UNIVERSITÉ DE LORRAINE

Ecole doctorale EMMA Lorraine

Modèles de comportement non linéaire des matériaux architecturés par des méthodes d'homogénéisation discrètes en grandes déformations. Application à des biomembranes et des textiles

THÈSE

Pour l'obtention du

Doctorat de l'Université de Lorraine

(Mention Mécanique et Energétique)

Présenté par

Khaled ElNady

Thèse soutenue publiquement le 18 février 2015 à Nancy devant le jury composé de :

Qi-Chang He	Pr	MSME, Université Paris Est	Rapporteur
Emmanuelle Vidal-Salle	Pr	LAMCOS, INSA de Lyon	Rapporteur
Stefan Diebels	Pr	LTM, Universität des Saarlandes	Examinateur
Francesco Dell Isola	Pr	Università di Roma La Sapienza and MEMOCS	Examinateur
Paul Lipinski	Pr	ENIM, Metz	Examinateur
Damien Durville	Dr	LMSSMaT, Ecole Centrale, Paris	Examinateur
Jean-François GANGHOFFER	Pr	LEMTA, Université de Lorraine	Directeur de thèse
Gérard Maurice	Pr	LEMTA, Université de Lorraine	Invité

Laboratoire d'énergétique et mécanique théorique et appliquée | UMR 7563 CNRS
Université de Lorraine

Table of Contents

List of Figures

List of Tables

List of Abbreviations

RVE	Representative volume element
RUC	Repeating unit cell
TL	Total Lagrangian formulation
UL	Updated Lagrangian formulation
DAH	Discrete asymptotic homogenization technique
dof	Degree of freedom
PET	polyethylene terephthalate

Nomenclature

$\mathbf{C}_{ijkl}, \mathbf{B}_{ijkl}, \mathbf{D}_{ijkl}$	Elastic tensors of rank four
E_s	Young's modulus
G	Shear modulus
ν	Poisson's ratio
N	Coupling number polar ratio
l_t	Characteristic length for torsion
l_b	Characteristic length for bending
$\mathbf{K}$	Tangent stiffness matrix
$\mathbf{d}$	Nodal displacement vector
$\mathbf{F}$	External nodal force vector
ε_L	Logarithmic strain
ε_G	Green Lagrangian strain
ε_E	Euler Almansi strain
$\mathbf{K}_o$	Linear stiffness matrix
$\mathbf{K}_u$	Initial displacement stiffness matrix
$\mathbf{K}_\sigma$	Initial stress stiffness matrix
$\mathbb{N}$	set of nodes of an elementary cell
$R\left(\lambda^1, \lambda^2\right)$	continuum node position
$\mathbb{Z}$	set of structural cells
$\mathbf{B}$	set of beams of an elementary cell
δ^{ib}	shift factor for nodes belonging to a neighboring cell
$\mathbf{e}_i^\lambda$	unit vectors of the curvilinear coordinate system associated to the lattice (generally non Cartesian)
λ^i	curvilinear coordinates associated with the vectors $\mathbf{e}_i^\lambda$
$\mathbf{e}_i$	vector of the Cartesian coordinate system
$\mathbf{e}^b$	unit vector in beam direction
$\mathbf{e}^{b\perp}$	unit vector perpendicular to beam direction
δ^{ib}	shift factor for nodes belonging to a neighboring cell
E_s	elastic modulus of structural material
l	characteristic length of the elementary cell
L	characteristic length of the whole structure
$\varepsilon = l / L$	Small scale parameter
$l^b = \varepsilon L^b$	length of the beam b
t^b	Width of the beam b
k_l	stiffness of a beam in extension
k_f	bending stiffness of a beam
$\boldsymbol{\sigma}_{ij}$	Cauchy stress tensor
$\mathbf{m}$	Couple stress tensor
$E_{h_{11}}, E_{h_{22}}$	Homogenized moduli along x and y direction
E_1, E_2	Green Lagrange strain along x and y direction

General Introduction

This thesis aims at the development of constitutive models for lattice-like structures and materials having an initially discrete and quasi periodical architecture at the microscopic scale, considering two important aspects: the non-linear constitutive response and the analysis of scale effects through the consideration of higher order gradients of the kinematic variables or additional micropolar degrees of freedom. The discrete homogenization technique is presently developed in order to substitute to an initially quasi periodical lattice-like structure by an effective continuum medium endowed with an effective mechanical behavior. Typical examples of applications of the proposed methodology and developed numerical schemes include dry textile preforms, biological membranes, trabecular bone, and artificial (man-made) structures involving a large number of repetitive structural one dimensional elements.

The mechanics of fibrous materials provides a wealth of interesting problems for the modelization, mathematical analysis and numerical simulations in modern applications in engineering and biomechanics. Especially, the tremendous amount of research on biological tissues and biosubstitutes has provided a new field to which the mechanics of fiber reinforced materials can be successfully applied.

In the first part of the work, we extend the first order homogenization schemes previously developed in LEMTA for the determination of effective mechanical properties of structures described as quasi periodical networks of beams, by the consideration of nonlinearities and internal length scale effects. We especially account for the geometrical nonlinearities arising from the large rotations of the beam elements, and build incremental scheme for the numerical computation of the overall nonlinear response of the effective continuum. The construction of homogenized effective continua leads to the calibration of strain energy density functions characterizing a hyperelastic effective continuum, which have been considered from a phenomenological viewpoint for fiber reinforced solids. The constructed effective response is validated by FE simulations performed over a representative unit cell of the lattice.

The kinematics of the lattice at the lower microscopic level may further lead to the emergence of non classical effects at a homogenized level, requiring the consideration of an enhanced kinematics or higher order gradients of the kinematic variables. Internal lengths scale effects are taken into account by generalized continua at the mesoscopic level; such effects have been proven to be noticeable when the specimen dimensions are comparable with the cell size. The

first order homogenization scheme is then accordingly extended towards the consideration of the second order gradient of the displacement, adopting a small strains framework. Thereby, the homogenized constitutive law includes the effective first order moduli and additional second order moduli. The methodology for the construction of the stress and hyperstress tensors versus the strain and strain gradient is first developed in a one dimensional context, before being extended to a more general 2D framework; these developments did benefit from discussions and joined work with Yosra Rahali in the frame of her PhD thesis.

The developed numerical schemes have been implemented in a dedicated code, using as an input the connectivity of the identified lattice unit cell and the beam mechanical moduli, and providing as an output the homogenized response of the effective continuum in the large strain regime.

Chapter 1

Motivations of the Thesis

Contents

1.1 Introduction

In recent years, new classes of cellular solid, lattice material and heterogeneous materials, such as composite material, solid foams, polycrystals, or bone are becoming increasingly popular in modern engineering applications because of their attractive properties, e.g. light weight, high specific stiffness, good damping capacity, high shock absorbability, etc. (Lorna and Gibson, 1997). The progress in civil engineering, aerospace industry, biomechanics and many other branches of technology has increased the role of these materials in the last two decades.

Complex heterogeneous materials may appear in shell-like structure such as laminated or textile reinforced composites. Textile are widely used nowadays in construction mechanics and in high added value fields such as aeronautics, due to their low weight, high capacity to sustain mechanical loads, good resistance to corrosion, and better distribution of efforts, to mention only a few main factors.

The prediction of elastic properties of dry textiles (preforms) in fibrous reinforced composites has been an active area of research in the past two decades, because the issues related to such parameters as fiber architecture, matrix properties, and fiber properties, affecting the mechanical characteristics of the composites, are highly complex. These factors make the modeling aspect of textile composites extremely challenging. Especially, it is important to be able to predict the orientation of the fibers during ongoing deformation of these structures, as it impacts the overall state of anisotropy and their effective mechanical properties; this is important in shape forming analysis of the dry perform, and also before the injection of resin.

The relation between the material microstructure and the resulting properties is the key to optimization and design of lightweight, strong, and tough materials.

Regarding the mechanical modeling, a composite material can be defined as a heterogeneous medium with effective mechanical properties at an upper level of description. Given the linear and/or nonlinear material properties of the constituents, one important goal of micromechanics of materials consists of predicting the response of the heterogeneous material on the basis of the geometries and properties of the individual phases, a task known as homogenization.

Foam-like structures, textiles in the form of 2D and 3D performs, morphing structures, large antennas made of many beam like repetitive structural elements, trabecular bone, as shown in Fig.1.1, all share common features: they can be described as lattice-like materials with a quasi-

repetitive geometry, and they are prone to large changes of their geometry, in addition to possible material nonlinearities. Those geometrical nonlinearities in such porous structures imply large density changes which will in turn impact the overall effective mechanical properties. Despite the available power of modern computers, it can be cumbersome to treat those structures as a full set of many structural members, so that one may search for a more convenient and simpler representation at an intermediate scale, especially when the goal is to perform structural computations at the level of a full structure.

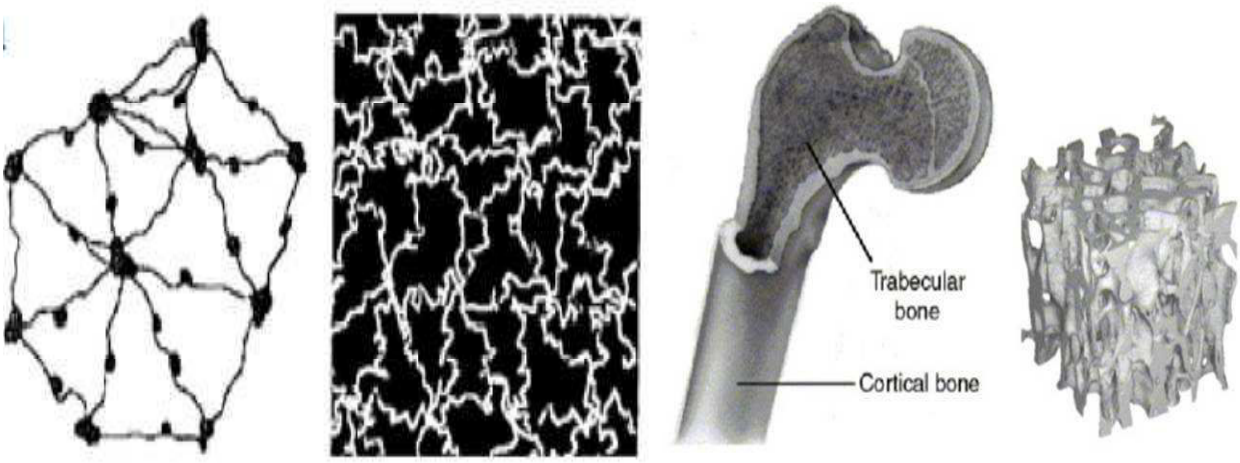

(a) (b)

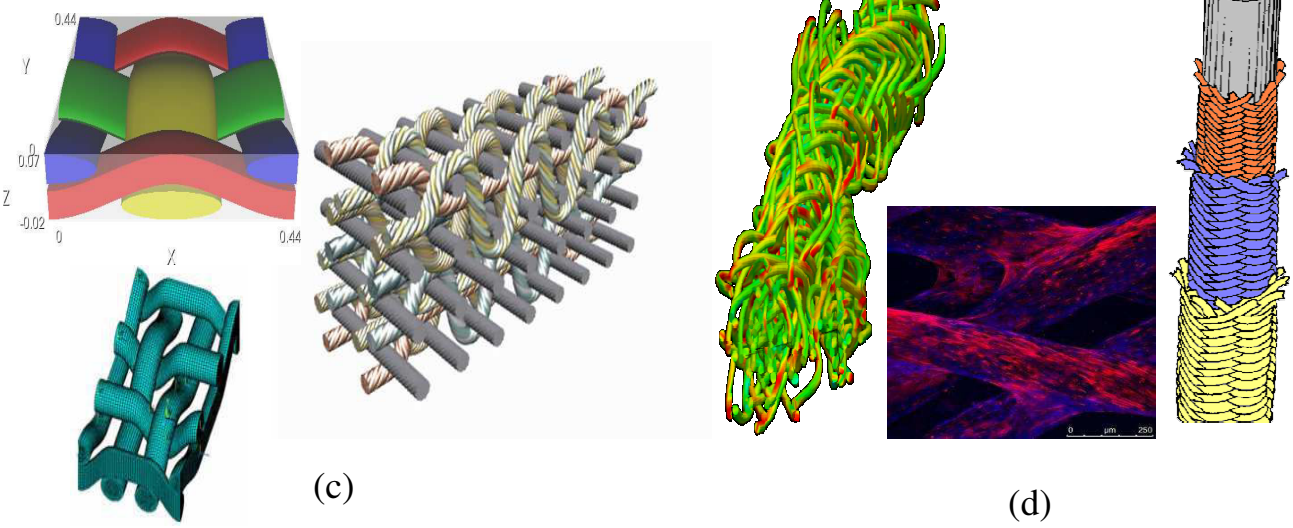

(c) (d)

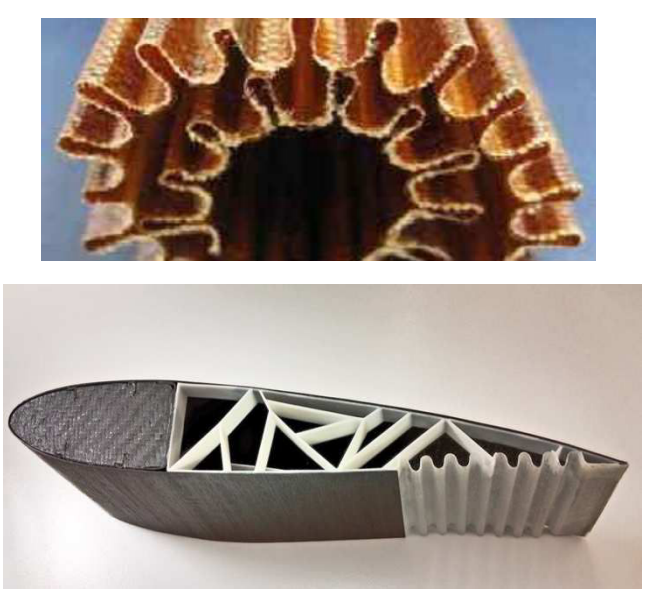

(e)

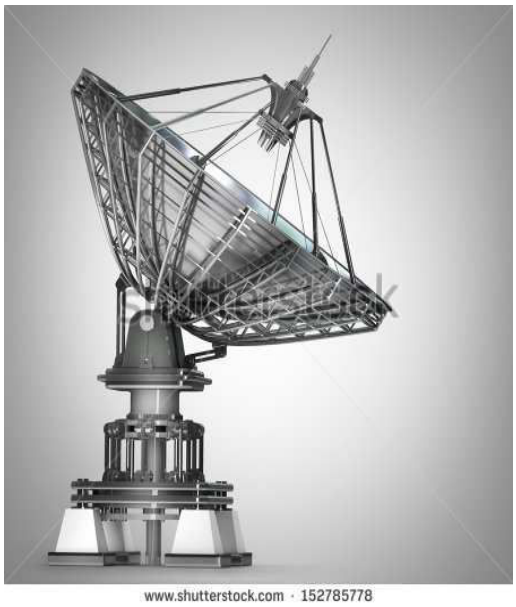

(f)

Fig. 1.1 Natural and artificial fibrous repetitive structures (a) Triangular network of the erythrocyte cytoskeleton (b) Human femur with cortical and trabecular bone. (c) 2D and 3D woven composite structures. (d) Scaffolds for tissue engineering (braided) Thesis C. Laurent (09/2012). (e) Morphing (reconfigurable) structures, Section of a morphing wing. (f) Large antennas made of many beam like repetitive structural elements.

1.2 Objective, strategy and outline

The principal objective of this thesis is to develop suitable homogenization schemes to construct the effective mechanical response of initially discrete structures representative of architecture materials, which will be substituted by an effective continuum at the intermediate mesoscopic level. An important category of structures which we shall focus in this thesis consists of lattices made of structural elements like articulated beams and bars, for which one may want to construct an effective continuum as a substitute for the initially discrete structure. They include both artificial (man-made) structures - such as articulated trusses, dry textiles and perform, fibers reinforced materials - and natural ones, like trabecular bone, fibrous reinforced soft tissues, and biological membranes. As one shall see, nonlinearities are mostly due to the modification of the internal geometry, with structural elements still undergoing small strains at the microscopic level (due to a large extension rigidity in comparison to the flexural rigidity), but large displacements and / or rotations due to weak flexural rigidity.

The kinematics of the lattice at the lower microscopic level may further lead to the emergence of non classical effects at a homogenized level, requiring considering an enhanced kinematics or higher order gradients of the kinematic variables. Such effects have been proven to be noticeable when the specimen dimensions are comparable with the cell size (Lakes, 1986). However, these effects are not easy to detect from a direct analysis at the macroscopic scale, based on experiments. Hence, micromechanical models are usually required to assess the impact of the lattice geometry and topology, and possibly of an internal microstructure within the lattice, on the computed effective mechanical behavior at an intermediate scale called the mesoscopic level, intermediate between the microscale (the scale of the microstructure) and the macroscale (scale of the entire structure). We shall address in this work the issue of construction both micropolar and second order grade effective constitutive models as substitutes of the initial structure, considering the occurrence of large deformations.

This contribution is based on the discrete asymptotic homogenization method, in contrast with a fully continuum homogenization strategy, in the sense that the initial medium is described as discrete. The method which has been developed in previous works (A. Mourad, 2003; D. Caillerie et al., 2006; Raoult et al., 2008; Dos Reis and Ganghoffer, 2012; I. Goda and Ganghoffer, 2013) shall presently be extended by the consideration of geometrical nonlinearities and internal length scale effects taken into account by generalized continua at the mesoscopic level.

This thesis aims at the development of constitutive models for lattice-like structures having an initially discrete and quasi periodical architecture at the microscopic scale considering two important aspects: the non-linear constitutive response due to large changes of the internal geometry (Andrea et al., 2014; Pindera et al., 2009; charalambakis, 2010) and the analysis of scale effects through the consideration of either additional degrees of freedom or higher order gradients of the kinematic variables (Kouznetsova et al., 2002, 2004; Nguyen et al., 2013). In order to exemplify the developed methodology and subsequent numerical algorithms, the specific case of fibrous media like dry textile monolayer's and biological membranes will be analyzed in this thesis; it is indeed well-know that those structures are prone to large changes in their geometry, while developing small strains.

The first objective is then to set up a novel methodology based on the discrete asymptotic homogenization method for the calculation of the equivalent effective mechanical response of

structures having a discrete topology, considering the occurrence of geometrical nonlinearities. We shall accordingly focus on the large displacement / small strains framework.

The nonlinear analysis is in the broad sense characterized by the non-proportional nature of the load-deformation behavior, which means that the structural response against an incremental loading is affected by the instantaneous loading level and the deformed geometry of the structure. In other words, the stiffness matrix of the structure is a function of element force as well as the deflection of the structure. Therefore, the instantaneous stiffness equation can only be solved numerically by an incremental and iterative procedure allowing for the geometrical change of the structure. Based on the Newton-Raphson scheme, the applied load is first divided into many small increments, and the displacement increment within each increment is computed using the tangent stiffness matrix.

This localization problem is next coupled with the homogenization procedure allowing the construction of the Cauchy and couple stress tensors, leading to an update the structure geometry and constitutive behavior.

The results in terms of the stress-strain relations obtained by homogenization shall then be validated by their numerical counterparts obtained by finite element simulations performed over an identified periodic unit cell. The interest of the developed micromechanical schemes is their ability to predict the response of the initial structure under different loadings; they are consequently useful to identify suitable hyperelastic constitutive models at the mesoscopic level.

The second objective we shall follow is an extension of the discrete asymptotic homogenization method recently developed for the determination of the effective mechanical properties of periodical lattices considered as Cauchy continua towards generalized continua accounting for internal scale effects; we shall consider successively two alternative routes for enriching the classical Cauchy continuum, namely micropolar continua (Dos Reis and Ganghoffer, 2012) and second order grade continua. As we will show, both approaches are complementary in the sense that the second order grade models capture internal lengths effects in tension, while micropolar models essentially capture the flexural response through the flexural rigidities and internal bending lengths.

Regarding the derivation of second order gradient effective continua, the homogenization technique will be introduced successively in a one-dimensional and a two-dimensional context.

Applications will be done to the computation of the effective mechanical response of biological membranes, considering successively the in-plane and out of plane responses.

The first part of the thesis is accordingly devoted to the presentation of the discrete homogenization technique accounting for geometrical nonlinearities, while the second part deals with the consideration of second order gradient effects. In fact, there are interconnections between both parts, as will be shown especially when computing the overall effective response of structures for which both the in-plane and bending properties are of interest.

The thesis is divided into five chapters, the content of which is next briefly described. Following a state of the art overview of the classification of nonlinearities in structural mechanics given in Chapter 2, we shall then introduce the general description of the asymptotic discrete homogenization technique, which is the cornerstone of this thesis, from a methodological point of view. More precisely, an extension of the simple framework of linear discrete homogenization elasticity towards the more involved framework of geometric nonlinearities will be done, in order to compute the effective constitutive relation between the Green's Lagrangian strain and the second Piola-Kirchhoff stress tensor. An incremental solution scheme is written to solve the non linear problem; several algorithms have been developed to follow the evolution of the lattice topology during increased loading of the microstructure, and providing as an output the equivalent effective stiffness (or rigidity) matrix of the effective continuum for each load increment. As an illustration of the proposed algorithms, the nonlinear response of biological membranes shall be investigated and a validation of the computed homogenized response will be validated thanks to FE simulations performed over a representative unit cell.

In Chapter 3, more general algorithms are presented for the purpose of computing the nonlinear response of arbitrary 2D lattices of beams, and their implementation into a dedicated code is achieved. We will determine as an illustration the nonlinear response of textiles (plain weave and twill), which will be validated by comparison with the response computed by FE simulations. In the same chapter, we shall further construct suitable hyperelastic models based on the calibration of a well-chosen form of the strain energy (density) function.

In the second part of this thesis exposed in chapters 4 and 5, we take into account the internal gradients of the mechanical fields within the representative unit cell, by incorporating second order gradient effects into the homogenized constitutive law. This is first done for 1D structures (chapter 4), and then further expanded to 2D structures (chapter 5). We first focus on one-dimensional homogenization, although the initially discrete lattice generally occupies a two-

dimensional domain in space: this means that the identified elementary unit cell is repeated by periodic translation in one dimension only. We shall first expose into details the technical steps required to construct the effective second order continuum, thereby highlighting the forces and hyperforces dual to the first and second order kinematic variables in the sense of the virtual power of internal forces. The proposed method is a variant of similar homogenization schemes already developed for second order continuum (Kouznetsova et al., 2002), with the main difference that the topology of the initial medium is discrete.

In chapter 5, two approaches are envisaged, based on the consideration (or not) of a second order gradient elasticity at the micro level, which then entail different second order grade continuum effective models for discrete beam lattices. The comparison of the effective behavior of simple lattices will be done in terms of the shear moduli based on three different schemes (Cauchy, Micropolar and second order gradient) in a small strains framework.

Finally, conclusions and possible directions of future research will be addressed in Chapter 6.

Chapter 2

General Introduction to Micromechanics

Contents

2.1 State of the art of micromechanical approaches

In this chapter, an overview of the relatively modern field of the multi-scale modeling of composite material is presented. We start with a review of the various micromechanical approaches developed to compute the overall effective mechanical properties of initially heterogeneous materials or structures, which are substituted by an equivalent homogeneous materials. There is often the need in heavy multiscale analysis of lattice materials to find the method that can provide the best trade-off between accuracy and computational cost (Bidanda and Bartolo, 2008; Ramirez et al., 2011; Schaedler et al., 2011). This method used to obtain the properties of macromaterial in terms of the effective properties of its repeated unit cell represents a process of homogenization. Several homogenization schemes exist in literature to characterize the mechanics of lattice materials. Those are known in the literature as cosserat elasticity theory (Cosserat and Cosserat, 1909), cosserat theory with constrained rotations our couple-stress theory (Mindlin and Tiersten, 1962; Koiter, 1964), strain gradient theory (Toupin, 1962) higher order strain gradient elastic theory(Mindlin, 1964, 1965a,b), micromorphic, microstretch and micropolar elasticity theories (Eringen, 1999) and Fully non-local elasticity (Eringen, 1992). More details on the above theories can be found in (Tiersten and Bleustein, 1974; Lakes, 1995 and Exadaktylos and Vardoulakis, 2001). The mutual connections of those theories is provided in the article of(Tekoglu and Onck, 2008).on other hand a large number of relevant works exploit homogenization techniques in order to establish micro-structural effects in a periodic non-homogenous continuum. In that case the unit cell of the periodic structure is employed and averaged, to obtain both the equation of motion and the new properties of the homogenized material including microstructure effects. In this category, representative works are those of (Ben-Amoz,1976; Forest et al., 1999, 2002; Forest and Trinh, 2010).

The interest of homogenization techniques is their use as a tool to conceive and calculate novel structural materials exhibiting unconventional mechanical properties or behavior; this includes additional degrees of freedom emerging from the homogenization and possibly due to the inclusion of a microstructure, or mechanical properties lying outside the range that pertain to homogeneous materials, such as negative Poisson's ratio, associated to the class of auxetic structures (Dos Reis and Ganghoffer, 2012; Yang et. Al, 2004). The derivation of mesoscopic models of lattices at an intermediate scale leads to a reduction of the computational cost associated to simulations of extended lattices incorporating a huge number

of degree of freedom; those lattices most often can be considered as quasi periodical for man-made structures (this would be more questionable for biological network), hence their homogenization makes sense.

An interesting classification of the two categories of micromechanical analysis will be discussed, the analysis of periodic materials based on the repeating unit cell (RUC) concept and the analysis of statistically homogeneous materials based on the representative volume element (RVE) concept. We shall then summarize the difference between RVE and RUC concepts as discussed in (Pindera and Hamed et al., 2009).

One of critical review that we prefer to discuss also in this chapter is chirality; Chirality is encountered in many branches of science, including physics, biology, chemistry and optics. An object is said to be chiral, or with handedness, if it cannot be superposed to its mirror image (Lord Kelvin, 1904). One shall found the difference between a general isotropic chiral (also known as non-centrosymmetric, a centric or hemitropic) micropolar versus the non-chiral (micropolar) theory as described in (Liu et al., 2012).

Micropolar model with chirality introduces three additional material constants compared to the non-chiral theory, the additional material parameters change their signs according to the handedness of the microstructure to represent the effect of chirality (Nowacki, 1986; Lakes and Benedict, 1982; Lakes, 2001; Joumaa and Ostoja-Starzewski, 2011).an over view about non-chiral and chiral (micropolar) will discuss later on.

2.2 Micromechanical schemes

While the area of micromechanics of heterogeneous materials continues to expand and new approaches are continuously being proposed, one shouldn't forget that micromechanical models are still only approximate models to the behavior of Heterogeneous materials. It is generally undesirable to use a model based on the actual spatial distribution of the reinforcing material within the specific composite which is to be used in a design: thus the modeling should begin with the approximation used for the geometry.

The determination of the effective mechanical moduli of these materials in the large deformation regime from mechanical measurements quite difficult; this makes micromechanical analyses a relevant alternative to evaluate those properties. For example, the

mechanics of woven materials as shown on the figure below can be addressed at three different scales (Fig 1.2): the **macroscopic scale** that is relevant to pieces of fabric, the **mesoscopic scale** related to the pattern, the smallest repeatable unit cell of fabric, and the **microscopic scale** of the yarn itself (itself generally an assembly of fibers).

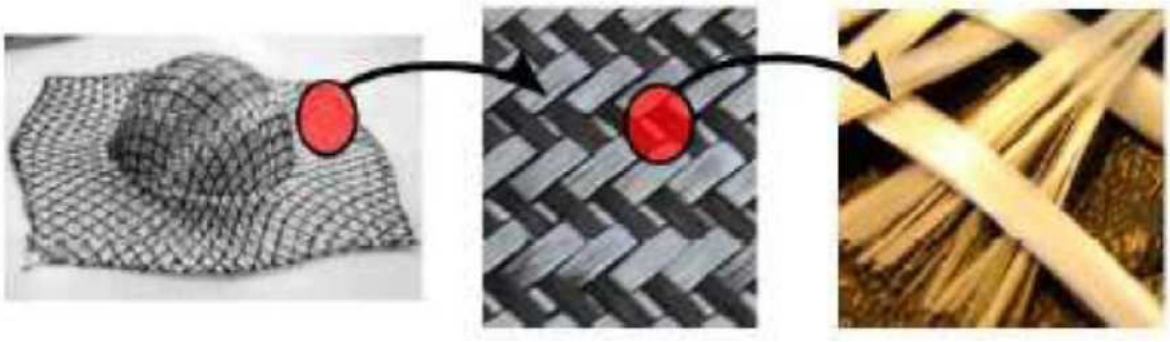

Fig. 2.1 Multiscale modeling of woven fabrics

Much work in the area of micromechanics of heterogeneous materials has been conducted during the past 50 years, starting with the simplest assumptions on the stress and strain sharing among the constituent phases and progressing to more detailed geometric models that require more demanding analytical and numerical treatment. The various approaches have been summarized in reports and monographs in (Hashin, 1972; Achenbach, 1975; Bensoussan et al., 1978; Christensen, 1979; Sanchez-Palencia, 1980; Suquet, 1987; Aboudi, 1991; Kalamkarov and Kolpakov, 1997; Nemat- Nasser and Hori, 1999; Markov and Preziosi, 2000; Buryachenko, 2007) among others. The development of these approaches has occurred along different paths, leading to interchangeable use of terminology in describing methods based on fundamentally different geometric models of material microstructure. The search for an ideal micromechanics model continues (Chaboche et al., 2001).While the structural with more complex microstructure lead to the widespread use of either purely numerical or semi-analytical approaches. These are based on approximate representations of local fields within the individual subregions into which the microstructure is discretized for analysis purposes. Such geometric discretization leads to large systems of algebraic equations for the unknown coefficients in the local field approximations upon solution of the governing field equations using variational or direct approaches. Rapid progress in the development of computational technology, which led to the advancement of numerical methods, such as finite-element, finite difference or finite-volume methods, has also stimulated a renewed interest in analytical techniques. In this communication, we will present an overview of key micromechanical

concepts needed in the determination of macroscopic and microscopic responses of heterogeneous materials.

2.3 Discrete asymptotic homogenization

The main idea of homogenization methods in a broad sense is to replace a real heterogeneous structure with an equivalent homogeneous one endow with the same average macroscopic behavior. The homogenization method assumes that all physical quantities vary at both local and global scales, and that those quantities are periodic with respect to the local scale, due to the periodicity of the existing microstructure. Gibson and Ashby,1999; Masters and Evans, 1996; Christensen, 2000; Wang and McDowell, 2004) presented the closed-form expressions of the effective mechanical properties of cellular materials. These authors generally assume that the cell walls behave like Euler–Bernoulli beams, examine the individual cell wall and determine the elastic constants of the cell by solving deformation and equilibrium problems. They work well for topologies that have a simple arrangement of the cell members, but present limitations if the geometry of the unit cell has a complex topology.

More recently, matrix-based techniques using the Bloch's theorem to homogenize the properties of planar lattice materials have been introduced (Elsayed and Pasini.,2010). Hutchinson and Fleck, 2006 proposed the first formulation of the microscopic nodal deformations of a lattice in terms of the macroscopic strain field. A methodology was proposed to characterize cell topologies with a certain level of symmetry, e.g. the Kagome lattice and the Triangular -Triangular lattice. (Elsayed and Pasini, 2010) extended this method to treat planar topologies that can possess any arbitrary geometry of the cell. Vigliotti and Pasini (2013) presented a more general matrix-based procedure for the analysis of arbitrary bidimensional and tridimensional cell topologies with open and closed cells.

Other models have been proposed to model these types of materials as equivalent micropolar media: micropolar elasticity (the Cosserat brothers, 1909; Eringen, 1992; Kumar and McDowell, 2004) means that an independent rotational degree of freedom is added to the translational one (the displacement vector). The micropolar elastic constants of the stiffness matrix are obtained through either an explicit structural analysis of the representative unit cell or an energy approach.

Among numerical approaches, the asymptotic homogenization (abbreviated as AH in the sequel) theory has been successfully applied to predict the effective mechanical properties of materials having a periodic or quasi periodic microstructure. Its mathematical basis was elaborated by various authors, especially (Bensoussan et al., 1978; Sanchez-Palencia, 1980; Bakhvalov and Panasenko, 1989). The method relies on an asymptotic expansion of the displacement and stress fields on the "natural length parameter", which is the ratio of a characteristic size of the heterogeneities to a measure of the macrostructure, see, e.g. (Tolenado and Murakami, 1987; Devries et al., 1989; Guedes and Kikuchi, 1990; Hollister and Kikuchi, 1992; Fish et al., 1999). Recent reviews on the asymptotic expansion homogenization method applied to composites can be found in (Kanouté et al., 2009; Oliveira et al., 2009). AH has been widely used not only for the analysis of composite materials and topology optimization of structures (Hassani and Hinton E, 1998; Sigmund, 1994; Bendsoe, 1989; Kikuchi and bendsoe, 1988) but also for the characterization of porous materials, such as tissue scaffolds (Lin, 2004; Fang et al., 2005; Sturm et al., 2010).

The underlying assumption of AH is that each field quantity depends on two different scales: one on the macroscopic level x , and the other on the microscopic level, $y = x / \varepsilon$, with ε a magnification factor that scales the dimensions of the unit cell to the dimensions of the material at the macroscale. Such an asymptotic homogenization approach provides the overall effective properties as well as local stress and strain values.

Micromechanical analyses are typically conducted based on either the concept of a representative volume element (RVE), which characterizes heterogeneous materials with macroscopically or statistically homogeneous microstructures at an appropriate scale (Hill, 1963), or a repeating unit cell (RUC) which characterizes periodic heterogeneous materials. These two concepts are discussed by (Drago and Pindera, 2007) and illustrated in Fig 1.3, based on different geometric representations of heterogeneous microstructures and require different boundary conditions in the micromechanical analysis of the smallest material subvolume, whose response is indistinguishable from that of the material-at-large.

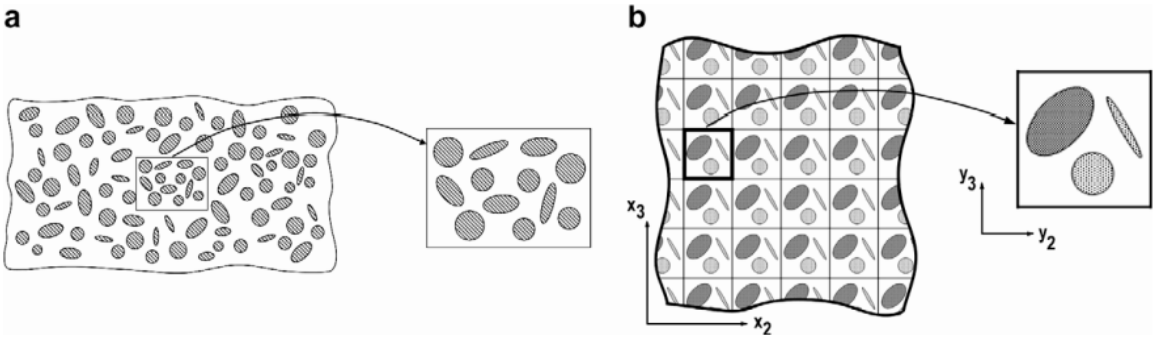

Fig. 2.2. Two geometric representations of a material microstructure: (a) statistically homogeneous microstructure characterized by an RVE; (b) periodic microstructure characterized by an RUC.

In particular, micromechanical analysis of an RVE is based on the equivalence of homogeneous traction and displacement boundary conditions, which in fact defines the RVE concept, while micromechanical analysis of an RUC is based on combined periodic displacement and traction boundary conditions. These concepts had been often confused in the literature. The RVE and RUC concepts have been re-examined recently in greater detail by several investigators; this was spurred by a sequence of papers by Huet.

2.3.1 Statistically homogeneous materials

The analysis of statistically homogeneous materials is based on the RVE concept. The suitable volume for homogenization is called ”representative volume element” (RVE). The RVE is the smallest subvolume of the statistically homogeneous microstructure which contains the same phase volume fractions and statistical distributions as the material-at-large, and which responds in a manner identical to that of the entire assemblage under either homogeneous displacement or homogeneous traction boundary conditions. The representative volume element must be large enough to include enough inhomogeneities (statistically homogeneous distribution of the defects or heterogeneities), but also small enough so that the stresses and strains within the RVE can be considered as uniform when viewed from a macroscopic level.

2.3.2 Periodic materials

In contrast, analysis of periodic materials is based on the RUC concept. The RUC is the smallest element of a periodic microstructure which serves as the basic building block for the material through replication regardless of its content. Thus, the response of the entire array under macroscopically uniform loading is identical to that of an arbitrary RUC subjected to the same loading. This loading is specified by periodic boundary conditions imposed on both the surface displacements and tractions.

The previous classification helps to clarify the often-confusing terminology used arbitrarily to describe the different micromechanics models and approaches that have evolved independently. One shall say that approaches based on the concept of a representative volume element are applicable to **statistically homogeneous microstructures**; and approaches based on the concept of a repeating unit cell are applicable to **periodic microstructures**.

2.3.3 Centrosymmetric micropolar elasticity

In the theory of classical continua, the displacement is the sole degree of freedom u_i , and the induced small strain measure is $\varepsilon_{ij} = \frac{1}{2}\left(u_{j,i} + u_{i,j}\right)$. The works of Euler and Bernoulli relative to beam mechanics suggest the novel idea to consider the displacements and rotations as independent quantities, as well as efforts and couple stresses. The idea of couple stress was explored in the middle of the 19th century by (MacCullagh, 1839; Lord Kelvin, 1882-1890; and viogt 1887), and was pursued later on by cosserat brothers (cosserat E and cosserat F, 1909), who proposed a theory based on a rigid triad of vectors attached to each point of a continuum, endowed with a local rotation independent on the local rotation due to deformation.

The micropolar theory has an intrinsic length scale and can describe various phenomena more accurately, e.g. liquid crystals, complex mixtures, granular media and lattice beam structures. As for the kinematics, we define the strain tensor γ_{ij} and curvature tensor κ_{ij} that are related to the displacement and rotation vectors as follows (e_{kij} is the Levi-Civita permutation tensor):

$$\gamma_{ij} = u_{j,i} - e_{kij}\phi_k \;\; ; \;\; \kappa_{ij} = \phi_{j,i} \tag{1.1}$$

The constitutive relations for stress $\boldsymbol{\sigma}_{ij}$ and couple-stress $\mathbf{m}_{ij}$ are specified as

$$\begin{aligned}
\boldsymbol{\sigma} &= \frac{1}{g}\mathbf{S}^{\mathrm{i}} \otimes \frac{\partial \mathbf{R}}{\partial \lambda^{\mathrm{i}}} = \frac{1}{g}\left(\mathbf{S}_1^{\mathrm{i}} + \varepsilon \mathbf{S}_2^{\mathrm{i}}\right) \otimes \frac{\partial \mathbf{R}}{\partial \lambda^{\mathrm{i}}} = \underbrace{\frac{1}{g}\mathbf{S}_1^{\mathrm{i}} \otimes \frac{\partial \mathbf{R}}{\partial \lambda^{\mathrm{i}}}}_{[\mathbf{A}]\{\gamma_{ij}\}} + \underbrace{\frac{1}{g}\varepsilon \mathbf{S}_2^{\mathrm{i}} \otimes \frac{\partial \mathbf{R}}{\partial \lambda^{\mathrm{i}}}}_{[\mathbf{B}]\{\kappa_{ij}\}} \\
\mathbf{m} &= \frac{1}{g}\boldsymbol{\mu}^{\mathrm{i}} \otimes \frac{\partial \mathbf{R}}{\partial \lambda^{\mathrm{i}}} = \frac{1}{g}\left(\varepsilon \boldsymbol{\mu}_1^{\mathrm{i}} + \varepsilon^2 \boldsymbol{\mu}_2^{\mathrm{i}}\right) \otimes \frac{\partial \mathbf{R}}{\partial \lambda^{\mathrm{i}}} = \underbrace{\frac{1}{g}\varepsilon \boldsymbol{\mu}_1^{\mathrm{i}} \otimes \frac{\partial \mathbf{R}}{\partial \lambda^{\mathrm{i}}}}_{[\mathbf{C}]\{\gamma_{ij}\}} + \underbrace{\frac{1}{g}\varepsilon^2 \boldsymbol{\mu}_2^{\mathrm{i}} \otimes \frac{\partial \mathbf{R}}{\partial \lambda^{\mathrm{i}}}}_{[\mathbf{D}]\{\kappa_{ij}\}}
\end{aligned} \tag{1.2}$$

This constitutive law can further be simplified basing on symmetry of the studied lattices. It has indeed shown that for centro-symmetrical lattices (Trovalusci and Masiani, 1999), the pseudo tensor [**B**] and [**C**] vanish; here, [**A**] and [**D**] are generalized elasticity tensors. The form of these tensors varies depending on the material isotropy/anisotropy and homogeneity. In the work of (Dos Reis and Ganghoffer, 2012), the micropolar elasticity constants are determined for square and honeycomb structures.

In the work of (Eringen, 1968), the constitutive equations for a linear isotropic Cosserat solid writes:

$$\begin{aligned}
\boldsymbol{\sigma}_{kl} &= \lambda_{\varepsilon rr}\delta_{kl} + (2\mu + \kappa)\varepsilon_{kl} + \kappa\varepsilon_{\kappa lm}(r_m - \phi_m), \\
\mathbf{m}_{kl} &= \alpha\phi_{r,r}\delta_{kl} + \beta\phi_{k,l} + \gamma\phi_{l,k},
\end{aligned} \tag{1.3}$$

In three dimensions, the isotropic cosserat elastic solid requires six elastic constants $\lambda, \mu, \alpha, \beta, \gamma$ and κ for its descriptions. A comparison of symbols used by various authors was presented by (Cowin, 1970). The following technical constants derived from tensorial constants are more beneficial in term of physical insight described by (Eringen, 1968) as:

Young's modulus $E = (2\mu + \kappa)(3\lambda + 2\mu + \kappa)/(2\lambda + 2\mu + \kappa)$

Shear modulus $G = (2\mu + \kappa)/2$

Poisson's ratio $\nu = \lambda/(2\lambda + 2\mu + \kappa)$

Characteristic length for torsion $l_t = \left[(\beta + \gamma)/(2\mu + \kappa)\right]^{1/2}$

Characteristic length for bending $l_b = \left[\gamma/2(2\mu + \kappa)\right]^{1/2}$

Coupling number polar ratio $N = \left[\kappa / 2(\mu + \kappa)\right]^{1/2}$, and

Polar ratio $\psi = (\beta + \gamma) / (\alpha + \beta + \gamma)$.

When $\alpha, \beta, \gamma, \kappa$ vanish, the solid becomes classical elastic. The case $N = 1$ is known as couple stress theory (Mindlin et al., 1962)

2.3.4 Non-centrosymmetric micropolar elasticity

So far, the constitutive relations relate the stresses to the strains, on the one hand, and the couple-stresses to the curvatures, on the other hand. Special microstructures of some materials make both the stress and the couple-stress directly dependent on both strains and curvatures, representing the phenomenon of chirality; this is most easily demonstrated in a one dimensional helix model.

Two examples of lattice structures that exhibit non-centrosymmetric micropolar behavior are shown in Fig.1.4

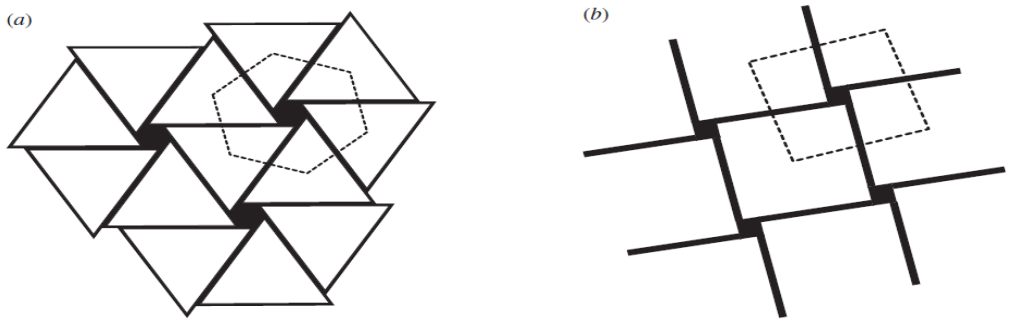

Fig. 2.3. Two-dimensional lattice structure: (a) triangular; (b) square lattice structures, involving rigidly connected elastic beams exhibiting both micropolar and chiral effects. Their corresponding representative volume elements are shown by dashed lines.

2.3.4.1 Isotropic micropolar model with chirality

In continuum mechanics, the non-centrosymmetric micropolar theory is usually used to capture the chirality inherent in materials. This theory provides an efficient tool for modeling the chiral effect presented in materials and structures, e.g., loading transfer in carbon nanotubes and chiral rods (Chandraseker and Mukherjee, 2006; Chandraseker et al, 2009;

Ieşan, 2010), mechanics of bone (Lakes et al, 1983), chirality transfer in nanomaterials (Wang et al, 2011) and wave propagation in chiral solids (Khurana and Tomar, 2009).However when reduced to a two dimensional (2D) isotropic problem, the resulting model becomes non-chiral. Therefore, influence of the chiral effect cannot be properly characterized by existing theories for 2D chiral solids. The work of (Liu at al., 2012) proposes a continuum theory to model the chiral effect for 2D isotropic chiral solids, based on reinterpretation of isotropic tensors in a 2D case. A single material parameter (A) related to chirality is introduced to characterize the coupling between the bulk deformation and the internal rotation which is a fundamental feature of 2D chiral solids.

The constitutive relation writes,

$$\begin{aligned} \boldsymbol{\sigma}_{ij} &= \mathbf{C}_{ijkl}\,\boldsymbol{\gamma}_{kl} + \mathbf{B}_{ijkl}\,\boldsymbol{\kappa}_{k,l} \\ m_{ij} &= \mathbf{B}_{ijkl}\,\gamma_{kl} + \mathbf{D}_{ijkl}\,\kappa_{k,l} \end{aligned} \tag{1.4}$$

Where $\mathbf{C}_{ijkl}$, $\mathbf{B}_{ijkl}$ and $\mathbf{D}_{ijkl}$ are elastic tensors of rank four. A micropolar solid with non-vanishing $\mathbf{B}_{ijkl}$ is usually referred as non-centrosymmetric.

The constitutive law can be rearranged in a matrix form as

$$\begin{Bmatrix} \sigma_x \\ \sigma_y \\ \sigma_{xy} \\ \sigma_{yx} \\ m_{xz} \\ m_{xz} \end{Bmatrix} = \begin{bmatrix} 2\mu+\lambda & \lambda & -A & A & 0 & 0 \\ \lambda & 2\mu+\lambda & -A & A & 0 & 0 \\ -A & -A & \mu+\kappa & \mu-\kappa & 0 & 0 \\ A & A & \mu-\kappa & \mu+\kappa & 0 & 0 \\ 0 & 0 & 0 & 0 & \gamma & 0 \\ 0 & 0 & 0 & 0 & 0 & \gamma \end{bmatrix} \begin{Bmatrix} \dfrac{\partial u_x}{\partial x} \\ \dfrac{\partial u_y}{\partial y} \\ \dfrac{\partial u_y}{\partial x} - \phi_z \\ \dfrac{\partial u_x}{\partial y} + \phi_z \\ \dfrac{\partial \phi_z}{\partial x} \\ \dfrac{\partial \phi_z}{\partial y} \end{Bmatrix} \tag{1.5}$$

It has four classical micropolar elastic constants and a new parameter A characterizing the chiral effect. It should be noted that this is not constitutive matrix for anisotropic material behavior, since the A parameter and its sign form a unique pattern in the constitutive matrix.

2.3.4.2 Anisotropic micropolar model with chirality

More detailed of this theory for anisotropic continuum, one shall found in the work of (Joumaa et al., 2011). Hooke's law expressed based on the differentiating of the energy expression with respect to strain and curvature, the following expressions was obtained:

$$\begin{aligned} \boldsymbol{\sigma}_{ij} &= \mathbf{C}^{(1)}_{ijkl}\,\boldsymbol{\gamma}_{kl} + \mathbf{B}_{ijkl}\,\boldsymbol{\kappa}_{k,l} \\ \mathbf{m}_{ij} &= \mathbf{B}_{ijkl}\,\boldsymbol{\gamma}_{kl} + \mathbf{C}^{(2)}_{ijkl}\,\boldsymbol{\kappa}_{k,l} \end{aligned} \tag{1.6}$$

The stiffness $\mathbf{C}^{(1,2)}_{ijkl}, \mathbf{B}_{ijkl}$ tensors can be explicitly determined from the unite cell structure. for anisotropic continuum, these tensors are defined as follows ($\delta_{ij} \equiv$ Kronecker's tensor):

$$\begin{aligned} \mathbf{C}^{(1)}_{ijkl} &= (\beta-\alpha)\,\delta_{jk}\delta_{il} + (\beta+\alpha)\,\delta_{jl}\delta_{ik} + \lambda\delta_{ij}\delta_{kl} \\ \mathbf{C}^{(2)}_{ijkl} &= (\psi-\varepsilon)\,\delta_{jk}\delta_{il} + (\psi+\varepsilon)\,\delta_{jl}\delta_{ik} + \eta\delta_{ij}\delta_{kl} \\ \mathbf{B}_{ijkl} &= (\rho-\sigma)\,\delta_{jk}\delta_{il} + (\rho+\sigma)\,\delta_{jl}\delta_{ik} + \omega\delta_{ij}\delta_{kl} \end{aligned} \tag{1.7}$$

The material model has nine independent stiffness constants, instead of six compared with non-chiral micropolar theory, as shown in the next table.

Table 2.1 Physical significance of stiffness constants

term	Interpretation
α, λ	Lame's constants
$\alpha, \psi, \varepsilon, \eta$	micropolar constants
ρ, σ, ω	Chirality constants

The chiral micropolar theory produce two independent form of length scales defined as

$$L_1 = \sqrt{\frac{\psi, \varepsilon, \eta}{\alpha, \beta, \lambda}} \quad \text{and} \quad L_2 = \frac{\rho, \sigma, \omega}{\alpha, \beta, \lambda}$$

However, the non-chiral micropolar model can only admit one set of length scales (L_1).

2.4 Discussion

The reminder of this thesis will be centered on the derivation and construction of the effective homogenized response of materials having a lattice like microstructure, considering two different aspects. We are firstly concerned with the derivation of constitutive models accounting for the geometrically non-linear behavior of lattices; an analytical homogenization scheme initially developed in a small transformations framework will accordingly be extended to consider the occurrence of geometrical nonlinearities. This formulation leads to a compact matrix expression for the macroscopic stress as a function of the macroscopic displacement gradient that can handle a priori both geometrical and material nonlinearities. Nevertheless, we shall focus on geometrical nonlinearities, since the structures and networks to which the developed homogenization schemes will be applied hardly exhibit any material non linearity.

As shall be described subsequently, this homogenization is mostly performed on the meso-level of the homogenized representative volume element, leading to constitutive models applicable at the macro-level in view of structural computations. Those homogenization methods lead to different choices for the equivalent continuum media that will be compared in terms of the nonlinear stress-strain response.

As a second aspect of homogenization schemes developed in this thesis, we shall rely on gradient elasticity as a convenient framework for materials and structures showing scale effects; this approach traces back to more than a century and a half ago as to the theoretical foundations. Scale effects become noticeable when the wavelengths of the loading or the deformation field become comparable to the microstructure size or spacing. In this work, the presence of localization phenomena in lattice-like structures motivate consideration of the second order multi scale computational homogenization scheme using a macroscopic Mindlin strain gradient continuum (Kouznetsova et al., 2004; Kaczmarczyk et al.,2008; Nguyen et al., 2013). One-dimensional microstructured beam and 2D chosen structures will be computed as illustrative examples of the proposed methodology for the scale transition accounting for strain gradient effects.

2.5 References

Aboudi J. Mechanics of composite materials – a unified micromechanical approach. Amsterdam: Elsevier; 1991.

Achenbach JD. A theory of elasticity with microstructure for directionally reinforced composites. New York: Springer-Verlag; 1975.

Assidi, M., Ben Boubaker, B., Ganghoffer, J.F., 2011. Equivalent properties of monolayer fabric from mesoscopic modelling strategies. Int. J. Solids Struct. 48, 2920–2930.

Bakhvalov, N.S., Panasenko, G.P., 1989. Homogenization Averaging Processes in Periodic Media. Kluwer Academic Publishing, Dordrecht.

Ben-Amoz, M., 1976. A dynamic theory for composite materials. J. Appl. Math. Phys. 27, 83–99.

Bensoussan A, Lions J-L, Papanicolaou G. Asymptotic analysis for periodic structures. Amsterdam: North Holland; 1978.

Bendsoe M. Optimal shape design as a material distribution problem. Struct. Multidisciplinary Optim. 1989;1:193–202.

Bidanda, B., Bartolo, P., 2008. Virtual Prototyping & Bio Manufacturing in Medical Applications. Springer, US.

Buryachenko VA. Micromechanics of heterogeneous materials. New York: Springer; 2007.

Caillerie, D., Mourad, A., Raoult, A., 2006. Discrete homogenization in graphene sheet modeling. J. Elast. 84, 33–68.

Chaboche JL, Kruch S, Maire JF, Pottier J. Towards a micromechanics based inelastic and damage modeling of composites. Int J Plasticity 2001;17(4):411–39.

Chandraseker, K., Mukherjee, S., 2006. Coupling of extension and twist in single-walled carbon nanotubes. J. Appl. Mech. 73, 315–326

Chandraseker, K., Mukherjee, S., Paci, J.T., Schatz, G.C., 2009. An atomistic-continuum Cosserat rod model of carbon nanotubes. J. Mech. Phys. Solids 57, 932–958.

Charalambakis, N., 2010. Homogenization techniques and micromechanics Asurvey and perspectives. Appl.Mech.Rev.63(3),1–10.

Christensen RM. Mechanics of composite materials. New York: John Wiley & Sons; 1979.

Christensen R M. Mechanics of cellular and other low-density materials. Int. J. Solids Struct.2000; 37:93–104.

Gibson LJ, AshbyMF.CellularSolids:StructureandProperties.Cambridge,UK: Cambridge University Press; 1999.

Cosserat, E., Cosserat, F., 1909. Theorie des Corps Deformables. Cornell University Library.

Cowin SC. Stress functions for Cosserat elasticity. International Journal of Solids and Structures 1970; 6: 389-98.

Drago AS, Pindera M-J. Micro-macromechanical analysis of heterogeneous materials: acroscopically homogeneous vs periodic microstructures. Compos Sci Technol 2007;67(6):1243–63.

Devries, F., Dumontet, H., Duvaut, G., Lene, F., 1989. Homogenization and damage for composite structures. Int. J. Numer. Meth. Engrg. 27, 285–298.

Dos Reis, F., Ganghoffer, J.F., 2012. Construction of micropolar continua from the asymptotic homogenization of beam lattices . Computers and Structures 112–113 (2012) 354–363.

Dos Reis, F., Ganghoffer, J.F., 2012. Equivalent mechanical properties of auxetic lattices from discrete homogenization. Comput. Mater. Sci. 51,314–321.

Elsayed MSA, Pasini D. Analysis of the elastostatic specific stiffness of 2D stretching-dominated lattice materials. Mech. Mater. 2010;42:709–25.

Eringen, A.C., 1992. Vistas of nonlocal continuum physics. Int. J. Eng. Sci. 30, 1551–1565.

Eringen, A.C., 1999. Microcontinuum Field Theories I: Foundations and Solids. Springer-Verlag, New York.

Exadaktylos, G.E., Vardoulakis, I., 2001. Microstructure in linear elasticity and scale effects: a reconsideration of basic rock mechanics and rock fracture mechanics. Tectonophysics 335, 81–109.

Fang Z, Starly B, Sun W. Computer-aided characterization for effective mechanical properties of porous tissue scaffolds. Comput.-Aided Des.2005;37:65–72.

Fish, J., Yu, Q., Shek, K., 1999. Computational damage mechanics for composite materials based on mathematical homogenisation. Int. J. Numer. Meth. Engrg., 45, 1657–1679.

Forest, S., Dendievel, R., Canova, G.R., 1999. Estimating the overall properties of heterogeneous Cosserat materials. Modell. Simul. Mater. Sci. Eng. 7, 829–840.

Forest, S., Pradel, F., Sab, K., 2001. Asymptotic analysis of heterogeneous Cosserat media. Int. J. Solids Struct. 38, 4585–4608.

Forest, S., Trinh, D.K., 2010. Generalized continua and non-homogeneous boundary conditions in homogenisation methods. ZAMM _ Z. Angew. Math. Mech. 91 (2), 90–109.

Green, A.E., Rivlin, R.S., 1964. Multipolar continuum mechanics. Arch. Ration. Mech. Anal. 17, 113–147.

Guedes, J. M., Kikuchi, N., 1990. Preprocessing and postprocessing for materials based on the homogenization method with adaptive finite element methods. Comput. Methods Appl. Mech. Engrg., 83,143–198.

Hashin Z. Theory of fiber reinforced materials. NASA Contractor Report-1974. NASA Langley Research Center, Washington, DC; 1972.

Hassani B, Hinton E. A review of homogenization and topology optimization III – topology optimization using optimality criteria. Comput. Struct. 1998;69:739–56.

Hill R. Elastic properties of reinforced solids: some theoretical principles. J Mech Phys Solids 1963;11:357–72.

Hollister, S. J., Kikuchi, N., 1992. A comparison of homogenization and standard mechanics analysis for periodic porous composites. Comput. Mech. 10, 73–95.

Hutchinson R, Fleck N. The structural performance of the periodic truss. J. Mech.Phys.Solids2006;54:756–82.

Joumaa, H., Ostoja-Starzewski, M., 2011. Stress and couple-stress invariance in non-centrosymmetric micropolar planar elasticity. Proc. R. Soc. A http://dx.doi.org/10.1098/rspa.2010.0660. (Published online).

Joumaa, H. and M. Ostoja-Starzewski, "Stress and Couple-stress Invariance in Non-centrosymetric Micropolar Planar Elasticity," Proceedings of the Royal Society, London A 467(2134), 2896-2911, 2011. doi: 101098/rspa2010.0660.

Kalamkarov AL, Kolpakov AG. Analysis, design and optimization of composite structures. New York: John Wiley & Sons; 1997.

Kanouté, P., Boso, D., Chaboche, J., Schrefler, B., 2009. Multiscale methods for composites: a review Arch. Comput. Meth. Eng. 16, 31–75.

Khurana, A., Tomar, S.K., 2009. Longitudinal wave response of a chiral slab interposed between micropolar solid half-spaces. Int. J. Solids Struct. 46, 135–150.

Kikuchi N, Bendsoe M. Generating optimal topologies in structural design using a homogenization method. Comput. Methods Appl. Mech. Eng.1988;71:197–224.

Koiter, W.T., 1964. Couple stress in the theory of elasticity I–II. Proc. Kon. Nederl. Akad. Wetensch. B 67, 17–44, 196.

Kouznetsova, V., Geers,M.G. D., and Brekelmans,W.A. M. [2002] "Multi-scale constitutive modelling of heterogeneous materials with a gradient–enhanced computational homogenization scheme," International Journal for Numerical Methods in Engineering 54, 11235–1260.

Kouznetsova,V.G.,Geers,M.G.D.,Brekelmans,W.A.M.,2004.Multi-scale second order computational homogenization of multi-phase materials: a nested finite element solution strategy. Comput. Methods Appl. Mech. Eng. 193(48–51), 5525–5550.

Lakes, R.S., Benedict, R.L., 1982. Noncentrosymmetry in micropolar elasticity. Int. J. Eng. Sci. 20, 1161–1167.

Lakes, R., Yoon, H.S., Katz, J.L., 1983. Slow compressional wave propagation in wet human and bovine cortical bone. Science 220, 513–515.

Lakes, R. S., 1986. "Experimental microelasticity of two porous solids," International Journal of solids and structures 22, 55–63.

Lakes, R., 1995. Experimental methods for study of Cosserat elastic solids and other generalized elastic continua. In: Mühlhaus, H.B. (Ed.), Continuum Models for Materials with Microstructure. John Wiley & Sons, Chichester, pp. 1–25.

Lakes, R., 2001. Elastic and viscoelastic behavior of chiral materials. Int. J. Mech. Sci. 43, 1579–1589.

Ies-an, D., 2010. Chiral effects in uniformly loaded rods. J. Mech. Phys. Solids 58, 1272–1285.

Liu, X.N, G.L., Huang, HU, G.K., 2012. Chiral effect in plane isotropic micropolar elasticity and its application to chiral lattices. Journal of the Mechanics and Physics of Solids 60 (2012) 1907–1921.

Loran J. Gibson and Michael F. Ashby. Cellular Solids. Presss syndicate of the university of Cambridge, 1997.

Lin CY, Kikuchi N, Hollister SJ. A novel method for biomaterial scaffold internal architecture design to match bone elastic properties with desired porosity.J. Biomech. 2004;37:623–36.

Markov K, Preziosi L. Heterogeneous media: micromechanics modeling methods and simulations. Boston: Birkhauser; 2000.

Masters I, Evans K. Models for the elastic deformation of honeycombs. Compos. Struct.1996;35:403–22.

Mindlin, R.D., Tiersten, H.F., 1962. Effects of couple stresses in linear elasticity. Arch. Rat. Mech. Anal. 11, 415–448.

Mindlin, R.D., 1964. Micro-structure in linear elasticity. Arch. Rat. Mech. Anal. 16, 51–78.

Mindlin, R.D., 1965a. On the equations of elastic materials with micro-structure. Int. J. Solids Struct. 1, 73–78.

Mindlin, R.D., 1965b. Second gradient of strain and surface-tension in linear elasticity. Int. J. Solids Struct. 1, 417–438.

Mourad, A., 2003. Description topologique de l'architecture fibreuse et modelisation mecanique du myocarde. Ph.D. thesis, I.N.P.L. Grenoble.

Nemat-Nasser S, Hori M. Micromechanics: overall properties of heterogeneous materials. 2nd rev. ed. New York: North-Holland; 1999.

Nguyen, V.-D., Becker, G., Noels, L., 2013. Multiscale computational homogenization methods with a gradient enhanced scheme based on the discontinuous Galerkin formulation. Comput. Methods Appl. Mech. Eng. 260, 63–77.

Nowacki, W., 1986. In: Theory of Asymmetric ElasticityPergamon Press, New York.

Oliveira, J.A., Pinho-da-Cruz, J., Teixeira-Dia, F., 2009. Asymptotic homogenisation in linear elasticity. Part II: Finite element procedures and multiscale applications. Comput. Mater. Sci. 45,1081–1096.

P. Trovalusci and R. Masiani. Material symmetries of micropolar continua equivalent to lattices. International Journal of Solids and Structures, 36:2091-2108, 1999.

Pindera, M-J, Khatam, H., Drago, A.S., Bansal, Y.,2009. Micromechanics of spatially uniform heterogeneous media: A critical review and emerging approaches. Compos. Struct. 40, 349–378.

Raoult, A., Caillerie, D., Mourad, A., 2008. Elastic lattices: equilibrium, invariant laws and homogenization. Ann. Univ. Ferrara 54, 297–318.

Ramirez,D.A.,Murr,L.E.,Li,S.J.,Tian,Y.X.,Martinez,E.,Martinez,J.L.,Machado,B.I.,Gaytan,S. M.,Medina,F.,Wicker,R.B.,2011. Open-cellular copper structures fabricated by additive manufacturing using electron beam melting. Mater. Sci. Eng.:A528(16–17), 5379–5386.

Sanchez-Palencia E. Non-inhomogeneous media and vibration theory. Lecture notes in physics, vol. 127. Berlin (New York): Springer-Verlag; 1980.

Schaedler,T.A.,Jacobsen,A.J.,Torrents,A.,Sorensen,A.E.,Lian,J.,Greer,J.R.,Valdevit,L.,Carter, W.B.,2011.Ultralightmetallicmicrolattices. Science334 (6058), 962–965.

Shahkarami, A., Vaziri, R., 2007. A continuum shell finite element model for impact simulation of woven fabrics. Int. J. Imp. Eng. 34, 104–119.

Sigmund O. Materials with prescribed constitutive parameters: an inverse homogenization problem. Int. J. Solids Struct. 1994;31:2313–29.

Sturm S, Zhou S, Mai Y-W, Li Q. On stiffness of scaffolds for bone tissue engineering – a numerical study. J. Biomech. 2010;43:1738–44.

Suquet PM. Elements of homogenization for inelastic solid mechanics. Lecture notes in physics, vol. 272. Berlin (New York): Springer-Verlag; 1987. p. 193–278.

Tekoglu, C., Onck, P.R., 2008. Size effects in two-dimensional Voronoi foams: a comparison between generalized continua and discrete models. J. Mech. Phys. Solids. 56, 3541–3564.

Tiersten, H.F., Bleustein, J.L., 1974. Generalized elastic continua. In: Herrmann, G.(Ed.), R.D. Mindlin and Applied Mechanics. Rergamon Press, New York, pp. 67–103.

Tolenado, A., Murakami, H., 1987. A high-order mixture model for periodic particulate composites, Int. J. Solids Struct. 23, 989–1002.

Toupin, R.A., 1964. Theories of elasticity with couple-stress. Arch. Rat. Mech. Anal. 17, 85–112.

Vigliotti A, Pasini D. Mechanical properties of hierarchical lattices .Mech. Mater.2013;62:32–43.

Wang A, McDowell D. In-plane stiffness and yield strength of periodic metal honeycombs.J.Eng.Mater.Technol.2004;126:137–56.

Wang, J.S., Jun, Feng X.Q., Qin, Q.H., Yu, S.W., 2011. Chirality transfer from molecular to morphological scales in quasi-one-dimensional nanomaterials: a continuum model. J. Comput. Theor. Nanosci. 8, 1–10.

Yang, W., Li, Z.M., Shi, W., Xie, B.H., Yang, M.B., 2004. Review on auxetic materials. J. Mater. Sci. 39, 3269-3279.

Part I

Discrete Homogenization Schemes considering Geometrical Nonlinearities within Large Strains Framework

CHAPTER Three: Discrete Homogenization Schemes with Geometrical Non-linearites.

CHAPTER Four: Initial Linear Response of Architectured Materials from Discrete Asymptotic Homogenization. Application to Textile Monolayers.

CHAPTER Five: Nonlinear Response of Textile Monolayers (Plain weave and Twill)

CHAPTER Three

Discrete Homogenization Schemes With Geometrical Non-linearites

Contents

Abstract

The goal of this chapter is to set up a novel methodology for structures having a discrete repetitive architecture, which changes during the motion of the structure under an external loading. This requires the modeling of those lattices into the nonlinear regime, especially to account for their changes of geometry. A new approach, based on general beam equations, is proposed to compute the non-linear constitutive behavior of the structure; the interest is focused on the large displacements, large rotations and small strain case. Thereby, a perturbed equilibrium problem is set up at the unit cell level, solved by Newton-Raphson method; the localization problem which has to be solved in an incremental manner is coupled with the homogenization procedure, allowing the construction of the Cauchy and couple stress tensors for a micropolar effective continuum, incorporating an update of the structure geometry and of the constitutive response. The computed response of those lattices is based on the DH (discrete homogenization) homogenization algorithm into a dedicated code. A classification of lattices with respect to the choice of the equivalent continuum model is then proposed: the Cauchy continuum and a micropolar continuum are adopted as two possible effective media, for a given beam model. The relative ratio of the characteristic length of the micropolar continuum to the unit cell size determines the relevant choice of the equivalent medium.

As an application of the proposed methodology, the following two simple planar repetitive structures are first analyzed, here described in terms of the topology of the unit cell: the square cell structure and the 'honeycomb' hexagonal structure, subjected to the following three elementary loading cases: uniaxial loading, bi-axial loading and simple shear. These simple lattices are submitted to different types of elementary loading: uniaxial tensile, biaxial and simple shearing. A satisfactory agreement is obtained between the stress-strain results obtained by homogenization and numerical stress-strain results obtained by finite element simulations performed over repeating unit cell.

3.1 Introduction

The formulation of constitutive models for repetitive lattice materials based on micromechanical modeling assumes that the essential macroscopic features of the mechanical behavior on the macro scale can be inferred from the deformation response of the repeating unit cell (RUC) which has been identified for each lattice or structure. We have mentioned a range of applications of those repetitive lattices (chapter 1) both in engineering and biomechanics. One of the essential aims of bioengineering today is to answer the basic question of how individual cell networks, viewed as continuum architectural biomaterials, interact with each other or behave under different loadings. The somewhat complex topology of these natural discrete structures (e.g biomembranes) poses a serious problem when setting up a mechanical model, in view of the determination of their effective mechanical behavior. The derivation of the equivalent mechanical properties of cellular biological structures is further interesting in order to understand the somewhat peculiar observed behavior, due to anisotropy, or such as negative Poisson ratio) (auxetic behaviors). Moreover, the established continuum mechanical model for discrete structures can provide details on the distribution of stress and strains induced in the unit cell and can be integrated in finite element simulations at the scale of the whole cell. However, the knowledge of the continuum behavior of biomembranes is challenging, as they may be highly anisotropic (the state of anisotropy will change during motion), due to unequal length and properties of the threads within the molecular network; furthermore, biological membranes are prone to large distensions and one should ideally consider material nonlinear effects. Hence, independently of any specific application, micromechanical approaches are needed in order to bridge the scales and to provide a physically based constitutive law at continuum scale, whereby the equivalent continuum properties emerge from micro-structural parameters related to both the geometry and mechanics of the network.

This chapter is organized as follows: Section 3.1 present the set up of general beam models accounting for large displacement and large rotations. In the next section 3.2, the discrete homogenization method is exposed. The nonlinear equilibrium problem of a lattice is written in section 3.3, which is solved by a Newton-Raphson iterative procedure. The algorithm used for the full incremental procedure with an update of the lattice geometry is described in section 3.4.

As an application, the equivalent mechanical properties of 2D simple lattices are derived, adopting first a linear framework, and extending next to the geometrical nonlinear situation for different types of macroscopic loadings in section 3.5. In section 3.7, we present a general description of biomembranes as biological networks and how it is classified to their connectivity.

The study of geometrical nonlinear behavior was extended for theses biological networks. Finally, the computed stress-strain homogenized response will be validated thanks to FE simulations performed over a well-chosen representative unit cell for each specific selected lattice.

3.2 Beam equations in the geometrically nonlinear framework

Complex heterogeneous materials may appear in shell-like structure, a typical example being biomembranes, which can be viewed as networks of connected filaments, each being modeled as an undulated beam undergoing both large displacements and rotations. We denote $\mathbf{B}_o$ the reference configuration of the beam under consideration. The kinematics of the curved beam is firstly established, in order to derive expressions of the resultant and moments for a given beam element. Torsion and warping are not taken into account, which restrict the present formulation to a certain class of problems. The constitutive relation is built as the relation between the Green-Lagrangian strain in tensor and second Piola-Kirchhoff stress tensor and strain potential formulation.

After lengthy calculations and considering only the first order expansion of the Taylor series of the trigonometric functions (Klaus Jurgen Bathe and Said Bolourchi, 1979), the forces and moments resultants can be written as follow:

$$\begin{aligned}
&N = E_s A\left(u' + \frac{1}{2}\left(u'^2 + v'^2\right) + \frac{\omega_3^2}{2} - \frac{1}{2}\left(\varepsilon_{01}^2 + \varepsilon_{02}^2 + \varepsilon_{03}^2\right)\right) + E_s I_z\left(\omega_3'^2 - \kappa_{03}^2\right)\\
&T_y = GA\left(\left|\omega_3\right|\left(1+u'\right) + v' - \varepsilon_{02}\right)\\
&T_z = -GA(\varepsilon_{03})\\
&M_x = 0, \qquad M_y = 0\\
&M_z = -E_s I_z\left(\omega_3'\left(1+u'\right) - \left|\omega_3\right|v' + \varepsilon_{01}\kappa_{03}\right)
\end{aligned} \tag{3.1}$$

Those expressions are written in a general case and exhibit a nonlinear elastic behavior. In order to apply the asymptotic homogenization method, some simplifications are made. We consider that all beams are initially rectilinear, so that no initial deformations or initial curvatures are present, implying that the corresponding kinematic variables $\varepsilon_{01}, \varepsilon_{02}, \varepsilon_{03}, \kappa_{03}$ are nil. From the continuous beam equations (3.142), we deduce the discrete relations by replacing the primed variable by their finite differences, in order to transform the initial continuous problem into a

more convenient system of discrete expressions for the asymptotic homogenization method. Thus, equations (2.42) can be rewritten in intrinsic format as

$$
\begin{aligned}
N &= E_s A\left(\frac{\Delta\mathbf{U}\cdot\mathbf{e}^b}{l}+\frac{1}{2}\left(\frac{\left(\Delta\mathbf{U}\cdot\mathbf{e}^b\right)^2}{l^2}+\frac{\left(\Delta\mathbf{U}\cdot\mathbf{e}^{b\perp}\right)^2}{l^2}\right)+\frac{\psi_c^2}{2}\right)+E_s I_z\left(\frac{\Delta\psi_c}{2}\right)^2 \\
T_y &= GA\left(\psi_c\left(1+\frac{\Delta\mathbf{U}\cdot\mathbf{e}^b}{l}\right)+\frac{\left(\Delta\mathbf{U}\cdot\mathbf{e}^{b\perp}\right)}{l}\right) \\
M_z &= -E_s I_z\left(\frac{\Delta\psi}{l}\left(1+\frac{\Delta\mathbf{U}\cdot\mathbf{e}^b}{l}\right)-\psi_c\frac{\left(\Delta\mathbf{U}\cdot\mathbf{e}^{b\perp}\right)}{l}\right)
\end{aligned}
\tag{3.2}
$$

In those expressions, A is the beam cross section, l the beam length, I_z the quadratic moment of the considered beam, $\mathbf{e}^b$ and $\mathbf{e}^{b\perp}$ are respectively the unite vector director of the beam and the transverse unit vector. E_s and G are the Young and the shear moduli respectively of the considered beam. ψ_c is the rotation of the central node of the beam.

3.3 Discrete Homogenization technique

The discrete homogenization method is considered as a mathematical technique to derive the equivalent continuous medium behavior of repetitive discrete structure made of elementary cells. This technique is inspired from the homogenization of periodic media developed thirty years ago by (Sanchez, 1980; Bakhvalov and Panasenko, 1989) and it was more recently applied by different authors including (Warren and Byskhov, 2002; Mourad and Caillerie, 2003; D. Caillerie et al., 2006; Raoult et al., 2008; Dos Reis and Ganghoffer, 2012). It has been also combined with the energy method by (Pradel and Sab, 1998) and applied to discrete homogenization. The DAH (short cut for discrete asymptotic homogenization) technique consists by essence in assuming asymptotic series expansions of both the node displacements, tension and external forces as successive powers of a small parameter labeled ε, defined as the ratio of a characteristic length of the unit cell to a characteristic length of the lattice structure. Those expansions are then inserted into the equilibrium equation, conveniently expressed in weak form. The balance equation of the nodes, the force–displacement relations and the moment-rotation relations of the beams are developed by inserting those series expansions and by using Taylor's series expansion of finite differences. The discrete sums are finally converted in the limit of a continuous density of beams into Riemann integrals, thereby highlighting continuous stress and

strain measures. The calculations have been completed for a quite general truss and the results give a general and closed form expression of elastic properties in the linear framework. .

In addition, several models analyze simple topologies to obtain closed form expressions of the linear behavior of the lattice stiffness and strength, by solving the equilibrium problem of the unit cell (Gibson and Ashby, 1982; Wang and McDowell, 2004; Gibson et al., 1982; Zhu et al., 1997; Hutchinson and Fleck, 2006). Despite the lack of a specific literature on non linear models for lattices, several works, mainly focused on the modeling of composites and of heterogeneous media, are available. These studies can offer insight into the general framework and theoretical basis for the development of a non linear constitutive model for lattices. Extensive reviews of these works can be found in (Pindera et al., 2009; Charalambakis, 2010).

The geometrical nonlinear behavior of cellular structures and networks was extensively studied by (Warren et al., 1989; Warren and Kraynik, 1991) considering the example of foams, using simplified pin jointed model for which the bending contribution of the skeleton struts was neglected. (Wang and Cuitino, 2000) proposed another approach where axial, bending and twisting deformations at local level were considered. One study based on homogenization technique was given in (Hohe and Beecker, 2003).

(Janus Michalska and Pecherski, 2003; Janus Michalska, 2005) presented linear effective models to analyze structures on the basis of a beam model, in which stretching and simultaneous bending occurs. More recently, Janus Michalska (2011) extended this linear model to construct the stress-strain relation and strain energy function for the hyperelastic cellular material with arbitrary symmetry. Let also mention the alternative approach proposed by (Andrea et al., 2014) using a computational homogenization to derive a nonlinear constitutive model for lattice materials.

3.3.1 Simplified beam model

In view of deriving a simplified beam model from the previous general one, and for the purpose of an easier treatment and numerical implementation, we neglect the nonlinear part of the strain (and the coupling term between displacement and rotation) in (3.3). The normal and transverse efforts, and the moment at the beam extremities can accordingly be successively expressed versus kinematical nodal variable as

$$
\begin{aligned}
N^{\varepsilon} &= \frac{E_s\, t}{l^{\varepsilon b}}\left[\left(\Delta \mathbf{U}^{b\varepsilon}.\mathbf{e}^{b}\right)\right] \\
T_t^{\varepsilon} &= \frac{12E_s I_z}{\left(l^{\varepsilon b}\right)^3}\left[\left(\Delta \mathbf{U}^{b\varepsilon}\cdot\mathbf{e}^{b\perp}\right)-\frac{l^{\varepsilon b}}{2}\left(\phi^{O(b)\varepsilon}+\phi^{E(b)\varepsilon}\right)\right] \\
M^{O(b)\varepsilon} &= \frac{-12E_s I_z}{\left(l^{\varepsilon b}\right)^3}\left[\left(\left(\frac{l^{\varepsilon b}}{2}\right)\left(\Delta \mathbf{U}^{b\varepsilon}\cdot\mathbf{e}^{b\perp}\right)\right)+\left(\frac{\left(l^{\varepsilon b}\right)^2}{6}\right)\left(2\phi^{O(b)\varepsilon}+\phi^{E(b)\varepsilon}\right)\right] \\
M^{E(b)\varepsilon} &= \frac{-12E_s I_z}{\left(l^{\varepsilon b}\right)^3}\left[\left(\left(\frac{l^{\varepsilon b}}{2}\right)\left(\Delta \mathbf{U}^{b\varepsilon}\cdot\mathbf{e}^{b\perp}\right)\right)+\left(\frac{\left(l^{\varepsilon b}\right)^2}{6}\right)\left(\phi^{O(b)\varepsilon}+2\phi^{E(b)\varepsilon}\right)\right]
\end{aligned}
\tag{3.3}
$$

The variables $M^{O(b)\varepsilon}$ and $M^{E(b)\varepsilon}$ therein are the moment at the origin and the end positions of a generic beam respectively. Details related to the asymptotic expansion of the kinematical variables can be found in (Thesis F. Dos Reis, 2010).

3.3.2 Position of the problem

The lattice under consideration is described as a quasi repetitive lattice of beams and is completely defined by the positions of the nodes and their connectivity. We denote by N_R and B_R respectively, the set of nodes and beams within the reference unit cell, which are finite dimensional. The lattice is also supposed to remain quasi periodic in its deformed state. The cells are numbered by the triplet of integers $\upsilon^i=\left(\upsilon^1,\upsilon^2,\upsilon^3\right)$; the nodes of the whole fabric can then be parameterized by the quadruplet $\tilde{n}=\left(n,\upsilon^1,\upsilon^2,\upsilon^3\right)\in N_R\times\mathbb{Z}^3$. In the same way, the beams of the fabric are described by the quadruplet $\tilde{b}=\left(b,\upsilon^1,\upsilon^2,\upsilon^3\right)\in B_R\times\mathbb{Z}^3$. Within the reference cell, one can select the origin node of a beam $O(\tilde{b})$ so that it belongs to the reference cell. This origin node can be represented by the quadruplet $\left(n,\upsilon^1,\upsilon^2,\upsilon^3\right)$. Wherein we have parameterized any point within the representative unit cell by curvilinear coordinates $\lambda^{\mathcal{E}}=\varepsilon\upsilon^i$ .Nevertheless, the end node $E(\tilde{b})$ does not necessarily belong to the reference cell, but is necessarily included in an adjacent cell numbered by $\left(\upsilon^1+\delta^1,\upsilon^2+\delta^2,\upsilon^3+\delta^3\right)$. The triplet $\left(\delta^1,\delta^2,\delta^3\right)\in\mathbb{Z}^3$ and the end node either belongs to the reference cell or to a cell next to it: this means that the shift parameter, the integer δ^i belongs to the set $\{-1,0,1\}$.We consider a static framework, which means we are entitled to neglect the inertia forces. Since each beam within the lattice is equilibrated, one has $T^{E(b)}=-T^{O(b)}$ (Fig. 3.1).

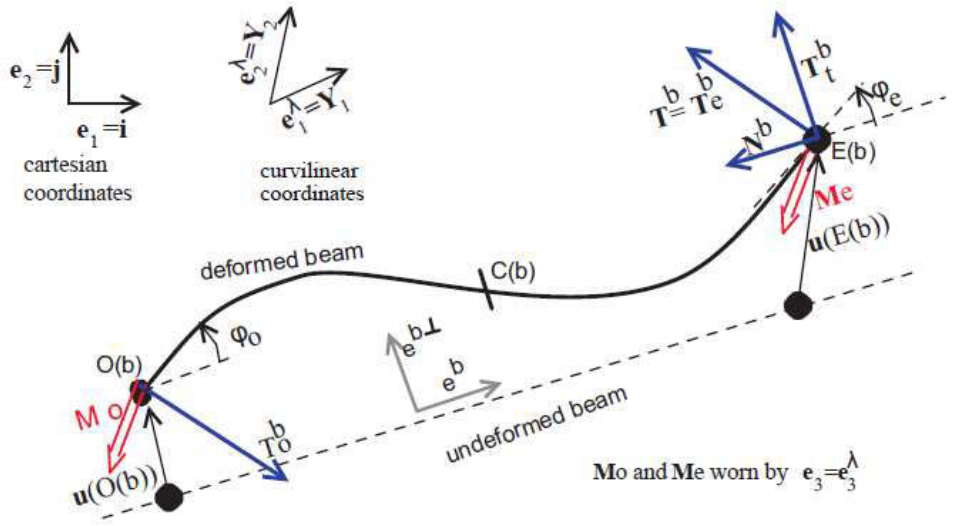

Fig. 3.1 Kinematic parameters of the beam

The equilibrium of forces over the lattice writes in virtual power form after insertion of the asymptotic development of the variables as

$$\sum_{i\in\mathbb{Z}^3}\sum_{b\in B_R} T^{\varepsilon b}.\left(\mathrm{v}^{\varepsilon}\left(O(b)\right)-\mathrm{v}^{\varepsilon}\left(E(b)\right)\right)=0 \tag{3.4}$$

with $\mathrm{v}^{\varepsilon}(.)$ a virtual velocity field choosing nil on the edges of the considered domain, and $\mathrm{T}^{\varepsilon b}$ the sum of N^{ε} the longitudinal force and T_t^{ε} the transversal force:

$$T^b = N^b\mathbf{e}^b + T_t^b\mathbf{e}^{b\perp} \tag{3.5}$$

For any virtual velocity field v^{ε}, supposed to be regular enough, a Taylor series's development at the first order leads to

$$\mathrm{v}^{\varepsilon}\left(O(b)\right)-\mathrm{v}^{\varepsilon}\left(E(b)\right)\approx\varepsilon\frac{\partial\mathrm{v}\left(\lambda^{\varepsilon}\right)}{\partial\lambda^{\mathrm{i}}}\delta^{ib} \tag{3.6}$$

Moment equilibrium proceeding similarly as for equilibrium of forces as

$$\sum_{i\in\mathbb{Z}^3}\sum_{b\in B_R}\left(\mathrm{M}^{O(b)\varepsilon}.\mathrm{w}^{\varepsilon}\left(O(b)\right)+\mathrm{M}^{E(b)\varepsilon}.\mathrm{w}^{\varepsilon}\left(E(b)\right)+\varepsilon L^b\left(\mathbf{e}^b\wedge\mathrm{T}^{\varepsilon b}\right).\mathrm{w}^{\varepsilon}\left(C(b)\right)\right)=0 \tag{3.7}$$

where w(C(b)) is the rotation rate of the incorporated central beam node. The rotation rate is further expanded as

$$\begin{aligned}
&\mathrm{w}^{O(b)\varepsilon}=\mathrm{w}_0(\lambda^{\varepsilon})\\
&\mathrm{w}^{E(b)\varepsilon}(\lambda+\varepsilon\delta^i)\approx\mathrm{w}_0(\lambda)+\varepsilon\frac{\partial w_0(\lambda)}{\partial\lambda^i}\delta^{ib}\\
&\mathrm{w}^{C(b)\varepsilon}=\frac{1}{2}\left(\mathrm{w}^{E(b)\varepsilon}+\mathrm{w}^{O(b)\varepsilon}\right)
\end{aligned} \tag{3.8}$$

3.3.3 Asymptotic parameters and description of the lattice geometry

For large enough lattice, the ratio of the beam length to a macroscopic lattice dimension constitutes the small scale parameter, $\varepsilon = l/L$, decrease of this parameter as shown in figure 3.2 shows that the structure with discrete architecture tends to appear as a continuum material.

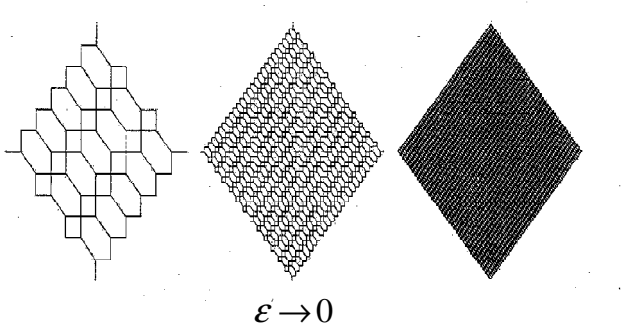

Fig. 3.2 Set of configurations parameterized by geometrical parameter (ε)

The discrete asymptotic technique requires the development of all variables as Taylor series; the beam length $l^{\varepsilon b}$, the beam width $t^{\varepsilon b}$, thickness $e^{\varepsilon b}$, the displacement $u^{\varepsilon n}$ and the rotation at the lattices nodes $\phi^{\varepsilon n}$ (they constitute the kinematic variables) vs. the small parameter ε. Bernoulli beam model is considered in this study, valid for slender enough beams. From the results of (A. Mourad, 2003), one can express the beam length and beam unit director as the following expansion versus ε.

$$l^{\varepsilon b} = \varepsilon l^{bo}\left(\lambda^{\varepsilon}\right) + \varepsilon^2 l^{b1}\left(\lambda^{\varepsilon}\right) + - - \tag{3.9}$$

$$e^{\varepsilon b} = e^{bo}\left(\lambda^{\varepsilon}\right) + \varepsilon e^{b1}\left(\lambda^{\varepsilon}\right) + - - - \tag{3.10}$$

The displacement difference $\Delta\mathbf{U}^{b\varepsilon}$ between the extremity and origin node of each beam is expressed by a Taylor series development, according to

$$\Delta\mathbf{U}^{b\varepsilon} = \mathbf{u}^{\varepsilon}(E(b)) - \mathbf{u}^{\varepsilon}(O(b)) = \underbrace{\varepsilon\left(\mathbf{u}_1^{E_{R(b)}}\left(\lambda^{\varepsilon}\right) - \mathbf{u}_1^{O_{R(b)}}\left(\lambda^{\varepsilon}\right) + \frac{\partial \mathbf{u}_0\left(\lambda^{\varepsilon}\right)}{\partial \lambda^i}\delta^{ib}\right)}_{\Delta U_1^b} + \varepsilon^2 \underbrace{\left(\mathbf{u}_2^{E_{R(b)}}\left(\lambda^{\varepsilon}\right) - \mathbf{u}_2^{O_{R(b)}}\left(\lambda^{\varepsilon}\right)\right)}_{\Delta U_2^b} \tag{3.11}$$

$$= \qquad \varepsilon\,\Delta\mathbf{U}_1^b \qquad + \qquad \varepsilon^2\,\Delta\mathbf{U}_2^b$$

With δ^{ib} the shift factor (equal to ± 1) for nodes belonging to a neighbouring cell, being nil for nodes located inside the considered cell.

The asymptotic expansion of the nodal microrotation $\phi^{n\varepsilon}$ is here limited to the first order in ε; it is defined successively at the origin and extremity of each beam as

$$\phi^{O(b)\varepsilon} = \phi_0^{O_{R(b)}} + \varepsilon\phi_1^{O_{R(b)}} ; \phi^{E(b)\varepsilon} = \phi_0^{E_{R(b)}} + \varepsilon\left(\frac{\partial\phi_0}{\partial\lambda^i}\delta^{ib} + \phi_1^{E_{R(b)}}\right) \tag{3.12}$$

The asymptotic expansion of the efforts and moments writes

$$N^\varepsilon = E_s\eta\left[\left(\left(\varepsilon\,\Delta\mathbf{U}_1 + \varepsilon^2\,\Delta\mathbf{U}_2\right).\mathbf{e}^b\right)\right]$$

$$N^\varepsilon \sim \left[\varepsilon\left(N_1^b\right) + \varepsilon^2\left(N_2^b\right)\right]$$

$$T_t^\varepsilon = E_s\eta^3\left(\mathbf{e}^{b\perp}.\left(\varepsilon\,\Delta\mathbf{U}_1^{\mathrm{b}} + \varepsilon^2\,\Delta\mathbf{U}_2^{\mathrm{b}}\right)\right) - \frac{1}{2}E_s\eta^3\varepsilon_L^{bo}\left(\left(\phi_0^{O_{R(b)}} + \phi_0^{E_{R(b)}} + \varepsilon\left(\phi_1^{O_{R(b)}} + \phi_1^{E_{R(b)}} + \frac{\partial\phi_0}{\partial\lambda^i}\delta^{ib}\right)\right)\right)$$

$$T_t^\varepsilon \sim \varepsilon T_{1t}^b + \varepsilon^2 T_{2t}^b$$

Similarly, the asymptotic expansion of the moments writes,

$$\mathrm{M}^{\mathrm{O(b)\varepsilon}} = -\left(\frac{1}{2}\right)\mathrm{E_s}\eta^3\varepsilon_{\mathrm{L}}{}^{\mathrm{bo}}\left(\Delta\mathbf{U}^{\mathrm{b}\varepsilon}\cdot\mathbf{e}^{\mathrm{b}\perp}\right) + \mathrm{E_s}\eta^3\varepsilon^2\left(\frac{\left(\mathrm{L}^{\mathrm{bo}}\right)^2}{6}\right)\left(2\phi^{\mathrm{O(b)\varepsilon}} + \phi^{\mathrm{E(b)\varepsilon}}\right)$$

$$\sim -\left(\frac{1}{2}\right)\mathrm{E_s}\eta^3\varepsilon_{\mathrm{L}}{}^{\mathrm{bo}}\mathbf{e}^{\mathrm{b}\perp}.\left(\varepsilon\,\Delta\mathbf{U}_1^{\mathrm{b}} + \varepsilon^2\,\Delta\mathbf{U}_2^{\mathrm{b}}\right) +$$

$$\mathrm{E_s}\eta^3\varepsilon^2\left(\frac{\left(\mathrm{L}^{\mathrm{bo}}\right)^2}{6}\right)\left(2\phi_0^{\mathrm{O_{R(b)}}} + \phi_0^{\mathrm{E_{R(b)}}} + \varepsilon\left(2\phi_1^{\mathrm{O_{R(b)}}} + \phi_1^{\mathrm{E_{R(b)}}} + \frac{\partial\phi_0}{\partial\lambda^{\mathrm{i}}}\delta^{\mathrm{ib}}\right)\right)$$

$$\sim \varepsilon^2\mathrm{M_1}^{\mathrm{O(b)}} + \varepsilon^3\mathrm{M_2}^{\mathrm{O(b)}}$$

$$\mathrm{M}^{\mathrm{E(b)\varepsilon}} = -\left(\frac{1}{2}\right)\mathrm{E_s}\eta^3\varepsilon_{\mathrm{L}}{}^{\mathrm{bo}}\left(\Delta\mathbf{U}^{\mathrm{b}\varepsilon}\cdot\mathbf{e}^{\mathrm{b}\perp}\right) + \mathrm{E_s}\eta^3\varepsilon^2\left(\frac{\left(\mathrm{L}^{\mathrm{bo}}\right)^2}{6}\right)\left(\phi^{\mathrm{O(b)\varepsilon}} + 2\phi^{\mathrm{E(b)\varepsilon}}\right)$$

$$\sim -\left(\frac{1}{2}\right)\mathrm{E_s}\eta^3\varepsilon_{\mathrm{L}}{}^{\mathrm{bo}}\mathbf{e}^{\mathrm{b}\perp}.\left(\varepsilon\,\Delta\mathbf{U}_1^{\mathrm{b}} + \varepsilon^2\,\Delta\mathbf{U}_2^{\mathrm{b}}\right) +$$

$$\mathrm{E_s}\eta^3\varepsilon^2\left(\frac{\left(\mathrm{L}^{\mathrm{bo}}\right)^2}{6}\right)\left(\phi_0^{\mathrm{O_{R(b)}}} + 2\phi_0^{\mathrm{E_{R(b)}}} + \varepsilon\left(\phi_1^{\mathrm{O_{R(b)}}} + 2\phi_1^{\mathrm{E_{R(b)}}} + \frac{\partial\phi_0}{\partial\lambda^{\mathrm{i}}}\delta^{\mathrm{ib}}\right)\right)$$

$$\sim \varepsilon^2\mathrm{M_1}^{\mathrm{E(b)}} + \varepsilon^3\mathrm{M_2}^{\mathrm{E(b)}}$$

We next express the equilibrium of forces according to the successive powers of ε as

$$\sum_{v^i\in\mathbb{Z}^3}\sum_{b\in B_R}\left[\begin{array}{l}\varepsilon^2\left(\begin{array}{l}E_s\eta\left(\Delta\mathbf{U}_1^{\mathrm{b}}\cdot\mathbf{e}^b\right)e^b+\left(E_s\eta^3\left(\Delta\mathbf{U}_1^{\mathrm{b}}.\mathbf{e}^{b\perp}\right)-\frac{1}{2}E_s\eta^3L^{bo}\left(\phi_0^{O_{R(b)}}+\phi_0^{E_{R(b)}}\right)\right)\mathbf{e}^{b\perp}\end{array}\right).\frac{\partial \mathrm{v}\left(\lambda^\varepsilon\right)}{\partial\lambda^{\mathrm{i}}}\delta^{ib}\\ +\varepsilon^3\left(\begin{array}{l}E_s\eta\left(\Delta\mathbf{U}_2^{\mathrm{b}}\cdot\mathbf{e}^b+\left(\frac{1}{2}\left(\Delta\mathbf{U}_1^{\mathrm{b}}\cdot e^b\right)\left(\Delta\mathbf{U}_1^{\mathrm{b}}\cdot\mathbf{e}^b\right)\right)\right)e^b+\\ \left(\begin{array}{l}E_s\eta^3\left(\Delta\mathbf{U}_1^{\mathrm{b}}.\mathbf{e}^{b\perp}\right)-\\ \frac{1}{2}E_s\eta^3L^{bo}\left(\phi_1^{O_{R(b)}}+\phi_1^{E_R(b)}+\frac{\partial\phi_0}{\partial\lambda^i}\delta^{ib}\right)\end{array}\right)e^{b\perp}\end{array}\right).\frac{\partial \mathrm{v}\left(\lambda^\varepsilon\right)}{\partial\lambda^{\mathrm{i}}}\delta^{ib}\\ +\varepsilon^4\left(\left(\left(\Delta\mathrm{U}_1^{\mathrm{b}}\cdot\mathbf{e}^b\right)\left(\Delta\mathbf{U}_2^{\mathrm{b}}\cdot\mathbf{e}^b\right)\right)\mathbf{e}^b\right).\frac{\partial \mathrm{v}\left(\lambda^\varepsilon\right)}{\partial\lambda^{\mathrm{i}}}\delta^{ib}\\ +\varepsilon^5\left(\left(\frac{1}{2}\left(\Delta\mathbf{U}_2^{\mathrm{b}}\cdot\mathbf{e}^b\right)\left(\Delta\mathbf{U}_2^{\mathrm{b}}\cdot\mathbf{e}^b\right)\right)\mathbf{e}^b\right).\frac{\partial \mathrm{v}\left(\lambda^\varepsilon\right)}{\partial\lambda^{\mathrm{i}}}\delta^{ib}\end{array}\right]=0 \tag{3.13}$$

Previous equilibrium equation gives in the limit of a vanishing small parameter the continuum equilibrium, relying on the following mathematical result: for any regular enough function *g*, the quantity $\varepsilon^3\sum_{v^i\in\mathbb{Z}^3}g\left(\varepsilon v^i\right)$ can be interpreted as the Riemann integral $\int_\Omega g(\lambda)d\lambda$ in 3-D when $\varepsilon\to 0$.

Accordingly, the previous discrete equation becomes the homogenized self-equilibrium equation

$$\int_\Omega \mathbf{S}^i.\frac{\partial \mathrm{v}(\lambda)}{\partial\lambda^{\mathrm{i}}}d\lambda=0 \tag{3.14}$$

with the stress vector $\mathbf{S}^i$, which splits into a first and a second order contribution, viz. $\mathbf{S}^i=\mathbf{S}_1^i+\varepsilon\mathbf{S}_2^i$, with both vectors given by

$$\begin{array}{l}\mathbf{S}_1^i=\sum_{b\in B_R}\left(\left(\begin{array}{l}E_s\eta\left(\Delta\mathbf{U}_1^{\mathrm{b}}\cdot\mathbf{e}^b\right)\mathbf{e}^b+\left(E_s\eta^3\left(\Delta\mathbf{U}_1^{\mathrm{b}}.\mathbf{e}^{b\perp}\right)-\frac{1}{2}E_s\eta^3{}_L{}^{bo}\left(\phi_0^{O_{R(b)}}+\phi_0^{E_{R(b)}}\right)\right)\mathbf{e}^{b\perp}\end{array}\right)\delta^{ib}\right)\\ \mathbf{S}_2^i=\sum_{b\in B_R}\left(E_s\eta\left(\Delta\mathbf{U}_2^{\mathrm{b}}\cdot\mathbf{e}^b+\left(\frac{1}{2}\left(\Delta\mathbf{U}_1^{\mathrm{b}}\cdot\mathbf{e}^b\right)\left(\Delta\mathbf{U}_1^{\mathrm{b}}\cdot\mathbf{e}^b\right)\right)\right)\mathbf{e}^b+\left(E_s\eta^3\left(\Delta\mathbf{U}_1^{\mathrm{b}}.\mathbf{e}^{b\perp}\right)-\frac{1}{2}E_s\eta^3{}_L{}^{bo}\left(\phi_1^{O_{R(b)}}+\phi_1^{E_{R(b)}}+\frac{\partial\phi_0}{\partial\lambda^i}\delta^{ib}\right)\right)\mathbf{e}^{b\perp}\right)\delta^{ib}\end{array} \tag{3.15}$$

Expressing the equilibrium of moment according to the successive powers of ε gives (for more details, the reader is referred to [Dos Reiss et al., 2012])

$$\sum_{v^i\in\mathbb{Z}^3}\sum_{b\in B_R}\left[\begin{array}{l}\varepsilon^3\left(E_s\eta^3\frac{\left(L^b\right)^2}{12}\left(\phi_0^{E_{R(b)}}-\phi_0^{O_{R(b)}}\right)\right).\frac{\partial w_o\left(\lambda^\varepsilon\right)}{\partial\lambda^{\mathrm{i}}}\delta^{ib}\\ +\varepsilon^4\left(E_s\eta^3\frac{\left(L^b\right)^2}{12}\left(-\phi_1^{O_{R(b)}}+\phi_1^{E_{R(b)}}+\frac{\partial\phi_0}{\partial\lambda^i}\delta^{ib}\right)\right).\frac{\partial w_o\left(\lambda^\varepsilon\right)}{\partial\lambda^{\mathrm{i}}}\delta^{ib}\end{array}\right]=0$$

Similarly, the previous equation can be rewritten in the limit $\varepsilon\to 0$ in the discrete sum in the following form

$$\int_{\Omega} \boldsymbol{\mu}^{i} . \frac{\partial \mathrm{w}(\lambda)}{\partial \lambda^{\mathrm{i}}} d\lambda = 0 \tag{3.16}$$

The couple stress vectors that incorporate moments $\boldsymbol{\mu}^{i}$ are also identified on two successive orders, viz. $\boldsymbol{\mu}^{i} = \varepsilon \boldsymbol{\mu}_1^{i} + \varepsilon^2 \boldsymbol{\mu}_2^{i}$, each as the following sums over the beams of the reference unit cell

$$\begin{aligned} \boldsymbol{\mu}_1^{i} &= \sum_{b \in B_R} \varepsilon \left(E_s \eta^3 \frac{\left(L^b\right)^2}{12} \left(\phi_0^{E_{R(b)}} - \phi_0^{O_{R(b)}} \right) \right) \delta^{ib} \\ \boldsymbol{\mu}_2^{i} &= \sum_{b \in B_R} \varepsilon^2 \left(E_s \eta^3 \frac{\left(L^b\right)^2}{12} \left(-\phi_1^{O_{R(b)}} + \phi_1^{E_{R(b)}} + \frac{\partial \phi_0}{\partial \lambda^i} \delta^{ib} \right) \right) \delta^{ib} \end{aligned} \tag{3.17}$$

The general form of the constitutive equations can presently be identified from the expressions of the homogenized stress and couple stress tensors together with S^{i} and μ^{i} expressions:

$$\begin{aligned} \boldsymbol{\sigma} &= \frac{1}{g} \mathbf{S}^{\mathrm{i}} \otimes \frac{\partial \mathrm{R}}{\partial \lambda^{\mathrm{i}}} = \frac{1}{g} \left(\mathbf{S}_1^{\mathrm{i}} + \varepsilon \mathbf{S}_2^{\mathrm{i}} \right) \otimes \frac{\partial \mathrm{R}}{\partial \lambda^{\mathrm{i}}} = \underbrace{\frac{1}{g} \mathbf{S}_1^{\mathrm{i}} \otimes \frac{\partial \mathrm{R}}{\partial \lambda^{\mathrm{i}}}}_{\left[\mathbf{K}^{s}\right]\{\epsilon\}} + \underbrace{\frac{1}{g} \varepsilon \mathbf{S}_2^{\mathrm{i}} \otimes \frac{\partial \mathrm{R}}{\partial \lambda^{\mathrm{i}}}}_{[\mathbf{B}]\{\chi\}} \\ \mathbf{m} &= \frac{1}{g} \boldsymbol{\mu}^{\mathrm{i}} \otimes \frac{\partial \mathrm{R}}{\partial \lambda^{\mathrm{i}}} = \frac{1}{g} \left(\varepsilon \boldsymbol{\mu}_1^{\mathrm{i}} + \varepsilon^2 \boldsymbol{\mu}_2^{\mathrm{i}} \right) \otimes \frac{\partial \mathrm{R}}{\partial \lambda^{\mathrm{i}}} = \underbrace{\frac{1}{g} \varepsilon \boldsymbol{\mu}_1^{\mathrm{i}} \otimes \frac{\partial \mathrm{R}}{\partial \lambda^{\mathrm{i}}}}_{[\mathbf{B}]\{\epsilon\}} + \underbrace{\frac{1}{g} \varepsilon^2 \boldsymbol{\mu}_2^{\mathrm{i}} \otimes \frac{\partial \mathrm{R}}{\partial \lambda^{\mathrm{i}}}}_{\left[\mathbf{K}^{\mu}\right]\{\chi\}} \end{aligned} \tag{3.18}$$

with g the Jacobian of the transformation from Cartesian to curvilinear coordinates and $\mathbf{R}$ the position vector of any material point.

For periodical uniform structures endowed with a central symmetry, the stiffness coefficients are invariant under a coordinate inversion, hence the pseudo-tensor B_{ijkl} vanishes. The previous constitutive equations then imply that the vectors μ_1^{i} and $\mathrm{S}_2^{\mathrm{i}}$ should vanish; this leads to an important simplification of the stress and couple stress vectors

$$\begin{aligned} \mathbf{S}^{i} = \mathbf{S}_1^{i} &= \sum_{b \in B_R} \left(\left(E_s \eta \left(\Delta \mathbf{U}_1^{\mathrm{b}} \cdot \mathbf{e}^{b} \right) \mathbf{e}^{b} + \left(E_s \eta^3 \left(\Delta \mathbf{U}_1^{\mathrm{b}} . \mathbf{e}^{b\perp} \right) - \frac{1}{2} E_s \eta^3 L^{bo} \left(\phi_0^{O_{R(b)}} + \phi_0^{E_{R(b)}} \right) \right) \mathbf{e}^{b\perp} \right) \right) \delta^{ib} \\ &= \sum_{b \in B_R} \left(N_1^{b} \mathbf{e}^{b} + T_{1t}^{b} \mathbf{e}^{b\perp} \right) \delta^{ib} \\ \boldsymbol{\mu}^{\mathrm{i}} = \boldsymbol{\mu}_2^{\mathrm{i}} &= \sum_{b \in B_R} \varepsilon^2 \left(E_s \eta^3 \frac{\left(L^b\right)^2}{12} \left(-\phi_1^{O_{R(b)}} + \phi_1^{E_{R(b)}} + \frac{\partial \phi_0}{\partial \lambda^i} \delta^{ib} \right) \right) \delta^{ib} \\ &= \sum_{b \in B_R} \frac{1}{2} \varepsilon^2 \left(M_2^{E(b)} - M_2^{O(b)} \right) \delta^{ib} \end{aligned} \tag{3.19}$$

In those expressions, N_1^b , T_{1t}^b and M_2^n are respectively, the first order normal and transverse effort and the second order moment, obtained when expanding the expressions (3.3) versus the small parameter ε. Those expressions still involve the unknown displacements and rotations which are determined for all nodes using the equilibrium equations (3.4) and (3.7).

3.4 Nonlinear equilibrium problem

We will extend the linear framework so far adopted and consider the impact of a variation of the lattice geometry on the equivalent moduli, and hence on the effective membrane behavior. We accordingly write down the non-linear equilibrium problem associated to the large perturbations of the network; the nonlinearity is due to the beam directors and beam lengths changing with the applied loading.

In order to set the stage, let consider the equilibriums equations (3.4) and (3.7). For every beam, one can write

$$b \in \mathbf{B}\,, \mathbf{B}^{b_o} = \mathbf{R}^{E_R(b)} - \mathbf{R}^{O_R(b)} + \frac{\partial \mathbf{R}^o}{\partial \lambda^{jb}} \delta^{jb},\ l^{b_o} = \left\| \mathbf{B}^{b_o} \right\| \text{and } \mathbf{e}^{b_o} = \frac{\mathbf{B}^{b_o}}{l^{b_o}}$$

For a given λ^{ε} and for each $\frac{\partial \mathbf{R}^o}{\partial \lambda^j} \delta^{jb}, j = 1,2,3,$ one can determine the quantities $\mathbf{B}^{b_o}, \mathbf{e}^{b_o}, N^{b_o}, T^{b_o}, M^{b_o}, b \in B,$ allowing to calculate the stress and the couple stress vectors S^{i_o} and μ^{i_o} resp. In other terms, this resolution has to be done for an imposed deformation gradient at the continuum level $\mathbf{G}^i$, for $b \in \mathbf{B}$, $\mathbf{B}^{b_o} = \mathbf{R}^{E_R(b)} - \mathbf{R}^{O_R(b)} + \mathbf{G}^i \delta^{jb}$

$l^b = \left\| \mathbf{B}^b \right\|$ and $\mathbf{e}^{b_o} = \frac{\mathbf{B}^{b_o}}{l^{b_o}}$ by considering N^b, T^b, M^b given by their expression in (3.3).

Since we are actually solving the nonlinear equilibrium equations over the deformed configuration, we have here introduced the non-linear map $\mathbf{G}^i$, which takes every material particle at the position $\mathbf{X}$ to its new position $\mathbf{x}$ in the current configuration $\mathbf{B}$.

By differentiating the equilibrium equations (3.2) and (3.5), the problem is solved with the well-known Newton-Raphson method, and can be written as follows. We introduce a projection operator $\mathbf{A} = \left[\mathbf{I} - \mathbf{e}^b \otimes \mathbf{e}^b \right], \mathbf{C} = \left[\mathbf{I} - \frac{1}{2} \mathbf{e}^b \otimes \mathbf{e}^b \right]$ with more detail in **Appendix B.2.1**., and the perturbation of the forces and moment's equation (3.4 and 3.7) writes

$$\begin{aligned}&\sum_{b\in B}\left(\delta N^{b(k)}\,\mathbf{e}^{b}+N^{b(k)}\,\delta\mathbf{e}^{b}\right).\Delta v+\sum_{b\in B}\left(N^{b(k)}\,\mathbf{e}^{b}\right).\Delta v+\\&\sum_{b\in B}\left(\delta T_t^{b(k)}\mathbf{e}^{b\perp}+T_t^{b(k)}\delta\mathbf{e}^{b\perp}\right).\Delta v+\sum_{b\in B}\left(T_t^{b(k)}\mathbf{e}^{b\perp}\right).\Delta v=0\end{aligned}\tag{3.20}$$

Similarly, the perturbation of the moment equilibrium (2.48) delivers

$$\begin{aligned}&\sum_{b\in B}\left(\delta M^{E(b)(k)}\mathbf{Y}_3.\Delta\underline{w}^{E(b)}+\delta M^{O(b)(k)}\mathbf{Y}_3.\Delta\underline{w}^{O(b)}\right)+\sum_{b\in B}\delta\left(B\wedge T_t^{b(k)}\,\mathbf{e}^{b\perp}\right).\Delta\underline{w}^{C(b)}+\\&\sum_{b\in B}\left(M^{E(b)(k)}\mathbf{Y}_3.\Delta\underline{w}^{E(b)}+M^{O(b)(k)}\mathbf{Y}_3.\Delta\underline{w}^{O(b)}\right)+\sum_{b\in B}\left(T_t^{b(k)}l^{b}\right)\mathbf{Y}_3.\Delta\underline{w}^{C(b)}=0\end{aligned}\tag{3.21}$$

In the two previous perturbed equations, the variation of the geometry is accounted for by the perturbed quantities, firstly the beam director

$$\delta\mathbf{e}^{b}=\frac{1}{l^{b}}\left(\mathbf{C}.\mathbf{A}\right).\delta\mathbf{B}\tag{3.22}$$

$$\delta\mathbf{e}^{b\perp}=\mathbf{\Omega}_Z.\delta\mathbf{e}^{b}\tag{3.23}$$

Introducing the orthogonal transformation

$$\mathbf{\Omega}_Z\left(\mathbf{e}^{b},\mathbf{e}^{b\perp},\mathbf{Y}_3\right)=\begin{bmatrix}\cos\left(\frac{\pi}{2}\right) & -\sin\left(\frac{\pi}{2}\right) & 0\\ \sin\left(\frac{\pi}{2}\right) & \cos\left(\frac{\pi}{2}\right) & 0\\ 0 & 0 & 1\end{bmatrix}\tag{3.24}$$

and

$$\delta\mathbf{e}^{b\perp}=\frac{1}{l^{b}}\mathbf{\Omega}_Z.\left(\mathbf{C}.\mathbf{A}\right).\delta\mathbf{B}\tag{3.25}$$

Secondly, the beam length variation is computed as

$$\begin{aligned}\delta l^{b}&=\delta\mathbf{B}.\mathbf{e}^{b}+\mathbf{B}.\delta\mathbf{e}^{b}\\&=\frac{\mathbf{B}}{l^{b}}.\left[\mathbf{I}+\mathbf{C}.\mathbf{A}\right].\delta\mathbf{B}\end{aligned}\tag{3.26}$$

Those variations induce in turn the following perturbations of the normal effort that have to be summed

$$\delta N^{bo}\,\mathbf{e}^{b}=\frac{EA_{b}}{L}\left[\left(\mathbf{e}^{b}\otimes\mathbf{e}^{b}\right)+\left(\frac{1}{l^{b}}\right)\left(\mathbf{e}^{b}\otimes\left(\mathbf{B}-\mathbf{B}_{o}\right)\right).\left(\mathbf{C}.\mathbf{P}\right)-\frac{\left(B-B_{o}\right).\mathbf{e}^{b}}{\left(l^{b}\right)^{2}}\left(\left(\mathbf{e}^{b}\otimes\mathbf{B}\right).\left[\mathrm{I}+\mathbf{C}.\mathbf{P}\right]\right)\right].\delta\mathbf{B} \tag{3.27}$$

$$N^{bo(k)}\,\delta\mathbf{e}^{b}=\left(\frac{N^{bo}}{l^{b}}\right)\mathbf{C}.\mathbf{P}.\delta\mathbf{B} \tag{3.28}$$

and of the transverse effort

$$\begin{aligned}\delta T^{t^{bo(k)}}\,\mathbf{e}^{b\perp}=&\left[\left(\frac{12EI_{z}}{\left(L\right)^{3}}\right)\left[\left(\left(\mathbf{e}^{b\perp}\otimes\mathbf{e}^{b\perp}\right)+\left(\frac{1}{l^{b}}\right)\left(\mathbf{e}^{b\perp}\otimes\left(\mathbf{B}-\mathbf{B}_{o}\right)\right).\left(\boldsymbol{\Omega}_{z}.\mathbf{C}.\mathbf{P}\right)-\right.\right.\right.\\&\left.\left.\left.\frac{\left(B-B_{o}\right).\mathbf{e}^{b\perp}}{\left(l^{b}\right)^{2}}\left(\left(\mathbf{e}^{b\perp}\otimes\mathbf{B}\right).\left[\mathrm{I}+\mathbf{C}.\mathbf{P}\right]\right)\right)\right]\right].\delta B\\&\left.-\left[\left(\frac{2T^{t^{bo(k)}}}{\left(l^{b}\right)^{2}}\right)\left(\left(\mathbf{e}^{b\perp}\otimes\mathbf{B}\right).\left[\mathrm{I}+\mathbf{C}.\mathbf{P}\right]\right)\right]\right]\\&+\left(\frac{-6EI_{z}}{\left(L\right)^{2}}\right)\left[\left(\mathbf{e}^{b\perp}\otimes\mathbf{Y}_{3}\right).\delta\Phi_{o}+\left(\mathbf{e}^{b\perp}\otimes\mathbf{Y}_{3}\right).\delta\Phi_{e}\right]\end{aligned}$$

$$T_{t}^{b}\,\delta\mathbf{e}^{b\perp}=\left(\frac{T_{t}}{l^{b}}\right)\left(\boldsymbol{\Omega}_{z}.\mathbf{C}.\mathbf{P}\right).\delta\mathbf{B} \tag{3.29}$$

By inserting equations (3.22-3.29) into the equilibrium relation (3.20), one obtains the following relation

$$
\begin{aligned}
&\sum_{b\in B}\left[\begin{array}{l}
\left[\begin{array}{l}
\left(\dfrac{EA}{L}\left[\begin{array}{l}\left(\mathbf{e}^b\otimes\mathbf{e}^b\right)+\left(\dfrac{1}{l^b}\right)\left(\mathbf{e}^b\otimes\left(\mathbf{B}-\mathbf{B}_o\right)\right).\left(\mathbf{C.P}.\delta\mathbf{B}\right)-\\ \dfrac{\left(\mathbf{B}-\mathbf{B}_o\right).\mathbf{e}^b}{\left(l^b\right)^2}\left(\left(\mathbf{e}^b\otimes\mathbf{B}\right).\left[\mathbf{I}+\mathbf{C.P}\right]\right)\end{array}\right]\right)+\\
\left(\dfrac{N^{bo}}{l^b}\right)\mathbf{C.P}
\end{array}\right]\\
\left[\begin{array}{l}
\left(\dfrac{12EI_z}{\left(L\right)^3}\right)\left[\left(\begin{array}{l}\left(\mathbf{e}^{b\perp}\otimes\mathbf{e}^{b\perp}\right)+\left(\dfrac{1}{l^b}\right)\left(\mathbf{e}^{b\perp}\otimes\left(\mathbf{B}-\mathbf{B}_o\right)\right).\left(\boldsymbol{\Omega}_z.\mathbf{C.P}\right)-\\ \dfrac{\left(\mathbf{B}-\mathbf{B}_o\right).\mathbf{e}^{b\perp}}{\left(l^b\right)^2}\left(\left(\mathbf{e}^{b\perp}\otimes\mathbf{B}\right).\left[\mathbf{I}+\mathbf{C.P}\right]\right)\end{array}\right)\right]\\
-\left[\left(\dfrac{2T^{t^{bo(k)}}}{\left(l^b\right)^2}\right)\left(\left(\mathbf{e}^{b\perp}\otimes\mathbf{B}\right).\left[\mathrm{I}+\mathbf{C.P}\right]\right)\right]\\
+\left(\dfrac{T_t}{l^b}\right)\left(\Omega_z.C.P\right)
\end{array}\right]
\end{array}\right].\delta\mathbf{B}.\Delta v\\
&+\sum_{b\in B}\left(\frac{-6EI_z}{\left(L\right)^2}\right)\left[\left(\mathbf{e}^{b\perp}\otimes\mathbf{Y}_3\right).\delta\Phi_o+\left(\mathbf{e}^{b\perp}\otimes\mathbf{Y}_3\right).\delta\Phi_e\right].\Delta v\\
&+\sum_{b\in B}\left(N^{bo(k)}\,\mathbf{e}^b\right).\Delta v+\sum_{b\in B}\left(T_t^b\mathbf{e}^{b\perp}\right).\Delta v=0
\end{aligned}
\tag{3.30}
$$

Similarly, the perturbation of the moment equilibrium equation writes:

$$
\begin{aligned}
&\sum_{b\in B}\left(\frac{EI_z}{l^b}\right)\left[-\left(\mathbf{Y}_3\otimes\mathbf{Y}_3\right).\delta\Phi_o+\left(\mathbf{Y}_3\otimes\mathbf{Y}_3\right).\delta\Phi_e\right].\Delta w^{E(b)}+\\
&\sum_{b\in B}\left(\frac{EI_z}{l^b}\right)\left[\left(\mathbf{Y}_3\otimes\mathbf{Y}_3\right).\delta\Phi_o-\left(\mathbf{Y}_3\otimes\mathbf{Y}_3\right).\delta\Phi_e\right].\Delta w^{O(b)}+\\
&\sum_{b\in B}\left(M^{E(b)_0(k)}\mathbf{Y}_3.\Delta w^{E(b)}+M^{O(b)_0(k)}\mathbf{Y}_3.\Delta w^{O(b)}\right)+\sum_{b\in B}\left(T^{t^{bo(k)}}l^b\right)\mathbf{Y}_3.\Delta w^{C(b)}=0
\end{aligned}
\tag{3.31}
$$

We observe that the perturbation of the normal force encapsulated into equations (3.27) and (3.28) leads to identify three types of stiffness matrices: the linear stiffness, the initial displacement stiffness, and the contribution of the initial stress as discussed in **Appendix A.6.1**. in equation (A.31), respectively the matrices:

$$\mathbf{K}_o = \frac{EA_b}{L}\left(\mathbf{e}^b \otimes \mathbf{e}^b\right),$$

$$\mathbf{K}_u = \frac{EA_b}{L}\left[\left(\frac{1}{l^b}\right)\left(\mathbf{e}^b \otimes \left(\mathbf{B}-\mathbf{B}_o\right)\right).\left(\mathbf{C.P}\right) - \frac{\left(\mathbf{B}-\mathbf{B}_o\right).\mathbf{e}^b}{\left(l^b\right)^2}\left(\left(\mathbf{e}^b \otimes \mathbf{B}\right).\left[\mathbf{I}+\mathbf{C.P}\right]\right)\right]$$

$$\mathbf{K}_\sigma = \left(\frac{N^{bo}}{l^b}\right)\mathbf{C.P}$$

Thus, the constitutive law can be rearranged in matrix form as,

$$\begin{bmatrix}\Delta v, \Delta w^{O(b)}, \Delta w^{E(b)}\end{bmatrix}\begin{bmatrix} \begin{pmatrix}\begin{bmatrix}\left(\frac{EA}{L}\left[\left(\mathbf{e}^b \otimes \mathbf{e}^b\right)+\left(\frac{1}{l^b}\right)\left(\mathbf{e}^b \otimes \left(\mathbf{B}-\mathbf{B}_o\right)\right).\left(\mathbf{C.P}.\delta\mathbf{B}\right)\right]\right)+ \\ \left(\frac{N^{bo}}{l^b}\right)\mathbf{C.P}\end{bmatrix}+ \\ \begin{bmatrix}\left(\frac{12EI_z}{(L)^3}\right)\left[\left(\left(\mathbf{e}^{b\perp} \otimes \mathbf{e}^{b\perp}\right)+\left(\frac{1}{l^b}\right)\left(\mathbf{e}^{b\perp} \otimes \left(\mathbf{B}-\mathbf{B}_o\right)\right).\left(\mathbf{\Omega}_z.\mathbf{C.P}\right)\right)\right] \\ +\left(\frac{T_t}{l^b}\right)\left(\mathbf{\Omega}_z.\mathbf{C.P}\right)\end{bmatrix}\end{pmatrix} & \left(\left(\frac{-6EI_z}{(L)^2}\right)\left(\mathbf{e}^{b\perp} \otimes \mathbf{Y}_3\right)\right) & \left(\left(\frac{-6EI_z}{(L)^2}\right)\left(\mathbf{e}^{b\perp} \otimes \mathbf{Y}_3\right)\right) \\ 0 & \left(\frac{EI_z}{l^b}\right)\left(\mathbf{Y}_3 \otimes \mathbf{Y}_3\right) & -\left(\frac{EI_z}{l^b}\right)\left(\mathbf{Y}_3 \otimes \mathbf{Y}_3\right) \\ 0 & -\left(\frac{EI_z}{l^b}\right)\left(\mathbf{Y}_3 \otimes \mathbf{Y}_3\right) & \left(\frac{EI_z}{l^b}\right)\left(\mathbf{Y}_3 \otimes \mathbf{Y}_3\right) \end{bmatrix}\begin{bmatrix}\delta\mathbf{B} \\ \delta\Phi_o \\ \delta\Phi_e\end{bmatrix}$$

$$+\begin{bmatrix}\Delta v, \Delta w^{O(b)}, \Delta w^{E(b)}\end{bmatrix}\begin{bmatrix} N^b\mathbf{e}^b + \left(T_t^b\mathbf{e}^{b\perp}\right) \\ \left(\frac{T^{t^{bo(k)}}l^b}{2}\right)\mathbf{Y}_3 + M^O\mathbf{Y}_3 \\ \left(\frac{T^{t^{bo(k)}}l^b}{2}\right)\mathbf{Y}_3 + M^E\mathbf{Y}_3 \end{bmatrix} = 0$$

Equations (3.30) and (3.31) provide the perturbed problem to be solved by an iterative Newton-Raphson technique. Let notify that this problem has a solution up to within a rigid body translation (and rotation); thus one has to fix at least one node of the structure to prevent the tangent stiffness matrix from becoming singular.

The solution of the localization problem at the unit cell scale involves the set of unknown variables $\mathbf{B}^{b(k+1)} = \mathbf{B}^{b(k)} + \delta\mathbf{B}^{b(k)}$ of the system formed by equations (3.30) and (3.31); its solution

provides the non-linear constitutive law of the unit cell. It can be considered as the (nonlinear) localization problem at the reference cell level. It has to be combined with the homogenization step of the network, based on the expression of the Cauchy stress and couple stress versus the actualized network topology at each loading increment. The main steps of the algorithm are given below in the next section.

A few comments related to the geometrical nonlinearities are in order: in the 1D situation in **Appendix A.6.2**., Table A.2 has shown that the contribution of the initial orientation of the beams has more impact on the overall response than the second order part of the strain. This means when extending this analysis for 2D lattices that we are also entitled to neglect the second order part of the strain when writing the expressions of the resultant and moments for the beams within any lattice. Based on the updated Lagrangian formulation in solving for the equilibriums, one is also entitled to neglect the initial displacement stiffness $\mathbf{K}_u$.

3.4.1 Illustrations of the algorithm based on the homogenization method

We extend the linear discrete asymptotic homogenization framework, relying on the idea of an update of lattice geometry, from which a linearized elastic computation will be done over one load increment.

A dedicated code has been constructed from the proposed algorithm to be exposed in the sequel, to solve for the nodal kinematical unknowns (displacements and microrotations) of each beam within the repetitive unit cell. The code uses an input file including the initial reference unit cell topology and mechanical properties, and delivering as an output the homogenized mechanical properties (classical and micropolar moduli) and stress-strain response over the load incremental change, and for a given elementary loading type.

In this work, we rely on the homogenization method based on the small perturbations framework, and use an alternative approach to the solution of the full incremental problem written previously: at each incremental computation, the expression of the constitutive law that relates stress to strain and involving the computed compliance matrix is used in order to determine the correct macroscopic displacement gradient that defines the controlled imposed strain loading over the unit cell. Thus, it provides the correct macroscopic boundary condition that are applied for each type of loading; this is a kind of inverse approach in comparison to what is done in Table 2.2, in which the external force is known and the unknown displacement is evaluated by solving a nonlinear equation. Note that in the present approach, we shall only consider the linear part of the strain (and neglect the second order quadratic contribution).

Based on this computation of the macroscopic kinematic boundary condition, one then updates the lattice geometry for each increment of the loading and one next determines the new homogenized rigidity matrix adapted to the new shape of the structure. We thus extract the equivalent homogenized mechanical properties at each load increment, up to the elastic limit as a material parameter that is specified for each structure topology. Such an evidence of the existence of an elastic limit will be discussed later on.

More details for this inverse methodology are discussed in **Appendix B.2.4.**

The algorithm that performs new elastic computation over one load increment and with an update of the lattice geometry is described next.

3.5 Algorithm for the discrete homogenization in a 2D framework

1. Initialization of the tables of initial data. For each beam, define beam length and director, and position vector, function **R** such that $\mathbf{x}=\mathbf{R}(\lambda^1,\lambda^2,\lambda^3)$

2. Transformation of the expressions

$$\left(\frac{\partial \mathbf{U}}{\partial \lambda_i}\right)_{(\mathrm{Y}_1,\mathrm{Y}_2,\mathrm{Y}_3)} \mapsto \left(\frac{\partial \mathbf{U}}{\partial \lambda_i}\right)_{(\mathrm{e}_x,\mathrm{e}_y,\mathrm{e}_z)} \text{ and } \left(\frac{\partial \phi}{\partial \lambda_i}\right)_{(\mathrm{Y}_1,\mathrm{Y}_2,\mathrm{Y}_3)} \mapsto \left(\frac{\partial \phi}{\partial \lambda_i}\right)_{(\mathrm{e}_x,\mathrm{e}_y,\mathrm{e}_z)}.$$

3. For each beam $b\in \mathbf{B}_R$, define the initial topology in terms of:

(a) The origin and end node of a beam respectively, $O=O_R(b),\ E=E_R(b)$.

(b) Express the displacement difference between extremity and origin node at first order: $\Delta\mathbf{U}_1^b=\mathbf{u}_1^E-\mathbf{u}_1^O+\frac{\partial \mathbf{U}}{\partial \lambda^i}\delta^i$, tensile rigidity: $k_l=\frac{A^bE_s^b}{L^b}$, flexural rigidity: $k_f=\frac{12E_s^bI_z^b}{\left(L^b\right)^3}$

(c) Express the first order efforts:

$$N=k_l\left(\mathbf{e}^b.\left(\Delta\mathbf{U}_1^{\mathrm{b}}\right)\right),$$

$$T_t=k_f\left(\mathbf{e}^{b\perp}.\left(\Delta\mathbf{U}_1^{\mathrm{b}}\right)-\frac{L^b}{2}\left(\mathbf{Y}_3.\left(\phi_0^O+\phi_0^E\right)\right)\right).$$

(d) Express the first order moments:

$$M_1^O=k_f\frac{L^b}{12}\left(6\mathbf{Y}_3.\left(\Delta\mathrm{U}_1^{\mathrm{b}}\right)+L^b\left(\mathbf{e}^{b\perp}.\left((4+\Phi_z)\phi_0^O+(2-\Phi_z)\phi_0^E\right)\right)\right),$$

$$M_1^E=k_f\frac{L^b}{12}\left(6\mathbf{Y}_3.\left(\Delta\mathbf{U}_1^{\mathrm{b}}\right)+L^b\left(\mathbf{e}^{b\perp}.\left((2-\Phi_z)\phi_0^O+(4+\Phi_z)\phi_0^E\right)\right)\right),$$

4. Calculate the unknowns displacement and rotation u_1^n and ϕ_0^n from (3.4) and (3.7).

5. Identify the homogenized microrotation.

6. Express the second order forces and moments as:

(a) $\Delta\mathbf{U}_2^b=\mathbf{u}_2^E-\mathbf{u}_2^O$ (b) $N_2=k_l\left(\mathbf{e}^b.\left(\Delta\mathbf{U}_2^{\mathrm{b}}\right)\right), T_{t2}=k_f\left(\mathbf{e}^{b\perp}.\left(\Delta\mathbf{U}_2^{\mathrm{b}}\right)-\frac{L^b}{2}\left(\mathbf{Y}_3.\left(\phi_1^O+\phi_1^E+\frac{\partial\phi}{\partial\lambda^i}\delta^i\right)\right)\right),.$

(c) $M_{2y}^{O}=k_f\frac{L^b}{12}\left(6\mathbf{e}_z\cdot\left(\Delta \mathrm{U}_2^{\mathrm{b}}\right)+L^b\left(\mathbf{e}_y\cdot\left((4+\Phi_z)\phi_1^{O}+(2-\Phi_z)\phi_1^{E}+(2-\Phi_z)\frac{\partial\phi}{\partial\lambda^i}\delta^i\right)\right)\right)$,

$M_{2}^{E}=k_f\frac{L^b}{12}\left(6\mathbf{e}_z\cdot\left(\Delta \mathrm{U}_2^{\mathrm{b}}\right)+L^b\left(\mathbf{e}_y\cdot\left((2-\Phi_z)\phi_1^{O}+(4+\Phi_z)\phi_1^{E}+(4+\Phi_z)\frac{\partial\phi}{\partial\lambda^i}\delta^i\right)\right)\right)$,

Solve for variables u_2^n and ϕ_1^n from (10) and (15).

7. Construct the stress and couple stress vectors,

$$\mathbf{S}^{\mathrm{i}}=\sum_{b\in B_R}\left(F_{x1}^b\mathbf{e}^b+F_{y1}^b\mathbf{e}^{b\perp}\right)\delta^i \text{ and } \mu^{\mathrm{i}}=\sum_{b\in B_R}\left(\frac{1}{2}\left(M_2^{E(b)}-M_2^{O(b)}\right)\mathbf{Y}_3\right)\delta^i$$

respectively.

8. Construct the stress tensor $\boldsymbol{\sigma}=\frac{1}{g}\mathbf{S}^{\mathrm{i}}\otimes\frac{\partial\mathbf{R}}{\partial\lambda^{\mathrm{i}}}$ and couple stress tensor $\mathbf{m}=\frac{1}{g}\boldsymbol{\mu}^{\mathrm{i}}\otimes\frac{\partial\mathbf{R}}{\partial\lambda^{\mathrm{i}}}$, such that

$$\begin{Bmatrix}\boldsymbol{\sigma}\\ \mathbf{m}\end{Bmatrix}=\begin{bmatrix}\mathbf{K}^s & 0\\ 0 & \mathbf{K}^{\mu}\end{bmatrix}\begin{Bmatrix}\epsilon\\ \chi\end{Bmatrix}.$$

9. Compute the effective mechanical properties $E_x^*,E_y^*,\nu_{xy}^*,G_{xy}^*,K_{55}^{\mu},K_{66}^{\mu}$ under this load increment.

10. Compute the incremental stress value versus the incremental strain with respect to the load case.

11. Solve the inverse problem gives the equivalent appropriate macroscopic displacement consistent with chosen load case.

11. Update lattice geometry to perform a new elastic computation under the new load increment (With a selected step size)

3.6 Homogenization examples and results

We shall consider as an application biological membranes, which can be idealized as quasi periodical networks of filaments in initially planar configurations. As we shall see into more details in section 3.7 of this chapter, these biomembranes can be classified based on the network connectivity. Anticipating forthcoming more detailed analyses of these biomembranes, we presently analyze the following networks: a) The square lattice b) The hexagonal lattice, in order to express the stress-strain behaviour for the following three types of loading:

A) Uniaxial load test.
B) Biaxial load test.
C) Simple shear test.

The deformation gradients for these three loadings are successively:

$$ {}^{A}\mathbf{F} = \begin{bmatrix} \lambda & 0 \\ 0 & \text{unprescribed} \end{bmatrix}, \quad {}^{B}\mathbf{F} = \begin{bmatrix} \lambda & 0 \\ 0 & \lambda \end{bmatrix}, \quad {}^{C}\mathbf{F} = \begin{bmatrix} 1 & \Gamma \\ 0 & 1 \end{bmatrix} \tag{3.32} $$

The following geometrical parameters and material properties for the chosen lattices are specified in Table 2.3 the elasticity domain of the overall lattice depends on the lattice material and geometrical parameters which determines the type of microstructure. The chosen parameters allow observing the nonlinear path in the small strain range (which is different to the infinitesimal domain).

Table 3.1 Specification of lattice geometry and micromechanical properties

Type	Geometric parameter of repeated unit cell [mm]	Material parameter [Mpa]
Square	$L_1 = L_2 = L = 20,\ t = 2$	$E_s = 2000$
Hexagonal	$L_1 = L_2 = L_3 = L = 20,\ t = 2$	$E_s = 2000$

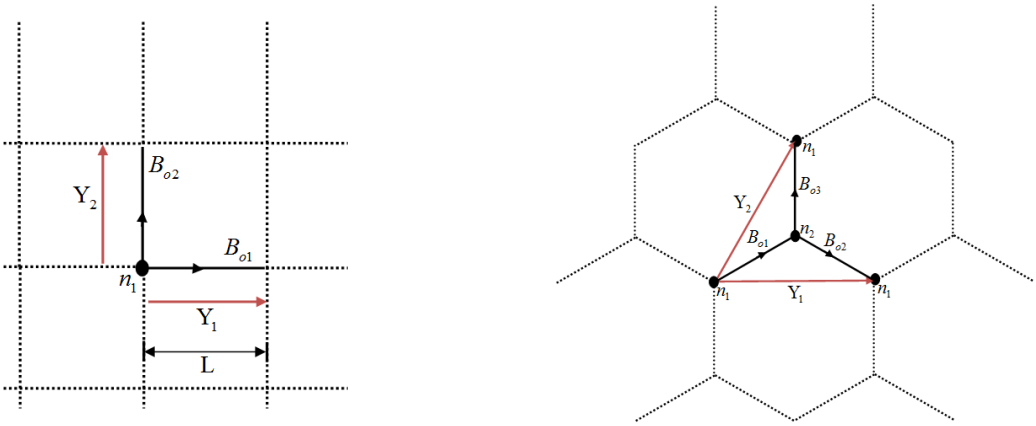

Fig. 3.3 Planar structures. Unit cells of the square lattice (left) and hexagonal lattice (right).

Plots of Cauchy's stress versus relative stretch are presented for the previous loadings as the result of a numerical analysis performed in combined symbolic and numeric language, using a dedicated Maple code. These plots are compared with the results of a linear analysis (the geometry is not updated) shown by dashed lines on those figures.

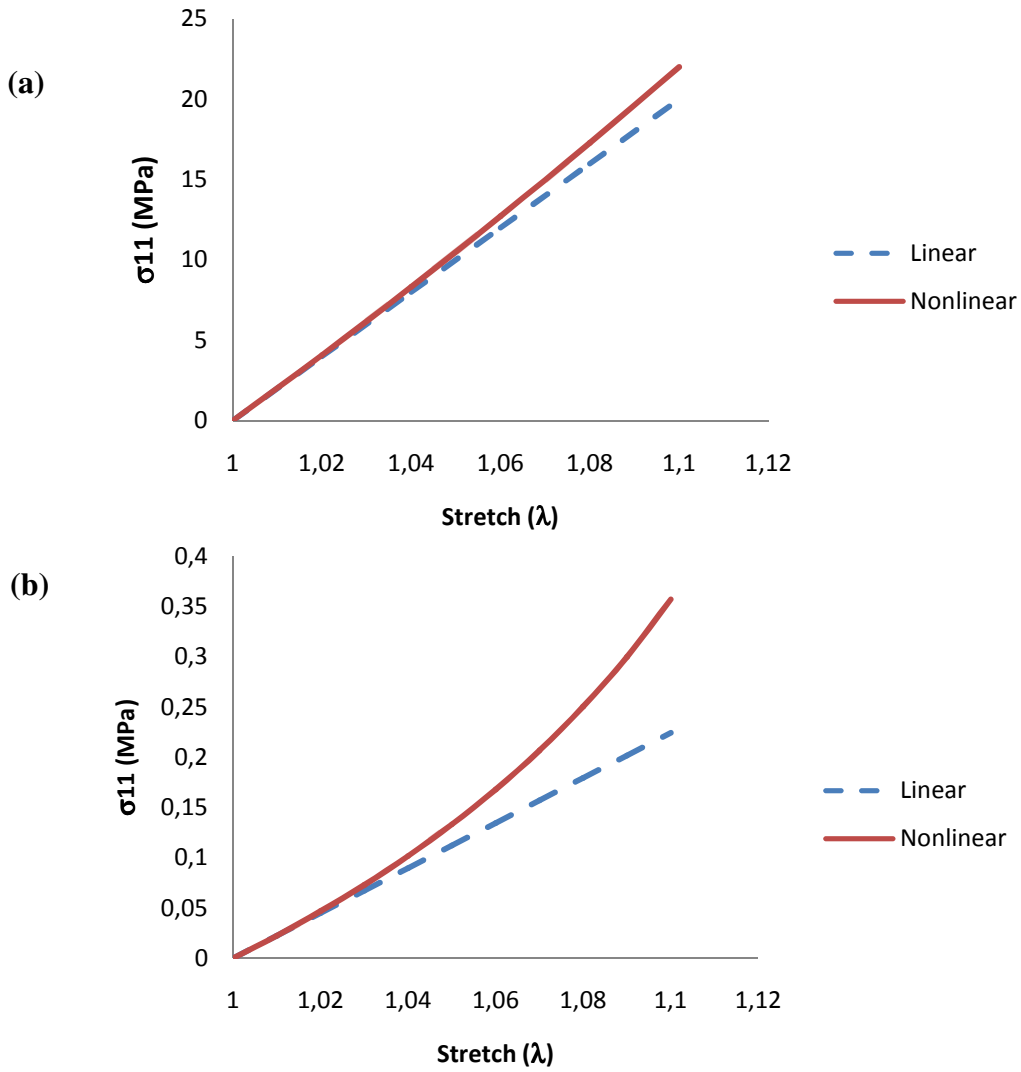

Fig. 3.4 Uniaxial tensile Cauchy stress σ_x versus the applied stretch λ, for two chosen planar lattices (square in a, hexagonal in b).

In the tensile loading test shown in Figure 3.4, we observe that the difference between the linear and geometrical nonlinear behaviours depends on the type of microstructure and its orientation with respect to the load direction. The square lattice is a relatively stiff structure, and the difference between geometrical nonlinear and linear behaviour is not significant; this can be explained by the fact that the beams will not rotate during extension, thus the square lattice responds in a quasi linear manner. This is also due to the fact that the beams do not present an initial inclination, a parameter which has been shown to strongly influence the response in 1D (as shown in previous Table 3.1).

Contrary to this, the hexagonal lattice responds as a compliant structure, since the bending of the microstructural beams dominate, even under a pure uniaxial tension. Thus, a neat difference in the response between the two lattices is observed. In this second situation, the inclined beams of

the hexagonal unit cell are responsible for the observed geometrical nonlinear effects (see Table A.2 for a similar analysis in 1D).

Figure 3.5 (a) show that hexagonal lattice is initially isotropic; it is evolving towards an anisotropic behaviour versus stretch. Figure 3.5 (b) shows the ratio between the mechanical moduli in both directions.

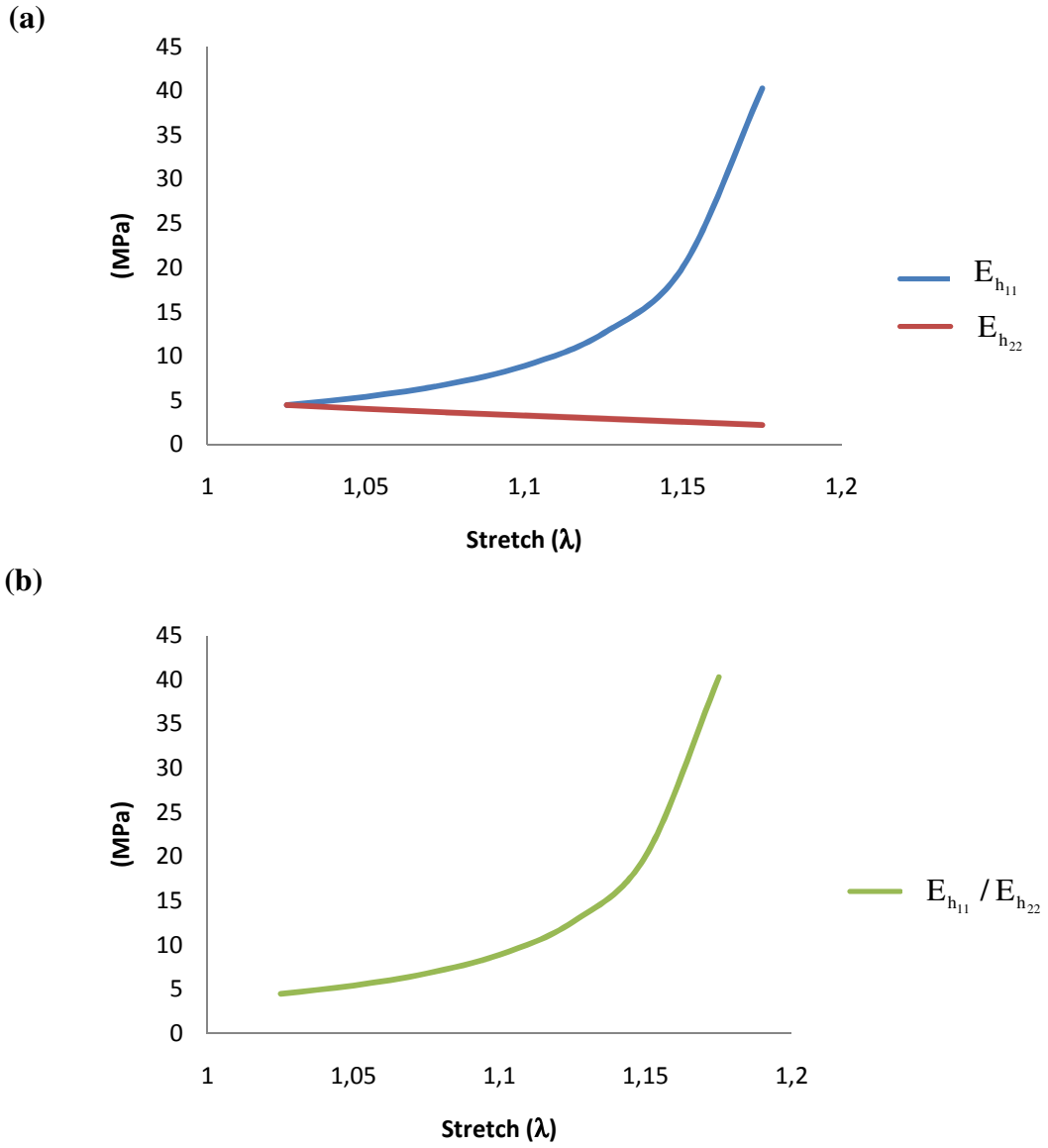

Fig. 3.5 homogenized mechanical parameters for hexagonal lattice (a) tensile moduli $E_{h_{11}}, E_{h_{22}}$ (b) homogenized tensile ratio $E_{h_{11}} / E_{h_{22}}$.

For the biaxial load test case B), the results are presented in Figure 3.6 for the two types of microstructures (lattices) under an equibiaxial loading, both leading to a nearly linear response.

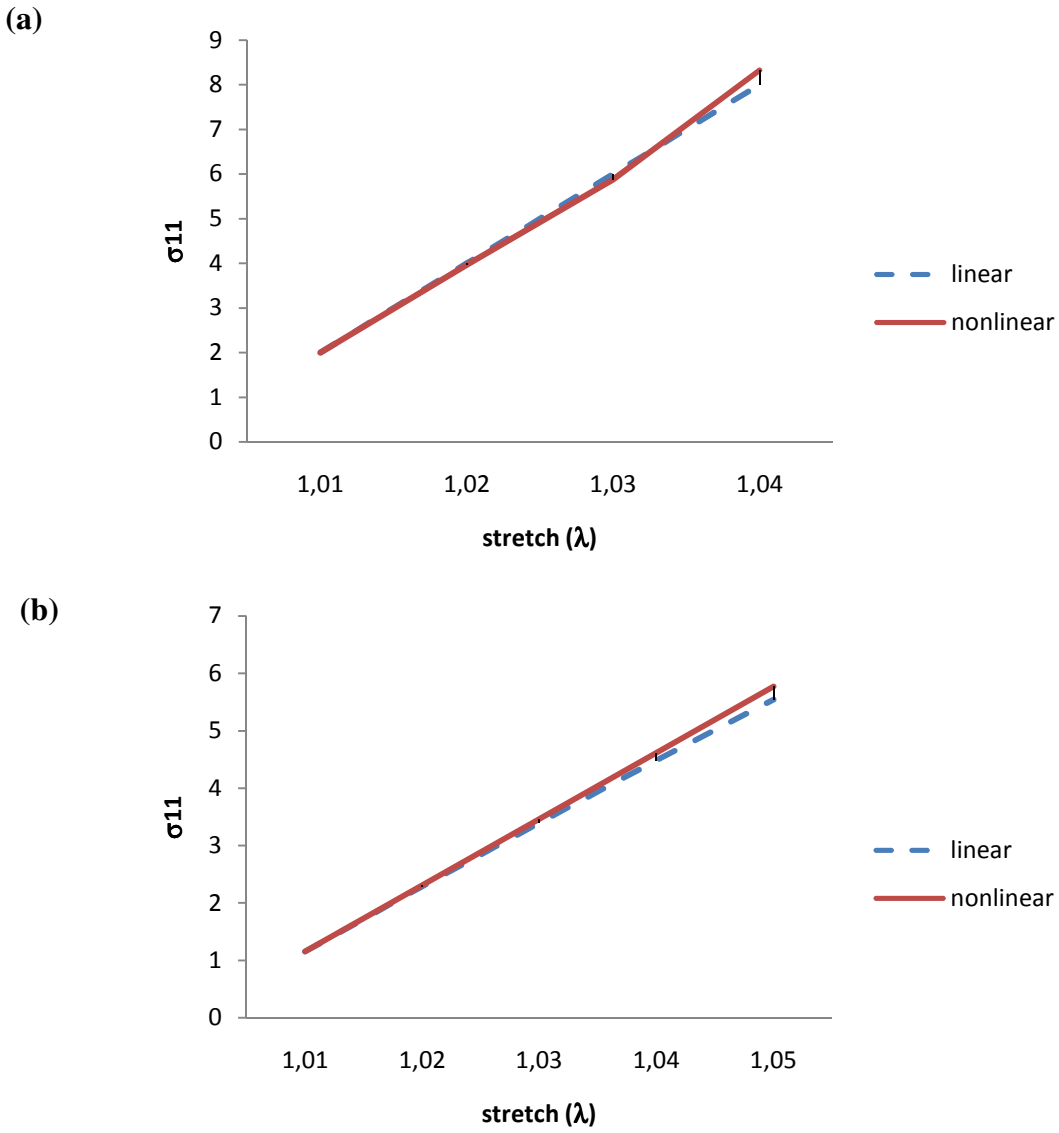

Fig. 3.6 Biaxial tensile Cauchy stress σ_1 versus the applied stretch λ for the chosen planar lattices (a, b).

This behaviour can be explained in this specific loading case by the fact that the beam orientation does not play an important role (but it would for a general non equibiaxial loading situation).

For the simple shear loading test referred to as case C), plots of the shear stress versus the shear angle show an important difference between the linear and geometrical nonlinear analysis, as pictured in fig. 3.7. This nonlinearity can be explained by the same reasons as before.

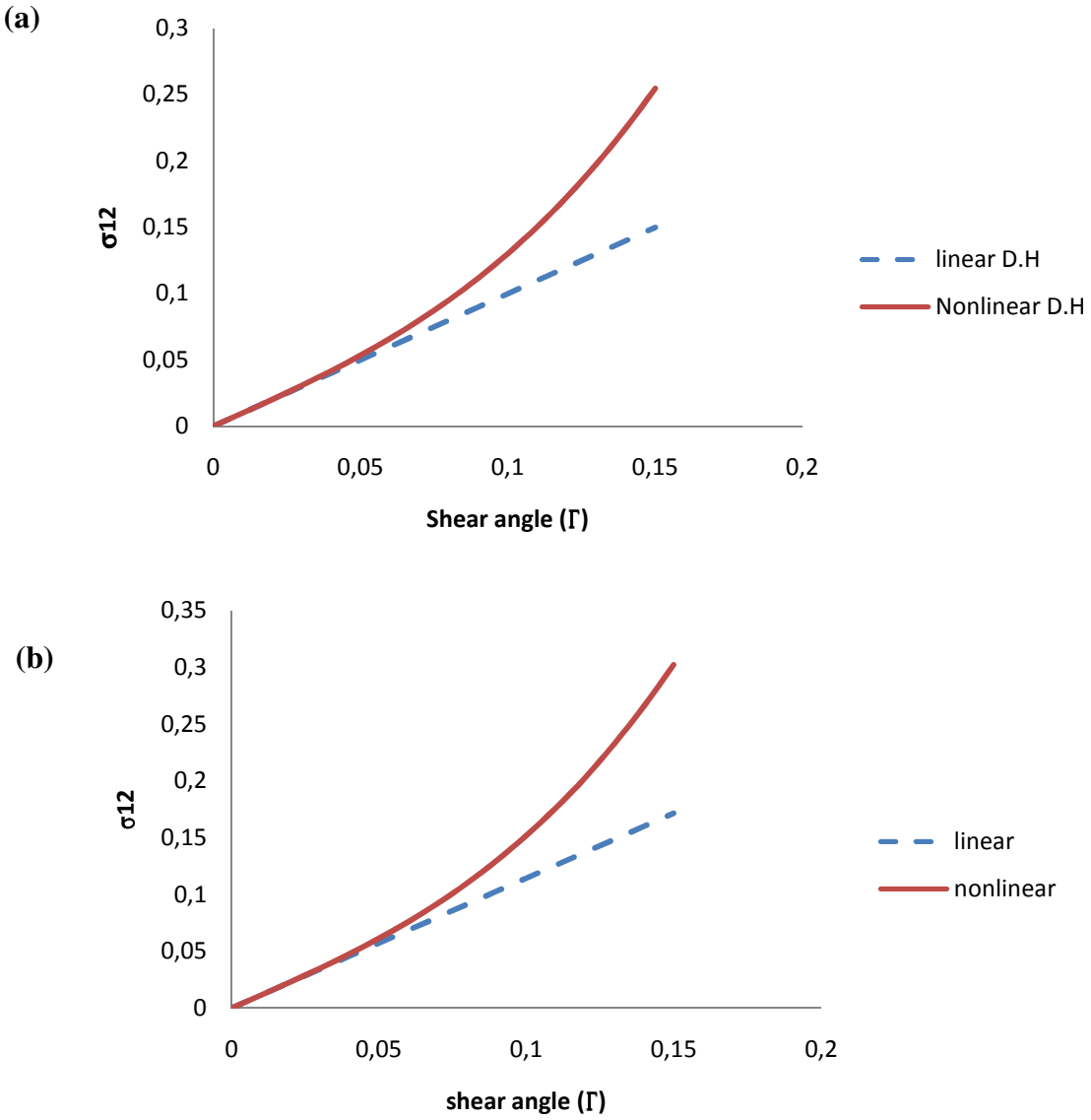

Fig. 3.7 Nonlinear response for the shear stress versus shear angle compared with linear predictions (dashed line)

Moreover, let consider the simple shear test for the Hexagonal lattice, in which nodal displacements and microrotations are considered as two independent degrees of freedom. The computed shear response for the micropolar continuum is compared (fig. 3.8) with the ones obtained for the classical Cauchy continuum (no microrotation) in both the geometrically linear and nonlinear settings.

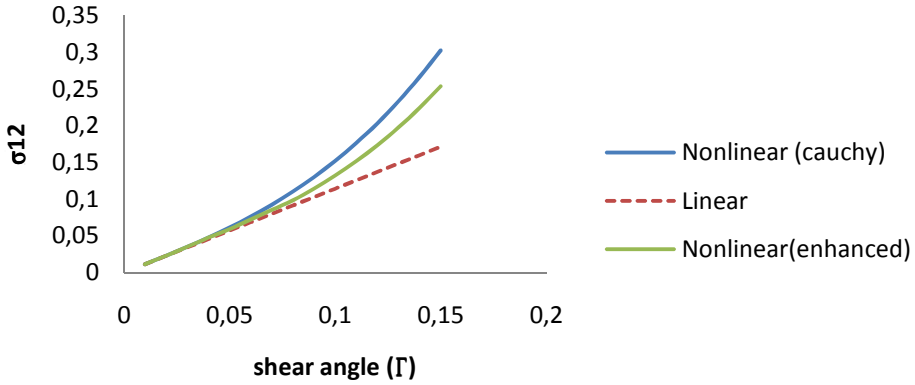

Fig. 3.8 Nonlinear path for shearing stress versus shear angle is compared with linear predictions (dashed line)

We note a softer response for the micropolar effective continuum in comparison to the two other effective media, due to the enhanced kinematics: part of the energy is distributed into both the displacement gradient and microrotation as far as the kinematics is concerned.

3.6.1 Effect of the slenderness ratio in elastic limit

For the hexagonal lattice, the effective homogenized tensile modulus under a uniaxial load test is plotted versus stretch, for different values of the slenderness parameter (η - ratio of beam thickness to beam length). We observe that the effective computed tensile modulus increases and reaches a maximum, followed by a decrease when the slenderness ratio is small enough, indicating a softening behaviour thereafter, related to the loss of ellipticity of the boundary value problem for the homogenized behaviour. An increase of (η) enhances the structure stability as shown in figure 3.9; the systematic detection of such instable behaviours can be implemented in future work, based on the eigenvalues of the acoustic tensor.

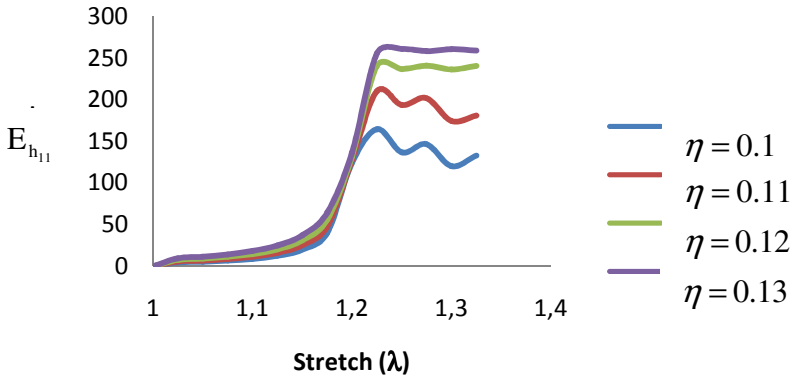

Fig. 3.9 Effective Young modulus in one direction versus stretch at different values of slenderness parameter

We next consider the following example of an arterial tissue modeled as a 2D planar sheet with a chosen configuration angle $\beta = 60°$ between the two families of fibers (G. A. Holzapfel, 2000). The lattice consists of inclined repeated inclined unit cells, described by two beams and two periodicity vectors $\mathbf{Y_1}, \mathbf{Y_2}$, as shown in figure 3.10 (a, b, c) respectively. The geometrical and material parameters for the beams within the unit cell are chosen as previously from Table 2.3.

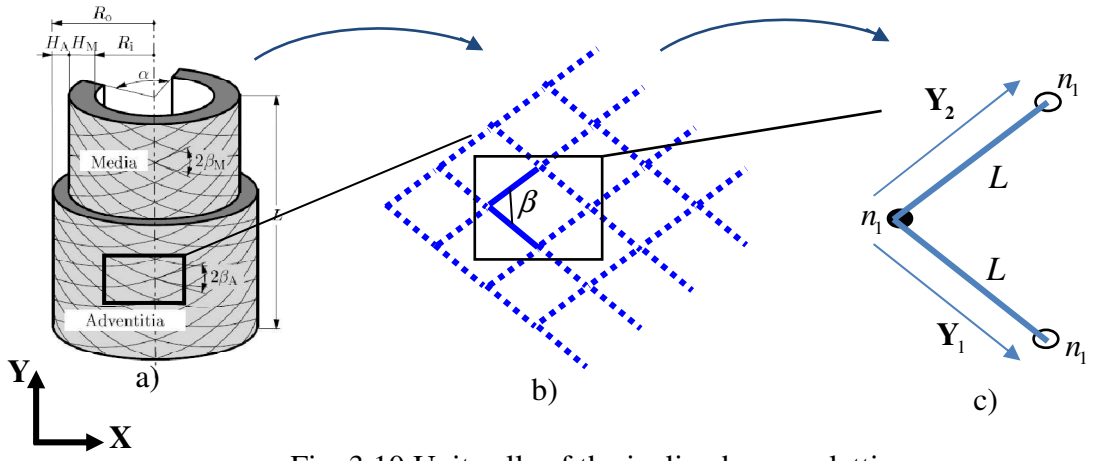

Fig. 3.10 Unit cells of the inclined square lattice

In the same manner, we perform the homogenization of this network to express the stress-strain behaviour for the previous three types of loading.

- **Uniaxial tension**

Plot of Cauchy stress versus the relative stretch are presented for the uniaxial loading test. One may observe a great difference between the linear (dashed line) and nonlinear response. This can be explained by the fact that the type of microstructure and its orientation give complaint structure for which bending of microstructural beams dominates as a deformation mode, as shown in figure 3.11.

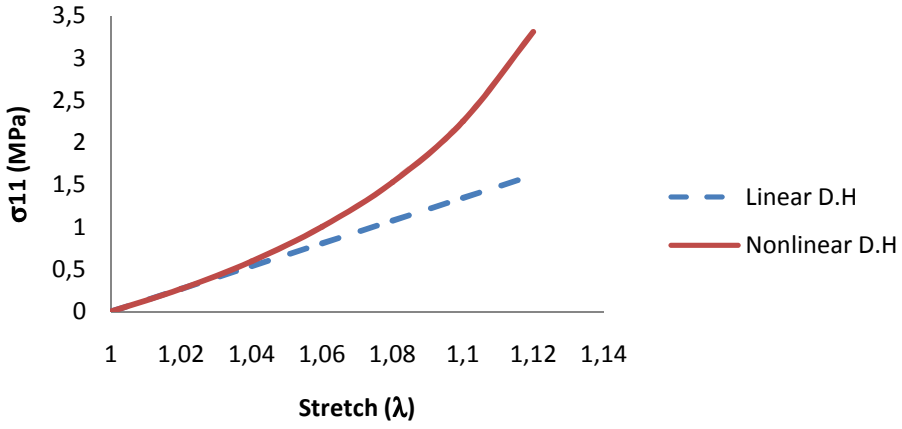

Fig. 3.11 Uniaxial tensile Cauchy stress σ_x versus the applied stretch λ, for the inclined square($\beta = 60°$).

- **Biaxial tension**

The stress-stain responses are represented in two directions (Figure 3.12) under an equibiaxial loading, both leading to a nearly linear response. This behaviour can be explained in this specific loading case by the fact that the beam orientation does not play an important role (but it would for a general non equibiaxial loading situation). Thus, let consider non equibiaxial loading test

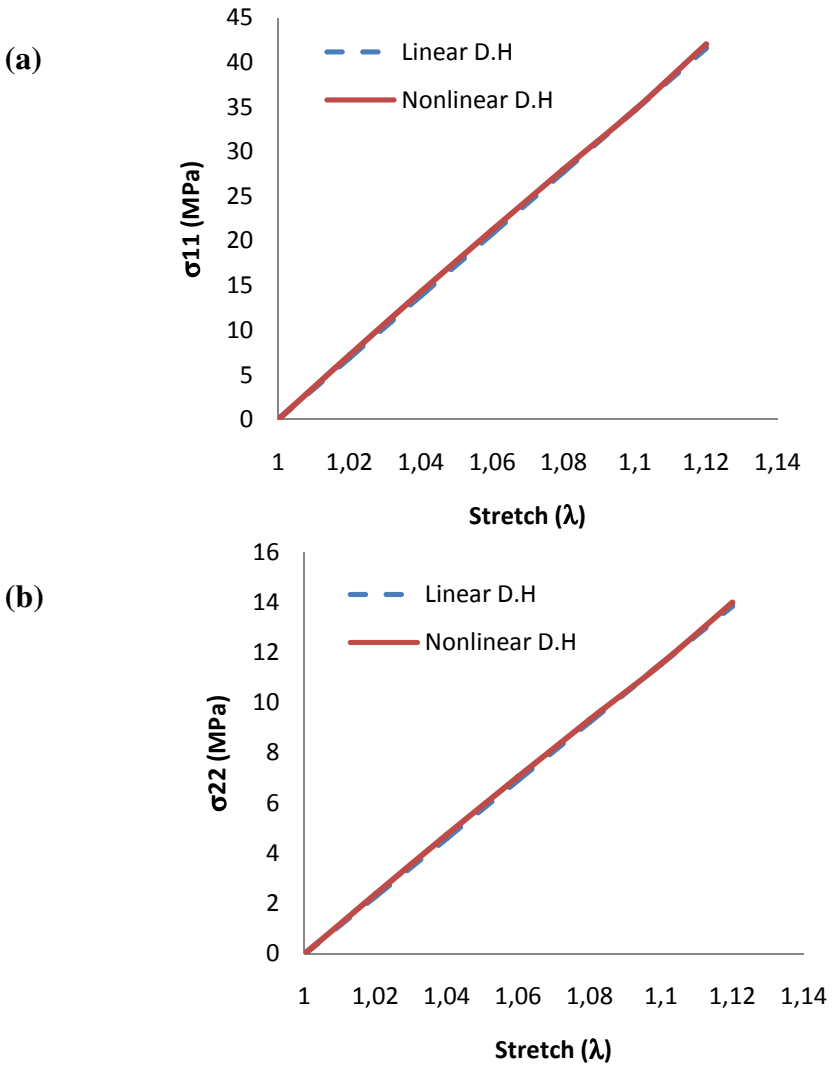

Fig. 3.12 Equibiaxial tensile Cauchy stress of (a) xx- direction and (b) yy-direction versus the applied stretch λ

.

Moreover, let consider non equibiaxial loading test elaborated with strain ratio $k = \frac{\varepsilon_2}{\varepsilon_1} = 3$ where ε_1 is the primary strain corresponding to x-axis, and ε_2 is the secondary strain corresponding to the y-axis. According to this condition one shall expect that the beam orientation will change versus stretch.Fig.3.13 shows: there is a softening in one direction (and conversely a hardening in transvers direction).

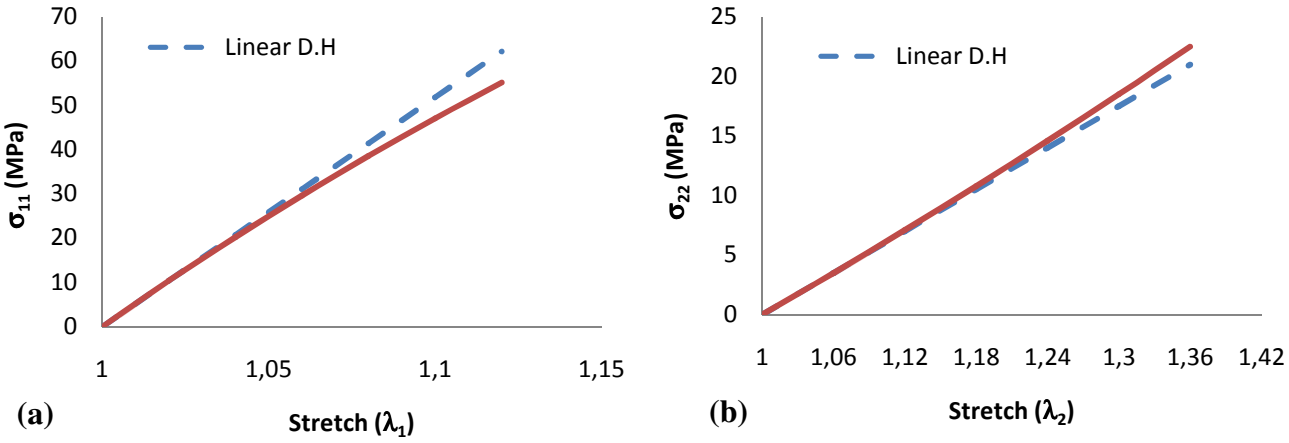

Fig. 3.13 Cauchy stress versus strain for biaxial strain ratio, k = 3. (a) xx- direction and (b) yy-direction.

- **Simple shear**

In the same manner, the response of the inclined square lattice subjected to simple shear is shown in Fig. 3.14: we note that there is no significant difference between the linear and geometrical nonlinear analysis. This quasi linearity is due to the fact that the fibbers locally experience a state of stress which is nearly uniaxial since the principal directions of stress are rotated by 45 degrees w.r.t the direction of shear.

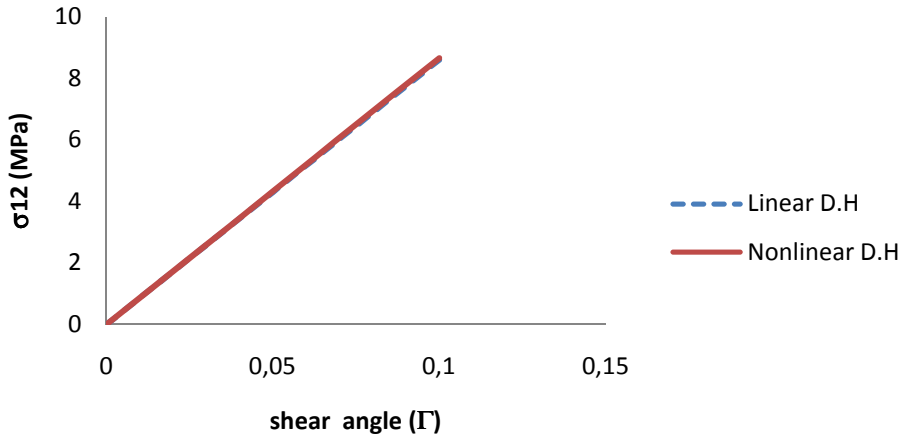

Fig. 3.14 Nonlinear response for the shear stress versus shear angle compared with linear predictions (dashed line)

We next compute the nonlinear response of biological membranes selected as an application of previous general nonlinear homogenization scheme. These membranes are here viewed as regular periodical networks of filaments, and they may be highly anisotropic due to unequal length and properties of the threads within the molecular network as will discussed below.

3.7 Two-dimensional biological networks

The membrane of biological cells is made of the assembly of filaments which are linked together as part of a network or are associated with the cell membrane to build a two dimensional thin sheet. Two-dimensional biological networks may be wrapped around a cell as its wall or are attached to its plasma or nuclear membrane. Membranes containing neither a nucleus nor other cytoskeletal components such as microtubules, for example the human red blood cell or the cortical lattice of an auditory outer hair cell Fig.3.15 (a, b) respectively, possess only a membrane associated cytoskeleton.

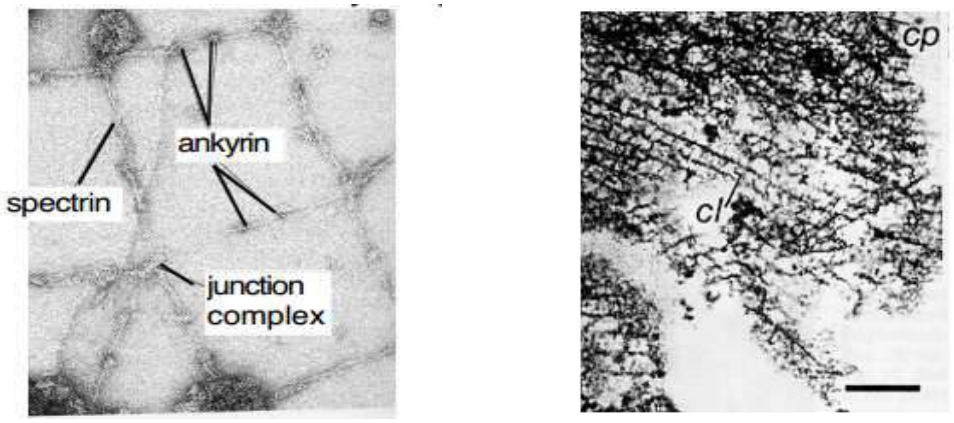

Fig. 3.15 (a) Membrane-associated cytoskeleton of the human erythrocyte (Byers and Branton, 1995). (b) Section from the cortical lattice of an auditory outer hair cell.

The boundary structure of bacteria can be classified in two ways. First, for the Gram-negative bacterium, there is a very thin peptidoglycan sandwiched between two membranes, while for the Gram-positive bacteria, one bilayer is present. The peptidoglycan blanket is much thicker, as shown in Fig.3.16 (a,b) respectively.

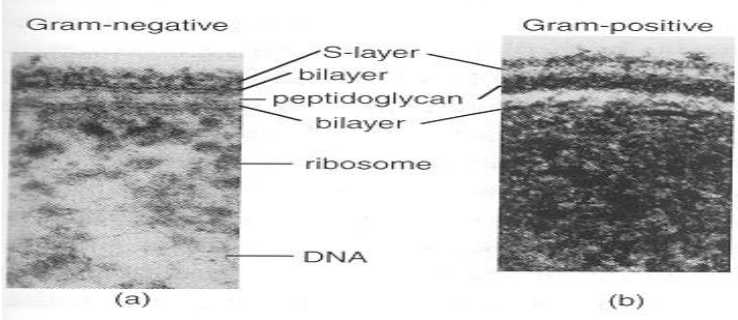

Figure 3.16 Boundary structure of bacteria (D. Boal, Mechanics of the cell, 2002)

3.7.1 Classifications of networks with three, four and sixfold connectivity

One shall presently classify the networks of biomembranes according to their connectivity: three fold, four fold and six fold connectivity. These networks are found in many cell structures, including the bacterial cell wall, the nuclear lamina and the membrane-associated cytoskeleton of mammalian erythrocytes. In biological membranes, the most encountered types of networks are the hexagonal, the square and the triangular networks respectively corresponding to a connectivity of 3, 4, 6 respectively. For example, the peptidoglycan network of the bacterial cell wall has T-shaped junctions with threefold coordination. The peptidoglycan network is built from two non-equivalent chains, as shown in the face view of a section Fig.3.17 (a) from (Koch and Woeste, 1992): sugar rings run in the direction supporting the maximum stress, while the softer peptide strings forming transverse links (and bearing less stress). It is believed that this molecular anisotropic organization is dictated by design principles of the cell, such that the stiffer chains act as reinforcement in the direction that shall sustain the maximal stress. Note that the knowledge of the mechanical properties of peptidoglycan is also of importance for understanding bacterial growth and form.

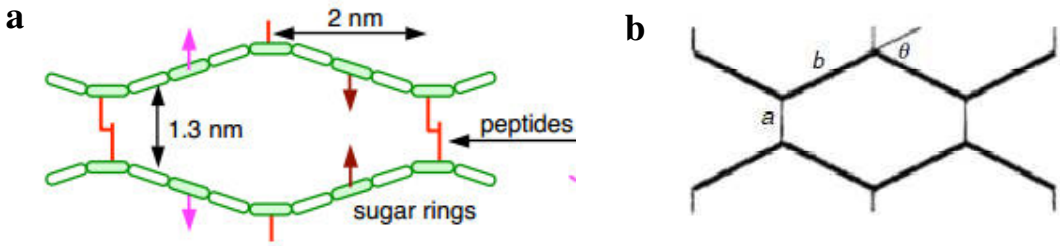

Fig. 3.17 Peptidoglycan network a) dimensions of network chains (peptides and sugar rings) Koch and Woeste (1992), (b) face view of the section of the peptidoglycan network and definition of the geometrical model.

The nuclear lamina is a further example contains junctions that have fourfold coordination (Aebi et al., 1986; McKeon et al., 1986). The nucleus is bounded by two membranes, and the lamina lies in the interior of the nucleus, adjacent to the inner nuclear membranes as shown in Figure 3.18.

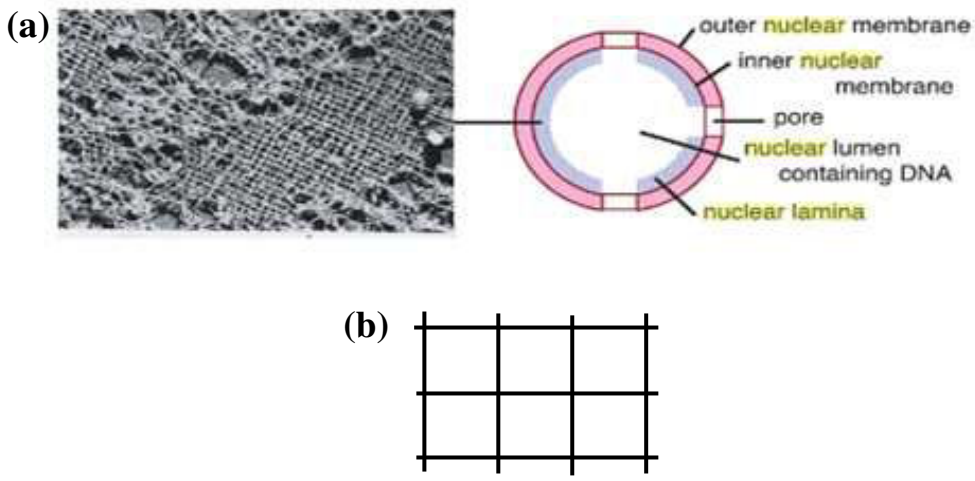

Fig. 3.18 Nuclear lamina showing its square lattice of intermediate filaments with (b) four-fold symmetry.

As a third example, the erythrocyte cytoskeleton is a network with at least partial C6 symmetry, which has both a low density and a high flexibility. Furthermore, the corresponding lattice has six-fold connectivity, with however 3% and 8% of the junctions presenting five or seven-folds respectively (Liu et al., 1987; Mohandas and Evan, 1994; Trovalusci and Masiani, 1999; Feyel and Chaboche, 2000). The description of the in-plane network, parameterized with the inclination angle θ, is pictured in Fig. 3.19.

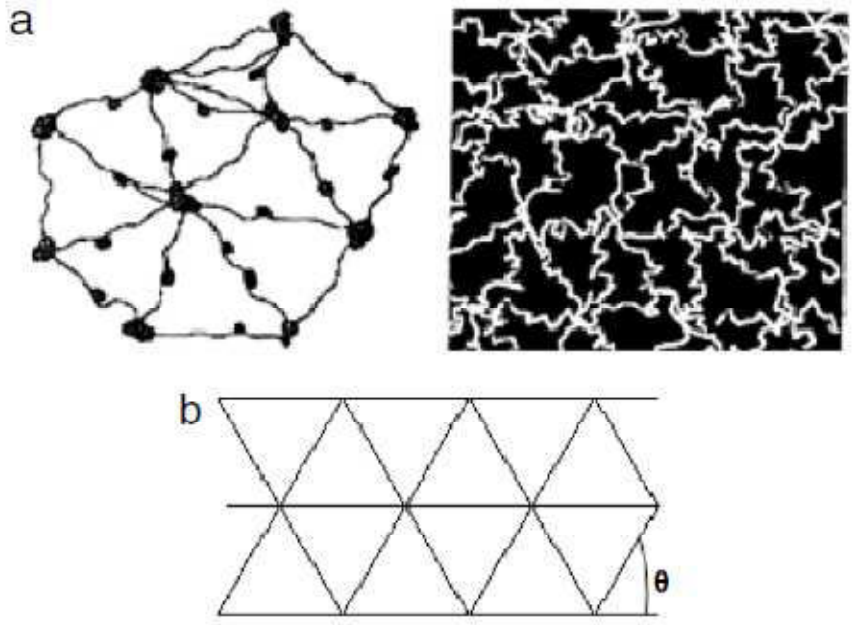

Fig.3.19 Triangular network of the erythrocyte cytoskeleton (a) with its idealization configuration parameterized by the angle θ (b).

In the next section, we will first study the effect of lattice randomness on effective properties of the triangular network, in order to validate the assumption of quasi periodicity we shall make to compute the effective nonlinear response of those lattices.

3.7.2 Impact of microstructural irregularity

Homogenization techniques for discrete media have been extensively used in the last decade, but they have a significant limitation in that they do not account for natural variations in the lattice topology, which are observed for most biological materials. Most models of 2D cellular structures are based on idealized unit cells intended to describe the micro-structural features of an average cell supposed to be representative of the real underlying structure. Those approaches do however not account for the complex and rather diverse mechanisms leading to membrane rearrangements usually referred to as remodeling; those mechanisms involving a complex machinery of proteins can be broadly classified as fusion or fission, including exocytosis and endocytosis, budding and fusion of transport carriers, relaxation of the elastic energy, as listed in the recent review paper (Kozlov et al., 2010).

The network topology may also vary as abnormal RBC skeletons have been reported, Hansen et al. (1997). Those variations lead to irregular cells and to non-periodic arrangement of the cell walls. Therefore, a quantitative study to investigate how the micro-structural variability can affect the macroscopic effective mechanical properties has been performed as a preliminary step. Statistical variations in the underlying models have been accounted for (Silva et al., 1995; Silva and Gibson, 1997; Zhu et al., 2001; Alkhader and Vural, 2008).

Several methods described in Kraynik et al. (1991) account for variability in the arrangement of cell walls of hexagonal honeycombs by modifying the initial two-dimensional unit cell analysis, see Warren and Kraynik (1987). Those authors develop structure-property relationships for arrays of hexagonal cells endowed with varying sizes and shapes, but they conserve an angle of 120° between the three struts common to each node. The results of those authors lead to the conclusion that the specific spatial arrangement and size distribution of the unit cells hardly affect their elastic response.

In order to generate a microstructural irregularity far from periodicity, a spatial perturbation has been applied to the vertices of a regular triangular truss network in random directions (Der Burg et al., 1997; Chen et al., 1999; Chen and Fleck, 2002; Alkhader and Vural, 2008), expressed by the following equations:

$$x_i^{'} = x_i + \lambda^{'} r\cos(\theta) \quad \gamma_i^{'} = \gamma_i + \lambda^{'} r\sin(\theta)$$

Where θ is a uniformly distributed random variable, r a random variable and $x_i^{'}$ and $\gamma_i^{'}$ are the perturbed coordinates, with the non primed component being the original coordinates. $\lambda^{'}$ is the perturbation parameter which specifies the degree of irregularity; note that it has been chosen in a manner that cell convexity is preserved. Fig. 3.20 shows different cellular structures generated for increasing values of $\lambda^{'}$.

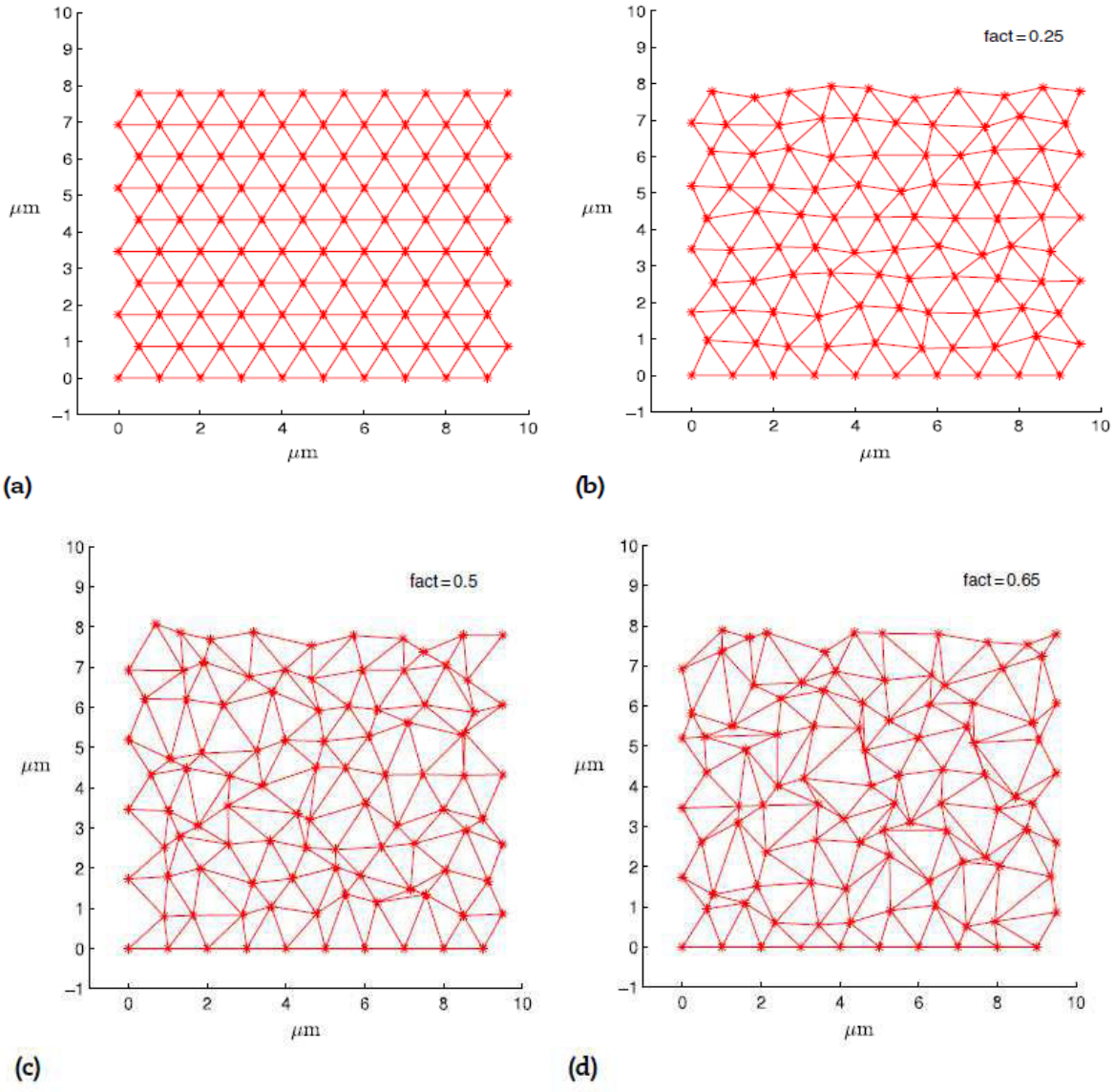

Fig.3.20 Cellular structures generated for FE analyses including stochastic triangular topologies. Sample microstructures subjected to various amounts of perturbation are shown. Note that nodal connectivity is 6 for these topologies. (a) Regular triangular topology. (b) The perturbation factor is 0.25, (c) 0.5, (d) 0.65.

We note that the last configuration obtained when $\lambda = 0.65$ looks very distorted.

Each topology is discretized by 9×9 cells and each beam element is 1 µm long within the initially regular topology. Accurate finite element analyses are performed (using the FE software Abaqus implicit) in order to get the effective tensile moduli, which are then compared with their counterpart for the regular topology (fig. 3.20a). Elastic linear and quasi-static framework has been considered; each cell element is modeled by three linear Bernoulli elements (Abaqus element type B23), considering a cubic formulation.

Simulation results show that the perturbed topology in the structure introduces a small amount of variances in the elastic constants for an isotropic triangular unit cell (the coefficient of variance lies in the interval [0.2%–4%]. The relative variation is represented versus the perturbation parameter λ' on Fig. 3.21 showing that the non-periodic arrangement of cells does only weakly affect the elastic properties of the overall network; hence it is legitimate to adopt in the sequel a quasi periodicity assumption. This finding is in agreement with many works in the literature, especially those dealing with cellular structural materials such as foam (Silva et al. (1995), Silva and Gibson (1997) and Zhu et al. (2001)). These results mean that random fluctuations do average in such a way that their net effect is nearly negligible. We may nevertheless be careful with these results, since introducing a controlled anisotropy amongst possible factors to control randomness would certainly modify substantially the effective properties.

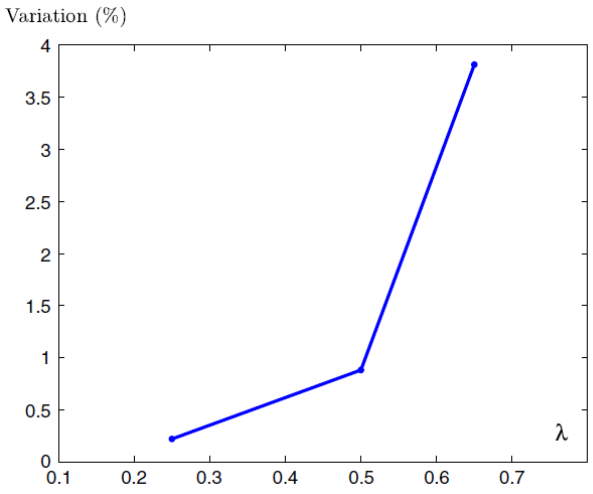

Fig. 3.21. Relative error in percent of the Young modulus versus the perturbation factor λ'.

3.7.3 Homogenized moduli of biological membranes

In the next section, we employ the proposed methodology based on discrete homogenization to analyze the mechanical response of the peptidoglycan, the erythrocyte and nuclear lamina networks subjected to uniaxial loading and simple shear. The filaments of the network are supposed to undergo small stretches, but they can easily bend, so that they are essentially prone to geometrical nonlinearities (material nonlinearities can be neglected). For a uniaxial loading, we shall plot the change of the area compression modulus and Poisson's ratio of these networks versus stretch, which are of high interest.

3.7.3.1 The peptidoglycan cell wall

The peptide and the glycan shown on Fig. 2.28 (left view) are modelled as beams with a regular circular cross section with radii respectively equal to 0.5 and 1 nm, Boal (2002); the angle θ is used as a descriptor of the topology of the glycan network. The whole lattice in a planar configuration is generated from the repetition of the unit cell shown in Fig. 3.22 (right) thanks to two periodicity vectors defined in the Cartesian basis.

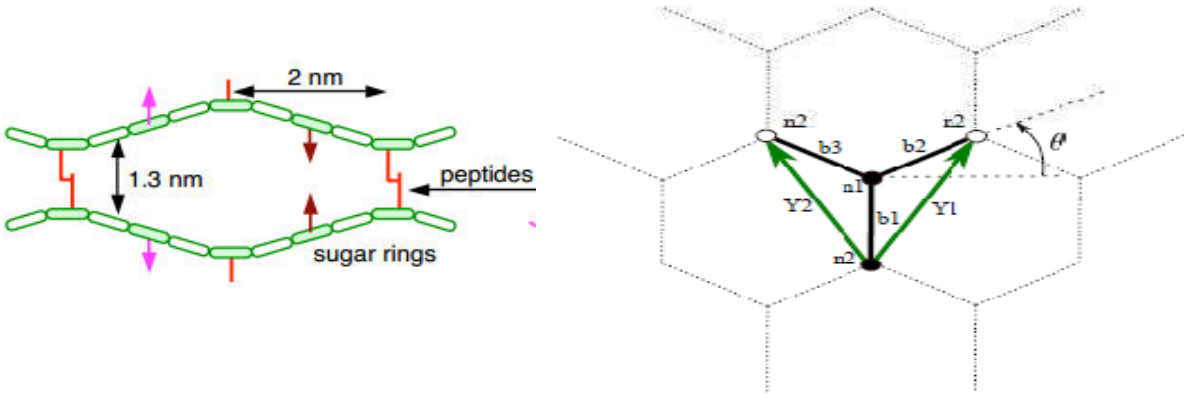

Fig. 3.22 Hexagonal unit cell for the peptidoglycan network

For this application, we choose (θ= 30) and select the dimensions of the molecular chains of the unit cell as indicated in Fig. 2.23: the average Young moduli of glycan at low temperature (T = 273 K), is given by Ygly = 4.799 × 107 J/m3 and Ypep = 1.53 × 107 J/m3 for peptides: the Young moduli are elaborated from the persistence length according to the relation $\xi_P = \frac{EI_Z}{K_B T}$ (Boal, 2002), wherein E, I_Z, T, K_B are the tensile modulus, the quadratic moment (dependent

on the beam cross section), the absolute temperature and Boltzmann constant respectively. Considering the properties of individual chain, the peptide is endowed with the classical properties of entropic springs, given that its end-to-end length in the network $l_{pep} = r_{ee} = 1.3\,\text{nm}$ is less than its contour length $L_c = 4.2\ \text{nm}$. The persistence length of the peptide string can be obtained from the simplified relation $\left\langle r_{ee}^2 \right\rangle = 2\xi_{P,peptide} L_c$, (the bracket denotes the average value) giving $\xi_{P,peptide} = 0.2\ \text{nm}$. The glycan chains are comparatively much stiffer, with $\xi_{P,glycan} \simeq 10\ \text{nm}$ (Stokke and Brant, 1990) and $l_{gly} = r_{ee} = 2\ \text{nm}$.

- **Uniaxial tension**

Plots of Cauchy stress versus the relative stretch are presented for the uniaxial loading test as the result of a numerical analysis performed in combined symbolic and numeric language, using a dedicated Maple code. Figure 3.23 shows the difference between the linear and nonlinear responses.

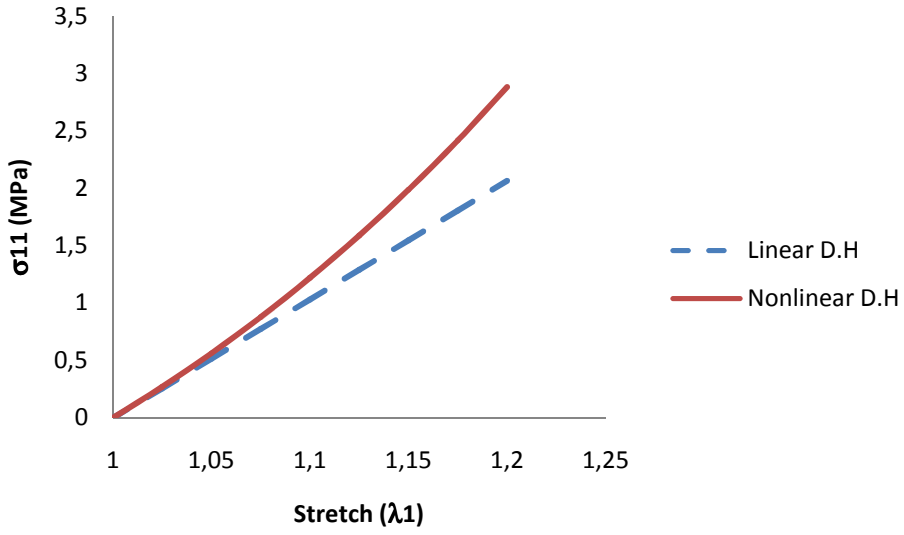

Fig. 3.23 Uniaxial tensile Cauchy stress versus stretch for the hexagonal lattice

In order to compute the evolution of both Poisson's ratio and area change under stretch, and as previously discussed in the first part of this chapter, the relation between the surface element (a vector) of in the reference configuration, $\mathbf{N}dS$, and its Eulerian counterpart, vector $\mathbf{n}ds$ after deformation writes (Nanson formula)

$$\mathbf{n}ds = J\mathbf{F}^{-\mathrm{T}}.\mathbf{N}dS \tag{3.33}$$

This entails the deformed area da in relation to the undeformed area dA using equation (3.34),

$$\frac{da}{dA}=\frac{\|\mathbf{n}ds\|}{\|\mathbf{N}dS\|}=\frac{\|J\mathbf{F}^{-\mathrm{T}}.\mathbf{N}dS\|}{\|\mathbf{N}dS\|}=\det(\mathbf{F})\|\mathbf{F}^{-\mathrm{T}}.\mathbf{N}\| \tag{3.34}$$

Thus, one can specify this ratio in a uniaxial loading test as

$$\frac{da}{dA}=\det(\mathbf{F})=\lambda_1\lambda_2 \rightarrow \frac{da-dA}{dA}=J-1$$

Values of the Jacobian above unity (resp. below unity) indicate that the area tends to increase (resp. decrease). Based on Poisson's ratio defined as $\nu_{12}=-E_2/E_1$, we can rewrite the area ratio as,

$$\frac{da}{dA}=\left(\nu_{12}(\lambda_1)+1\right)\lambda_1-\nu_{12}(\lambda_1)\lambda_1^2 \tag{3.35}$$

with Poisson's ratio depending on the applied stretch λ_1 .We can see from previous formula that there is a competition between the first positive contribution on the right hand side and the second term, which is negative. For large stretches, the negative term, which is at least quadratic in the stretch, is expected to dominate over the first term.

The change of area ratio and Poisson's ratio versus stretch are shown in figure 3.24.

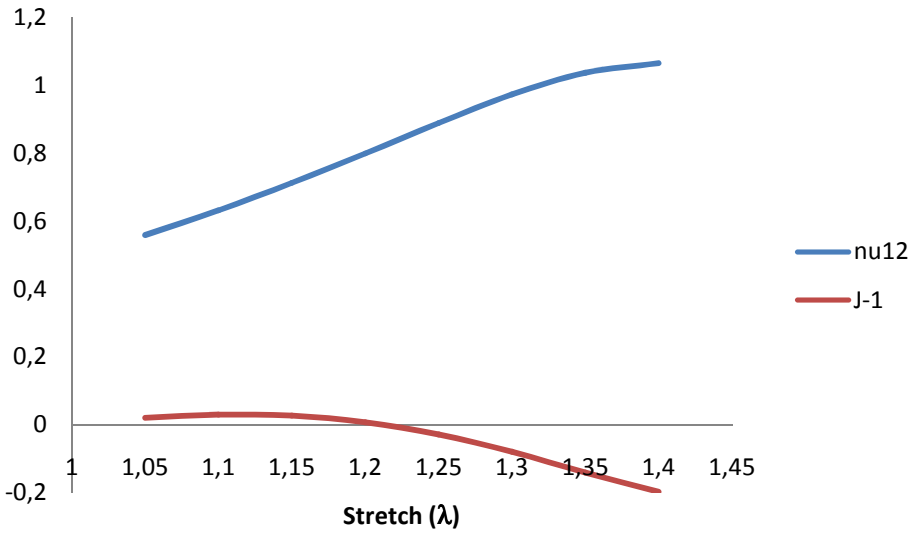

Fig. 3.24 change of area ratio (red curve) and Poisson's ratio (blue curve) versus stretch for the hexagonal lattice

Poisson's ratio increases from its initial value at low strains (0.56) up to a maximum slightly above unit at 40% elongation; this means that the membrane will undergo an increased lateral contraction with ongoing stretch. The area remains nearly constant for low and moderate values

of the stretch (it slightly increases towards a maximum), and it then decreases nearly linearly for higher values of the stretch (above 17% deformation), due to the dominant negative contribution in (3.35).

Moreover, the planar modulus of compressibility, denoted K_A, is elaborated as the hydrostatic part of the stress divided by the determinant of deformation gradient representing the change of area (as shown just above) as,

$$K_A = \frac{\mathrm{tr}(\boldsymbol{\sigma})}{\mathrm{tr}(\mathbf{F})} \tag{3.36}$$

Figure 3.25 shows that the modulus of area compressibility increases monotonously versus stretch, indicating a greater resistance of the membrane to area change at higher stretches.

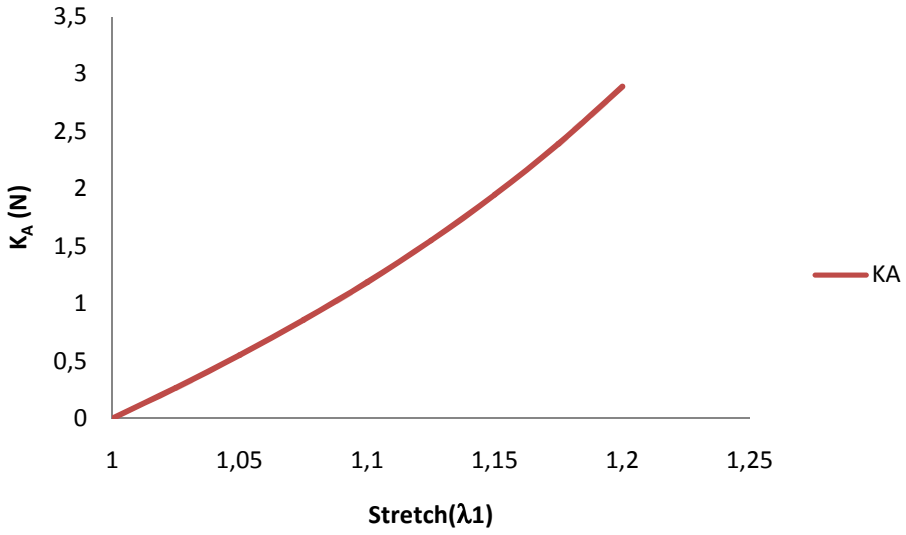

Fig. 3.25. Change of modulus of compressibility versus stretch for hexagonal lattice

- **Simple shear test**

Plot of the shear stress versus the shear angle shows not significant difference between the linear and geometrical nonlinear analysis, as pictured in fig. 3.26. This can be explained by the fact that the hexagonal lattice has a relatively high effective shear modulus.

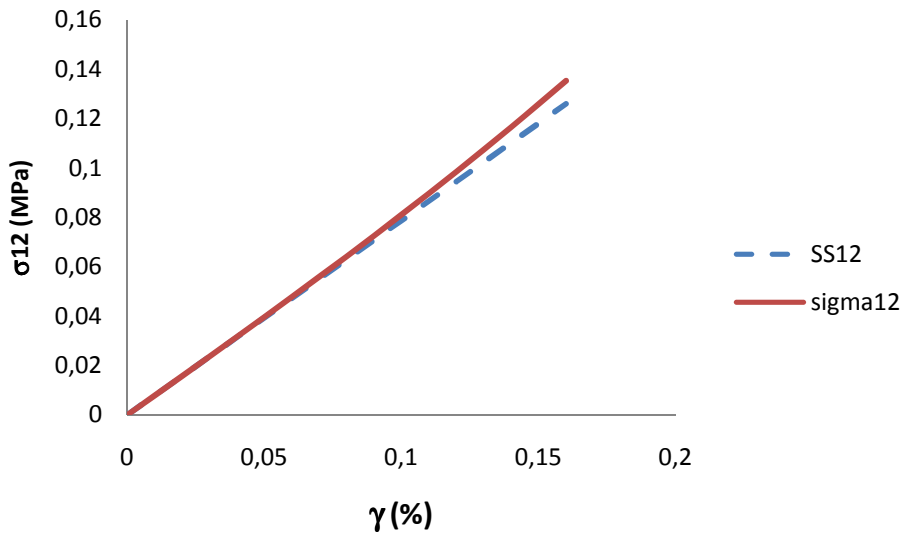

Fig. 3.26 Nonlinear shear stress versus shear strain response and comparison with linear predictions for the hexagonal lattice

3.7.3.2 The erythrocyte network

In the same manner, the erythrocyte network with connectivity 6 is modeled based on triangular repeated unit cells, each of them described by three beams and two periodicity vectors $\mathbf{Y}_1, \mathbf{Y}_2$ at a chosen configuration $\theta = 60^\circ$, as shown in figure 3.27.

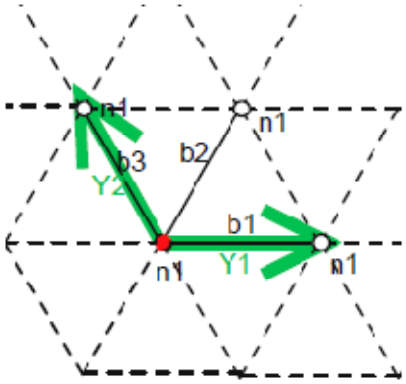

Fig. 3.27 Triangular unit cell for the erythrocyte network

One shall first define the geometrical and mechanical parameters of the beams within the repeated unit cell as described below. Considering a low temperature (close to T = 273 K) and an initially non-stressed membrane, the spring constant for any chain in the network is considered as constant, with an average value given in (Boey et al., 1998),

$$\beta \kappa_{eff} a^2 = 0.23 \qquad (3.37)$$

with β the inverse temperature $\frac{1}{K_B T}$, a=6.4 nm the bead diameter (Boey et al., 1998) and $\kappa_{eff} = \frac{YS}{l^b}$ the tensile modulus of a beam. Using Eq. (3.37), the Young modulus Y for any chain in the network is then calculated from the following expression

$$Y = \frac{0.23}{\beta a^2} \frac{l^b}{S}$$

with S the section of the considered chain. In the sequel, we consider a rectangular beam section with a chain width $t = 9.96 .10^{-3}$ nm (hence assigning the quadratic moment) and an average end to-end beam length $l^b = 200$ nm (Feyel and Chaboche, 2000).

From previous data, the chosen geometrical and mechanical parameters of the repeated unit cell feed an input file into a dedicated Maple code. For a uniaxial loading, we plot Cauchy stress versus the relative stretch in figure 3.23. The nonlinearity is less pronounced in comparison to networks having three-fold connectivity (fig. 3.28).

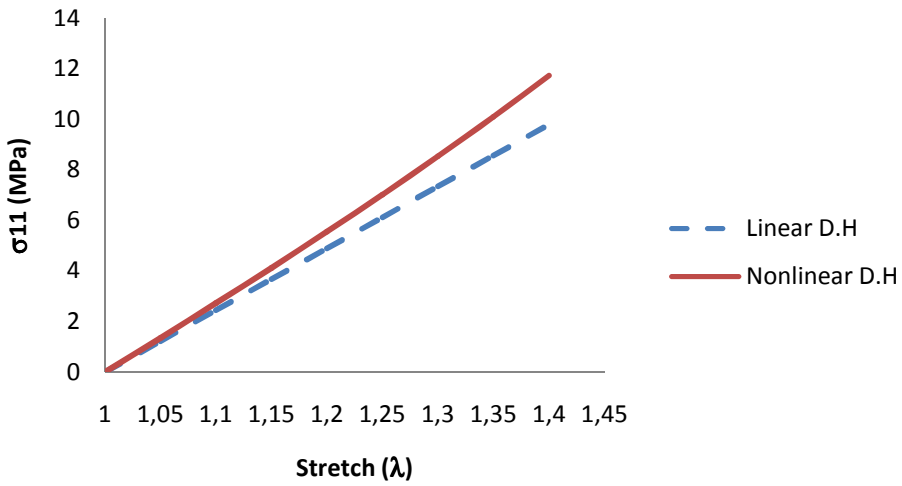

Fig. 3.28 Uniaxial tensile Cauchy stress versus stretch for the triangular lattice

Moreover, we plot the changes of area, Poisson's ratio and the planar modulus of compressibility K_A, as shown in Figures (3.29, 3.30) respectively.

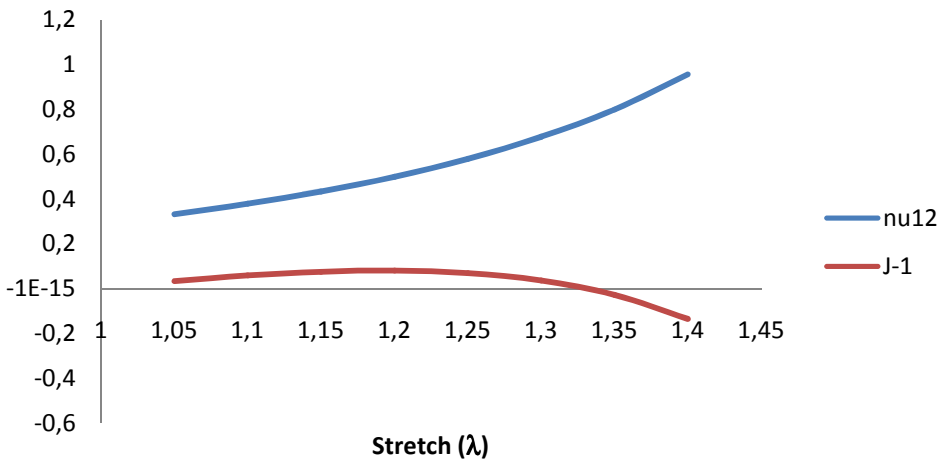

Fig. 3.29 change of area ratio and Poisson's ratio versus stretch for the triangular lattice

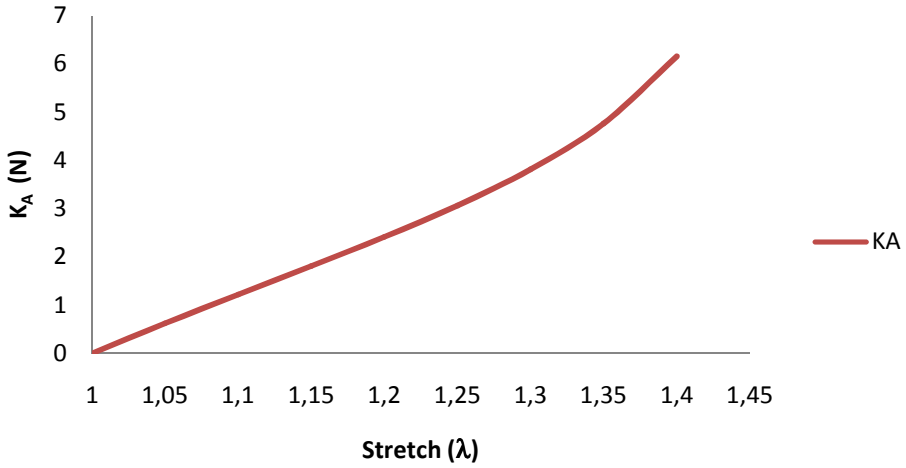

Fig. 3.30 change of modulus of compressibility versus stretch for the triangular lattice

Evolutions of Poisson's ratio and area show similar evolutions compared to the previous 3 fold connectivity lattice.

- **Simple shear test**

The triangular lattice has a high effective shear modulus. Thus, the evolution of shear stress shows similar evolutions compared to the previous 3-fold connectivity lattice.

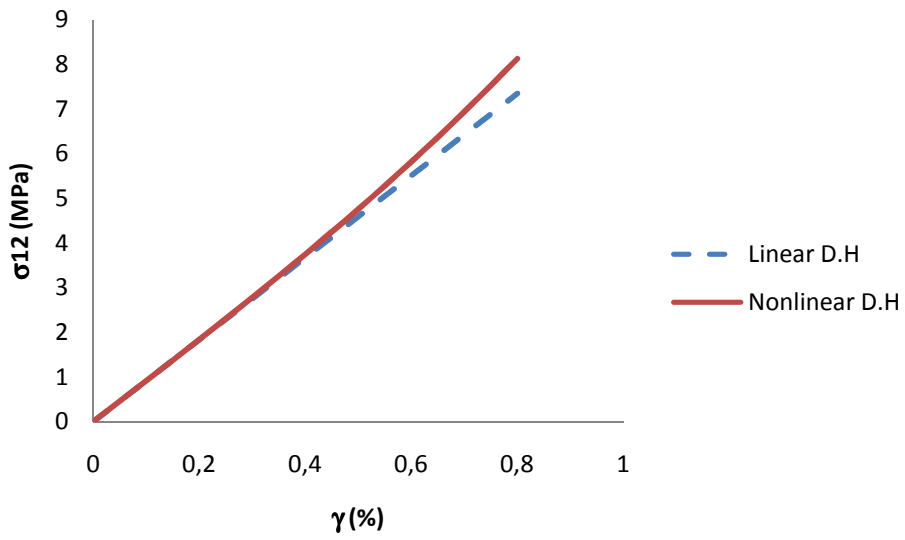

Fig. 3.31 Nonlinear shear stress versus shear strain response and comparison with linear predictions for triangular lattice

3.7.3.3 The nuclear lamina network

For the nuclear lamina network with connectivity 4 is modeled based on square repeated unit cells, each of them described by two beams and two periodicity vectors $\mathbf{Y_1}, \mathbf{Y_2}$, as shown in figure 3.32.

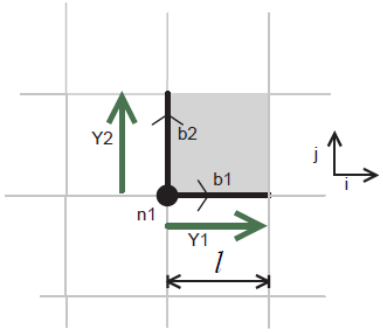

Fig. 3.32. Square unit cell for the erythrocyte network

We assume that the beams within the repeated unit have the same geometrical and mechanical parameters as described above for the triangular cell.

For a uniaxial loading, we plot Cauchy stress versus the relative stretch in figure 3.33 the nonlinearity is less pronounced in comparison to the triangular unit cell (fig. 3.28). This can be explained by the fact that the square lattice is a relatively stiff structure.

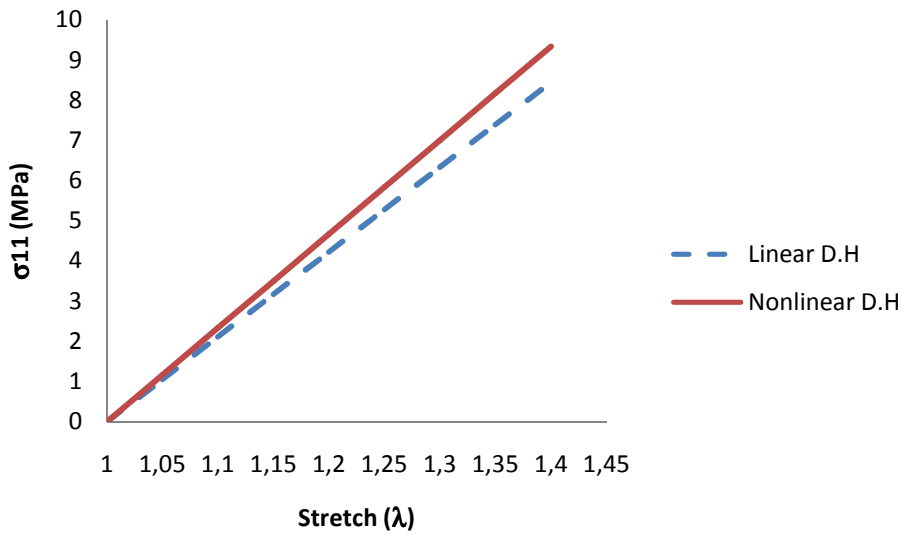

Fig. 3.33 Cauchy stress versus stretch for the square lattice.

Moreover, we plot the changes of area, Poisson's ratio and the planar modulus of compressibility K_A, as shown in Fig.3.34 (a,b) and Fig.3.35 respectively. Due to the fact that that the square lattice is a relatively stiff structure.Poisson's ratio has very small value compared to the triangular lattice; this means that the membrane will undergo slightly lateral contraction with ongoing stretch. The area will increase linearly versus stretch as shown in Fig. 2.34 (a, b).

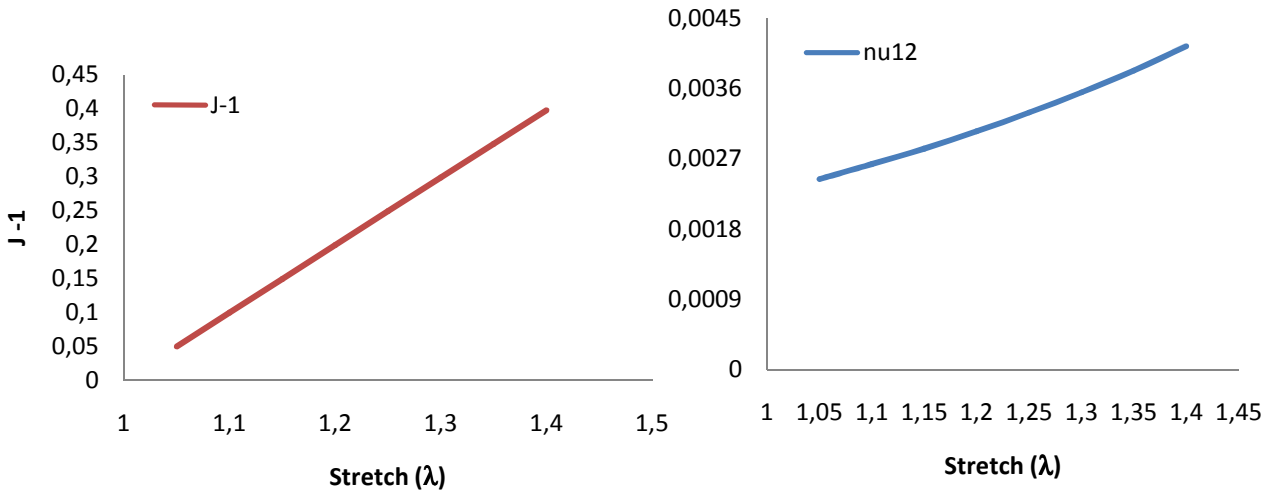

(a) **(b)**

Fig. 3.34 change of area ratio and Poisson's ratio versus stretch for the square lattice (a, b).

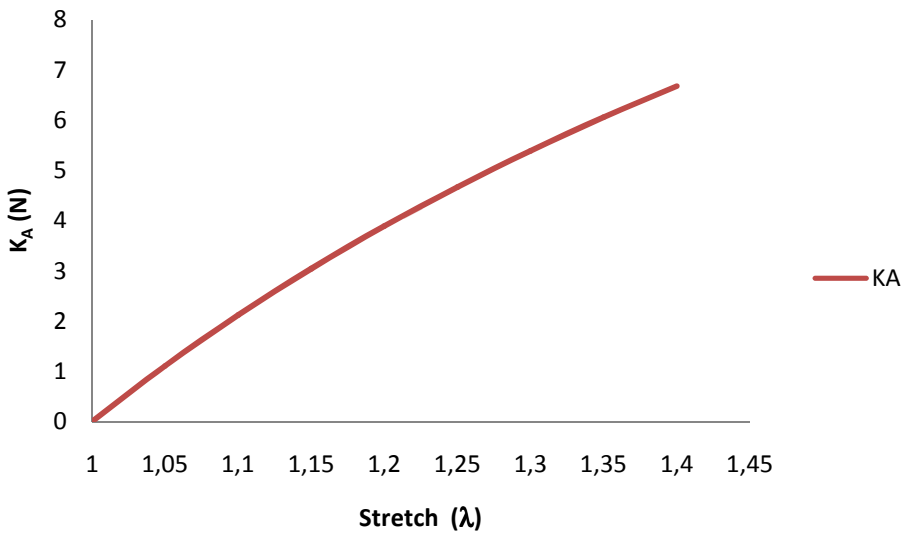

Fig. 3.35 Change of modulus of compressibility versus stretch for the square lattice

- **Simple shear test**

The plot of the shear stress versus the shear angle shows an important difference in comparison to networks having six-fold connectivity, as pictured in fig. 3.36. This important difference between the linear and nonlinear can be explained due to the fact that the square structure has a small effective shear modulus.

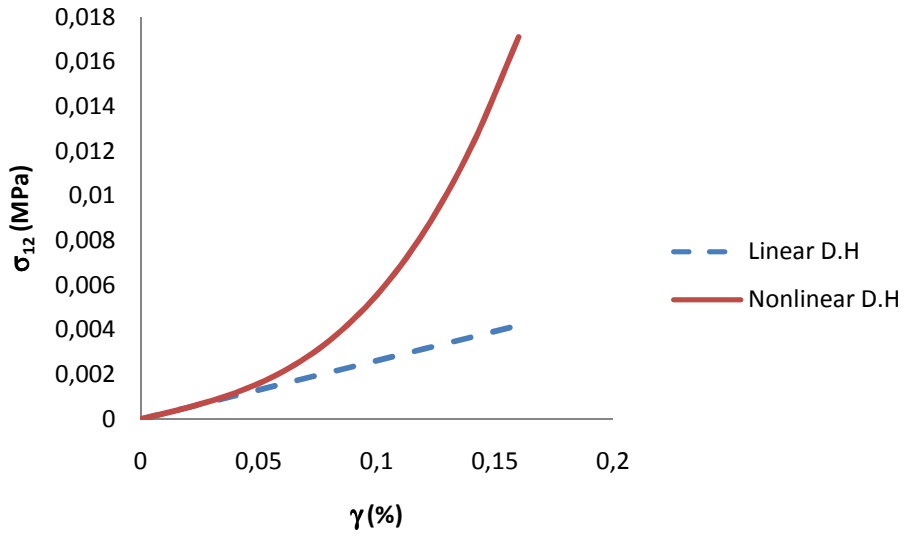

Fig. 3.36 Nonlinear shear stress versus shear strain response and comparison with linear predictions for the square lattice

In the next section, based on the previous nonlinear discrete homogenization analysis, we will validate the stress-strain responses obtained for the considered biomembranes, by comparing the homogenized responses with full FE computations over a representative unit cell.

3.8 Comparison of homogenized responses with FE computations

The previous results shown in Fig. 3.4 (a,b) obtained with the DH technique are now compared with numerical results obtained from the FE method (ABAQUS), under the specified types of loadings (we restrict the validation of the computed response to uniaxial tests), with appropriate boundary conditions. The beams within the full lattices are discretized by Timoshenko beam elements, adopting 36 elements per unit cell.

The uniaxial response for both the square and hexagonal lattices is shown in Fig. 3.37 for the two chosen planar lattices (a) and (b); a good agreement is obtained of both methods, with a maximum discrepancy close to 10.4%.

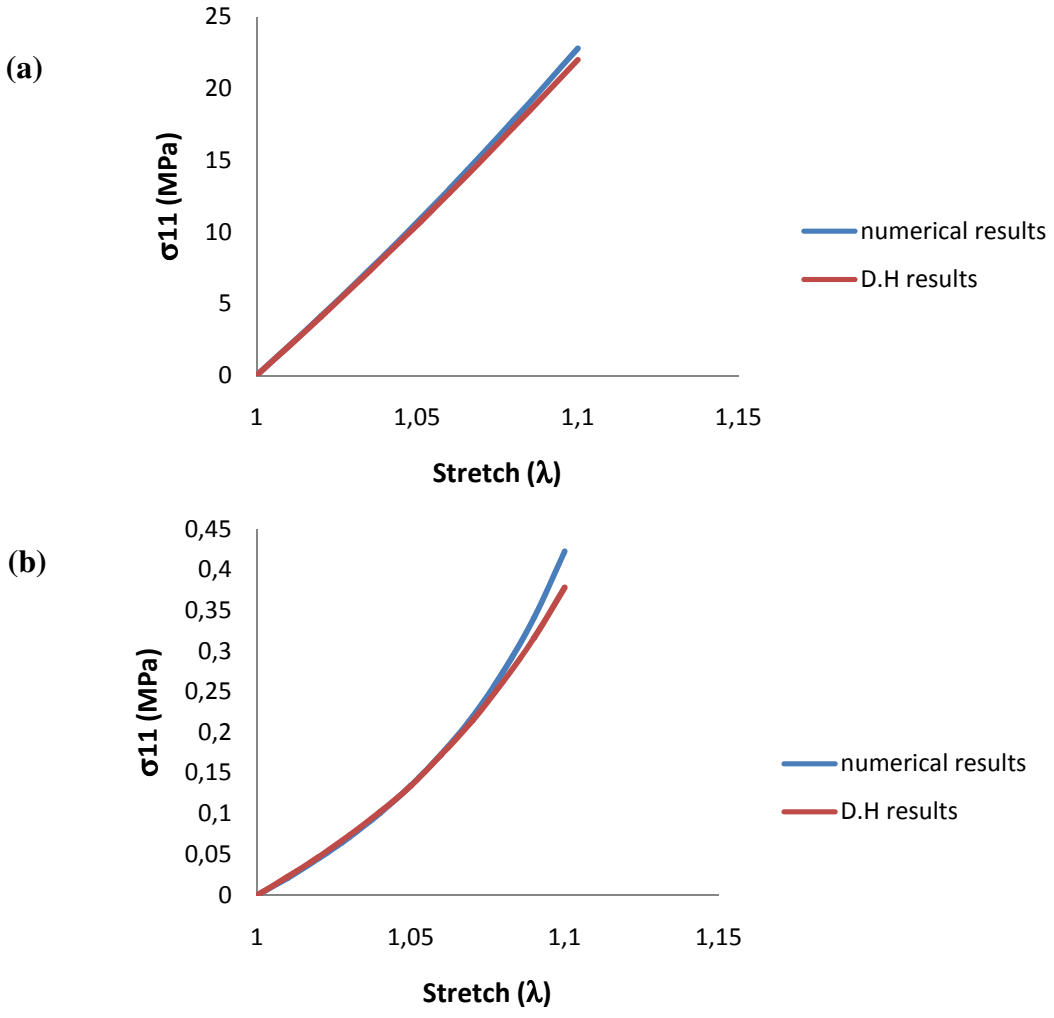

Fig. 3.37 Comparison of results from the DH technique and FEM code (ABAQUS).

One possible reason for the observed small difference may be attributed to the assumption that the second order part of the strain can be neglected.

3.9 Conclusions and discussion

The interest of the developed homogenization technique lies in its flexibility and capability to handle any planar lattice; however, in this work, we restricted ourselves to centrosymmetric lattices so that the coupling coefficients between stress and curvature vanish. Further interest of the homogenization method lies in it is ability to deliver the expressions of the forces and hyperforces at the beam extremities of the lattice, based on the kinematical nodal variables (displacement and microrotation). From those expressions, one is able to construct the full compliance (or rigidity) matrix, reflecting the complex and evolving anisotropy of the so-built equivalent continuum, and the evolution of the anisotropy with the change of geometry induced by the loading. In the elastic case, and for small perturbations, the effective properties are derived as closed-form expressions of the geometry (characterized by the beam length and the quadratic moment of inertia) and mechanical properties (Young modulus). We have extended the linear discrete asymptotic homogenization framework to the nonlinear setting, based on an update of the lattice geometry and an elastic computation done over each load increment. These theoretical developments have been implemented into a dedicated code using the lattice geometry and microstructural properties as an input, and delivering as an output the effective response.

The detailed analysis of the considered types of structure from the proposed methodology shows that the main reason of nonlinearity lies in the beam reorientation, whereas other geometrical effects are negligibly small. The stress-strain behavior under the three types of loading has been computed.

A comparison of the response under uniaxial loading computed based on DH and on FE simulations has been done in order to validate the homogenized response (by the DH technique), showing a good agreement between the results from discrete homogenization and those computed numerically.

3.10 References

Caillerie, D., Mourad, A., Raoult, A., 2006. Discrete homogenization in graphene sheet modeling. J. Elast. 84, 33–68.

Dos Reis, F., Ganghoffer, J.F., 2012. Construction of micropolar continua from the asymptotic homogenization of beam lattices . Computers and Structures 112–113 (2012) 354–363.

Gibson, L.J., Ashby, M.F., 1982. The mechanics of 3-dimensional cellular materials. Proc. R. Soc. Lond. Ser. A: Math. Phys. Eng. Sci. 382 (1782), 43.

Gibson,L.J.,Ashby,M.F.,Schajer,G.S.,Robertson,C.I.,1982. The mechanics of two-dimensional cellular materials. Proc. R. Soc. Lond. Ser. A:Math. Phys.Eng. Sci. 382(1782),25–42.

Hutchinson,R.G.,Fleck,N.A.,2006. The structural performance of the periodic truss. J. Mech. Phys. Solids 54(4), 756–782.

Klaus-Jürgen Bathe, Saïd Bolourchi. Large Displacement Analysis of three-dimensional Beam Structures. International Journal for Numerical Methods in Engineering. VOL. 14, 961-986 (1979).

Mourad, A., 2003. Description topologique de l'architecture fibreuse et modélisation mécanique du myocarde. Ph.D. thesis, I.N.P.L. Grenoble.

Raoult, A., Caillerie, D., Mourad, A., 2008. Elastic lattices: equilibrium, invariant laws and homogenization. Ann. Univ. Ferrara 54, 297–318.

Sanchez-Palencia E. Non-homogeneous media and vibration theory. Lect Notes Phys 1980;127.

Zhu, H.X., Knott, J.F., Mills, N.J., 1997. Analysis of the elastic properties of open-cell foams with tetrakaidecahedral cells. J. Mech. Phys. Solids 45 (3), 319.

Wang,A.J.,McDowell,D.L.,2004. In plane stiffness and yield strength of periodic metal honeycombs. J.Eng.Mater.Technol.Trans.ASME126(2),137–156.

Bakhvalov N, Panasenko G. Averaging processes in period media. Mathematic problem in mechanics of composite materials. Dortrecht: Kluwer Academic Publishers; 1989.

Warren WE, Byskov E. Three-fold symmetry restrictions on two-dimensional micropolar material. Eur J Mech A/Solid 2002;21:779–92.

Pradel F, Sab K. Homogenization of discrete media, 1998. J Phys IV France 1998;08:P317–24.

Pindera, M-J, Khatam, H., Drago, A.S., Bansal, Y.,2009. Micromechanics of spatially uniform heterogeneous media: A critical reviewand emerging approaches. Compos. Struct. 40, 349–378.

Charalambakis, N., 2010. Homogenization techniques and micromechanics Asurvey and perspectives. Appl.Mech.Rev.63(3),1–10.

Warren, W. E., Kraynik, A. M., The nonlinear elastic behaviour of open-cell foams, Transactions of ASME, 58, 375–381, June 1991.

Warren, W. E., Kraynik, A. M., Stone, C. M., A constitutive model for two-dimensional nonlinear elastic foams, Journal of the Mechanics and Physics of Solids and Structures, 37, 717–733, 1989.

Wang, Y., Cuitino, A. M., Three-dimensional nonlinear open cell foams with large deformations, journals of the Mechanics and Physics of Solids, 48, 961–988, 2000.

Hohe, J., Becker, W., Effective mechanical behavior of hyperelastic honeycombs and two dimensional model foams at finite strain, International Journal of Mechanical Sciences, 45, 891–913, 2003.

Janus-Michalska, M., Pęcherski, R. P., Macroscopic properties of open-cell foams based on micromechanical modeling, Technische Mechanik, Band 23, Heft 2-4, 221–231, 2003.
Janus-Michalska, J., Effective models describing elastic behavior of cellular materials, Archives of Metallurgy and Materials, 50, 595–608, 2005.
Janus-Michalska, J., Hyperelastic behavior of cellular structures based on micromechanical modeling at small strain, Arch. Mech., 63, 1, pp. 3–23, Warszawa 2011.

CHAPTER Four

Initial linear response of Architectured Materials from Discrete Asymptotic Homogenization. Application to Textile Monolayers

Contents

Abstract

The goal of this chapter is to develop computational discrete homogenization schemes to derive nonlinear continuum constitutive models for initially discrete structures prone to geometrical nonlinearities. In order to exemplify the method, we consider as specific structures textile monolayer fabrics patterns, viz plain weave and twill. A representative unit cell (RUC) of the fabric is constructed and modeled as a network of trusses connected by nodes at cross points of the interwoven yarns within the fabric. These trusses have extensional and bending rigidities to represent yarn stretching and flexion. The contact interactions between yarns at the cross-over points are captured by beam segments connecting the nodes. The proposed methodology has been used for the analysis of plain weave and twill fabrics subjected to large applied strains. The stress-strain responses are evaluated after applying appropriate boundary condition to the RUC, considering the three elementary loading cases, namely uniaxial tension, bi-axial tension and simple shear. The computed response of those fabrics is based on a micropolar discrete homogenization algorithm, which has been implemented into a dedicated code. A calibration of a selected form of the strain energy density is done by identifying the set of material constants based on comparisons with the stress-strain response computed by discrete homogenization. The mechanical responses obtained by discrete homogenization with finite element simulation performed over periodic unit cells are in good agreement.

4.1 Introduction

Over the past decade, considerable attention from the composite manufacturing sector has been devoted to textile composites and especially woven fabrics. These materials have become increasingly popular for use in structural applications in recent years due to their advantages such as low fabrication costs, light weight, ease of handling and high adaptability, over tape laminates and several other engineering materials. These factors provide strong motivation for the textile industry to develop simulation technology for understanding the deformation, kinematics and mechanical behavior of textile composite.

Woven fabrics are produced by weaving continuous fiber also called reinforcement by multiple weaving patterns viz. plain, twill, satin, basket etc. The mechanical behavior of woven fabrics is of interest in numerous applications, including apparel, fabric reinforced

composites, and body armor for ballistic protection. The development of these technologies requires a thorough understanding of the mechanical behavior of woven fabrics. Different levels of analysis and modeling can be adopted in the case of fabric. Figure 4.1 shows three different levels, namely the microscopic (i.e. single fiber), mesoscopic (i.e. fiber yarn and yarn architecture) and macroscopic scales (the structural scale of the entire fabric).

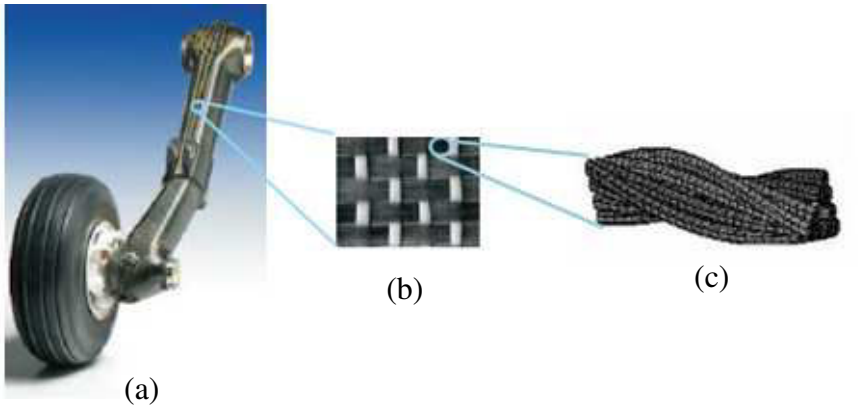

Figure. 4.1 Different scales in textile analysis.(a) Trailing arm at the macroscopic level. (b) Plain weave pattern composite at the mesoscopic level. (b) Single fiber at the microscopic level

The mechanical behavior of fabrics is clearly a multi-scale problem: at the macroscopic scale, the fabric consists of an assembly of yarns in the armor (meso-scale), themselves composed of fibers (micro-scale), leading overall to a complex mechanical behavior. Micro-scale approaches take the distribution and the contact between thousands of fibers into account. Some studies have been performed at this scale (Durville, 2002), but the analyses of the mechanical behavior of the woven unit cell at this scale is very difficult accounting for the number of fibers (some thousands) in a unit cell. In macro-scale approaches, fabrics are modeled as membranes (or shells if bending is taken into account). These approaches are used in forming simulations. Macroscale analyses focus on the characterization of fabric behavior without explicitly modeling the geometric structure of the textile. Usually the fabric is modeled as a homogeneous continuum which obeys a certain constitutive relation. These continuous models do not include crimp and interlacement effects which are important features of the fabric reinforcement behavior. The analyses at mesoscale consider the geometry of the woven unit cell but consider the yarns as continuous domains. Single yarn interactions are also taken into account in analyses on the mesoscale. These analyses ensure a good compromise between realism and complexity.

To this end, woven fabrics can be considered as structured, hierarchical materials, having the three structural levels previously described (Lomov et al., 2007). The mechanical behavior of woven fabrics is complex due to the intricate interactions of the yarns that constitute the fabric ‘‘mesostructure’’. Despite many attempts to develop effective models for fabric behavior, there is currently no widely accepted modeling approach that can accurately describe all the important aspects of the fabric mechanical behavior. This is due in part to the variability of requirements for fabric models in different applications (Parsons et al., 2010). A number of these models are next reviewed.

The macromechanical properties of the woven fabric are evaluated with the help of periodic unit cell structure by using micromechanical approach

This chapter is organized as follows: we first introduce the recent modeling techniques (both analytical and numerical) pertaining to the mechanical behavior of woven fabric textile in section 4.2. In section 4.4, we extend the homogenization technique proposed in chapter two and an expression of forces and hyperforces in the framework of 3D Timoshenko beams is exposed. Then we construct the effective continuum behavior of the textile monolayers. The macromechanical properties of the woven fabric are evaluated with the help of periodic unite cell structure. Applications to two different woven textile architectures will be given in Section 3.6, leading to an equivalent behavior at the mesoscopic scale. The discrete homogenization approach adopted first a linear framework, and extended next to the geometrical nonlinear situation for different types of macroscopic loadings. In the next section we then propose the calibration of a strain energy density of a hyperelastic model for the two chosen textile fabrics (plain weave and twill). Finally, the computed stress-strain homogenized response will be validated thanks to FE simulations performed over a well-chosen representative unit cell structure for each specific selected type of fabric.

4.2 Review of modeling approaches to predict the mechanical behavior of woven fabrics

Many modeling approaches have been used to analyze the mechanical behavior of fabrics, which can be classified into analytical and numerical models. The literature review (Tan et al., 1997; Crookston et al., 2005) shows that finite element analysis and analytical methods are powerful tools for studying the mechanical properties of woven fabrics. However, the complexity of the micro-structure is proportional to the number of parameters controlling the mechanical properties. So, various assumptions should be proposed for simplifying the

analysis. Most of the models for woven fabrics are based on the definition of a unit cell geometry and include the major architectural parameters in predicting the mechanical properties. The unit cell to be modeled is described as being the smallest unit of textile that, when tiled, will generate the full scale textile. The fibers within a yarn are not modeled individually; instead, yarns are represented as solid volume elements representing the approximate bounds of the fibers they are made of. There are several reasons for this: first of all it is much easier to represent the yarn as a solid volume, and secondly this kind of representation is much more useful in view of the computational analysis of textile properties.
A lot of mesostructurally based analytical models have been developed for the study of woven fabrics behavior. Such analytical models use mathematical relations to predict the mechanical response of the fabric and its component yarns in specific modes of deformation. In addition, these models can be used to quantify the homogenized material properties for use in continuum models. (Hearle et al., 1969) described a number of classical analytical fabric models. (Kawabata et al., 1973; 1973a; 1973b) presented general models for uniaxial, biaxial and shear deformation properties of plain weave fabrics based on a simplified model representing the structure of the fabric unit cells. The basic geometry used in these models is based on one dimensional stiffness elements (bars) representing yarns, and the connecting stiffness elements at intersection of yarns to model the compression between yarns. Other researchers have developed improved analytical models, including (Realff et al., 1997) who modify Kawabata's uniaxial model to include more complex behaviors such as yarn flattening and consolidation. (Kato et al., 1999) proposed an analytical model for predicting the constitutive behavior of a coated fabric composite that is based on the pin-joined lattice-type geometry. Recently, (Ben Boubaker et al., 2007a,b,c) developed a meso-level discrete model for a woven structure. The woven structure was considered as being organized in two sets of intertwined yarns, the warp yarns and the weft yarns. Each subsystem is considered as a sum of n single yarns. One single yarn is discretized and consists of a set of point masses mutually connected by extensional springs. Each node (point mass) is provided with rotational stiffness. Moreover, (Ben Boubaker et al., 2007d) proposed a discrete model of woven textile in which the basic pattern is represented by stretching springs, connected at nodes where a rotational stiffness is represented by flexional springs. More recently, (Assidi et al., 2011) developed mesostructurally-based continuum model, relating the fabric behavior at the macroscopic continuum scale to the response and geometry of the fabric's mesostructure (geometrical configuration of the weave and the yarn properties). For a more detailed description of several other analytical models, see (Realff, 1992).

Analytical models of the fabric mesostructure can be incorporated into anisotropic continuum formulations to yield models that track the fabric mesostructure as the continuum deforms. A number of authors have presented models for woven fabrics with continuum properties calculated from a deforming unit cell. (Boisse et al., 1997, 2001) constructed a three-dimensional unit cell like that of Kawabata for quasi-static and dynamic simulations of composite forming, but did not incorporate the resistance to yarn rotation or the inertia of uncrimping. (Rattensperger et al., 2003) take a similar approach for modeling fabric-reinforced hydraulic hoses, with fabric lattice geometry similar to that used by Kato, and use a conventional finite element formulation with rebar reinforcements. (Tanov and Brueggert, 2003) presented a mesostructurally-based continuum model that includes shear and locking resistance through diagonal spar elements within the assumed unit cell network. (Boisse et al., 2005, 2006) later used a planar unit cell for dynamic simulations by incorporating shear resistance at the cross-over point, but they did not include cross-locking. (Hamila et al., 2009) extended this approach to a shell finite element which includes the resistance to bending of the yarns. Some models are specific to the ballistic impact of woven fabrics. (Ivanov and Tabiei, 2004) constructed a Kawabata type unit cell for the simulation of ballistic impact but did not consider transverse compression, cross-locking, or the inertia of uncrimping. (Shahkarami and Vaziri, 2007) also used the Kawabata geometry in the simulation of ballistic impact.

Other mesostructurally analytical models have also been proposed for the study of woven fabrics behaviors. These models fall into two categories, namely orthogonal and non orthogonal constitutive models. (Peng and Cao, 2002) developed a systematic framework for predicting the effective nonlinear orthotropic elastic moduli of textile composites using the combination of the homogenization method and finite element analysis, considering orthogonal textiles. This approach mainly depends on the geometric description of the unit cell and the homogenized material properties imposed; a unit cell is built for the yarn section to estimate the effective elastic constants of fiber yarn. Then, another unit cell at meso-level is constructed to represent the periodic structure of the woven fabric. (Peng and Cao, 2005) developed a continuum mechanics-based non-orthogonal constitutive model to characterize the anisotropic material behavior of woven composite fabrics undergoing large deformations. The aim of their work was to overcome the difficulties involved in the purely numerical approach and to capture the anisotropic material behavior of woven composite fabrics during forming. Moreover, (Xue et al., 2005) developed an integrated meso-macro model for the prediction of the mechanical properties of woven fabrics in the range of large deformations.

Those authors previously suggested a non-orthogonal constitutive model for the prediction of mechanical properties at the macro scale (Xue et al., 2003), relying on experimental measurements to identify the constants of their model. (Khan et al., 2010) proposed a hypoelastic behavior for the numerical and experimental analyses of woven composite reinforcement forming. (Baseau, 2003) developed continuum formulations for "filamentary networks" appropriate for non-reinforced fabrics. (King et al., 2005) also proposed a new approach for continuum modeling of fabrics by selecting a geometric model for the fabric weave coupled with constitutive models for the yarns behavior. These authors used an energy minimization method to relate the fabrics structural configuration to the macroscopic deformation.

4.3 Unit cell geometrical model

The unit cell can be described as the smallest possible building block for the textile fabric, such that the fabric can be created by assembling the unit cell in the two periodic directions; the initial geometry is modeled using TexGen. TexGen is free and open source license software, operates on Windows and Linux, developed from research on technical textiles at the University of Manchester (www.texeng.co.uk). It is powerful appearing in speedy and accurate design and manufacture of 3D solid fabric of multilayer as well as single layer .Two typical textile patterns are considered in the present work, plain weave and twill fabrics (figure 4.2). Modeling this architecture is relatively difficult with conventional CAD, so we instead use TexGen in order to save time in the generation of the geometrical model and to export the geometric files to ABAQUS where the finite element analysis is done.

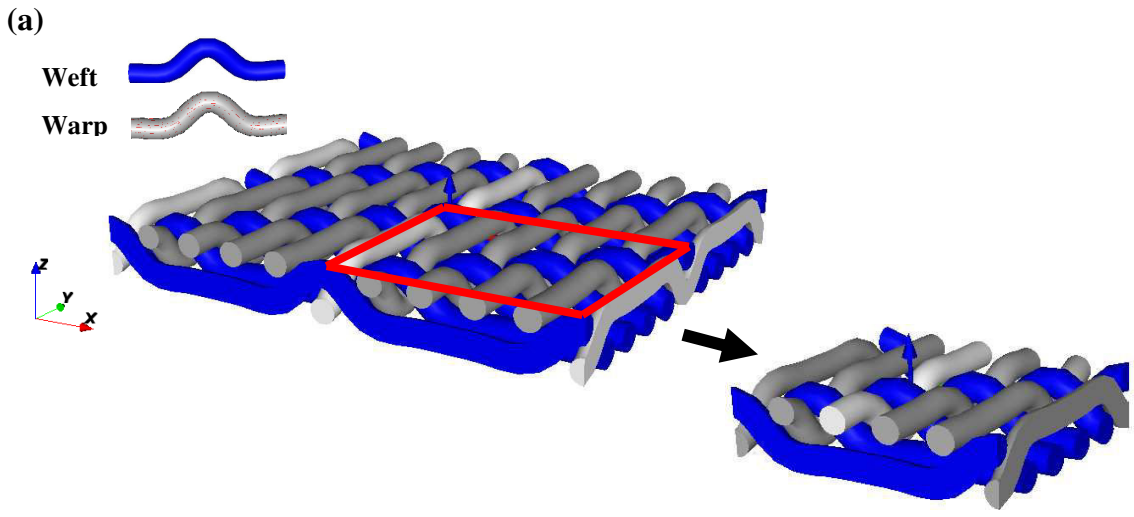

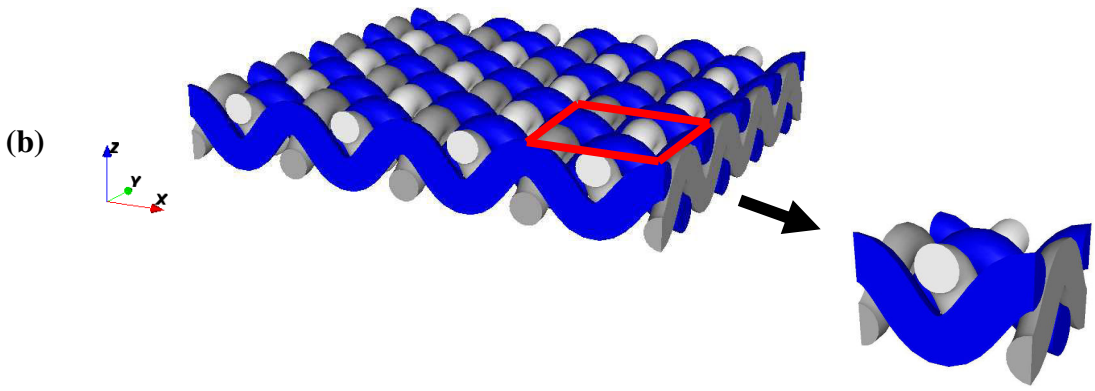

Fig. 4.2 Periodic reinforcement and Representative Unit Cell (RUC). (a) Macrostructure of twill fabric and its periodic macro-unit cell, (b) Macrostructure of plain weave fabric and its periodic macro-unit cell.

4.4 Expression of forces and moments

We extend in this chapter the homogenization technique introduced in chapter two to the consideration of the bending and torsion of the yarns modeled as thick beam elements, thus leading to the expression of internal forces and moments. The asymptotic expansion of the nodal displacement u^{ε} is written up to the second order as

$$\mathrm{u}^{\varepsilon}(\lambda^{\varepsilon}) = \mathrm{u}_0(\lambda^{\varepsilon}) + \varepsilon\ \mathrm{u}_1(\lambda^{\varepsilon}) + \varepsilon^2 \mathrm{u}_2(\lambda^{\varepsilon}) \tag{4.1}$$

The displacement difference $\Delta \mathrm{U}^{\mathrm{b}\varepsilon}$ between the extremity and origin node of each beam is expressed by a Taylor series development, according to

$$\begin{aligned} \Delta \mathrm{U}^{\mathrm{b}\varepsilon} = \mathrm{u}^{\varepsilon}(E(b)) - \mathrm{u}^{\varepsilon}(O(b)) &= \underbrace{\varepsilon\left({}^{E}_{\mathrm{u}_1} R(b)\left(\lambda^{\varepsilon}\right) - {}^{O}_{\mathrm{u}_1} R(b)\left(\lambda^{\varepsilon}\right) + \frac{\partial \mathrm{u}_0\left(\lambda^{\varepsilon}\right)}{\partial \lambda^i}\delta^{ib} \right)}_{\Delta \mathrm{U}_1^{\mathrm{b}}} \\ &\quad + \underbrace{\varepsilon^2\left({}^{E}_{\mathrm{u}_2} R(b)\left(\lambda^{\varepsilon}\right) - {}^{O}_{\mathrm{u}_2} R(b)\left(\lambda^{\varepsilon}\right) \right)}_{\Delta \mathrm{U}_2^{\mathrm{b}}} \\ &= \varepsilon\, \Delta \mathrm{U}_1^{\mathrm{b}} + \varepsilon^2\, \Delta \mathrm{U}_2^{\mathrm{b}} \end{aligned} \tag{4.2}$$

with δ^{ib} the shift factor (equal to ± 1) for nodes belonging to a neighbouring cell, and nil for nodes located inside the considered cell.

The asymptotic expansion of nodal microrotation $\phi^{n\varepsilon}$ is here limited to the first order in ε; it is defined successively at the origin and extremity of each beam as

$$\phi^{O(b)\varepsilon} = \phi_0^{O_{R(b)}} + \varepsilon\phi_1^{O_{R(b)}} \; ; \; \phi^{E(b)\varepsilon} = \phi_0^{E_{R(b)}} + \varepsilon\left(\frac{\partial\phi_0}{\partial\lambda^i}\delta^{ib} + \phi_1^{E_{R(b)}}\right) \tag{4.3}$$

wherein we have parameterized any point within the surface element representative of the fabric by curvilinear coordinates λ^i; this allows treating fabrics with curved material lines following the fibers in their reference state.

The normal and transverse efforts as well as the moments exerted on the beam extremities in the framework of 3D Timoshenko beams are obtained after lengthy calculations as

$$F_x^{\varepsilon b} = \frac{E_s^b A^{\varepsilon b}}{l^{\varepsilon b}} \left(e_x.\left(\varepsilon\,\Delta \mathrm{U}_1^{\mathrm{b}} + \varepsilon^2\,\Delta \mathrm{U}_2^{\mathrm{b}}\right)\right) \tag{4.4}$$

$$F_y^{\varepsilon b} = \frac{12E_s^b I_z^{\varepsilon b}}{\left(l^{\varepsilon b}\right)^3}\left(\begin{array}{l} e_y.\left(\varepsilon\,\Delta \mathrm{U}_1^{\mathrm{b}} + \varepsilon^2\,\Delta \mathrm{U}_2^{\mathrm{b}}\right) \\ -\frac{l^{\varepsilon b}}{2}\left(e_z.\left(\phi_0^{O_{R(b)}} + \phi_0^{E_{R(b)}} + \varepsilon\left(\phi_1^{O_{R(b)}} + \phi_1^{E_R(b)} + \frac{\partial\phi_0}{\partial\lambda^i}\delta^{ib}\right)\right)\right)\end{array}\right) \tag{4.5}$$

$$F_z^{\varepsilon b} = \frac{12E_s^b I_y^{\varepsilon b}}{\left(l^{\varepsilon b}\right)^3}\left(\begin{array}{l} e_z.\left(\varepsilon\,\Delta \mathrm{U}_1^{\mathrm{b}} + \varepsilon^2\,\Delta \mathrm{U}_2^{\mathrm{b}}\right) \\ +\frac{l^{\varepsilon b}}{2}\left(e_y.\left(\phi_0^{O_{R(b)}} + \phi_0^{E_{R(b)}} + \varepsilon\left(\phi_1^{O_{R(b)}} + \phi_1^{E_R(b)} + \frac{\partial\phi_0}{\partial\lambda^i}\delta^{ib}\right)\right)\right)\end{array}\right) \tag{4.6}$$

$$\begin{aligned} M_x^{O(b)\varepsilon} &= \frac{G_s^b J^{\varepsilon b}}{l^{\varepsilon b}}\varepsilon\left(e_x.\left(\phi_1^{O_{R(b)}} - \left(\frac{\partial\phi_0}{\partial\lambda^i}\delta^{ib} + \phi_1^{E_{R(b)}}\right)\right)\right) \\ M_x^{E(b)\varepsilon} &= \frac{G_s^b J^{\varepsilon b}}{l^{\varepsilon b}}\varepsilon\left(e_x.\left(\phi_1^{E_{R(b)}} - \phi_1^{O_{R(b)}} + \frac{\partial\phi_0}{\partial\lambda^i}\delta^{ib}\right)\right) \end{aligned} \tag{4.7}$$

$$\begin{aligned} M_y^{O(b)\varepsilon} &= \frac{6E_s^b I_y^{\varepsilon b}}{\left(l^{\varepsilon b}\right)^2}\left(e_z.\left(\varepsilon\,\Delta \mathrm{U}_1^{\mathrm{b}} + \varepsilon^2\,\Delta \mathrm{U}_2^{\mathrm{b}}\right)\right) \\ &+ \frac{E_s^b I_y^{\varepsilon b}}{l^{\varepsilon b}}\left(e_y.\left((4+\Phi_z^{\varepsilon})\phi_0^{O_{R(b)}} + (2-\Phi_z^{\varepsilon})\phi_0^{E_{R(b)}} + \varepsilon\left(\begin{array}{l}(4+\Phi_z^{\varepsilon})\phi_1^{O_{R(b)}} + (2-\Phi_z^{\varepsilon})\phi_1^{E_R(b)} \\ +(2-\Phi_z^{\varepsilon})\frac{\partial\phi_0}{\partial\lambda^i}\delta^{ib}\end{array}\right)\right)\right) \end{aligned} \tag{4.8}$$

$$
\begin{aligned}
M_y^{E(b)\varepsilon} &= \frac{6E_s^b I_y^{\varepsilon b}}{\left(l^{\varepsilon b}\right)^2}\left(e_z\cdot\left(\varepsilon\,\Delta U_1^b + \varepsilon^2\,\Delta U_2^b\right)\right) \\
&\quad + \frac{E_s^b I_y^{\varepsilon b}}{l^{\varepsilon b}}\left(e_y\cdot\left(\begin{array}{l}(2-\Phi_z^{\varepsilon})\phi_0^{O_{R(b)}} + (4+\Phi_z^{\varepsilon})\phi_0^{E_{R(b)}} + \varepsilon\left(\begin{array}{l}(2-\Phi_z^{\varepsilon})\phi_1^{O_{R(b)}} + (4+\Phi_z^{\varepsilon})\phi_1^{E_{R(b)}} \\ +(4+\Phi_z^{\varepsilon})\dfrac{\partial\phi_0}{\partial\lambda^i}\delta^{ib}\end{array}\right)\end{array}\right)\right) \\
M_z^{O(b)\varepsilon} &= \frac{6E_s^b I_z^{\varepsilon b}}{\left(l^{\varepsilon b}\right)^2}\left(-e_y\cdot\left(\varepsilon\,\Delta U_1^b + \varepsilon^2\,\Delta U_2^b\right)\right) \\
&\quad + \frac{E_s^b I_z^{\varepsilon b}}{l^{\varepsilon b}}\left(e_z\cdot\left(\begin{array}{l}(4+\Phi_y^{\varepsilon}))\phi_0^{O_{R(b)}} + (2-\Phi_y^{\varepsilon}))\phi_0^{E_{R(b)}} + \varepsilon\left(\begin{array}{l}(4+\Phi_y^{\varepsilon}))\phi_1^{O_{R(b)}} + (2-\Phi_y^{\varepsilon}))\phi_1^{E_{R(b)}} \\ +(2-\Phi_y^{\varepsilon}))\dfrac{\partial\phi_0}{\partial\lambda^i}\delta^{ib}\end{array}\right)\end{array}\right)\right) \\
M_z^{E(b)\varepsilon} &= \frac{6E_s^b I_z^{\varepsilon b}}{\left(l^{\varepsilon b}\right)^2}\left(-e_y\cdot\left(\varepsilon\,\Delta U_1^b + \varepsilon^2\,\Delta U_2^b\right)\right) \\
&\quad + \frac{E_s^b I_z^{\varepsilon b}}{l^{\varepsilon b}}\left(e_z\cdot\left(\begin{array}{l}(2-\Phi_y^{\varepsilon})\phi_0^{O_{R(b)}} + (4+\Phi_y^{\varepsilon})\phi_0^{E_{R(b)}} + \varepsilon\left(\begin{array}{l}(2-\Phi_y^{\varepsilon})\phi_1^{O_{R(b)}} + (4+\Phi_y^{\varepsilon})\phi_1^{E_{R(b)}} \\ +(4+\Phi_y^{\varepsilon})\dfrac{\partial\phi_0}{\partial\lambda^i}\delta^{ib}\end{array}\right)\end{array}\right)\right)
\end{aligned}
\tag{4.9}
$$

where E_s^b and G_s^b the tensile and shear modulus of bulk material. In the forthcoming development, a circular section of the beams is considered, hence the following geometrical parameters are computed: the cross-sectional area $A^{\varepsilon b} = \pi(\varepsilon r)^2$, the quadratic moment of the beam $I_y^{\varepsilon b} = I_z^{\varepsilon b} = \pi\frac{(\varepsilon r)^4}{4}$, and the torsional constant $J^{\varepsilon b} = \pi\frac{(\varepsilon r)^4}{2}$. Note that the present beam model and subsequent derivations of the effective mechanical response is not specific to textile materials, but can be applied to any lattice materials showing coupling effects between tension, bending and torsion (3D bone fall in this category).

We introduce the unit vectors $e_x = \left[Cxx' \quad Cyx' \quad Czx'\right]^T$, $e_y = \left[Cxy' \quad Cyy' \quad Czy'\right]^T$, and $e_z = \left[Cxz' \quad Cyz' \quad Czz'\right]^T$, where $Cxx' = \cos\theta_x$, $Cyx' = \cos\theta_y$, and $Czx' = \cos\theta_z$ are the direction cosines of x', describing the transformation between the local and global coordinate system in 3D (Fig. 4.3). Similarly, the components of e_y and e_z are the direction cosines of y' and z', respectively.

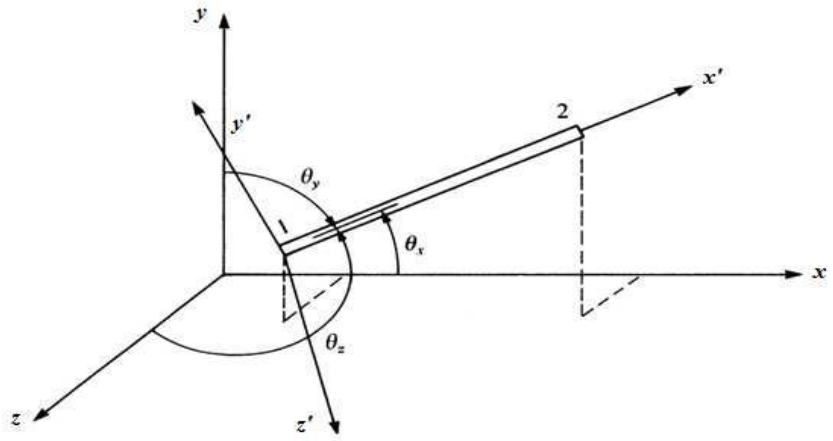

Fig. 4.3 Direction cosines associated with the x axis.

Previous expressions of the resultant forces and moments correspond to a Timoshenko beam model expressed in discrete form. The model takes into account the contribution of both shear and flexural rigidity to the deformation of a beam, which proves necessary to represent complex yarns made of the assembly of many filaments. On the tow scale, the obtained properties of fiber tows through the first level of evaluation and the properties of multi-layer matrices are combined with the geometrical parameters (the geometrical size of the tow's cross-section).

Since each beam within the fabric is equilibrated, the following equality holds true $\mathrm{F}^{\mathrm{E(b)}} = -\mathrm{F}^{\mathrm{O(b)}} = \mathrm{F}^{\mathrm{b}}$. The equilibrium of forces over the entire fabric (lattice) writes in virtual power form after insertion of the asymptotic development of the variables as

$$\sum_{i\in\mathbb{Z}^3}\sum_{b\in B_R} F^{\varepsilon b}.\left(\mathrm{v}^{\varepsilon}\left(O(b)\right)-\mathrm{v}^{\varepsilon}\left(E(b)\right)\right)=0 \tag{4.10}$$

with v^{ε} (.) a virtual velocity field choosing nil on the edges of the considered domain, and $\mathrm{F}^{\varepsilon\mathrm{b}}$ the sum of the extensional force $F_x^{\varepsilon b}$ and transversal forces, $F_y^{\varepsilon b}$ and $F_z^{\varepsilon b}$ (Eqs. (4.4-4.6)). For any virtual velocity field v^{ε}, supposed to be regular enough, a Taylor series development at the first order leads to

$$\mathrm{v}^{\varepsilon}\left(O(b)\right)-\mathrm{v}^{\varepsilon}\left(E(b)\right)\approx\varepsilon\frac{\partial\mathrm{v}\left(\lambda^{\varepsilon}\right)}{\partial\lambda^{\mathrm{i}}}\delta^{ib} \tag{4.11}$$

The fabric under consideration is described as a quasi repetitive lattice of beams and is completely defined by the positions of the nodes and their connectivity. We denote by N_R and B_R respectively, the set of nodes and beams within the reference unit cell, which are finite dimensional. The fabric is quasi periodic in its deformed state. The cells are numbered by the

triplet of integers $\upsilon^i=\left(\upsilon^1,\upsilon^2,\upsilon^3\right)$. The nodes of the whole fabric can then be parameterized by the quadruplet $\tilde{n}=\left(n,\upsilon^1,\upsilon^2,\upsilon^3\right)\in N_R\times\mathbb{Z}^3$. In the same way, the beams of the fabric are described by the quadruplet $\tilde{b}=\left(b,\upsilon^1,\upsilon^2,\upsilon^3\right)\in B_R\times\mathbb{Z}^3$. Within the reference cell, one can select the origin node of a beam $O(\tilde{b})$ so that it belongs to the reference cell. This origin node can be represented by the quadruplet $\left(n,\upsilon^1,\upsilon^2,\upsilon^3\right)$. Nevertheless, the end node $E(\tilde{b})$ does not necessarily belong to the reference cell, but is necessarily included in an adjacent cell numbered by $\left(\upsilon^1+\delta^1,\upsilon^2+\delta^2,\upsilon^3+\delta^3\right)$. The triplet $\left(\delta^1,\delta^2,\delta^3\right)\in\mathbb{Z}^3$, and the end node either belongs to the reference cell or to a cell next to it: this means that the shift parameter, the integer δ^i belongs to the set $\{-1,0,1\}$.

At the present stage, we rewrite the equilibrium Eq. (3.64) after substituting expressions of the forces from (3.58) to (3.60) therein and ordering according to the successive powers of ε as

$$\sum_{\upsilon^i\in\mathbb{Z}^3}\sum_{b\in B_R}\left[\begin{array}{l}\varepsilon^3\left(\begin{array}{l}\dfrac{\pi E_s^b\left(r^b\right)^2}{L^b}\left(e_x.\Delta\mathrm{U}_1^{\mathrm{b}}\right)e_x+\left(\dfrac{3\pi E_s^b\left(r^b\right)^4}{\left(L^b\right)^3}\left(e_y.\Delta\mathrm{U}_1^{\mathrm{b}}-\dfrac{L^b}{2}\left(e_z.\left(\phi_0^{O_{R(b)}}+\phi_0^{E_{R(b)}}\right)\right)\right)\right)e_y\\ +\left(\dfrac{3\pi E_s^b\left(r^b\right)^4}{\left(L^b\right)^3}\left(e_z.\Delta\mathrm{U}_1^{\mathrm{b}}+\dfrac{L^b}{2}\left(e_y.\left(\phi_0^{O_{R(b)}}+\phi_0^{E_{R(b)}}\right)\right)\right)\right)e_z\end{array}\right).\dfrac{\partial\mathrm{v}\left(\lambda^\varepsilon\right)}{\partial\lambda^{\mathrm{i}}}\delta^{ib}\\ +\varepsilon^4\left(\begin{array}{l}\dfrac{\pi E_s^b\left(r^b\right)^2}{L^b}\left(e_x.\Delta\mathrm{U}_2^{\mathrm{b}}\right)e_x+\left(\dfrac{3\pi E_s^b\left(r^b\right)^4}{\left(L^b\right)^3}\left(e_y.\Delta\mathrm{U}_2^{\mathrm{b}}-\dfrac{L^b}{2}e_z.\left(\begin{array}{l}\phi_1^{O_{R(b)}}+\phi_1^{E_{R(b)}}\\ +\dfrac{\partial\phi_0}{\partial\lambda^i}\delta^{ib}\end{array}\right)\right)\right)e_y\\ +\left(\dfrac{3\pi E_s^b\left(r^b\right)^4}{\left(L^b\right)^3}\left(e_z.\Delta\mathrm{U}_2^{\mathrm{b}}+\dfrac{L^b}{2}e_y.\left(\phi_1^{O_{R(b)}}+\phi_1^{E_{R(b)}}+\dfrac{\partial\phi_0}{\partial\lambda^i}\delta^{ib}\right)\right)\right)e_z\end{array}\right).\dfrac{\partial\mathrm{v}\left(\lambda^\varepsilon\right)}{\partial\lambda^{\mathrm{i}}}\delta^{ib}\end{array}\right]=0 \qquad (4.12)$$

Previous equilibrium equation gives in the limit of a vanishing small parameter the continuum equilibrium, relying on the following mathematical result: for any regular enough function g, the quantity $\varepsilon^3\sum_{\upsilon^i\in\mathbb{Z}^3}g\left(\varepsilon\upsilon^i\right)$ can be interpreted as the Riemann integral $\int_\Omega g(\lambda)d\lambda$ in 3-D when $\varepsilon\to 0$. Accordingly, the previous discrete equation becomes the homogenized self-equilibrium equation

$$\int_\Omega \mathrm{S}^i.\frac{\partial\mathrm{v}(\lambda)}{\partial\lambda^{\mathrm{i}}}d\lambda=0 \qquad (4.13)$$

with the stress vector S^i, which splits into a first and a second order contribution, viz. $\mathrm{S}^i = \mathrm{S}_1^i + \varepsilon \mathrm{S}_2^i$, with

$$\mathrm{S}_1^i = \sum_{b \in B_R} \left(\begin{array}{l} \dfrac{\pi E_s^b \left(r^b\right)^2}{L^b} \left(e_x . \Delta \mathrm{U}_1^{\mathrm{b}}\right) e_x + \left(\dfrac{3\pi E_s^b \left(r^b\right)^4}{\left(L^b\right)^3} \left(e_y . \Delta \mathrm{U}_1^{\mathrm{b}} - \dfrac{L^b}{2} \left(e_z . \left(\phi_0^{O_{R(b)}} + \phi_0^{E_{R(b)}} \right) \right) \right) \right) e_y \\ + \left(\dfrac{3\pi E_s^b \left(r^b\right)^4}{\left(L^b\right)^3} \left(e_z . \Delta \mathrm{U}_1^{\mathrm{b}} + \dfrac{L^b}{2} \left(e_y . \left(\phi_0^{O_{R(b)}} + \phi_0^{E_{R(b)}} \right) \right) \right) \right) e_z \end{array} \right) \delta^{ib}$$

$$\mathrm{S}_2^i = \sum_{b \in B_R} \left(\begin{array}{l} \dfrac{\pi E_s^b \left(r^b\right)^2}{L^b} \left(e_x . \Delta \mathrm{U}_2^{\mathrm{b}}\right) e_x + \left(\dfrac{3\pi E_s^b \left(r^b\right)^4}{\left(L^b\right)^3} \left(e_y . \Delta \mathrm{U}_2^{\mathrm{b}} - \dfrac{L^b}{2} \left(e_z \left(\phi_1^{O_{R(b)}} + \phi_1^{E_R(b)} + \dfrac{\partial \phi_0}{\partial \lambda^i} \delta^{ib} \right) \right) \right) \right) e_y \\ + \left(\dfrac{3\pi E_s^b \left(r^b\right)^4}{\left(L^b\right)^3} \left(e_z . \Delta \mathrm{U}_2^{\mathrm{b}} + \dfrac{L^b}{2} \left(e_y . \left(\phi_1^{O_{R(b)}} + \phi_1^{E_R(b)} + \dfrac{\partial \phi_0}{\partial \lambda^i} \delta^{ib} \right) \right) \right) \right) e_z \end{array} \right) \delta^{ib} \qquad (4.14)$$

The moment equilibrium is written in two different ways: one can first consider the equilibrium of moments for the fabric unit cell nodes, which is necessary to solve for the unknowns; it writes in asymptotic form as

$$\sum_{v^i \in \mathbb{Z}^3} \sum_{b \in B_R} \left(\mathrm{M}^{O(b)\varepsilon} . \mathrm{w}^{\varepsilon}\left(O(b)\right) + \mathrm{M}^{E(b)\varepsilon} \mathrm{w}^{\varepsilon}\left(E(b)\right) \right) = 0 \qquad (4.15)$$

Another approach involving the local equilibrium of each individual beam is considered for the purpose of homogenization; equilibrium is written at the center of each beam in asymptotic form as

$$\sum_{v^i \in \mathbb{Z}^3} \sum_{b \in B_R} \left(\mathrm{M}^{O(b)\varepsilon} . \mathrm{w}^{\varepsilon}\left(O(b)\right) + \mathrm{M}^{E(b)\varepsilon} . \mathrm{w}^{\varepsilon}\left(E(b)\right) + \varepsilon L^b \left(e_x \wedge \mathrm{F}^{\varepsilon b}\right) . \mathrm{w}^{\varepsilon}\left(C(b)\right) \right) = 0 \qquad (4.16)$$

where w(C(b)) is the rotation rate of the incorporated central beam node. The rotation rate is further expanded as

$$\begin{aligned} \mathrm{w}^{O(b)\varepsilon} &= \mathrm{w}_0(\lambda) \\ \mathrm{w}^{E(b)\varepsilon}(\lambda + \varepsilon\delta^i) &\approx \mathrm{w}_0(\lambda) + \varepsilon \frac{\partial \mathrm{w}_0(\lambda)}{\partial \lambda^i} \delta^{ib} \\ \mathrm{w}^{c(b)\varepsilon}(\lambda + \varepsilon\delta^i) &= \frac{1}{2}\left(\mathrm{w}^{E(b)\varepsilon} + \mathrm{w}^{O(b)\varepsilon} \right) \end{aligned} \qquad (4.17)$$

Similarly as for the equilibrium of efforts, the moment equilibrium (4.16) is homogenized. After some developments and simplifications and passing to the limit $\varepsilon \to 0$ in the discrete sum, the moment equilibrium equation after homogenization takes the following form

$$\int_{\Omega} \mu^i . \frac{\partial \mathrm{w}(\lambda)}{\partial \lambda^{\mathrm{i}}} d\lambda = 0 \qquad (4.18)$$

with the couple stress vectors that incorporate moments μ^i, also identified on two orders, viz. $\mu^i = \varepsilon\mu_1^i + \varepsilon^2\mu_2^i$, with

$$\mu_1^i = \sum_{b\in B_R}\left(\frac{1}{2}\left(M_{1y}^{E(b)} - M_{1y}^{O(b)}\right)e_y + \frac{1}{2}\left(M_{1z}^{E(b)} - M_{1z}^{O(b)}\right)e_z\right)\delta^{ib}$$
$$\mu_2^i = \sum_{b\in B_R}\left(M_{2x}^{E(b)}e_x + \frac{1}{2}\left(M_{2y}^{E(b)} - M_{2y}^{O(b)}\right)e_y + \frac{1}{2}\left(M_{2z}^{E(b)} - M_{2z}^{O(b)}\right)e_z\right)\delta^{ib} \quad (4.19)$$

with

$$M_{1y}^{O(b)} = \frac{3\pi E_s^b\left(r^b\right)^4}{2\left(L^b\right)^2}\left(e_z.\Delta U_1^b\right) + \frac{\pi E_s^b\left(r^b\right)^4}{4L^b}\left(e_y.\left((4)\phi_0^{O_{R(b)}} + (2)\phi_0^{E_{R(b)}}\right)\right)$$

$$M_{1z}^{O(b)} = \frac{3\pi E_s^b\left(r^b\right)^4}{2\left(L^b\right)^2}\left(-e_y.\Delta U_1^b\right) + \frac{\pi E_s^b\left(r^b\right)^4}{4L^b}\left(e_z.\left((4)\phi_0^{O_{R(b)}} + (2)\phi_0^{E_{R(b)}}\right)\right)$$

$$M_{2y}^{O(b)} = \frac{3\pi E_s^b\left(r^b\right)^4}{2\left(L^b\right)^2}\left(e_z.\Delta U_2^b\right) + \frac{\pi E_s^b\left(r^b\right)^4}{4L^b}\left(e_y.\left((4)\phi_1^{O_{R(b)}} + (2)\left(\phi_1^{E_{R(b)}} + \frac{\partial\phi_0}{\partial\lambda^i}\delta^{ib}\right)\right)\right)$$

$$M_{2z}^{O(b)} = \frac{3\pi E_s^b\left(r^b\right)^4}{2\left(L^b\right)^2}\left(-e_y.\Delta U_2^b\right) + \frac{\pi E_s^b\left(r^b\right)^4}{4L^b}\left(e_z.\left((4)\phi_1^{O_{R(b)}} + (2)\left(\phi_1^{E_{R(b)}} + \frac{\partial\phi_0}{\partial\lambda^i}\delta^{ib}\right)\right)\right)$$

$$M_{1y}^{E(b)} = \frac{3\pi E_s^b\left(r^b\right)^4}{2\left(L^b\right)^2}\left(e_z.\Delta U_1^b\right) + \frac{\pi E_s^b\left(r^b\right)^4}{4L^b}\left(e_y.\left((2)\phi_0^{O_{R(b)}} + (4)\phi_0^{E_{R(b)}}\right)\right) \quad (4.20)$$

$$M_{1z}^{E(b)} = \frac{3\pi E_s^b\left(r^b\right)^4}{2\left(L^b\right)^2}\left(-e_y.\Delta U_1^b\right) + \frac{\pi E_s^b\left(r^b\right)^4}{4L^b}\left(e_z.\left((2)\phi_0^{O_{R(b)}} + (4)\phi_0^{E_{R(b)}}\right)\right)$$

$$M_{2x}^{E(b)} = \frac{\pi G_s^b\left(r^b\right)^4}{2L^b}\left(e_x.\left(\phi_1^{E_{R(b)}} - \phi_1^{O_{R(b)}} + \frac{\partial\phi_0}{\partial\lambda^i}\delta^{ib}\right)\right)$$

$$M_{2y}^{E(b)} = \frac{3\pi E_s^b\left(r^b\right)^4}{2\left(L^b\right)^2}\left(e_z.\Delta U_2^b\right) + \frac{\pi E_s^b\left(r^b\right)^4}{4L^b}\left(e_y.\left((2)\phi_1^{O_{R(b)}} + (4)\left(\phi_1^{E_{R(b)}} + \frac{\partial\phi_0}{\partial\lambda^i}\delta^{ib}\right)\right)\right)$$

$$M_{2z}^{E(b)} = \frac{3\pi E_s^b\left(r^b\right)^4}{2\left(L^b\right)^2}\left(-e_y.\Delta U_2^b\right) + \frac{\pi E_s^b\left(r^b\right)^4}{4L^b}\left(e_z.\left((2)\phi_1^{O_{R(b)}} + (4)\left(\phi_1^{E_{R(b)}} + \frac{\partial\phi_0}{\partial\lambda^i}\delta^{ib}\right)\right)\right)$$

The constitutive equations for a micropolar linear (in general anisotropic) elastic solid are given by:

$$\sigma_{ij} = K_{ijkl}^s\epsilon_{kl} + B_{ijkl}\chi_{kl},\ m_{ij} = B_{klij}\epsilon_{kl} + K_{ijkl}^\mu\chi_{kl}\quad (i,j,k,l = x,y,z) \quad (4.21)$$

Where K_{ijkl}^s, B_{ijkl} and K_{ijkl}^μ are the micropolar fourth rank stiffness tensors. As a matter of comparison, for a linear and isotropic micropolar continuum, the previous general constitutive model simplifies to

$$
\begin{aligned}
K^{s}_{ijkl} &= \lambda\delta_{ij}\delta_{kl} + \mu^{*}\delta_{il}\delta_{jk} + \left(\mu^{*} + \kappa\right)\delta_{ik}\delta_{jl}, \\
K^{\mu}_{ijkl} &= \alpha\delta_{ij}\delta_{kl} + \beta\delta_{il}\delta_{jk} + \gamma\delta_{ik}\delta_{jl}.
\end{aligned}
\tag{4.22}
$$

Where δ_{ij} is the Kronecker symbol, and $\lambda, \mu^{*}, \kappa, \alpha, \beta$ and γ are six micropolar elastic constants, satisfying the relation $\mu = \mu^{*} + \kappa/2$. λ and μ are the classical Lamé constants with dimensions of force/length^2, κ, α, β and γ are new micropolar constants which vanish for classical materials.

The general form of the constitutive equations can presently be identified from the expressions of the homogenized stress and couple stress tensors together with S^{i} and μ^{i} expressions:

$$
\begin{aligned}
\sigma &= \frac{1}{g} S^{i} \otimes \frac{\partial R}{\partial \lambda^{i}} = \frac{1}{g}\left(S_1^{i} + \varepsilon S_2^{i}\right) \otimes \frac{\partial R}{\partial \lambda^{i}} = \underbrace{\frac{1}{g} S_1^{i} \otimes \frac{\partial R}{\partial \lambda^{i}}}_{\left[K^{s}\right]\{\epsilon\}} + \underbrace{\frac{1}{g}\varepsilon S_2^{i} \otimes \frac{\partial R}{\partial \lambda^{i}}}_{[B]\{\chi\}} \\
m &= \frac{1}{g}\mu^{i} \otimes \frac{\partial R}{\partial \lambda^{i}} = \frac{1}{g}\left(\varepsilon\mu_1^{i} + \varepsilon^{2}\mu_2^{i}\right) \otimes \frac{\partial R}{\partial \lambda^{i}} = \underbrace{\frac{1}{g}\varepsilon\mu_1^{i} \otimes \frac{\partial R}{\partial \lambda^{i}}}_{[B]\{\epsilon\}} + \underbrace{\frac{1}{g}\varepsilon^{2}\mu_2^{i} \otimes \frac{\partial R}{\partial \lambda^{i}}}_{\left[K^{\mu}\right]\{\chi\}}
\end{aligned}
\tag{4.23}
$$

with ***g*** the Jacobian of the transformation from Cartesian to curvilinear coordinates and **R** the position vector of any material point.

For periodical uniform structures endowed with a central symmetry, the stiffness coefficients are invariant under a coordinate inversion, hence the pseudo-tensor B_{ijkl} vanishes. The previous constitutive equations then implies that the vectors μ_1^{i} and S_2^{i} should vanish; this leads to an important simplification of the stress and couple stress vectors

$$
\begin{aligned}
S^{i} = S_1^{i} &= \sum_{b \in B_R} \left(\begin{array}{l}
\dfrac{\pi E_s^{b}\left(r^{b}\right)^{2}}{L^{b}} \left(e_x . \Delta U_1^{b}\right) e_x + \left(\dfrac{3\pi E_s^{b}\left(r^{b}\right)^{4}}{\left(L^{b}\right)^{3}} \left(e_y . \Delta U_1^{b} - \dfrac{L^{b}}{2}\left(e_z . \left(\phi_0^{O R(b)} + \phi_0^{E R(b)} \right) \right) \right) \right) e_y \\
+ \left(\dfrac{3\pi E_s^{b}\left(r^{b}\right)^{4}}{\left(L^{b}\right)^{3}} \left(e_z . \Delta U_1^{b} + \dfrac{L^{b}}{2}\left(e_y . \left(\phi_0^{O R(b)} + \phi_0^{E R(b)} \right) \right) \right) \right) e_z
\end{array} \right) \delta^{ib} \\
&= \sum_{b \in B_R} \left(F_{x1}^{b} e_x + F_{y1}^{b} e_y + F_{z1}^{b} e_z \right) \delta^{ib}
\end{aligned}
\tag{4.24}
$$

and

$$\mu^{i}=\mu_{2}^{i}=\sum_{b\in B_R}\left(\begin{array}{l}\left(\frac{\pi G_s^b\left(r^b\right)^4}{2L^b}\left(e_x\cdot\left(\phi_1^{E}{}_{R(b)}-\phi_1^{O}{}_{R(b)}+\frac{\partial\phi_0}{\partial\lambda^i}\delta^{ib}\right)\right)e_x\right)\\ +\frac{\pi E_s^b\left(r^b\right)^4}{4L^b}\left(\left(e_y\cdot\left(\begin{array}{l}\phi_1^{E}{}_{R(b)}-\phi_1^{O}{}_{R(b)}\\ +\frac{\partial\phi_0}{\partial\lambda^i}\delta^{ib}\end{array}\right)\right)e_y+\left(e_z\cdot\left(\begin{array}{l}\phi_1^{E}{}_{R(b)}\\ -\phi_1^{O}{}_{R(b)}\\ +\frac{\partial\phi_0}{\partial\lambda^i}\delta^{ib}\end{array}\right)\right)e_z\right)\end{array}\right)\delta^{ib} \tag{4.25}$$

$$=\sum_{b\in B_R}\left(M_{2x}^{E(b)}e_x+\frac{1}{2}\left(M_{2y}^{E(b)}-M_{2y}^{O(b)}\right)e_y+\frac{1}{2}\left(M_{2z}^{E(b)}-M_{2z}^{O(b)}\right)e_z\right)\delta^{ib}$$

with F_{x1}^b, F_{y1}^b, F_{z1}^b, M_{2x}^n, M_{2y}^n, and M_{2z}^n respectively, the first order normal and transverse efforts and the second order moment about x', y', and z'. Those expressions still involve the unknown displacements u_1^n, u_2^n and rotations ϕ_0^n, ϕ_1^n, which are determined for all nodes by solving the equilibrium Eqs. (3.64) and (3.69). After solving for the previous unknowns, one uses the expressions of the efforts and moments previously exposed to build the stress and couple stress vectors, S^i and μ^i, respectively; these vectors will then allow constructing the stress and couple stress tensors.

A dedicated code has been constructed from the proposed algorithms for the calculation of the effective classical and micropolar elastic constants of general repetitive fabric unit cells endowed with an arbitrary topology. The code uses an input file including the fabric topology and mechanical properties within a selected unit cell, and delivering as an output the homogenized mechanical properties (classical and micropolar moduli).

The algorithm that performs each new elastic computation over one load increment and with an update of the lattice geometry is described next.

4.5 Algorithm for the discrete homogenization in 3D framework

1. Initialization of the tables of initial data. Definition of the function **R** such That $x=R(\lambda^1,\lambda^2,\lambda^3)$
2. Transformation of the expressions

$\left(\frac{\partial \mathrm{U}}{\partial \lambda_i}\right)_{(\mathrm{Y}_1,\mathrm{Y}_2,\mathrm{Y}_3)} \mapsto \left(\frac{\partial \mathrm{U}}{\partial \lambda_i}\right)_{(\mathrm{e}_x,\mathrm{e}_y,\mathrm{e}_z)}$ and $\left(\frac{\partial \phi}{\partial \lambda_i}\right)_{(\mathrm{Y}_1,\mathrm{Y}_2,\mathrm{Y}_3)} \mapsto \left(\frac{\partial \phi}{\partial \lambda_i}\right)_{(\mathrm{e}_x,\mathrm{e}_y,\mathrm{e}_z)}$

3. For each beam in the fabric elementary cell (weft, warp and contact) $b \in B_R$, define

(a) The origin and end node of a beam respectively, $O=O_R(b),\ E=E_R(b)$.

(b) Express the displacement difference between extremity and origin node at first order: $\Delta \mathrm{U}_1^b = \mathrm{u}_1^E - \mathrm{u}_1^O + \frac{\partial \mathrm{U}}{\partial \lambda^i}\delta^i$, tensile rigidity: $k_l = \frac{A^b E_s^b}{L^b}$, flexural rigidity: $k_{ty} = \frac{12 E_s^b I_z^b}{\left(L^b\right)^3}$, $k_{tz} = \frac{12 E_s^b I_y^b}{\left(L^b\right)^3}$, torsional rigidity: $k_r = \frac{G_s^b J^b}{L^b}$

(c) Express the first order efforts:

$$F_{x1} = k_l\left(\mathbf{e}_x.\left(\Delta \mathrm{U}_1^b\right)\right), F_{y1} = \frac{k_{ty}}{(1+\Phi_y)}\left(\mathbf{e}_y.\left(\Delta \mathrm{U}_1^b\right) - \frac{L^b}{2}\left(\mathbf{e}_z.\left(\phi_0^O + \phi_0^E\right)\right)\right),$$

$$F_{z1} = \frac{k_{tz}}{(1+\Phi_z)}\left(\mathbf{e}_z.\left(\Delta \mathrm{U}_1^b\right) + \frac{L^b}{2}\left(\mathbf{e}_y.\left(\phi_0^O + \phi_0^E\right)\right)\right)$$

(d) Express the first order moments:

$$M_{1y}^O = k_{tz}\frac{L^b}{12(1+\Phi_z)}\left(6\mathbf{e}_z.\left(\Delta \mathrm{U}_1^b\right) + L^b\left(\mathbf{e}_y.\left((4+\Phi_z)\phi_0^O + (2-\Phi_z)\phi_0^E\right)\right)\right),$$

$$M_{1y}^E = k_{tz}\frac{L^b}{12(1+\Phi_z)}\left(6\mathbf{e}_z.\left(\Delta \mathrm{U}_1^b\right) + L^b\left(\mathbf{e}_y.\left((2-\Phi_z)\phi_0^O + (4+\Phi_z)\phi_0^E\right)\right)\right),$$

$$M_{1z}^O = k_{ty}\frac{L^b}{12(1+\Phi_y)}\left(-6\mathbf{e}_y.\left(\Delta \mathrm{U}_1^b\right) + L^b\left(\mathbf{e}_z.\left((4+\Phi_y)\phi_0^O + (2-\Phi_y)\phi_0^E\right)\right)\right),$$

$$M_{1z}^E = k_{ty}\frac{L^b}{12(1+\Phi_y)}\left(-6\mathbf{e}_y.\left(\Delta \mathrm{U}_1^b\right) + L^b\left(\mathbf{e}_z.\left((2-\Phi_y)\phi_0^O + (4+\Phi_y)\phi_0^E\right)\right)\right).$$

4. Calculate the unknowns displacement and rotation u_1^n and ϕ_0^n from (4.10) and (4.14).

5. Identify the homogenized microrotation

$$\phi_x = \frac{1}{2}\left(\frac{\partial u_z}{\partial y} - \frac{\partial u_y}{\partial z}\right),\ \phi_y = \frac{1}{2}\left(\frac{\partial u_x}{\partial z} - \frac{\partial u_z}{\partial x}\right),\ \phi_z = \frac{1}{2}\left(\frac{\partial u_y}{\partial x} - \frac{\partial u_x}{\partial y}\right).$$

6. Express the second order forces and moments as:

(a) $\Delta \mathrm{U}_2^b = \mathrm{u}_2^E - \mathrm{u}_2^O$ (b) $F_{x2} = k_l\left(\mathbf{e}_x.\left(\Delta \mathrm{U}_2^b\right)\right), F_{y2} = \frac{k_{ty}}{(1+\Phi_y)}\left(\mathbf{e}_y.\left(\Delta \mathrm{U}_2^b\right) - \frac{L^b}{2}\left(\mathbf{e}_z.\left(\phi_1^O + \phi_1^E + \frac{\partial \phi}{\partial \lambda^i}\delta^i\right)\right)\right),$

$$F_{z2} = \frac{k_{tz}}{(1+\Phi_z)}\left(\mathbf{e}_z.\left(\Delta \mathrm{U}_2^b\right) + \frac{L^b}{2}\left(\mathbf{e}_y.\left(\phi_1^O + \phi_1^E + \frac{\partial \phi}{\partial \lambda^i}\delta^i\right)\right)\right).$$

(c) $M_{2x}^{O}=k_r\left(\mathbf{e}_x\cdot\left(\phi_1^{O}-\left(\frac{\partial\phi}{\partial\lambda^i}\delta^i+\phi_1^{E}\right)\right)\right), M_{2x}^{E}=k_r\left(\mathbf{e}_x\cdot\left(\phi_1^{E}-\phi_1^{O}+\frac{\partial\phi}{\partial\lambda^i}\delta^i\right)\right),$

$M_{2y}^{O}=k_{tz}\frac{L^b}{12(1+\Phi_z)}\left(6\mathbf{e}_z\cdot\left(\Delta\mathrm{U}_2^{\mathrm{b}}\right)+L^b\left(\mathbf{e}_y\cdot\left((4+\Phi_z)\phi_1^{O}+(2-\Phi_z)\phi_1^{E}+(2-\Phi_z)\frac{\partial\phi}{\partial\lambda^i}\delta^i\right)\right)\right),$

$M_{2y}^{E}=k_{tz}\frac{L^b}{12(1+\Phi_z)}\left(6\mathbf{e}_z\cdot\left(\Delta\mathrm{U}_2^{\mathrm{b}}\right)+L^b\left(\mathbf{e}_y\cdot\left((2-\Phi_z)\phi_1^{O}+(4+\Phi_z)\phi_1^{E}+(4+\Phi_z)\frac{\partial\phi}{\partial\lambda^i}\delta^i\right)\right)\right),$

$M_{2z}^{O}=k_{ty}\frac{L^b}{12(1+\Phi_y)}\left(-6\mathbf{e}_y\cdot\left(\Delta\mathrm{U}_2^{\mathrm{b}}\right)+L^b\left(\mathbf{e}_z\cdot\left((4+\Phi_y)\phi_1^{O}+(2-\Phi_y)\phi_1^{E}+(2-\Phi_y)\frac{\partial\phi}{\partial\lambda^i}\delta^i\right)\right)\right),$

$M_{2z}^{E}=k_{ty}\frac{L^b}{12(1+\Phi_y)}\left(-6\mathbf{e}_y\cdot\left(\Delta\mathrm{U}_2^{\mathrm{b}}\right)+L^b\left(\mathbf{e}_z\cdot\left((2-\Phi_y)\phi_1^{O}+(4+\Phi_y)\phi_1^{E}+(4+\Phi_y)\frac{\partial\phi}{\partial\lambda^i}\delta^i\right)\right)\right).$

Solve for variables u_2^n and ϕ_1^n from (4.10) and (4.14).

7. Construct the stress and couple stress vectors,

$\mathrm{S}^{\mathrm{i}}=\sum_{b\in B_R}\left(F_{x1}^{b}e_x+F_{y1}^{b}e_y+F_{z1}^{b}e_z\right)\delta^i$ and

$\mu^{\mathrm{i}}=\sum_{b\in B_R}\left(M_{2x}^{E(b)}e_x+\frac{1}{2}\left(M_{2y}^{E(b)}-M_{2y}^{O(b)}\right)e_y+\frac{1}{2}\left(M_{2z}^{E(b)}-M_{2z}^{O(b)}\right)e_z\right)\delta^i$ respectively.

8. Construct the stress tensor $\sigma=\frac{1}{g}\mathrm{S}^{\mathrm{i}}\otimes\frac{\partial\mathrm{R}}{\partial\lambda^{\mathrm{i}}}$ and couple stress tensor $\mathrm{m}=\frac{1}{g}\mu^{\mathrm{i}}\otimes\frac{\partial\mathrm{R}}{\partial\lambda^{\mathrm{i}}}$,

such that $\begin{Bmatrix}\sigma\\ \mathrm{m}\end{Bmatrix}=\begin{bmatrix}K^s & 0\\ 0 & K^{\mu}\end{bmatrix}\begin{Bmatrix}\epsilon\\ \chi\end{Bmatrix}$.

9. Compute the effective mechanical properties $E_x^*, E_y^*, \nu_{xy}^*, G_{xy}^*, K_{55}^{\mu}, K_{66}^{\mu}$ in the small strain regime.

10. Compute the incremental stress value versus the incremental strain with respect to the load case.

11. Solve the inverse problem gives the equivalent appropriate macroscopic displacement consistent with chosen load case.

12. Update pattern geometry to perform a new elastic computation under the new load increment (with a selected step size).

This algorithm has been implemented into a dedicated code written in symbolic language to compute the overall response of different woven structures subjected to different loadings at the mesoscopic scale.

It includes two successive parts: one first determines the effective mechanical properties of the considered periodic lattice in the initial small strain regime descriptive of the initial response of the structure (this step is described in the subsequent section 4.6). Afterwards, this

information is used to initialize the incremental scheme for the construction of the structural response in the nonlinear regime, as described in section 4.7.
We shall consider as a specific application the modelling of dry textiles (without the resin into which the perform is impregnated), which consist of two (at least) families of fibbers, for monolayers. Nevertheless, the proposed methodology is quite general and can be potentially applied to any structure including two families of fibers, such as arteries or biological membranes.

4.6 Effective mechanical properties of woven fabrics

A woven fabric consists of two sets of interwoven yarns, called warp and weft. From a geometrical point of view and without considering a specific pattern, each of these yarn elements can be considered to be either inclined (as it passes from top to bottom of the fabric) or straight (as it passes over or under another yarn), as depicted earlier in Figure 3.8. In this section, we apply the discrete homogenization technique exposed in the previous section to two important types of woven fabrics, plain weave and twill (Fig. 3.8) to calculate their equivalent effective properties. For this purpose, simplified models based on a 3D geometrical description of the unit cell at the mesoscopic scale are proposed, in which the fabrics are assumed to be represented as networks of beams linked by articulations. The main assumption made throughout the construction of these models is that the yarn section remains constant along the curvilinear trajectory. This trajectory, namely the mean line of the yarn, is modeled as straight segments of beams from which the 3D yarns of the fabric are constructed.
The first step is to build a geometrical model that is consistent and able to take into account the diversity of fabric geometries. For this intention, the textile is represented as a network of beams connected by nodes at their crossover points. These beams do not lie in the plane of the fabric but are interwoven to capture crimp interchange; they have axial and bending rigidities to allow for yarn stretch and flexion. Yarn-yarn interactions at the yarns crossing points clearly influence the effective properties of the material at the meso-level. Interactions between warp and weft yarns at the crossover points are here captured by beam segments connecting the nodes (see figure 3.10 (a), (b)). The crossover beams also have two modes of deformation, namely extension and flexion.

The proposed geometric description therefore is adequate for capturing the relevant behaviors and is more computationally efficient for effective mechanical behaviors than more

sophisticated geometrical descriptions. Its chief limitation is that the yarns are modeled as straight beams with sharp corners at the crossover points, whereas they warp around the crossing yarns with a smooth radius of curvature in reality. This geometry consequently permits configurations that are incompatible because of interpenetrations between the yarns, and cannot capture complex behaviors that are controlled by yarn wrapping.

4.6.1 Unit cell of plain weave and twill fabric

The first order homogenization schemes was recently developed by (Goda et al., 2013) for the determination of the effective mechanical properties of these two chosen architectures, stiffness matrix components are expressed as a function of material and micro structural geometric parameter.

For the two chosen applications of (a) plain weave (b) Twill, the proposed geometric description for the unit cell of fabric and the corresponding periodicity vectors are represented on the same figure 4.4.

(a)

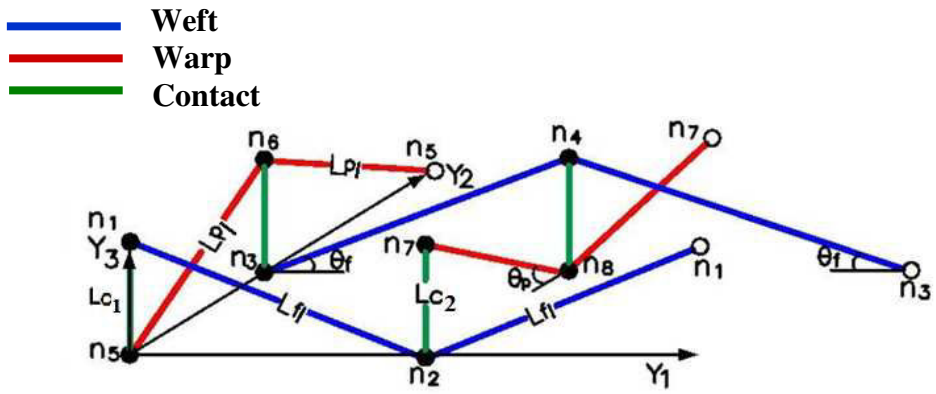

(b)

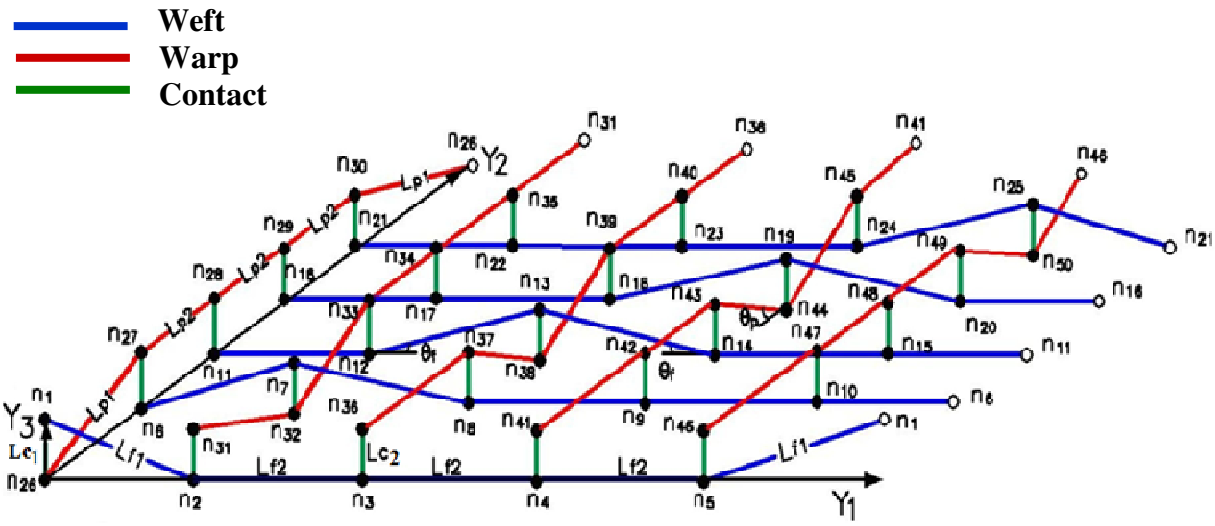

Fig. 4.4 Proposed geometric description for the unit cell of the fabric. (a) A 3D lattice model of 2D plain weave. (b) Geometrical model of an elementary cell of twill.

The following geometrical parameters and material properties for plain weave and twill are given in Table 4.1.

Table 4.1 Plain weave and twill fabric configuration parameter.

weave	Set of input geometric data required for modeling					
Plain	Weft	L_{f1} = 0.618 mm	--	θ_f =40°	d_f = 0.27 mm
	Warp	L_{p1} = 0.56 mm	--	θ_p =40°	d_p = 0.25 mm
Twill	Weft	L_{f1} = 0.618 mm	L_{f2} = 0.487 mm	θ_f =40°	d_f = 0.27 mm
	Warp	L_{p1} = 0.56 mm	L_{p2} = 0.41 mm	θ_p =40°	d_p = 0.25 mm

The mechanical properties of weft and warp made of PET (Polyethylene terephthalate) are given in Table 4.2; we intentionally choose very different moduli to represent an unbalanced fabric, leading to an expected anisotropic behavior.

Table 4.2 Elastic properties of weft and warp yarns.

	Set of input material data		
Weft	E_{sf} =1889 MPa	G_{sf} =756 MPa	v_f =0.25
Warp	E_{sp}= 13853 Mpa	G_{sp}= 5541 Mpa	v_p =0.25

The mechanical properties of the yarns are the same for both unit cells. The tensile, flexural, and torsion rigidities of the beam segments are quantified as follows:

Table 4.3 Mechanical properties of weft warp and contact beams.

Beams at / Beam rigidity	Weft	warp	contact
Tensile	$k_{lf_{1,2}} = \frac{E_{sf} A_f}{L_{f_{1,2}}}$	$k_{lp_{1,2}} = \frac{E_{sp} A_p}{L_{p_{1,2}}}$	$k_{lc_{1,2}} = \frac{E_{sc} A_c}{L_{c_{1,2}}}.$
Flexural	$k_{tf1} = \frac{12 E_{sf} I_f}{\left(L_{f1}\right)^3}$	$k_{tp1} = \frac{12 E_{sp} I_p}{\left(L_{p1}\right)^3}$	$k_{tc_{1,2}} = \frac{12 E_{sc} I_c}{\left(L_{c_{1,2}}\right)^3}.$
Torsional	$k_{rf1} = \frac{G_{sf} J_f}{L_{f1}}$	$k_{rp1} = \frac{G_{sp} J_p}{L_{p1}}$	$k_{rc_{1,2}} = \frac{G_{sc} J_c}{L_{c_{1,2}}}.$

Furthermore, the geometric and material parameters for the contact beam are

$$L_{c_{1,2}} = Lf_1 Sin\theta_f, Lp_1 Sin\theta_p,\ r_c = \frac{r_f + r_p}{2},\ G_{sc} = \frac{G_{sf} + G_{pf}}{2}, \text{ and } E_{sc} = \frac{E_{sf} + E_{pf}}{2}$$

where $L_{c1,2}$, r_c, G_{sc}, and E_{sc}, respectively, represent the lengths, radius, shear and Young's modulus of the contact beams (beams connecting the warp and weft yarns at their crossing points). As an assumption, we consider the beam in contact has radius and mechanical modulus as the average value from weft and warp values.

After homogenization, the equivalent stiffness matrix is obtained as a function of the geometrical and mechanical parameters of the two weave fabric. One can accordingly write the equivalent form of the constitutive law under the form

$$\begin{Bmatrix} \sigma \\ \mathrm{m} \end{Bmatrix} = \begin{bmatrix} K^s & 0 \\ 0 & K^\mu \end{bmatrix} \begin{Bmatrix} \boldsymbol{\varepsilon} \\ \boldsymbol{\kappa} \end{Bmatrix}$$

The deformation and microcurvature components write versus the displacement gradient and the microrotations as

$$\varepsilon_x = \frac{\partial u_x}{\partial x},\ \varepsilon_y = \frac{\partial u_y}{\partial y},\ \varepsilon_{xy} = \frac{\partial u_y}{\partial x} - \phi_z,\ \varepsilon_{yx} = \frac{\partial u_x}{\partial y} + \phi_z$$

$$\kappa_{xx} = \frac{\partial \phi_x}{\partial x},\ \kappa_{yy} = \frac{\partial \phi_y}{\partial y},\ \kappa_{xy} = \frac{\partial \phi_y}{\partial x},\ \kappa_{yx} = \frac{\partial \phi_x}{\partial y},\ \kappa_{xz} = \frac{\partial \phi_z}{\partial x}, \kappa_{yz} = \frac{\partial \phi_z}{\partial y}$$

The following stiffness's matrices K^s and K^μ describing respectively the in-plane and bending behaviour are obtained for the plain weave fabric:

$$\left[K^{s}\right]=\begin{bmatrix}121.7 & 49.70 & 0 & 0\\ 49.7 & 302.2 & 0 & 0\\ 0 & 0 & 25.7 & -9.9\\ 0 & 0 & -58.1 & 78.4\end{bmatrix}\ \text{MPa}$$

$$\left[K^{\mu}\right]=\begin{bmatrix}1.22 & 0 & 0 & 0 & 0 & 0\\ 0 & 6.24 & 0 & 0 & 0 & 0\\ 0 & 0 & 2.00 & 0 & 0 & 0\\ 0 & 0 & 0 & 5.04 & 0 & 0\\ 0 & 0 & 0 & 0 & 1.69 & 0\\ 0 & 0 & 0 & 0 & 0 & 6.92\end{bmatrix}\ \text{N}$$

In the same manner, the equivalent stiffness matrix corresponding to the twill fabric,

$$\left[K^{s}\right]=\begin{bmatrix}194.7 & 93.6 & 0 & 0\\ 93.6 & 360.6 & 0 & 0\\ 0 & 0 & 34.5 & -15.6\\ 0 & 0 & -89.4 & 115.6\end{bmatrix}\ \text{MPa}$$

$$\left[K^{\mu}\right]=\begin{bmatrix}3.25 & 0 & 0 & 0 & 0 & 0\\ 0 & 10.72 & 0 & 0 & 0 & 0\\ 0 & 0 & 3.64 & 0 & 0 & 0\\ 0 & 0 & 0 & 8.37 & 0 & 0\\ 0 & 0 & 0 & 0 & 4.0 & 0\\ 0 & 0 & 0 & 0 & 0 & 10.45\end{bmatrix}\ \text{N}$$

The mechanical moduli extracted from those matrices are given in a synthetic form in the following table.

Table 4.4 Effective homogenized moduli of plain weave and twill fabrics.

Effective homogenized moduli	Plain weave fabric	Twill fabric
$E_x^*(MPa)$	113.5	170.4
$E_y^*(MPa)$	281.9	315.6
υ_{xy}^*	0.16	0.26
υ_{xy}^*	0.4	0.48
$G^*(MPa)$	7.90	9.44
$l_{c1}(mm)$	0.23	0.33
$l_{c1}(mm)$	0.41	0.45

Here, $E^*_{x,y}, \upsilon^*_{xy,yx}, G^*$ and $l_{c_{1,2}}$ are Young's moduli, Poisson's ratios, shear moduli and characteristics length's of the fabrics, respectively.

In the next section, based on the previous linear discrete homogenization analysis, we will describe how we extend this approach to account for the geometrical nonlinear behavior.

4.7 Nonlinear modelling framework implementation by the discrete homogenization approach

The discrete homogenization approach as explained in section 2.4 has been implemented for the two types of fabric. The analyses of the periodic reinforcement as representative unit cell (RUC) have been implemented within a dedicated code considering the impact of a variation of the structure geometry simultaneously in a nested manner. First, the deformation gradient tensor at each macroscopic incremental load (or at each macroscopic iteration) is assigned based on the macroscopic constitutive law. Second, we based on previous linear framework involving the computed compliance matrix to be transferred to the correct macroscopic displacement gradient that defines the controlled imposed strain loading over the representative unit cell.
The incremental–iterative approach for the macro–micro computational homogenization method is schematically illustrated in Figure 4.5.

In the next sections, the proposed methodology based on the discrete homogenization framework implementation is performed for the two chosen pattern of fabric under the three types of loading as explained in section 3.6. The verification of the correctness of the present methodology will be discussed from the comparison with numerical computation on the representative unit cell generated by TexGen and exported to ABAQUS.

4.7.1 Steps of incremental–iterative discrete homogenization modelling approach

STEP 1: At the beginning of first incremental iteration, define the constitutive law involving the computed compliance matrix from the linear discrete homogenization framework.

Step 2: Solve the RVE boundary value problem for the unknown components of the unprescribed strain; this is an inverse problem, the solution of which giving for each load type the incrementally controlled imposed strain to be applied over the representative unit cell.

STEP 3: compute and store the incremental second Piola-Kirchhoff stress tensor.

STEP 4: then push forward the incremental second Piola-Kirchhoff stress tensor to get the incremental Cauchy stress tensor.

STEP 5: A new geometric and mechanical description is initialized for the RUC analysis job. (i.e update pattern geometry).

STEP 6: next iteration start with solve the equilibrium of forces and hyper forces over the updated geometry of the representative unite cell. Then repeat steps from 1-5 with accumulation of the incremental Cauchy stress values versus the strain.

The work flow steps of the coupling between the linear and geometrical nonlinear discrete homogenization approaches is described next as shown in figures 4.5.

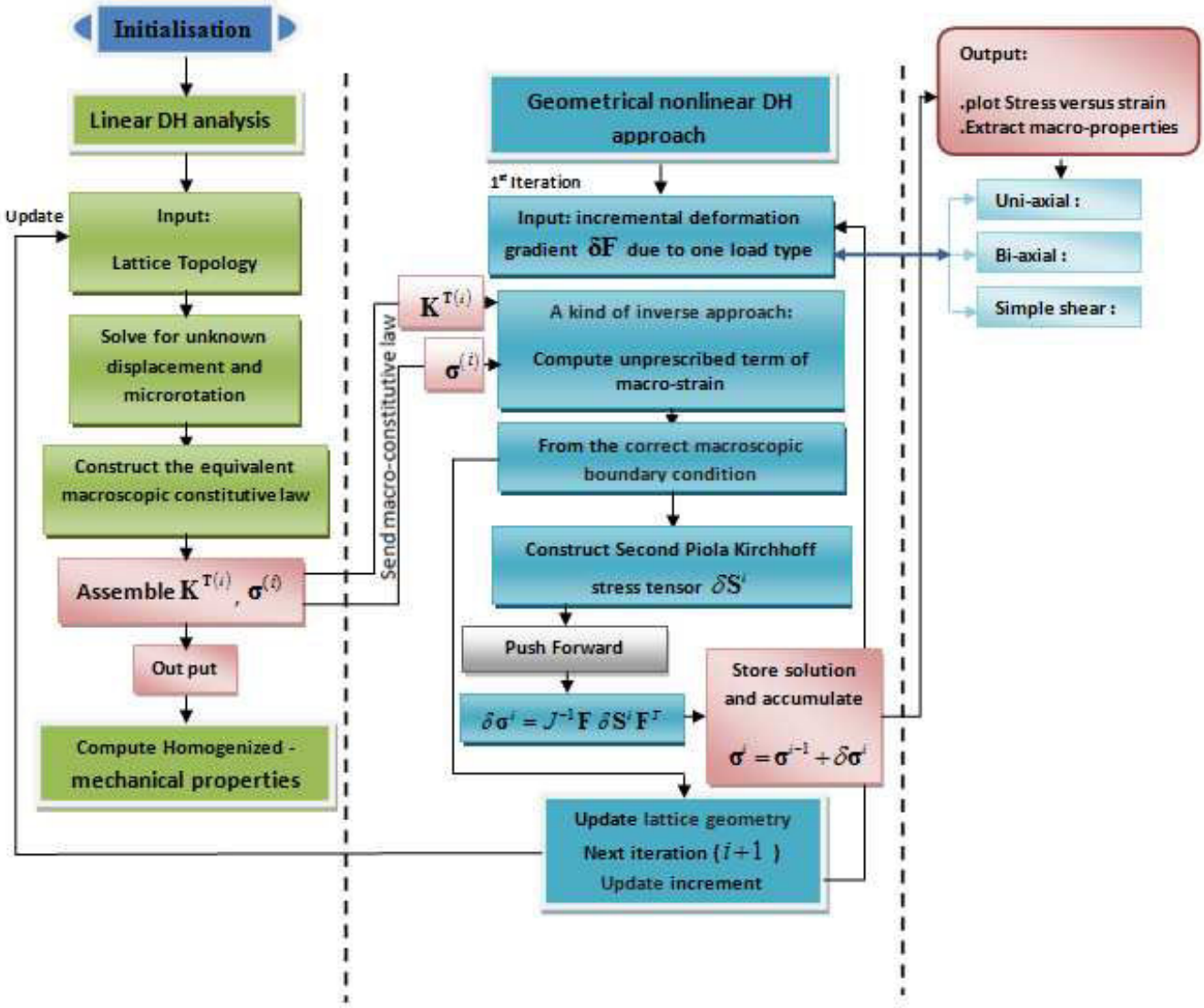

Fig. 4.5 Schematic view of the proposed methodology

CHAPTER Five

Nonlinear Response of Textile Monolayers (Plain weave and Twill)

Contents

We next compute the nonlinear response of textile monolayers which exhibit strong geometrical nonlinearities, as discussed in the literature overview in the second part of this chapter. The constitutive yarns can be considered as flexible beam elements with low stretch. The interlacing and crossing of yarns give rise to complex internal deformation mechanisms, responsible for the nonlinear response.

5.1 Homogenization examples and results

The following representative unit cells are analyzed: a) plain weave fabric b) twill fabric, in order to express the stress-strain behaviour under the three types of loading, as explained previously for the simple 2D applications treated in section 3.6.

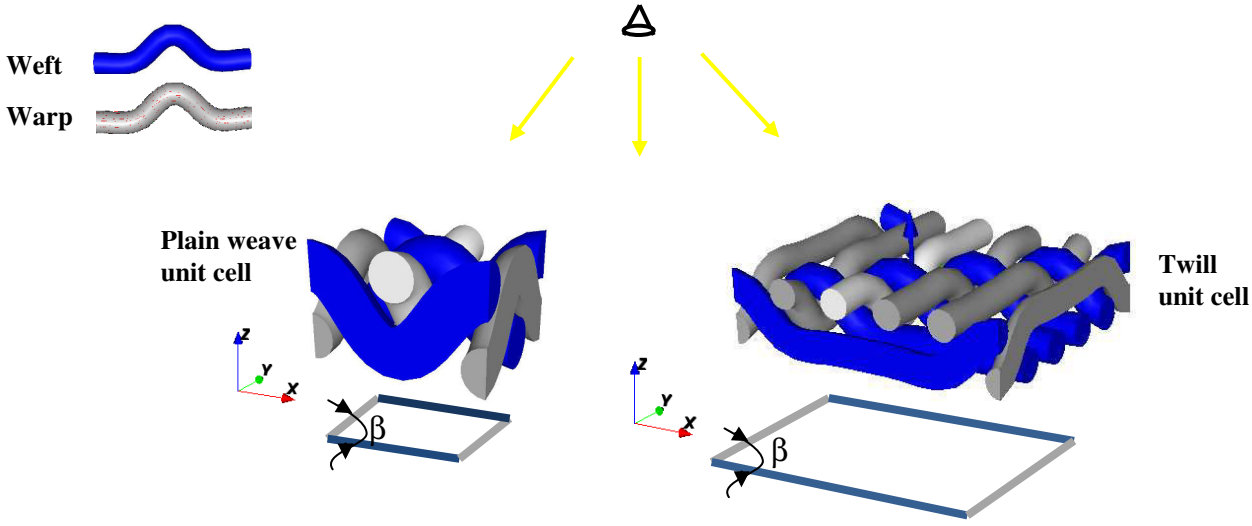

Fig. 5.1 Representative plain weave and twill unit cells top views ($\beta = 90^{\circ}$).

The deformation gradient tensor expresses as

$$\mathbf{F} = \begin{bmatrix} 1+\varepsilon_{xx} & \gamma_{xy} \\ \gamma_{yx} & 1+\varepsilon_{yy} \end{bmatrix}$$

It is applied to the RUC fabric describing the total deformation through the displacement gradient that is imposed by the periodic boundary conditions, where ε and γ_{xy} are the normal strain and shear strain respectively. The subscripts “x” and “y” denote the direction of the axes of the global coordinate system. Recall that only part of the total deformation gradient is actually controlled in a specific loading, so that one solves the RUC boundary value problem for the unknown components of the unprescribed strain.

5.1.1 Unit cell of plain weave fabric

5.1.1.1 Uniaxial tension

In the case of a uniaxial tensile test on a textile RUC, yarns under tensile strain tend to straighten, whereas the crimps of yarns in transverse direction tend to increase: this phenomenon is called crimp interchange. The crimp C_r characterize the degree of out-of-plane waviness of a yarn, by measuring the length of the yarn in fabric state l_{yarn} within the periodic RUC, and the periodic length l_{RUC} of the representative unit cell that define the fabric, one shall defined from the previous two lengths the crimp ratio at each load increment as,

$$C_{r_{11,22}}(\%) = \frac{l_{\text{yarn}_{1,2}} - l_{\text{RUC}_{1,2}}}{l_{\text{RUC}_{1,2}}}$$

Where the subscripts “11” and “22” denote the direction of the axes of the global coordinate system(x, y) as (weft and warp) respectively.

The prescribed deformation applied on the RVEs for the uniaxial tension in weft and warp directions are

$$\mathbf{F}_f = \begin{bmatrix} 1+\varepsilon_{xx} & \gamma_{xy}=0 \\ \gamma_{yx}=0 & 1+\varepsilon_{yy} \end{bmatrix} = \begin{bmatrix} 1+\varepsilon_{xx} & 0 \\ 0 & \textit{unprescribed} \end{bmatrix}$$

And

$$\mathbf{F}_p = \begin{bmatrix} 1+\varepsilon_{xx} & \gamma_{xy} \\ \gamma_{yx} & 1+\varepsilon_{yy} \end{bmatrix} = \begin{bmatrix} \textit{unprescribed} & 0 \\ 0 & 1+\varepsilon_{yy} \end{bmatrix}$$

In the tensile loading test in weft direction shown in Figure 5.2, we observe that there is an important difference between the linear and geometrical nonlinear behaviour with increasing stretch (from 1.15 to 1.3): one obtains as one can expect from simple mechanical considerations a stiffer response in comparison to the linear response (from 10% to 24%), due to the yarns being more aligned in the direction of the applied tension.

- **Uniaxial tension in weft**

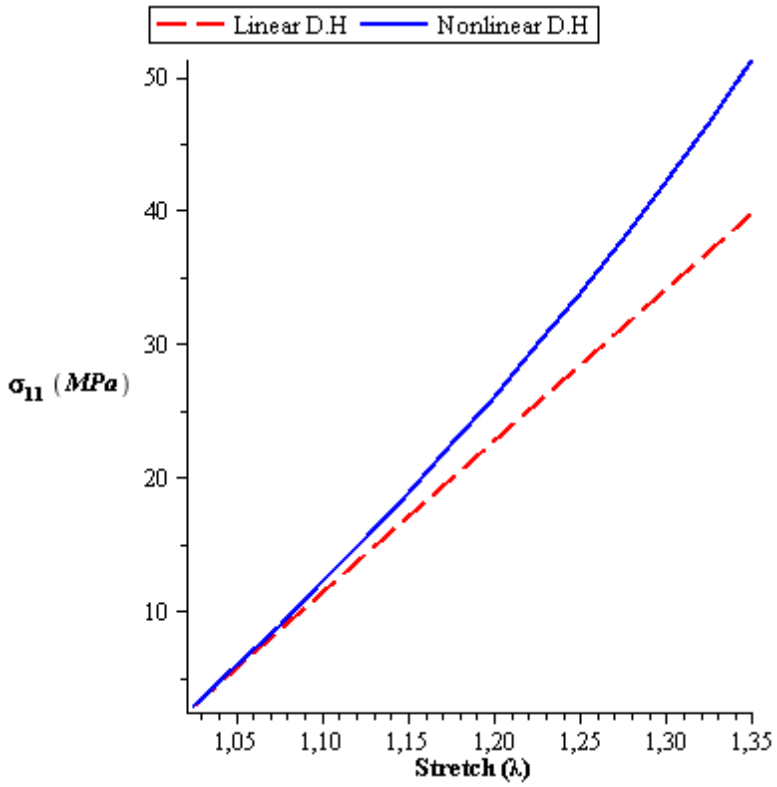

Fig. 5.2 Cauchy stress versus stretch for plain weave fabric. (a) Cauchy stress in xx-direction versus stretch in the same direction

We next plot the evolution of the homogenized geometrical and mechanical effective properties versus the stretch applied in the in xx-direction. The mechanical parameters characterizing the derived effective micropolar behaviour are: two tensile moduli $E_{h_{11}}, E_{h_{22}}$. The crimp ratio in both direction $\%C_{r_1}, \%C_{r_2}$ .and Poisson's ratio $\nu_{h_{12}}, \nu_{h_{21}}$ as shown in the next figure 5.3 (a, b and c) respectively.

The equivalent tensile modulus along x-direction increases continuously in the selected range of stretch. The tensile modulus along yy-direction has its maximum value initially and decreases versus stretch thereafter: this is expected due to the structure becoming stiffer in xx-direction due to the straightening of the yarns, and softer in transverse direction, due to increasing crimp. The contraction $\nu_{h_{21}}$ and the crimp ratio $\%C_{r_{11}}$ decrease monotonously versus stretch. The Poisson's ratio $\nu_{h_{12}}$ shows a complex evaluation as shown in figure 5.3(c), increasing through a maximum (the transverse contraction is maximal for $\lambda = 1.15$) and decreasing thereafter. Finally, one shall expect the increase of crimp ratio in warp direction

$\%C_{r_{22}}$ versus stretch as shown in figure 5.3 (b) that comes from the contraction in this direction.

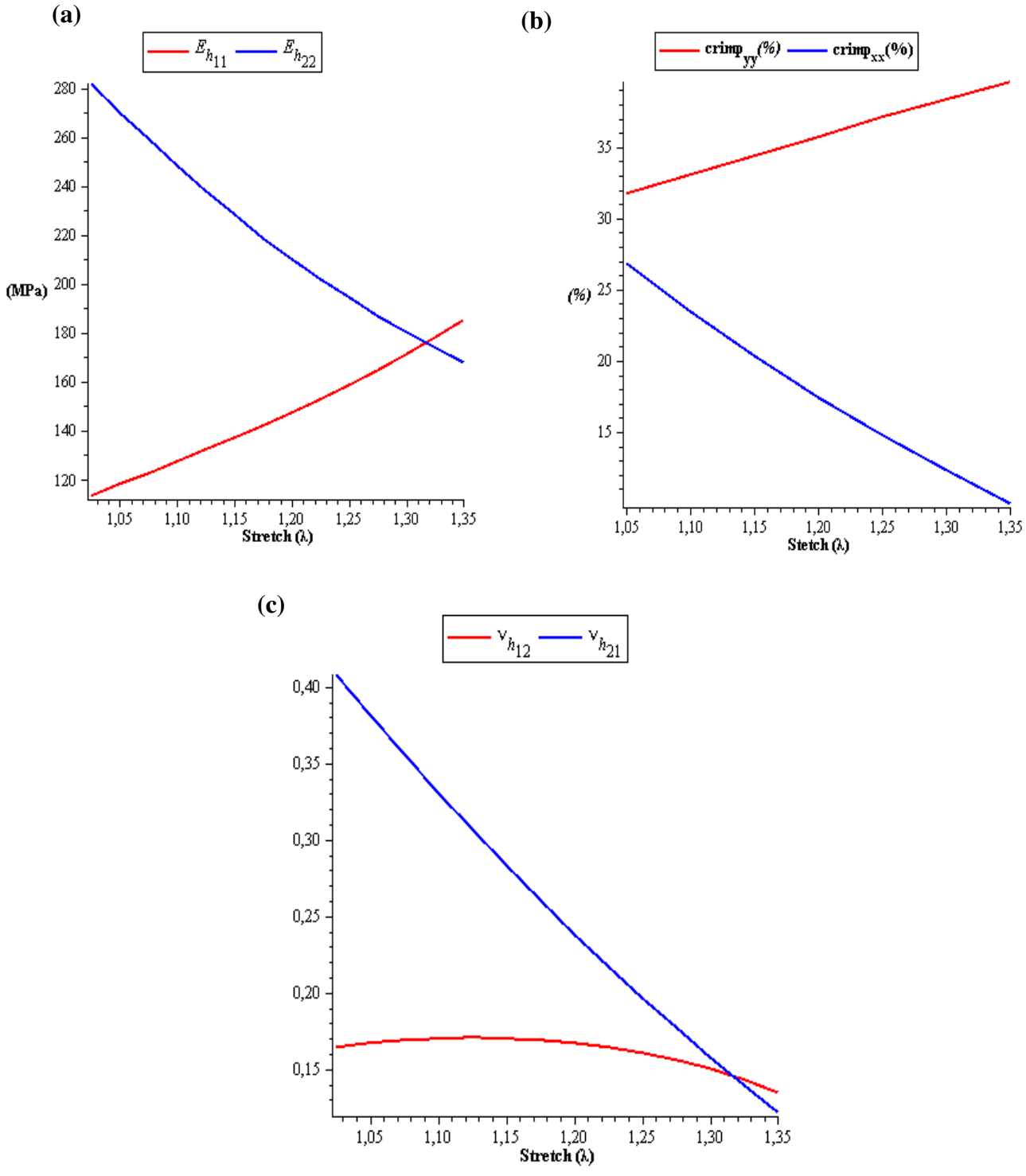

Fig. 5.3: homogenized mechanical and geometrical parameters (a) tensile moduli $E_{h_{11}}, E_{h_{22}}$ (b) crimp ratio $\%C_{r_{11}}, \%C_{r_{22}}$. (c) Poisson's ratio $\nu_{h_{12}}, \nu_{h_{21}}$ versus stretch in xx- direction.

- **Uniaxial tension in warp**

In the same manner, we plot the evaluation of Cauchy stress and the change of the homogenized geometrical and mechanical parameters versus stretch applied in yy-direction.

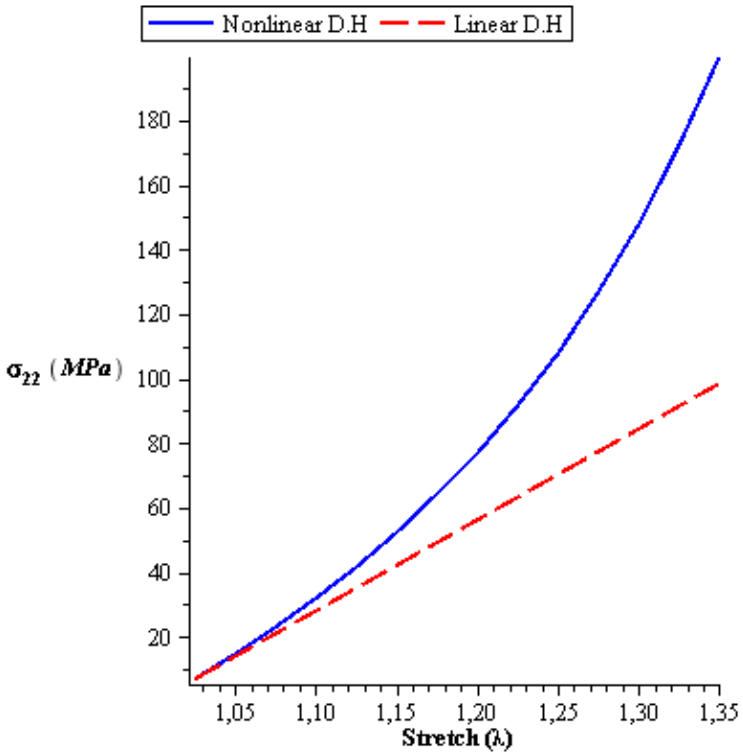

Fig. 5.4 Cauchy stress versus stretch for plain weave fabric. (a) Cauchy stress in yy-direction versus stretch in the same direction

Uniaxial tension in warp direction shows an important difference between the linear and the geometrical nonlinear analysis (figure 5.4). In this case, the difference between the linear and geometrical nonlinear response increases when increasing stretch (from 1 to 1.35), with a maximum difference for 35% deformation equal to 102%; this is in line with the continuous increase of both the tensile modulus $E_{h_{22}}$ along y-direction and the contraction $\nu_{h_{21}}$, as shown in figure 4.10 (a, c). Contrary to this, the tensile modulus $E_{h_{11}}$ along x-direction and the contraction $\nu_{h_{12}}$ decrease. In this case, the crimp ratio decreasing in the axes of loading and increase in the transverse direction as shown in figure5.5 (b).

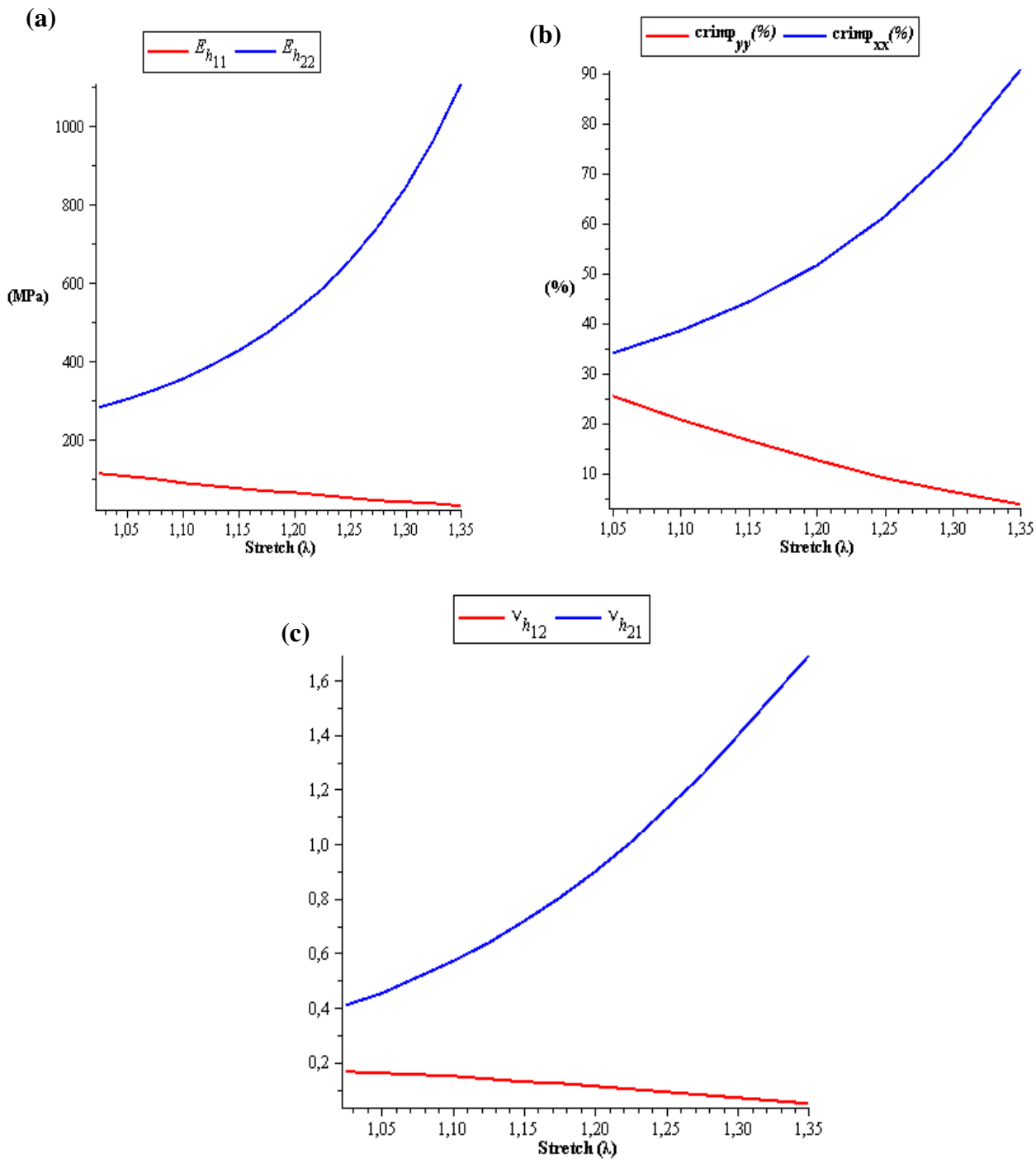

Fig. 5.5 homogenized mechanical and geometrical parameters (a) tensile moduli $E_{h_{11}}, E_{h_{22}}$ (b) crimp ratio $\%C_{r_{11}}, \%C_{r_{22}}$. (c) Poisson's ratio $\nu_{h_{12}}, \nu_{h_{21}}$ versus stretch in yy- direction.

Moreover, we next consider plain weave RUC (non-orthogonal) under uniaxial test for various β-angles (90 - 45), namely the angle between the periodicity vectors in weft and warp direction.

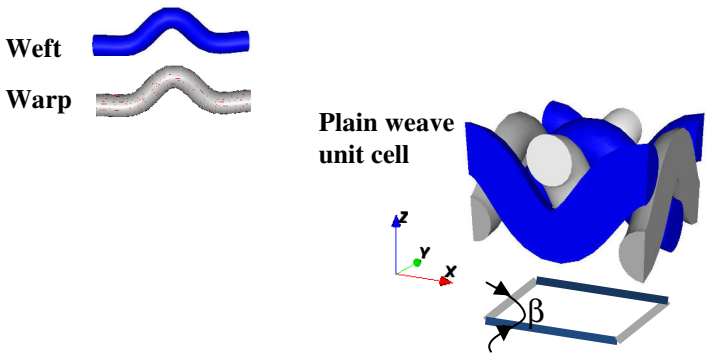

Fig. 5.6 Representative plain weave unit cells top views ($\beta = 90^{\circ}$).

Figure 5.7 shows that decreasing the angle β between the two sets of yarns from 90 up to 45 degrees brings some more pronounced non linear effects. Moreover, it is observed that decreasing of β up to half of its value increases the tensile stress by about 55%; this is logical since there is an additional geometrical hardening effect due to the reorientation of the two yarns under load

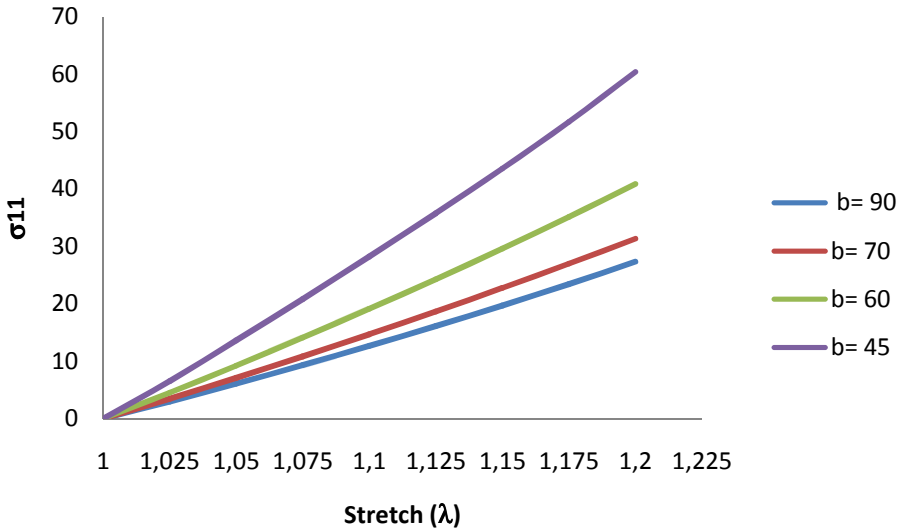

Fig. 5.7 Tensile Cauchy stress versus strain for the non-orthogonal plain weave $\beta \in \{90°, 70°, 60°, 45°\}$

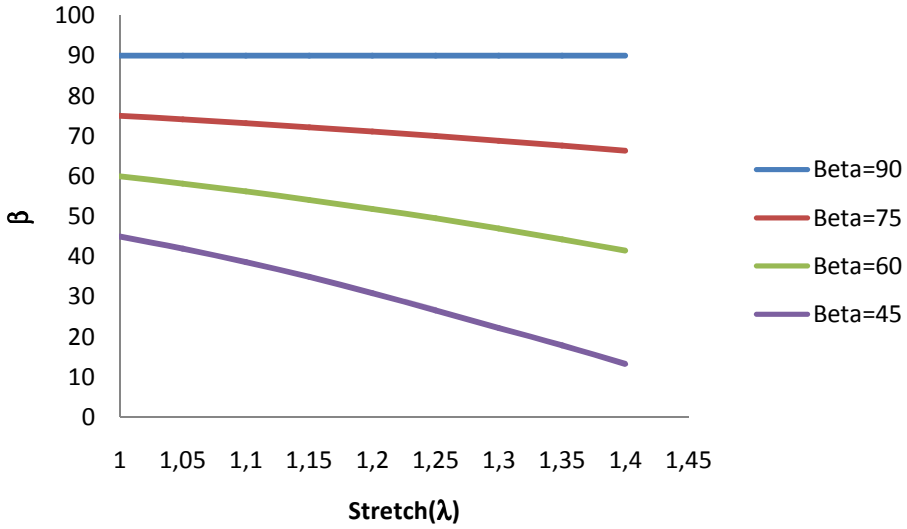

Fig. 5.8 β angle versus stretch in weft direction.

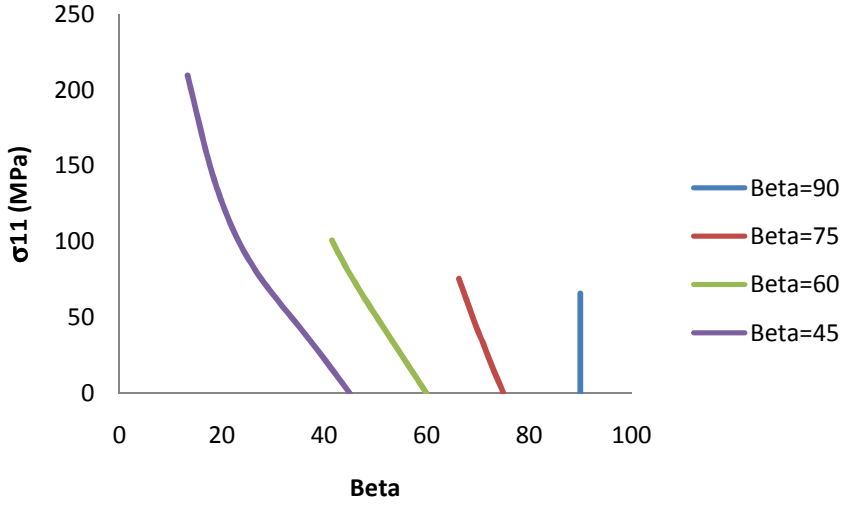

Fig. 5.9 β angle versus Cauchy stresses

In figure 4.8, we choose different initial configurations of plain weave with a varying mutual orientation between warp and weft; the variation of this orientation versus uniaxial stress (itself computed from the applied controlled stretch) is pictured in fig. 5.9, showing overall a decrease of the angle between the two sets of yarns.

It is observed that for the fabric which initially orthogonal yarns ($\beta = 90^\circ$), the β value does not change versus stress due to the uniaxial load being applied in the warp direction. But with lower values of ($\beta \ll 90^\circ$), the increase of stress leads to a decrease of β up to reaching a kinematic locking between yarns: for instance, fig. 5.9 shows that this locking occurs for about 10 degrees when the stress reaches 250 MPa. Since we do not include contact

conditions between the warp and weft as physical factors responsible for the locking, we overestimate the locking angle in our simulations.

It is also observed that although we initially choose different moduli of the warp and weft thus leading to an initially anisotropic behaviour, the structure becomes isotropic for a certain shear β angle (at $\beta \approx 59.2$), as shown in Fig. 5.10 and 5.11, which compares the effective initial properties of plain weave structures having different relative orientations of the warp and weft yarns.

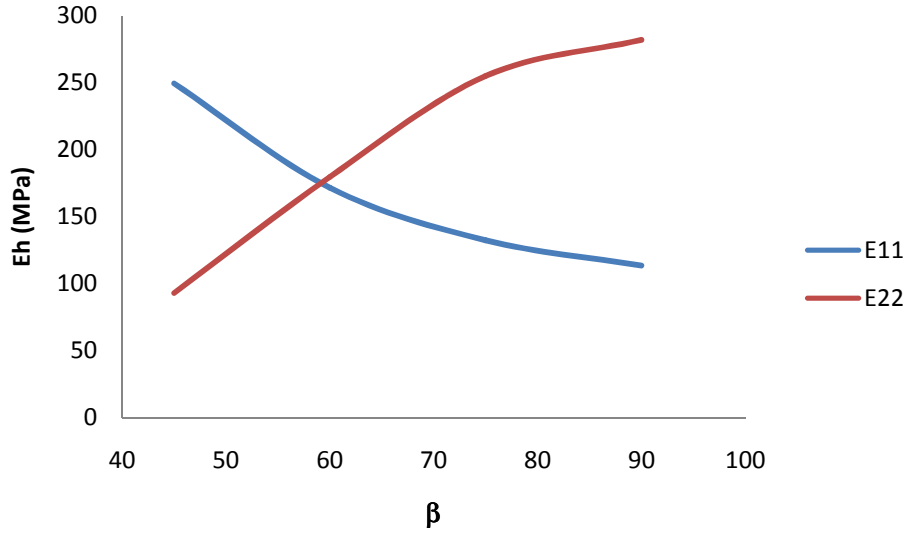

Fig. 5.10 Effective tensile modulus in weft and warp direction, (E_{11}, E_{22})

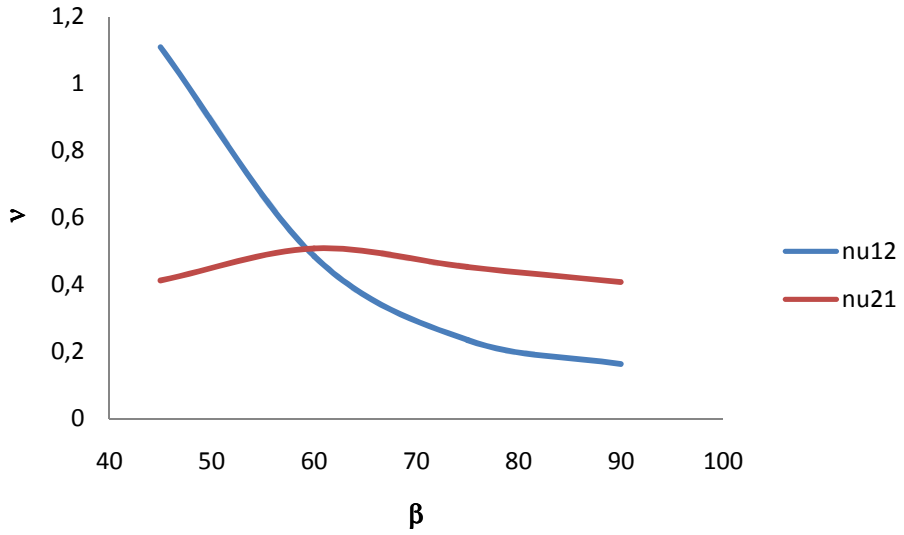

Fig. 5.11 Effective Poisson's ratio (υ_{xy}, υ_{yx})

5.1.1.2 Biaxial tension

The biaxial tensile strain simulation can be achieved by applying a strain in the longitudinal direction of warp and weft yarns for various biaxial strain ratios, elaborated as

$$k = \frac{\varepsilon_2}{\varepsilon_1}$$

where ε_1 is the primary textile strain corresponding to weft direction, and ε_2 is the secondary strain corresponding to the warp direction. The deformation gradient tensor for biaxial tension then reads

$$\mathbf{F} = \begin{bmatrix} 1+\varepsilon_{xx} & \gamma_{xy}=0 \\ \gamma_{yx}=0 & 1+\varepsilon_{yy} \end{bmatrix}$$

The responses under biaxial strain tension are next computed: figure 5.12 (a,b) shows the evolution of Cauchy stress in directions xx and yy for different values of the biaxial strain ratio, namely $k \in \{1,2,3\}$ respectively. It can be observed that a nearly linear behaviour is obtained in all cases. By comparison, the uniaxial case (k=0) is constructed such that no contraction occurs in the transverse direction.

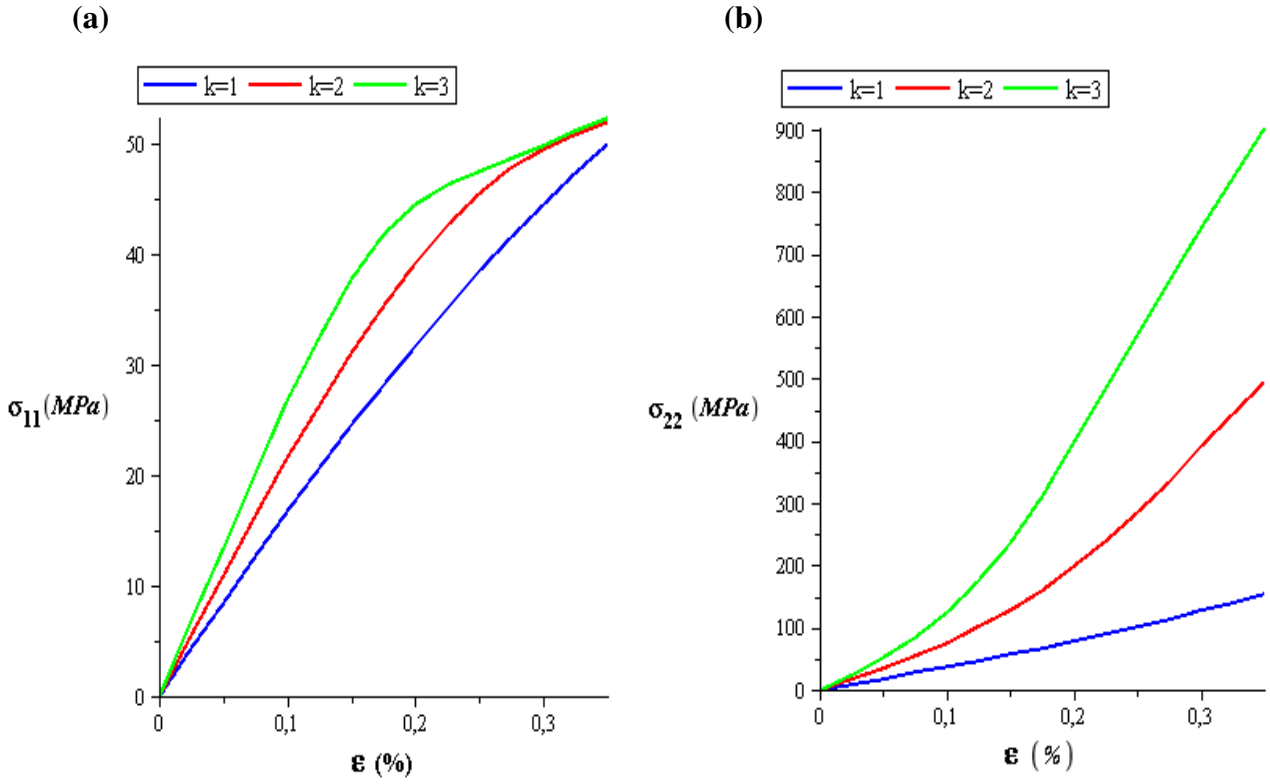

Fig. 5.12 The Cauchy stress of (a) xx- direction and (b) yy-direction versus strain for the unbalanced plain weave different biaxial strain ratio, k =1, 2 and 3.

We notice that the response is stiffer when the biaxiality ratio is increased, as expected.

As shown previously in figure 5.12 (a,b), a relatively complex behavior emerges for the biaxial loading test. A balanced weave was studied with the biaxial strain ratio $k \in \{1, 2\}$ to have a better understanding of the fabric response under a biaxial load test. The entire geometry of the unit cell is constructed based on the geometrical and mechanical micro parameters as summarized in the table 5.1 below.

Table 5.1 Balanced Plain weave mechanical and geometric parameters

weave	Set of input geometric data required for modeling				
Plain(balanced)	Weft / warp	E= 1889 MPa	L = 0.618 mm	θ =40°	d = 0.27 mm

For a equibiaxial loading (k=1), the stress increases linearly with relatively small change of the tensile moduli versus stretch (figure5.13 (a,b)). For k=2, one expects by comparison with previous equibiaxial situation a decrease of the crimp ratio in both directions, thus a stiffening of the response in both directions. But this is not exactly what happens, as shown in figure 5.14 (c,e): there is a softening in weft direction (and conversely a hardening in warp direction) corresponding to a decrease (resp. an increase) of the homogenized moduli versus stretch, as shown in figure 5.14 (d,f).

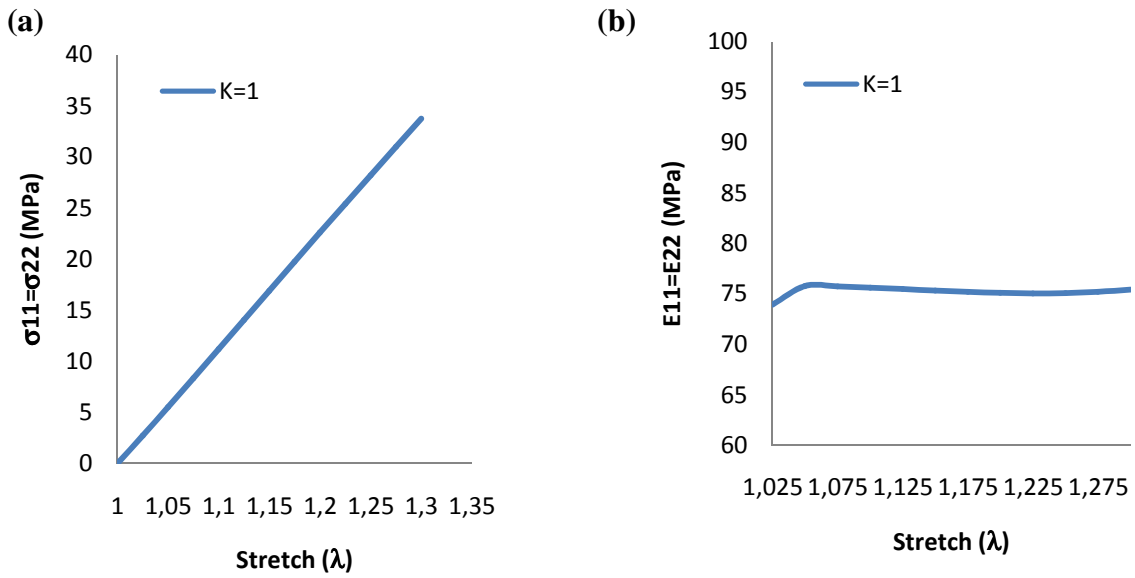

Fig. 5.13 Cauchy stress for the balanced plain weave in xx- direction, yy-direction and tensile moduli versus strain for different biaxial strain ratio, k =1.

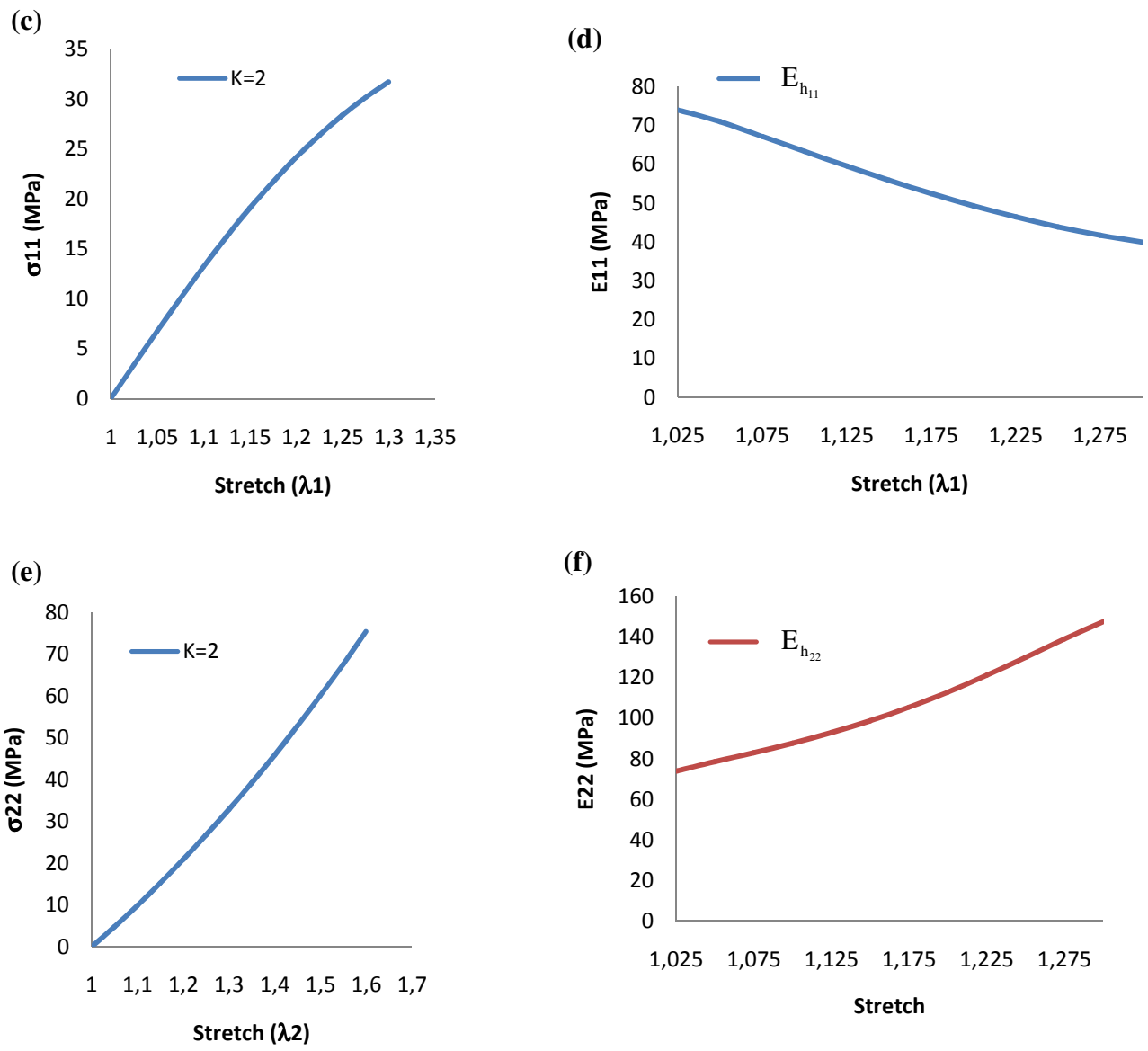

Fig. 5.14 Cauchy stress for the balanced plain weave in xx- direction, yy-direction and tensile moduli versus strain for different biaxial strain ratio, k = 2.

Due to the fact that the strain in warp is twice the strain in weft, there will be faster alignment of the warp with applied strain, so that this crimp change mechanism explains the computed response.

5.1.1.3 Simple shear test

In this section, the shear stress is plotted versus shear angle with the following deformation gradient as shown in the figure 5.15; it can be observed that the shear stress response shows an important difference between the linear and geometrical nonlinear analysis.

$$\mathbf{F} = \begin{bmatrix} 1+\varepsilon_{xx} & \gamma_{xy} \\ 0 & 1+\varepsilon_{yy} \end{bmatrix} = \begin{bmatrix} 1 & \gamma_{xy} \\ 0 & 1 \end{bmatrix}$$

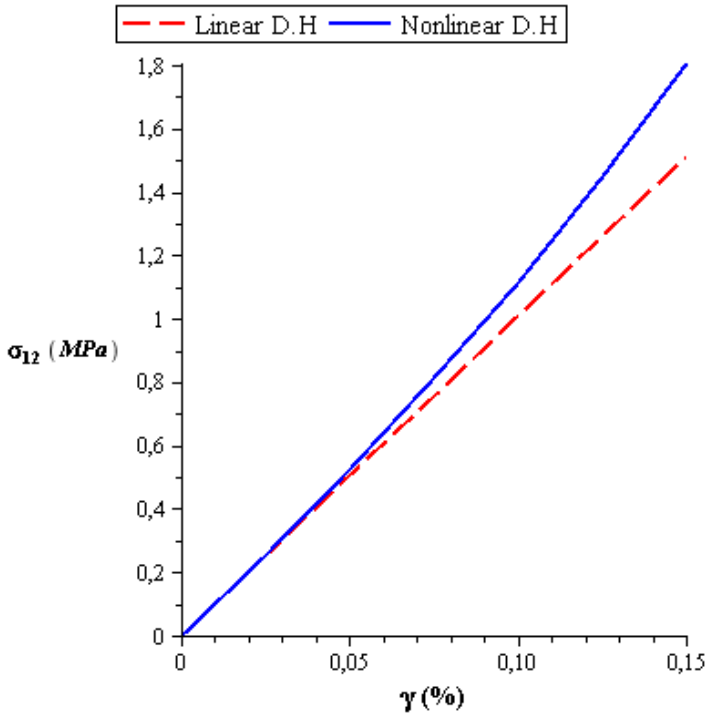

Fig. 5.15 Nonlinear shear stress versus shear strain response and comparison with linear predictions

5.1.1.4 Flexural behavior based on micropolar model for the balanced plain weave RUC

We next compute the flexural behavior based on micropolar model for the balanced plain weave representative unit cell selected as an application of previous general nonlinear homogenization scheme subjected to pure bending. The general features for a beam in pure bending will discussed below.

Let consider a beam with original length L_o (undeformed) figure5.16 (left); we assume the location of the position within the cross-section where $\rho\theta = L_o$, in which ρ is the radius of

curvature and θ the angle, is known as the Neutral Axis: it is the place where the final deformed length is the same as the original undeformed length, so that no stretching takes place due to bending figure 5.16 (right). When the path is straight, ρ is infinite, and when the path has a sharp curve in it, ρ is small.

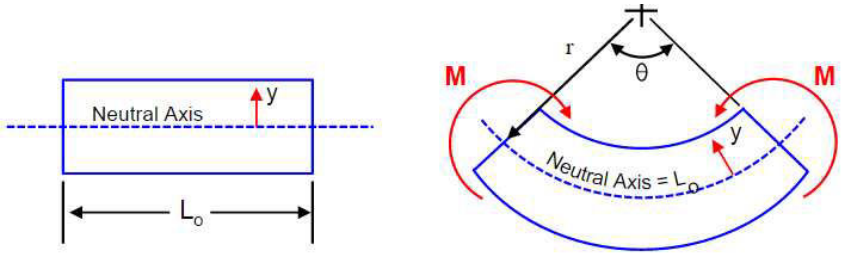

Fig. 5.16 beam in bending

One may further introduce the variable y as the distance from the neutral axis to any other radius in the cross-section as shown in figure 5.16 above. As a result, the radius of curvature at any y is $(\rho - y)$ and the final length at any y is given by

$$L = (\rho - y)\theta$$

Recall that $L_o = \rho\theta$. Now one can express the bending strain as,

$$\varepsilon = \frac{L - L_o}{L_o} = \frac{(\rho - y)\theta - \rho\theta}{\rho\theta}$$

$$\varepsilon = -\frac{y}{\rho} \tag{5.1}$$

Thus, equation (5.1) shows that the strain is zero at $y = 0$, the neutral axis, and varies linearly with the distance from it. For thick beams, y can take large values, but for thin beams, y remains small. This is fundamentally why thick beams have higher bending stiffness in comparison thin ones. If the angle of rotation θ is very small; there the curvature $\kappa = \frac{1}{\rho}$.

The bending strain can be expressed as a function of curvature as,

$$\varepsilon = \kappa y \tag{5.2}$$

We presently employ the following procedure to analyze the deformation of the balanced plain weave subjected to pure bending. Relying on the previous geometrical and material data (Table 5.1), which are used to define the geometrical and material parameters for the balanced

plain weave RUC. One shall observe that the crimp angle is a function in the representative unit cell thickness. According to this, we study the bending response with lower values of crimp angle, namely $\theta_f = \theta_p \in \{5^\circ, 2^\circ\}$, as shown in figure 5.17. We assume the applied bending strain reaches values up to 20%. Thus, based on equation (5.2), one shall get the corresponding curvature value as $\kappa = \varepsilon / h$; the height of the RUC $h = L\sin(\theta_f)$. The effective bending modulus is expected to depend on the ratio of the effective medium thickness, parameter h, to the unit cell length, evaluated as $2L\cos\theta$, so that $h / L = \tan\theta_f / 2 \cong \theta_f / 2$, which has a small value. This rough analysis explains the weak nonlinear bending effect, and the fact that the overall bending modulus will increase when the effective stiffness increases.

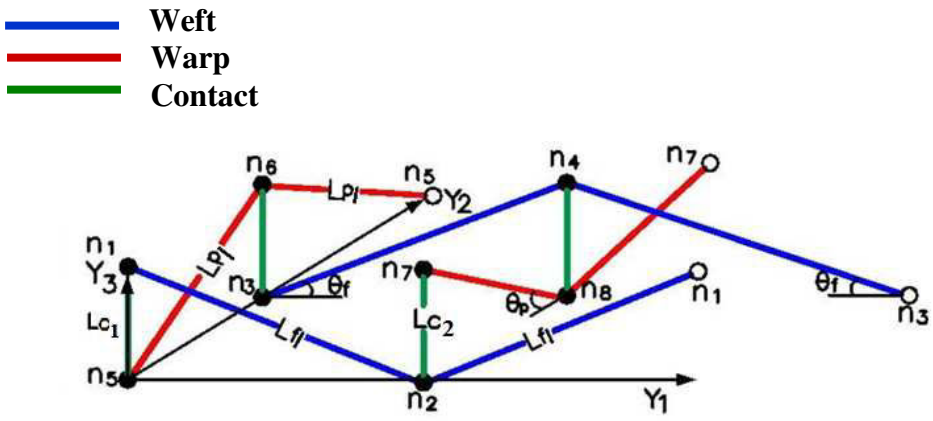

Fig. 5.17 A 3D lattice model of balanced plain weave.

One shall notice that smaller crimp angles give larger range of the applied curvatures. This is related to the fact that thick sheets of plain weave need larger bending moment to bring significant differences between the linear and geometrical nonlinear bending behaviors. Figure 5.18 shows that the difference between the linear and geometrical nonlinear behavior increases with curvature κ (from 3 to 6); a softer response is obtained in comparison to the linear response (from 2 % to 4%).

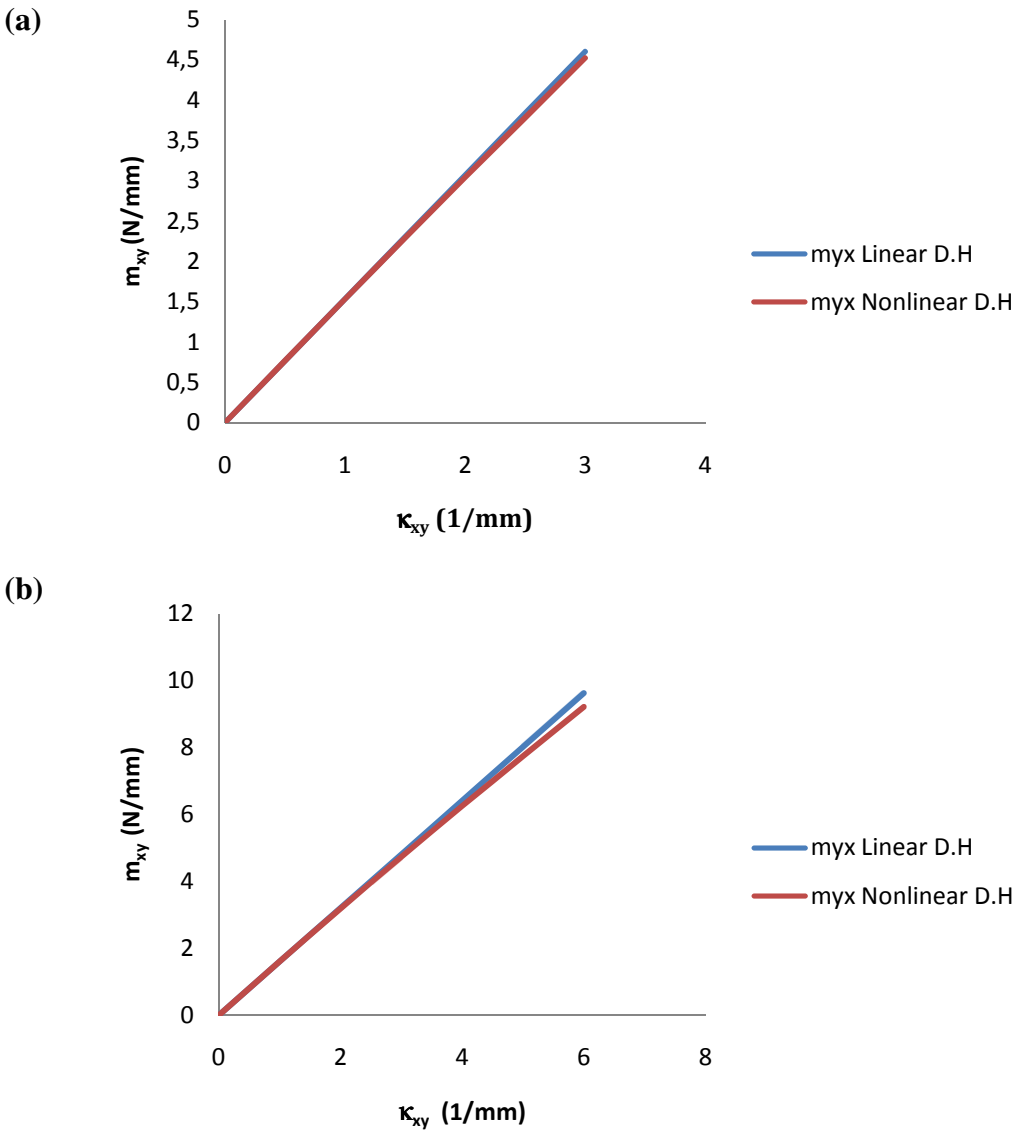

Fig. 5.18 Linear versus geometrical nonlinear evolutions of couple stress versus microcurvature (a) $\theta_f = 5^\circ$ (b) $\theta_f = 2^\circ$.

One shall rely on the bending stiffness previously written in section 4.6.1, the couple stress of the out of plane bending m_{xy} expresses versus curvature κ_{xy} as follows,

$$m_{xy} = k_{33}\,\kappa_{xy}$$

Thus, the softening response corresponds to a decrease of the homogenized moduli (k_{33}) versus curvature. Moreover, the characteristic length of the micropolar behaviour for the in-plane bending is calculated from the rigidities: $l_c = \sqrt{K_{55}^{\mu} \Big/ 2\left(K_{33}^{s} + K_{34}^{s}\right)}$, which decreases versus curvature, as shown in figure 5.19 (a,b) respectively.

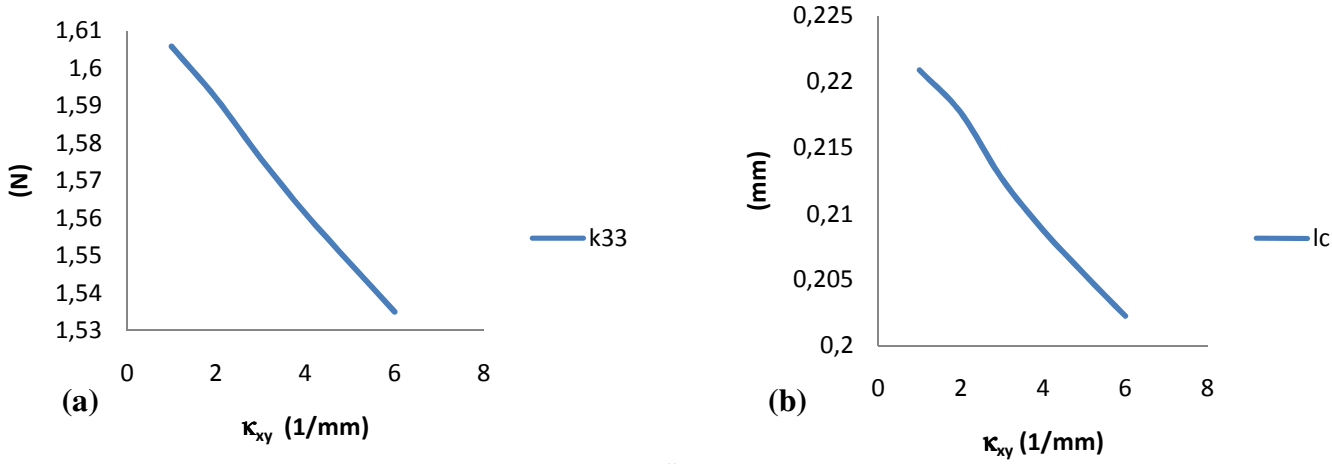

Fig. 5.19 (a) Micropolar homogenized moduli K_{33}^{μ} versus curvature (b) characteristic length versus curvature

Note that the determination of out of plane bending lengths requires to make an homogenization also in the thickness direction, a situation representative of a pile up of such textile monolayer.

5.1.1.5 Relocalization of the mechanical fields from the DH technique

The DH technique leads to an effective substitution medium with uniform mechanical fields by construction. The underlying RVE used to construct the homogenized response is nevertheless heterogeneous, so it is interesting to compute the distribution of the mechanical fields inside the RVE, which is the purpose of this paragraph. In order to illustrate the relocalization technique, we consider the weft yarn within the balanced plain weave unit cell discretized as two inclined beams(as shown in previous figure 4.22). The evaluation of normal (N), transverse (T) forces and moments (M) within uniaxial tension test versus stretch (λ) has been done after homogenization. The loading is applied in 4 increments of stretch(see figure 5.20 (a,b,c,d,e) respectively)

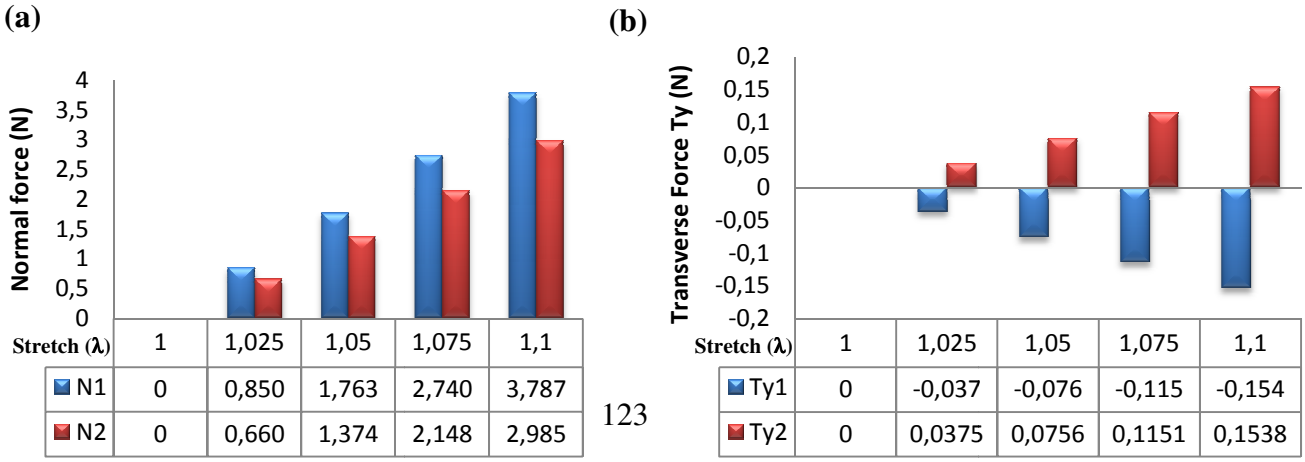

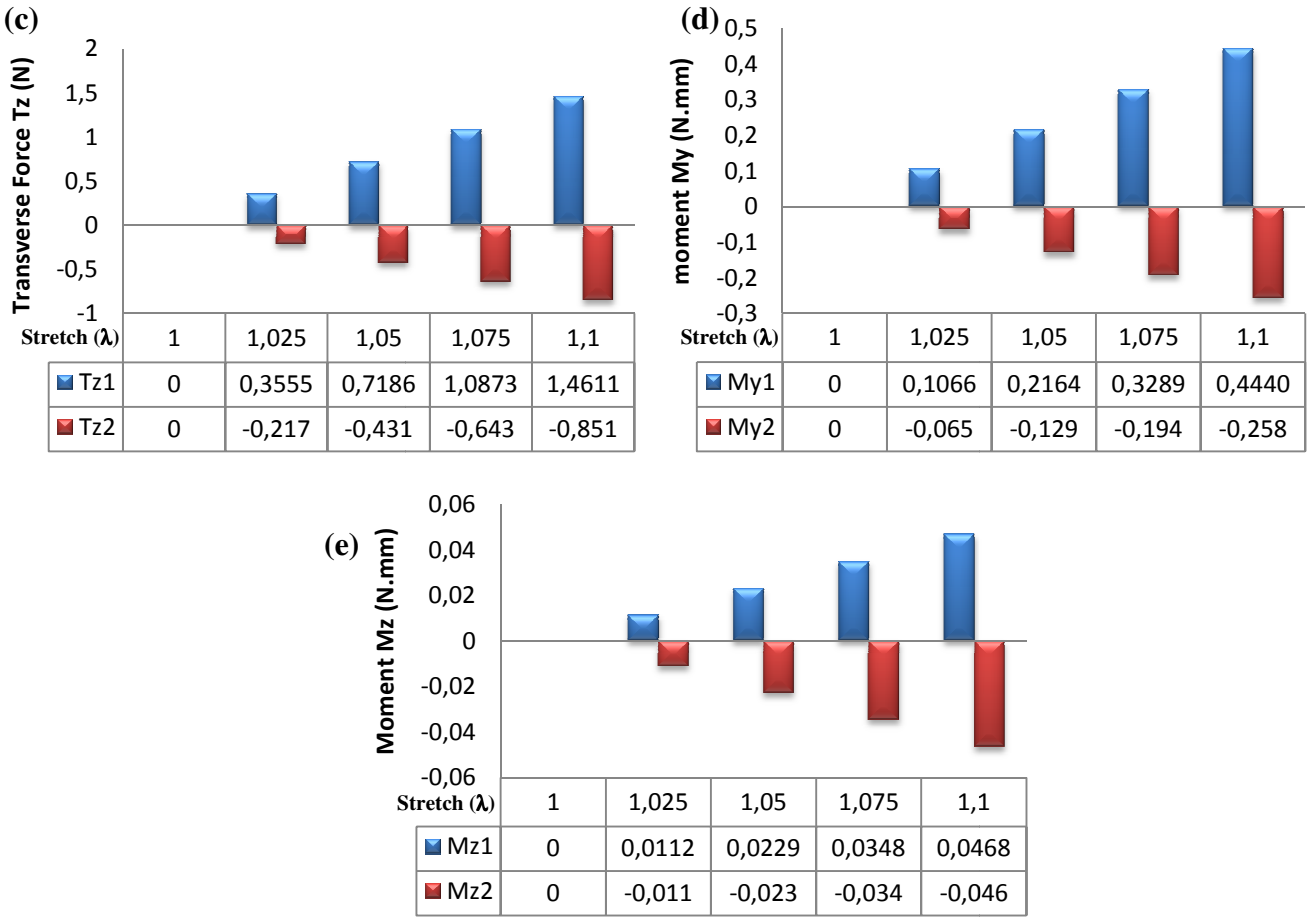

Stretch (λ)	1	1,025	1,05	1,075	1,1
Tz1	0	0,3555	0,7186	1,0873	1,4611
Tz2	0	-0,217	-0,431	-0,643	-0,851

Stretch (λ)	1	1,025	1,05	1,075	1,1
My1	0	0,1066	0,2164	0,3289	0,4440
My2	0	-0,065	-0,129	-0,194	-0,258

Stretch (λ)	1	1,025	1,05	1,075	1,1
Mz1	0	0,0112	0,0229	0,0348	0,0468
Mz2	0	-0,011	-0,023	-0,034	-0,046

Fig. 5.20 evolutions of forces and moments for uniaxial tension versus stretch (λ)

5.1.2 Unit cell of twill fabric

In the same manner, we plot the stress response for the three type of loadings applied over the RUC of the twill fabric.

5.1.2.1 Uniaxial tension

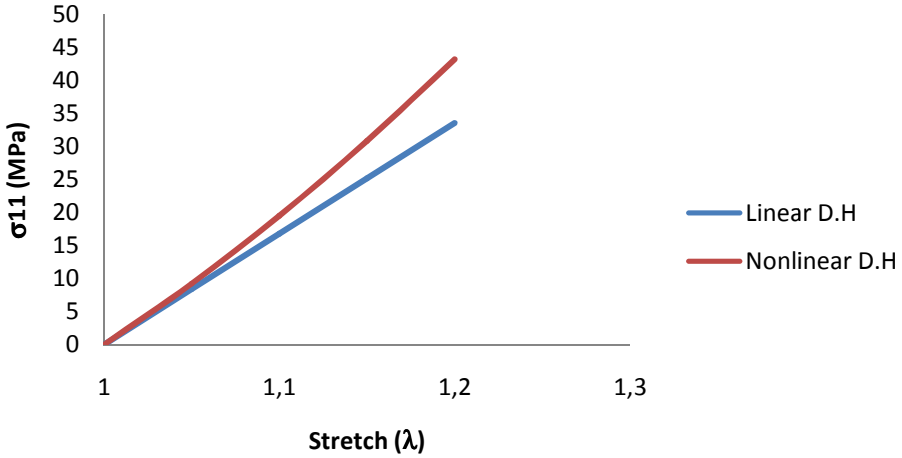

Figure 5.21 Cauchy stress in xx-direction versus stretch (in the same direction) for twill.

In the tensile loading test in weft direction for the twill fabric (Figure 5.21), we observe that there is an important difference between the linear and geometrical nonlinear behaviour with increasing stretch (from 1.05 to 1.2): one obtains as one can expect from simple mechanical considerations a stiffer response in comparison to the linear response (from 10% to 28%), due to the yarns becoming more aligned with increasing stretch in the direction of the applied tension.

5.1.2.2 Biaxial tension

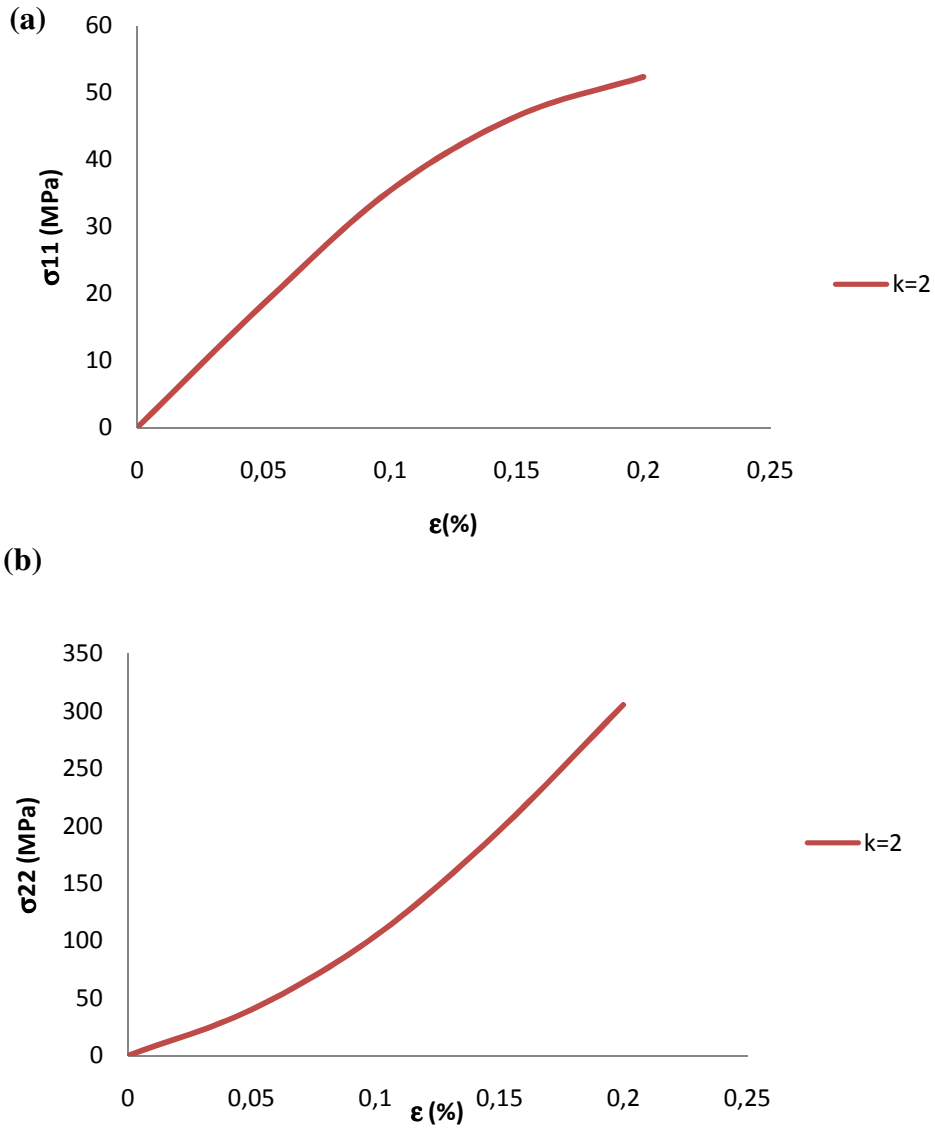

Fig. 5.22 Cauchy stress versus strain for tests in (a) xx- direction and (b) yy-direction. Biaxial strain ratio k =2.

The responses under biaxial strain tension are next computed: figure 5.22 (a,b) shows the evolution of Cauchy stress in directions xx and yy for the value of the biaxial strain ratio,

$k = 2$ respectively. It can be observed that a nearly linear behaviour is obtained in weft direction.

5.1.2.3 Simple shear test

Now, the shear stress is plotted versus shear angle with the following deformation gradient as shown in the figure 5.23; it can be observed that the shear stress response shows an important difference between the linear and geometrical nonlinear analysis.

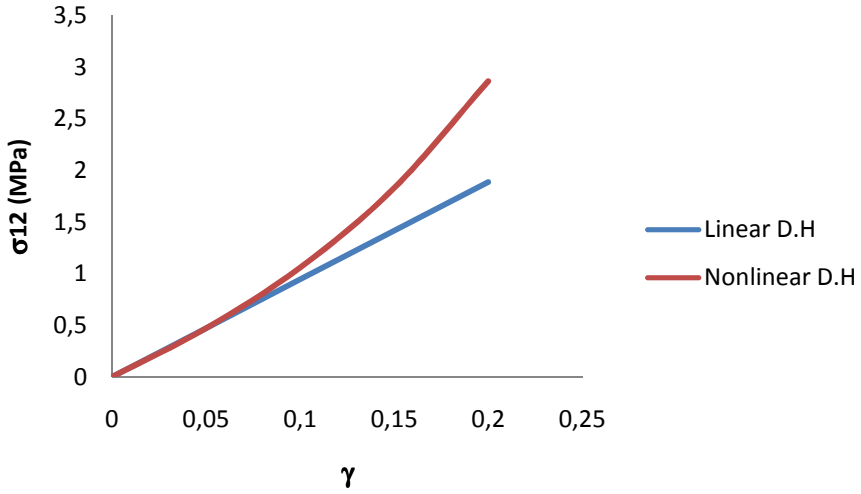

Fig. 5.23 Nonlinear path for shearing stress versus shear strain is compared with linear predictions

5.1.3 Comparison of mechanical responses for tows constructed from plain weave and twill unit cell

Now we compare the results obtained previously for the plain weave and twill fabric during the three types of loading tests.

5.1.3.1 Uniaxial tension

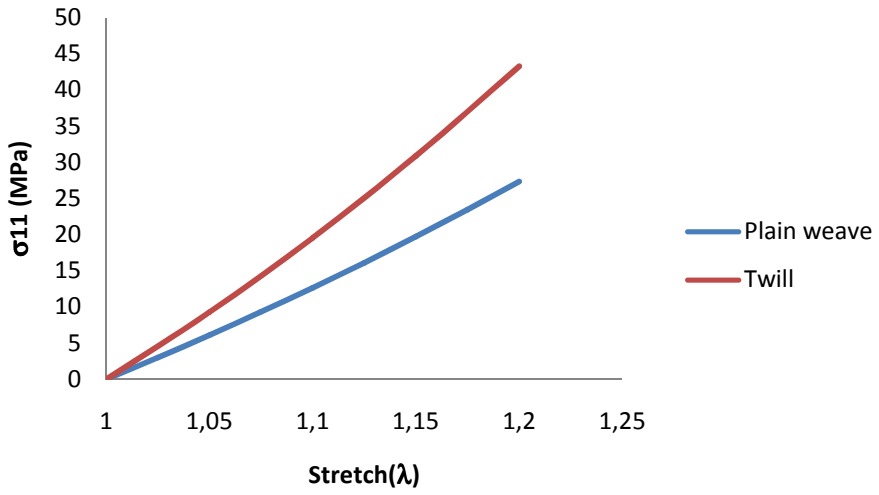

Figure 5.24 comparisons between Cauchy stress evolutions for plain weave and twill.

Figure 5.24 shows a comparison between the Cauchy stress response versus stretch for both plain weave and twill. The initial homogenized tensile rigidity in the weft direction are respectively 113.5 MPa and 170.4MPa for plain weave and twill, which leads to higher stress for the twill response compared to plain weave response. The stiffest response obtained for twill can be explained by the fact that yarns within the representative unit cell are more aligned in the direction in traction; we expect this tendency to be valid for any loading.

5.1.3.2 Biaxial tension

(a)

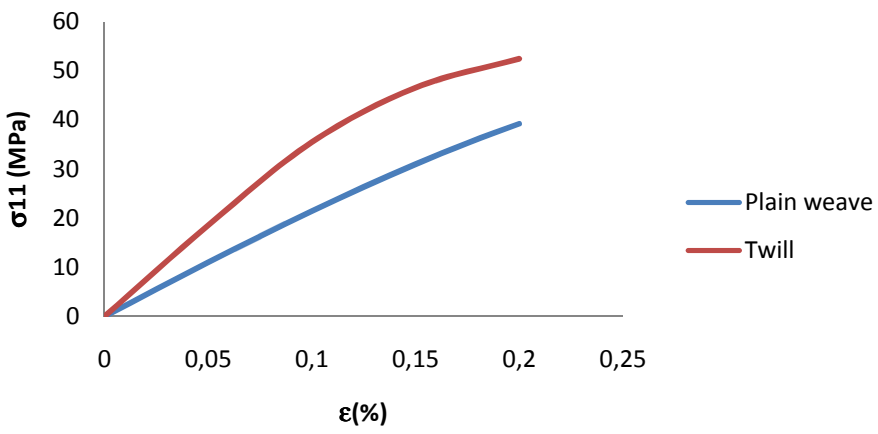

(b)

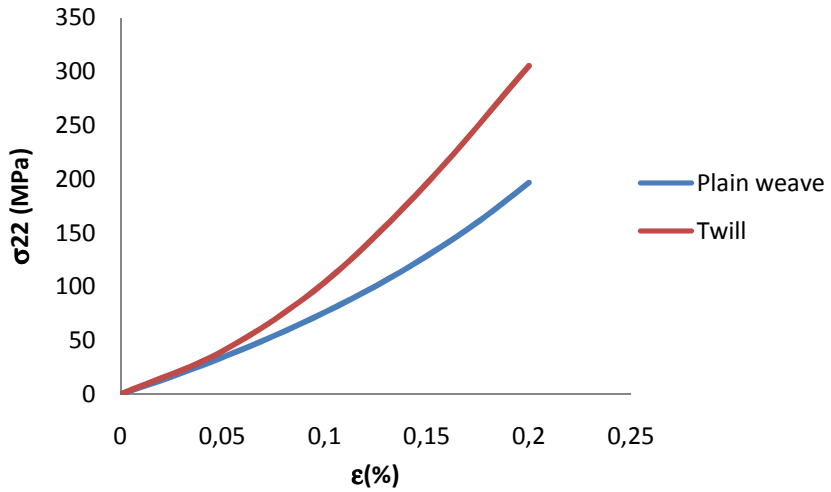

Fig. 5.25 Comparison between Cauchy stress of both type of fabric in (a) xx- direction and (b) yy-direction versus strain with biaxial strain ratio, k =2.

Figure 5.25 shows the comparison of the biaxial response for both types of fabric for (k=2): here also, twill shows a stiffer response, as for uniaxial loading conditions. Those differences extend the comparison of the initial homogenized moduli summarized in (Table 4.4) to the large strains regime.

5.1.3.3 Simple shear test

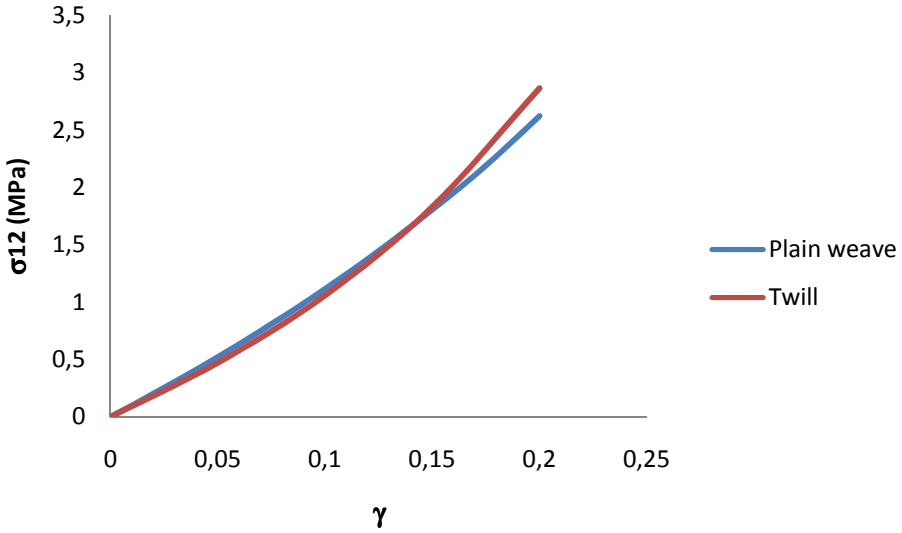

Fig. 5.26 Comparison between the shear stress response for plain weave and twill.

The shear response shows nearly the same trend for both types of fabrics up to 0.15 shear strain, with a small difference occurring for large strains, as shown in figure 4.31; this can be

explained by the fact that the initial yarn crimp does not play an important role in simple shear (contrary to uniaxial loading conditions).
In the next section, based on the previous nonlinear discrete homogenization analysis, we will validate the stress-strain responses obtained for the considered textile performs, by comparing the homogenized responses with full FE computations for a representative unit cell initially generated by TexGen and next exported to ABAQUS.

5.2 Finite element method

The practical stress analysis of solids and structures is unlikely to be studied based on classical methods, and currently numerical analysis, as a matter of fact in the form of the finite element method, is the only way by which the behavior of a structure subjected to complex loading can be successfully simulated. The study of the numerical analysis of nonlinear continua using a computer is called nonlinear computational mechanics. One shall summarize the finite element method as follows. It is a procedure whereby the continuum behavior described at infinity of points is approximated in terms of a finite number of points, called nodes, located at specific points in the continuum. These nodes are used to define regions, called finite elements, over which both the geometry and the primary variables (which is the dependent displacement and its derivative) in the governing equations is approximated. thus in the stress analysis of a solid the finite element could be for example a tetrahedral element defined by four nodes and the primary variables the three displacements components in the Cartesian direction. The governing equations describing the nonlinear behavior of the solid are usually formulated in a so-called weak integral form using, for example, the principle of virtual work or the principal of minimum potential energy. The finite element approximations are then introduced into these integral equations, and a standard textbook manipulation yields a finite set of nonlinear algebraic equations in the primary variable. These equations are then usually solved using the Newton-Raphson iterative technique (Javer Bonet and Richard D. Wood, 1997)

In the current section, 3D finite element models of woven fabrics at meso-level are developed to evaluate the accuracy of the effective properties predicted from discrete homogenization. The FE model is capable of simulating elementary cells under simultaneous axial loading along the yarn directions. The stress evolution versus strain is calculated using the strain energy-based method, based on the relationship established between the strain energy of the

microstructure and that of the homogenized equivalent model under specific boundary conditions. The homogenized material properties macroscopically account for the heterogeneity in the tows.

The finite element procedure at the meso-level involves the modeling of a single unit cell instead of modeling the whole fabric structure. In defining such a unit cell, it should be noted that it is not isolated from the adjacent cells in the fabric. Subsequently, the boundary effects from the adjacent cells should be taken into account: this is done by imposing a specific type of geometric constraints known as ‘‘periodic boundary conditions’’ on the unit cells.

The displacement field is split into an affine part and a fluctuation u_i^* with zero average,

$$u_i = \tilde{\epsilon}_{ij} x_j + u_i^*$$

with $\tilde{\epsilon}_{ij}$ the mesoscopic average strain imposed over the unit cell boundary.

The boundary surfaces of the unit cell must always appear in parallel pairs; the displacements on a pair of parallel opposite boundary surfaces can be written as

$$u_i^{k+} = \tilde{\epsilon}_{ij} x_j^{k+} + u_i^*,\ u_i^{k-} = \tilde{\epsilon}_{ij} x_j^{k-} + u_i^* \tag{5.3}$$

where indices "k^+" and "k^-" identify the k^{th} pair of two opposite parallel boundary surfaces of a repeated unit cell. Note that u_i^* is the same at the two parallel boundaries (periodicity), thus the difference between the above two equations gives

$$u_i^{k+} - u_i^{k-} = \tilde{\epsilon}_{ij}(x_j^{k+} - x_j^{k-}) = \tilde{\epsilon}_{ij} \Delta x_j^k \tag{5.4}$$

Since the quantities Δx_j^k are constants for each pair of the parallel boundary surfaces, for a specified macro strain $\tilde{\epsilon}_{ij}$, the right-hand side in (5.4) becomes constant. The constraint equations are applied as nodal displacement constraint equations, instead of giving Eq. (5.3) directly as boundary conditions.

5.3 Comparison of homogenized moduli with finite element results

The previous results for stress-strain response are obtained with the DH technique are now compared with numerical results obtained from the FE method (ABAQUS), under the specified types of loadings (we restrict the validation of the computed response to uniaxial and Biaxial tests), with appropriate boundary conditions. The warp and weft yarns are meshed with the eight-node solid linear hexahedral element (ABAQUS element type C3D8); a total of

14,804 elements are used to model the balanced plain weave. In order to account for the possible relative displacements between the yarns, the contact with friction is introduced with a master/slave approach. Contact is considered to be an intrinsic character of woven fabrics which cannot be neglected during the meso-level analysis. Contact conditions are prescribed between the possible interlacing surfaces of the yarns under loading and are the same for all loading cases. The tangential behavior at the contact surfaces in the frame of Coulomb friction is defined using the penalty method with a friction coefficient selected here as 0.05, relying on date from (Peng and Cao, 2002).

The deformation gradient tensor

$$\mathbf{F} = \begin{bmatrix} 1+\varepsilon_{xx} & \gamma_{xy} \\ \gamma_{yx} & 1+\varepsilon_{yy} \end{bmatrix}$$

is applied as the RUC total deformation through the displacement of the four corner nodes and additional periodic boundary conditions (BCs) are imposed, where ε and γ are the normal and shear strains respectively.

The results obtained with the DH technique are now validated with numerical results obtained from the FE method (ABAQUS), under the two types of loadings (uniaxial and biaxial loads), with appropriate boundary conditions. The uniaxial response for the balanced plain weave is shown in Fig. 5.27; a good agreement is obtained using both methods, with a maximum discrepancy close to 1.41% in the uniaxial test, and a relatively larger discrepancy close 15 % in biaxial testing conditions (Fig. 5.28). We have tested two types of element, namely the four-node solid linear tetrahedral element C3D 4, and the eight-node solid linear hexahedral element C3D8; it appears from the literature that element C3D4 behaves poorly, so we presently used the second element type.

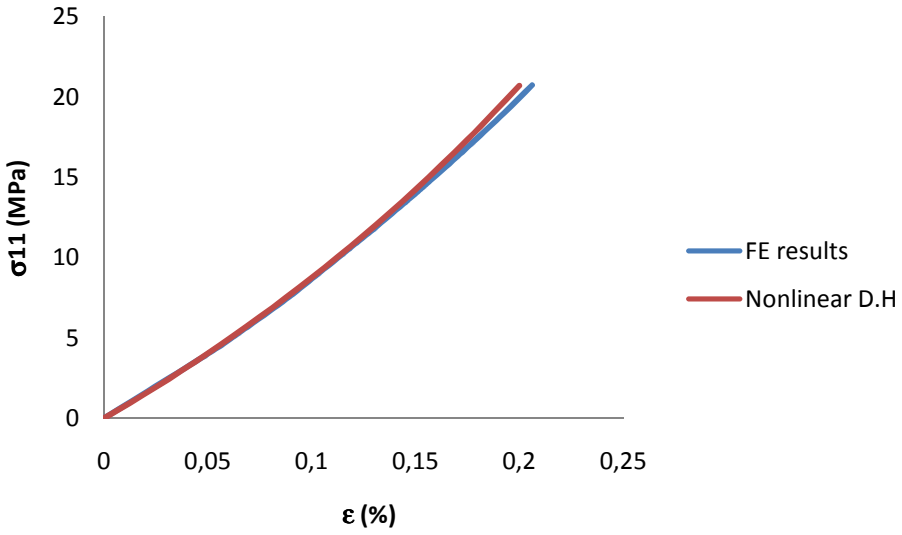

Fig. 5.27 Comparison of the uniaxial tensile response in xx- direction for the balanced plain weave between the DH method and FEM simulations (ABAQUS).

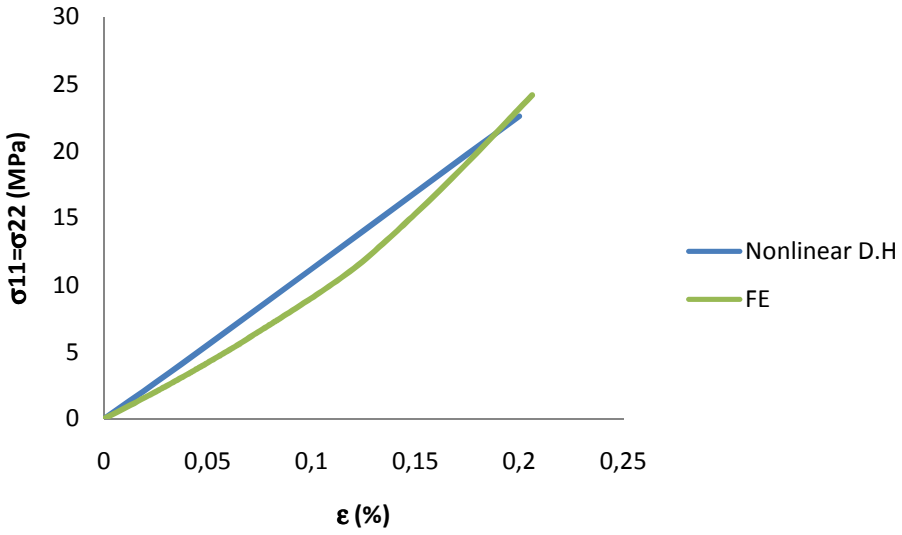

Fig. 5.28 Comparison of the equibiaxial tensile response for the balanced plain weave between the DH method and FEM simulations (ABAQUS).

The discrepancy for the biaxial test is maximum for about 13% stretch, and may be due to the adopted number of elements (we consider beams as solid elements). The displacement and stress distributions over the RUC for both uniaxial and biaxial testing conditions for the balanced plain weave are pictured on Fig. 5.29 and Fig. 5.30.

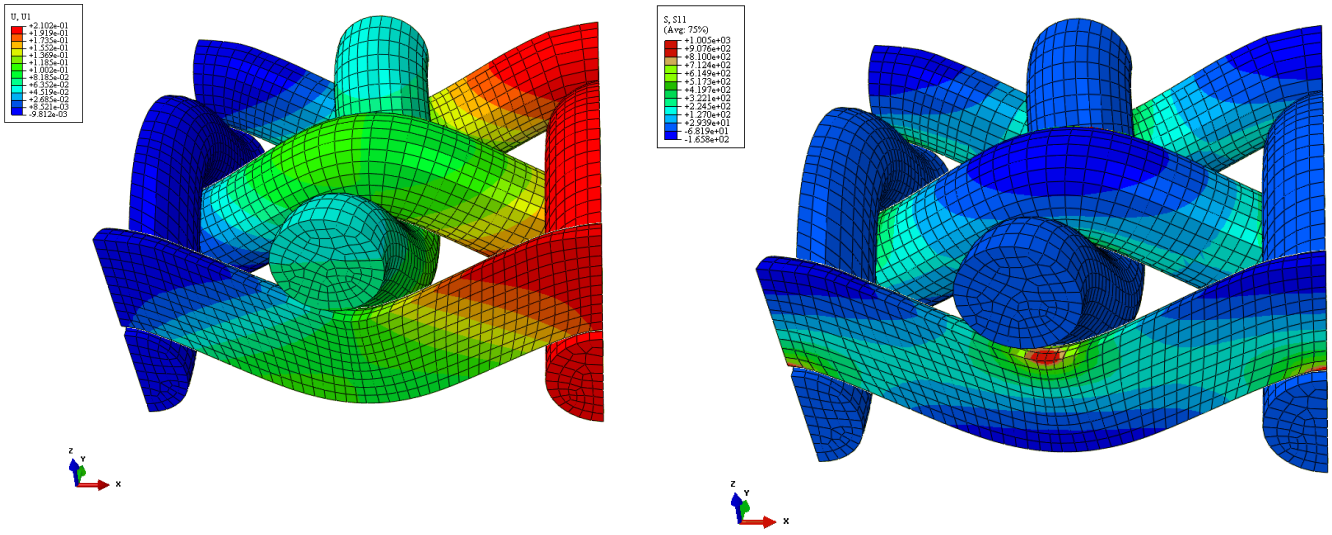

Fig. 5.29 displacement (left) and stress distributions (right) over the balanced plain weave submitted to a uniaxial test

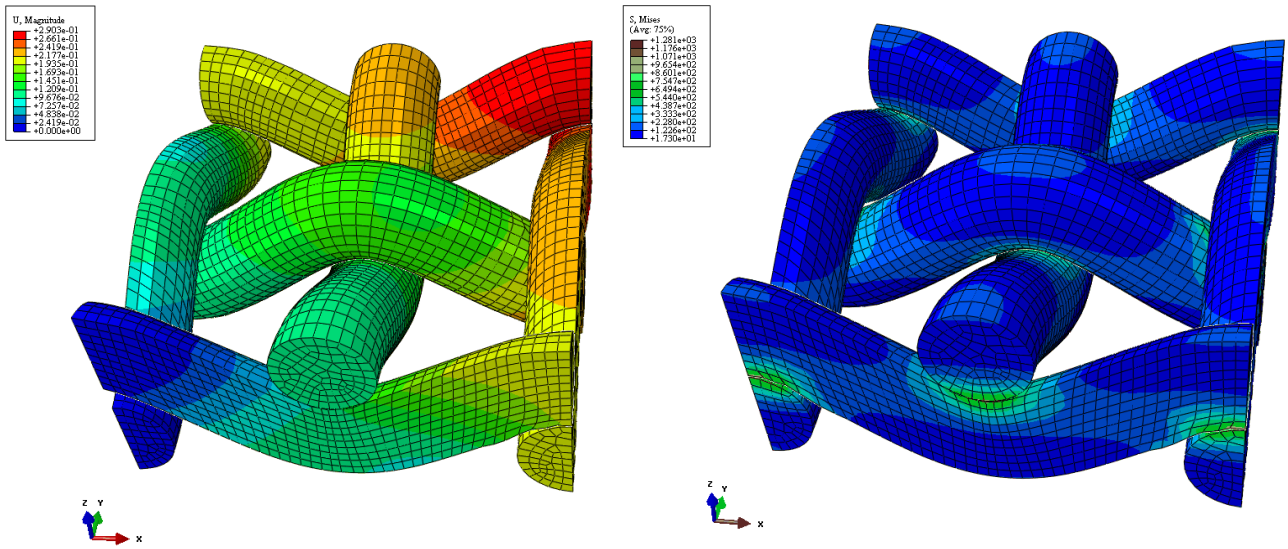

Fig. 5.30 displacement (left) and stress distributions (right) over the balanced plain weave submitted to a biaxial test

5.4 Identification of a strain energy density of a hyperelastic model of textile structures

In the next section, we perform the calibration of a strain energy density inherent to an hyperelastic model for the plain weave tows. We rely on the expressions of the strain energy density given in **Appendix C.7** Written in expressions (C.51) to (C.53), and we identify a set of material constants based on uniaxial (in weft and warp directions) and simple shear virtual tests. The set of material parameters shall minimize the difference between the responses obtained on one hand by the DH method, and on the other hand when directly computing the stress-strain response under the same loading conditions form the strain energy density.

Based on the numerical responses computed in terms of the second Piola-Kirchhoff stress S_{ii} versus stretch λ_1, a polynomial of degree three is used for interpolating the response curve $S_{ii}-\lambda_1$. We rely on the polynomial hyperelastic model written in expressions (C.51) and (C.52), with a strain energy density given by

$$\tilde{W}=\sum_{\alpha=0}^{m}\frac{1}{\alpha+2}a_\alpha\left(\lambda_1^{\alpha+2}-1\right)+\sum_{\beta=0}^{n}\frac{1}{\beta+2}b_\beta\left(\lambda_2^{\beta+2}-1\right)+\sum_{\gamma=0}^{p}\frac{1}{\gamma+1}c_\gamma\cos^{\gamma+1}\theta+k_{r1}\lambda_1\lambda_2+k_{r2}\left(\lambda_1\lambda_2\right)^2$$

with $a_\alpha, b_\beta, c_\gamma, k_{r1}, k_{r2}$ the set of material parameters to be identified. Note that the two coefficients k_{r1}, k_{r2} are required to introduce a dependency of the two stress components S_{11}, S_{22} versus both stretches.The plain weave fabric is initially orthogonal and will remain orthogonal (so that $\cos(\theta)=0$), so that the coefficients c_γ can be given nil values.

One may further simplify the previous expressions as

$$S_{11}=\sum_{\alpha=0}^{m}a_\alpha\lambda_1^{\alpha+1}+k_{r1}\left(\lambda_2\right)+2k_{r2}\left(\lambda_1\lambda_2^2\right),\ S_{22}=\sum_{\alpha=0}^{m}b_\beta\lambda_2^{\beta}++k_{r1}\left(\lambda_1\right)+2k_{r2}\left(\lambda_2\lambda_1^2\right) \tag{5.5}$$

$$S_{12}=\sum_{\gamma=0}^{p}c_\gamma\cos^\gamma\theta$$

The material parameters are identified based on virtual tension, biaxial and simple shear tests performed over the unit cell of balanced plain weave; their identification proceeds from the minimization of the following functional with respect to the set of parameters $a_\alpha, b_\beta, c_\gamma, k_{r1}, k_{r2}$

$$\underset{a_\alpha, b_\beta, c_\gamma, k_{r1}, k_{r2}}{\text{Min}} S^e\left(a_\alpha, b_\beta, c_\gamma, k_{r1}, k_{r2}\right) := \left\{ \left\| \mathbf{S}_{11}^{DH} - \mathbf{S}_{11} \right\|^2 + \left\| \mathbf{S}_{22}^{DH} - \mathbf{S}_{22} \right\|^2 + \left\| \mathbf{S}_{12}^{DH} - \mathbf{S}_{12} \right\|^2 \right\}^{1/2}$$

built as the quadratic measure of the error between the DH stress components and their analytical counterpart obtained from the hyperelastic potential. Note that it is necessary to incorporate therein the stresses obtained from the three considered deformation modes simultaneously, so that the identified strain energy density has the capability to properly describe the response of the networks under different loadings. The stress responses are adjusted with a third order polynomial, using the least square procedure in the Matlab toolbox.

Relying on these first two expressions of the two components of the second Piola-Kirchhoff stress and on the computed responses obtained by DH, the material constants of the model are identified from a least square method (9 sampling points are used), within uniaxial tension and biaxial tension with strain ratio, namely k=2 load tests as shown below.

(a)

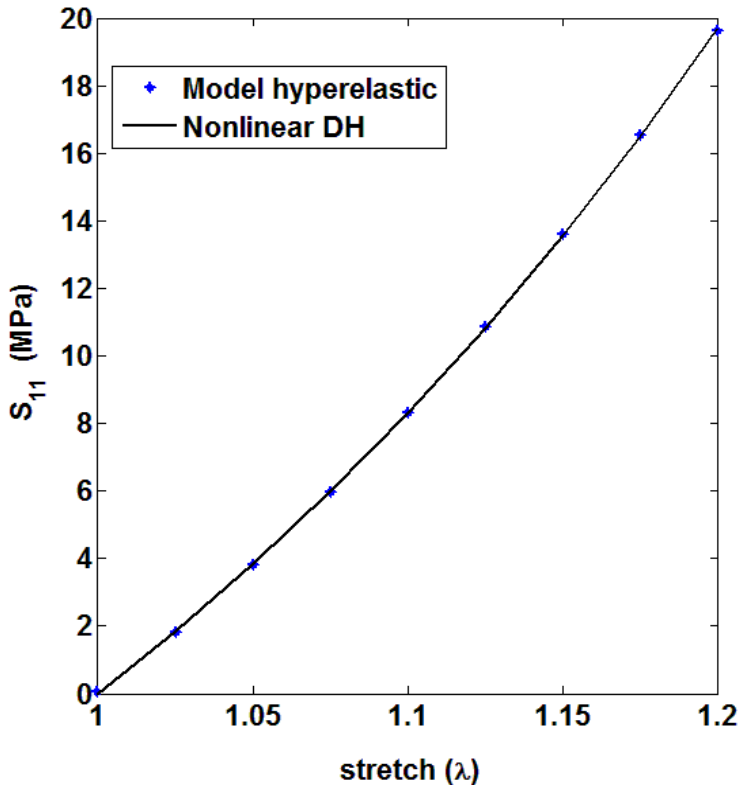

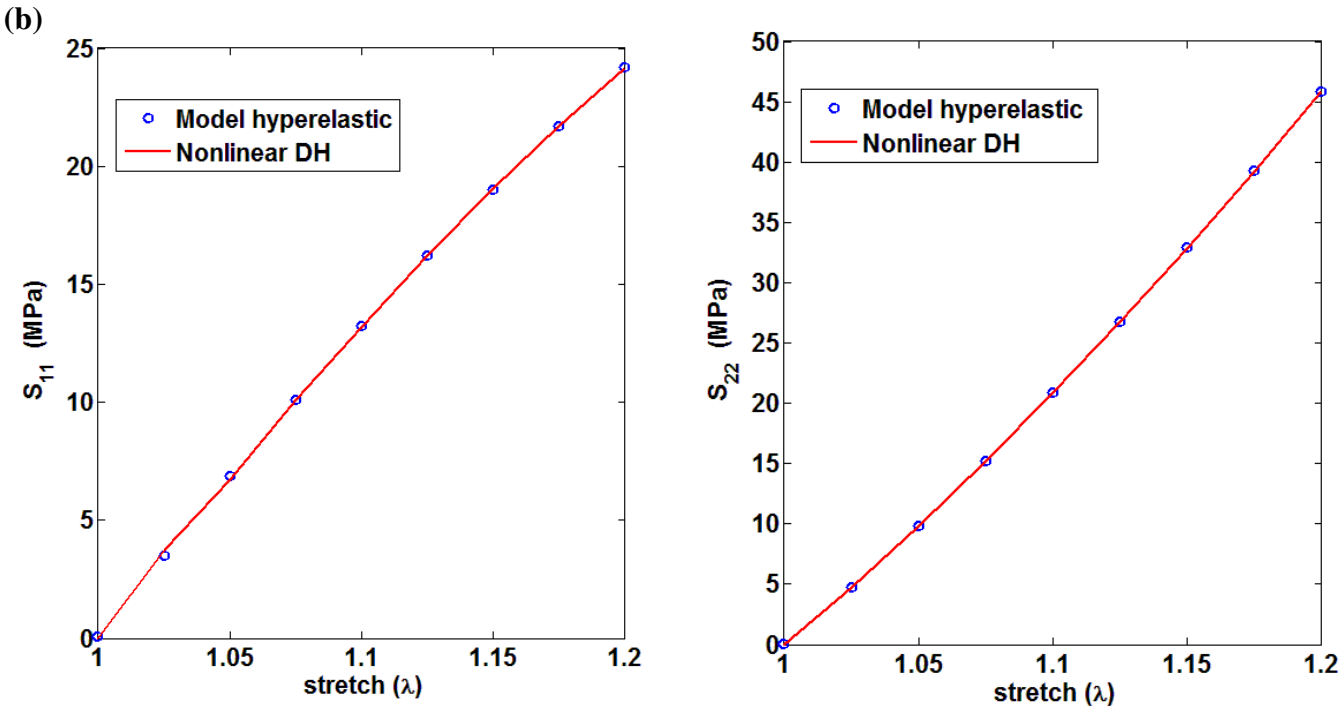

Fig. 5. 31 Second Piola-Kirchhoff stress components within (a) uniaxial tension (b) biaxial tension for biaxial strain ratio (k=2), response from nonlinear discrete homogenization and from the hyperelastic model

Figure 5.31 (a) shows a good agreement between the prediction of the hyperelastic model as to the evolution of S_{11} versus the stretch applied in weft and the evolutions computed by DH.

Similarly, the stress component S_{11} and S_{22} within biaxial load test: fig. 5.31 (b) shows that the identified model is able to capture accurately the numerical response computed by discrete homogenization. Note that the stress amplitude in warp direction is higher compared to the stress magnitude in weft direction, as expected from the choice of biaxial strain ratio k=2.

In the same manner, we identify the set of remaining coefficients $\{c_\gamma\}$ based on numerical results corresponding to simple shear tests. The expression of the components S_{12} obtained by the proposed hyperelastic model has been previously given in equation (C.53), with the angle θ between both sets of fibers changing during ongoing shear. A polynomial of degree three in the cosines of the angle is used for interpolating the numerical response obtained by homogenization.

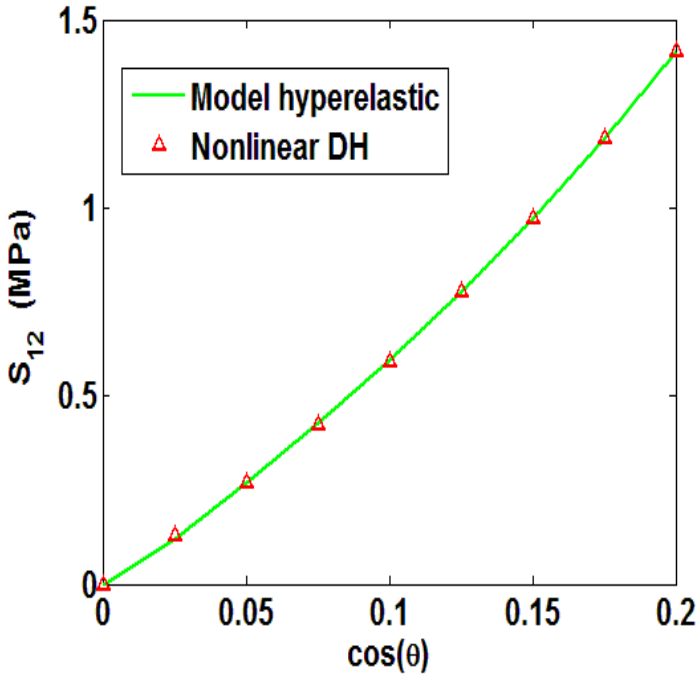

Fig. 5.32 Second Piola-Kirchhoff stress S_{12} response based on the nonlinear discrete homogenization analysis and equivalent response from hyperelastic model

The identified material constants of the strain energy function are summarized in the table 5.2 below.

Table 5.2: Optimal material parameters of the potential function within multi-mode of deformation.

a_1 [MPa]	a_2 [MPa]	a_3 [MPa]	b_1 [MPa]	b_2 [MPa]	b_3 [MPa]	k_{r1} [MPa]	k_{r2} [MPa]	c_1 [MPa]	c_2 [MPa]	c_3 [MPa]
-7.73	-211.3	153.6	-106.5	-164.1	151.2	94.25	-14.39	4.83	10.514	3.521

The strain energy density depends in general on at most only three independent invariants, which are the components of the right Cauchy-Green tensor along the fibers. If we want to express the strain energy density versus the 6 invariants, we easily can show that only three of those six invariants will be really independent. Previous classification highlights that the true invariants are in fact the three projections of the Cauchy Green tensor on the fiber directions, and that using the set of 8 invariants I_1 through I_8 is somewhat artificial (especially the decoupling between pure matrix influence via invariants I_1, I_2 and influence of the fibers via the other invariants).

It is further obvious that many structures prone to such geometrical nonlinearities can be modeled by a hyperelastic response; the interest to develop computational schemes based on discrete homogenization lies in the ability to determine efficiently and accurately the coefficients of such hyperelastic models, without recourse to a FE expensive analysis.
Note that we have used one possible formulation of the strain energy density versus the stretches, but we could also alternatively express it though the independent principal invariants considering two structural tensors representative of the two principal geometrical orientations present in such textile monolayer's.

5.5 Conclusions

We have performed meso-level analysis of the mechanical behavior of textile monolayers to construct effective anisotropic micropolar continuum models. The discrete asymptotic homogenization method delivers a micropolar effective medium at the mesoscopic level, from the description of the textile as a lattice of beams. Each yarn within the textile is modeled as a Timoshenko beam at the microscopic scale. As the main novel aspect, the nonlinear behavior of such networks under large strains was investigated. The plain weave and twill tows have been selected as case studies and have been analyzed in detailed. The derivation of such effective mechanical properties of textile from micromechanical analyses is quite interesting, moreover the change of these properties during incremental deformation have been identified, since those properties haven't been measured up to now, due to the discrete nature of textiles. On the other hand, the nonlinear stress strain response was analyzed incrementally under three type of loading cases: uniaxial, biaxial and simple shear, taking into consideration the structure geometry changes. The homogenization scheme is quite general and versatile enough to be applicable for any networks having a periodical architecture. The obtained effective continuum models at the mesoscopic level may be further used at the next scale level to perform simulations of shape forming operations involving dry textiles. as the nonlinear hyperelastic constitutive laws for fabric consists of two families of fiber has shown, one shall use the stress strain values in calibration of strain energy hyperelastic model and identify of the material constants.A relatively good agreement has been obtained between the stress strain results determined from discrete homogenization and those computed numerically by the sequential FE homogenization from the fiber scale to the tow scale.

The representation of yarns could be improved by implementing a more elaborate model of the yarn behavior. This micromechanical approach is particularly interesting and novel, due to the difficulty to measure such effective properties for textiles considering their discreteness. The proposed homogenization technique proves efficient from a numerical point of view, and it has a great versatility as to the topology of the textile armor, which makes it a suitable tool to explore and compare various textile architectures for both single and multilayers configurations in future developments. Other factors that have been discarded in the present contribution can be incorporated in extensions of the model, like yarn transverse compressibility, a more accurate representation of the shape of the yarn, and a better description of contact between yarns up to friction

5.6 References

Assidi, M., Ben Boubaker, B., Ganghoffer, J.F., 2011. Equivalent properties of monolayer fabric from mesoscopic modelling strategies. Int. J. Solids Struct. 48, 2920–2930.

Aimene Y., Hagege B., Sidoroff F., Salle E., Boisse P., 2008. "Hyperelastic approch for composite reinforcing forming simulations" ESAFORM 2008 International Journal of Material Forming, Springer Paris, Vol.1 pp. 811-814.

Aimene Y., Badel P., Vidal-Sallé E. Boisse P., 2008. "Analyse of textile composite reinforcement deformation using hyperelastic and hypoelastic constitutive laws", 11th Euromech-Mecamat conference: Mechanics of microstructured solids: cellular materials, fibre reinforced solids and soft tissues. Torino, Italie.

Baseau, E., 2003. Finite deformation of elastic–plastic filamentary networks. Int. J. Nonlinear Mech. 38, 1473– 1479.

Ben Boubaker, B., Haussy, B., Ganghoffer, J.F., 2007a. Consideration of the yarn-yarn interactions in meso/macro discrete model of the fabric. Part I: Single yarn behavior, Mechanics Research Comminucations 34, 359-370.

Ben Boubaker, B., Haussy, B., Ganghoffer, J.F., 2007b. Consideration of the yarn-yarn interactions in meso/macro discrete model of the fabric, Part II: Woven fabric under uniaxial and biaxial extension. Mechanics Research Comminucations 34, 371-378.

Ben Boubaker, B., Haussy, B., Ganghoffer, J.F., 2007c. Discrete woven structure model: yarn-on-yarn friction. C. R. Mecanique 335, 150-158.

Ben Boubaker, B. Haussy, B., Ganghoffer, J.F., 2007d. Discrete models of woven structures. Macroscopic approach. Compos. B 38 498-505.

Bensoussan, A., Lions, J.L., Papanicolaou, G., 1978. Asymptotic Analysis for Periodic Structures. North Holland, Amsterdam.

Boisse, P., Borr, M., Buet, K., Cherouat, A., 1997. Finite element simulations of textile composite forming including the biaxial fabric behaviour. Compos. B 28, 453–464.

Boisse, P., Gasser, A., Hivet, G., 2001. Analyses of fabric tensile behaviour: determination of the biaxial tension-strain surfaces and their use in forming simulations. Compos. A 32, 1395–1414.

Boisse, P., Zouari, B., Gasser, A., 2005. A mesoscopic approach for the simulation of woven fibre composite forming. Compos. Sci. Technol. 65, 429–436.

Boisse, P., Zouari, B., Daniel, J., 2006. Importance of in-plane shear rigidity in finite element analyses of woven fabric composite preforming. Compos. A 37, 2201–2212.

Crookston, J.J., Long, A.C., Jones, I.A., 2005 Asummary review of mechanical properties prediction methods for textile reinforced polymer composites. Proc. IMechE, Part L: J. Materials : Design and applications 219:91-109.

Hamila, N., Boisse, P., Sabourin, F., Brunet, M., 2009. A semi-discrete shell finite element for textile composite reinforcement forming simulation. Int. J. Numer. Methods Eng. 79, 1443–1466.

Hearle, J.W.S., Grosberg, P., Baker, S., 1969. Structural Mechanics of Fibers, Yarns, & Fabrics, Vol. 1, John Wiley& Sons, New York, USA.

Ivanov, I., Tabiei, A., 2004. Loosely woven fabric model with viscoelastic crimped fibres for ballistic impact simulations. Int. J. Numer. Methods Eng. 61 (10), 1565–1583.

Kato, S., Yoshiro, T., Minami, H., 1999. Formulation of constitutive equations for fabric membranes based on the concept of fabric lattice model. Eng. Struct. 21, 691–708.

Kawabata S., Niwa, M., Kawai, H.,1973. Finite-deformation theory of plain-weave fabrics – 1. The biaxial-deformation theory. J. Text. Inst. 64, 21–46.

Kawabata, S., Niwa, M., Kawai., H., 1973. Finite-deformation theory of plain-weave fabrics – 2. The uniaxial-deformation theory. J. Text. Inst. 64,47–61.

Kawabata, S., Niwa, M., Kawai, H., 1973. Finite-deformation theory of plain-weave fabrics – 3. The shear-deformation theory. J. Text. Inst. 64, 62–85.

Khan M. A., Mabrouki T. Vidal-Sallé E. Boisse P. 2010. Numerical and exprimental analyses of woven composite reinforcement forming using a hypoelastic behavior. Application to the double dome benchmark. J mater proc Technol 2010:210:378-88

King, M.J., Jearanaisilawong, P., Socrate, S., 2005. A continuum constitutive model for the mechanical behavior of woven fabrics. Int. J. Solids Struct. 42, 3867–3896.

Parsons, E. M., Weerasooriya, T., Sarva, S. and Socrate, S., 2010. Impact of woven fabric: Experiments and mesostructure-based continuum-level simulations. J. Mech. Phys. Solids 58, 1995-2021.

Peng, X., Cao, J., 2000. Numerical determination of mechanical elastic constants of textile composites. Proceedings-American Society for Composites 677–688.

Peng, X., Cao, J., 2002. A dual homogenization and finite element approach for material characterization of textile composites. Compos. B 33, 45–56.

Peng, X. Cao, J., 2005. A continuum mechanics-based non-orthogonal constitutive model for woven composite fabrics. Compos. A 36, 859–874.

Rattensperger, H., Eberhardsteiner, J., Mang, H.A., 2003. Numerical investigation of high pressure hydraulic hoses with steel wire braid. In: IUTAM Symposium on Computational Mechanics of Solid Materials at Large Strains 407–416.

Realff, M.L., 1992. Mechanical properties of fabrics woven from yarns produced by different spinning technologies. Ph.D. Thesis, Massachusetts Institute of Technology.

Realff, M.L., Boyce, M.C., Backer, S., 1997. A micromechanical model of the tensile behavior of woven fabric. Text. Res. J. 67, 445–459.

Shahkarami, A., Vaziri, R., 2007. A continuum shell finite element model for impact simulation of woven fabrics. Int. J. Imp. Eng. 34, 104–119.

Tan, P., Tong L., Steven, G.P., 1997, Modeling for predicting the mechanical properties of textile composites – A review. Composite Part A- Applied Sience and manufacturing 28(11): 903-922.

Xue, P., Peng, X., Cao, J., 2003. A non-orthogonal constitutive model for characterizing woven composites. Compos. A 34, 183–193.

Xue, P., Cao, J. Chen, J., 2005. Integrated micro/macro-mechanical model of woven fabric composites under large deformation. Compos. Struct. 70, 69-80.

Bonet, J., & Wood, R. D., 1997. Nonlinear continuum mechanics for finite element analysis. Cambridge: Cambridge University Press.

Belytschko T, Liu WK and Moran B 2000b Nonlinear Finite Elements for Continua and Structures.Wiley, Chichester, UK

Part II

Second Order Grade Continua
Adopting a small strain Framework

CHAPTER Six: Construction of Second Order Gradient Continuous Media by the Discrete Asymptotic Homogenization Method.

CHAPTER Seven: Two-Dimensional Discrete Homogenization Towards Second Order grade Continua.

CHAPTER Six

Construction of Second Order Gradient Continuous Media by the Discrete Asymptotic Homogenization Method

Contents

Abstract

The consideration of higher order gradients of the kinematic variables is required when localization of the deformation takes place within distances comparable or less than the typical microstructure size or spacing. This issue is of relevance in homogenization theories when the load applied to a representative unit cell can no more be considered as homogeneous. We presently address the issue of constructing an effective continuum medium from an initially discrete medium (lattice material) exhibiting such strong variations of the deformation field, due to non affine motions of the internal degrees of freedom under an externally applied strain field. We presently focus on lattice structures having a regular architecture, so that a representative unit cell can be identified at a mesoscopic level. The individual elements of the unit cell are described as beams endowed with a tensile and flexural rigidity.

We presently extend the first order homogenization schemes recently developed for the determination of the effective mechanical properties of periodical lattices considered as Cauchy or micropolar continua (Dos Reis and Ganghoffer, 2012) towards second order gradient continua. The expressions of the stresses and hyperstresses of the second order effective continuum are obtained by an identification of the principle of virtual power of internal forces for both the postulated equivalent second order continuum and the obtained homogenized continuum. The internal lengths of the second order gradient continua are evaluated versus the obtained effective second order mechanical moduli. The proposed methodology for the scale transition accounting for strain gradient effects is firstly developed in a 1D situation; the first and second order effective tensile and bending rigidities of a one-dimensional microstructured beam are evaluated; these moduli are then used at the structural level to determine the overall tensile response of an effective beam obeying a second order grade continuum behavior.

An extension of the homogenization technique to the two-dimensional case is then presented. The obtained constitutive law relates the stress and hyperstress tensors to their conjugates kinematic variables, respectively the first and second order displacement gradients, which are evaluated from the topology and microstructural properties of the initial lattice. First applications to different lattices illustrate the proposed methodology, including the square, hexagonal, triangular lattices

representative of biological membranes, and the zig-zag lattice, representative of an undulated filament or yarn. The internal lengths reflecting scale effects have been formally computed for the two types of enrichment of the classical Cauchy continuum, either by considering higher order gradients of the kinematic variables or micropolar degrees of freedom.

It is observed that there is a similarity in the methodologies used to express the transverse forces and hyper forces in the second order grade model, and the corresponding transverse forces and moments in the micropolar continuum model. This similarity noticed in such comparison between the expressions (see equation (33)) written in the second order grade model, and the corresponding expression (see Appendix B (20)) in micropolar continuum model. In both methodologies, the stiffness matrix relating the nodal forces and moments to their conjugated kinematic nodal variables are assembled by evaluating and assembling the work of internal forces versus the vector of kinematic d.o.f. The work of internal forces is required in order to obtain the second order derivative of the vertical displacement and to extract the coefficient of the kinematic conditions in each model lead to the determination of the stuffiness matrix ((B (26))). Finally, it is easy to integrate the virtual work of inter-efforts to get the expression of the forces and hyperforces in the second order gradient elastic model (equations (34) through (37)), or to express the transverse forces and moments in the micropolar model. This is discussed in detailed manner later on in this chapter in section three based on a one-dimensional homogenization example.

When we especially consider the beam undergoing flexion, a third order displacement function with four constants is considered at the onset. In the micropolar (or Cosserat) theory, the four kinematic conditions are expressed versus the vertical displacement and microrotation as two independents degree of freedoms. Instead of that, the four kinematic conditions are expressed versus the vertical displacement and its derivatives at the origin and extremity nodes in the second order gradient model.

This chapter is organized as follows: we first present the description of the kinematics (section 2), whereby the discrete virtual displacement field of the lattice nodes is related to the controlled gradients imposed on the unit cell, up to the second order. The forces and hyperforces of the discrete lattice are then identified, based on the expression of the virtual power of internal forces (section 3). The

homogenization process leading to the identification of the effective second order continuum is presented in section 4. The example of a one-dimensional microstructured beam subjected to flexion and extension is treated to illustrate the proposed homogenization scheme (section 5). We conclude this contribution (section 6) by a synthetic overview of the main thrust of the paper and a few perspectives of development.

A few words regarding notations are in order: vectors and higher order tensors are denoted as boldface symbols (expect in the 1D case where they reduce to scalars).

We submitted the present work of this chapter as an article in the proceedings of the 5th International Conference on Computational Methods, Vol.1, 2014, (ICCM2014), which was held in Cambridge, at 28th-30th July 2014. This work has been published as a special issue assigned an ISSN 23743948 (online), with Scientech Publisher llc, USA as the official publisher.

International Journal of Applied Mechanics

Construction of second order gradient continuous media by the discrete asymptotic homogenization method

KHALED ELNADY*
LEMTA, Université de Lorraine, 2, Avenue de la Forêt de Haye TSA 60604. 54518, Vandoeuvre-les-Nancy, France

FRANCISCO DOS REIS
LEMTA, Université de Lorraine, 2, Avenue de la Forêt de Haye TSA 60604. 54518, Vandoeuvre-les-Nancy, France

JEAN-FRANCOIS GANGHOFFER
LEMTA, Université de Lorraine, 2, Avenue de la Forêt de Haye TSA 60604. 54518, Vandoeuvre-les-Nancy, France

The consideration of higher order gradients of the kinematic variables is required when localization of the deformation takes place within distances comparable or less than the typical microstructure size or spacing. This issue is of relevance in homogenization theories when the load applied to a representative unit cell can no more be considered as homogeneous. We presently address the issue of constructing an effective continuum medium from an initially discrete medium exhibiting such strong variations of the deformation field due to non affine motions of the internal nodes under an externally applied strain field. We presently focus on fibrous structures having a regular architecture of a discrete nature, so that a representative unit cell can be identified at a mesoscopic level. The individual segments of the fibrous architecture are described as beams endowed with a tensile and flexural rigidity. We presently extend the first order homogenization schemes recently developed for the determination of the effective mechanical properties of periodical lattices considered as Cauchy or micropolar continua [Dos Reis and Ganghoffer, 2012] towards second order gradient continua. The expressions of the stresses and hyperstresses of the second order effective continuum are obtained by an identification of the principle of virtual power of internal forces for both the postulated equivalent second order continuum and the obtained homogenized continuum. The internal lengths of the second order gradient continua are evaluated versus the obtained effective second order mechanical moduli. The first and second order effective tensile and bending rigitities of a one-dimensional microstructured beam are computed as an illustrative example of the proposed methodology for the scale transition accounting for strain gradient effects. The obtained moduli are then used at the structural level to determine the overall tensile response of an effective beam obeying such a second order gradient continuum behavior.

Keywords: lattices; discrete homogenization; second order grade continua; micropolar continuum; elasticity; higher order tensile and flexural moduli; structural computations.

*LEMTA, Université de Lorraine, 2, Avenue de la Forêt de Haye. 54518 Vandoeuvre-les-Nancy, France.

1. Introduction

The recent period has witnessed the development of new classes of cellular solids and lattice materials used in a wide range of applications in engineering, including lightweight structures and energy absorption systems, especially due to the fact that lattice-like materials have an architecture that usually enhances the static and dynamic properties in comparison to bulk materials. Periodic lattice structures consist of the assembly of structural elements (typically beam elements) jointed at hinges and organized according to a specific discrete topology. The effective properties of such lattices are depending upon the internal topology of the beam elements within the representative unit cell, the relative density and the material properties of the structural microelements. Lattices endowed with an original mechanical behavior due to the presence of an inherent microstructure still raise the continuous interest of researchers [Gibson, 2005]. The relationship between the material microstructure and the resulting properties is the key to optimization and design of lightweight, strong, and tough materials and structures [McVeigh *et al.*, 2006].

An important category consists of lattices having a (discrete) kinematics and topology leading to an effective behavior requiring generalized continuum models at the macroscopic scale of description. Such effects are noticeable when the specimen dimensions are comparable with the cell size [Lakes, 1986]. However, they are not easy to evidence from a direct analysis at the macroscopic scale. The first motivation of micromechanically inspired analyses is then an increased understanding of the behavior of those lattices in certain loading situations (concentrated forces, tolerance to damage, perforations), [Warren and Byskov, 2008], certain geometries [Liu and Su, 2009; Yoo and Jasiuk, 2006], or when submitted to heat exchanges [Kumar and McDowell, 2009; Gu, 2001]. For example, contributions of [Fatemi *et al.*, 2002] and [Rosenberg and Cimran, 2003] show that the variation of the stress concentration at the interface between bone and prosthesis can be explained by the micropolar structure of the medium. A second motivation of homogenization techniques is their use as a tool to conceive and calculate novel structural materials exhibiting unconventional mechanical properties or behaviors, like generalized continua, as exposed in recent contributions, [Forest, 1998, 2002], [Hirschberger *et al.*, 2009], [DosReis and Ganghoffer, 2012], and references therein. A third motivation of deriving mesoscopic models of lattices at an intermediate scale is the reduction of the induced computational cost, since direct numerical simulations for full lattices would be computationally too expensive for large scales structures, if useful at all. Therefore, methods have been developed over the last two decades to replace the initial lattice by an effective continuum endowed with representative mechanical effective properties. One such method that has been prolific is the double-scale asymptotic expansion, its principle goes back to the work of [Sanchez-Palencia, 1983]. This approach has been applied to reticulated structures in [Cioranescu and Saint-Jean Paulin, 1999] and to other periodical structures in [Boutin, 1996]. Several variations were then developed for the homogenization of beam lattices: [Pradel and

Sab, 1998] and [Sab and Pradel, 2009] suggested to treat homogenization of beam lattice in a way similar as the homogenization of media made of discrete particles; the resolution of the unknowns is done by those authors by minimizing an energy functional. [Moreau and Caillerie, 1998] and [Tollenaere and Caillerie, 1998] developed a method which uses only one variable in the asymptotic expansions; the work of those authors is however limited to lattices endowed mainly with an extensional behavior. Later on, [Boutin and Hans, 2003; Boutin *et al.*, 2010] proposed a dynamical formulation of the balance of forces to solve vibration problems, essentially applied to square unit cells.

The use of gradient elasticity as a convenient framework for materials and structures showing scale effects traces back to more than a century and a half ago. Such scale effects become noticeable when the wavelength of the loading or deformation field become comparable to the microstructure size or spacing, in such situations, and due to the lack of internal lengths scales, the classical elasticity theory fails to describe such behaviors, thus requiring enhanced elastic theories incorporating intrinsic parameters and length scales to correlate the microstructure with the macrostructure. Such extensions fall into different classes of models, known in the literature as micropolar theory developed by the Cosserat brothers, couple-stress theory (Cosserat model with constrained rotations [Koiter, 1964], strain gradient theory [Toupin, 1962], micromorphic, microstretch and micropolar elasticity theories [Eringen, 1999], and fully non-local elasticity [Eringen, 1992].

In this work devoted to the construction of second order elastic models for discrete beam lattices, we expose a new homogenization scheme developed to substitute an initially discrete medium in the form of a periodic lattice by a second order effective continuum in the elastic range. We focus in this contribution on one-dimensional homogenization, although the initially discrete lattice generally occupies a two-dimensional domain in space: this means that the identified elementary unit cell is repeated by periodic translation in one dimension only. We shall first expose into details the technical steps required to construct the effective second order continuum, thereby highlighting the forces and hyperforces dual to the first and second order kinematic variables in the sense of the virtual power of internal forces. The proposed method is a variant of similar homogenization schemes already developed for second order continuum [Kouznetsova et al., 2002], with the main difference that the topology of the initial medium is discrete.

The outline of this contribution is as follows: section 2 is devoted to the description of the kinematics, whereby the discrete virtual displacement field of the lattice nodes is related to the controlled gradients (imposed on the unit cell), up to the second order. The forces and hyperforces of the discrete lattice are then identified, based on the expression of the virtual power of internal forces (section 3). The homogenization process leading to the identification of the effective second order continuum is presented in section 4. The example of a one-dimensional microstructured beam subjected to flexion and extension is treated to illustrate the proposed homogeniza-

tion scheme (section 5). We conclude this contribution (section 6) by a synthetic overview of the main thrust of the paper and a few perspectives of development.

A few words regarding notations are in order: vectors and higher order tensors are dentoed as boldface symbols (expect in the 1D case where they reduce to scalars).

2. Displacement functions and derivatives for a beam

In order to set the stage, we write a general displacement function within a periodic continuous lattice, variable $V^{\varepsilon}(x, y)$, writes [Boutin, 1996]

$$V^{\varepsilon}(x,y) = V_0(x,y) + \varepsilon V_1(x,y) + \varepsilon^2 V_2(x,y) + ... \tag{1}$$

with x the macroscopic variable of the overall lattice (describing variations of the field for different unit cells) and $y = \dfrac{x}{\varepsilon}$ the microscopic periodical variable of period $l = \varepsilon L$, describing fine variations within the considered unit cell [Cioranescu and Paulin, 1999; Sanchez-Palencia, 1983]. The small non-dimensional parameter ε represents the ratio of the identified unit cell size l to a macroscopic length L representative of the whole lattice. We accordingly rely on the double asymptotic expansion versus the spatial variables x and y at macroscopic and microscopic scales respectively. Any kinematic variable like the virtual velocity field is then made dependent upon both scales through these two variables.

Since the first order leading term of previous asymptotic expansion is supposed to be representative of the whole unit cell kinematics, the dependency on the microscopic variable is dropped therein, thus the differential of the previous displacement field then writes

$$dV^{\varepsilon}(x,y) = \frac{\partial V_0(x)}{\partial x}dx + \varepsilon\left(\frac{\partial V_1(x,y)}{\partial x}dx + \frac{\partial V_1(x,y)}{\partial y}dy\right) + \varepsilon^2\left(\frac{\partial V_2(x,y)}{\partial x}dx + \frac{\partial V_2(x,y)}{\partial y}dy\right) + ... \tag{2}$$

with the relation linking the macroscopic to the microscropic variables $dy = \dfrac{1}{\varepsilon}dx$. Equation 2 then becomes

$$\frac{\partial V^{\varepsilon}(x,y)}{\partial x} = \frac{\partial V_0(x)}{\partial x} + \frac{\partial V_1(x,y)}{\partial y} + \varepsilon\left(\frac{\partial V_2(x,y)}{\partial y} + \frac{\partial V_1(x,y)}{\partial x}\right) + ... \tag{3}$$

The variable x is the slow variable, considered to be constant within any representative unit cell, whereas $y = \dfrac{x}{\varepsilon}$ is the fast variable describing the variations occurring within the unit reference cell. This means that one can rewrite equations (**??**) and (3) under the form:

$$V^{n,\varepsilon}(x,y) = V_0(x) + \varepsilon V_1^n(x,y) + \varepsilon^2 V_2^n(x,y) + ... \tag{4}$$

$$\frac{\partial V^{n,\varepsilon}(x,y)}{\partial x} = \frac{\partial V_0(x)}{\partial x} + \frac{\partial V_1^n(x,y)}{\partial y} + \varepsilon\left(\frac{\partial V_2^n(x,y)}{\partial y} + \frac{\partial V_1^n(x,y)}{\partial x}\right) + ... \quad (5)$$

The integer subscript n associated to the node numbering indicates that the function varies within the unit cell (its absence would indicate that the function is constant within the unit cell).

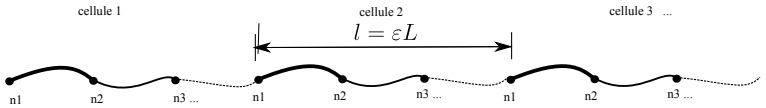

Fig. 1. Structured one-dimensional beam

We next set a relation between the displacement function of a generic node n_i and the displacement function of the similar node n_i, but which belongs to the neighbouring cell, as pictured on figure 1. We consider a node n_i occupying the position $(x, y) = (a, y)$; equations (5) and (4) then deliver:

$$V^{n,\varepsilon}(a,y) = V_0(a) + \varepsilon V_1^n(a,y) + \varepsilon^2 V_2^n(a,y) + ... \quad (6)$$

$$\frac{\partial V^{n,\varepsilon}}{\partial x}(a,y) = \frac{\partial V_0}{\partial x}(a) + \frac{\partial V_1^n}{\partial y}(a,y) + \varepsilon\left(\frac{\partial V_2^n}{\partial y}(a,y) + \frac{\partial V_1^n}{\partial x}(a,y)\right) + ... \quad (7)$$

The similar node n_i that belongs to a neighbouring cell occupies the position $(x_1, y) = (a + \varepsilon L, y)$; one can then write a Taylor series expansion of the equations (6) and (7), as follows:

$$\begin{aligned} V^{n,\varepsilon}(a+\varepsilon L, y) \approx V_0(a) &+ \varepsilon\left(V_1^n(a,y) + L\frac{\partial V_0}{\partial x}(a)\right) \\ &+ \varepsilon^2\left(V_2^n(a,y) + L\frac{\partial V_1^n}{\partial x}(a,y) + \frac{L^2}{2}\frac{\partial^2 V_0}{\partial^2 x}(a)\right) \end{aligned} \quad (8)$$

$$\begin{aligned} \frac{\partial V^{n,\varepsilon}(a+\varepsilon L, y)}{\partial x} \approx &\frac{\partial V_0}{\partial x}(a) + \frac{\partial V_1^n}{\partial y}(a,y) \\ &+ \varepsilon\left(\frac{\partial V_2^n}{\partial y}(a,y) + \frac{\partial V_1^n(a,y)}{\partial x} + L\left(\frac{\partial^2 V_0}{\partial^2 x}(a) + \frac{\partial^2 V_1^n}{\partial x \partial y}(a,y)\right)\right) \end{aligned} \quad (9)$$

One may then formulate the assumption that the second order cross-derivative $\frac{\partial^2 V_1^n}{\partial x \partial y}(a,y)$ vanishes. One justification of this assumption is to get rid of an additional (useless) degree of freedom in view of the forthcoming resolution procedure. Based on this assumption, equations (8) and (9) become

$$V^{n,\varepsilon}(a+\varepsilon L,y) \approx V_0(a) + \varepsilon\left(V_1^n(a,y) + L\frac{\partial V_0}{\partial x}(a)\right) + \varepsilon^2\left(V_2^n(a,y) + L\frac{\partial V_1^n}{\partial x}(a,y) + \frac{L^2}{2}\frac{\partial^2 V_0}{\partial^2 x}(a)\right) \tag{10}$$

$$\frac{\partial V^{n,\varepsilon}(a+\varepsilon L,y)}{\partial x} \approx \frac{\partial V_0}{\partial x}(a) + \frac{\partial V_1^n}{\partial y}(a,y) + \varepsilon\left(\frac{\partial V_2^n}{\partial y}(a,y) + \frac{\partial V_1^n(a,y)}{\partial x} + L\frac{\partial^2 V_0}{\partial^2 x}(a)\right) \tag{11}$$

As a summary of previous steps, the equations to be used in the sequel are (6), (7), (10) and (11). The forces and hyperforces conjugated to the kinematic first and second order variables are next identified based on the writing of the virtual internal work.

3. Determination of the forces and hyperforces from the virtual work principle

We consider a single beam of length $l_b = \varepsilon L_b$ in equilibrium under the action of two types of forces (the reader is referred to figure 2): classical forces T_O, T_E and hyperforces m_O, m_E (equivalent in some sense to couples in the case of bending) applied to the beam extremities.

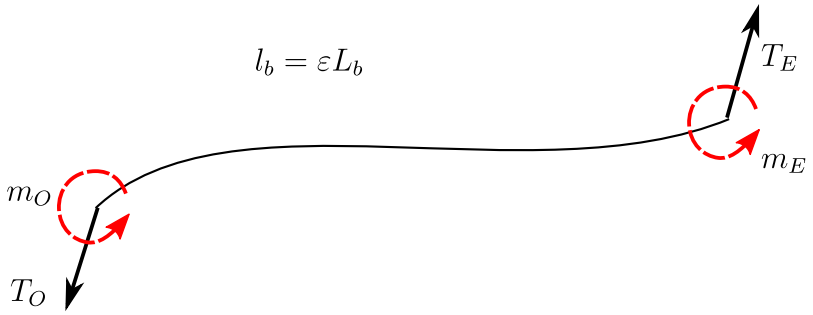

Fig. 2. Static variables attached to a beam

We express the displacement field of the representative deformation of the beam, described as a third order polynomial

$$v(s) = a\,s^3 + b\,s^2 + c\,s + d \tag{12}$$

The first and second order derivatives follow successively as

$$\frac{dv(s)}{ds} = 3as^2 + 2bs + c \tag{13}$$

$$\frac{d^2v(s)}{d^2s} = 6as + 2b \tag{14}$$

One considers the origin and extremity nodes, denoted successively O et E, with actual coordinates on the double spatial scale (x, o) and (x, e) respectively. The expression of the displacements (6) and (7) of the extremity nodes of the beam are then

$$V^{O,\varepsilon}(x, o) = V_0(x) + \varepsilon V_1^O(x, o) + \varepsilon^2 V_2^O(x, o) + ... \tag{15}$$

$$\frac{\partial V^{O,\varepsilon}}{\partial x}(x, o) = \frac{\partial V_0}{\partial x}(x) + \frac{\partial V_1^O}{\partial y}(x, o) + \varepsilon \left(\frac{\partial V_2^O}{\partial y}(x, o) + \frac{\partial V_1^O}{\partial x}(x, o) \right) + ... \tag{16}$$

$$V^{E,\varepsilon}(x, e) = V_0(x) + \varepsilon V_1^E(x, e) + \varepsilon^2 V_2^E(x, e) + ... \tag{17}$$

$$\frac{\partial V^{E,\varepsilon}}{\partial x}(x, e) = \frac{\partial V_0}{\partial x}(x) + \frac{\partial V_1^E}{\partial y}(x, e) + \varepsilon \left(\frac{\partial V_2^E}{\partial y}(x, e) + \frac{\partial V_1^E}{\partial x}(x, e) \right) ... \tag{18}$$

One may further simplify the notations by rewriting previous equations as

$$V_0(a_o) = V_0(a_e) = V_0 \tag{19}$$

$$V_1^O(x, o) = V_{O1}; \quad V_2^O(x, o) = V_{O2} \tag{20}$$

$$V_1^E(x, e) = V_{E1}; \quad V_2^E(x, e) = V_{E2} \tag{21}$$

$$\frac{\partial V_0}{\partial x}(x) = dV_0 \tag{22}$$

$$\frac{\partial^2 V_0}{\partial^2 x}(x) = d^2 V_0 \tag{23}$$

$$\frac{\partial V_1^O}{\partial y}(x, o) = dV_{O1} \tag{24}$$

$$\frac{\partial V_2^O}{\partial y}(x,o) + \frac{\partial V_1^O}{\partial x}(x,o) = dV_{O2} \tag{25}$$

$$\frac{\partial V_1^E}{\partial y}(x,e) = dV_{E1} \tag{26}$$

$$\frac{\partial V_2^E}{\partial x}(x,e) = dV_{E2} \tag{27}$$

One can then express the displacement function of the beam, previous third order polynomial expression (12), using the terms of the displacement function at the extremity nodes, based on equations (15) through (18), by solving for the unknowns a, b, c and d the following equations:

$$v(0) = V^{O,\varepsilon}(x,o) \tag{28}$$

$$v(\varepsilon L_b) = V^{E,\varepsilon}(x,e) \tag{29}$$

$$\frac{dv}{ds}(0) = \frac{\partial V^{O,\varepsilon}}{\partial x}(x,o) \tag{30}$$

$$\frac{dv}{ds}(\varepsilon L_b) = \frac{\partial V^{E,\varepsilon}}{\partial x}(x,e) \tag{31}$$

After solving these equations, using the simplified terms of the equations (19) through (27), one then obtains for the second order derivative $\frac{d^2v(s)}{d^2s}$ the following expression:

$$\begin{aligned}\frac{d^2v(s)}{d^2s} = \frac{-2}{{L_b}^3\varepsilon^2}(&-3sL_b\,dV_{E1} - 3s\varepsilon L_b\,dV_{O2} - 6s\varepsilon\,V_{O2} + 6s\varepsilon\,V_{E2} - 3sL_b\,dV_{O1}\\ &- 3s\varepsilon L_b\,dV_{E2} - 6s\,V_{O1} - 6sL_b\,dV_0 + 6s\,V_{E1} + 2\varepsilon^2{L_b}^2\,dV_{O2}\\ &+ 3\varepsilon^2 L_b\,V_{O2} - 3\varepsilon^2 L_b\,V_{E2} + 2\varepsilon{L_b}^2\,dV_{O1} + \varepsilon^2{L_b}^2\,dV_{E2} + 3\varepsilon L_b\,V_{O1}\\ &+ 3\varepsilon{L_b}^2\,dV_0 + \varepsilon{L_b}^2\,dV_{E1} - 3\varepsilon L_b\,V_{E1}\end{aligned} \tag{32}$$

Extracting the coefficients of the vector
$[dV_0, V_{O1}, V_{O2}, dV_{O1}, dV_{O2}, V_{E1}, V_{E2}, dV_{E1}dV_{E2}]$
then leads to the determination of the stiffness matrix; multiplication by $E_sI_z = \frac{E_s\varepsilon^3 t_b^3}{12}$ and integrating further lead to the following expressions of the forces and hyperforces:

$$T_O = k_{fb}\left(\frac{L_b}{2}\left(2dV_0 + dV_{O1} + dV_{E1} + \varepsilon\left(dV_{O2} + dV_{E2}\right)\right)\right.$$
$$\left. + V_{O1} - V_{E1} + \varepsilon\left(V_{O2} - V_{E2}\right)\right)\Big) \tag{33}$$

$$T_E = -k_{fb}\left(\frac{L_b}{2}\left(2dV_0 + dV_{O1} + dV_{E1} + \varepsilon\left(dV_{O2} + dV_{E2}\right)\right)\right.$$
$$\left. + V_{O1} - V_{E1} + \varepsilon\left(V_{O2} - V_{E2}\right)\right)\Big) \tag{34}$$

$$m_O = k_{fb}\left(\frac{L_b^2}{6}\left(3dV_0 + 2dV_{O1} + dV_{E1} + \varepsilon\left(2dV_{O2} + dV_{E2}\right)\right)\right.$$
$$\left. + \frac{L_b}{2}\left(V_{O1} - V_{E1} + \varepsilon\left(V_{O2} - V_{E2}\right)\right)\right) \tag{35}$$

$$m_E = k_{fb}\left(\frac{L_b^2}{6}\left(3dV_0 + dV_{O1} + 2dV_{E1} + \varepsilon\left(dV_{O2} + 2dV_{E2}\right)\right)\right.$$
$$\left. + \frac{L_b}{2}\left(V_{O1} - V_{E1} + \varepsilon\left(V_{O2} - V_{E2}\right)\right)\right) \tag{36}$$

with the bending stiffness therein $k_{fb} = \dfrac{E_s\varepsilon^2 t_b^3}{L_b^3}$.

The method used to obtain these results relies on the finite element method leading to the stifness matrices for a beam element, as described in the two Appendices.

4. Homogenization of the discrete lattice based on the virtual work of internal forces

The expressions of the efforts obtained in previous section have been obtained from the principle of virtual work, or equivalently the principle of virtual power, since we restrict to a static situation. We are still faced with the issue of the choice of the virtual velocity field: we presently select a first order velocity field at the first order in the small parameter ε. Drawing a parallel with the expressions of the displacement vectors, equations (5) and (4) deliver

$$\dot{V}^{n,\varepsilon}(x,y) = \dot{V}_0(x) = \dot{V}_0 \tag{37}$$

$$\frac{\partial \dot{V}^{n,\varepsilon}(x,y)}{\partial x} = \frac{\partial \dot{V}_0(x)}{\partial x} + \frac{\partial \dot{V}_1^n(x,y)}{\partial y} = d\dot{V}_0 + d\dot{V}_{n1} \tag{38}$$

A Taylor series expansion to the second order of previous equation (37) allows us to write at a point with the same index n, but located in a contiguous cell (at a distance εL of the slow variable x) the following expansion of the virtual velocity field up to the second order gradient (based on previous notations)

$$\dot{V}^n(x+\varepsilon L, y) \approx \dot{V}_0 + \varepsilon\, L\, d\dot{V}_0 + \frac{\varepsilon^2}{2} L^2\, d^2\dot{V}_0 \tag{39}$$

In a similar manner, a first order Taylor series development of equation (38) allows writing

$$\frac{\partial \dot{V}^{n,\varepsilon}(x+\varepsilon L, y)}{\partial x} \approx d\dot{V}_0 + d\dot{V}_{n1} + L\, d^2\dot{V}_{n1} + \varepsilon\, L\, d^2\dot{V}_0 \tag{40}$$

Using the same hypothesis as done before for the virtual displacements (2), one shall assume that $d^2\dot{V}_{n1} = 0$; this assumption will provde a simplification in the forthcoming developments. Equation (40) then becomes

$$\frac{\partial \dot{V}^{n,\varepsilon}(x+\varepsilon L, y)}{\partial x} \approx d\dot{V}_0 + d\dot{V}_{n1} + \varepsilon\, L\, d^2\dot{V}_0 \tag{41}$$

The virtual power for the whole lattice writes as the sum of the product of forces by their conjugated kinematic quantities at each node,

$$P = \sum T_i \dot{V}_i + m_i \frac{\partial \dot{V}_i}{\partial x} \tag{42}$$

One can further decompose the sum as a double sum on the cells and on the nodes within each cell

$$P = \sum_{c\in\mathbb{Z}} \left(\sum_{n\in\mathbb{B}} T_i \dot{V}_i + m_i \frac{\partial \dot{V}_i}{\partial x} \right) = \sum_{c\in\mathbb{Z}} P_e \tag{43}$$

with $i = (c, n)$, $\mathbb{Z}$ the set of all cells of the lattice, $\mathbb{B}$ the set of all nodes of an elementary cell, and P_e the virtual power expressed on an elementary cell. One can further decompose the virtual power over the elementary unit cell as

$$P_e = \sum_{n\in\mathbb{B}} T_i \dot{V}_i + m_i \frac{\partial \dot{V}_i}{\partial x} \tag{44}$$

Since the sum of efforts vanishes for each node of the lattice due to equilibrium, it only remains the two edge nodes since the contribution of the internal nodes to the virtual power vanishes, so that one obtains

$$P_e = T_o \dot{V}_o + m_o \frac{\partial \dot{V}_o}{\partial x} + T_e \dot{V}_e + m_e \frac{\partial \dot{V}_e}{\partial x} \tag{45}$$

Due to the considered self-equilibrium of the beam, one further obtains the efforts $T_o = -T_e$ and hyperforces $m_o = -m_e$, thus one can simplify the expression of P_e

$$P_e = T_e \left(\dot{V}_e - \dot{V}_o \right) + m_e \left(\frac{\partial \dot{V}_e}{\partial x} - \frac{\partial \dot{V}_o}{\partial x} \right) \tag{46}$$

One further expands the differences therein as follows

$$\begin{aligned} \left(\dot{V}_e - \dot{V}_o \right) &= \dot{V}_0 + \varepsilon\, L\, d\dot{V}_0 + \frac{\varepsilon^2}{2} L^2\, d^2\dot{V}_0 - \dot{V}_0 \\ &= \varepsilon\, L\, d\dot{V}_0 + \frac{\varepsilon^2}{2} L^2\, d^2\dot{V}_0 \end{aligned} \tag{47}$$

$$\begin{aligned} \left(\frac{\partial \dot{V}_e}{\partial x} - \frac{\partial \dot{V}_o}{\partial x} \right) &= d\dot{V}_0 + d\dot{V}_{n1} + \varepsilon\, L\, d^2\dot{V}_0 - d\dot{V}_0 + d\dot{V}_{n1} \\ &= \varepsilon\, L\, d^2\dot{V}_0 \end{aligned} \tag{48}$$

Thus, we obtain the virtual power of internal forces in discrete form as

$$P = \sum_{c \in \mathbb{Z}} T_e \left(\varepsilon\, L\, d\dot{V}_0 + \frac{\varepsilon^2}{2} L^2\, d^2\dot{V}_0 \right) + m_e \left(\varepsilon\, L\, d^2\dot{V}_0 \right) \tag{49}$$

If one considers the fact that a unit cell is a small material element, so that $dx = \varepsilon L$ at constant macroscopic length L, letting the length of a small element tend to zero $\varepsilon \to 0$, it follows then the homogenized expression of the virtual power of internal forces

$$\lim_{\varepsilon \to 0} P = \int_\Omega \left(T_e \left(d\dot{V}_0 + \frac{\varepsilon}{2} L\, d^2\dot{V}_0 \right) + m_e\, d^2\dot{V}_0 \right) dx \tag{50}$$

$$= \int_\Omega \left(T_e d\dot{V}_0 + \left(T_e \frac{\varepsilon}{2} L + m_e \right) d^2\dot{V}_0 \right) dx \tag{51}$$

with Ω representing the domain of the whole structure. Previous Riemann integral represents the virtual power of internal forces in the constructed effetive second order gradient 1D continuum. One can notice therein the appearance of two products of forces with conjugated kinematic variables, the force T_e multiplied by the derivative of the velocity $d\dot{V}_0$, and the hyperforce $\left(T_e \frac{\varepsilon}{2} L + m_e \right)$ equivalent to a couple multiplied by the second order derivative of the velocity, quantity $d^2\dot{V}_0$.

We recall in general that in the discrete homogenization scheme, the static variables highlighted as dual to the kinematic variables (the first and second order spatial strain gradients) are not directly the Cauchy first and second order stress tensors, but (first and second order) stress vectors. The first order Cauchy stress is

then simply reconstructed in this 1D example from the obtained transverse force dual to the kinematic variable $d\dot{V}_0$, second order tensor

$$\sigma = T_e \mathbf{e}^b \otimes \mathbf{e}^{b\perp} + \mathbf{e}^{b\perp} \otimes \mathbf{e}^b$$

with $\mathbf{e}^b$ the unit vector along the beam, and $\mathbf{e}^{\mathbf{b}\perp}$ the unit orthogonal vector. Similarly, the hyperstress third order tensor $\mathbf{S}$ is reconstructed from the static variable $\left(T_e \varepsilon \frac{L}{2} + m_e\right)$ dual to the kinematic scalar quantity $d^2\dot{V}_0$ in the virtual power of internal forces, thus giving

$$\mathbf{S} = \left(T_e \varepsilon \frac{L}{2} + m_e\right) \mathbf{e}b\perp \otimes \mathbf{e}^b \otimes \mathbf{e}^b$$

in which the tensor basis has to be symmetrized with respect to the second and third indices, since $\mathbf{S}$ is an eulerian stress enjoying symmetry as does the first order Cauhy stress.

It remains at this stage to solve the localization problem, that is to determine the four kinematic unknowns V_{n1}, V_{n2}, dV_{n1} and dV_{n2} for each node. The balance of forces defined in equations (33) through (36) have to be satisfied for each node and for each of the successive powers of ε. There are two series of forces T_e and m_e and two different powers in ε, thus there are in total four series of (different) equations per node to be solved for the same number of kinematic variables. Plugging then back the expression of those kinematic variables into the static variables (forces and moments), delivers the final expression of the forces and moments fully expressed versus the macroscopic controlles gradients of the displacement.

The next section is devoted to the application of previous second order homogenization scheme to a one dimensional microstructured beam subjected to combined tension and flexion, for which the effective first and second order moduli will be evaluated. Due to the linear framework, one can consider separately the two loading cases of uniaxial tension and flexion.

5. Case of a one-dimensional microstructured beam: first and second order tensile and flexural rigidities

We consider a beam made of a periodic microstructure defining the representative unit cell, including two beams presenting different geometrical and mechanical characteristics, as pictured in figure (3)). Beam p_1 has an elastic modulus E_1, a width t_1, and length l_1; similarly, beam p_2 has an elastic modulus E_2, a width t_2, and a length l_2.

Based on expressions (33) to (36), we identify the forces and hyperforces for the present example; setting $k_{fb} = \dfrac{E_i \varepsilon^2 t_i^3}{L_i^3}$, we first write the resultants and moments for the first beam p_1:

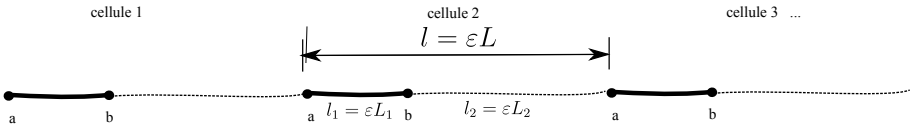

Fig. 3. Example of a microstructured beam made of two beams with different microstructural properties

$$T_O^{p1} = k_{f1}\left(\frac{L_1}{2}\left(2dV_0 + dV_{a1} + dV_{b1} + \varepsilon\left(dV_{a2} + dV_{b2}\right)\right)\right.$$
$$\left. + V_{a1} - V_{b1} + \varepsilon\left(V_{a2} - V_{b2}\right)\right) \tag{52}$$

$$T_E^{p1} = -k_{f1}\left(\frac{L_1}{2}\left(2dV_0 + dV_{a1} + dV_{b1} + \varepsilon\left(dV_{a2} + dV_{b2}\right)\right)\right.$$
$$\left. + V_{a1} - V_{b1} + \varepsilon\left(V_{a2} - V_{b2}\right)\right) \tag{53}$$

$$m_O^{p1} = k_{f1}\left(\frac{L_1^2}{6}\left(3dV_0 + 2dV_{a1} + dV_{b1} + \varepsilon\left(2dV_{a2} + dV_{b2}\right)\right)\right.$$
$$\left. + \frac{L_1}{2}\left(V_{a1} - V_{b1} + \varepsilon\left(V_{a2} - V_{b2}\right)\right)\right) \tag{54}$$

$$m_E^{p1} = k_{f1}\left(\frac{L_1^2}{6}\left(3dV_0 + dV_{a1} + 2dV_{b1} + \varepsilon\left(dV_{a2} + 2dV_{b2}\right)\right)\right.$$
$$\left. + \frac{L_1}{2}\left(V_{a1} - V_{b1} + \varepsilon\left(V_{a2} - V_{b2}\right)\right)\right) \tag{55}$$

In order to get similar exprsssions for the second beam p_2, one has to exploit the series of equations (6), (7), (10) and (11) in order to determine the expressions corresponding to the displacement of the node a located at the right extremity of the beam p_2, but at a distance εL from node a, the left origin of the first beam p_1:

$$V^{n_1 \in p_1} \approx V_0 + \varepsilon V_{a1} + \varepsilon^2 V_{a2} \tag{56}$$

$$dV^{n_1 \in p_1} \approx dV_0 + dV_{a1} + \varepsilon dV_{a2} \tag{57}$$

$$V^{n_1 \in p_2} \approx V_0 + \varepsilon\left(V_{a1} + L\left(dV_0 + dV_{a1}\right)\right) + \varepsilon^2\left(V_{a2} + \frac{L^2}{2}d^2V_0\right) \tag{58}$$

$$dV^{n_1 \in p2} \approx dV_0 + dV_{a1} + \varepsilon\left(dV_{a2} + L\,d^2V_0\right) \tag{59}$$

Thus, the forces and hyperforces are derived for the second beam p_2 as

$$T_O^{p2} = k_{f2}\left(\frac{L_2}{2}\left(2dV_0 + dV_{a1} + dV_{b1} + \varepsilon\left(\left(dV_{a2} + L\,d^2V_0\right) + dV_{b2}\right)\right)\right.$$
$$\left. + V_{b1} - \left(V_{a1} + L\left(dV_0 + dV_{a1}\right)\right) + \varepsilon\left(V_{b2} - \left(V_{a2} + \frac{L^2}{2}d^2V_0\right)\right)\right) \tag{60}$$

$$T_E^{p2} = -k_{f2}\left(\frac{L_2}{2}\left(2dV_0 + dV_{a1} + dV_{b1} + \varepsilon\left(\left(dV_{a2} + L\,d^2V_0\right) + dV_{b2}\right)\right)\right.$$
$$\left. + V_{b1} - \left(V_{a1} + L\left(dV_0 + dV_{a1}\right)\right) + \varepsilon\left(V_{b2} - \left(V_{a2} + \frac{L^2}{2}d^2V_0\right)\right)\right) \tag{61}$$

$$m_O^{p2} = k_{f2}\left(\frac{L_2^2}{6}\left(3dV_0 + 2dV_{b1} + dV_{a1} + \varepsilon\left(2dV_{b2} + \left(dV_{a2} + L\,d^2V_0\right)\right)\right)\right.$$
$$\left. + \frac{L_2}{2}\left(V_{b1} - \left(V_{a1} + L\left(dV_0 + dV_{a1}\right)\right) + \varepsilon\left(V_{b2} - \left(V_{a2} + \frac{L^2}{2}d^2V_0\right)\right)\right)\right) \tag{62}$$

$$m_E^{p2} = k_{f2}\left(\frac{L_2^2}{6}\left(3dV_0 + dV_{b1} + 2dV_{a1} + \varepsilon\left(dV_{b2} + 2\left(dV_{a2} + L\,d^2\,V_0\right)\right)\right)\right.$$
$$\left. + \frac{L_2}{2}\left(V_{b1} - \left(V_{a1} + L\left(dV_0 + dV_{a1}\right)\right) + \varepsilon\left(V_{b2} - \left(V_{a2} + \frac{L^2}{2}d^2V_0\right)\right)\right)\right) \tag{63}$$

It holds in addition the additive decomposition of the overall length of the unit cell of the two beam lengths

$$L = L_1 + L_2 \tag{64}$$

One then writes the equilibrium of forces and hyperforces for the nodes a and b in order to determine the six kinematic unknowns, $dV_{a1}, dV_{a2}, dV_{b1}, dV_{b2}, V_{a1}, V_{a2}$:

$$E_{q1} = T_O^{p1} + T_E^{p2} = 0 \tag{65}$$

$$E_{q2} = m_O^{p1} + m_E^{p2} = 0 \tag{66}$$

$$E_{q3} = m_E^{p1} + m_O^{p2} = 0 \tag{67}$$

These equations express on two orders in the small parameter ε; one obtains

$$dV_{a2} = \frac{(k_{f1}L_1L_1^3 - k_{f2}L_2^3)d^2V_0}{k_{f1}L_1^2 + k_{f2}L_2^2} \tag{68}$$

$$dV_{b2} = \frac{(k_{f1}L_1^3 + 2k_{f2}L_2^2L_1 + k_{f2}L_2^3)d^2V_0}{2(k_{f1}L_1^2 + k_{f2}L_2^2)} \tag{69}$$

$$V_{a2} = \frac{L_1^2 d^2 V_0}{2} + V_{b2} \tag{70}$$

$$dV_{a1} = dV_{b1} = 0 \tag{71}$$

$$V_{a1} = -L_1 dV_0 + V_{b1} \tag{72}$$

From the solution of the localization problem giving the kinematic displacements versus the continuous gradients of the displacement, we are then able to fully express the static variables T_E and m_E in terms of the first and second order gradients of the vertical displacement:

$$m_E^{p2} = \varepsilon \frac{k_{f2} k_{f1} L_2^2 L_1^2 (L_1 + L_2)}{12\left(k_{f1} L_1^2 + k_{f2} L_2^2\right)} d^2 V_0 \tag{73}$$

$$T_E^{p2} = 0 \tag{74}$$

Previous relation between the hyperforce and the second order kinematic variable then leads to the identification of the second order effective modulus of the beam, representing a flexural rigidity B, expressing as

$$B = \frac{k_{f2} k_{f1} L_2^2 L_1^2 (L_1 + L_2)}{12\left(k_{f1} L_1^2 + k_{f2} L_2^2\right)}$$

This modulus coincides with the one that would be obtained from a micropolar effective continuum. Lastly, we determine the internal bending length from the relation between the bending moment and the curvature of the micropolar constitutive model,

$$M_{XZ} = \left(2\mu\, l_c^2\right) \frac{\partial \varphi}{\partial x}$$

.

The shear modulus therein, the scalar quantity μ, is obtained from the relation between the effective shear stress σ_{12} and the shear strain, variable $\frac{\partial V}{\partial x}$, as

$$\sigma_{12} = \left(\frac{1}{2} k_{f2} l_2\right)\left(\frac{\partial V}{\partial x}\right)$$

The effective shear modulus is computed from discrete homogenization as

$$\mu = \frac{1}{4} k_{f2} l_2$$

This gives the internal length for bending as

$$l_{bending} = \sqrt{\frac{L_2\left(L_1 + L_2\right)}{3\left(1 + \frac{k_{f2}}{k_{f1}}\left(\frac{L_2}{L_1}\right)^2\right)}}$$

depending upon the ratio of the bending stifnesses of the two internal beams, and the relative length of the second beam. It is straightforward to see that l_c has a maximum value of $\frac{1}{\sqrt{3}}$, obtained when the ratio of bending stiffness is very small and when the first beam is of negligible length in comparison to the second one.

Considering now a beam under pure extension, the virtual power of internal work writes in a similar format, replacing the kinematic virtual velocities $\dot{V}_0, d^2\dot{V}_0$ by $\dot{U}_0, d^2\dot{U}_0$ respectively. We accordingly obtain

$$\dot{U}^{n,\varepsilon}(x,y) = \dot{U}_0(x) = \dot{U}_0 \tag{75}$$

and

$$\dot{U}^{n}(x+\varepsilon L,y) \approx \dot{U}_0 + \varepsilon\, L\, d\dot{U}_0 + \frac{\varepsilon^2}{2} L^2\, d^2\dot{U}_0 \tag{76}$$

Thus, the virtual power for the whole lattice writes as the sum of the product of forces by their conjugated kinematic quantities at each node. After transforming the double summation into a Riemann integral as previously done for pure flexion, and considering the fact that the unit cell is a small element of vanishing size $\varepsilon \to 0$, we arrive at the continuum version of the virtual power of internal forces in case of pure extension, viz

$$\lim_{\varepsilon\to 0} P = \int_{\Omega} \left(N_e d\dot{U}_o + N_e \frac{\varepsilon}{2} L d^2\dot{U}_o \right) dx \tag{77}$$

One can then identify from the previous equation and in a general situation the first and second order forces as the static variables dual respectively to the first and second gradients of the virtual normal velocity.

We next extend previous example to the computation of the effective bending modulus to an undulated beam modeled as a zig-zag beam (the initial slope of the yarn is an adjustable configuration parameter), an approximation of a sine function, and relying on a micropolar effective continuum model for the evalulation of the effective mechanical properties.

The flexural rigidity is recorded versus the inclination of the beams, showing a continuous decrease when the crimp increases (the straight beam then has the highest flexural rigidity).

This problem is representative of the tensile response of a single undulated beam, and the update of the geometry is descriptive of geometrical nonlinearities. Some additional work is nevertheless required to perform a similar homogenization, but relying on a second order gradient scheme instead.

The effective second order grade continuum is next built for the situation of pure extension.

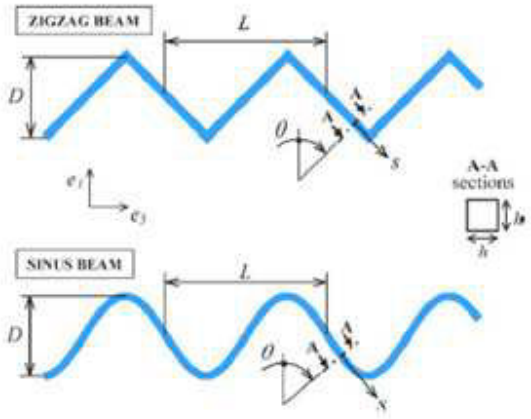

Fig. 4. Initial configuration of an undulated beam, corrugated structure [Siad and Potier Ferry, 1992]

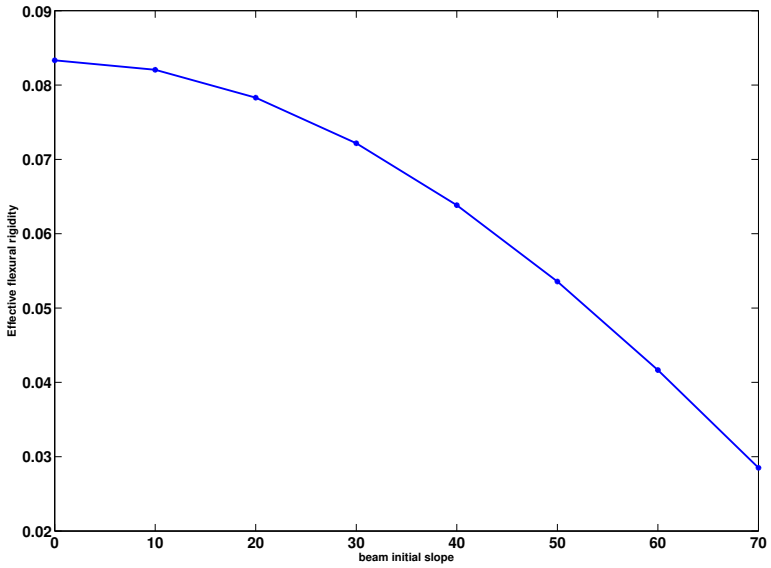

Fig. 5. Effective second order flexural rigidity vs. different beam initial slope

5.1. *Tensile rigidity for a microstructured beam*

We consider the beam subjected to pure uniaxial tension, thus the kinematic unknown is the sole longitudinal displacement expressing at two orders of the small parameter ε. One obtains the following expressions of the normal forces similar to

the previous formula (34) to (37), based on the results described in the Appendix (case of beam in tension) The following expressions of the normal forces is obtained, setting $k_{lb} = \frac{E_s \varepsilon^2 t}{L}$:

$$N_O = k_{lb} \left(U_{O1} - U_{E1} + \varepsilon \left(U_{O2} - U_{E2} \right) \right) \tag{78}$$

and

$$N_E = -k_{lb} \left(U_{O1} - U_{E1} + \varepsilon \left(U_{O2} - U_{E2} \right) \right) \tag{79}$$

For the first beam p_1, this gives:

$$N_O^{p1} = k_{l1} \left(U_{a1} - U_{b1} + \varepsilon \left(U_{a2} - U_{b2} \right) \right) \tag{80}$$

$$N_E^{p1} = -k_{l1} \left(U_{a1} - U_{b1} + \varepsilon \left(U_{a2} - U_{b2} \right) \right) \tag{81}$$

In order to get analogous formula for the second beam p_2, one has to exploit a similar series of equations derived in previous section for bending: one expresses the longitudinal displacement of the node a located at the right extremity of the beam p_2, but at a distance εL from node a, the left origin of beam p_1.

$$U^{n_1 \in p1} \approx U_o + \varepsilon U_{a1} + \varepsilon^2 U_{a2} \tag{82}$$

$$U^{n_1 \in p2} \approx U_o + \varepsilon \left(U_{a1} + L \left(dU_o \right) \right) + \varepsilon^2 \left(U_{a2} + \frac{L^2}{2} d^2 U_o \right) \tag{83}$$

Thus, it holds for beam p_2:

$$N_O^{p2} = k_{l2} \left(U_{b1} - \left(U_{a1} + L \left(dU_o \right) \right) + \varepsilon \left(U_{b2} - \left(U_{a2} + \frac{L^2}{2} d^2 U_o \right) \right) \right) \tag{84}$$

$$N_E^{p2} = -k_{l2} \left(U_{b1} - \left(U_{a1} + L \left(dU_o \right) \right) + \varepsilon \left(U_{b2} - \left(U_{a2} + \frac{L^2}{2} d^2 U_o \right) \right) \right) \tag{85}$$

One sets in addition equation (65), and then writes the equilibrium of normal forces for the nodes a and b in order to determine the four unknowns U_{a1} , U_{a2} , U_{b1}, U_{b2} :

$$E_{q1} = N_E^{p1} + N_O^{p2} = 0 \tag{86}$$

$$E_{q2} = N_O^{p1} + N_E^{p2} = 0 \tag{87}$$

These equations express on two orders in ε ; one obtains

$$U_{a1} = -\frac{k_{l2}\,(L_1+L_2)}{k_{l1}+k_{l2}}\,dU_o + U_{b1} \tag{88}$$

$$U_{a2} = \frac{k_{l2}(L_1+L_2)^2}{2\,(k_{l1}+k_{l2})}\,d^2U_o + U_{b2} \tag{89}$$

so that

$$N_E^{p2} = \frac{k_{l1}\,k_{l2}\,(L_1+L_2)\,dU_o}{(k_{l1}\,+k_{l2}\,)} + \varepsilon\frac{k_{l1}\,k_{l2}(L_1+L_2)^2 d^2U_o}{2\,(k_{l1}\,+k_{l2}\,)} \tag{90}$$

It is then straightforward to identify from the previous expression of the normal force the first and second order effective tensile moduli of the beam, representing the effective tensile rigidities: the first order effective tensile modulus is identified from the first order term of N_E^{p2} as

$$\frac{k_{l1}\,k_{l2}\,(L_1+L_2)}{(k_{l1}\,+k_{l2}\,)}$$

The second order effective tensile modulus writes as the second order contribution of N_E^{p2}, term

$$\varepsilon\frac{k_{l1}k_{l2}(L_1+L_2)^3}{4\,(k_{l1}+k_{l2})}$$

It shall be noted that the first order tensile rigidity coincides with the one that would be obtained from a Cauchy effective continuum.

As a summary, we obtain the following effective first and second order tensile and flexural rigidities, as summarized in the following Table:

Table1: Identified effective first and second order results.

Equivalent flexural rigidity from second gradient continuum	Equivalent flexural rigidity from discrete micropolar homogenization
$\frac{k_{f1}\,k_{f2}L_1^2L_2^2(L_1+L_2)}{12\left(k_{f1}\,L_1^2+k_{f2}\,L_2^2\right)}$	$\frac{k_{f1}\,k_{f2}L_1^2L_2^2(L_1+L_2)}{12\left(k_{f1}\,L_1^2+k_{f2}\,L_2^2\right)}$
Equivalent tensile rigidity for second order gradient continuum	Equivalent first order tensile rigidity from discrete homogenization
$\frac{k_{l1}\,k_{l2}(L_1+L_2)}{(k_{l1}+k_{l2}\,)}$, $\frac{k_{l1}\,k_{l2}(L_1+L_2)^3}{4(k_{l1}+k_{l2}\,)}$	$\frac{k_{l1}\,k_{l2}(L_1+L_2)}{(k_{l1}+k_{l2}\,)}$

The internal length for pure extension is obtained as the square root of the ratio of the second order to first order effective moduli, as $l_{tension} = \frac{(L_1+L_2)}{2}$, so one can see that second order effects in extension are always important (for any choice of microstructural parameters).

In the next section, the obtained homogenized mechanical properties are used to perform the scale transition from the mesoscopic to the macroscopic structural level.

6. Structural computations based on the discrete homogenization scheme

We here rely on the determination of the effective mechanical properties of 1D beam to make the transition from the mesoscopic to the macroscopic level, and perform structural calculations of the response of a second order grade beam submitted to a tensile loading. The formulation of continuum models for second order grade continua together with the suitable required higher order boundary conditions can be found e.g. in [Forest, 2002].

A bar of length l is clamped at the left extremity at position $x = 0$, and we assume no double volume forces, no couples and no triple forces to simplify the analysis. The external volume loading then resumes to a simple constant body force f. Based on the derivation of the boundary conditions in previous section, a double normal force M is applied to the right edge located at position $x = l$. The virtual powers of external and contact forces then successively simplify in the present 1D context to

$$P^{(e)} = \int\limits_{[0,l]} f.\delta u dx$$

and

$$P^{(c)} = \int\limits_{\partial D} \{t.\delta u + MD_n\delta u\}\, dx = [t.\delta u + MD_n\delta u]_0^l$$

The field equations accordingly become:

$$\begin{array}{l} \tau := \sigma - divS, \mathrm{x} \in [0, l] \\ \sigma(x) = E\frac{\partial u(x)}{\partial x}, S(x) = A\frac{\partial^2 u(x)}{\partial^2 x} \\ div\tau(x) + f = 0 \rightarrow div\left\{E\frac{\partial u(x)}{\partial x} - div\left(A\frac{\partial^2 u(x)}{\partial^2 x}\right)\right\} + \mathrm{f} = 0 \end{array}$$

Those equations are associated to the boundary conditions

$$BC : \begin{cases} u(x=0) = 0 \\ t = \left(\tau - \frac{\partial S}{\partial x}\right)(x = l) \\ M = S(x = l) \end{cases}$$

with t, M given quantities. It follows from simple dimensional analysis that the ratio of the first to second order moduli has the dimension of a length, so that $l_c = E/A$ defines an internal length for the second order gradient continuum.
The response of the bar under tension is obtained by evaluating the relation between the applied tension and the strain, defined as the relative displacement, that is the scalar $\varepsilon := \Delta l/l$, with Δl the increase of length, which has to be determined from the end displacement, $\Delta l := u\,(x = l)$. The applied tension to be considered as a static boundary condition is

$$t = \left(\tau - \frac{\partial S}{\partial x}\right)(x = l) = \left(\sigma - 2\frac{\partial S}{\partial x}\right)(x = l) = \left(E\frac{\partial u}{\partial x} - 2A\frac{\partial^2 u\,(x)}{\partial^2 x}\right)(x = l)$$

while the second order boundary condition writes in the present 1D context as

$$M = A\frac{\partial^2 u}{\partial^2 x}\,(x = l)$$

These two boundary conditions deliver the following conditions for the first and second partial derivatives

$$\frac{\partial u}{\partial x}\,(x = l) = \frac{(t + 2M)}{E}$$
$$\frac{\partial^2 u}{\partial^2 x}\,(x = l) = M/A$$

The continuous displacement for the second order effective bar then writes

$$u(x) = \frac{A\,(Af + EM)}{E^3 e^{El/A}} e^{Ex/A} - \frac{fx^2}{2E} + \frac{(Efl - Af + EM + Et)}{E^2} x - \frac{A\,(Af + EM)}{E^3} e^{-El/A}$$

The strain over the bar denoted ϵ is then evaluated from previous expression as a linear function of the applied traction t as $\epsilon := \frac{\Delta l}{l} = \frac{u(l)}{l}$.

The bar compliance C^{hom} is then defined as the ratio of the overall strain to the applied tension, the scalar quantity

$$C^{hom} = \frac{fl + 2t}{2Et}$$

.

The obtained second order gradient solution is next compared with the first order gradient solution: the first order gradient problem writes

$$\sigma\,(x) = E\frac{\partial u(x)}{\partial x},$$
$$div\sigma\,(x) + f = 0 \rightarrow E\frac{\partial^2 u(x)}{\partial^2 x} + \mathrm{f} = 0$$

associated to the boundary conditions

$$BC : \begin{cases} u(x=0) = 0 \\ t = E\frac{\partial u(x)}{\partial x}\,(x=l) \end{cases}$$

The solution is

$$u(x) = -\frac{1}{2}\frac{fx^2}{E} + \frac{(fl+t)\,x}{E}$$

We easily see that the first order displacement field is recovered from the second order gradient displacement for nil values of the second order parameters, that is for $A = 0 = M$.

7. Conclusion

We have developed a discrete homogenization scheme up to the second order gradient of the imposed displacement field in order to formulate constitutive models for media exhibiting strong deformation gradients at the unit cell level, due to the impact of an inherent microstructure. The derived effective continuum is characterized by first and second order mechanical moduli relating the stress to the first order strain and the hyperstress to the second order strain. The method is systematic in the sense that it can handle any lattice, with an homogenization restricted to one direction in space in the present contribution. From a numerical viewpoint, a dedicated homogznization code has been developed combining symbolic and numerical evaluations, using as an input file the topology and mechanical parameters of the beams within the identified unit cell of the lattice. The proposed methdology has been applied to the evaluation of the second order tensile and flexural rigidity of a microstructured beam; the flexural rigidiy calculated by the second order gradient scheme is identical to that computed by a micropolar effective continuum model. However, in from a technical point of view, the effective second order modulus (51) is obtained in a simpler manner by the second order gradient homogenization scheme. The computation of effective mechanical properties of materials endowed with a microstructure exhibiting effectively second order gradient effects is the basis for performing structural computations in a efficient manner, whereby the identified effective constitutive law is implemented at each Gauss point of a finite element computation. An extension of the present methodology to the 2D homogenization of periodical discrete structures towards second order gradient continua constitutes a promising perspective of development of the present work.

8. References

Dos Reis, F., and Ganghoffer, J.F. [2012] "Construction of micropolar continua from the asymptotic homogenization of beam lattices," *Computers and Structures* **112-113**, 354–363.

Gibson, L. J [2005] "Biomechanics of cellular solids," *Journal of Biomechanics* **38**, 377–399.

McVeigh, C., Vernerey, F., Liu, W. K., and Brinson, L. C. [2006] "Multiresolution analysis for material design," *Computer Methods Applied Mechanics and Engineering* **195**, 5053–5076.

Lakes, R. S. [1986] "Experimental microelasticity of two porous solids," *International Journal of solids and structures* **22**, 55–63.

Warren, W. E., and Byskov, E. [2008] "A general solution to some plane problems of micropolar elasticity," *European Journal of Mechanics A/Solids* **27**, 18–27.

Liu, S., and Su, W. [2009] "Effective couple-stress continuum model of cellular solids and size effects analysis," *International Journal of Solids and Structures* **46** (14-15), 2787–2799.

Yoo, A., and Jasiuk, I. [2006] "Couple-stress moduli of a trabecular bone idealized as a 3D periodic cellular network," *Journal of Biomechanics* **39**, 2241–2252.

Kumar, R. S., and McDowell, D. L. [2009] "Multifunctional Design of Two-Dimensional Cellular Materials with Tailored Mesostructure," *International Journal of Solids and Structures* **46** (14-15), 2871–2885.

Fatemi, J., Van Keulen, F., and Onck, P. R. [2002] "Generalized Continuum Theories: Application to Stress Analysis in Bone," *Meccanica* **37**, 385–396.

Potier-Ferry, M., and Siad, L. [1992] "Homognisation gomtrique dune poutre ondule," *C.R. Academy of Sciences, Paris* **314** (II), 3425–430.

Rosenberg, J., Cimrman, R. [2003] "Microcontinuum approach in biomechanical modeling," *Mathematics and Computers in Simulation* **61**, 249–260.

Forest, S. [2002] "Homogenization methods and the mechanics of generalized continua - part 2," *Theoretical and Applied Mechanics* **28-29**, 113–143.

Forest, S. [1998] "Mechanics of generalized continua : construction by homogenization," *J. Phys. IV France* **8**, 39–48.

Sanchez-Palencia, E. [1983] "Centrifuge testing," in *Homogenization method for the study of composite medi*, ed. F. Verhulst (Asymptotic Analysis II, Vol. 985 of Lecture Notes in Mathematics, Springer Berlin / Heidelberg), pp. 192–214.

Cioranescu, D., and Paulin, S. J. [1999] *Homogenization of reticulated structures* (Springer).

Boutin, C. [1996] " Microstructural effects in elastic composites," *International journal of solids and structures* **33** (7), 1023–1051.

Pradel, F., and Sab, K. [1998] " Cosserat modelling of elastic periodic lattice structures," *Comptes Rendus de lAcadmie des Sciences, Paris* **326** (IIb), 699–704.

Sab, K., and Pradel, F. [2009] "Homogenisation of periodic Cosserat media," *International Journal of Computer Applications in Technology* **34**, 60–71.

Moreau, G., and Caillerie, D. [2009] "Continuum modeling of lattice structures in large displacement applications to buckling analysis," *Computers and Structures* **68**, 181–189.

Kouznetsova, V., Geers, M.G. D., and Brekelmans, W.A. M. [2002] "Multi-scale con-

stitutive modelling of heterogeneous materials with a gradient–enhanced computational homogenization scheme," *International Journal for Numerical Methods in Engineering* **54**, 11235–1260.

Tollenaere, H., and Caillerie, D. [1998] "Continuous modeling of lattice structures by homogenization," *Advances in Engineering Software* **29**, 699–705.

Boutin, C., and Hans, S. [2003] "Homogenisation of periodic discrete medium: Application to dynamics of framed structures," *Computers and Geotechnics* **30**, (4) 303–320.

Boutin, C., Hans, S., and Chenais, C. [2010] "Generalized beams and continua. dynamics of reticulated structures," *Mechanics of Generalized Continua*, ed.G. A. Maugin, A. V. Metrikine (Mechanics of Generalized Continua: One Hundred Years After the Cosserats), pp. 131–141.

Eringen, A. C. [1992] "Balance laws of micromorphic continua revisited," *Int. J. Engng Sci.* **30**, 805–810.

Eringen, A. C. [1999] *Microcontinuum field theories* (Springer), New York.

Toupin, R. [1962] "Elastic materials with couple stresses," *Archives Rational Mechanics Analysis* **11**, 385–413.

Koiter, W. [1964] "Couple stresses in the theory of elasticity," *i,ii, Proc. Kon. Ned. Akad. Wetenscha* **B 67**, 17–44.

Hirschberger, C. B., Ricker, S., Steinmann, P., and Sukumar, N. [2009] "Computational multiscale modelling of heterogeneous material layers," *Engineering Fracture Mechanics* **76**, 793–812.

CHAPTER Seven

Two-Dimensional Discrete Homogenization Towards Second Order grade Continua

Content

We extend in this chapter the homogenization technique introduced in 1D to a full 2D context; these developments did benefit from discussions and joined work with Yosra Rahali in the frame of her PhD thesis.

7.1 Introduction

It is relevant to reduce the size of structural problems for repetitive lattice materials by recourse to homogenization, with the underlying idea of replacing the initially discrete lattice by an equivalent continuum at an intermediate mesoscopic scale. The lattices made of heterogeneous materials are generally considered as multiscale, in the sense that the characteristic dimensions of their constituents are very different from the dimension of the structure. On the other hand, the occurrence of instability phenomena associated to the consideration of strong fluctuations of the deformation within an identified representative volume element is one key objective of the multiscale analysis of these structures. These phenomena may occur at both microscopic and macroscopic levels and they mutually interact. The classical framework of continuum mechanics does not allow in general describing the microstructural phenomena. In many problems characterized by stress or strain concentrations or singular mechanical fields, such as localization of deformation and rupture, standard continuum models do not properly capture those phenomena (T. Duy Khanh, 2011; F. Samuel, 1996; 2006).

Generalized continua (Cosserat and second order grade continua, micromorphic continua...) are prone to capture microstructural effects on the macroscopic behavior, by refining the kinematic description(C. Eugène et al., 1909). In this context, numerous models have been proposed since the early sixties, especially by (Toupin in 1962; 1964; Mindlin et al., 1962). This work is a contribution in this spirit, based on the discrete asymptotic homogenization (of discrete media) towards second order grade continua. We thereby extend the first order homogenization scheme for discrete media, by including second order terms in the asymptotic expansion. The methodology for the construction of the stress and hyperstress tensors hyperstress representative of the statics of second order grade continua versus their conjugated kinematic variables, the strain and the strain gradient respectively, is developed. The obtained constitutive law shall be evaluated from the topology and microstructural properties of the initial lattices; applications to different lattices will illustrate the proposed

methodology, including the square, hexagonal, triangular lattices representative of biological membranes, and the zig-zag lattice. The internal lengths reflecting scale effects have been formally computed for the two types of enrichment of the classical Cauchy continuum, either through the consideration of higher order gradients of the kinematic variables or by additional micropolar degrees of freedom. We first start by computing the expression of the forces and hyperforces for a beam within the lattice.

7.2 Expression of forces and hyperforces

We consider a 2D beam of length $l_b = \varepsilon L_b$ working in traction-compression due to the action of the forces $\mathbf{N}_O$ et $\mathbf{N}_E$ applid to its extremity node, and in flexion under the action of the transverse forces $\mathbf{T}_O$, $\mathbf{T}_E$, as pictured on Figure 7.1.

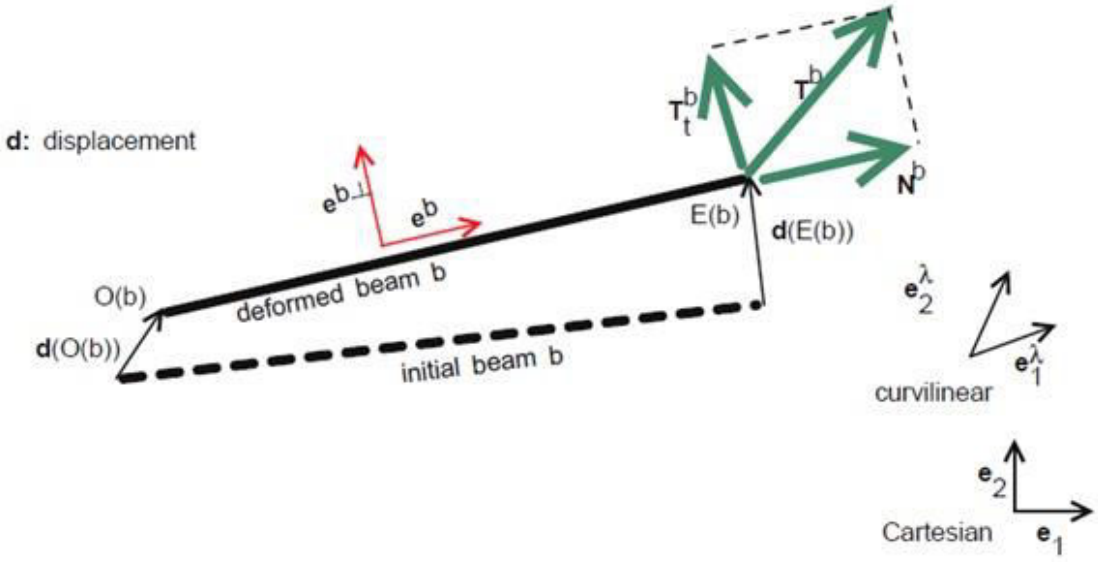

Fig. 7.1 kinematic and static description of a single beam element in equilibrium

Based on the equations of beam theory written by (Thesis F. Dos Reis, 2010), one shall next determine the expression of the forces incorporating the second order displacement gradient; we summarize below the expression of the forces for the Cauchy continuum in vector (intrinsic) format:

$$\mathbf{N}_O = k_l^b \left(\mathrm{u}_O - \mathrm{u}_E\right)\mathbf{e}^b \tag{7.1}$$

$$\mathbf{N}_E = -\mathbf{N}_O \tag{7.2}$$

$$\mathbf{T}_O = k_f^b \left(\mathrm{v}_O - \mathrm{v}_E \right) \mathbf{e}^{b\perp} \tag{7.3}$$

$$\mathbf{T}_E = -\mathbf{T}_O \tag{7.4}$$

The following notations have been introduced there above:

$\mathbf{D}_O^\varepsilon$, $\mathbf{D}_E^\varepsilon$ the displacement vectors at the origin and extremity nodes of the beam element

l_b^ε the beam length.

$k_l^b = \dfrac{ES}{l_b^\varepsilon}$ the tensile rigidity and $k_f^b = \dfrac{12EI_z}{l_b^3}$ the flexural rigidity.

One presently considers beams with a square section $S = t^{\varepsilon b}.ep^{\varepsilon b}$, with $t^{\varepsilon b}$ the width and $ep^{\varepsilon b}$ the thickness of the beam. Let I_z be the quadratic moment of the beam: $I_z = \dfrac{\left(t^{\varepsilon b}\right)^3}{12}$. One imposes $t \neq ep$ and a constant thickness $ep = Cte = 1 \Rightarrow S = t^{\varepsilon b} = \varepsilon t^b$; this entails simplifications of the expression of the forces without reducing the generality of the method, thus:

$$k_{l_1}^b = \frac{ES}{l_b^\varepsilon} = \frac{E\varepsilon t^b}{\varepsilon L_b} = \frac{Et^b}{L_b}$$

$$\text{and } k_f^b = \frac{12EI}{l_b^{\varepsilon 3}} = \frac{12E\left(\varepsilon t^b\right)^3}{12\left(\varepsilon L_b\right)^3} = \frac{Et^{b3}}{L_b{}^3}$$

In this work, we shall essentially consider planar problems, thus the use of boldface symbols refers to vectors written in 2D.

7.3 Asymptotic expansion of the kinematic displacement variables $\mathbf{D}^\varepsilon$ and $d\mathbf{D}^\varepsilon$

One considers displacement fields parameterized by a curvilinear coordinate (denoted λ in the sequel), according to:

$$\mathbf{D} = (\mathrm{u}, \mathrm{v})$$

Let first express the asymptotic expansion of the displacement at second order, using Cartesian coordinates:

$$\mathbf{D}^{\varepsilon}\left(\mathbf{x},\mathbf{y}\right)=\mathbf{D}_{o}(\mathbf{x})+\varepsilon\mathbf{D}_{1}\left(\mathbf{x},\mathbf{y}\right)+\varepsilon^{2}\mathbf{D}_{2}\left(\mathbf{x},\mathbf{y}\right)+... \tag{7.5}$$

The first order term therein, vector $\mathbf{D}_{o}(\mathbf{x})$, is considered as independent of the microscopic variable **y,** defined as $\mathbf{y}=\frac{\mathbf{x}}{\varepsilon}$, with **x** the global variable for the lattice (macroscopic scale) and **y** the periodicity variable (microscopic scale), the unit cell being of period $l=\varepsilon L_{i}$

The same expansion writes in curvilinear coordinates

$$\mathbf{D}^{\varepsilon}(\lambda_{i})=\mathbf{D}_{o}(\lambda_{i})+\varepsilon\mathbf{D}_{1}(\lambda_{i})+\varepsilon^{2}\mathbf{D}_{2}(\lambda_{i})+... \tag{7.6}$$

We express the difference of displacement between the origin and extremity nodes of the beam via the Taylor series expansion:

$$\mathbf{D}_{1}^{n}=\mathbf{D}_{1}^{n}(\lambda_{i})+L_{1}\frac{\partial\mathbf{D}_{O}(\lambda_{i})}{\partial\lambda_{1}}\delta^{1b}+L_{2}\frac{\partial\mathbf{D}_{O}(\lambda_{i})}{\partial\lambda_{2}}\delta^{2b}+... \tag{7.7}$$

$$\begin{aligned}\mathbf{D}_{2}^{n}=\mathbf{D}_{2}^{n}(\lambda_{i})&+L_{1}\frac{\partial\mathbf{D}_{1}^{n}(\lambda_{i})}{\partial\lambda_{1}}\delta^{1b}+\frac{L_{1}^{2}}{2}\frac{\partial\mathbf{D}_{o}^{2}(\lambda_{i})}{\partial\lambda_{1}^{2}}\delta^{1b}+L_{2}\frac{\partial\mathbf{D}_{1}^{n}(\lambda_{i})}{\partial\lambda_{2}}\delta^{2b}+\frac{L_{2}^{2}}{2}\frac{\partial\mathbf{D}_{o}^{2}(\lambda_{i})}{\partial\lambda_{2}^{2}}\delta^{2b}\\&+L_{1}L_{2}\frac{\partial\mathbf{D}_{o}^{2}(\lambda_{i})}{\partial\lambda_{1}\partial\lambda_{2}}\delta^{1b}\delta^{2b}\end{aligned} \tag{7.8}$$

Thus

$$(\mathrm{u}_{O}^{\varepsilon}-\mathrm{u}_{E}^{\varepsilon})=\mathbf{e}^{b}.\left(\varepsilon\left(\mathbf{D}_{1}^{O}-\mathbf{D}_{1}^{E}\right)+\varepsilon^{2}\left(\mathbf{D}_{2}^{O}-\mathbf{D}_{2}^{E}\right)\right) \tag{7.9}$$

$$(\mathrm{v}_{O}^{\varepsilon}-\mathrm{v}_{E}^{\varepsilon})=\mathbf{e}^{b\perp}.\left(\varepsilon\left(\mathbf{D}_{1}^{O}-\mathbf{D}_{1}^{E}\right)+\varepsilon^{2}\left(\mathbf{D}_{2}^{O}-\mathbf{D}_{2}^{E}\right)\right) \tag{7.10}$$

with the shift factor $\delta^{i}\in\{0,1,-1\}$ written as a Kronecker symbol, the index $i\in\{1,2\}$ indicating whether the considered axis is e_1 or e_2.

One notices that the displacement is expressed versus both the first and second order gradients of the displacement.

Inserting equation (7.9-7.10) into equations (7.1) to (7.4), one obtains the expressions of the normal and transverses forces, successively $\mathbf{N}^{\varepsilon b}$ and $\mathbf{T}^{\varepsilon b}$ at the extremity nodes of the beam element:

$$\mathbf{N}_O = k_i^b \mathbf{e}^b \left(\mathbf{e}^b . \left(\varepsilon \left(\mathbf{D}_1^O - \mathbf{D}_1^E \right) + \varepsilon^2 \left(\mathbf{D}_2^O - \mathbf{D}_2^E \right) \right) \right) \tag{7.11}$$

$$\mathbf{N}_E = -\mathbf{N}_O \tag{7.12}$$

$$\mathbf{T}_O = k_r^b \left(\left(\mathbf{e}^{b\perp} . \left(\varepsilon \left(\mathbf{D}_1^O - \mathbf{D}_1^E \right) + \varepsilon^2 \left(\mathbf{D}_2^O - \mathbf{D}_2^E \right) \right) \right) + \frac{\varepsilon L_b}{2} \left(\mathbf{e}^{b\perp} . \left(2 d\mathbf{D}_0 + \varepsilon \left(d\mathbf{D}_1^O + d\mathbf{D}_1^E \right) \right) \right) \right) \tag{7.13}$$

$$\mathbf{T}_E = -\mathbf{T}_O \tag{7.14}$$

In order to simplify notations, one sets:

$$u_{O1} = \mathbf{D}_1^O . \mathbf{e}^b \tag{7.15}$$

$$u_{E1} = \left(\mathbf{D}_1^E + L_i \delta^{ib} \frac{\partial \mathbf{D}_o(\lambda^\varepsilon)}{\partial \lambda_i} \right) . \mathbf{e}^b \tag{7.16}$$

$$u_{O2} = \mathbf{D}_2^O . \mathbf{e}^b \tag{7.17}$$

$$u_{E2} = \left(\mathbf{D}_2^E + L_i \delta^{ib} \frac{\partial \mathbf{D}_1^E(\lambda^\varepsilon)}{\partial \lambda_i} + L_i^2 \delta^{ib} \frac{\partial^2 \mathbf{D}_o(\lambda^\varepsilon)}{\partial \lambda_i^2} \right) . \mathbf{e}^b \tag{6.18}$$

$$v_{O1} = \mathbf{D}_1^O . \mathbf{e}^{b\perp} \tag{7.19}$$

$$v_{E1} = \left(\mathbf{D}_1^E + L_i \delta^{ib} \frac{\partial \mathbf{D}_o(\lambda^\varepsilon)}{\partial \lambda_i} \right) . \mathbf{e}^{b\perp} \tag{7.20}$$

$$v_{O2} = \mathbf{D}_2^O . \mathbf{e}^{b\perp} \tag{7.21}$$

$$v_{E2} = \left(\mathbf{D}_2^E + L_i \delta^{ib} \frac{\partial \mathbf{D}_1^E(\lambda^\varepsilon)}{\partial \lambda_i} + L_i^2 \delta^{ib} \frac{\partial^2 \mathbf{D}_o(\lambda^\varepsilon)}{\partial \lambda_i^2} \right) . \mathbf{e}^{b\perp} \tag{7.22}$$

Thus finally, the forces write:

$$\mathbf{N}_O = k_i^b \mathbf{e}^b \left(\varepsilon \left(u_{O1} - u_{E1} \right) + \varepsilon^2 \left(u_{O2} - u_{E2} \right) \right) \tag{7.23}$$

$$\mathbf{N}_E = -\mathbf{N}_O \tag{7.24}$$

$$\mathbf{T}_O = k_r^b \left(\varepsilon \left(v_{O1} - v_{E1} \right) + \varepsilon^2 \left(v_{O2} - v_{E2} \right) \right) \tag{7.25}$$

$$\mathbf{T}_E = -\mathbf{T}_O \tag{7.26}$$

We next determine the derivatives of the displacement, expressions $L_i \delta^{ib} \frac{\partial \mathbf{D}_o(\lambda^\varepsilon)}{\partial \lambda_i}$,

$L_i \delta^{ib} \frac{\partial \mathbf{D}_1^E(\lambda^\varepsilon)}{\partial \lambda_i}$ and $L_i^2 \delta^{ib} \frac{\partial^2 \mathbf{D}_o(\lambda^\varepsilon)}{\partial \lambda_i^2}$.

After resolution and simplifications, the derivatives express as:

$$L_i\delta^{ib}\frac{\partial \mathbf{D}_o(\lambda^\varepsilon)}{\partial\lambda_i}=L_1\delta^1\left(\cos\theta_x\ \frac{\partial \mathbf{D}_o}{\partial x}+\sin\theta_x\ \frac{\partial \mathbf{D}_o}{\partial y}\right)+L_2\delta^2\left(\cos\theta_y\ \frac{\partial \mathbf{D}_o}{\partial x}+\sin\theta_y\ \frac{\partial \mathbf{D}_o}{\partial y}\right) \tag{7.27}$$

$$L_i\delta^{ib}\frac{\partial \mathbf{D}_1^E(\lambda^\varepsilon)}{\partial\lambda_i}=L_1\delta^1\left(\cos\theta_x\ \frac{\partial \mathbf{D}_1^E}{\partial x}+\sin\theta_x\ \frac{\partial \mathbf{D}_1^E}{\partial y}\right)+L_2\delta^2\left(\cos\theta_y\ \frac{\partial \mathbf{D}_1^E}{\partial x}+\sin\theta_y\ \frac{\partial \mathbf{D}_1^E}{\partial y}\right) \tag{7.28}$$

$$L_i^2\delta^{ib}\frac{\partial^2 \mathbf{D}_o(\lambda^\varepsilon)}{\partial\lambda_i^2}=\left(\begin{array}{l}\dfrac{L_1^2\delta^1}{2}\left(\cos^2\theta_x\ \dfrac{\partial^2 \mathbf{D}_o}{\partial x^2}+\sin^2\theta_x\ \dfrac{\partial^2 \mathbf{D}_o}{\partial y^2}+2\sin\theta_x\cos\theta_x\dfrac{\partial^2 \mathbf{D}_o}{\partial x\partial y}\right)\\ +\dfrac{L_2^2\delta^2}{2}\left(\cos^2\theta_y\ \dfrac{\partial^2 \mathbf{D}_o}{\partial x^2}+\sin^2\theta_y\dfrac{\partial^2 \mathbf{D}_o}{\partial y^2}+2\sin\theta_y\cos\theta_y\dfrac{\partial^2 \mathbf{D}_o}{\partial x\partial y}\right)\end{array}\right) \tag{7.29}$$

The next step is the homogenization processes, leading to the expression of the constitutive law**.**

7.4 Homogenization

7.4.1 Writing of the equilibrium equations in virtual power form

The virtual velocity field has the same form as the displacement field evaluated in section 6.3; we shall select a simple field reducing to the term in order 0 in the small parameter (ε). The virtual velocity field then writes:

$$\dot{\mathbf{D}}^\varepsilon(\mathbf{P})=\dot{\mathbf{D}}_o(\mathbf{P})+... \tag{7.30}$$

P is the coordinate vector of the considered point within the global lattice; this field can be decomposed into a transversal and a longitudinal velocity; the transversal velocity writes:

$$\begin{aligned}\dot{V}^\varepsilon(\mathbf{P})&=\dot{\mathbf{D}}^\varepsilon(\mathbf{P}).\,\mathbf{e}^{b\perp}\\ &=\dot{V}_o(\mathbf{P})+...\end{aligned} \tag{7.31}$$

The longitudinal virtual velocity writes:

$$\dot{U}^{\varepsilon}(\mathbf{P}) = \dot{\mathbf{D}}^{\varepsilon}(\mathbf{P}).\,\mathbf{e}^{b} \tag{7.32}$$

$$= \dot{U}_{o}(\mathbf{P}) + \ldots$$

The virtual power of the forces within the lattice writes as a product of internal forces by their dual kinematic quantity at each node:

$$P = \sum T_i \dot{V}_i + N_i \dot{U}_i \tag{7.33}$$

One can decompose the sum as a double summation on the cells and on the nodes within a cell:

$$P = \sum_{c \in \mathbb{C}} \left(\sum_{n \in B} T_i \dot{V}_i + N_i \dot{U}_i \right) = \sum_{c \in \mathbb{C}} P_e \tag{7.34}$$

with $i = (c,n)$, $\mathbb{C}$ the set of cells of the lattice, $\mathbb{B}$ the set of nodes of an elementary cell and P_e the virtual power of internal forces in an elementary cell. One can accordingly express the virtual power as:

$$P_e = \sum_{n \in B} T_i \dot{V}_i + N_i \dot{U}_i \tag{7.35}$$

Since the sum of efforts vanish at each node of the lattice, it only remains for each of the considered nodes the edge nodes, since the virtual power of the internal nodes (to the elementary unit cell) vanish:

$$P_e = \sum_{b} \left(T_O \dot{V}_O + N_o \dot{U}_O + T_e \dot{V}_e + N_e \dot{U}_e \right) \tag{7.36}$$

The cell is under equilibrium at each node, and the efforts are periodical with a period equal to the cell width; this means that each edge node n has a duplicate (see figure 7.2): one edge node belongs to the elementary cell (it is called n_e in figure 7.2), and the other node belongs to the adjacent cell, called n_a on the same figure 7.2. The position of the nodes relative to the beam they belong to is not identical: the nodes of type n_e are origin nodes of the beam, whereas the nodes of type n_a are extremity nodes for this beam.

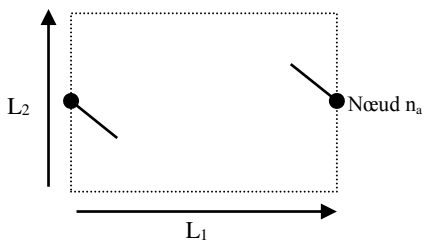

Nœud n_e

Fig. 7.2 elementary cell in a 2D space.

One can thus write :

$$\sum T_{n_e=o} = -\sum T_{n_a=e} \tag{7.37}$$

$$\sum N_{n_e=o} = -\sum N_{n_a=e} \tag{7.38}$$

One can accordingly simplify the expression of P_e in eq.(7.36)

$$P_e = \sum_b \left(T_e \left(\dot{V}_e - \dot{V}_O \right) + N_e \left(\dot{U}_e - \dot{U}_O \right) \right) \tag{7.39}$$

Let then develop the expressions $\left(\dot{V}_e - \dot{V}_O \right) and \left(\dot{U}_e - \dot{U}_O \right)$: a Taylor series expansion of equations (7.31) and (7.32) allows writing

$$\dot{V}_O \left(\lambda^\varepsilon \right) = \dot{V}_o \left(\lambda^\varepsilon \right) + ...$$

$$\dot{V}_e = \dot{V}_o(\lambda^\varepsilon + \varepsilon L_i \delta^{ib}) = \dot{V}_o + \varepsilon L_i \delta^{ib} \frac{\partial \dot{V}_o(\lambda^\varepsilon)}{\partial \lambda_i} + \varepsilon^2 L_i^2 \delta^{ib} \frac{\partial^2 \dot{V}_o(\lambda^\varepsilon)}{\partial \lambda_i^2} + ..$$

Thus

$$(\dot{V}_e - \dot{V}_O) = \varepsilon L_i \delta^{ib} \frac{\partial \dot{V}_o(\lambda^\varepsilon)}{\partial \lambda_i} + \varepsilon^2 L_i^2 \delta^{ib} \frac{\partial^2 \dot{V}_o(\lambda^\varepsilon)}{\partial \lambda_i^2} \tag{7.40}$$

Similarly, one obtains

$$(\dot{U}_e - \dot{U}_O) = \varepsilon L_i \delta^{ib} \frac{\partial \dot{U}_o(\lambda^\varepsilon)}{\partial \lambda_i} + \varepsilon^2 L_i^2 \delta^{ib} \frac{\partial^2 \dot{U}_o(\lambda^\varepsilon)}{\partial \lambda_i^2} \tag{7.41}$$

From equations (6.27) and (6.28), one can develop the expressions $L_i \delta^{ib} \frac{\partial \dot{V}_o(\lambda^\varepsilon)}{\partial \lambda_i}$

, $L_i \delta^{ib} \frac{\partial \dot{U}_o(\lambda^\varepsilon)}{\partial \lambda_i}, L_i^2 \delta^{ib} \frac{\partial^2 \dot{V}_o(\lambda^\varepsilon)}{\partial \lambda_i^2}$ et $L_i^2 \delta^{ib} \frac{\partial^2 \dot{U}_o(\lambda^\varepsilon)}{\partial \lambda_i^2}$, and replace their expressions in equations (7.40) and (7.41):

$$L_i\delta^{ib}\frac{\partial \dot{V}_o(\lambda^\varepsilon)}{\partial \lambda_i}=L_1\delta^1\left(\mathrm{c}\theta_x\ \frac{\partial \dot{V}_o}{\partial x}+\mathrm{s}\theta_x\ \frac{\partial \dot{V}_o}{\partial y}\right)+L_2\delta^2\left(\mathrm{c}\theta_y\ \frac{\partial \dot{V}_o}{\partial x}+\mathrm{s}\theta_y\ \frac{\partial \dot{V}_o}{\partial y}\right) \tag{7.42}$$

$$L_i\delta^{ib}\frac{\partial \dot{U}_o(\lambda^\varepsilon)}{\partial \lambda_i}=L_1\delta^1\left(\mathrm{c}\theta_x\ \frac{\partial \dot{U}_o}{\partial x}+\mathrm{s}\theta_x\ \frac{\partial \dot{U}_o}{\partial y}\right)+L_2\delta^2\left(\mathrm{c}\theta_y\ \frac{\partial \dot{U}_o}{\partial x}+\mathrm{s}\theta_y\ \frac{\partial \dot{U}_o}{\partial y}\right) \tag{7.43}$$

$$L_i^2\delta^{ib}\frac{\partial^2 \dot{V}_o(\lambda^\varepsilon)}{\partial \lambda_i^2}=\left(\begin{array}{l}\dfrac{L_1^2\delta^1}{2}\left(\mathrm{c}^2\theta_x\ \dfrac{\partial^2 \dot{V}_o}{\partial x^2}+\mathrm{s}^2\theta_x\ \dfrac{\partial^2 \dot{V}_o}{\partial y^2}+2\mathrm{s}\theta_x\mathrm{c}\theta_x\dfrac{\partial^2 \dot{V}_o}{\partial x\partial y}\right)\\ +\dfrac{L_2^2\delta^2}{2}\left(\mathrm{c}^2\theta_y\ \dfrac{\partial^2 \dot{V}_o}{\partial x^2}+\mathrm{s}^2\theta_y\ \dfrac{\partial^2 \dot{V}_o}{\partial y^2}+2\mathrm{s}\theta_y\mathrm{c}\theta_y\dfrac{\partial^2 \dot{V}_o}{\partial x\partial y}\right)\end{array}\right) \tag{7.44}$$

$$L_i^2\delta^{ib}\frac{\partial^2 \dot{U}_o(\lambda^\varepsilon)}{\partial \lambda_i^2}=\left(\begin{array}{l}\dfrac{L_1^2\delta^1}{2}\left(\mathrm{c}^2\theta_x\ \dfrac{\partial^2 \dot{U}_o}{\partial x^2}+\mathrm{s}^2\theta_x\ \dfrac{\partial^2 \dot{U}_o}{\partial y^2}+2\mathrm{s}\theta_x\mathrm{c}\theta_x\dfrac{\partial^2 \dot{U}_o}{\partial x\partial y}\right)\\ +\dfrac{L_2^2\delta^2}{2}\left(\mathrm{c}^2\theta_y\ \dfrac{\partial^2 \dot{U}_o}{\partial x^2}+\mathrm{s}^2\theta_y\ \dfrac{\partial^2 \dot{U}_o}{\partial y^2}+2\mathrm{s}\theta_y\mathrm{c}\theta_y\dfrac{\partial^2 \dot{U}_o}{\partial x\partial y}\right)\end{array}\right) \tag{7.45}$$

Thus, the virtual power of an elementary cell becomes written in (7.39), becomes:

$$P_e=\sum_b\left[\begin{array}{l}T_e\left(\begin{array}{l}\varepsilon\left(L_1\delta^1\left(\mathrm{c}\theta_x\ \dfrac{\partial \dot{V}_o}{\partial x}+\mathrm{s}\theta_x\ \dfrac{\partial \dot{V}_o}{\partial y}\right)+L_2\delta^2\left(\mathrm{c}\theta_y\ \dfrac{\partial \dot{V}_o}{\partial x}+\mathrm{s}\theta_y\ \dfrac{\partial \dot{V}_o}{\partial y}\right)\right)\\ +\varepsilon^2\left(\dfrac{L_1^2\delta^1}{2}\left(\mathrm{c}^2\theta_x\ \dfrac{\partial^2 \dot{V}_o}{\partial x^2}+\mathrm{s}^2\theta_x\ \dfrac{\partial^2 \dot{V}_o}{\partial y^2}+2\mathrm{s}\theta_x\mathrm{c}\theta_x\dfrac{\partial^2 \dot{V}_o}{\partial x\partial y}\right)+\dfrac{L_2^2\delta^2}{2}\left(\mathrm{c}^2\theta_y\ \dfrac{\partial^2 \dot{V}_o}{\partial x^2}+\mathrm{s}^2\theta_y\ \dfrac{\partial^2 \dot{V}_o}{\partial y^2}+2\mathrm{s}\theta_y\mathrm{c}\theta_y\dfrac{\partial^2 \dot{V}_o}{\partial x\partial y}\right)\right)\end{array}\right)\\ +N_e\left(\begin{array}{l}\varepsilon\left(L_1\delta^1\left(\mathrm{c}\theta_x\dfrac{\partial \dot{U}_o}{\partial x}+\mathrm{s}\theta_x\ \dfrac{\partial \dot{U}_o}{\partial y}\right)+L_2\delta^2\left(\mathrm{c}\theta_y\ \dfrac{\partial \dot{U}_o}{\partial x}+\mathrm{s}\theta_y\ \dfrac{\partial \dot{U}_o}{\partial y}\right)\right)\\ +\varepsilon^2\left(\dfrac{L_1^2\delta^1}{2}\left(\mathrm{c}^2\theta_x\ \dfrac{\partial^2 \dot{U}_o}{\partial x^2}+\mathrm{s}^2\theta_x\ \dfrac{\partial^2 \dot{U}_o}{\partial y^2}+2\mathrm{s}\theta_x\mathrm{c}\theta_x\dfrac{\partial^2 \dot{U}_o}{\partial x\partial y}\right)+\dfrac{L_2^2\delta^2}{2}\left(\mathrm{c}^2\theta_y\ \dfrac{\partial^2 \dot{U}_o}{\partial x^2}+\mathrm{s}^2\theta_y\ \dfrac{\partial^2 \dot{U}_o}{\partial y^2}+2\mathrm{s}\theta_y\mathrm{c}\theta_y\dfrac{\partial^2 \dot{U}_o}{\partial x\partial y}\right)\right)\end{array}\right)\end{array}\right] \tag{7.46}$$

Let recall the discrete expression of the virtual power of the internal forces over the lattice:

$$P=\sum_{c\in\mathcal{C}}P_e \tag{7.47}$$

A continuum expression on the domain Ω of the double summation is obtained based on Riemann integral, when $\varepsilon \to 0$:

$$\lim_{e \to 0} P = e \sum_{c \in \Omega} P_e = \int_{\Omega} P_e dl$$

considering that the elementary cell is a small surface element, thus $dv = g\ d\lambda \to d\lambda = \frac{1}{g} dv$,

with λ the curvilinear coordinate and g the determinant of the Jacobian transformation matrix:

$$g = \det \begin{bmatrix} \frac{\partial R[1]}{\partial \lambda_1} & \frac{\partial R[1]}{\partial \lambda_2} \\ \frac{\partial R[2]}{\partial \lambda_1} & \frac{\partial R[2]}{\partial \lambda_2} \end{bmatrix}$$

The vector **R** defines the coordinate change between the Cartesian basis and the curvilinear basis, expressed as $\mathbf{R} = \left[L_1 \lambda_1 Y_1[1] + L_2 \lambda_2 Y_2[1], L_1 \lambda_1 Y_1[2] + L_2 \lambda_2 Y_2[2] \right]_{(i,j)}$, with $\mathbf{Y_1} = \begin{bmatrix} c\theta_x \\ s\theta_x \end{bmatrix}_{(i,j)}$ and $\mathbf{Y_2} = \begin{bmatrix} c\theta_y \\ s\theta_y \end{bmatrix}_{(i,j)}$ the two periodicity vectors (figure 6.3).

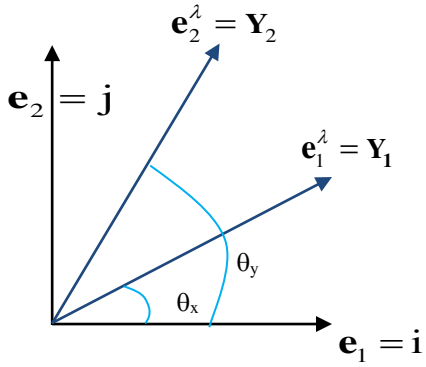

Fig. 7.3 Change of basis.

One obtains after developments:

$$d\lambda = \frac{1}{L_1 L_2 \left(c\theta_x s\theta_y - s\theta_x c\theta_y \right)} dv \tag{7.48}$$

This results in the continuum form of the virtual power of internal forces:

$$\lim_{\varepsilon\to 0} P =$$

$$\int_{\Omega}\left[\sum_{b}\left[\begin{array}{l}\dfrac{T_e}{L_1L_2\left(\mathrm{c}\theta_x\mathrm{s}\theta_y-\mathrm{s}\theta_x\mathrm{c}\theta_y\right)}\left(\begin{array}{l}\left(L_1\delta^1\left(\mathrm{c}\theta_x\dfrac{\partial\dot{V}_o}{\partial x}+\mathrm{s}\theta_x\dfrac{\partial\dot{V}_o}{\partial y}\right)+L_2\delta^2\left(\mathrm{c}\theta_y\dfrac{\partial\dot{V}_o}{\partial x}+\mathrm{s}\theta_y\dfrac{\partial\dot{V}_o}{\partial y}\right)\right)\\ +\varepsilon\left(\begin{array}{l}\dfrac{L_1^2\delta^1}{2}\left(\mathrm{c}^2\theta_x\dfrac{\partial^2\dot{V}_o}{\partial x^2}+\mathrm{s}^2\theta_x\dfrac{\partial^2\dot{V}_o}{\partial y^2}+2\mathrm{s}\theta_x\mathrm{c}\theta_x\dfrac{\partial^2\dot{V}_o}{\partial x\partial y}\right)\\ +\dfrac{L_2^2\delta^2}{2}\left(\mathrm{c}^2\theta_y\dfrac{\partial^2\dot{V}_o}{\partial x^2}+\mathrm{s}^2\theta_y\dfrac{\partial^2\dot{V}_o}{\partial y^2}+2\mathrm{s}\theta_y\mathrm{c}\theta_y\dfrac{\partial^2\dot{V}_o}{\partial x\partial y}\right)\end{array}\right)\end{array}\right)\\ +\dfrac{N_e}{L_1L_2\left(\mathrm{c}\theta_x\mathrm{s}\theta_y-\mathrm{s}\theta_x\mathrm{c}\theta_y\right)}\left(\begin{array}{l}\left(L_1\delta^1\left(\mathrm{c}\theta_x\dfrac{\partial\dot{U}_o}{\partial x}+\mathrm{s}\theta_x\dfrac{\partial\dot{U}_o}{\partial y}\right)+L_2\delta^2\left(\mathrm{c}\theta_2\dfrac{\partial\dot{U}_o}{\partial x}+\mathrm{s}\theta_2\dfrac{\partial\dot{U}_o}{\partial y}\right)\right)\\ +\varepsilon\left(\begin{array}{l}\dfrac{L_1^2\delta^1}{2}\left(\mathrm{c}^2\theta_x\dfrac{\partial^2\dot{U}_o}{\partial x^2}+\mathrm{s}^2\theta_x\dfrac{\partial^2\dot{U}_o}{\partial y^2}+2\mathrm{s}\theta_x\mathrm{c}\theta_x\dfrac{\partial^2\dot{U}_o}{\partial x\partial y}\right)\\ +\dfrac{L_2^2\delta^2}{2}\left(\mathrm{c}^2\theta_y\dfrac{\partial^2\dot{U}_o}{\partial x^2}+\mathrm{s}^2\theta_y\dfrac{\partial^2\dot{U}_o}{\partial y^2}+2\mathrm{s}\theta_y\mathrm{c}\theta_y\dfrac{\partial^2\dot{U}_o}{\partial x\partial y}\right)\end{array}\right)\end{array}\right)\end{array}\right]\right]dv \qquad (7.49)$$

7.4.2 Equivalence with a second order continuum gradient medium

This expression is next used to identify the statics of a second order gradient continuum; the virtual power of internal forces for a second order grade continuum writes in the framework of linear elasticity choosing a virtual velocity nil on the edges of the domain as

$$P^i=\int_{\Omega}\left(\left(\boldsymbol{\sigma}-\mathbf{S}\cdot\underline{\nabla}\right)\cdot\underline{\nabla}\right)\cdot\underline{\dot{D}}\,dV \qquad (7.50)$$

Introducing therein the first order Cauchy stress $\boldsymbol{\sigma}$ (a second order tensor) and the third order hyperstress tensor **S,** with the gradient operator $\underline{\nabla}=\dfrac{\partial\mathbf{e}_i}{\partial x_i}$.

Previous equation then writes in index format as:

$$P^i = \int_\Omega \left(\left(\left(\boldsymbol{\sigma}_{ij} \mathbf{e}_i \otimes \mathbf{e}_j \right) - \left(\mathbf{S}_{klm} \mathbf{e}_k \otimes \mathbf{e}_l \otimes \mathbf{e}_m \right) \cdot \left(\frac{\partial \mathbf{e}_p}{\partial x_p} \right) \right) \cdot \left(\frac{\partial \mathbf{e}_q}{\partial x_q} \right) \right) \cdot \left(\dot{D}_r \, \mathbf{e}_r \right) dV$$

$$= \int_\Omega \left(\left(\boldsymbol{\sigma}_{ij} \mathbf{e}_i \otimes \mathbf{e}_j \right) \cdot \left(\frac{\partial \mathbf{e}_q}{\partial x_q} \right) \cdot \left(\dot{D}_r \, \mathbf{e}_r \right) - \left(\mathbf{S}_{klm} \mathbf{e}_k \otimes \mathbf{e}_l \otimes \mathbf{e}_m \right) \cdot \left(\frac{\partial \mathbf{e}_p}{\partial x_p} \right) \cdot \left(\frac{\partial \mathbf{e}_q}{\partial x_q} \right) \cdot \left(\dot{D}_r \, \mathbf{e}_r \right) \right) dV$$

$$= \int_\Omega \left(\left(\boldsymbol{\sigma}_{ij} \mathbf{e}_i \otimes \mathbf{e}_j \cdot \mathbf{e}_q \right) \cdot \left(\frac{\partial \dot{D}_r \, \mathbf{e}_r}{\partial x_q} \right) - \left(\left(\mathbf{S}_{klm} \mathbf{e}_k \otimes \mathbf{e}_l \otimes \mathbf{e}_m \cdot \mathbf{e}_p \right) \cdot \mathbf{e}_q \right) \cdot \left(\frac{\partial^2 \dot{D}_r \, \mathbf{e}_r}{\partial x_p \partial x_q} \right) \right) dV$$

$$= \int_\Omega \left(\left(\boldsymbol{\sigma} \cdot \mathbf{e}_q \right) \cdot \left(\frac{\partial \dot{\underline{D}}}{\partial x_q} \right) - \left(\left(\mathbf{S} \cdot \mathbf{e}_p \right) \cdot \mathbf{e}_q \right) \cdot \left(\frac{\partial^2 \dot{\underline{D}}}{\partial x_p \partial x_q} \right) \right) dV$$

Thus,

$$P^i = \int_\Omega \left(\mathbf{F}^q \cdot \left(\frac{\partial \dot{\underline{D}}}{\partial x_q} \right) - \mathbf{H}^{pq} \cdot \left(\frac{\partial^2 \dot{\underline{D}}}{\partial x_p \partial x_q} \right) \right) dV \tag{7.51}$$

with

$$\mathbf{F}^q = \boldsymbol{\sigma} \cdot \mathbf{e}_q = \boldsymbol{\sigma}_{ij} \mathbf{e}_i \otimes \mathbf{e}_j \cdot \mathbf{e}_q = \boldsymbol{\sigma}_{iq} \mathbf{e}_i \tag{7.52}$$

and

$$\mathbf{H}^{pq} = \left(\mathbf{S} \cdot \mathbf{e}_p \right) \cdot \mathbf{e}_q = \left(\mathbf{S}_{klm} \mathbf{e}_k \otimes \mathbf{e}_l \otimes \mathbf{e}_m \cdot \mathbf{e}_p \right) \cdot \mathbf{e}_q = \mathbf{S}_{kqp} \mathbf{e}_k \tag{7.53}$$

From equations (7.52) and (7.53), one is able to reconstruct the tensors $\boldsymbol{\sigma}$ and $\mathbf{S}$ as

$$\boldsymbol{\sigma} = \left(\boldsymbol{\sigma}_{iq} \mathbf{e}_i \right) \otimes \mathbf{e}_q = \mathbf{F}^q \otimes \mathbf{e}_q \tag{7.54}$$

$$\mathbf{S} = \left(\mathbf{S}_{kqp} \mathbf{e}_k \right) \otimes \mathbf{e}_q \otimes \mathbf{e}_p = \mathbf{H}^{pq} \otimes \mathbf{e}_q \otimes \mathbf{e}_p \tag{7.55}$$

Recalling the previous homogenized expression (7.49)

$$\lim_{\varepsilon\to 0} P =$$

$$\int_{\Omega}\left[\sum_{b}\left[\begin{array}{l}\dfrac{T_e}{L_1L_2\left(\mathrm{c}\theta_x\mathrm{s}\theta_y-\mathrm{s}\theta_x\mathrm{c}\theta_y\right)}\left(\begin{array}{l}\left(L_1\delta^1\left(\mathrm{c}\,\theta_x\dfrac{\partial\dot{V}_o}{\partial x}+\mathrm{s}\,\theta_x\dfrac{\partial\dot{V}_o}{\partial y}\right)+L_2\delta^2\left(\mathrm{c}\,\theta_y\dfrac{\partial\dot{V}_o}{\partial x}+\mathrm{s}\,\theta_y\dfrac{\partial\dot{V}_o}{\partial y}\right)\right)\\ +\varepsilon\left(\begin{array}{l}\dfrac{L_1^2\delta^1}{2}\left(\mathrm{c}^2\,\theta_x\dfrac{\partial^2\dot{V}_o}{\partial x^2}+\mathrm{s}^2\,\theta_x\dfrac{\partial^2\dot{V}_o}{\partial y^2}+2\mathrm{s}\theta_x\mathrm{c}\theta_x\dfrac{\partial^2\dot{V}_o}{\partial x\partial y}\right)\\ +\dfrac{L_2^2\delta^2}{2}\left(\mathrm{c}^2\,\theta_y\dfrac{\partial^2\dot{V}_o}{\partial x^2}+\mathrm{s}^2\,\theta_y\dfrac{\partial^2\dot{V}_o}{\partial y^2}+2\mathrm{s}\theta_y\mathrm{c}\theta_y\dfrac{\partial^2\dot{V}_o}{\partial x\partial y}\right)\end{array}\right)\end{array}\right)\\ +\dfrac{N_e}{L_1L_2\left(\mathrm{c}\theta_x\mathrm{s}\theta_y-\mathrm{s}\theta_x\mathrm{c}\theta_y\right)}\left(\begin{array}{l}\left(L_1\delta^1\left(\mathrm{c}\,\theta_x\dfrac{\partial\dot{U}_o}{\partial x}+\mathrm{s}\,\theta_x\dfrac{\partial\dot{U}_o}{\partial y}\right)+L_2\delta^2\left(\mathrm{c}\,\theta_2\dfrac{\partial\dot{U}_o}{\partial x}+\mathrm{s}\,\theta_2\dfrac{\partial\dot{U}_o}{\partial y}\right)\right)\\ +\varepsilon\left(\begin{array}{l}\dfrac{L_1^2\delta^1}{2}\left(\mathrm{c}^2\,\theta_x\dfrac{\partial^2\dot{U}_o}{\partial x^2}+\mathrm{s}^2\,\theta_x\dfrac{\partial^2\dot{U}_o}{\partial y^2}+2\mathrm{s}\theta_x\mathrm{c}\theta_x\dfrac{\partial^2\dot{U}_o}{\partial x\partial y}\right)\\ +\dfrac{L_2^2\delta^2}{2}\left(\mathrm{c}^2\,\theta_y\dfrac{\partial^2\dot{U}_o}{\partial x^2}+\mathrm{s}^2\,\theta_y\dfrac{\partial^2\dot{U}_o}{\partial y^2}+2\mathrm{s}\theta_y\mathrm{c}\theta_y\dfrac{\partial^2\dot{U}_o}{\partial x\partial y}\right)\end{array}\right)\end{array}\right)\end{array}\right]\right]dv$$

Introducing the notations $\mathbf{T}_e = T_E\mathbf{e}^{b\perp}$ et $\mathbf{N}_e = N_{_E}\mathbf{e}^b$, a more compact formulation is obtained as:

$$\lim_{\varepsilon\to 0} P = \int_{\Omega}\sum_{b}\left(\mathbf{F}^q\cdot\left(\frac{\partial\dot{\mathbf{D}}_o}{\partial x_q}\right)-\underline{\mathbf{H}^{pq}}\cdot\frac{\partial^2\dot{\mathbf{D}}_o}{\partial x_p\partial x_q}\right)dv \tag{7.56}$$

with

$$q\in\{1,2\},\ \mathbf{F}^1=\left(\frac{\mathbf{T}_e+\mathbf{N}_e}{L_1L_2\left(\mathrm{c}\theta_x\mathrm{s}\theta_y-\mathrm{s}\theta_x\mathrm{c}\theta_y\right)}\right)\left(L_1\delta^1\mathrm{c}\theta_x+L_2\delta^2\mathrm{c}\theta_y\right) \tag{7.57}$$

$$\mathbf{F}^2=\left(\frac{\mathbf{T}_e+\mathbf{N}_e}{L_1L_2\left(\mathrm{c}\theta_x\mathrm{s}\theta_y-\mathrm{s}\theta_x\mathrm{c}\theta_y\right)}\right)\left(L_1\delta^1\mathrm{s}\theta_x+L_2\delta^2\mathrm{s}\theta_y\right) \tag{7.58}$$

and the pair $(p,q)\in\{(1,1),(2,2),(1,2)\}$. There are not four, but only three combinations, since one sums up combinations of the mixed derivatives (1,2) and (2,1):

$$\mathbf{H}^{11}=\varepsilon\left(\frac{\mathbf{T}_e+\mathbf{N}_e}{L_1L_2\left(\mathrm{c}\theta_x\mathrm{s}\theta_y-\mathrm{s}\theta_x\mathrm{c}\theta_y\right)}\right)\left(\frac{L_1^2\delta^1\mathrm{c}^2\theta_x}{2}+\frac{L_2^2\delta^2\mathrm{c}^2\theta_y}{2}\right) \tag{7.59}$$

$$\mathbf{H}^{22} = \varepsilon \left(\frac{\mathbf{T}_e + \mathbf{N}_e}{L_1 L_2 \left(\mathrm{c}\theta_x \mathrm{s}\theta_y - \mathrm{s}\theta_x \mathrm{c}\theta_y \right)} \right) \left(\frac{L_1^2 \delta^1 \mathrm{s}^2\theta_x}{2} + \frac{L_2^2 \delta^2 \mathrm{s}^2\theta_y}{2} \right) \tag{7.60}$$

Et

$$\mathbf{H}^{12} = \varepsilon \left(\frac{\mathbf{T}_e + \mathbf{N}_e}{L_1 L_2 \left(\mathrm{c}\theta_x \mathrm{s}\theta_y - \mathrm{s}\theta_x \mathrm{c}\theta_y \right)} \right) \left(L_1^2 \delta^1 \mathrm{c}\theta_x \mathrm{s}\theta_x + L_2^2 \delta^2 \mathrm{s}\theta_y \mathrm{c}\theta_y \right) \tag{7.61}$$

Simple lattice topologies are next consider as an application of the previous general methodology.

7.5 Identification of internal lengths

In this subsection, we develop a general method to identify the internal lengths of the second order effective grade continuum; our approach is based on the writing of the equilibrium equations. An alternative method could also be envisaged, based on the writing of the strain energy density of the effective continuum, and its decomposition into the different deformation modes, as followed in the thesis of Y. Rahali.

We recall the previous expression of the virtual power of internal and external forces for the obtained effective second order continuum:

$$P^i = \int_\Omega \left(\mathbf{F}^q \cdot \left(\frac{\partial \underline{\underline{D}}}{\partial x_q} \right) - \mathbf{H}^{pq} \cdot \left(\frac{\partial^2 \underline{\underline{D}}}{\partial x_p \partial x_q} \right) \right) dV,$$

$$P^e = \int_\Omega \mathbf{f}.\dot{\mathbf{D}} dV$$

with therein

$$\boldsymbol{\sigma}.\mathbf{e}_\mathrm{j} = \left(\boldsymbol{\sigma}_{\mathrm{ij}} \mathbf{e}_\mathrm{i} \otimes \mathbf{e}_\mathrm{j} \right).\mathbf{e}_\mathrm{i} = \boldsymbol{\sigma}_{\mathrm{ij}} \mathbf{e}_\mathrm{i}$$

We further evaluate the term

$$\boldsymbol{\sigma}.\mathbf{e}_\mathrm{j}.\frac{\partial \dot{\mathbf{D}}}{\partial \mathrm{x}_\mathrm{j}} = \sigma_{\mathrm{ij,j}} \mathbf{e}_\mathrm{i}.\dot{\mathbf{D}} = \sigma_{\mathrm{kj,j}} \dot{\mathrm{D}}_\mathrm{k}$$

Here, $\dot{\mathbf{D}}$ is a virtual velocity, allowing localizing the principle of virtual power into the strong form of the equilibrium equations. Similarly, we transform the term

$$\left(\frac{\partial^2 \mathbf{S}}{\partial x_i \partial x_j}\right) : \left(\mathbf{e}_i \otimes \mathbf{e}_j\right).\dot{\mathbf{D}} = \left(-\frac{\partial \mathbf{F}^p}{\partial x_p} + \frac{\partial^2 \mathbf{H}^{ij}}{\partial x_i \partial x_j}\right).\dot{\mathbf{D}}$$

by integration by part, with the subscript 0 referring to the first order term of the asymptotic expansion. Furthermore, it holds that

$$\mathbf{F}^p = \boldsymbol{\sigma}.\mathbf{e}_p, \quad \mathbf{H}^{ij} = \mathbf{S} : \left(\mathbf{e}_i \otimes \mathbf{e}_j\right)$$

This allows rewriting the virtual power principle as

$$\int_\Omega \left(-\frac{\partial}{\partial x_p}\sigma_{kp} + \frac{\partial^2 S_{ijk}}{\partial x_i \partial x_j}\right)\dot{D}_k + f_k \dot{D}_k = 0, \quad k = 1..3, \ \forall \dot{D}_k \Rightarrow \left(-\frac{\partial}{\partial x_p}\sigma_{kp} + \frac{\partial^2 S_{ijk}}{\partial x_i \partial x_j}\right) + f_k = 0, \quad k = 1..3$$

The static equilibrium equations written here in 3D will next be analyzed in 2D for planar lattices, in order to identify the internal lengths associated to the different deformation modes. The two equilibrium equations expand as

$$-\left(\frac{\partial \sigma_{k1}}{\partial x_1} + \frac{\partial \sigma_{k2}}{\partial x_2}\right) + \frac{\partial^2 S_{11k}}{\partial x_1 \partial x_1} + \frac{\partial^2 S_{12k}}{\partial x_1 \partial x_2} + \frac{\partial^2 S_{21k}}{\partial x_2 \partial x_1} + \frac{\partial^2 S_{22k}}{\partial x_2 \partial x_2} + f_k = 0, \quad k = 1,2$$

Inserting therein the expressions obtained for Cauchy stress and hyperstress versus the corresponding kinematic variables lead to a factorization of a second order partial derivative acting on a degree of freedom (displacement component in the plane of the lattice), of the form

$$\left(1 - l_{jk}{}^2 \nabla^2{}_{jk}\right)\frac{\partial^2 U_i}{\partial x_j \partial x_k}, i = 1,2, \ j,k=1..3$$

with l_{jk} the internal length associated to directions j and k for the deformation mode U_i.

Observe that since Cauchy stress is only expressed versus first order gradient of displacement, and the hyperstress only depends upon the second order displacement gradient, one can see that the second order derivative (resp. fourth order derivative) of the displacement in previous equation arises respectively from $\boldsymbol{\sigma}$ and $\mathbf{S}$. It is nevertheless expected that non centrosymmetric media will give rise to mutual interactions.

Note that the internal lengths appear as ratio of second order to first order effective moduli; their direct identification from the effective tensors of first and second order rigidities is however challenging (especially their definition) for a general anisotropic medium, so that the present methodology is useful for this purpose due its degree of generality.

The internal length for bending are similarly obtained by considering now the lattice as embedded into 3D Euclidean space, so that one has to write the equilibrium equation involving the third vertical coordinate, for instance

$$\left(-\frac{\partial}{\partial x_3}\sigma_{13} + \frac{\partial^2 S_{ij1}}{\partial x_i \partial x_j} \right) + f_1 = 0$$

which gives a sum of terms, for instance (after insertion of the constitutive law) the specific bending contribution $\left(1 - l_{33}{}^2 \nabla^2{}_{33}\right) \frac{\partial^2 U_1}{\partial x_3 \partial x_3}$, with the internal bending length l_{33} therein.

7.6 Examples

We will consider applications of the developed general framework to the specific case of biological membranes, and analyze successively the in-plane behaviors. Biological membranes have been presented in chapter 3 from a biological viewpoint, and classified according to node connectivity.

7.6.1 Biomembranes with four connectivity networks

Let consider the following example of a nuclear lamina with connectivity 4 is modeled based on two orthogonal beam elements (figure 7.4). The nodes with black circles belong to the reference unit cell, whereas nodes with empty circles belong to the adjacent unit cell.

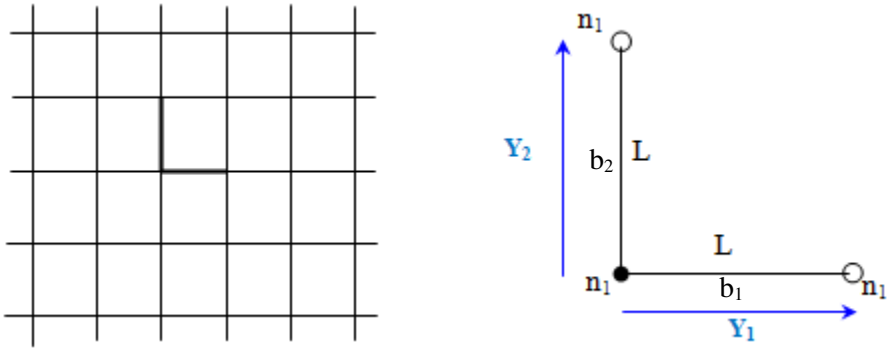

Fig. 7.4 square lattice

Each beam is of length $L_b = [L, L]$. The lengths of the periodicity vectors $\mathbf{Y}_1 = \begin{bmatrix} 1 \\ 0 \end{bmatrix}$ and $\mathbf{Y}_2 = \begin{bmatrix} 0 \\ 1 \end{bmatrix}$ are respectively $L_1 = L$ and $L_2 = L$. The connectivity of this lattice is given in Table 5.1.

Table 7.1 Mechanical properties connectivity of the square lattice

beam	**1**	**2**
O(b)	1	1
E(b)	1	1
δ^1	1	0
δ^2	0	1

We first compute the effective second order gradient response of this lattice in order to compare it with the classical Cauchy continuum. The Cauchy stress tensor writes at first order in $\boldsymbol{\varepsilon}$ as for the classical first order continuum:

$$\boldsymbol{\sigma} = \begin{bmatrix} k_{l_1} \dfrac{\partial U}{\partial x} & k_f \dfrac{\partial U}{\partial y} \\ k_f \dfrac{\partial V}{\partial x} & k_{l_1} \dfrac{\partial V}{\partial y} \end{bmatrix}$$

One here recovers the Cauchy stress for the first order grade continuum, $\boldsymbol{\sigma}_{\mathbf{Cauchy}}$.

The hyperstress tensor $\mathbf{S}$ writes at second order in ε and in terms of the second order derivatives of the displacement as:

$$\mathbf{S}[1..2,1..2,1]=\varepsilon\begin{bmatrix}\frac{1}{4}k_{l_1}L^2\left(\frac{\partial^2U(x,y)}{\partial x^2}\right) & 0\\ \frac{1}{4}k_fL^2\left(\frac{\partial^2V(x,y)}{\partial x^2}\right) & 0\end{bmatrix}=\begin{bmatrix}S_{112} & S_{122}\\ S_{212} & S_{222}\end{bmatrix}$$

$$\mathbf{S}[1..2,1..2,2]=\varepsilon\begin{bmatrix}0 & \frac{1}{4}k_fL^2\left(\frac{\partial^2U(x,y)}{\partial y^2}\right)\\ 0 & \frac{1}{4}k_{l_1}L^2\left(\frac{\partial^2V(x,y)}{\partial y^2}\right)\end{bmatrix}=\begin{bmatrix}S_{111} & S_{121}\\ S_{211} & S_{221}\end{bmatrix}$$

with the extension and flexural rigidities therein given by

$$k_{l_1}=\frac{Et}{L_b},k_f=\frac{Et^3}{L_b^3}.$$

7.6.1.1 Computation of internal lengths for the square topology of biomembranes

We next compute the internal lengths for the square lattice, relying on the effective second order behavior computed with the second gradient approach; these lengths are identified from the writing of the equilibrium equations.

Isolating first the contributions in extension, that is the derivatives $\frac{\partial\sigma_{11}}{\partial x_1}$, $\frac{\partial S_{111}}{\partial x_1\partial x_1}$, and inserting the expressions of those two components of the hyperstress tensor versus $\frac{\partial^2U(x,y)}{\partial x^2}$, one identifies a contribution

$$\left(-k_l+\frac{\varepsilon}{4}L^2\right)\frac{\partial^2U(x,y)}{\partial x^2}\equiv-\left(k_l-l_{xx}{}^2k_l\left(\nabla^2\right)_{xx}\right)\frac{\partial^2U(x,y)}{\partial x^2}$$

with ∇^2_{xx} the square of the xx component of the gradient, thus one identifies the internal extensional length as $l_{xx}{}^2=\frac{\varepsilon}{4}L^2\Rightarrow l_{xx}=\frac{\sqrt{\varepsilon}}{2}L$

This length clearly vanishes with the small parameter ε, in fact as its square root. In practical situations for whioch the lattice is bounded (thus the number of repetitive unit cells is finite),

parameter ε takes a finite value, since it is the ratio of unit cell size to the overall lattice size (which is finite in applications); for instance, adopting the finite value $\varepsilon = 1/100$, we get $l_{xx} = \frac{1}{20} L$. We shall compute the internal lengths for other deformation modes, and we shall see that it depends more generally not only on geometrical parameters (such as beam lengths), but also on the microstructural moduli, which can counterbalance the impact of the geometrical parameters.

We proceed in a similar manner to evaluate the internal extensional length in direction y, the flexural and torsional internal lengths that are associated to the other partial second order derivatives.

Let first express the balance of linear momentum for a first order Cauchy continuum in 2D,

$$-\left(\frac{\partial \sigma_{11}}{\partial x}+\frac{\partial \sigma_{12}}{\partial y}\right)+f_1=0,\ \ (k=1)\rightarrow -k_1\frac{\partial^2 U}{\partial x\partial x}-k_f\frac{\partial^2 U}{\partial y\partial y}+f_1=0$$
$$-\left(\frac{\partial \sigma_{21}}{\partial x}+\frac{\partial \sigma_{22}}{\partial y}\right)+f_2=0,\ \ (k=2)\rightarrow -k_f\frac{\partial^2 V}{\partial x\partial x}-k_1\frac{\partial^2 V}{\partial y\partial y}+f_2=0$$

We see the involvement of the four second order derivatives of the displacement, $\frac{\partial^2 U}{\partial x\partial x},\frac{\partial^2 U}{\partial y\partial y},\frac{\partial^2 V}{\partial x\partial x},\frac{\partial^2 V}{\partial y\partial y}$, with derivatives $\frac{\partial^2 U}{\partial x\partial x},\frac{\partial^2 V}{\partial y\partial y}$ that will be factored out in the expression of the hyperstress tensor $\mathbf{S}$ in order to isolate and identify the corresponding internal length in extension, as well as the mixed partial derivatives $\frac{\partial^2 U}{\partial y\partial y},\frac{\partial^2 V}{\partial x\partial x}$ describing in – plane shear (with the shear rigidity as a multiplicative factor), and the isolation of which shall deliver two a priori distinct internal shear lengths in the plane.

Accordingly, isolating the derivatives $\frac{\partial^2 U}{\partial y\partial y},\frac{\partial^2 V}{\partial x\partial x}$ in the two equilibrium equations gives:

$$-\left(\frac{\partial \sigma_{11}}{\partial x}+\frac{\partial \sigma_{12}}{\partial y}\right)+\frac{\partial^2 S_{111}}{\partial x\partial x}+\frac{\partial^2 S_{121}}{\partial x\partial y}+\frac{\partial^2 S_{211}}{\partial y\partial x}+\frac{\partial^2 S_{221}}{\partial y\partial y}+f_1=0$$
$$-\left(\frac{\partial \sigma_{21}}{\partial x}+\frac{\partial \sigma_{22}}{\partial y}\right)+\frac{\partial^2 S_{112}}{\partial x\partial x}+\frac{\partial^2 S_{122}}{\partial x\partial y}+\frac{\partial^2 S_{212}}{\partial y\partial x}+\frac{\partial^2 S_{222}}{\partial y\partial y}+f_2=0$$

Since the second order derivative $\frac{\partial^2 U}{\partial y \partial y}$ intervenes only in σ_{12} for the first equation and not at second order, this gives the term $-\frac{\partial \sigma_{12}}{\partial y}$ in the first equation, so there will be no internal length for this term. The same term $\frac{\partial^2 U}{\partial y \partial y}$ intervenes now uniquely at the second order in the second equation, that is in term $\frac{\partial^2 S_{122}}{\partial x \partial y} = \frac{1}{4} \varepsilon k_f L^2 \left(\nabla^2\right)_{xy} \frac{\partial^2 U(x,y)}{\partial y^2}$, which tend to identify an internal length for the shear along x-y as

$$l_{int,xy} = \frac{1}{2}\sqrt{\varepsilon} L$$

One can further proceed in the same manner for the derivative $\frac{\partial^2 V}{\partial x \partial x}$ and identify now an internal length for shear along y-x : previous second order derivative intervenes respectively in the terms $\frac{\partial^2 S_{211}}{\partial y \partial x}, -\frac{\partial \sigma_{21}}{\partial x}$ within the first and second equations, thus giving $\frac{1}{4} \varepsilon k_f L^2 \left(\nabla^2\right)_{yx} \left(\frac{\partial^2 V(x,y)}{\partial x^2} \right)$, from which one can identify the internal length in shear $l_{int,yx} = \frac{1}{2}\sqrt{\varepsilon} L$, which turns out to be the same as $l_{int,xy}$.

Due to the obtained non symmetrical stress and hyperstress tensors, one could nevertheless obtain two different shear internal lengths when considering arbitrary lattices.

We notice that there is no bending behavior due to the fact we have considered a planar lattice embedded into the 2D Euclidean space R^2, so that an embedding into the 3D Euclidean space will be necessary to capture the bending response. This highlights that the micropolar continuum brings bending as additional information in comparison to the second order gradient continuum, so that micropolar and second order grade continuum are complementary.

7.6.2 Biomembranes with threefold connectivity networks

In the same manner, we consider the peptidoglycan network with connectivity 3, modeled as hexagonal repeated unit cells, each of them described by three beams and two periodicity vectors $\mathbf{Y_1}, \mathbf{Y_2}$ at a selected configuration angle $\theta = 30^\circ$, as shown in figure 7.5.

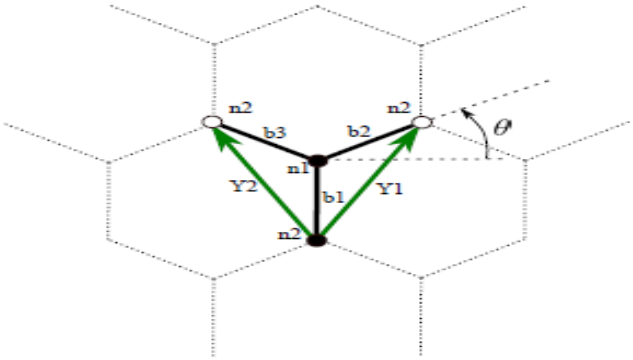

Fig. 7.5 Hexagonal lattice

Each beam is of length $L_b = [L, L, L]$. The lengths of the periodicity vectors $\mathbf{Y}_1 = \begin{bmatrix} \frac{1}{2} \\ \frac{\sqrt{3}}{2} \end{bmatrix}$ and $\mathbf{Y}_2 = \begin{bmatrix} -\frac{1}{2} \\ \frac{\sqrt{3}}{2} \end{bmatrix}$ are respectively $L_1 = \sqrt{3}L$ and $L_2 = \sqrt{3}L$. The connectivity of this lattice is given in Table 7.2.

Table 7.2 Mechanical properties connectivity of the hexagonal lattice

beam	**1**	**2**	**3**
O(b)	2	1	1
E(b)	1	2	2
δ^1	0	1	0
δ^2	0	0	1

One obtains the Cauchy stress

$$\boldsymbol{\sigma} = \begin{bmatrix} \sigma_{11} & \sigma_{12} \\ \sigma_{21} & \sigma_{22} \end{bmatrix}$$

with the components

$$\sigma_{11} = \frac{1}{6}\frac{k_l\sqrt{3}}{k_f + k_l}\left(\left(3k_f + k_l\right)\frac{\partial U(x,y)}{\partial x} + \left(k_l - k_f\right)\frac{\partial V(x,y)}{\partial y}\right)$$

$$\sigma_{12} = -\frac{1}{6}\frac{k_f\sqrt{3}}{k_f + k_l}\left(\left(3k_l - k_f\right)\frac{\partial U(x,y)}{\partial y} + \left(k_f - k_l\right)\frac{\partial V(x,y)}{\partial x}\right)$$

$$\sigma_{21} = \frac{1}{6}\frac{k_f\sqrt{3}}{k_f + k_l}\left(\left(k_l - k_f\right)\frac{\partial U(x,y)}{\partial y} + \left(k_f + 3k_l\right)\frac{\partial V(x,y)}{\partial x}\right)$$

$$\sigma_{22} = -\frac{1}{6}\frac{k_l\sqrt{3}}{k_f + k_l}\left(\left(k_f - k_l\right)\frac{\partial U(x,y)}{\partial x} + \left(-k_l - 3k_f\right)\frac{\partial V(x,y)}{\partial y}\right)$$

The hyperstress tensor $\mathbf{S}$ writes at second order in ε and in terms of the second order derivatives of the displacement as:

$$\mathbf{S}[1..2,1..2,1] = \begin{bmatrix} S_{111} & S_{121} \\ S_{211} & S_{221} \end{bmatrix}, \text{ with}$$

$$S_{111} = \frac{1}{32}\varepsilon L^2\left(-10k_f\frac{\partial^2 V(x,y)}{\partial x^2} + \left(\sqrt{3}k_f - 8\sqrt{3}k_l\right)\frac{\partial^2 U(x,y)}{\partial x^2} - 3\sqrt{3}k_f\frac{\partial^2 U(x,y)}{\partial y^2} - 6k_f\frac{\partial^2 U(x,y)}{\partial x \partial y}\right)$$

$$S_{121} = -\frac{1}{32}\varepsilon k_f L^2\left(-2\sqrt{3}\frac{\partial^2 V(x,y)}{\partial x^2} + 3\frac{\partial^2 U(x,y)}{\partial x^2} - 9\frac{\partial^2 U(x,y)}{\partial y^2} - 6\sqrt{3}\frac{\partial^2 U(x,y)}{\partial y \partial x}\right)$$

$$S_{211} = -\frac{1}{8}\varepsilon L^2\left(-2\sqrt{3}k_f\frac{\partial^2 V(x,y)}{\partial x^2} + k_l\frac{\partial^2 U(x,y)}{\partial x^2}\right)$$

$$S_{221} = \frac{1}{8}\sqrt{3}\varepsilon L^2\left(k_l\frac{\partial^2 U(x,y)}{\partial x^2}\right)$$

$$\mathbf{S}[1..2,1..2,2] = \begin{bmatrix} S_{112} & S_{122} \\ S_{212} & S_{222} \end{bmatrix}, \text{ with}$$

$$S_{112} = -\frac{1}{32}\varepsilon k_f L^2\left(-2\sqrt{3}\frac{\partial^2 V(x,y)}{\partial x^2} + 3\frac{\partial^2 U(x,y)}{\partial x^2} - 9\frac{\partial^2 U(x,y)}{\partial y^2} - 6\sqrt{3}\frac{\partial^2 U(x,y)}{\partial y \partial x}\right)$$

$$S_{122} = \frac{1}{8}\sqrt{3}\varepsilon L^2\left(k_l\frac{\partial^2 U(x,y)}{\partial x^2}\right)$$

$$S_{212} = -\frac{1}{32}\varepsilon k_f L^2\left(-2\sqrt{3}\frac{\partial^2 V(x,y)}{\partial x^2} + 3\frac{\partial^2 U(x,y)}{\partial x^2} - 9\frac{\partial^2 U(x,y)}{\partial y^2} - 6\sqrt{3}\frac{\partial^2 U(x,y)}{\partial y \partial x}\right)$$

$$S_{222} = \frac{3}{8}\varepsilon L^2\left(k_l\frac{\partial^2 U(x,y)}{\partial x^2}\right)$$

7.6.2.1 Computation of internal lengths for the hexagonal topology of biomembranes

We next compute the internal lengths for the hexagonal lattice, relying on the effective second order behavior computed with the second gradient approach.

Isolating first the contributions in extension, that is the derivatives $\frac{\partial \sigma_{11}}{\partial x_1}$, $\frac{\partial S_{111}}{\partial x_1 \partial x_1}$, and inserting the expressions of those two components of the hyperstress tensor versus $\frac{\partial^2 U(x,y)}{\partial x^2}$, one identifies the internal extensional length as

$$l_{xx}{}^2 = \frac{3}{16}\varepsilon L^2 \frac{(8k_1 - k_f)(k_1 - k_f)}{k_1(3k_f + k_1)} \Rightarrow l_{xx} = \frac{\sqrt{3}}{4}\sqrt{\varepsilon} L \sqrt{\frac{(8k_1 - k_f)(k_1 - k_f)}{k_1(3k_f + k_1)}} =$$
$$= \frac{\sqrt{3}}{4}\sqrt{\varepsilon} L \sqrt{\frac{(8 - k_f / k_1)(1 - k_f / k_1)}{(3k_f / k_1 + 1)}}$$

This length depends now on both the geometry through the factor $\sqrt{\varepsilon} L$, but also on the ratio of the beam flexural to tension rigidity, factor k_f / k_1, which is usually very small, unless the beams within the representative unit cell have themselves a microstructure. If we integrate in previous expression of the internal length the relation between the extension and bending stiffness's versus the slenderness ratio, that is

$$k_l = k_s \eta,\ k_f = k_s \eta^3 \Rightarrow k_f / k_l = \eta^2$$

we arrive at

$$l_{xx} = \frac{\sqrt{3}}{4}\sqrt{\varepsilon} L \sqrt{\frac{(8 - k_f / k_1)(1 - k_f / k_1)}{(3k_f / k_1 + 1)}} = \frac{\sqrt{3}}{4}\sqrt{\varepsilon} L \sqrt{\frac{(8 - \eta^2)(1 - \eta^2)}{(3\eta^2 + 1)}}$$

The parameter η take values of the order of 0.5 in general for biomembranes, which determines the value of the second factor in previous expression.

We proceed in a similar manner as described previously to evaluate the internal length for the shear along x-y and y-x respectively: the internal length for shearing along x-y is

$$l_{int,xy}^2 = \frac{9\sqrt{3}}{32}\varepsilon L^2 k_f$$

One can further proceed in the same manner for the derivative $\frac{\partial^2 V}{\partial x \partial x}$ and further identify an internal length for shear along y-x $l^2_{int,yx} = \frac{10\sqrt{3}}{32}\varepsilon L^2$, which is not the same as $l_{int,xy}$.

7.6.3 Biomembranes with sixfold connectivity networks

Here, we consider the erythrocyte network with connectivity 6, which is modeled based on triangular repeated unit cells, each of them described by three beams and two periodicity vectors $\mathbf{Y_1}, \mathbf{Y_2}$ at a chosen configuration $\theta = 30^\circ$, as shown in figure 7.6.

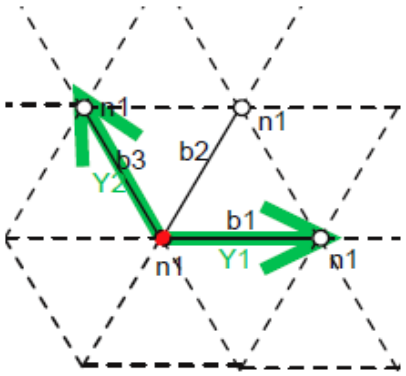

Fig. 7.6 Triangular lattice

Each beam is of length $L_b = [L, L, L]$. The lengths of the periodicity vectors $\mathbf{Y}_1 = \begin{bmatrix} 1 \\ 0 \end{bmatrix}$ and $\mathbf{Y}_2 = \begin{bmatrix} -\frac{1}{2} \\ \frac{\sqrt{3}}{2} \end{bmatrix}$ are respectively $L_1 = L$ and $L_2 = L$. The connectivity of this lattice is given in Table 7.3.

Table 7.3 Mechanical properties connectivity of the triangular lattice

beam	1	2	3
O(b)	1	1	1
E(b)	1	1	1
δ^1	1	1	0
δ^2	0	1	1

One obtains the Cauchy stress

$$\boldsymbol{\sigma} = \begin{bmatrix} \sigma_{11} & \sigma_{12} \\ \sigma_{21} & \sigma_{22} \end{bmatrix}$$

with the components

$$\sigma_{11} = \frac{1}{4}\sqrt{3}\left(\left(3k_l + k_f\right)\frac{\partial U(x,y)}{\partial x} + \left(k_l - k_f\right)\frac{\partial V(x,y)}{\partial y} \right)$$

$$\sigma_{12} = -\frac{1}{4}\sqrt{3}\left(\left(-k_l - 3k_f\right)\frac{\partial U(x,y)}{\partial y} + \left(k_f - k_l\right)\frac{\partial V(x,y)}{\partial x} \right)$$

$$\sigma_{21} = \frac{1}{4}\sqrt{3}\left(\left(k_l - k_f\right)\frac{\partial U(x,y)}{\partial y} + \left(3k_f + k_l\right)\frac{\partial V(x,y)}{\partial x} \right)$$

$$\sigma_{22} = -\frac{1}{4}\sqrt{3}\left(\left(k_f - k_l\right)\frac{\partial U(x,y)}{\partial x} + \left(-3k_l - k_f\right)\frac{\partial V(x,y)}{\partial y} \right)$$

The hyperstress tensor $\mathbf{S}$ writes at second order in ε as:

$$\mathbf{S}[1..2,1..2,1] = \begin{bmatrix} S_{111} & S_{121} \\ S_{211} & S_{221} \end{bmatrix}, \text{ with}$$

$$S_{111} = \frac{1}{64}\varepsilon L^2 \left(\begin{array}{l} \left(12k_l - 12k_f\right)\frac{\partial^2 V(x,y)}{\partial x^2} + \left(13\sqrt{3}k_f - 15\sqrt{3}k_l\right)\frac{\partial^2 U(x,y)}{\partial x^2} + \left(3\sqrt{3}k_l + 9\sqrt{3}k_f\right)\frac{\partial^2 U(x,y)}{\partial y^2} \\ -\left(6k_l + 18k_f\right)\frac{\partial^2 U(x,y)}{\partial y \partial x} + \left(6k_l - 6k_f\right)\frac{\partial^2 V(x,y)}{\partial y^2} + \left(4\sqrt{3}k_f - 4\sqrt{3}k_l\right)\frac{\partial^2 V(x,y)}{\partial y \partial x} \end{array} \right)$$

$$S_{211} = \frac{1}{64}\varepsilon L^2 \left(\begin{array}{l} \left(15\sqrt{3}k_f + 13\sqrt{3}k_l\right)\frac{\partial^2 V(x,y)}{\partial x^2} + \left(-12k_f + 12k_l\right)\frac{\partial^2 U(x,y)}{\partial x^2} + \left(6k_l - 6k_f\right)\frac{\partial^2 U(x,y)}{\partial y^2} \\ +\left(4\sqrt{3}k_f - 4\sqrt{3}k_l\right)\frac{\partial^2 U(x,y)}{\partial y \partial x} + \left(9\sqrt{3}k_l + 8\sqrt{3}k_f\right)\frac{\partial^2 V(x,y)}{\partial y^2} - \left(6k_f + 18k_l\right)\frac{\partial^2 V(x,y)}{\partial y \partial x} \end{array} \right)$$

$$S_{121} = \frac{1}{64}\varepsilon L^2 \left(\begin{array}{l} \left(2\sqrt{3}k_f - 2\sqrt{3}k_l\right)\frac{\partial^2 V(x,y)}{\partial x^2} - \left(9k_f + 3k_l\right)\frac{\partial^2 U(x,y)}{\partial x^2} - \left(3k_l + 9k_f\right)\frac{\partial^2 U(x,y)}{\partial y^2} \\ +\left(6\sqrt{3}k_f + 2\sqrt{3}k_l\right)\frac{\partial^2 U(x,y)}{\partial y \partial x} \end{array} \right)$$

$$S_{221} = -\frac{1}{64}\varepsilon L^2 \left(\begin{array}{l} \left(3k_f + 9k_l\right)\frac{\partial^2 V(x,y)}{\partial x^2} + \left(-2\sqrt{3}k_f + 2\sqrt{3}k_l\right)\frac{\partial^2 U(x,y)}{\partial x^2} + \left(9k_l + 3k_f\right)\frac{\partial^2 V(x,y)}{\partial y^2} \\ -\left(2\sqrt{3}k_f + 6\sqrt{3}k_l\right)\frac{\partial^2 V(x,y)}{\partial y \partial x} \end{array} \right)$$

$$\mathbf{S}[1..2,1..2,2]=\begin{bmatrix} S_{112} & S_{122} \\ S_{212} & S_{222} \end{bmatrix}$$

$$S_{112}=\frac{1}{64}\varepsilon L^2\left(\begin{array}{l}\left(-2\sqrt{3}k_l+2\sqrt{3}k_f\right)\dfrac{\partial^2 V(x,y)}{\partial x^2}-\left(9k_f+3k_l\right)\dfrac{\partial^2 U(x,y)}{\partial x^2}-\left(3k_l+9k_f\right)\dfrac{\partial^2 U(x,y)}{\partial y^2}\\ +\left(2\sqrt{3}k_l+6\sqrt{3}k_f\right)\dfrac{\partial^2 U(x,y)}{\partial y\partial x}\end{array}\right)$$

$$S_{212}=-\frac{1}{64}\varepsilon L^2\left(\begin{array}{l}\left(3k_f+9k_l\right)\dfrac{\partial^2 V(x,y)}{\partial x^2}+\left(-2\sqrt{3}k_f+2\sqrt{3}k_l\right)\dfrac{\partial^2 U(x,y)}{\partial x^2}+\left(9k_l+3k_f\right)\dfrac{\partial^2 V(x,y)}{\partial y^2}\\ -\left(2\sqrt{3}k_f+6\sqrt{3}k_l\right)\dfrac{\partial^2 V(x,y)}{\partial y\partial x}\end{array}\right)$$

$$S_{122}=-\frac{3}{64}\varepsilon L^2\left(\begin{array}{l}\left(2k_f-2k_l\right)\dfrac{\partial^2 V(x,y)}{\partial x^2}-\left(3\sqrt{3}k_f+\sqrt{3}k_l\right)\dfrac{\partial^2 U(x,y)}{\partial x^2}-\left(\sqrt{3}k_l+3\sqrt{3}k_f\right)\dfrac{\partial^2 U(x,y)}{\partial y^2}\\ +\left(6k_f+2k_l\right)\dfrac{\partial^2 U(x,y)}{\partial y\partial x}\end{array}\right)$$

$$S_{222}=\frac{3}{64}\varepsilon L^2\left(\begin{array}{l}\left(\sqrt{3}k_f+3\sqrt{3}k_l\right)\dfrac{\partial^2 V(x,y)}{\partial x^2}+\left(-2k_f+2k_l\right)\dfrac{\partial^2 U(x,y)}{\partial x^2}+\left(3\sqrt{3}k_l+\sqrt{3}k_f\right)\dfrac{\partial^2 V(x,y)}{\partial y^2}\\ -\left(2k_f+6k_l\right)\dfrac{\partial^2 V(x,y)}{\partial y\partial x}\end{array}\right)$$

7.6.3.1 Computation of internal lengths for the triangular topology of biomembranes

We next compute the internal lengths for the hexagonal lattice, relying on the effective second order behavior computed with the second gradient approach. Isolating first the contributions in extension, that is the derivatives $\frac{\partial \sigma_{11}}{\partial x_1}$, $\frac{\partial S_{111}}{\partial x_1 \partial x_1}$, and inserting the expressions of those two components of the hyperstress tensor versus $\frac{\partial^2 U(x,y)}{\partial x^2}$, one identifies the internal extensional length as

$$l_{xx}^{\ 2}=\frac{1}{16}\varepsilon L^2\frac{\left(15k_l+13k_f\right)}{\left(3k_l+k_f\right)}\Rightarrow l_{xx}=\frac{1}{4}\sqrt{\varepsilon}L\sqrt{\frac{\left(15k_l+13k_f\right)}{\left(3k_l+k_f\right)}}$$

This length clearly vanishes with the small parameter ε, in fact as its square root.

We proceed in a similar manner as described previously to evaluate the internal length for the shear along x-y and y-x respectively, the internal length for the shear along x-y as

$$l^2_{int,xy} = \frac{\sqrt{3}}{64}\varepsilon L^2\left(9k_f + 3k_l\right)$$

One can further proceed in the same manner for the derivative $\frac{\partial^2 V}{\partial x \partial x}$ and identify now an internal length for shear along y-x, $l^2_{int,yx} = \frac{\sqrt{3}}{64}\varepsilon L^2\left(17k_f + 11k_l\right)$, which is not the same as $l_{int,xy}$.

7.7 Application to the Zig-Zag lattice

We consider the description of a flexible yarn as an undulated beam with periodical crimp along direction x, and we compute the first and second order effective moduli, from the homogenized response involving Cauchy stress and hyperstress expressed versus the kinematic variables.

Let consider an undulated beam with a geometry discretized by a Zig-Zag lattice represented by two inclined beams, as shown in figure 7.7.

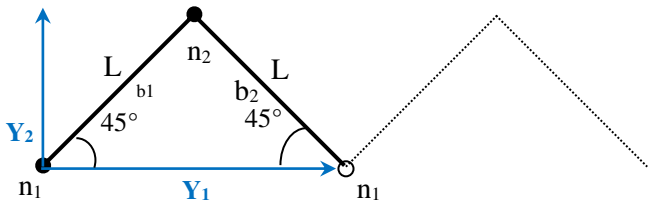

Fig. 7.7 Geometry of the Zig-Zag lattice.

The length of each beam is $L_b = [L, L]$. The periodicity vectors are $\mathbf{Y}_1 = \begin{bmatrix} 1 \\ 0 \end{bmatrix}$ and $\mathbf{Y}_2 = \begin{bmatrix} 0 \\ 1 \end{bmatrix}$, with lengths $L_1 = \sqrt{2}\,L$ and $L_2 = 1$.

The connectivity of this lattice is given in Table 7.4.

Table 7.4 Mechanical properties connectivity of the Zig-Zag lattice

beam	**1**	**2**
O(b)	1	2
E(b)	2	1
δ^1	0	1
δ^2	0	0

From the previous general framework, one first obtains the Cauchy stress

$$\boldsymbol{\sigma} = \begin{bmatrix} \dfrac{k_f k_{l_1} L\sqrt{2}\left(\dfrac{\partial U(x,y)}{\partial x}\right)}{k_f + k_{l_1}} & 0 \\ \dfrac{k_f k_{l_1} L\sqrt{2}\left(\dfrac{\partial V(x,y)}{\partial x}\right)}{k_f + k_{l_1}} & 0 \end{bmatrix}$$

The hyperstress tensor $\mathbf{S}$ is obtained as:

$$\mathbf{S}[1..2,1..2,1] = \begin{bmatrix} \dfrac{\varepsilon L^3}{48}\dfrac{k_{l_2} k_f \sqrt{2}}{k_{l_2} + k_f}\left(\dfrac{\partial^2 U(x,y)}{\partial x^2}\right) & 0 \\ \dfrac{\varepsilon L^3}{48}\dfrac{k_{l_2} k_f \sqrt{2}}{k_{l_2} + k_f}\left(\dfrac{\partial^2 V(x,y)}{\partial x^2}\right) & 0 \end{bmatrix}$$

$$\mathbf{S}[1..2,1..2,2] = \begin{bmatrix} 0 & 0 \\ 0 & 0 \end{bmatrix}$$

The flexural rigidity is extracted from the expression of $S[1,1,1]$ as

$$S[1,1,1] = \frac{\varepsilon L^3}{48}\frac{k_{l_2} k_f \sqrt{2}}{k_{l_2} + k_f}\frac{\partial^2 V(x,y)}{\partial x^2}$$

The internal extensional length is defined as

$$l_{xx}^{\,2} = \frac{1}{4}\varepsilon L^2 \frac{(k_l + k_f)^2}{(k_l k_f)} \Rightarrow l_{xx} = \frac{1}{2}\sqrt{\varepsilon} L \sqrt{\frac{(k_l + k_f)^2}{(k_l k_f)}}$$

The nonlinear response of lattices under out of plane bending is next analysed.

7.8 Flexural behavior of biomembranes based on micropolar models for a nuclear lamina

In the last decade, the growing availability of advanced microscopy and imaging techniques has led to a blooming of interest in the study of biological membranes, revealing often spectacular examples of the intricate interplay of the various features characterizing their behavior (see, e.g., Baumgart et al. 2003). The main literature on the modeling of the mechanical behavior of biological membranes can be traced back to the pioneering works of

(Canham, 1970 and Helfrich, 1973), who derived elastic models describing the bending behavior of lipid bilayers, the building blocks of all types of biological membranes.

In this section, we consider the homogenization technique towards a micropolar continuum for a nuclear lamina subjected to in/out of plane bending test. Namely, the in plane bending test over square lattice based on two orthogonal beam elements, as shown in figure below.

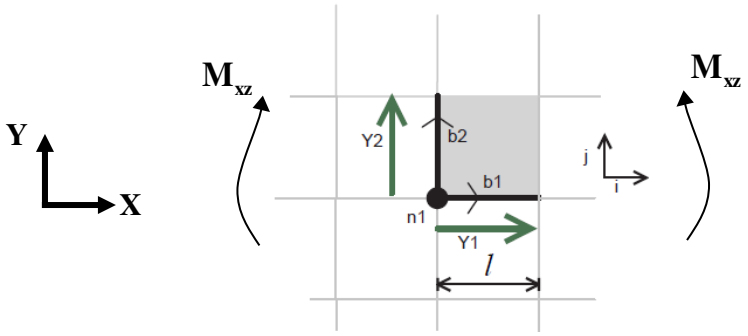

Fig. 7.8 In plane bending test of the tetragonal lattice

(biomembrane with connectivity four).

and the out of plane bending test over a lamina with small undulation angle $\theta_L = 5^\circ$ modeled as square topology repeated unit cells (RUC), with the four beams configuration shown in figure 7.9 (a,b) respectively.

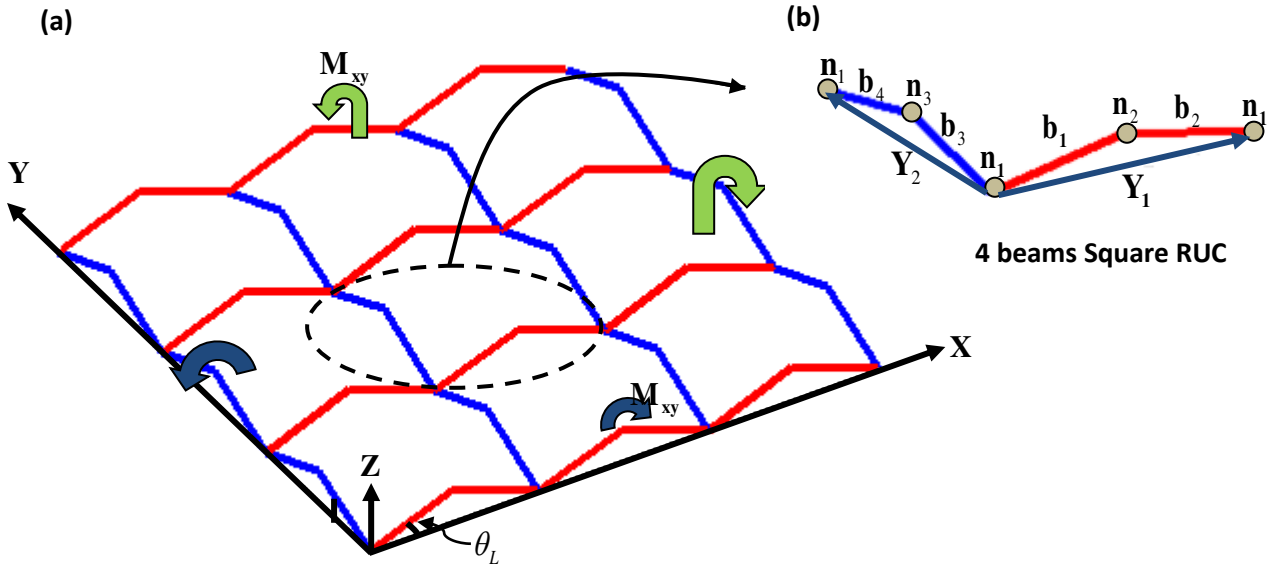

Fig. 7.9 Out of plane bending test: (a) lamina based on repeated (b) 4 beams square lattice .

We shall extract the micropolar moduli from the rigidity and compliance matrices to identify the homogenized micropolar moduli corresponding to the couple stress component. The constitutive equation of linear micropolar continuum write the couple stress (moment per unit surface) m_{xz}, m_{xy} versus the microcurvatures $k_{xz} = \frac{\partial \phi_z}{\partial x}$, $k_{xy} = \frac{\partial \phi_y}{\partial x}$ as follows

$$m_{xz,xy} = k^{\mu}_{55,33} k_{xz,xy}$$

With $k^{\mu}_{55}, k^{\mu}_{33}$ therein the in-plane and out of plane homogenized micropolar modulus respectively, which depend (in a complicated way) of the microstructural lattice parameters.

We employ the following procedure to analyze the deformation of the lamina subjected to (in and out plane) pure bending respectively. As previously discussed (chapter Three), the constitutive law can be identified from the expression of the second order forces and moments, based on the kinematical nodal displacement at the second order of (ε) and the nodal microrotation at first order in (ε). One solves the equilibrium equation at this stage under a pure bending load involving the gradient of the microrotation imposed over the reference unit cell to evaluate the kinematical nodal displacement for each beam versus its flexural rigidity.

- **In plane bending for the 2-beams square RUC**

The repeated unit cell (RUC) is chosen with beam length $L^b = 2\,\text{nm}$, a beam width $t = 0.5\,\text{nm}$ and elastic moduli $E_s = 47.99\,\text{MPa}$ (as previously discussed in chapter two: section 3.7.3.1).

The response of the square lattice subjected to in plane pure bending is shown in Fig. 7.10: we note that the macroscopic couple stress does not display a nonlinear evolution during the corresponding incremental increase of the bending strain. This shows that each beam undergoes in fact a very small rotation, with all rotations cumulated giving rise to nearly no geometrical nonlinear effect at the structural level.

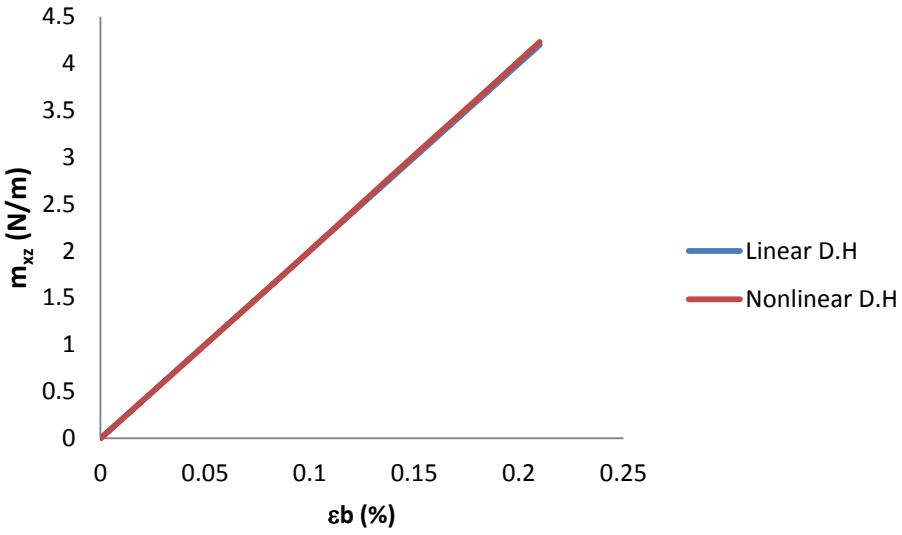

Fig. 7.10 In plane bending test: couple stress versus bending strain.

- **Out-of-plane bending for the 4-beams square RUC**

Next, let consider the square repeated unit cell (RUC) within the lamina having small undulation, described by the angle $\theta_L = 5^\circ$. Each beam has length $L^b = 2\,\text{nm}$, width $t = 0.5\,\text{nm}$ and elastic moduli $E_s = 4.799\times10^7\text{Pa}$. The periodicity vectors are $Y_1 = \begin{bmatrix}1\\0\\0\end{bmatrix}$, $Y_2 = \begin{bmatrix}0\\1\\0\end{bmatrix}$ and $Y_3 = \begin{bmatrix}0\\0\\1\end{bmatrix}$, with lengths $L_1 = 2\,L\cos(\theta_L)$ *and* $L_2 = 2\,L\cos(\theta_L)$. The connectivity of this lattice is given in Table 7.5.

Table 7.5 Mechanical properties connectivity of the square lattice

beam	**1**	**2**	**3**	**4**
O(b)	1	2	1	3
E(b)	2	1	3	1
δ^1	0	1	0	0
δ^2	0	0	0	1
δ^3	0	0	0	0

The response of the square lattice subjected to out of plane bending (m_{xy}) is shown in Fig. 7.11: we note that at 20% of bending strain, there is a relatively large difference between the

linear and geometrical nonlinear analysis of about 10%, with bending requiring less moments in comparison to a linear response. This contrasts with the in-plane behavior which remains linear, thus stiffer.

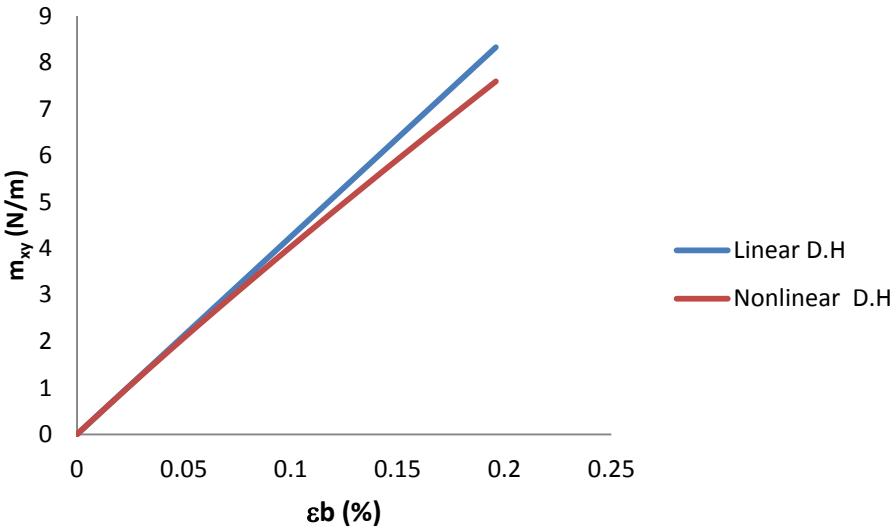

Fig. 7.11 Out of plane bending test: couple stress versus bending strain.

7.9 Conclusion

We have developed a theoretical framework for the evaluation of second order gradient effects arising from the non affine motions of the internal nodes of the representative unit cell within lattice materials. The internal lengths have been formally computed based on the writing of the equilibrium equations. One-dimensional applications have been made as a first step, followed by computations of the bending properties of biological membranes, relying on the micropolar effective continuum. The case of bending is illustrative of the links between the homogenization scheme towards micropolar and second order grade continuous media. Especially, it has been shown that the developed homogenization scheme does not capture the bending behavior since it is restricted to 2D lattices; accordingly, the micropolar model is complementary in the sense that it is able to capture the bending response and provide the internal bending lengths. Furthermore, there is a strong similarity in the methodology for the derivation of the effective properties of micropolar and second order grade continua, especially the construction of the expression of the moments (at beam level and for the

micropolar continuum) and of the hyperforces (at the beam level for the second order grade continuum).

The developed predictive numerical model can be used as a design tool to explore lattices giving rise to more pronounced size effects; especially, one shall imagine microstructured beams within the representative unit cell giving rise to more pronounced size effects at the mesoscopic level.

Future planed work includes the development of numerical schemes for the computation of the effective second order properties for discrete media having a 3D geometry, such as textile or trabecular bone. One shall then expect that both extension and bending lengths shall be computed for such 3D geometries; the internal lengths for bending shall then coincide with those evaluated from the micropolar continuum.

The effective second order models evaluated at the mesoscopic level shall further be used at the macroscopic scale to perform structural computations for media showing such scale effects.

7.10 References

[1] Trinh Duy-Khanh. Thèse de doctorat : Méthodes d'homogénéisation d'ordre supérieur pour les matériaux architecturés. École nationale supérieure des Mines de Paris, 2011.

[2] Forest Samuel. Milieux continus généralisés et matériaux hétérogènes. Presses des Mines, 2006.

[3] Forest Samuel. Thèse de doctorat : Modèles mécaniques de la déformation hétérogène des monocristaux. École nationale supérieure des Mines de Paris, 1996.

[4] Cosserat Eugène, et al. Théorie des corps déformables. Librairie scientifique A. Hermann et fils, Paris,1909.

[5] R. A. Toupin. Elastic materials with couple-stresses. Archive for Rational Mechanics and Analysis. Springer.Vol. 11, Issue 1, pp. 385-414, 1962.

[6] R.D. Mindlin, H.F. Tiersten. Effect of couple stresses in linear elasticity. Archive for Rational Mechanics and Analysis. Springer. Vol. 11, pp. 415-448, 1962

[7] Dos Reis Francisco. Thèse de doctorat: Homogénéisation automatique de milieux discrets périodiques: applications aux mousses polymères et aux milieux auxétiques, Institut national polytechnique de Lorraine. 2010.

[8] Luc Chevalier. Mécanique des systèmes et des milieux déformables. Chevalier 2004.

[9] J.C. Craveur, C. Cheze. Mécanique des structures. 2008.

[10] F. dell'Isola and D. Steigmann "A two-dimensional gradient-elasticity theory for woven fabrics", *Journal of Elasticity*, 14 May 2014, 13.

[11] M. Ferretti, A. Madeo, F. dell'Isola and P. Boisse "Modelling the onset of shear boundary layers in fibrous composite reinforcements by second gradient theory", Zeitschrift für angewandte Mathematik und Physik, vol.65 (3), 2014, pp.587-612.

General Conclusions and Recommendations for future work

The development of suitable micromechanical schemes for the computation of the effective mechanical response of architecture materials such as fibrous networks is quite important, in order to have at hand predictive models to analyze the overall computed response in terms of the underlying microscopic mechanisms. When a RUC can be identified for a quasi periodic network, it is possible to develop specific homogenization schemes relying on the assumption of inherent periodicity. Although a lot of attention has been devoted to replacing large periodic networks of lattice materials by effective continuum models, less attention has been paid to the consideration of both geometrical nonlinearities and microstructure effects leading to generalized continua at the continuum level.

This is the main goal of this thesis, in which we shall develop a modeling and numerical platform to determine in a general and systematic way the overall continuum response of periodical networks representative of the initial structure.

The interest of the developed discrete homogenization technique (DH in short) lies in its flexibility and capability to handle any planar lattice; however in this work, we restricted ourselves to centro-symmetric lattices for simplicity. A further interest of the homogenization method lies in it is ability to deliver the expressions of the forces and hyperforces at the beam extremities of the lattice for generalized continua, based on the kinematical nodal variables (displacement and microrotation). From those expressions, one is able to construct the full compliance (or rigidity) matrix, reflecting the complex and evolving anisotropy of the so-built equivalent continuum. In the elastic case, and for small perturbations, the effective properties are derived as closed-form expressions of the geometry (characterized by the beam length and the quadratic moment of inertia) and mechanical properties (Young modulus). We extended the linear discrete asymptotic homogenization framework to the nonlinear setting, based on an update of the lattice geometry and an elastic computation done over each load increment. These theoretical developments have been implemented into a dedicated code using the lattice geometry and microstructural properties as an input, and delivering as an output the effective response.

We observe that for depending on the type of structure topology, a linear analysis is not acceptable, since the difference between linear and nonlinear is significant. The detailed analysis of the considered types of structure from the proposed methodology shows that the

main reason of nonlinearity lies in the reorientation of the structural beam elements under the local stresses, whereas other geometric effects such as extension are negligibly small in comparison. A source of difficulty lies in the fact that due to the existing nonlinearity, it is not possible as for the homogenization in the linear setting to superpose the response obtained for individual loadings.

A comparison of the response under uniaxial loading computed based on DH and on FE simulations has been done systematically in order to validate the homogenized response obtained by the DH technique, showing overall a good agreement between the results from discrete homogenization and those computed numerically. Especially, we have shown that the flexural response is well predicted by the DH technique, with a gain in rigidity due to micropolar effects that the DH is able to capture.

We have performed as an application of those models meso-level analysis of the mechanical behavior of textile monolayers and biological membranes to construct their effective anisotropic micropolar representative continuum models at the mesosopic level. The discrete asymptotic homogenization method delivers for such thin layers a micropolar effective medium at the mesoscopic level, from the description of the network as a lattice of thick (or thin) beams. As the main novel aspect, the nonlinear behavior of such networks under large strains was investigated.

The micropolar concept is natural for textile since it captures the change of crimp and the local discrete rotations at the crossing zones between yarns. It further allows computing the flexural rigidity of such thin layers, the determination of which would otherwise be difficult to access. Plain weave and twill tows have been selected as case studies and have been analyzed in detailed. The derivation of such effective mechanical properties of textile from micromechanical analyses is quite interesting; moreover, the change of these properties during incremental deformation has been identified. On the other hand, the nonlinear stress strain response was analyzed incrementally under three classical types of loading cases: uniaxial, biaxial and simple shear, taking into consideration the structure geometry changes.

The homogenization scheme is quite general and versatile enough to be applicable for any networks having a periodical architecture. The obtained effective continuum models at the mesoscopic level may be further used at the next scale level to perform structural simulations; for textiles, it paves the way towards the simulation of shape forming operations involving dry textiles. In view of this objective, we have identified strain energy functions for effective

hyperelastic continua, as the nonlinear hyperelastic constitutive laws for fabric consisting of two independent families of fiber.

The representation of yarns could be improved by implementing a more elaborate model of the yarn behavior. This micromechanical approach is particularly interesting and novel, due to the difficulty to measure such effective properties for textiles considering their discreteness. The proposed homogenization technique proves efficient from a numerical point of view, and it has a great versatility as to the topology of the textile armor, which makes it a suitable tool to explore and compare various textile architectures for both single and multilayer 3D configurations in future developments. Other factors that have been discarded in the present contribution can be incorporated in extensions of the model, like yarn transverse compressibility, a more accurate representation of the shape of the yarn, and a better description of contact between yarns up to friction.

In the second part of this work, we have developed a discrete homogenization scheme up to the second order gradient of the imposed displacement field in order to formulate constitutive models for media exhibiting strong deformation gradients at the unit cell level, due to the non affine motion of internal nodes with the RUC. The derived effective continuum is characterized by first and second order mechanical moduli relating the stress to the first order strain and the hyperstress to the second order strain, in a decoupled manner. The proposed methodology has been first applied to the evaluation of the second order tensile and flexural rigidity of a microstructured beam; the flexural rigidity calculated by the second order gradient scheme is identical to that computed by a micropolar effective continuum model. From a technical point of view, it has been shown that the effective second order modulus is obtained in a simpler manner by the second order gradient homogenization scheme.

The method is systematic in the sense that it can handle any lattice; these analyses are preliminary in the sense that we have mostly considered 2D or 2.5D geometries with essentially an in-plane behavior (without bending). From a numerical viewpoint, a dedicated homogenization code has been developed combining symbolic and numerical evaluations, using as an input file the topology and mechanical parameters of the beams within the identified unit cell of the lattice.

The internal lengths for both the micropolar and second order gradient continua have been formally computed based on the writing of the equilibrium equations. One-dimensional applications have been made as a first step, followed by computations of the bending properties of biological membranes, relying on the micropolar effective continuum. The case

of bending is illustrative of the links between the homogenization scheme towards micropolar and second order grade continuous media. Especially, it has been shown that the developed homogenization scheme towards second order gradient continua does not capture the bending behavior, when restricted to 2D geometries; accordingly, the micropolar model is complementary in the sense that it is able to capture the bending response. Furthermore, there is a strong similarity in the methodology for the derivation of the effective properties of micropolar and second order grade continua, especially the construction of the expression of the moments (at beam level and for the micropolar continuum) and of the hyperforces (at the beam level for the second order grade continuum).

The developed predictive numerical model can be used as a design tool to explore lattices giving rise to more pronounced size effects. The effective second order models evaluated at the mesoscopic level can further be used at the macroscopic scale to perform structural computations for media showing such scale effects. Before that, we need to validate by FE simulations the computed homogenized second order moduli; this is an issue as one has to apply proper boundary conditions involving non uniform strains and uniform curvatures to capture second order gradient or internal bending effects.

The computation of effective mechanical properties of materials endowed with microstructure exhibiting effectively second order gradient effects is the basis for performing structural computations in an efficient manner, whereby the identified effective constitutive law is implemented at each Gauss point of a finite element computation. More detailed investigations of both the theoretical basis of the 2D homogenization of periodical discrete structures towards second order gradient continua are needed, before going to more complex 2D and 3D geometries exhibiting more pronounced scale effects. The analysis of 3D textiles is a natural perspective of development of the present work.

The mechanical response of random fibrous networks such as biomembranes is another perspective, for which a proper definition of a RUC together with the analysis of internal length scale effects are important issues.

Appendix A: General Introduction to Nonlinear Elasticity Theory

Contents

In this appendix, we present a short review of number of features associated with the nonlinear elasticity theory. First, we recall some ideas for linear and nonlinear material modeling; we then focus on the different sources of nonlinearities in the analysis of solid continua, and nonlinear trusses will be considered to determine the main aspects of the nonlinear analysis as a final goal of this appendix.

A.1. Introduction

Nonlinear and linear continuum mechanics deal with the same topics including kinematics, statics, equilibrium, and the constitutive behavior. But in the linear analysis, an assumption is made that the deformation is sufficiently small to ignore the effect of changes in the geometrical configuration of the solid, whereas in the nonlinear case, the magnitude of the deformation is unrestricted so that this situation requires an extension of the small strain analysis.

The principal problem in Elasticity Theory is to find the relation between the stress and the strain in a body under certain forces. Hooke's Law is applied when the strains are small.
However rubber-like materials at large deformations are considered as nonlinear elastic, so that new expressions are required to characterize the behavior of the material. During uniaxial loading the difference between the linear and nonlinear behavior is represented in the shape of the curve of stress-strain behavior as shown in Figure A.1.1, in which stresses cannot be described as a linear function of strains. In both cases however, the curves during loading and unloading follow the same path; the stress is a unique function of the strain or deformation.

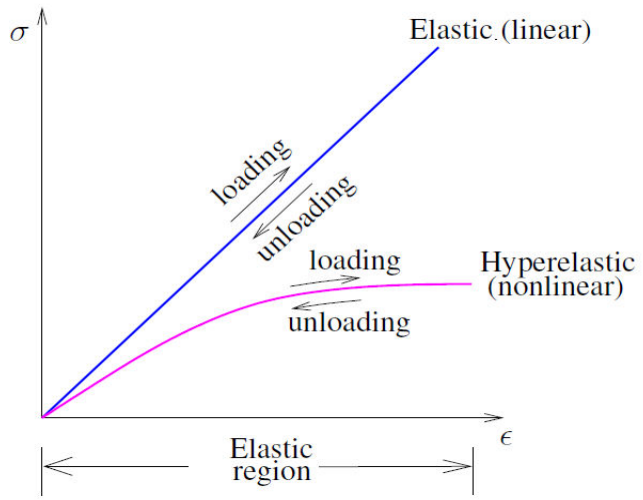

Fig. A.1.1 types of stress strain responses

In a nonlinear analysis, the shape of the response is characterized by non-proportional nature between load and deformation. Thus, the structural response presented versus incremental loading with taking into consideration the new shape of the structure. In other words, the stiffness matrix of the structure is a function of element force as well as the deflection of the structure. Therefore, the instantaneous stiffness equation can only be solved numerically by an incremental and iterative procedure allowing for the geometrical change of the structure. Based on the Newton-Raphson scheme, the applied load is first divided into many small increments, and the displacement increment within each increment is computed by using the tangent stiffness matrix.

A.1.1. Linear material modeling

In this type of material modeling the constitutive equation that relates the relation between stress and deformation is represented by linear relation between the stress tensor σ_{ij} and the strain tensor ε_{kl} is given by Hooke's law (linear proportional relationship named after Robert Hooke, 1676).

$$\boldsymbol{\sigma}_{ij} = \mathbf{C}_{ijkl}\, \boldsymbol{\varepsilon}_{kl} \tag{A.1}$$

Where σ_{ij} components of the Cauchy stress tensor are, ε_{kl} are components of the strain tensor and C_{ijkl} is called the elastic constants tensor of fourth order.

Consequently, in the linear Finite Element Analysis (FEA) the set of equations, describing the material behavior is linear. In this analysis the equivalent stiffness matrix (K) is independent on the value of the load level and the displacements are proportional to the loads.

$$\mathbf{K\,d = F} \tag{A.2}$$

where $\mathbf{d}$ is the nodal displacement vector and $\mathbf{F}$ the external nodal force vector.

A.1.2. Nonlinear material modeling

For many materials, the relationship between the deformation and the applied load is no longer in a linear proportional; linear elastic models don't accurately describe the observed material behavior. However at large deformations, new expressions to characterize the behavior of materials like rubber are required.

In the next section we discuss the constitutive equations which interrelates the stress and the strain components within a nonlinear regime. With present a nonlinear constitutive theory to describe a wide variety of physical phenomena in which the strains may be large, i.e. finite.
For the case of hyperelastic material the resulting theory is called finite hyperelasticity and the constitutive equations for these materials postulates the existence of a Helmholtz free energy function (strain energy or stored energy function) ψ , in which $\psi = \psi(\mathbf{F})$ is a function of the transformation gradient **F** or of a suitable strain tensor.
Consequently, the nonlinear Finite Element Analysis is needed when the loading on the material cause's significant changes in stiffness. The stiffness changes arises amongst all possible factors from strains beyond the elastic limit (plasticity), large deflections, modifications of the structure geometry, elastic properties depending upon strain, contact between two bodies. To trace the nonlinear load-deflection curve, a suitable numerical solution technique shall be adopted. As a consequence, the stiffness matrix is a function of element force as well as the deformation. Thus, for these phenomena, the set of equilibrium equations becomes nonlinear and instead of the set of linear equations (5.2) we obtain a set of nonlinear algebraic equations.

$$R(\mathbf{d}) = \mathbf{F} \tag{A.3}$$

The instantaneous stiffness equation can only be solved numerically by an incremental and iterative procedure allowing for the geometrical change of the structure. Based on the Newton-Raphson scheme (or modified Newton-Raphson), the applied load is first divided into many small increments, and the displacement increment within each increment is computed by using the tangent stiffness matrix from the set of linear simultaneous equations.

$$\mathbf{K}_T^{i-1} \Delta\mathbf{d}^i = \Delta\mathbf{F}^i \tag{A.4}$$

And an update solution is obtained as shown in figure 5.2, with recognize that in nonlinear only one load case can be handled at a time and the results of several load cases cannot be combined.

$$\mathbf{d}^i = \mathbf{d}^{i-1} + \Delta\mathbf{d}^i \tag{A.5}$$

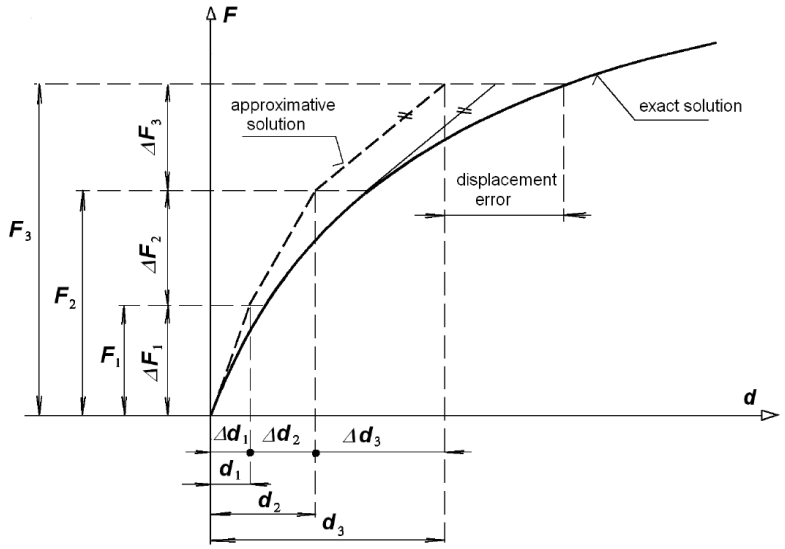

Fig. A.1.2 Incremental method [Steen Krenk]

A.2. Nonlinear computational mechanics

Nonlinearities exist in an equation of motion, for whatever reason, the stress strain behavior given by the constitutive relation is nonlinear, from exist of products of variables, or their derivatives. The important is to understand the system in terms of the material model, loading and expected response to be able to determine where a linear approximation is adequate and where the use of a nonlinear theory is needed. The two main sources of nonlinearity exist in the analysis of solid continua, namely, material and geometric nonlinearity. Contact can also be classified as a geometric nonlinearity because the area of contact is a function of the deformation, but some author's puts contact in another class called nonlinear boundary conditions.

A.3. Types of nonlinearities

A.3.1. Material nonlinearities

Material nonlinearities occur when the stress-strain or force-displacement law is not linear, or when material properties change with the applied loads.

It is important to note that no material has a perfectly linear elastic modulus or is perfectly isotropic; these are just approximations that are satisfactory for most situations.

If the material behavior is nonlinear, the displacement is infinitesimal, strain is infinitesimal and the stress-strain relationship is nonlinear. Possible material models are:
nonlinear elastic, elastoplastic, viscoelastic and viscoplastic.
The assumption of material linearity is adopted in this thesis for simplicity and we concentrate on geometric effects only.

A.3.2. Geometrical nonlinearities

Geometric nonlinearities in solid bodies and structures involve nonlinearities in kinematic quantities, which entail nonlinear strain-displacement relations. Such nonlinearities can occur due to the occurrence of large displacements, large strains, large rotations, and combination of these. Changes in geometry, whenever large or small, have a significant effect on the load-deformation behavior.
If the effect of large displacements and large rotations on the overall geometric configuration of the structure exists, this effect can be dividing in two cases as exposed next.

- **Large displacements / large rotations but small strains**

• Displacements and rotations are large.
• Strains are small.
• Stress – strain relations are linear or nonlinear.

- **Large displacements, large rotations, large strains**

• Displacements are large.
• Rotations are large.
• Strains are large.
• The stress-strain relation is probably nonlinear.

A.3.3. Boundary nonlinearities

The most frequent boundary nonlinearities are encountered in contact problems, displacement dependent boundary conditions. Let consider simple examples to facilitate the understanding of these different types of nonlinearities.

A.4. Simple example of nonlinear structure behavior

Let consider a cantilever torsion spring model as shown in Figure (A.4.1) that provides a gentle introduction to some aspects of nonlinear analysis.

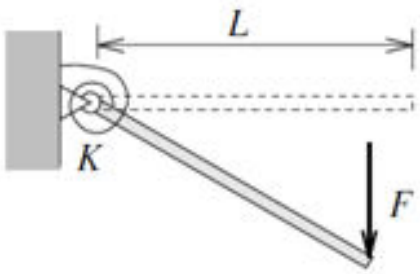

Fig. A.4.1 Rigid bar attached to linear elastic torsion spring

Taking the balance of moments about the hinge gives the equilibrium equation as,

$$M = F\,L\cos(\theta) \tag{A.6}$$

where M is the moment at the pinned end of the bar. We can further relate the moment M to the rotation of the spring by the constitutive equation for a torsion spring as,

$$M = K(\theta) \tag{A.7}$$

where K is the torsional spring constant. Therefore, by substitute of eqn.(A.6) into eqn.(A.7) we can write,

$$F = \frac{K(\theta)}{L\cos(\theta)} \tag{A.8}$$

Therefore, the force-rotation relationship is nonlinear in θ, typical of a non-linearity due to geometry. If the angle $\theta \to 0$, then $\cos(\theta) \to 1$, and the linear equilibrium equation is recovered as,

$$F = \frac{K}{L}(\theta) \tag{A.9}$$

If we assume that the torsion spring is nonlinear elastic the constitutive equation for the spring writes,

$$M = (k_o + k_1\theta)\left(\theta\right) \tag{A.10}$$

In this case, substituting eqn. (2.6) into eqn. (2.10), the force-rotation relation becomes,

$$F = \frac{(k_o + k_1\theta)(\theta)}{L\cos(\theta)} \tag{A.11}$$

Therefore, the force-rotation relationship contains both material and geometrical nonlinearities. Assuming small rotations leads to

$$F = \frac{(k_o + k_1\theta)}{L}(\theta) \tag{A.12}$$

which traduces the fact that the force-rotation relationship traduces only material nonlinearity.

A.5. One dimensional nonlinear strain measures

In the theory of infinitesimal deformations, the simplest possible quantity that we can use to measure the strain in one dimensional bar is the so-called engineering strain ε defined as,

$$\varepsilon = \frac{l - l_o}{l_o} \quad or \quad \varepsilon = \lambda - 1 \tag{A.13a,b}$$

This strain definition is used for small displacement problems only, in which there is no significant difference between the second Piola-Kirchhoff stress and Cauchy stress.

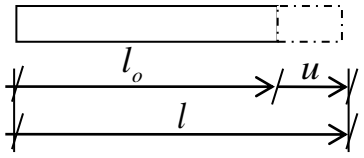

Fig. A.5.1 one–dimensional strain

An alternative large strain measure can be obtained by multiple choices for the way of reporting strain in the theory of large deformation. The various strain measures for a tensile rods having original length (L) and deformed length (l) are shown in fig. (A.5.1). This large strain measure can be obtained by adding up all the small strain increments that take place when the rod is continuously stretched from its original length L to its final length l; this integration process leads to the definition of the natural or logarithmic strain ε_L as,

$$\varepsilon_L = \int_L^l \frac{\delta l}{l} \quad or \quad \varepsilon_L = \ln\left(\frac{l}{L}\right) = \ln\lambda \tag{A.14a,b}$$

Although the above strain definition can in fact be extrapolated to the deformation of a three dimensional continuum body, this generalization process is complex and computationally costly. Strain measures that are much more readily generalized to continuum cases are the so-called Green strain ε_G and Almansi strain ε_E defined as,

$$\varepsilon_G = \frac{l^2 - L^2}{2L^2} \quad or \quad \varepsilon_G = \frac{1}{2}\left(\lambda^2 - 1\right) \tag{A.15a,b}$$

$$\varepsilon_E = \frac{l^2 - L^2}{2l^2} \quad or \quad \varepsilon_E = \frac{1}{2}\left(1 - \frac{1}{\lambda^2}\right) \tag{A.16a,b}$$

A.6. Nonlinear truss example

Simple one-dimensional problems (single incompressible truss member) will be analyzed based on an incremental iterative method in order to introduce a number of features associated to finite deformation theory. Based on the principle of virtual displacements, one shall express the external force versus displacement, with the total stiffness divided by three different types of tangent stiffness. The external force is plotted versus displacement in two types of loading. Type one is loading is when the bar is initially inclined and the external force acts in y-direction. The second loading type of when the bar initially horizontal (y=0) and the external force act in the same axis of the bar.

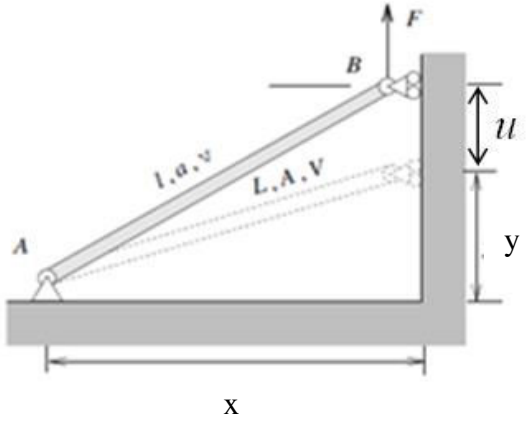

Fig. A.6.1 single incompressible truss member

The chosen material and geometrical parameters of the bar are as shown in the Table A.1.

Table A.1 Material and Geometric parameters

A_b **(mm²)**	E_b **(MPa)**	y **(mm)**	x **(mm)**
Truss bar type one			
2	2000	2	20
Truss bar type two			
2	2000	0	20

A.6.1. Type one the bar initially inclined (a)

We consider the truss member shown in Figure A.6.1 with initial and deformed lengths, and cross-sectional areas and volumes: L, A, V and l, a, v in initial and deformed configurations respectively. We assume large displacements and small strains, hence V = v or AL = al. The constitutive equations are chosen based on Green's definition of strain; hence the Cauchy stress writes,

$$\sigma = \frac{N}{A} = E\frac{l^2 - L^2}{2L^2} \tag{A.23}$$

The original bar length L and the bar length l corresponding to the current deformed state write:

$$L = \sqrt{x^2 + y^2} \qquad l = \sqrt{x^2 + (y+u)^2} \tag{A.24a,b}$$

The axial force in the bar expresses in terms of the Green strain as,

$$N = EA\varepsilon_G \; EA\left[\frac{y}{L}\frac{u}{L} + \frac{1}{2}\left(\frac{u}{L}\right)^2\right] \tag{A.25}$$

- **Equilibrium**

The principle of virtual displacements (PVD) is a convenient way to obtain the equilibrium equation, when the bar is in equilibrium; the virtual works of internal and external forces are equal for every kinematic admissible set of virtual displacements. In this case, the truss member has one degree of freedom, only one virtual displacement δu is possible and the principle of virtual displacement receives the form

$$\delta V = \int_V \sigma\, \delta\varepsilon_G \, dV = F\, \delta u \tag{A.26}$$

where $\delta\varepsilon_G$ is virtual strain corresponding to virtual displacement δu . The virtual strain can be expressed from equation (2.25) as

$$\delta\varepsilon_G = \frac{d\varepsilon_G}{du}\delta u = \frac{d}{du}\left[\frac{y}{L}\frac{u}{L} + \frac{1}{2}\left(\frac{u}{L}\right)^2\right]\delta u = \left[\frac{y+u}{L^2}\right]\delta u \tag{A.27}$$

Therefore, substituting eqn.(2.23, 2.25) and (2.27) into eqn. (2.26) delivers

$$\left(\frac{N}{A}\right)\left[\frac{y+u}{L^2}\right]\delta u(AL) = F\,\delta u \tag{A.28}$$

Thus, equilibrium of the node B in the deformed state (Fig. 2.5) requires that the external force F is equal to the internal force g(u) generated by deformation of the bar:

$$\begin{aligned} g(u) &= N\left[\frac{y+u}{L}\right] \;\; ; \quad g(u) = F \\ EA&\left[\frac{y}{L}\frac{u}{L}+\frac{1}{2}\left(\frac{u}{L}\right)^2\right]\left[\frac{y+u}{L}\right] = F \end{aligned} \tag{A.29}$$

The tangent stiffness is a measure of the change in force for a given change in displacement and is defined by,

$$K = \frac{dg}{du} = \frac{d}{du}\left(N\left[\frac{y+u}{L}\right]\right) \tag{A.30}$$

$$\begin{aligned} K &= \frac{EA}{L}\left(\frac{y}{L}\right)^2 + \frac{EA}{L}\left(\frac{yu+u^2}{L^2}\right) + \frac{N}{L} \\ &= \quad K_o \quad + \quad K_u \quad + K_\sigma \end{aligned} \tag{A.31}$$

In which K_o is the linear stiffness, K_u is the initial displacement stiffness, and K_σ is the initial stress stiffness.

A.6.2. Type two loading of the bar initially horizontal (b)

We next consider the same previous problem however in a second situation when the truss bar is initially horizontal as shown in figure (A.5.1), thus one rewrites equation (A.23) as

$$\sigma = \frac{N}{A} = E\frac{l^2 - L^2}{2L^2} \tag{A.32}$$

One sets in addition the relation between the original bar length L and the deformed one l as:

$$l = L + u \tag{A.33}$$

The axial force in the bar expresses in terms of the Green strain as,

$$N = EA\varepsilon_G \;\square\; EA\left[\frac{u}{L}+\frac{1}{2}\left(\frac{u}{L}\right)^2\right] \tag{A.34}$$

One then writes the virtual strain as,

$$\delta\varepsilon_G = \frac{d\varepsilon_G}{du}\delta u = \frac{d}{du}\left[\frac{u}{L}+\frac{1}{2}\left(\frac{u}{L}\right)^2\right]\delta u = \left[\frac{L+u}{L^2}\right]\delta u \tag{A.35}$$

Therefore, equation (A.26) becomes,

$$\left(\frac{N}{A}\right)\left[\frac{L+u}{L^2}\right]\delta u\left(AL\right) = F\,\delta u \tag{A.36}$$

Thus, equilibrium of node B in the deformed state requires that the external force F is equal to the internal force g(u) generated by the deformation of the bar.

$$g(u) = N\left[\frac{L+u}{L}\right] \;\; ; \;\; g(u) = F$$
$$EA\left[\frac{u}{L} + \frac{1}{2}\left(\frac{u}{L}\right)^2\right]\left[\frac{L+u}{L}\right] = F \tag{A.37}$$

The tangent stiffness is defined as,

$$K = \frac{dg}{du} = \frac{d}{du}\left(N\left[\frac{L+u}{L}\right]\right) \tag{A.38}$$

$$K = \frac{EA}{L}\left(\frac{L+u}{L}\right) + \frac{EA}{L}\left(\frac{Lu+u^2}{L^2}\right) + \frac{N}{L} \tag{A.39}$$
$$= \quad K_o \qquad + \qquad K_u \qquad\qquad + K_\sigma$$

Finally, we use an incremental procedure to solve the equilibrium equations (A.29) and /or (A.37) for the unknown displacement u corresponding to a given value of the external load F. But in this one-degree-of-freedom case, it is easier to specify a value for u and find the corresponding external load F. As a summary, we obtain the following tangent stiffness, as the sum of three types of stiffnesses mentioned above in each case, shown in Table A.2.

Table A.2 Identification of the total tangent stiffness

Case one: initially inclined beam			**Case two: initially horizontal beam**		
K_o	K_u	K_σ	K_o	K_u	K_σ
$\frac{EA}{L}\left(\frac{y}{L}\right)^2$	$\frac{EA}{L}\left(\frac{yu+u^2}{L^2}\right)$	$\frac{N}{L}$	$\frac{EA}{L}\left(\frac{L+u}{L}\right)$	$\frac{EA}{L}\left(\frac{Lu+u^2}{L^2}\right)$	$\frac{N}{L}$
Internal force			**Internal force**		
$N = EA\left[\frac{y}{L}\frac{u}{L} + \frac{1}{2}\left(\frac{u}{L}\right)^2\right]$			$N = EA\left[\frac{u}{L} + \frac{1}{2}\left(\frac{u}{L}\right)^2\right]$		
External force			**External force**		
$F = EA\left[\frac{y}{L}\frac{u}{L} + \frac{1}{2}\left(\frac{u}{L}\right)^2\right]\left[\frac{y+u}{L}\right]$			$F = EA\left[\frac{u}{L} + \frac{1}{2}\left(\frac{u}{L}\right)^2\right]\left[\frac{L+u}{L}\right]$		

We denote by type one and two the cases of initially inclined and horizontal beams respectively, which means that type one will account for the linear and the initial displacement stiffnesses.

The external force is recorded versus each displacement increment, showing a nonlinear relation of type one and a linear relation of type two, as represented in figure A.6.2 (a, b) respectively.

Obviously, the equilibriums equations (A.29-A.37) are nonlinear with respect to the displacement u, which means that one expects the relation between external load F and displacement u to be represented by a nonlinear curve. But one shall notice from figures 2.6a,b that this occurs only with type one loading. Understanding the reasons of the difference of behaviors (linear versus nonlinear responses) in the present 1D case will be of great help to understand the response of 2D lattices within a geometrical nonlinear analysis.

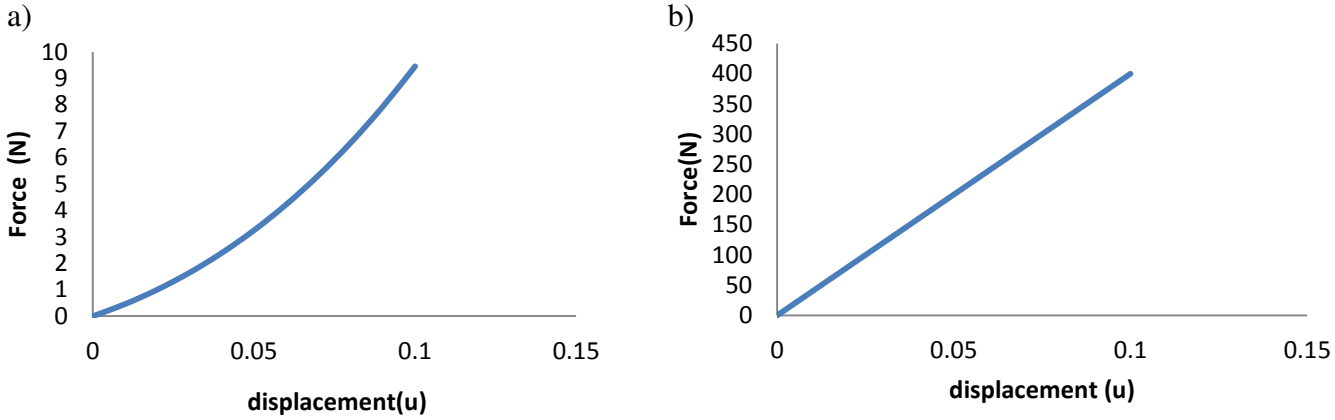

Fig. A.6.2 External force (F) versus the applied incremental displacement (u), for the previous two types of structures

One shall notice that there is a slight difference in the definitions of internal force in equations (A.25 - A.34), which is obvious with the linear part of strain ($\frac{u}{L}$) times this factor $\frac{y}{L}$ in case of type one loading (Fig. A.6.2a). Rewriting these equations in terms of the stress- strain relation leads to,

For the first type of structure (Fig. A.6.2a): $\frac{N}{A}=\sigma=E\left[\frac{y}{L}+\frac{1}{2}\varepsilon\right]\varepsilon;\ \Delta\sigma=E\left[\frac{y}{L}+\frac{1}{2}\Delta\varepsilon\right]\Delta\varepsilon$

For the second type of structure (Fig. A.6.2b): $\frac{N}{A}=\sigma=E\left[1+\frac{1}{2}\varepsilon\right]\varepsilon;\ \Delta\sigma=E\left[1+\frac{1}{2}\Delta\varepsilon\right]\Delta\varepsilon$

One shall notice that in both types (a, b), the tensile modulus E is not a function of strain, so that there is no material nonlinearity. In order to plot the stress-strain response, one shall solve for equilibrium using a small incremental value of the strain at each step, and neglect the second

order part of the strain, thereby using the linearized form of the constitutive law. However, the factor y/L is still present, leading to a nonlinear force-displacement relation.

In the general case (more than one-degree of freedom), an incremental procedure is needed to solve the equilibrium equations as mentioned above. The solution can be formulated in two ways. In the total Lagrangian formulation, one uses the full tangent stiffness matrix, including the displacement stiffness matrix during all steps of the computation. The Second-Piola Kirchhoff stress should be associated with Green's strain and not Cauchy stress;

The principle of virtual displacement gives

$$\int_{{}^{o}V} {}^{t+\Delta t}_{0}S_{ij}\, \delta\, {}^{t+\Delta t}_{0}\varepsilon_{G_{ij}}\, dV = {}^{t+\Delta t}R \tag{A.40}$$

where ${}^{t+\Delta t}_{0}S_{ij}$ are the components of the 2nd Piola Kirchhoff stress tensor.

In the alternative Updated Lagrangian formulation, the geometry is updated, and the current value of displacement (u) is absorbed in the updated value of (a), and in that case the initial displacement stiffness K_u vanishes.

In the Updated Lagrangian formulation, a known deformed configuration (i) is taken as initial state for the subsequent configuration (i+1) and this process is continually updated as the calculation proceeds.

The principle of virtual displacement gives

$$\int_{V^i} \sigma_{ij}^{(i+1)}\, \delta\varepsilon_{A_{ij}}^{(i+1)}\, dV = {}^{t+\Delta t}R \tag{A.41}$$

where $\sigma_{ij}^{(i+1)}$ is Cauchy stress tensor and $\varepsilon_{A_{ij}}^{(i+1)}$ is Almansi strain tensor, the notaion (i+1) means that the stress and strain are evaluated in configuration (i+1), but the integration is done over the known volume at the known deformed configuration (i).

Appendix B: Non-linear Equilibrium Problems with Large Perturbations of the Networks: Technical Aspects

Contents

B.1. perturbation with respect to beam length and directors

We next write into a detailed manner the perturbed expression used in the non-linear equilibrium problem associated to the large perturbations of the network.

In order to set the stage, we write the beam in vector form as a function of its length (l^b) and directory ($\mathbf{e}^b$) as follow,

$$\mathbf{B} = l^b \, \mathbf{e}^b \tag{B. 1}$$

One may then formulate the variation of the beam from the perturbation with respect to the beam length and director as,

$$\delta\mathbf{B} = \delta l^b \, \mathbf{e}^b + l^b \, \delta\mathbf{e}^b \tag{B.2}$$

We next formulate an expression for the perturbed beam geometry

$$\delta\mathbf{e}^b = \left(\frac{1}{l^b}\right)\left[\delta\mathbf{B} - \delta l^b \, \mathbf{e}^b\right] \tag{B.3}$$

and length

$$\delta l^b = \delta\mathbf{B}.\mathbf{e}^b + \mathbf{B}.\delta\mathbf{e}^b \tag{B.4}$$

We substitute equation (B.4) into equation (B.3), thus one obtains

$$\delta\mathbf{e}^b = \left(\frac{1}{l^b}\right)\left[\delta\mathbf{B} + \left(\delta\mathbf{B}.\mathbf{e}^b - \mathbf{B}.\delta\mathbf{e}^b\right)\mathbf{e}^b\right]$$

$$\delta\mathbf{e}^b \, l^b = \left[\delta\mathbf{B} + \left(\delta\mathbf{B}.\mathbf{e}^b\right)\mathbf{e}^b - \left(\mathbf{B}.\delta\mathbf{e}^b\right)\mathbf{e}^b\right]$$

$$\delta\mathbf{e}^b \, l^b + \left(\mathbf{B}.\delta\mathbf{e}^b\right)\mathbf{e}^b = \left[\delta\mathbf{B} + \left(\delta\mathbf{B}.\mathbf{e}^b\right)\mathbf{e}^b\right] \tag{B.5}$$

One then divides equation (B.5) by $\left(l^b\right)$, thus

$$\delta\mathbf{e}^b + \left(\frac{\mathbf{B}}{l^b}.\delta\mathbf{e}^b\right)\mathbf{e}^b = \frac{1}{l^b}\left[\delta\mathbf{B} - \left(\delta\mathbf{B}.\mathbf{e}^b\right)\mathbf{e}^b\right]$$

$$\delta\mathbf{e}^b + \left(\mathbf{e}^b.\delta\mathbf{e}^b\right)\mathbf{e}^b = \frac{\delta\mathbf{B}}{l^b}\left[\mathbf{I} - \left(\mathbf{e}^b \otimes \mathbf{e}^b\right)\right]$$

$$\left[\mathbf{I} + \left(\mathbf{e}^b \otimes \mathbf{e}^b\right)\right].\delta\mathbf{e}^b = \frac{\delta\mathbf{B}}{l^b}.\left[\mathbf{I} - \left(\mathbf{e}^b \otimes \mathbf{e}^b\right)\right]$$

$$\left[\mathbf{I}+\left(\mathbf{e}^b\otimes\mathbf{e}^b\right)\right]^{-1}=\left[\mathbf{I}-\frac{1}{2}\left(\mathbf{e}^b\otimes\mathbf{e}^b\right)\right]$$

We can then introduce a projection operator as

$$\mathbf{C}=\left[\mathbf{I}-\frac{1}{2}\left(\mathbf{e}^b\otimes\mathbf{e}^b\right)\right],\quad \mathbf{P}=\left[\mathrm{I}-\left(\mathbf{e}^b\otimes\mathbf{e}^b\right)\right] \tag{B.6}$$

Finally, the perturbation of the beam director in the beam direction writes,

$$\delta e^b=\frac{1}{l^b}\left(C.P\right).\delta B \tag{B.7}$$

Substituting equation (B.7) in equation (B.4), one then obtain

$$\delta l^b=\delta\mathbf{B}.\mathbf{e}^b+\mathbf{B}.\left(\frac{1}{l^b}\left(\mathbf{C}.\mathbf{P}\right).\delta\mathbf{B}\right)$$

$$\delta l^b=\delta\mathbf{B}.\mathbf{e}^b+l^b\,\mathbf{e}^b.\left(\frac{1}{l^b}\left(\mathbf{C}.\mathbf{P}\right).\delta\mathbf{B}\right)$$

$$\delta l^b=\mathbf{e}^b.\left[\mathbf{I}+\mathbf{C}.\mathbf{P}\right].\delta\mathbf{B}$$

Finally, the perturbation of beam length writes,

$$\delta l^b=\frac{\mathbf{B}}{l^b}.\left[\mathbf{I}+\mathbf{C}.\mathbf{P}\right].\delta\mathbf{B} \tag{B.8}$$

One can remark that it is easier to get the expression of the perturbation in the perpendicular direction of the beam by introducing the orthogonal transformation ($\mathbf{\Omega}_Z$) such that

$$\mathbf{e}^{b\perp}=\mathbf{\Omega}_Z.\mathbf{e}^b$$

where

$$\mathbf{\Omega}_Z\left(e^b,e^{b\perp},Y_3\right)=\begin{bmatrix}\cos\left(\frac{\pi}{2}\right) & -\sin\left(\frac{\pi}{2}\right) & 0\\ \sin\left(\frac{\pi}{2}\right) & \cos\left(\frac{\pi}{2}\right) & 0\\ 0 & 0 & 1\end{bmatrix}$$

$$\delta\mathbf{e}^{b\perp}=\mathbf{\Omega}_Z.\delta\mathbf{e}^b$$

Finally, the perturbation of the beam director in perpendicular direction of the beam writes

$$\delta \mathbf{e}^{b\perp} = \frac{1}{l^b} \boldsymbol{\Omega}_Z . (\mathbf{C}.\mathbf{P}) . \delta \mathbf{B} \tag{B.9}$$

B.2. Kinematics of deformable Bodies

Classical continuum mechanics studies the deformation and motion of bodies ignoring the discrete nature of matter. The deformation gradient F is the fundamental measure of deformation in continuum mechanics, which is involved in all equations relating quantities before deformation to the corresponding quantities after (or during) deformation. The deformation gradient tensor enables the relative spatial position of two neighbouring particles after deformation to be described in terms of their relative material position before deformation; consequently, it is central to the description of deformation and hence strain.

In such a nonlinear localization problem, involving (large displacements, large rotations), the most important point is to use the strain definition without "self straining", a condition that precludes generation of strais for arbitrary rigid body motion.

The Green Lagrangian strain ($\mathbf{E}$) tensor is defined with respect to the initial configuration. When the deformation is given by the deformation gradient $\mathbf{F}$, the strain tensor can be obtained based on this formula:

$$\mathbf{E} = \frac{1}{2}\left(\mathbf{F}^T\mathbf{F} - \mathbf{I}\right) \tag{B.10}$$

with $\mathbf{I}$ the unit tensor.

The second Piola-Kirchhoff stress ($\mathbf{S}$) tensor is the stress conjugated to the Green lagrangian strain tensor. A push-forward of the second Piola-Kirchhoff stress to the actual configuration Cauchy gives the following expression of the Cauchy stress,

$$\boldsymbol{\sigma} = J^{-1}\mathbf{F}\mathbf{S}\mathbf{F}^{\mathrm{T}} \tag{B.11}$$

One may then formulate the deformation gradient and the Green Lagrangian strain versus the displacement gradients as,

$$\mathbf{F} = \mathrm{Grad}\,\mathbf{x} = \mathbf{I} + \mathrm{Grad}\,\mathbf{u} \tag{B.12}$$

where $\mathbf{I}$ is the identity tensor and $\mathrm{Grad}\,\mathbf{u}$ is the displacement gradient.

The Lagrangian strain writes based on the displacement gradient as,

$$\mathbf{E} = \frac{1}{2}\left(\nabla \mathbf{u} + \nabla \mathbf{u}^T\right) + \frac{1}{2}\nabla \mathbf{u}^T \nabla \mathbf{u}$$
$$E_{ij} = \frac{1}{2}\left(\frac{\partial u_i}{\partial x_j} + \frac{\partial u_j}{\partial x_i} + \frac{\partial u_i}{\partial x_i}\frac{\partial u_j}{\partial x_j}\right) \tag{B.13}$$

The stretch (or the stretch ratio) λ is defined as the ratio of the length of a deformed line element $d\mathbf{x}$ to length of the corresponding undeformed line element $\mathrm{d}\mathbf{X}$

$$\lambda = \frac{d\mathbf{x}}{d\mathbf{X}} \tag{B.14}$$

For a line element in the 1-direction, the unit extension is

$$\frac{\left|d\mathbf{x}_{(1)}\right| - \left|d\mathbf{X}_{(1)}\right|}{\left|d\mathbf{X}_{(1)}\right|} = \lambda - 1$$

Denoting the unit extension of by $d\mathbf{X}_{(1)}$ by $\mathbf{E}_{(1)}$, one can write the strain in this direction, based on equation (A.2.4) as

$$E_{11} = \mathbf{E}_{(1)} + \frac{1}{2}\mathbf{E}_{(1)}^2$$

and similarly for the other diagonal elements of the Lagrangian strain E_{22}, E_{33}. When the deformation is small, $\mathbf{E}_{(1)}^2$ is small in comparison to $\mathbf{E}_{(1)}$, it results in $E_{11} \approx \mathbf{E}_{(1)}$.

B.3. Micro to mesolevel transition

The first order homogenization schemes has been recently developed in [Dos Reis and Ganghoffer, 2012] for the determination of the effective mechanical properties of periodical lattices at the mesoscopic scale; thereby, the stiffness matrix components are expressed as a function of the material and micro structural geometric parameters.

We analyze overall the following networks: a) the square lattice b) the inclined square lattice c) the hexagonal lattice d) the triangular lattice, in order to evaluate the stress-strain behaviour for three different types of loading tests. The unit cell for each lattice and the corresponding periodicity vectors are represented on the same figure below.

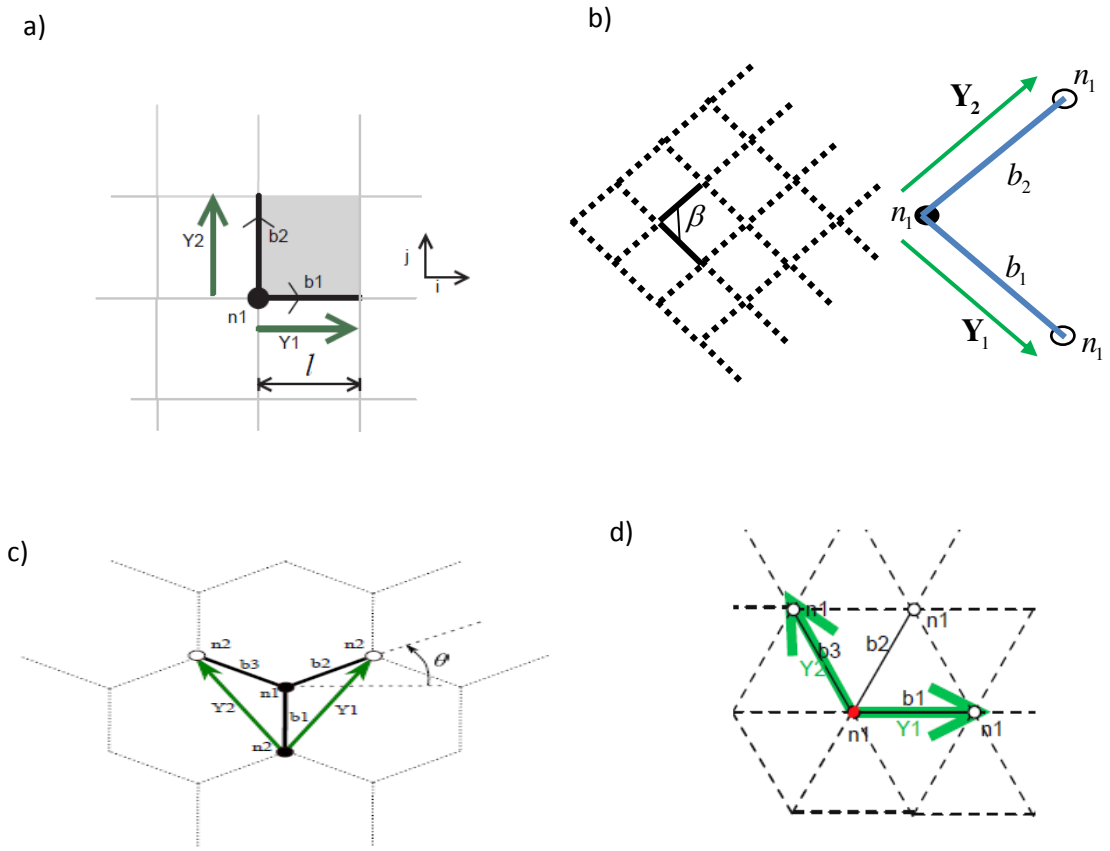

Fig. B.3.1 The analyzed 2D planar Unit cell: (a) square lattice (b) inclined square lattice (c) hexagonal lattice (d) Triangular lattice

The constitutive relations for a plane problem may be written under the form

$$\{\sigma\}=\begin{Bmatrix}\sigma_x\\ \sigma_y\\ \sigma_{xy}\\ \sigma_{yx}\\ m_{xz}\\ m_{yz}\end{Bmatrix}=\begin{bmatrix}K_{11} & K_{12} & 0 & 0 & 0 & 0\\ K_{21} & K_{22} & 0 & 0 & 0 & 0\\ 0 & 0 & K_{33} & K_{34} & 0 & 0\\ 0 & 0 & K_{43} & K_{44} & 0 & 0\\ 0 & 0 & 0 & 0 & K_{55} & 0\\ 0 & 0 & 0 & 0 & 0 & K_{66}\end{bmatrix}\begin{Bmatrix}\varepsilon_x\\ \varepsilon_y\\ \varepsilon_{xy}\\ \varepsilon_{yx}\\ \kappa_{xz}\\ \kappa_{yz}\end{Bmatrix}=[K]\begin{Bmatrix}\frac{\partial u}{\partial x}\\ \frac{\partial v}{\partial y}\\ \frac{\partial v}{\partial x}-\phi\\ \frac{\partial u}{\partial y}+\phi\\ \frac{\partial \phi}{\partial x}\\ \frac{\partial \phi}{\partial x}\end{Bmatrix} \tag{B.15}$$

The following initial stiffness matrix K is obtained for the square lattice, the effective extensional and bending stiffness's are successively given by $k_l=\frac{E_s t}{L}$, and $k_f=\frac{12E_s I^3}{L^3}$,

$$[K]=\begin{bmatrix} k_l & 0 & 0 & 0 & 0 & 0 \\ 0 & k_l & 0 & 0 & 0 & 0 \\ 0 & 0 & k_f & 0 & 0 & 0 \\ 0 & 0 & 0 & k_f & 0 & 0 \\ 0 & 0 & 0 & 0 & \dfrac{k_f L^2}{12} & 0 \\ 0 & 0 & 0 & 0 & 0 & \dfrac{k_f L^2}{12} \end{bmatrix}$$

The initial stiffness matrix K of the inclined square lattice expresses as,

$$K=\begin{bmatrix} K_{11} & K_{12} & 0 & 0 & 0 & 0 \\ K_{21} & K_{22} & 0 & 0 & 0 & 0 \\ 0 & 0 & K_{33} & K_{34} & 0 & 0 \\ 0 & 0 & K_{43} & K_{44} & 0 & 0 \\ 0 & 0 & 0 & 0 & K_{55} & 0 \\ 0 & 0 & 0 & 0 & 0 & K_{66} \end{bmatrix}$$

with the rigidities therein

$$K_{11}=\frac{\sqrt{3}}{4}\left(3k_l+k_f\right);\ K_{22}=\frac{\sqrt{3}}{12}\left(k_l+3k_f\right);K_{12}=K_{21}=-\frac{\sqrt{3}}{4}\left(-k_l+k_f\right);K_{33}=\frac{\sqrt{3}}{12}\left(3k_l+2k_f\right)\ ;$$

$$K_{44}=\frac{\sqrt{3}}{4}\left(k_l+2k_f\right)\ ;K_{34}=-\frac{\sqrt{3}}{12}\left(-3k_l+2k_f\right);K_{43}=-\frac{\sqrt{3}}{4}\left(-k_l+2k_f\right);\ K_{55}=\frac{\sqrt{3}L^2k_f}{12};$$

$$K_{66}=\frac{\sqrt{3}L^2k_f}{36}$$

The initial stiffness matrix K of the hexagonal lattice expresses with the rigidities therein evaluated as,

$$K_{11}=K_{22}=\frac{\sqrt{3}k_l(k_l+3k_f)}{6(k_l+k_f)};\ K_{12}=K_{21}=\frac{\sqrt{3}k_l(k_l-k_f)}{6(k_l+k_f)};\ K_{33}=K_{44}=\frac{\sqrt{3}k_f(k_f+3k_l)}{6(k_l+k_f)}$$

$$K_{34}=K_{43}=\frac{\sqrt{3}k_f(k_l-k_f)}{6(k_l+k_f)};\ K_{55}=K_{66}=\frac{\sqrt{3}L^2k_f}{12}$$

Similarly, the initial stiffness matrix K of the triangular lattice expresses with the rigidities therein evaluated as,

$$K_{11} = K_{22} = \frac{\sqrt{3}}{4}\left(3k_l + k_f\right);\ K_{12} = K_{21} = -\frac{\sqrt{3}}{4}\left(-k_l + k_f\right);\ K_{33} = K_{44} = \frac{\sqrt{3}}{4}\left(k_l + 3k_f\right)$$

$$K_{34} = K_{43} = -\frac{\sqrt{3}}{4}\left(-k_l + k_f\right);\ K_{55} = K_{66} = \frac{\sqrt{3}L^2 k_f}{12}$$

The mechanical moduli extracted from the effective stiffness matrices are given in a synthetic form in the following table,

	Square	**Inclined Square**	**Hexagonal**	**Triangular**
E^*	k_l	$\frac{4\sqrt{3}\left(k_f k_l\right)}{\left(k_l + 3k_f\right)}$	$\frac{4\sqrt{3}\left(k_f k_l\right)}{3\left(k_l + 3k_f\right)}$	$\frac{4\sqrt{3}\left(k_f k_l\right)}{\left(k_l + 3k_f\right)}$
υ^*	**0**	$\frac{4\sqrt{3}\left(k_f k_l\right)}{3\left(3k_l + k_f\right)}$	$\frac{\left(k_l - k_f\right)}{\left(k_l + 3k_f\right)}$	$\frac{\left(-k_l + k_f\right)}{\left(3k_l + k_f\right)}$
G^*	$\frac{k_f}{2}$	$\frac{\sqrt{3}}{4}k_l$	$\frac{\sqrt{3}\left(k_f k_l\right)}{3\left(k_l + k_f\right)}$	$\frac{\sqrt{3}}{4}\left(k_l + k_f\right)$
μ^*	**0**	$\frac{\sqrt{3}}{4}\left(k_l - \frac{4}{6}k_f\right)$	$\frac{1}{6}\frac{\sqrt{3}k_f\left(k_l - k_f\right)}{\left(k_l + k_f\right)}$	$\frac{\sqrt{3}}{4}\left(k_l - \frac{4}{6}k_f\right)$
γ	$\frac{k_f L^2}{12}$	$\frac{\sqrt{3}L^2 k_f}{12}$	$\frac{\sqrt{3}k_f L^2}{36}$	$\frac{\sqrt{3}k_f L^2}{12}$
L^2_{cara}	$\frac{l^2}{24}$	$\frac{L^2 k_f}{12k_l}$	$\frac{L^2\left(k_l + k_f\right)}{48k_l}$	$\frac{L^2 k_f}{12\left(k_l + k_f\right)}$
N^2_{coupl}	$\frac{1}{2}$	$\frac{2k_f}{\left(3k_l + 2k_f\right)}$	$\frac{k_l + k_f}{\left(3k_l + k_f\right)}$	$\frac{2k_f}{\left(k_l + 3k_f\right)}$

Table B.3.1: Summary of the homogenized moduli of the chosen 2D lattices

B.4. Transition of homogenous deformation to macroscopic boundary condition

Within a specified type of load test, we next determine the adequate macroscopic displacement boundary conditions that have to be imposed over the representative unit cell (RUC).

- **Uniaxial tension**

In the uniaxial tensile loading test, we control and impose the stretch (λ) in the xx-direction. One is then entitled to first assume that there is no contraction in yy-direction, as shown in figure B. 4.1 (a). We will see next that this assumption is incorrect, and we will determine the adequate kinematic bouindary condition to be imposed in the yy-direction.

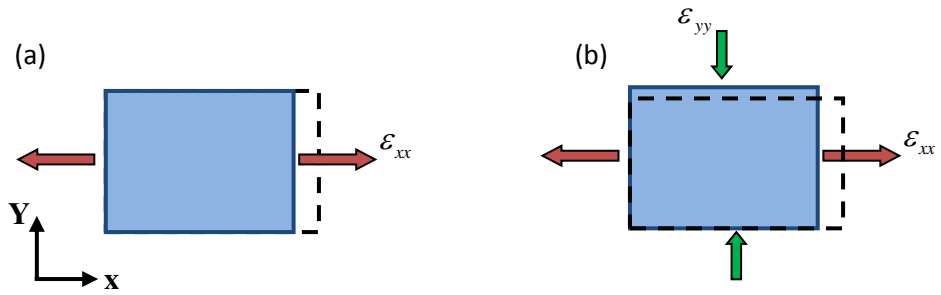

Fig. B. 4.1 Tensile loading in xx-direction

Based on previous assumption, the deformation gradient is described as $\mathbf{F}=\begin{bmatrix}\lambda & 0\\ 0 & 1\end{bmatrix}$. One next expresses Green's strain based on equation (B.10) as

$$\mathbf{E}=\begin{bmatrix}\dfrac{\lambda^2-1}{2} & 0\\ 0 & 1\end{bmatrix} \tag{B.16}$$

One may then reformulate Green's strain versus the displacement gradient, based on equation (A.2.4); interrelating this form with equation (B.16) leads to the imposed displacement gradient versus stretch as,

$$\varepsilon_{xx}=\frac{\partial u}{\partial x}=\lambda-1,\ \varepsilon_{yy}=\frac{\partial v}{\partial y}=0$$

As shown next in figure 4.1 (b), the material locally reacts to the imposed stretch in xx-direction with a stretch in the transverse direction which remains unprescribed, thus the deformation gradient should include an a priori unprescribed strain in yy-direction, in contradiction to what has been initially assumed.

Thus, the deformation gradient for this loading type is defined as follow

$$ {}^{A}\mathbf{F} = \begin{bmatrix} 1+\varepsilon_{xx} & \gamma_{xy}=0 \\ \gamma_{yx}=0 & 1+\varepsilon_{yy} \end{bmatrix} \tag{B.17} $$

The a priori unprescribed strain, the component (ε_{yy}) therein, first requires to initialize the solution of the full incremental problem from the homogenization method based on the small perturbations framework. The correct macroscopic boundary condition shall be extracted, based on the constitutive law that relates stress to strain and involving the computed compliance matrix (A.3). The constitutive law for the stress component in the direction of the imposed xx-stretch loading writes specifically,

$$ \begin{aligned} \left[\sigma_{11}\right] &= \mathrm{K}_{11}\left[\varepsilon_{\mathrm{xx}}\right] + \mathrm{K}_{12}\left[\varepsilon_{\mathrm{yy}}\right] \\ &= \mathrm{K}_{11}\left[\frac{\partial \mathrm{u}}{\partial \mathrm{x}}\right] + \mathrm{K}_{12}\left[\frac{\partial \mathrm{v}}{\partial \mathrm{y}}\right] \end{aligned} $$

One then obtains the macroscopic displacement gradient by the following expressions versus stretch,

$$ \varepsilon_{xx} = (\lambda - 1);\ \varepsilon_{yy} = -\nu_{xy}.\varepsilon_{xx} = -\nu_{12}.(\lambda - 1) $$

involving Poisson's ratio ν_{xy} in the transverse direction. It is thus clearly Poisson's ratio which controls the boundary condition in terms of the stretch to be applied in the transverse yy-direction.

One then updates the lattice geometry for each increment of the loading and determines the new homogenized rigidity matrix adapted to the new shape of the structure, in terms of the stiffness coefficients relative to the new geometry of the lattice unit cell. We thus extract the effective Poisson's ratio (ν_{xy}) at each load increment. This general procedure is applied for each specific loading condition to determine the correct a priori unspecified kinematic control loadings that have to be applied to the unit cell boundaries.

- **Biaxial tension**

In the biaxial tensile loading test, we impose the stretch in both directions; this can be achieved by applying a strain in xx and yy-directions for various biaxial strain ratios, defined as $k = \dfrac{\varepsilon_{xx}}{\varepsilon_{yy}}$, here selected to be an integer $k \in \{0,1,2,3\}$.

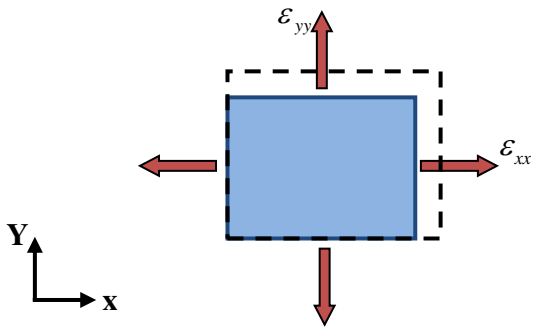

Fig. B.4.2 Biaxial tensile loading in both directions.

The specific case $k = 1$ means one applies a equibiaxial loading with deformation gradient $\mathbf{F} = \begin{bmatrix} \lambda & 0 \\ 0 & \lambda \end{bmatrix}$. One next expresses in this case the Green's strain from equation (B.10) as

$$\mathbf{E} = \begin{bmatrix} \dfrac{\lambda^2 - 1}{2} & 0 \\ 0 & \dfrac{\lambda^2 - 1}{2} \end{bmatrix} \tag{B.18}$$

One then obtains the imposed macroscopic displacements as,

$$\varepsilon_{xx} = \varepsilon_{yy} = (\lambda - 1)$$

In the same manner, we then update the lattice geometry for each increment of the loading and determine the new homogenized rigidity matrix adapted to the new shape of the structure.

- **Simple shear**

In the simple shear test, we impose (Γ), the shear angle as shown in figure B.4.3; considering g of small incremental shear angle lead to $\gamma_{xy} \approx \Gamma$. The deformation gradient is computed as follows

$$F = \begin{bmatrix} 1+\varepsilon_{xx} & \gamma_{xy} \\ 0 & 1+\varepsilon_{yy} \end{bmatrix} = \begin{bmatrix} 1 & \gamma_{xy} \\ 0 & 1 \end{bmatrix} \tag{B.19}$$

One next expresses Green's strain from equation (B.10) as

$$\mathbf{E} = \begin{bmatrix} 0 & \frac{\Gamma}{2} \\ \frac{\Gamma}{2} & \frac{\Gamma^2}{2} \end{bmatrix} \tag{B.20}$$

One may further write the imposed macroscopic displacements versus the shear strain angle as,

$$\varepsilon_{xy} = \varepsilon_{yx} = \frac{\Gamma}{2}$$

It can be observed from equation (B.20) that a compressive strain needs to be imposed in the transverse direction at each increment of the numerical solution procedure, evaluated versus the shear Γ as

$$\varepsilon_{yy} = -1 - \sqrt{\left(1+\Gamma^2\right)}$$

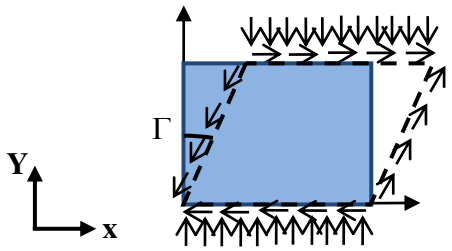

Fig. B.4.3 Simple shear loading test.

Appendix C: Constitutive Theory of Hyperelastic Material for Fiber Reinforced Solids

Contents

C.1. Introduction

In this chapter based on the proposed 2D discrete homogenization discussed in chapter two, we briefly describe the method in a framework of 3D model to derive the macroscopic elastic properties of woven structures – and more generally solids reinforced by two families of fibers - by taking into account axial, transverse shearing, flexural and torsional deformations of the yarns building the woven fabrics. Furthermore, we evaluate the effective mechanical properties of structures having a discrete architecture, relying on the discrete asymptotic homogenization method developed for the large deformation regime.

In the first section of this chapter, we present a short review of nonlinear hyperelastic constitutive laws for isotropic and transversely isotropic solids; a special attention is paid to dry textiles which consist of two families of fibers (before impregnation by the resin).

We aim in this chapter at computing the overall response of a surface made of two families of fibers embedded into an elastic matrix, based on the four basic structures that characterize the symmetry properties of a network of fibers. As a final objective of this first part, we then formulate the strain energy function of such anisotropic surfaces by using the set of invariants incorporating the structural tensors of the fibers; appropriate expressions are given for the different families of surfaces relying on the classification introduced previously.

In second part of this chapter, we shall compute the nonlinear response of fibrous reinforced solid materials, and identify from these numerically computed responses suitable forms of strain energy densities.

C.2. Basic issues concerning strain and stress measures in finite theory

In continuum mechanics, the finite strain theory also called large strain theory, or large deformation theory deals with deformations in which both rotations and strains can be large. Finite strain measures and stress-deformation relations play a basic role in the analysis and computation of finite deformation problems of materials and structures. The next section will describe some of the aspects related to the large deformation theory.

C.2.1. Kinematics of large deformation

Classical continuum mechanics studies the deformation and motion of bodies ignoring the discrete nature of matter. The **deformation gradient** $\mathbf{F}$ is the fundamental measure of deformation in continuum mechanics; it is the second order tensor which maps line elements in the reference configuration $d\mathbf{X}$ into line elements (consisting of the same material particles) in the current configuration $d\mathbf{x}$. Figure C.2.1 considers a line element $d\mathbf{X}$ emanating from position $\mathbf{X}$ in the reference configuration which becomes $d\mathbf{x}$ in the current configuration at a position $\mathbf{x}$. Most of the following results are taken from, or based on, Ogden (1997).

$$d\mathbf{x} = \mathbf{F}.d\mathbf{X} \tag{C.1}$$

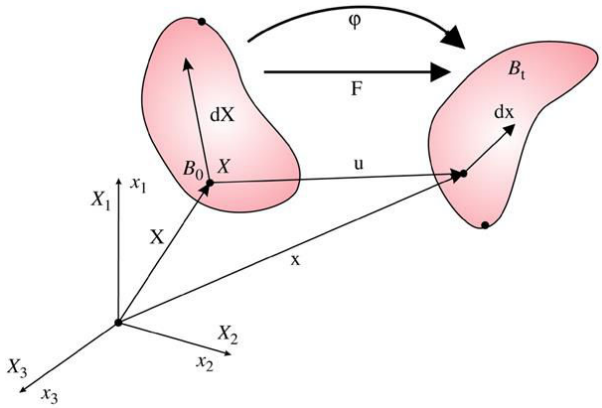

Fig. C.2.1 Material and spatial configurations and motion of a continuum body.

Moreover, a different view of the deformation can be obtained when $\mathbf{F}$ is written in terms of its polar decomposition, given by

$$\mathbf{F} = \mathbf{RU} = \mathbf{VR} \tag{C.2}$$

where $\mathbf{R}$ is a proper orthogonal tensor, i.e. $\mathbf{R}^T\mathbf{R} = \mathbf{I}$ with determinant equal to unity, corresponding to a finite rotation, and $\mathbf{U}$ and $\mathbf{V}$ are second-order positive definite symmetric tensors, known as the right and left stretch tensors If, $\mathbf{R} = \mathbf{I}$, $\mathbf{F} = \mathbf{U} = \mathbf{V}$ the deformation is known as pure strain. If $\mathbf{U} = \mathbf{V} = \mathbf{I}$, $\mathbf{F} = \mathbf{R}$ the deformation corresponding to a rigid body rotation. Using the polar decomposition of $\mathbf{F}$, previous decomposition (C.2) then delivers the relation between small material vectors

$$d\mathbf{x} = \mathbf{R}(\mathbf{U}d\mathbf{X}) \tag{C.3}$$

which means that the unreformed line element $d\mathbf{X}$ is first stretched by $\mathbf{U}$ and is then rotated by $\mathbf{R}$ into the deformed element $d\mathbf{x}$.

In the nonlinear localization problem, the strain is measured locally by changes in the length of line elements. The strain shall be formulated in one of these two forms:

- **Green-Lagrange strain** ($\mathbf{E}_G$) is formulated with respect to the initial configuration.
- **Eulerian (Almansi) strain** ($\mathbf{E}_e$) is formulated with respect to the deformed configuration.

Let consider a differential material line segment in the reference configuration is

$$dS^2 = d\mathbf{X}^T d\mathbf{X}$$

The same material line in the current configuration is

$$ds^2 = d\mathbf{x}^T d\mathbf{x} = d\mathbf{x}^T \mathbf{F}^\mathbf{T} \mathbf{F} d\mathbf{x}$$

Thus, the difference of the square of the length of an infinitesimal segment in the current (deformed) configuration and the reference (unreformed) configuration is given by:

$$ds^2 - dS^2 = d\mathbf{X}^T \left(\mathbf{F}^\mathbf{T}\mathbf{F} - \mathbf{I} \right) d\mathbf{X}$$

The tensor $\mathbf{F}^\mathbf{T}\mathbf{F} - \mathbf{I}$ is a measure of strain; it entails the so-called Green Lagrange strain ($\mathbf{E}_G$ defined by

$$\mathbf{E}_G = \frac{1}{2}\left(\mathbf{F}^\mathbf{T}\mathbf{F} - \mathbf{I} \right) \tag{C.4}$$

Using the polar decomposition equation (C.2) for the deformation gradient $\mathbf{F}$, we may also form the following tensors as possible deformation measures,

$$\mathbf{C} = \mathbf{F}^\mathbf{T}.\mathbf{F} = \mathbf{U}^\mathbf{2}, \quad \mathbf{B} = \mathbf{F}.\mathbf{F}^\mathbf{T} = \mathbf{V}^\mathbf{2} \tag{C.5}$$

We refer to $\mathbf{C}$ and $\mathbf{B}$ as the right and left Cauchy-Green deformation tensors respectively.

Thus $\mathbf{E}_G$ may be written as

$$\mathbf{E}_G = \frac{1}{2}\left(\mathbf{C} - \mathbf{I} \right) = \frac{1}{2}\left(\mathbf{U}^2 - \mathbf{I} \right)$$

The corresponding Euler strain tensor $\mathbf{E}_e$, based on $\mathbf{V}$, is defined by

$$\mathbf{E}_e = \frac{1}{2}\left(\mathbf{I} - \left(\mathbf{F}^\mathbf{T}\mathbf{F} \right)^{-1} \right) = \mathbf{F}^{-\mathbf{T}}\, \mathbf{E}_G.\mathbf{F}^{-1} \tag{C.6}$$

Finally, in this section, it is useful to note that the displacement $\mathbf{u}$ of a particle is defined as

$$\mathbf{u} = \mathbf{x} - \mathbf{X} \tag{C.7}$$

So that

$$\mathbf{x} = \mathbf{X} + \mathbf{u} \tag{C.8}$$

and

$$\mathbf{F} = \text{Grad}\,\mathbf{x} = \mathbf{I} + \text{Grad}\,\mathbf{u} \tag{C.9}$$

where $\mathbf{I}$ is the identity tensor and $\text{Grad}\,\mathbf{u}$ is the displacement gradient.

Using this form (C.9) for the deformation gradient $\mathbf{F}$, gives a variant expression for the Green Lagrangian strain based on the displacement gradient as,

$$\mathbf{E}_G = \frac{1}{2}\left(\nabla\mathbf{u} + \nabla\mathbf{u}^T\right) + \frac{1}{2}\nabla\mathbf{u}^T\nabla\mathbf{u} \tag{C.10}$$

when the deformations are small, it is reasonable to neglect the term involving product of the displacement gradient, thus one recovers the small strain tensor

$$\mathbf{E}_G \approx \varepsilon = \frac{1}{2}\left(\nabla\mathbf{u} + \nabla\mathbf{u}^T\right) \tag{C.11}$$

C.2.2. Statics for large deformation

When the deformations are large, there are a number of different possible ways of defining the action of surface forces; some of these stress measures often do not have as clear a physical meaning as the Cauchy stress, but are useful nonetheless. The force per unit area in the current, deformed, configuration has been described in terms of the Cauchy stress tensor σ . The Cauchy stress is also called the **true stress**, to distinguish it from other stress tensors, some of which will be discussed below.

Figure C.2.2 shows that a vector element of surface in the reference configuration, $\mathbf{N}dS$, where dS is the area of the element and $\mathbf{N}$ is the unit normal. After deformation, the material particles making up this area element now occupy the element defined by $\mathbf{n}ds$, where ds is the area element and $\mathbf{n}$ the unit exterior normal in the current configuration. Suppose that a force $d\mathbf{f}$ acts on the surface element (in the current configuration). Then by definition of the Cauchy stress

$$d\mathbf{f} = \boldsymbol{\sigma}\,\mathbf{n}\,ds \tag{C.12}$$

the (Cauchy) traction vector is defined as

$$\mathbf{t} = \frac{d\mathbf{f}}{ds}\ ,\ \mathbf{t} = \boldsymbol{\sigma}.\mathbf{n} \tag{C.13}$$

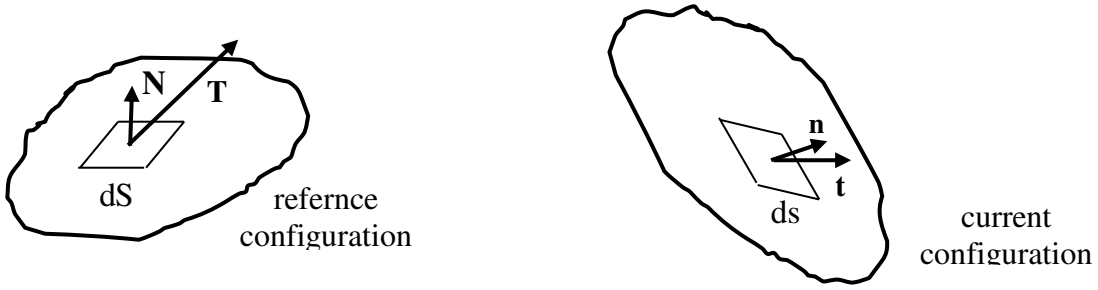

Fig. C.2.2 Traction vectors $\mathbf{T}, \mathbf{t}$ in undeformed and deformed configurations respectively

Similarly, one can introduce the **first Piola-Kirchhoff stress** tensor **P** (called **PK1 stress**) defined by

$$d\mathbf{f} = \mathbf{P}\,\mathbf{N}\,dS \tag{C.14}$$

The PK1 stress relates the force acting in the current configuration to the surface element in the reference configuration. Since it relates to both configurations, it is in fact a two-point tensor, which does not truly deserve the status of a second order tensor.

The (first Piola Kirchhoff) traction vector is defined as

$$\mathbf{T} = \frac{d\mathbf{f}}{dS}\ ,\ \mathbf{T} = \mathbf{P}\,\mathbf{N} \tag{C.15}$$

The Cauchy traction is the actual physical force per area on the element in the current configuration, the PK1 traction is a fictitious quantity, defined as the force acting on an element in the current configuration divided by the area of the corresponding element in the reference configuration.

Thus, one shall notice that, since $d\mathbf{f} = \mathbf{t}ds = \mathbf{T}dS$, it means that $\mathbf{t}$ and $\mathbf{T}$ have the same direction but different magnitude.

The second Piola Kirchhoff stress tensor, or the **PK2** stress, $\mathbf{S}$, is defined by

$$\mathbf{S} = J\mathbf{F}^{-1}\boldsymbol{\sigma}\,\mathbf{F}^{-\mathrm{T}} \tag{C.16}$$

The PK2 is a material tensor field, in the same way as the Cauchy stress is a spatial tensor field. The relations between the different types of stresses mentioned above are next written.

- Cauchy stress $\boldsymbol{\sigma}$ and PK1 are related through

$$\mathbf{P} = J\boldsymbol{\sigma}\mathbf{F}^{-\mathrm{T}} \Leftrightarrow \boldsymbol{\sigma} = J^{-1}\mathbf{P}\mathbf{F}^{\mathrm{T}} \tag{C.17}$$

- The PK1 and PK2 stresses are related through

$$\mathbf{P} = \mathbf{F}\mathbf{S} \Leftrightarrow \mathbf{S} = \mathbf{F}^{-1}\mathbf{P} \tag{C.18}$$

Finally, one shall notice that the Cauchy stress is symmetric, but the deformation gradient is not. Hence, the PK1stress tensor is not symmetric, and this restricts its use as an alternative stress measure to the Cauchy stress measure. Moreover, one can easily obtain the following relations

$$\left(\mathbf{F}^{-1}\boldsymbol{\sigma}\,\mathbf{F}^{-\mathrm{T}}\right)^{\mathrm{T}} = \left(\boldsymbol{\sigma}\,\mathbf{F}^{-\mathrm{T}}\right)^{\mathrm{T}}\left(\mathbf{F}^{-1}\right)^{\mathrm{T}} = \mathbf{F}^{-1}\boldsymbol{\sigma}^{\mathrm{T}}\,\mathbf{F}^{-\mathrm{T}} \tag{C.19}$$

Since the Cauchy stress is symmetric, so the PK2 is also symmetric, $\mathbf{S} = \mathbf{S}^{\mathrm{T}}$.

C.3. Nonlinear elasticity models

For many materials, linear elastic models do not accurately describe the observed material behavior. Elastic materials for which the work done on the material is independent of the load path are said to be hyperelastic (they are also called Green elastic materials). Nonlinear elastic behavior of materials can be formulated in several ways. The simplest formulation is called the total formulation, whereby the stress and strains are defined in terms of the secant modulus of elasticity E_s , see Figure C.3.1,

$$\sigma = E_s \varepsilon \tag{C.20}$$

In a hypo-elastic formulation for which finite stress cannot directly be related to finite strain, the relationship between stress and strain increments is defined by the tangential modulus of elasticity E_t, such that

$$d\sigma = E_t(\varepsilon)\, d\varepsilon \tag{C.21}$$

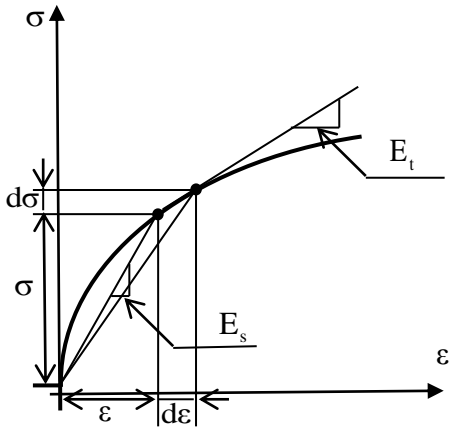

Fig. C.3.1 Nonlinear elastic response

The nonlinear elastic material law can also be formulated in terms of hyperelastic formulation: a hyperelastic material has a nonlinear behavior, which means that its answer to the load is not directly proportional to the deformation; the most common example of this kind of material is rubber, but also biological tissues and several woven fabrics like Lycra can be modeled using an hyperelastic constitutive law.

Hyperelasticity accounts for the capability of a material to experience large elastic strain due to small or large forces, without losing its original properties when unloaded back to the initial configuration. In this section, we discuss the phenomenological equations which interrelate the

stress and the strain tensors within the nonlinear regime. We present a nonlinear constitutive theory to describe a wide variety of physical phenomena in which the strains may be large, that is finite (in opposition to the small strain regimes). For hyperelastic materials, the resulting theory is called finite hyperelasticity and the constitutive equations for these materials postulates the existence of a Helmholtz free energy function W (the strain energy or stored energy function in the absence of thermal effects, elaborated as a density per unit volume), in which W=W(F) is a function of F or some alternative strain tensor. Its derivative with respect to the strain tensor E determines the corresponding stress, as

$$\mathbf{S}_{ij} = \frac{\partial W}{\partial E_{ij}} = 2\frac{\partial W}{\partial C_{ij}} \tag{C.22}$$

where:

$\mathbf{S}_{ij}$ is the components of the second Piola-Kirchhoff stress tensor

W is the strain-energy function per unit undeformed volume

$\mathbf{E}_{ij}$ denote the components of the Lagrangian strain tensor

$\mathbf{C}_{ij}$ are the component of the right Cauchy-Green deformation tensor

The principal features of a nonlinear elastic material are:

1. The presence of large deformations, such that the analysis is nonlinear,
2. It does not have permanent deformations,
3. There is no proportionality between stress and strain,
4. As a corollary, the elastic stiffness tensor $\mathbf{C}_{ij}$, is not a matrix of constant coefficients. Instead, finite stress-strain relations with elasticity constants depending upon the strain are derived from a strain energy function W; the strain energy may be expressed in terms of the principle invariants of $\mathbf{C}$ for an isotropic material, viz

$$\mathrm{W} = \mathrm{f}(\mathrm{I}_1, \mathrm{I}_2, \mathrm{I}_3) \tag{C.23}$$

I_1, I_2 and I_3 are the three invariants of the green deformation tensor given in terms of the principle extension ratios λ_1, λ_2 and λ_3 by:

$$\begin{aligned} \mathrm{I}_1 &= tr\,\mathbf{C} = \lambda_1^2 + \lambda_2^2 + \lambda_3^2 \\ \mathrm{I}_2 &= \frac{1}{2}\left(\left(tr\,\mathbf{C}\right)^2 - tr\left(\mathbf{C}\right)^2\right) = \lambda_1^2\lambda_2^2 + \lambda_2^2\lambda_3^2 + \lambda_3^2\lambda_1^2 \\ \mathrm{I}_3 &= \det\mathbf{C} = \lambda_1^2\lambda_2^2\lambda_3^2 \end{aligned} \tag{C.24}$$

C.4. Isotropic hyperelastic material Models

We next review some hyperelastic constitutive models developed for isotropic and anisotropic solid bodies undergoing large strains.

C.4.1. Saint-Venant Kirchhof Model

The simplest hyperelastic material model is the Saint Venant–Kirchhoff model, which is an extension of the linear elastic material model to the nonlinear regime. This model is a straightforward generalization of Hooke's law to finite strains when the effects of the large deformation are primarily due to rotations such as in the bending of a marine riser or a fishing rod, for example. The St. Venant-Kirchhoff material is fully nonlinear in the displacements. This model is suitable for large displacement calculations, when the material undergoes only small strains (but large displacements and rotations) through the use of Green-Lagrange strain (E) measure. This model has a strain energy function of the form:

$$\psi(\mathbf{E}_G) = \frac{\gamma}{2}\left[Tr(\mathbf{E}_G)\right]^2 + \mu Tr(\mathbf{E}_G{}^2) \tag{C.25}$$

in which, $\gamma \succ 0$ and $\mu \succ 0$ are the two Lamé constants.

From the given strain energy function $\psi(\mathbf{E}_G)$, one derives the second Piola-Kirchhof stress $(\mathbf{S})$, which linearly depend on the Green-Lagrange strain $(\mathbf{E}_G)$, as

$$\mathbf{S} = \gamma \,\mathrm{Tr}(\mathbf{E}_\mathrm{G})\mathbf{I} + 2\mu(\mathbf{E}_\mathrm{G}) \tag{C.26}$$

For rubber and biological materials, more sophisticated models are necessary to describe the materials that exhibit modest strain, or are elastic in the regime of very large strains. From experiments, it is known that rubbery materials can develop moderate strains up to 30-70%.

C.4.2. Neo-Hookean Solid Model

The neo-Hooekean hyperelastic material model was proposed by Ronald Rivlin in 1984; it is similar to Hooke's law, and can be used for predicting the nonlinear stress-strain behavior of materials undergoing large deformations. The form of the strain energy potential is as follows:

$$W = c_1(I_1 - 3) \tag{C.27}$$

where c_1 is a material constant (a shear modulus), and $I_1 := Tr(C)$ is the first invariant of the left Cauchy-Green deformation tensor. The Neo-Hookean model can be replaced by more general model, such as the Mooney-Rivlin solid where the strain energy is a linear combination of the first two invariants.

C.4.3. Mooney-Rivlin Model

Rivlin and Sunders developed in 1951 a hyperelastic model for large deformations of elastomers, typically rubber for an automobile tire. The form of the strain energy potential for a Mooney-Rivlin material is given as:

$$W = c_{10}(I_1 - 3) + c_{01}(I_2 - 3) \tag{C.28}$$

where, c_{10}, c_{01} are material constants. The Mooney Rivlin material was originally developed for rubber, but is today often applied to model (incompressible) biological tissues. For modeling rubbery and biological materials at even higher strains, the more sophisticated Ogden material model described subsequently has been developed.

C.4.4. Signorini Model

It is an extension of Mooney-Rivlin model including a quadratic contribution in the first invariant

$$W = c_{10}(I_1 - 3) + c_{01}(I_2 - 3) + c_{20}(I_1 - 3)^2 \tag{C.29}$$

C.4.5. Yeoh Model

The original model proposed by Yeoh has a cubic form with a sole dependence on the first invariant I_1 and is applicable to purely incompressible materials. The strain energy density for this model is written as

$$W = c_{10}(I_1 - 3) + c_{20}(I_1 - 3)^2 + c_{30}(I_1 - 3)^3 \tag{C.30}$$

C.4.6. Ogden Model

This model was developed by Ray W. Ogden in 1972; like other hyperelastic materials models, the Ogden assumes that the material behavior is described by a strain energy density function, from which the stress-strain relationship can be derived.

The Ogden form of strain energy is based on the principal stretches of left-Cauchy strain tensor, which has the form:

$$W = \sum_{p=1}^{N} \frac{\mu_p}{\alpha_p} \left(\lambda_1^{\alpha_p} + \lambda_2^{\alpha_p} + \lambda_3^{\alpha_p} - 3 \right) \tag{C.31}$$

where N, μ_p and α_p are material constants.

C.4.7. Arruda–Boyce Model

This model was developed by Arruda–Boyce in 1993; it is used to describe the mechanical behavior of rubber and other polymeric substances. This model is based on the statistical mechanics of a polymeric material with a cubic representative volume element containing eight chains along the diagonal directions. The material is assumed to be incompressible, so that the strain energy density function for the incompressible Arruda–Boyce model is given by

$$W = N k_B \theta \sqrt{n} \left[\beta \lambda_{\text{chain}} - \sqrt{n} \ln \left(\frac{\sinh \beta}{\beta} \right) \right] \tag{C.32}$$

where n is the number of chain segments. k_B is the Boltzmann constant, θ is the temperature in Kelvin, and N is the number of chains in the network of a cross-linked polymer.

C.5. Transversely isotropic material models

Fiber-reinforced composites material and also many biological tissues such as ligaments or blood vessels are modeled by the hyperelastic idealization; the reader is referred to chapter I for an overview of such materials and structures. Fiber-reinforced materials are composed of a network of fibers with different choices of fiber distribution: when the reinforcement is randomly arranged, they can be modeled as isotropic materials; when they are composed of one family of fibers only (with a single preferred direction), they can usually be considered as transversely isotropic; finally, when two or more families of fibers are present, the tissue is modeled as a fully anisotropic solid material.

We consider herewith a 3-D fiber-reinforced composite made of isotropic matrix and a single family of reinforcing fibers. The fibers are continuously distributed and have a common unique direction in the reference configuration of the material. We denote by $\mathbf{A}$ the unit vector parallel to the fiber direction in the reference configuration, and $\mathbf{a} = \mathbf{F}.\mathbf{A}$ the corresponding unit vector in the current configuration, transported by the deformation gradient $\mathbf{F}$.

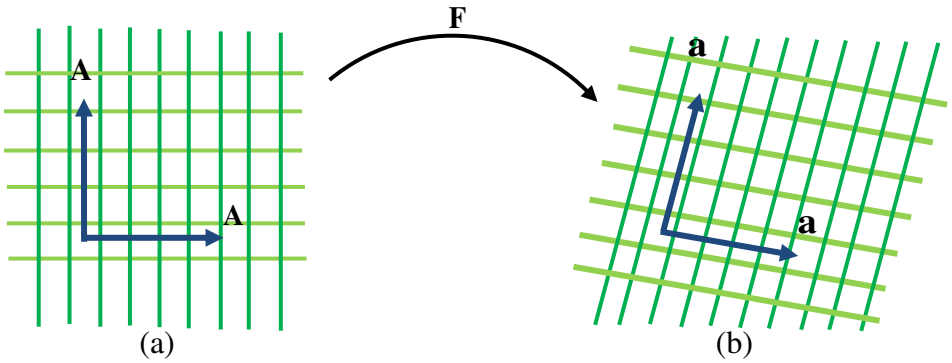

Fig. C.5.1 Top view of piece of fabric made of single family of reinforcing fibers (a) orientation initial (b) orientation after deformation

For such hyperelastic anisotropic materials, the isotropic part of the elastic strain energy function descriptive of the matrix response can be written in terms of the right Cauchy-Green tensor $W^M = W^M(\mathbf{C})$. The presence of a family of reinforcing fibers in the isotropic matrix gives the material transversely isotropic properties, characterized by the invariance of W under rotations that preserve the fibers direction in the reference configuration. In the sequel, a classification of the possible forms of the strain energy density is proposed.

Let **G** be the group of orthogonal transformations which leave the axis parallel to $\mathbf{A}$ invariant, i.e

$$\mathbf{G} = \{\mathbf{R} \in o(3) / \mathbf{R}\mathbf{A} = \pm\mathbf{A}\} \tag{C.33}$$

Its elements are the rotations with axis parallel to $\mathbf{A}$ and the reflections in the planes parallel or orthogonal to $\mathbf{A}$. If we assume the matrix material to be hyperelastic, then it is customary to assume that, in the presence of fibers, the following transverse isotropy condition holds

$$W(\mathbf{C}) = W(\mathbf{R}\mathbf{C}\mathbf{R}^T), \forall \mathbf{R} \in \mathbf{G}. \tag{C.34}$$

Transverse isotropy can also be characterized alternatively in terms of the so-called structural tensor built from the fiber direction,

$$\mathbf{M} = \mathbf{A} \otimes \mathbf{A} \tag{C.35}$$

In fact, the group of orthogonal transformations that leaves the structural tensor invariant is clearly **G** itself, viz

$$\mathbf{G} = \{\mathbf{R} \in o(3) : \mathbf{R}\mathbf{M}\mathbf{R}^T = \mathbf{M}\} \tag{C.36}$$

We next assume that the elastic energy W can be written as a function of $\mathbf{C}$ and the structural tensor $\mathbf{M}$

$$W = \hat{W}(\mathbf{C}, \mathbf{A} \otimes \mathbf{A}) \tag{C.37}$$

In order to describe the constitutive law of the fiber reinforced composites at finite strains, the Helmholtz free energy function W is proposed which depends not only on the deformation

gradient F but also on the fiber directions. Hence, W can be written for one family of fiber as a function of the right green strain tensor $\mathbf{C}$ and the structural tensor $\mathbf{M}$, such that:

$$W = W(\mathbf{C}, \mathbf{M}) \tag{C.38}$$

where $\mathbf{M} = \mathbf{A} \otimes \mathbf{A}$, with $\mathbf{A}$ a unit vector which denotes the fiber direction.

For two families of fibers as shown in Figure 3.5, the free energy is written analogically as:

$$W = W(\mathbf{C}, \mathbf{M}_1, \mathbf{M}_2) \tag{C.39}$$

where $\mathbf{M}_1 = \mathbf{A}_1 \otimes \mathbf{A}_1$ and $\mathbf{M}_2 = \mathbf{A}_2 \otimes \mathbf{A}_2$ are the structural tensors of the two fiber directions $\mathbf{A}_1, \mathbf{A}_2$.

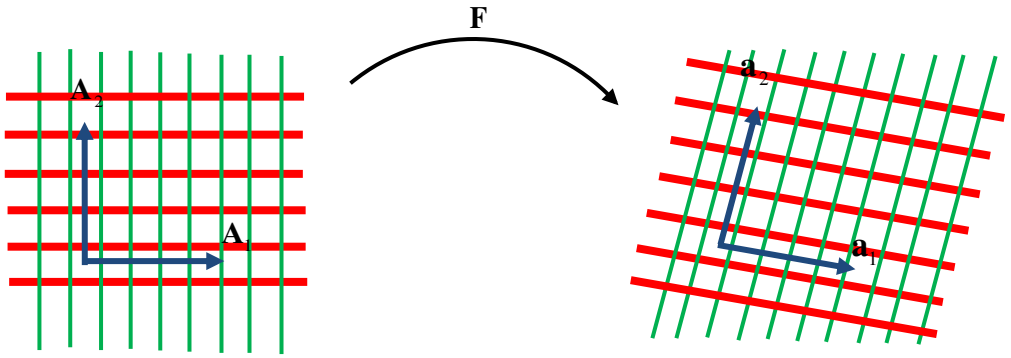

Fig. C.5.2 Top view of a piece of fabric made of two different families of reinforcing fibers (a) initial orientation (b) orientation after deformation

Next, we introduce the free energy function in terms of the invariants of the tensor $\mathbf{C}$ and the fiber directions, viz

$$W = W\left[I_1(\mathbf{C}), I_2(\mathbf{C}), I_3(\mathbf{C}), I_4(\mathbf{C}, \mathbf{A}_1), I_5(\mathbf{C}, \mathbf{A}_1), I_6(\mathbf{C}, \mathbf{A}_2), I_7(\mathbf{C}, \mathbf{A}_2), I_8(\mathbf{C}, \mathbf{A}_1, \mathbf{A}_2)\right]$$

The first three invariants account for the isotropic matrix material contribution, while the remaining invariant represents the contribution of the fiber material:

$$\begin{aligned} &I_1(\mathbf{C}) = tr\mathbf{C}, \qquad I_2(\mathbf{C}) = \frac{1}{2}\left[(tr\mathbf{C})^2 - tr(\mathbf{C}^2)\right], \quad I_3(\mathbf{C}) = \det(\mathbf{C}), \\ &I_4(\mathbf{C}, \mathbf{A}_1) = \mathbf{A}_1.\mathbf{C}\mathbf{A}_1, \quad I_5(\mathbf{C}, \mathbf{A}_1) = \mathbf{A}_1.\mathbf{C}^2\mathbf{A}_1, \qquad I_6(\mathbf{C}, \mathbf{A}_2) = \mathbf{A}_2.\mathbf{C}\mathbf{A}_2, \\ &I_7(\mathbf{C}, \mathbf{A}_2) = \mathbf{A}_2.\mathbf{C}^2\mathbf{A}_2, \qquad I_8(C, \mathbf{A}_1, \mathbf{A}_2) = (\mathbf{A}_1.\mathbf{A}_2)\mathbf{A}_1.\mathbf{C}\mathbf{A}_2 \end{aligned} \tag{C.40}$$

In the next section, we describe surfaces made of two families of fibers and introduce the four basic structures that characterize the symmetry properties of a network of fibers.

For slightly compressible materials, the free energy can be additively decoupled into volumetric, isochoric and anisotropic parts:

$$W = W_{vol}(J) + W_{iso}(I_1, I_2) + W_{ani}(I_\alpha) \tag{C.41}$$

where $\alpha = 4,5$ for the one family of fiber and $\alpha = 4,5,6,7,8$ for the two families of fibers; W_{vol}, W_{iso} and W_{ani} are the volumetric, isotropic and anisotropic deviatoric part, respectively, J is the ratio of the deformed elastic volume, $J = \det(\mathbf{F})$, I_1, I_2 and I_α are the corresponding invariants.

The constitutive equation for the second Piola Kirchhoff stress then writes,

$$S_{ij} = 2\frac{\partial W}{\partial C_{ij}} = S_{vol} + S_{iso} + S_{ani} \tag{C.42}$$

C.6. Surfaces made of two families of fibers

In what follows, we consider a surface formed by two families of fibers, as in the previous section. The fibers are continuously distributed and those of each family have the same direction in the reference configuration.

We denote by $\mathbf{A}_1$ and $\mathbf{A}_2$ are the unit vectors associated to the fiber directions in the reference configuration while $\mathbf{A}^1$ and $\mathbf{A}^2$ are their dual, such that $\mathbf{A}_i.\mathbf{A}^j = \delta_i^j$ and by $\mathbf{a}_1, \mathbf{a}_2$ the corresponding unit vectors in the current configuration. A classification of the form of the strain energy function for such reinforced materials by two families of fibers is next done, based on symmetry arguments. Details related to this approach can be found in (Giuliana Indelicato, 2008)

C.6.1. The four basic patterns: square, rectangular, rhombic and parallelogram

We now introduce the four basic structures that characterize the symmetry properties of a network of two families of fibers.

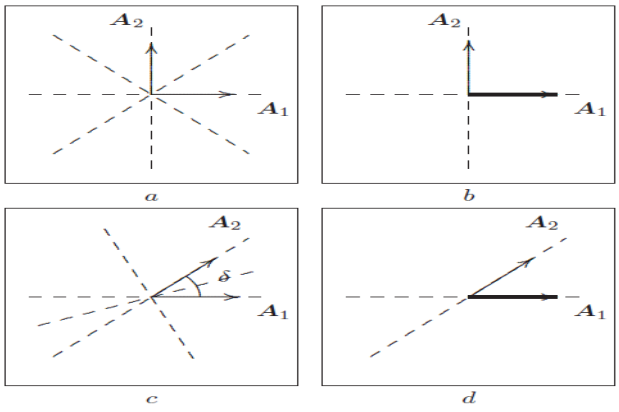

Fig. C.6.1 The four basic structure of a weave pattern. a: square, b: rectangular, c: rhombic and d: parallelogram

C.6.1.1. The square structure

In case of two families of fibers which are mutually orthogonal in the reference configuration and have the same material properties, we refer to this structure as the square structure (Figure C.6.1 a). The full symmetry group H_{sq} describing the anisotropy of this material is generated by the orthogonal transformations of $\mathbb{Z}_2$, whose matrix representation in the orthonormal basis $(\mathbf{A}_1, \mathbf{A}_2)$ is

$$\mathbf{R}_{(\pi/2)} = \begin{pmatrix} 0 & -1 \\ 1 & 0 \end{pmatrix}, \qquad \mathbf{R}_1 = \begin{pmatrix} -1 & 0 \\ 0 & 1 \end{pmatrix};$$

The set of permutations associated to the full symmetry group of the square structure is $H_{sq} = s_2$, and the corresponding homomorphism is

$$\mathbf{R}_{(\pi/2)} \mapsto (12), \qquad \mathbf{R}_1 \mapsto (1)(2),$$

with (1)(2) the identity permutation and (12) the transposition of 1 in 2. Also, the homomorphism $H \to \mathbb{Z}_2 \times \mathbb{Z}_2$ associated to the group generators is

$$\mathbf{R}_{(\pi/2)} \mapsto (\lambda(1) = 0, \lambda(2) = 1), \qquad \mathbf{R}_1 \mapsto (\lambda(1) = 1, \lambda(2) = 0).$$

C.6.1.2. The rectangular structure

In case the two families of fibers are mutually orthogonal but have different material properties so that A_1 and A_2 are not interchangeable, we refer to the resulting structure as the rectangular structure (Figure C.6.1 b). The full symmetry group describing the anisotropy of this material is generated by the two transformations

$$\mathbf{R}_1 = \begin{pmatrix} -1 & 0 \\ 0 & 1 \end{pmatrix}, \qquad \mathbf{R}_2 = \begin{pmatrix} 1 & 0 \\ 0 & -1 \end{pmatrix};$$

with R_1 and R_2 the reflections about the two axes. In this case, the fibers are not interchangeable, so that H'rt = {(1)(2)} reduces to the identity permutation. The homomorphism $H \to \mathbb{Z}_2 \times \mathbb{Z}_2$ associated to the group generators is

$$\mathbf{R}_1 \mapsto (\lambda(1) = 1, \lambda(2) = 0), \qquad \mathbf{R}_2 \mapsto (\lambda(1) = 0, \lambda(2) = 1).$$

C.6.1.3. The rhombic structure

In case of two families of fibers having the same material properties, but which are not orthogonal, we refer to the resulting structure as to the rhombic structure (Figure C.6.1 c).
The symmetry group describing the anisotropy of this material is generated by the transformations

$$\mathbf{R}_3 = \begin{pmatrix} \cos\delta & \sin\delta \\ \sin\delta & -\cos\delta \end{pmatrix}, \qquad \mathbf{R}_4 = \begin{pmatrix} \cos\delta & \sin\delta \\ \sin\delta & -\cos\delta \end{pmatrix}$$

with δ the angle between the fibers, and the matrix representation is taken in the orthonormal basis $(\mathbf{A}_1, \mathbf{A}_2)$, with j orthogonal to $\mathbf{A}_1$. Notice that $\mathbf{R}_3$ and $\mathbf{R}_4$ are the reflections about the lines bisecting the angle between A_1 and A_2, and the axis orthogonal to it.
In this case, the fibers are interchangeable, it follows that the set of permutations associated to the full symmetry group of the rhombic structure is $H'_{rb} = \{(1)(2),(1,2)\} = S_2$, and the corresponding homomorphism is

$$\mathbf{R}_3 \mapsto (12), \qquad \mathbf{R}_4 \mapsto (1)(2),$$

The homomorphism $H \to \mathbb{Z}_2 \times \mathbb{Z}_2$ associated to inversion of the fibers is

$$\mathbf{R}_3 \mapsto (\lambda(1)=0, \lambda(2)=0), \qquad \mathbf{R}_2 \mapsto (\lambda(1)=1, \lambda(2)=1).$$

C.6.1.4. The parallelogram structure

Finally, if the two families of fibers are not orthogonal and have different material properties, we have the parallelogram structure of Figure C.6.1 d. The symmetry group describing the anisotropy of this material is

$$H_{pr} = \left\{ \mathbf{I} = \begin{pmatrix} 1 & 0 \\ 0 & 1 \end{pmatrix}, -\mathbf{I} = \begin{pmatrix} -1 & 0 \\ 0 & -1 \end{pmatrix} \right\}$$

and H'pr reduces to the identity, while the homomorphism H $\to \mathbb{Z}_2 \times \mathbb{Z}_2$ is just

$$-\mathbf{I} \mapsto (\lambda(1)=1, \lambda(2)=1).$$

C.7. Application to a fibered surface without bending and twisting stiffness

We apply the above results to find a representation for the surface strain energy function of the form $W = W(\mathbf{C})$, that is invariant under the action of the material symmetry group associated to the fibers. As a first step, we neglect the bending and twisting effects in this section.

Let H be the full material symmetry group of the structure; then, according to the generalized Rychlewski's theorem (J. Rychlewski et al., 1990), the condition

$$W(\mathbf{C}) = W(\mathbf{R}\mathbf{C}\mathbf{R}^{\top}) \qquad \forall R \in H$$

is satisfied if and only if the strain energy can be written as an isotropic function $\hat{W}$ of C and the two structural tensors $\mathbf{A}_1 \otimes \mathbf{A}_1, \mathbf{A}_2 \otimes \mathbf{A}_2$

$$\hat{W}\left(Q\mathbf{C}Q^T, Q\mathbf{A}_1 \otimes \mathbf{A}_1 Q^T, Q\mathbf{A}_2 \otimes \mathbf{A}_2 Q^T\right) = \hat{W}\left(\mathbf{C}, \mathbf{A}_1 \otimes \mathbf{A}_1, \mathbf{A}_2 \otimes \mathbf{A}_2\right)$$

This strain energy function is additionally invariant under the permutations of the structure tensors corresponding to H, i.e,

$$\hat{W}\left(\mathbf{C}, \mathbf{A}_1 \otimes \mathbf{A}_1, \mathbf{A}_2 \otimes \mathbf{A}_2\right) = \hat{W}\left(\mathbf{C}, \mathbf{A}_{\sigma(1)} \otimes \mathbf{A}_{\sigma(1)}, \mathbf{A}_{\sigma(2)} \otimes \mathbf{A}_{\sigma(2)}\right)$$

In fact, the eight invariants introduced previously are needed to fully describe the material response; we know that, in general, all polynomial isotropic functions of three 2 × 2 symmetric tensors

$$f = f\left(s_1, s_2, s_3\right)$$

Can be written as a function of the basic invariants

$$tr(s_i), \quad tr(s_i^2), \quad tr(s_i s_j), \quad tr(s_i^2 s_j),$$
$$tr(s_i s_j^2), \quad tr(s_i^2 s_j^2), \quad tr(s_1 s_2 s_3).$$

Specifying to our case of absence of bending and twisting, and neglecting trivial invariants (such as $\mathbf{A}_1.\mathbf{A}_2$), we find that the elastic energy W must be a function of the following eight invariants

$$
\begin{aligned}
&\mathrm{I}_1(\mathbf{C}) = \mathrm{tr}\mathbf{C}, \quad , \quad \mathrm{I}_2(\mathbf{C}) = \det(\mathbf{C}), \quad \mathrm{I}_3(\mathbf{C}, \mathbf{A}_1) = \mathbf{A}_1.\mathbf{C}\mathbf{A}_1, \\
&\mathrm{I}_4(\mathbf{C}, \mathbf{A}_1) = \mathbf{A}_1.\mathbf{C}^2\mathbf{A}_1, \quad \mathrm{I}_5(\mathbf{C}, \mathbf{A}_2) = \mathbf{A}_2.\mathbf{C}\mathbf{A}_2, \quad \mathrm{I}_6(\mathbf{C}, \mathbf{A}_2) = \mathbf{A}_2.\mathbf{C}^2\mathbf{A}_2, \\
&\mathrm{I}_7(\mathbf{C}, \mathbf{A}_1, \mathbf{A}_2) = \left(\mathbf{A}_1.\mathbf{A}_2\right)\mathbf{A}_1.\mathbf{C}\mathbf{A}_2
\end{aligned} \tag{C.43}
$$

Now, by the standard representation for quadratic forms, one obtains

$$
\mathbf{C} = C_{11}\,\mathbf{A}^1 \otimes \mathbf{A}^1 + C_{12}\left(\mathbf{A}^1 \otimes \mathbf{A}^2 + \mathbf{A}^2 \otimes \mathbf{A}^1\right) + C_{22}\,\mathbf{A}^2 \otimes \mathbf{A}^2 \ , \ \mathbf{C}_{ij} = \mathbf{A}_i.\mathbf{C}\mathbf{A}_j
$$

Hence, the invariants become functions of the right-Cauchy Green components as

$$
\begin{aligned}
&I_1 = C_{11}\left|\mathbf{A}^1\right|^2 + 2C_{12}\mathbf{A}^1.\mathbf{A}^2 + C_{22}\left|\mathbf{A}^2\right|^2, \\
&I_2 = P\left(C_{11}, C_{12}, C_{22}\right) \\
&I_3 = C_{11}, \\
&I_4 = C_{11}^2\left|\mathbf{A}^1\right|^2 + 2C_{11}C_{12}\mathbf{A}^1.\mathbf{A}^2 + C_{12}^2\left|\mathbf{A}^2\right|^2, \\
&I_5 = C_{22} \\
&I_6 = C_{12}^2\left|\mathbf{A}^1\right|^2 + 2C_{12}C_{22}\mathbf{A}^1.\mathbf{A}^2 + C_{22}^2\left|\mathbf{A}^2\right|^2, \\
&I_7(C, \mathbf{A}_2) = \left(\mathbf{A}^1.\mathbf{A}^2\right)C_{12},
\end{aligned} \tag{C.44}
$$

with $P\ (C11,\ C12,\ C22)$ there above a second degree-polynomial in its arguments. Hence, two cases are possible:

(i) $\mathbf{A}_1.\mathbf{A}_2 = 0 \ \Leftrightarrow \mathbf{A}^1.\mathbf{A}^2 = 0$, i.e., the fibers are orthogonal (square and rectangular structures). Then (3.11) reduces to

$$
\begin{aligned}
&\mathrm{I}_1 = \mathrm{C}_{11} + \mathrm{C}_{22}, \\
&\mathrm{I}_2 = \mathrm{C}_{11}\mathrm{C}_{22} - \mathrm{C}_{12}^2 \\
&\mathrm{I}_3 = \mathrm{C}_{11}, \\
&\mathrm{I}_4 = \mathrm{C}_{11}^2 + \mathrm{C}_{12}^2, \\
&\mathrm{I}_5 = \mathrm{C}_{22} \\
&\mathrm{I}_6 = \mathrm{C}_{12}^2 + \mathrm{C}_{22}^2,
\end{aligned} \tag{C.45}
$$

So that the independent invariants are the three coefficients

$$
C_{11}, \quad C_{22}, \quad C_{12}^2 \tag{C.46}
$$

Notice that the shear coefficient C_{12} only intervenes through its square, which entails that the sign of the shear does not intervene

(ii) $A_1.A_2 \neq 0$, i.e., the fibers are not orthogonal (rhombic and parallelogram structures). In this case, (3.44) reduces to the set of independent invariants

$$C_{11}, \quad C_{22}, \quad C_{12} \tag{C.47}$$

which are exactly the components of C in the basis (A_1, A_2); here, the sign of the shear is important.

Notice that if the fibers are supposed inextensible, the equality $C_{11} = C_{22} = 1$ holds identically (in the basis made of the two fibers). Taking into account permutations, we may henceforth propose the following classification of two fibers families:

- for networks with **square symmetry**, formed by two orthogonal families of equivalent fibers, the permutation group H_{sq} is s_2 ,so that the energy is a symmetric function of C_{11} and C_{22} ,but depend from the square of C_{12} i.e.,

$$W = W\left(C_{11} + C_{22}, C_{11}C_{22}, C_{12}^2\right) \tag{C.48}$$

- for networks with **rectangular symmetry**, formed by two orthogonal families of non equivalent fibers, the permutation group H'rt is the identity, so that the energy has the form

$$W = W\left(C_{11}, C_{22}, C_{12}^2\right) \tag{C.49}$$

Notice that, in the above both cases, the restriction imposed by invariance forces the energy to depend from the square C_{12}^2, which is just $\sin^2\gamma$, with γ the angle of shear Physically, this means that a shear of angle γ has the same effect than the shear of angle −γ on the shear density.

- for networks with **rhombic symmetry**, formed by two non-orthogonal families of equivalent fibers, the permutation group $H_{rb}^{'}$ is again s_2, so that the energy is a symmetric function of C_{11} and C_{22} i.e.,

$$W = W\left(C_{11} + C_{22}, C_{11}C_{22}, C_{12}\right) \tag{C.50}$$

- In the general case of networks with parallelogram symmetry, for networks with **parallelogram symmetry**, formed by two non-orthogonal families of non equivalent fibers, the permutation group H'_{pr} is the identity, so that the energy has the form

$$W = W\left(C_{11}, C_{22}, C_{12}\right) \tag{C.51}$$

So that is is just an arbitrary function of the components of C.

In both cases above, the situation is radically different from the square and rectangular structures: since the energy depends arbitrarily on coefficient C_{12}, a shear of angle γ does no more have the same effect than the shear of angle $-\gamma$.

The previous classification shows that there are at most three independent invariants for a network of two families of fibers, consisting of the components of C in the basis of the fibers. In this representation, there is thus no split of the energy into a pure matrix contribution and contributions due to the fibers. Instead, the strain energy density has arguments reflecting directly interactions between the fibers and the matrix.Considering previous classification, there is still some freedom in the choice of the argument of the strain energy function, since one may for instance express the components C_{11}, C_{22}, C_{12} versus the eigenvalues of the $\mathbf{C}$ tensor. In the thesis of (Y. Aimene et al., 2008), the author makes different choices for the argument of the strain energy density for anisotropic hyperelastic solids reinforces by two families of fibers; the three choices of arguments of the strain energy function are shown in the following Table C.1.

Table C.1 Different sets of invariants consider as arguments of the strain energy function.

Invariants type	Strain energy function	Tension	Shear
Type 1	$W(\mathbf{C}) = \overset{\square}{W}(\mathbf{C}, \mathbf{L}_{11}, \mathbf{L}_{22})$	$\mathrm{I}_i = \mathrm{Tr}(\mathbf{C}.\mathbf{L}_{ii})\ (i = 1,2)$	$\mathrm{I}_{12} = \frac{1}{\mathrm{I}_1\mathrm{I}_2}\mathrm{Tr}(\mathbf{C}.\mathbf{L}_{11}.\mathbf{C}.\mathbf{L}_{22})$
Type 2	$W = \overset{\square}{W}(\lambda_1, \lambda_2, \cos\theta)$	$\lambda_i\,(\text{elongation})\ (i = 1,2)$	$\cos(\theta)$
Type 3	$\overset{\square}{W}(\mathbf{C}, \mathbf{L}_{11}, \mathbf{L}_{22}) = \overset{\approx}{W}(\mathrm{I}_1, \mathrm{I}_2, \mathrm{I}_{12})$	$\mathrm{I}_i = \mathrm{Tr}(\mathbf{C}.\mathbf{L}_{ii})\ (i = 1,2)$	$\mathrm{I}_{12} = \mathrm{Tr}(\mathbf{C}.\mathbf{L}_{11}.\mathbf{C}.\mathbf{L}_{22})$

where $\mathbf{L}_{ii} = L_i \otimes L_i \ (i = 1,2)$, I_1 and I_2 and I_{12} are the structural tensors of the two fiber directions L_1,L_2, the tension invariants and the shear invariant respectively.

Focusing on the type two, we express the strain energy function of a surface made of two families of intersecting fibers based on the invariants $\lambda_1, \lambda_2, \cos\theta$, viz

$$W = \bar{W}(\lambda_1, \lambda_2, \cos\theta)$$

where λ_1, λ_2 are the elongations in two directions and $\cos\theta$ is the angle between the two fiber directions. After several steps and choosing a polynomial function of the strain energy in terms of the elongation λ_1, λ_2 for the first part, and a polynomial function of the cosine of angle θ in the expression of the shear strain energy delivers the strain energy function

$$\bar{W} = \sum_{\alpha=0}^{m} \frac{1}{\alpha+2} a_\alpha \left(\lambda_1^{\alpha+2} - 1\right) + \sum_{\beta=0}^{n} \frac{1}{\beta+2} b_\beta \left(\lambda_2^{\beta+2} - 1\right) + \sum_{\gamma=0}^{p} \frac{1}{\gamma+1} c_\gamma \cos^{\gamma+1}\theta$$

The derivative of the strain function with respect to the strain gives the Second Piola-Kirchhoff stress as

$$S_{ij} = 2\frac{\partial \bar{W}}{\partial C_{ij}} = 2\left(\frac{\partial \bar{W}_1}{\partial \lambda_1}\frac{\partial \lambda_1}{\partial C} + \frac{\partial \bar{W}_2}{\partial \lambda_2}\frac{\partial \lambda_2}{\partial C} + \frac{\partial \bar{W}_c}{\partial \cos\theta}\frac{\partial \cos\theta}{\partial C}\right)$$

$$S_{11} = \sum_{\alpha=0}^{m} a_\alpha \lambda_1^\alpha - \frac{\cos\theta}{\lambda_1^2}\sum_{\gamma=0}^{p} c_\gamma \cos^\gamma\theta \qquad \text{(C.52)}$$

$$S_{22} = \sum_{\alpha=0}^{m} b_\beta \lambda_2^\beta - \frac{\cos\theta}{\lambda_2^2}\sum_{\gamma=0}^{p} c_\gamma \cos^\gamma\theta \qquad \text{(C.53)}$$

$$S_{12} = \frac{1}{\lambda_1\lambda_2}\sum_{\gamma=0}^{p} c_\gamma \cos^\gamma\theta \qquad \text{(C.54)}$$

The three unknown sets of constants a_α , b_β and c_γ of this phenomenological constitutive model written at the mesoscopic scale of a continuum shall be identified for dry textile monolayers in the second part of this chapter, based on numerical results of the homogenization of the fibrous microstructure. Before that, we expose a review of the modeling approaches of woven fabrics.

Appendix D: Methodology Used to Express the Transverse Forces and Hyper Forces in the Second Order Gradient Model

Contents

Appendix

.1. *D1. Application of the principle of virtual power for the writing of the resultant and moments*

In case of a beam loaded by a distribution of efforts $\{\mathbf{F}(s)\}$ along the mean line parameterized by the curvilinear abscissa s, the local equilibrium equations write

$$\left\{\frac{d\mathbf{T}(s)}{ds}\right\} + \{\mathbf{F}(s)\} = \{\mathbf{A}(s)\} \tag{.1}$$

The edge conditions at the terminal abscissa $s1$ and $s2$ of the beam write

$$\{\mathbf{T}(s1)\} = -\{\mathbf{F}(s1)\} \tag{.2}$$

and

$$\{\mathbf{T}(s2)\} = +\{\mathbf{F}(s2)\} \tag{.3}$$

One can perform the comment of any torsor $\{\mathbf{V}^*(s)\}$, and integrate over the beam length for equation .1. In equations .2 et .3, one can sum the product with the terms $\{\mathbf{V}^*(s1)\}$ and $\{\mathbf{V}^*(s2)\}$. This leads to the following formulation, often coined the principal of virtual power:

$$\int_{s1}^{s2}\left[\left\{\frac{d\mathbf{T}(s)}{ds}\right\} + \{\mathbf{F}(s)\} - \{\mathbf{A}(s)\}\right]\otimes\{\mathbf{V}^*(s)\}\,ds + [\{\mathbf{T}(s1)\} + \{\mathbf{F}(s1)\}]\otimes\{\mathbf{V}^*(s1)\} + [-\{\mathbf{T}(s2)\} + \{\mathbf{F}(s2)\}]\otimes\{\mathbf{V}^*(s12)\} = 0 \tag{.4}$$

Integrating by part the term $\int_{s1}^{s2}\left\{\frac{d\mathbf{T}(s)}{ds}\right\}\otimes\{\mathbf{V}^*(s)\}\,ds$, one can notice:

$$\int_{s1}^{s2}\left\{\frac{d\mathbf{T}(s)}{ds}\right\}\otimes\{\mathbf{V}^*(s)\}\,ds = \{\mathbf{T}(s2)\}\otimes\{\mathbf{V}^*(s2)\} - \{\mathbf{T}(s1)\}\otimes\{\mathbf{V}^*(s1)\} - \int_{s1}^{s2}\{\mathbf{T}(s)\}\otimes\left\{\frac{d\mathbf{V}^*(s)}{ds}\right\}ds \tag{.5}$$

Inserting then previous development .5 into equation .4, one notices that the edge contributions cancel to deliver a simpler expression of the form

$$-\int_{s1}^{s2}\{\mathbf{T}(s)\}\otimes\left\{\dot{\mathbf{D}}^*(s)\right\}ds + \int_{s1}^{s2}\{\mathbf{F}(s)\}\otimes\left\{V^*(s)\right\}ds + \sum_i\{\mathbf{F}(s_i)\}\otimes\{\mathbf{V}^*(s_i)\} = \int_{s1}^{s2}\{\mathbf{A}(s)\}\otimes\{\mathbf{V}^*(s)\}\,ds \tag{.6}$$

denoting therein $\left\{\frac{d\mathbf{V}^*(s)}{ds}\right\} = \left\{\dot{\mathbf{D}}^*(s)\right\}$. The first term corresponds to the virtual power of the inter-efforts, the second one to the virtual power of line efforts; the right-hand side includes the virtual power of acceleration quantities. This last

equation .6 is the point of departure of the approximate solution method by finite elements.

.2. *D2.Application of the FE method to beams*

A few authors present equation .6 under the virtual work principle, replacing the virtual velocity $\{\mathbf{V}^*(s)\}$ by the virtual displacement $\{\mathbf{U}^*(s)\}$, corresponding to the integration of $\{\mathbf{V}^*(s)\}$ during an interval of time dt. We can then write the following equation

$$-\int_{s1}^{s2}\{\mathbf{T}(s)\}\otimes\{\mathbf{D}^*(s)\}\,ds+\int_{s1}^{s2}\{\mathbf{F}(s)\}\otimes\{\mathbf{U}^*(s)\}\,ds+\sum_i\{\mathbf{F}(s_i)\}\otimes\{\mathbf{U}^*(s_i)\}=\int_{s1}^{s2}\{\mathbf{A}(s)\}\otimes\{\mathbf{U}^*(s)\}\,ds \tag{.7}$$

We assume no line effort, and restrict to the static situation; equation .7 then simplifies to

$$-\int_{s1}^{s2}\{\mathbf{T}(s)\}\otimes\{\mathbf{D}^*(s)\}\,ds+\sum_i\{\mathbf{F}(s_i)\}\otimes\{\mathbf{U}^*(s_i)\}=0 \tag{.8}$$

The virtual work of inter-efforts is equal to the work of external nodal forces; accounting for the small displacements torsor, the small strains torsor $\{\mathbf{D}(s)\}$ writes

$$\{\mathbf{U}(s)\}=\left\{\begin{matrix}\alpha\ \beta\ \phi\\ u\ v\ w\end{matrix}\right\}\Longrightarrow\{\mathbf{D}(s)\}=\left\{\frac{d\mathbf{U}(s)}{ds}\right\}=\left\{\begin{matrix}\frac{d\alpha}{ds} & \frac{d\beta}{ds} & \frac{d\phi}{ds}\\ \frac{du}{ds} & \frac{dv}{ds}-\phi & \frac{dw}{ds}+\beta\end{matrix}\right\} \tag{.9}$$

Under Bernoulli beam assumption, this torsor simplifies, as two of its components can be considered as nil

$$\{\mathbf{D}(s)\}=\left\{\begin{matrix}\frac{d\alpha}{ds} & -\frac{d^2w}{ds^2} & \frac{d^2v}{ds^2}\\ \frac{du}{ds} & 0 & 0\end{matrix}\right\} \tag{.10}$$

In the same manner, we can write the torsor of the virtual strain

$$\{\mathbf{D}^*(s)\}=\left\{\begin{matrix}\frac{d\alpha^*}{ds} & -\frac{d^2w^*}{ds^2} & \frac{d^2v^*}{ds^2}\\ \frac{du^*}{ds} & 0 & 0\end{matrix}\right\} \tag{.11}$$

The left hand side of equation .8, representing the virtual work principle then writes as

$$W_i^* = -\int_{s1}^{s2} \{\mathbf{T}(s)\} \otimes \{\mathbf{D}^*(s)\}\, ds$$
$$= -\int_{s1}^{s2} \left\{ M_t \frac{d\alpha^*}{ds} - M_{fz} \frac{d^2w^*}{ds^2} + M_{fy} \frac{d^2v^*}{ds^2} + N \frac{du^*}{ds} \right\} ds$$
$$= -\int_{s1}^{s2} \left\{ GI_0 \frac{d\alpha}{ds}\frac{d\alpha^*}{ds} - EI_z \frac{d^2w}{ds^2}\frac{d^2w^*}{ds^2} + EI_y \frac{d^2v}{ds^2}\frac{d^2v^*}{ds^2} + ES \frac{du}{ds}\frac{du^*}{ds} \right\} ds \quad (.12)$$

.3. *D3.Discretization of the beam problem*

For a 2D beam subjected to traction-compression and flexion, with local axes $(\mathbf{x}_p, \mathbf{y}_p, \mathbf{z}_p)$, and under flexion in the $\mathbf{x}O\mathbf{y}$ plane, each of the node has three degrees of freedom, pictured in figure ??: two translations along the (two) beam axes, $\mathbf{x}_p$, $\mathbf{y}_p$, and the rotation around the axis orthogonal to the plane $\mathbf{z}_p$. The vector of d.o.f. is of dimension 6, as well as the load vector, and thus the stiffness matrix is of size 6x6.

The beam section is considered as constant, and the neutral axis is supposed to have the required symmetries so that the torsion center and gravity center coincide. The beam is supposed to be slender enough to neglect the deformation due to transverse shear, thus Bernoulli beam kinematics holds. According to those assumptions, the beam behavior is the superposition of two simple independent behaviors: traction-compression and flexion in the principal plane; one can separate both behaviors to construct the rigidity matrix.

.4. *D4.Beam under traction-compression*

Although the result is simple and well-known in this loading situation, the methodology proves useful to treat next the more complex case of a beam undergoing pure flexion. For a beam submitted to a concentrated tension $N\mathbf{x}_p$ in the direction of its axis $\mathbf{x}_p$, the only deformations arise from the component $\mathbf{u}$ of the torsor of small displacements

$$\{\mathbf{U}(x)\} = \left\{ \begin{array}{c} \psi = 0 \\ \mathbf{u} = u(x)\mathbf{x} \end{array} \right\} \Rightarrow \{\mathbf{D}(x)\} = \left\{ \begin{array}{c} \gamma = 0 \\ \varepsilon = \dfrac{du(x)}{dx}\mathbf{x} \end{array} \right\} \quad (.13)$$

The virtual work of inter-efforts is evaluated as

$$W_i^* = \int_{s1}^{s2} \left\{ ES \frac{du}{ds}\frac{du^*}{ds} \right\} ds \quad (.14)$$

One selects a displacement field expressing versus the displacements of nodes 1 and 2; since there are two d.o.f., a linear displacement field involving two constants is considered:

$$u(x) = ax + b \tag{.15}$$

with the following edge conditions

$$u(0) = u1 \text{ et } u(L) = u2$$

thus giving

$$u(x) = u1\frac{L-x}{L} + u2\frac{x}{L} = [\phi(x)]\,[\mathbf{U}] \tag{.16}$$

denoting

$[\mathbf{U}] = \begin{bmatrix} u1 \\ u2 \end{bmatrix}$

the column vector of displacements and the vector of shape functions

$[\phi(x)] = \begin{bmatrix} \frac{L-x}{L} & \frac{x}{L} \end{bmatrix}$,

the row of the shape functions of the element. The derivative $\frac{du(x)}{dx}$ is easily calculated as

$$\frac{du(x)}{dx} = -u1\frac{1}{L} + u2\frac{1}{L} = [\psi]\,[\mathbf{U}] \tag{.17}$$

We notice that the terms of $[\psi]$ are constants. It is easy to next integrate the virtual work of inter-efforts

$$W_i^* = -\int_0^L ES\,[\mathbf{U}]^t\,[\psi]^t\,[\psi]\,[\mathbf{U}^*]\,dx = -ELS\,[\mathbf{U}]^t\,[\psi]^t\,[\psi]\,[\mathbf{U}^*] \tag{.18}$$

One next notes $[\mathbf{K}_{tc}]$ the square matrix obtained by

$$[\mathbf{K}_{tc}] = ELS\,[\psi]^t\,[\psi] \tag{.19}$$

The product $[\psi]^t\,[\psi]$ is evaluated as

$$[\psi]^t\,[\psi] = \frac{1}{L^2}\begin{bmatrix} 1 & -1 \\ -1 & 1 \end{bmatrix} \tag{.20}$$

Finally, the virtual work of inter-efforts writes under traction-compression as

$$W_i^* = [\mathbf{U}]^t\,[K_{tc}]\,[\mathbf{U}^*] \tag{.21}$$

with

$$[\mathbf{K}_{tc}] = \frac{ES}{L}\begin{bmatrix} 1 & -1 \\ -1 & 1 \end{bmatrix} \tag{.22}$$

Regarding the virtual work of external forces, since we do only consider concentrated forces at the nodes, the formulation is quite simple:

$$W_e^* = \sum_i \{\mathbf{F}(s_i)\} \otimes \{\mathbf{U}^*(s_i)\} = \sum_i N_i u_i^* = [\mathbf{F}]^t [\mathbf{U}^*] \tag{.23}$$

with $[\mathbf{F}]$ the column of nodal forces.

.5. *D5.Beam under flexion*

In the case of a beam undergoing flexion, four kinematic conditions are available at the nodes:

$v(0) = v1$; $v(L) = v2$; $\frac{dv}{dx}(0) = \phi 1$; $\frac{dv}{dx}(L) = \phi 2$

In this condition, it is necessary to consider a third order displacement function, involving four constants:

$$v(x) = ax^3 + bx^2 + cx + d \Rightarrow \frac{dv(x)}{dx} = 3ax^2 + 2bx + c \tag{.24}$$

One obtains the constants from the initial conditions:

$c = \phi 1$; $d = v1$;

$a = \frac{2}{L^3}(v1 - v2) + \frac{1}{L^2}(\phi 1 + \phi 2)$; $b = -\frac{3}{L^2}(v1 - v2) - \frac{1}{L}(2\phi 1 + \phi 2)$

This leads to the matrix like expression of the vertical displacement

$$v(x) = \left[1 - 3\xi^2 + 2\xi^3 \; L\left(\xi - 2\xi^2 + \xi^3\right) \; 3\xi^2 - 2\xi^3 \; L\left(-\xi^2 + \xi^3\right)\right] \begin{bmatrix} v1 \\ \phi 1 \\ v2 \\ \phi 2 \end{bmatrix} = [\phi(x)]\,[\mathbf{U}] \tag{.25}$$

with $\xi = \frac{x}{L}$.

In the expression of the work of internal forces, one needs the following second ordre derivative

$$\frac{d^2v(x)}{dx^2} = \left[\frac{6}{L^2}(-1 + 2\xi) \; \frac{2}{L}(-2 + 3\xi) \; \frac{6}{L^2}(1 - 2\xi) \; \frac{2}{L}(-1 + 3\xi)\right] \begin{bmatrix} v1 \\ \phi 1 \\ v2 \\ \phi 2 \end{bmatrix} = [\psi(x)]\,[\mathbf{U}] \tag{.26}$$

The terms therein are no more constants, so that one has to integrate these functions over the element to derive the expression of the virtual work:

$$W_i^* = -\int_0^L EI \frac{d^2v}{dx^2}\frac{d^2v^*}{dx^2}dx = -EI\,[\mathbf{U}]^t \int_0^L [\psi(x)]^t\,[\psi(x)]\,dx\,[\mathbf{U}^*] \tag{.27}$$

The square stiffness matrix for flexion $[\mathbf{K}_{fl}]$ is obtained as

$$[\mathbf{K}_{fl}] \quad = \quad -EI\int_0^L [\psi(x)]^t\,[\psi(x)]\,dx \quad = \quad \frac{EI}{L^3}\begin{bmatrix} 12 & 6L & -12 & 6L \\ 6L & 4L^2 & -6L & 2L^2 \\ -12 & -6L & 12 & -6L \\ 6L & 2L^2 & -6L & 4L^2 \end{bmatrix} \tag{.28}$$

By assembling the two matrices $[\mathbf{K}_{tc}]$ and $[\mathbf{K}_{fl}]$, we obtain the elementary stiffness matrix in the local system of axes $\mathbf{K}$, so that the virtual work principle writes

$$W_i^* + W_e^* = 0 \tag{.29}$$

$$\Rightarrow [\mathbf{U}]^t\,[\mathbf{K}]\,[\mathbf{U}^*] = [\mathbf{F}]^t\,[\mathbf{U}^*] \tag{.30}$$

Previous relation is valid for any $[\mathbf{U}^*]$, and can thus be rewritten under the form

$$[\mathbf{K}]\,[\mathbf{U}] = [\mathbf{F}] \tag{.31}$$

with

$$[\mathbf{U}] = \begin{bmatrix} u1 \\ v1 \\ \phi 1 \\ u2 \\ v2 \\ \phi 2 \end{bmatrix};\ [\mathbf{F}] = \begin{bmatrix} F1x \\ F1y \\ M1z \\ F2x \\ F2y \\ M2z \end{bmatrix}$$

$$[\mathbf{K}] = \begin{bmatrix} \frac{ES}{L} & 0 & 0 & -\frac{ES}{L} & 0 & 0 \\ 0 & \frac{12EI}{L^3} & \frac{6EI}{L^2} & -\frac{12EI}{L^3} & 0 & \frac{6EI}{L^2} \\ 0 & \frac{6EI}{L^2} & \frac{4EI}{L} & -\frac{6EI}{L^2} & 0 & \frac{2EI}{L} \\ -\frac{ES}{L} & 0 & 0 & \frac{ES}{L} & 0 & 0 \\ 0 & -\frac{12EI}{L^3} & -\frac{6EI}{L^2} & \frac{12EI}{L^3} & 0 & -\frac{6EI}{L^2} \\ 0 & \frac{6EI}{L^2} & \frac{2EI}{L} & -\frac{6EI}{L^2} & 0 & \frac{4EI}{L} \end{bmatrix} \tag{.32}$$

Part III

Résumé des Travaux en Langue Française

CHAPITER Huit: Comportement mécanique nonlinéaire de milieux fibreux par des méthodes d'homogénéisation discrète.

CHAPITER Huit

Comportement Mécanique Nonlinéaire de Milieux Fibreux par des Méthodes d'Homogénéisation Discrète

Contents

8.1 Introduction

L'objectif de ce chapitre est de développer une nouvelle méthodologie pour homogénéiser le comportement mécanique de structures d'architecture discrète, dont la géométrie change en raison des déplacements et rotations importants subis par les éléments structuraux lors de l'application d'un chargement externe. Les structures envisagées peuvent être assimilées en général à des réseaux de poutres quasi périodiques. Les applications concernent aussi bien les milieux fibreux artificiels (les tissages 2D et 3D en construction mécanique et en aéronautique) que naturels (les membranes biologiques, l'os trabéculaire), que des structures reconfigurables (antennes déployables de grande taille, structure interne d'ailes d'avion à géométrie variable). Le calcul de ces structures de grande taille à un coût qui peut être prohibitif en raison du grand nombre de degrés de liberté présent ; aussi est-t'il préférable de remplacer ces structures par un milieu homogénéisé continu doté de propriétés effectives.

Les modifications de géométrie que subissent ces structures nécessitent de prendre en compte les grandes transformations dans les lois de comportement homogénéisées (effectives), ce qui constitue l'aspect novateur principal de la thèse. Nous proposons une nouvelle approche qui repose sur les équations de poutres à l'échelle microscopique d'un volume élémentaire représentatif, qui sont ensuite homogénéisées dans un contexte de nonlinéarités de nature géométrique, afin de construire par un schéma d'homogénéisation discret asymptotique la réponse de la structure, vue comme un milieu continu. Les modèles d'homogénéisation développés ont vocation à traiter a priori autant les nonlinéarités matérielles que géométrique ; en raison des faibles déformations des éléments structuraux (les modules de traction sont d'un ou plusieurs ordres de grandeur supérieur aux modules de flexion), il est cependant raisonnable de négliger les nonlinéarités matérielles, pour ne considérer que les nonlinéarités géométrique.

Une classification des milieux continus effectifs visés est proposée dans ce travail, en fonction des échelles de longueur relatives présentes. Nous considérons dans ce chapitre des milieux continus de type micropolaire, qui comportent un degré de liberté en translation et en rotation.

8.2 Equations de poutres dans un contexte de nonlinéarités géométriques

On note $\mathbf{B}_o$ la configuration de référence de chaque poutre du réseau ; on écrit tout d'abord la cinématique des poutres, afin d'en déduire des expressions des résultantes et des moments pour chaque élément de poutre. La torsion et le gauchissement de la section ne sont pas pris en compte. Après de longs calculs et en considérant uniquement l'expansion au premier ordre de la série de Taylor des fonctions trigonométriques (Klaus Jurgen Bathe and Said Bolourchi, 1979), les forces et les moments résultant peuvent s'écrire :

$$
\begin{aligned}
&N = E_s A\left(u^{'} + \frac{1}{2}\left(u^{'2} + v^{'2}\right) + \frac{\omega_3^2}{2} - \frac{1}{2}\left(\varepsilon_{01}^2 + \varepsilon_{02}^2 + \varepsilon_{03}^2\right)\right) + E_s I_z\left(\omega_3^{'2} - \kappa_{03}^2\right)\\
&T_y = GA\left(\left|\omega_3\right|\left(1+u^{'}\right) + v^{'} - \varepsilon_{02}\right)\\
&T_z = -GA(\varepsilon_{03})\\
&M_x = 0, \qquad M_y = 0\\
&M_z = -E_s I_z\left(\omega_3^{'}\left(1+u^{'}\right) - \left|\omega_3\right| v^{'} + \varepsilon_{01}\kappa_{03}\right)
\end{aligned}
\tag{8.1}
$$

Ces expressions sont générales dans un contexte de réponse élastique nonlinéaire. Cependant, afin de pouvoir appliquer la méthode d'homogénéisation asymptotique, des simplifications sont apportées : on considère des poutres initialement rectilignes, d'où il résulte l'absence de déformations et de courbures initiales, ce qui implique la nullité des variables $\varepsilon_{01}, \varepsilon_{02}, \varepsilon_{03}, \kappa_{03}$. On déduit alors des expressions précédentes les relations discrètes correspondantes en replaçant les dérivées par rapport à l'abscisse curviligne par des différences finies, afin de transformer le problème continu initial en un système d'expressions discrètes en vue du schéma d'homogénéisation :

$$
\begin{aligned}
&N = E_s A\left(\frac{\Delta\mathbf{U}\cdot\mathbf{e}^b}{l} + \frac{1}{2}\left(\frac{\left(\Delta\mathbf{U}\cdot\mathbf{e}^b\right)^2}{l^2} + \frac{\left(\Delta\mathbf{U}\cdot\mathbf{e}^{b\perp}\right)^2}{l^2}\right) + \frac{\psi_c^2}{2}\right) + E_s I_z\left(\frac{\Delta\psi_c}{2}\right)^2\\
&T_y = GA\left(\psi_c\left(1 + \frac{\Delta\mathbf{U}\cdot\mathbf{e}^b}{l}\right) + \frac{\left(\Delta\mathbf{U}\cdot\mathbf{e}^{b\perp}\right)}{l}\right)\\
&M_z = -E_s I_z\left(\frac{\Delta\psi}{l}\left(1 + \frac{\Delta\mathbf{U}\cdot\mathbf{e}^b}{l}\right) - \psi_c\frac{\left(\Delta\mathbf{U}\cdot\mathbf{e}^{b\perp}\right)}{l}\right)
\end{aligned}
\tag{8.2}
$$

On a introduit dans ces expressions les variables suivantes : A est la section de la poutre, l sa longueur, I_z le moment quadratique, $\mathbf{e}^b$ et $\mathbf{e}^{b\perp}$ les vecteurs unitaires directeurs et normal à l'élément de poutre respectivement, E_s et G les modules de traction et de cisaillement, et ψ_c la rotation du nœud central de chaque élément de poutre.

8.3 Méthode d'homogénéisation discrète

L'homogénéisation discrète est une technique mathématique pour construire le comportement d'un milieu continu homogénéisé représentatif d'un réseau de poutres quasi périodique constitué de la répétition d'un motif élémentaire. Cette technique est inspirée de l'homogénéisation de milieux continus périodiques développée dans les années 1980 par différents auteurs ((Sanchez, 1980; Bakhvalov et Panasenko, 1989) et plus récemment (Warren and Byskhov, 2002; Mourad and Caillerie, 2003; D. Caillerie et al., 2006; Raoult et al., 2008; Dos Reis and Ganghoffer, 2012 ; Pradel et Sab, 1998 ; Pindera et al., 2009; Charalambakis, 2010, Warren et al.,1989; Warren and Kraynik, 1991 ; Wang and Cuitino, 2000 ; Hohe and Beecker, 2003 ; (Janus Michalska and Pecherski, 2003; Janus Michalska, 2005, 2011 ; Andrea et al., 2014). Elle consiste en l'écriture de développements asymptotiques des variables cinématiques à l'échelle des nœuds du treillis de poutres en fonction d'un petit paramètre ε, rapport de la taille de la cellule de base à une dimension macroscopique du treillis, qui sont ensuite insérées dans les expressions des variables statiques (forces et moments).

Les équations d'équilibre des forces et des moments sont ensuite écrites sous forme de puissances virtuelles discrètes, et sont finalement converties dans la limite $\varepsilon \to 0$ en des intégrales de Riemann continues, faisant ainsi apparaitre des mesures continues de contraintes et de déformation ainsi que la loi de comportement homogénéisée.

8.3.1 Modèle de poutre simplifié

On néglige dans ce qui suit la partie nonlinéaire de la déformation ainsi que le couplage entre déplacement et rotation dans (2.44). On peut alors écrire les expressions de l'effort normal et transverse, ainsi que le moment aux extrémités de chaque poutre $\mathrm{M}^{\mathrm{O(b)\varepsilon}}$ et $\mathrm{M}^{\mathrm{E(b)\varepsilon}}$, en fonction des variables cinématiques nodales, selon

$$
\begin{aligned}
N^{\varepsilon} &= \frac{E_s\, t}{l^{\varepsilon b}}\left[\left(\Delta \mathbf{U}^{b\varepsilon}.\mathbf{e}^{b}\right)\right] \\
T_t^{\varepsilon} &= \frac{12E_s I_z}{\left(l^{\varepsilon b}\right)^3}\left[\left(\Delta \mathbf{U}^{b\varepsilon}\cdot\mathbf{e}^{b\perp}\right)-\frac{l^{\varepsilon b}}{2}\left(\phi^{O(b)\varepsilon}+\phi^{E(b)\varepsilon}\right)\right] \\
M^{O(b)\varepsilon} &= \frac{-12E_s I_z}{\left(l^{\varepsilon b}\right)^3}\left[\left(\left(\frac{l^{\varepsilon b}}{2}\right)\left(\Delta \mathbf{U}^{b\varepsilon}\cdot\mathbf{e}^{b\perp}\right)\right)+\left(\frac{\left(l^{\varepsilon b}\right)^2}{6}\right)\left(2\phi^{O(b)\varepsilon}+\phi^{E(b)\varepsilon}\right)\right] \\
M^{E(b)\varepsilon} &= \frac{-12E_s I_z}{\left(l^{\varepsilon b}\right)^3}\left[\left(\left(\frac{l^{\varepsilon b}}{2}\right)\left(\Delta \mathbf{U}^{b\varepsilon}\cdot\mathbf{e}^{b\perp}\right)\right)+\left(\frac{\left(l^{\varepsilon b}\right)^2}{6}\right)\left(\phi^{O(b)\varepsilon}+2\phi^{E(b)\varepsilon}\right)\right]
\end{aligned}
\tag{8.3}
$$

Les details relatifs à la méthode asymptotique sont exposés dans (F. Dos Reis, 2010).

8.3.2 Position du Problème

Le treillis est décrit par la répétition périodique d'un motif élémentaire constitué d'un assemblage de poutres, et il est parfaitement décrit par la position des nœuds et leur connectivité. On note N_R et B_R respectivement les ensembles de nœuds et de poutres au sein de la cellule unité de référence. Le treillis est supposé périodique dans sa configuration déformée. Les cellules sont numérotées par le triplet d'entiers $\upsilon^i = \left(\upsilon^1, \upsilon^2, \upsilon^3\right)$; les noeuds du treillis sont alors paramétrés par le quadruplet $\tilde{n} = \left(n, \upsilon^1, \upsilon^2, \upsilon^3\right) \in N_R \times \square^3$. De la même façon, les poutres du treillis sont numérotées par le quadruplet $\tilde{b} = \left(b, \upsilon^1, \upsilon^2, \upsilon^3\right) \in B_R \times \square^3$. On peut sélectionner un nœud origine dans la cellule de référence, soit $O(\tilde{b})$, positionné par le quadruplet $\left(n, \upsilon^1, \upsilon^2, \upsilon^3\right)$. Le nœud extrémité $E(\tilde{b})$ n'appartient pas nécessairement à la cellule de référence, mais à une cellule adjacente $\left(\upsilon^1+\delta^1, \upsilon^2+\delta^2, \upsilon^3+\delta^3\right)$, avec le triplet $\left(\delta^1, \delta^2, \delta^3\right) \in \square^3$ et où l'entier $\delta^i \in \{-1, 0, 1\}$ indique la translation vers la cellule adjacente correspondante. On néglige les forces d'inertie, soit on considère un équilibre statique. L'équilibre de chaque poutre au sein du réseau se traduit par l'équation $T^{E(b)} = -T^{O(b)}$ (Fig. 8.1).

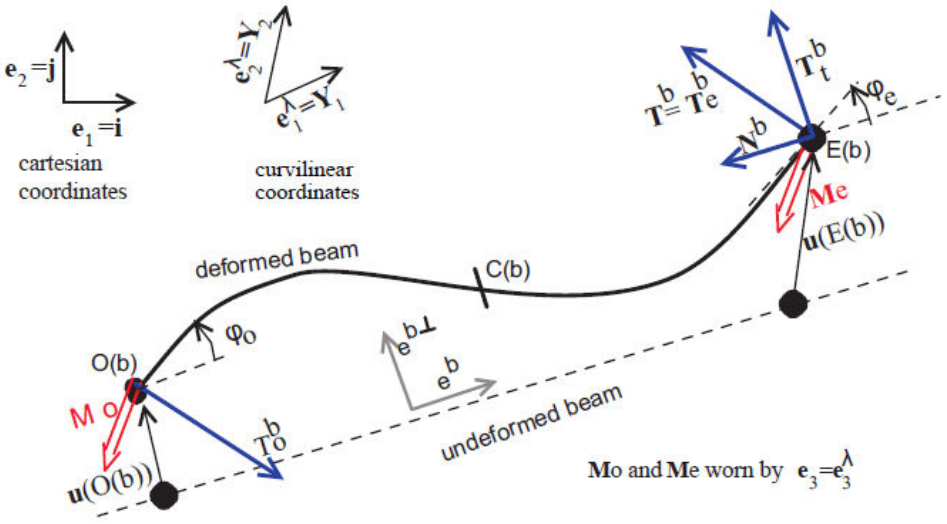

Figure 8.1. Grandeurs cinématiques et statiques pour une poutre

L'équilibre des forces s'écrit après insertion des développements asymptotiques des variables cinématiques selon

$$\sum_{v^i \in \mathbb{R}^3} \sum_{b \in B_R} T^{\varepsilon b} . \left(\mathrm{v}^{\varepsilon} \left(O(b) \right) - \mathrm{v}^{\varepsilon} \left(E(b) \right) \right) = 0 \tag{8.4}$$

Avec v^{ε} (.) un champ de vitesse virtuel, choisi nul sur les bords du réseau, et $\mathrm{T}^{\varepsilon b}$ le vecteur qui assemble la somme des résultantess, et qui se décompose en un effort normal N^{ε} et transverse T_t^{ε}, soit :

$$T^b = N^b \mathbf{e}^b + T_t^b \mathbf{e}^{b\perp} \tag{8.5}$$

Pour tout champ de vitesse virtuel assez régulier v^{ε}, un développement en série de Taylor conduit à

$$\mathrm{v}^{\varepsilon} \left(O(b) \right) - \mathrm{v}^{\varepsilon} \left(E(b) \right) \approx \varepsilon \frac{\partial \mathrm{v} \left(\lambda^{\varepsilon} \right)}{\partial \lambda^{\mathrm{i}}} \delta^{ib} \tag{8.6}$$

L'équilibre des moments s'écrit de façon similaire selon

$$\sum_{v^i \in \mathbb{R}^3} \sum_{b \in B_R} \left(\mathrm{M}^{O(b)\varepsilon} . \mathrm{w}^{\varepsilon} \left(O(b) \right) + \mathrm{M}^{E(b)\varepsilon} . \mathrm{w}^{\varepsilon} \left(E(b) \right) + \varepsilon L^b \left(\mathbf{e}^b \wedge \mathrm{T}^{\varepsilon b} \right) . \mathrm{w}^{\varepsilon} \left(C(b) \right) \right) = 0 \tag{8.7}$$

avec w(C(b)) la vitesse de rotation virtuelle du noeud central de chaque pouter ; on écrit les développements suivants des taux de rotation virtuels :

$$\mathrm{w}^{O(b)\varepsilon} = \mathrm{w}_0(\lambda^{\varepsilon})$$

$$\mathrm{w}^{E(b)\varepsilon}(\lambda + \varepsilon\delta^i) \approx \mathrm{w}_0(\lambda) + \varepsilon \frac{\partial w_0(\lambda)}{\partial \lambda^i}\delta^{ib} \qquad (8.9)$$

$$\mathrm{w}^{C(b)\varepsilon} = \frac{1}{2}\left(\mathrm{w}^{E(b)\varepsilon} + \mathrm{w}^{O(b)\varepsilon}\right)$$

8.3.3 Description de la géométrie du treillis

La méthode d'homogénéisation asymptotique requiert le développement de toutes les variables en série de Taylor, soit la longueur de la poutre $\mathrm{l}^{\varepsilon b}$ (uniquement en grandes perturbations), sa largeur $\mathrm{t}^{\varepsilon b}$, son épaisseur $\mathrm{e}^{\varepsilon b}$, le déplacement $\mathrm{u}^{\varepsilon n}$ et la rotation des nœuds tu réseau $\phi^{\varepsilon n}$ en fonction du petit paramètre ε. On peut selon (A. Mourad, 2003) écrire

$$l^{\varepsilon b} = \varepsilon l^{bo}\left(\lambda^{\varepsilon}\right) + \varepsilon^2 l^{b1}\left(\lambda^{\varepsilon}\right) + - - \qquad (8.10)$$

$$e^{\varepsilon b} = e^{bo}\left(\lambda^{\varepsilon}\right) + \varepsilon e^{b1}\left(\lambda^{\varepsilon}\right) + - - - \qquad (8.11)$$

La difference de déplacement $\Delta\mathbf{U}^{\mathrm{b}\varepsilon}$ entre les noeuds d'extrémité de chaque poutre s'exprime selon

$$\Delta\mathbf{U}^{\mathrm{b}\varepsilon} = \mathbf{u}^{\varepsilon}(E(b)) - \mathbf{u}^{\varepsilon}(O(b)) = \varepsilon \underbrace{\left(\mathbf{u}_1^{E_{R(b)}}\left(\lambda^{\varepsilon}\right) - \mathbf{u}_1^{O_{R(b)}}\left(\lambda^{\varepsilon}\right) + \frac{\partial \mathbf{u}_0\left(\lambda^{\varepsilon}\right)}{\partial \lambda^i}\delta^{ib}\right)}_{\Delta\mathrm{U}_1^{\mathrm{b}}} + \varepsilon^2 \underbrace{\left(\mathbf{u}_2^{E_{R(b)}}\left(\lambda^{\varepsilon}\right) - \mathbf{u}_2^{O_{R(b)}}\left(\lambda^{\varepsilon}\right)\right)}_{\Delta\mathrm{U}_2^{\mathrm{b}}} \qquad (8.12)$$

$$= \quad \varepsilon\ \Delta\mathbf{U}_1^{\mathrm{b}} \quad + \quad \varepsilon^2\ \Delta\mathbf{U}_2^{\mathrm{b}}$$

Le développement asymptotique de la microrotation nodale $\phi^{n\varepsilon}$ est ici limité au premier ordre en ε; la rotation nodale s'écrit aux noeuds extrémité de chaque poutre selon

$$\phi^{O(b)\varepsilon} = \phi_0^{O_{R(b)}} + \varepsilon\phi_1^{O_{R(b)}}\ ;\ \phi^{E(b)\varepsilon} = \phi_0^{E_{R(b)}} + \varepsilon\left(\frac{\partial \phi_0}{\partial \lambda^i}\delta^{ib} + \phi_1^{E_{R(b)}}\right)$$

Le développement asymptotique des efforts et moments s'écrit selon

$$N^{\varepsilon} = E_s\eta\left[\left(\left(\varepsilon\,\Delta\mathbf{U}_1 + \varepsilon^2\,\Delta\mathbf{U}_2\right).\mathbf{e}^b\right)\right]$$

$$N^{\varepsilon} \square \left[\varepsilon\left(N_1^b\right) + \varepsilon^2\left(N_2^b\right)\right]$$

$$T_t^{\varepsilon} = E_s\eta^3\left(\mathbf{e}^{b\perp}.\left(\varepsilon\ \Delta\mathbf{U}_1^{\mathrm{b}} + \ \varepsilon^2\ \Delta\mathbf{U}_2^{\mathrm{b}}\right)\right) - \frac{1}{2}E_s\eta^3\varepsilon L^{bo}\left(\left(\phi_0^{O_{R(b)}} + \phi_0^{E_{R(b)}} + \varepsilon\left(\phi_1^{O_{R(b)}} + \phi_1^{E_{R(b)}} + \frac{\partial\phi_0}{\partial\lambda^i}\delta^{ib}\right)\right)\right)$$

$$T_t^{\varepsilon} \square\ \varepsilon T_{1t}^b + \varepsilon^2 T_{2t}^b$$

Celui des moments se formule selon

$$\mathrm{M}^{\mathrm{O(b)}\varepsilon} = -\left(\frac{1}{2}\right)\mathrm{E_s}\eta^3\varepsilon\mathrm{L}^{\mathrm{bo}}\left(\Delta\mathbf{U}^{\mathrm{b}\varepsilon}\cdot\mathbf{e}^{\mathrm{b}\perp}\right) + \mathrm{E_s}\eta^3\varepsilon^2\left(\frac{\left(\mathrm{L}^{\mathrm{bo}}\right)^2}{6}\right)\left(2\phi^{\mathrm{O(b)}\varepsilon} + \phi^{\mathrm{E(b)}\varepsilon}\right)$$

$$\square\ -\left(\frac{1}{2}\right)\mathrm{E_s}\eta^3\varepsilon\mathrm{L}^{\mathrm{bo}}\mathbf{e}^{\mathrm{b}\perp}.\left(\varepsilon\ \Delta\mathbf{U}_1^{\mathrm{b}} + \ \varepsilon^2\ \Delta\mathbf{U}_2^{\mathrm{b}}\right) + \mathrm{E_s}\eta^3\varepsilon^2\left(\frac{\left(\mathrm{L}^{\mathrm{bo}}\right)^2}{6}\right)\left(2\phi_0^{\mathrm{O_{R(b)}}} + \phi_0^{\mathrm{E_{R(b)}}} + \varepsilon\left(2\phi_1^{\mathrm{O_{R(b)}}} + \phi_1^{\mathrm{E_{R(b)}}} + \frac{\partial\phi_0}{\partial\lambda^{\mathrm{i}}}\delta^{\mathrm{ib}}\right)\right)$$

$$\square\ \varepsilon^2\mathrm{M_1}^{\mathrm{O(b)}} + \varepsilon^3\mathrm{M_2}^{\mathrm{O(b)}}$$

$$\mathrm{M}^{\mathrm{E(b)}\varepsilon} = -\left(\frac{1}{2}\right)\mathrm{E_s}\eta^3\varepsilon\mathrm{L}^{\mathrm{bo}}\left(\Delta\mathbf{U}^{\mathrm{b}\varepsilon}\cdot\mathbf{e}^{\mathrm{b}\perp}\right) + \mathrm{E_s}\eta^3\varepsilon^2\left(\frac{\left(\mathrm{L}^{\mathrm{bo}}\right)^2}{6}\right)\left(\phi^{\mathrm{O(b)}\varepsilon} + 2\phi^{\mathrm{E(b)}\varepsilon}\right)$$

$$\square\ -\left(\frac{1}{2}\right)\mathrm{E_s}\eta^3\varepsilon\mathrm{L}^{\mathrm{bo}}\mathbf{e}^{\mathrm{b}\perp}.\left(\varepsilon\ \Delta\mathbf{U}_1^{\mathrm{b}} + \ \varepsilon^2\ \Delta\mathbf{U}_2^{\mathrm{b}}\right) + \mathrm{E_s}\eta^3\varepsilon^2\left(\frac{\left(\mathrm{L}^{\mathrm{bo}}\right)^2}{6}\right)\left(\phi_0^{\mathrm{O_{R(b)}}} + 2\phi_0^{\mathrm{E_{R(b)}}} + \varepsilon\left(\phi_1^{\mathrm{O_{R(b)}}} + 2\phi_1^{\mathrm{E_{R(b)}}} + \frac{\partial\phi_0}{\partial\lambda^{\mathrm{i}}}\delta^{\mathrm{ib}}\right)\right)$$

$$\square\ \varepsilon^2\mathrm{M_1}^{\mathrm{E(b)}} + \varepsilon^3\mathrm{M_2}^{\mathrm{E(b)}}$$

L'équilibre des forces prend la forme d'une somme double ordonnées selon les puissances successives de ε selon

$$\sum_{\upsilon^i\in\square^3}\sum_{b\in B_R}\left[\begin{array}{l}
\varepsilon^2\left(\ E_s\eta\left(\Delta\mathbf{U}_1^{\mathrm{b}}\cdot\mathbf{e}^b\right)e^b + \left(E_s\eta^3\left(\Delta\mathbf{U}_1^{\mathrm{b}}.\mathbf{e}^{b\perp}\right) - \frac{1}{2}E_s\eta^{3\,bo}_{L}\left(\phi_0^{O_{R(b)}} + \phi_0^{E_{R(b)}}\right)\right)\mathbf{e}^{b\perp}\right).\frac{\partial\mathrm{v}\left(\lambda^{\varepsilon}\right)}{\partial\lambda^{\mathrm{i}}}\delta^{ib} \\
+\varepsilon^3\left(E_s\eta\left(\Delta\mathbf{U}_2^{\mathrm{b}}\cdot\mathbf{e}^b + \left(\frac{1}{2}\left(\Delta\mathbf{U}_1^{\mathrm{b}}\cdot e^b\right)\left(\Delta\mathbf{U}_1^{\mathrm{b}}\cdot\mathbf{e}^b\right)\right)\right)e^b + \left(E_s\eta^3\left(\Delta\mathbf{U}_1^{\mathrm{b}}.\mathbf{e}^{b\perp}\right) - \frac{1}{2}E_s\eta^{3\,bo}_{L}\left(\phi_1^{O_{R(b)}} + \phi_1^{E_{R(b)}} + \frac{\partial\phi_0}{\partial\lambda^i}\delta^{ib}\right)\right)e^{b\perp}\right).\frac{\partial\mathrm{v}\left(\lambda^{\varepsilon}\right)}{\partial\lambda^{\mathrm{i}}}\delta^{ib} \\
+\varepsilon^4\left(\left(\left(\Delta\mathrm{U}_1^{\mathrm{b}}\cdot\mathbf{e}^b\right)\left(\Delta\mathbf{U}_2^{\mathrm{b}}\cdot\mathbf{e}^b\right)\right)\mathbf{e}^b\right).\frac{\partial\mathrm{v}\left(\lambda^{\varepsilon}\right)}{\partial\lambda^{\mathrm{i}}}\delta^{ib} \\
+\varepsilon^5\left(\left(\frac{1}{2}\left(\Delta\mathbf{U}_2^{\mathrm{b}}\cdot\mathbf{e}^b\right)\left(\Delta\mathbf{U}_2^{\mathrm{b}}\cdot\mathbf{e}^b\right)\right)\mathbf{e}^b\right).\frac{\partial\mathrm{v}\left(\lambda^{\varepsilon}\right)}{\partial\lambda^{\mathrm{i}}}\delta^{ib}
\end{array}\right] = 0 \qquad (8.13)$$

La limite continue est ensuite obtenue à partir du résultat mathématique suivant : pour toute fonction régulière *g*, la quantité $\varepsilon^3\sum_{\upsilon^i\in\square^3} g\left(\varepsilon\upsilon^i\right)$ s'interprète comme l'intégrale de Riemann $\int_\Omega g(\lambda)d\lambda$ en 3-D quand $\varepsilon\to 0$.

Cela conduit aux équations d'auto-équilibre suivantes :

$$\int_\Omega \mathbf{S}^i.\frac{\partial\mathrm{v}\left(\lambda\right)}{\partial\lambda^{\mathrm{i}}}d\lambda = 0 \qquad (8.14)$$

Avec le vecteur contrainte $\mathbf{S}^i$ qui se décompose en une contribution du premier et du second ordre, soit $\mathbf{S}^i = \mathbf{S}_1^i + \varepsilon\mathbf{S}_2^i$, avec

$$\mathbf{S}_1^i = \sum_{b\in B_R}\left(\left(E_s\eta\left(\Delta\mathbf{U}_1^b\cdot\mathbf{e}^b\right)\mathbf{e}^b + \left(E_s\eta^3\left(\Delta\mathbf{U}_1^b.\mathbf{e}^{b\perp}\right) - \frac{1}{2}E_s\eta^3 {}^{bo}_{L}\left(\phi_0^{O_{R(b)}} + \phi_0^{E_{R(b)}}\right)\right)\mathbf{e}^{b\perp}\right)\right)\delta^{ib}$$

$$\mathbf{S}_2^i = \sum_{b\in B_R}\left(E_s\eta\left(\Delta\mathbf{U}_2^b\cdot\mathbf{e}^b + \left(\frac{1}{2}\left(\Delta\mathbf{U}_1^b\cdot\mathbf{e}^b\right)\left(\Delta\mathbf{U}_1^b\cdot\mathbf{e}^b\right)\right)\right)\mathbf{e}^b + \left(E_s\eta^3\left(\Delta\mathbf{U}_1^b.\mathbf{e}^{b\perp}\right) - \frac{1}{2}E_s\eta^3 {}^{bo}_{L}\left(\phi_1^{O_{R(b)}} + \phi_1^{E_{R(b)}} + \frac{\partial\phi_0}{\partial\lambda^i}\delta^{ib}\right)\right)\mathbf{e}^{b\perp}\right)\delta^{ib} \tag{8.15}$$

L'équilibre des mopents s'écrit selon les puissances succesives de ε selon ives (plus de détails sont donnés dans (Dos Reis et al., 2012)

$$\sum_{\upsilon^i\in\square^3}\sum_{b\in B_R}\left[\begin{array}{l}\varepsilon^3\left(E_s\eta^3\frac{\left(L^b\right)^2}{12}\left(\phi_0^{E_{R(b)}} - \phi_0^{O_{R(b)}}\right)\right).\frac{\partial w_o\left(\lambda^\varepsilon\right)}{\partial\lambda^{\mathrm{i}}}\delta^{ib} \\ +\varepsilon^4\left(E_s\eta^3\frac{\left(L^b\right)^2}{12}\left(-\phi_1^{O_{R(b)}} + \phi_1^{E_{R(b)}} + \frac{\partial\phi_0}{\partial\lambda^i}\delta^{ib}\right)\right).\frac{\partial w_o\left(\lambda^\varepsilon\right)}{\partial\lambda^{\mathrm{i}}}\delta^{ib}\end{array}\right] = 0$$

L'équation précédente peut s'écrire dans la limite $\varepsilon \to 0$ sous la forme de l'équation d'auto-équilibre en flexion

$$\int_\Omega \boldsymbol{\mu}^i.\frac{\partial \mathrm{w}(\lambda)}{\partial\lambda^{\mathrm{i}}}d\lambda = 0 \tag{8.16}$$

Le vecteur couple de contraintes incorpore les vecteurs de micro-moments également écrits sur deux ordres $\boldsymbol{\mu}^i = \varepsilon\boldsymbol{\mu}_1^i + \varepsilon^2\boldsymbol{\mu}_2^i$, chacun d'eux prenant la forme d'une somme sur les poutres de la cellule de référence

$$\boldsymbol{\mu}_1^i = \sum_{b\in B_R}\varepsilon\left(E_s\eta^3\frac{\left(L^b\right)^2}{12}\left(\phi_0^{E_{R(b)}} - \phi_0^{O_{R(b)}}\right)\right)\delta^{ib}$$

$$\boldsymbol{\mu}_2^i = \sum_{b\in B_R}\varepsilon^2\left(E_s\eta^3\frac{\left(L^b\right)^2}{12}\left(-\phi_1^{O_{R(b)}} + \phi_1^{E_{R(b)}} + \frac{\partial\phi_0}{\partial\lambda^i}\delta^{ib}\right)\right)\delta^{ib} \tag{8.17}$$

La forme générale de la loi de comportement en régime linéaire relie les contraintes et couples de contraintes homogénéisées aux déformations et micro courbures homogénéisées, formés des produits dyadiques des vecteurs contrainte et couple de contraintes avec le gradient de position $\frac{\partial\mathbf{R}}{\partial\lambda^{\mathrm{i}}}$:

$$\boldsymbol{\sigma} = \frac{1}{g}\mathbf{S}^{\mathrm{i}} \otimes \frac{\partial \mathbf{R}}{\partial \lambda^{\mathrm{i}}} = \frac{1}{g}\left(\mathbf{S}_1^{\mathrm{i}} + \varepsilon \mathbf{S}_2^{\mathrm{i}}\right) \otimes \frac{\partial \mathbf{R}}{\partial \lambda^{\mathrm{i}}} = \underbrace{\frac{1}{g}\mathbf{S}_1^{\mathrm{i}} \otimes \frac{\partial \mathbf{R}}{\partial \lambda^{\mathrm{i}}}}_{\left[\mathbf{K}^{s}\right]\{\dot{\mathrm{o}}\}} + \underbrace{\frac{1}{g}\varepsilon \mathbf{S}_2^{\mathrm{i}} \otimes \frac{\partial \mathbf{R}}{\partial \lambda^{\mathrm{i}}}}_{[\mathbf{B}]\{\chi\}}$$

$$\mathbf{m} = \frac{1}{g}\boldsymbol{\mu}^{\mathrm{i}} \otimes \frac{\partial \mathbf{R}}{\partial \lambda^{\mathrm{i}}} = \frac{1}{g}\left(\varepsilon \boldsymbol{\mu}_1^{\mathrm{i}} + \varepsilon^2 \boldsymbol{\mu}_2^{\mathrm{i}}\right) \otimes \frac{\partial \mathbf{R}}{\partial \lambda^{\mathrm{i}}} = \underbrace{\frac{1}{g}\varepsilon \boldsymbol{\mu}_1^{\mathrm{i}} \otimes \frac{\partial \mathbf{R}}{\partial \lambda^{\mathrm{i}}}}_{[\mathbf{B}]\{\dot{\mathrm{o}}\}} + \underbrace{\frac{1}{g}\varepsilon^2 \boldsymbol{\mu}_2^{\mathrm{i}} \otimes \frac{\partial \mathbf{R}}{\partial \lambda^{\mathrm{i}}}}_{\left[\mathbf{K}^{\mu}\right]\{\chi\}} \tag{8.19}$$

avec ***g*** le Jacobien de la transformation des coordonnées cartésiennes en curvilignes.

Pour des structures périodiques uniformes dotes d'une symétrie centrale, les coefficients d'élasticité sont invariant par inversion, d'où il résulte que le pseudo-tenseur B_{ijkl} s'annule ; cela implique la nullité des vecteurs μ_1^{i} et $\mathrm{S}_2^{\mathrm{i}}$, d'où la simplification importante des expressions des vecteurs contrainte et couple de contrainte :

$$\begin{aligned}\mathbf{S}^i = \mathbf{S}_1^i &= \sum_{b\in B_R}\left(\left(E_s\eta\left(\Delta\mathbf{U}_1^{\mathrm{b}}\cdot\mathbf{e}^b\right)\mathbf{e}^b + \left(E_s\eta^3\left(\Delta\mathbf{U}_1^{\mathrm{b}}.\mathbf{e}^{b\perp}\right) - \frac{1}{2}E_s\eta^3{}_L^{bo}\left(\phi_0^{O_{R(b)}} + \phi_0^{E_{R(b)}}\right)\right)\mathbf{e}^{b\perp}\right)\right)\delta^{ib} \\ &= \sum_{b\in B_R}\left(N_1^b\mathbf{e}^b + T_{1t}^b\mathbf{e}^{b\perp}\right)\delta^{ib}\end{aligned}$$

$$\begin{aligned}\boldsymbol{\mu}^{\mathrm{i}} = \boldsymbol{\mu}_2^{\mathrm{i}} &= \sum_{b\in B_R}\varepsilon^2\left(E_s\eta^3\frac{\left(L^b\right)^2}{12}\left(-\phi_1^{O_{R(b)}} + \phi_1^{E_{R(b)}} + \frac{\partial\phi_0}{\partial\lambda^i}\delta^{ib}\right)\right)\delta^{ib} \\ &= \sum_{b\in B_R}\frac{1}{2}\varepsilon^2\left(M_2^{E(b)} - M_2^{O(b)}\right)\delta^{ib}\end{aligned} \tag{8.20}$$

Les grandeurs N_1^b, T_{1t}^b et M_2^n sont respectivement l'effort normal et transverse au premier ordre et le moment au second ordre, obtenu par l'expansion des expressions (8.3) en fonction de ε. Ces expressions impliquent les variables cinématiques inconnues de déplacement et rotation aux nœuds, qui sont calculées en résolvant le problème de localisation à partir des équations d'équilibre (8.4) et (8.7).

Comme on le verra plus loin, la résolution du problème linéaire sur une configuration de treillis donnée constitue aussi bien l'étape initiale de détermination des modules effectifs dans le régime linéaire que la base d'un schéma incrémental pour calculer la réponse d'une structure de treillis dans le régime nonlinéaire.

8.4 Problème nonlinéaire

On décrit dans cette section l'impact d'une modification de la géométrie du treillis sur les propriétés effectives afin de modéliser la réponse nonlinéaire du treillis. La nonlinéarité principale est ici de nature géométrique, compte tenu des modules de flexion très faibles en regard des modules de traction des poutres du treillis. On vise ainsi à prendre en compte la variation de longueur et d'orientation des poutres.

On écrit pour chaque poutre

$$b \in \mathbf{B}, \mathbf{B}^{b_o} = \mathbf{R}^{E_R(b)} - \mathbf{R}^{O_R(b)} + \frac{\partial \mathbf{R}^o}{\partial \lambda^{jb}} \delta^{jb},\ l^{b_o} = \left\| \mathbf{B}^{b_o} \right\| \text{and } \mathbf{e}^{b_o} = \frac{\mathbf{B}^{b_o}}{l^{b_o}}$$

Pour un λ^{ε} donné (variable d'élongation, donc de déformation) et pour un macrogradient de deformation fixé $\frac{\partial \mathbf{R}^o}{\partial \lambda^j} \delta^{jb}, j = 1,2,3,$ on détermine les quantités $\mathbf{B}^{b_o}, \mathbf{e}^{b_o}, N^{b_o}, T^{b_o}, M^{b_o}, b \in B,$ afin de calculer les vecteurs contraintes et couples de contrainte S^{i_o} et μ^{i_o} respectivement. La résolution se fait pour un macrogradient de déformation imposé au niveau du continuum équivalent, soit l'application tangente $\mathbf{G}^i$, pour chaque poutre $b \in \mathbf{B}$, $\mathbf{B}^{b_o} = \mathbf{R}^{E_R(b)} - \mathbf{R}^{O_R(b)} + \mathbf{G}^i \delta^{jb}$, avec la longueur $l^b = \left\| \mathbf{B}^b \right\|$ et le vecteur unitaire directeur de la poutre $\mathbf{e}^{b_o} = \frac{\mathbf{B}^{b_o}}{l^{b_o}}$, avec N^b, T^b, M^b donnés par leurs expressions en (8.3).

En différentiant les equations d'équilibre (8.2) et (8.5), le problème incrémental induit est résolu avec la méthode de Newton-Raphson :

$$\begin{aligned} &\sum_{b \in B} \left(\delta N^{b(k)} \mathbf{e}^b + N^{b(k)} \delta \mathbf{e}^b \right).\Delta v + \sum_{b \in B} \left(N^{b(k)} \mathbf{e}^b \right).\Delta v + \\ &\sum_{b \in B} \left(\delta T_t^{b(k)} \mathbf{e}^{b\perp} + T_t^{b(k)} \delta \mathbf{e}^{b\perp} \right).\Delta v + \sum_{b \in B} \left(T_t^{b(k)} \mathbf{e}^{b\perp} \right).\Delta v = 0 \end{aligned} \tag{8.21}$$

La perturbation des équations d'équilibre des moments (8.7) s'écrit

$$\begin{aligned} &\sum_{b \in B} \left(\delta M^{E(b)(k)} \mathbf{Y}_3.\Delta \underline{w}^{E(b)} + \delta M^{O(b)(k)} \mathbf{Y}_3.\Delta \underline{w}^{O(b)} \right) + \sum_{b \in B} \delta \left(B \wedge T_t^{b(k)} \mathbf{e}^{b\perp} \right).\Delta \underline{w}^{C(b)} + \\ &\sum_{b \in B} \left(M^{E(b)(k)} \mathbf{Y}_3.\Delta \underline{w}^{E(b)} + M^{O(b)(k)} \mathbf{Y}_3.\Delta \underline{w}^{O(b)} \right) + \sum_{b \in B} \left(T_t^{b(k)} l^b \right) \mathbf{Y}_3.\Delta \underline{w}^{C(b)} = 0 \end{aligned} \tag{8.22}$$

Dans les équations d'équilibre précédents, la variation de la géométrie est prise en compte par la perturbation des longueurs et orientations des poutres, selon

$$\delta \mathbf{e}^b = \frac{1}{l^b}\left(\mathbf{C}.\mathbf{A}\right).\delta \mathbf{B} \tag{8.23}$$

$$\delta \mathbf{e}^{b\perp} = \mathbf{\Omega}_Z.\delta \mathbf{e}^b, \quad \delta \mathbf{e}^{b\perp} = \frac{1}{l^b}\mathbf{\Omega}_Z.\left(\mathbf{C}.\mathbf{A}\right).\delta \mathbf{B} \tag{8.24}$$

En introduisant l'opérateur de projection $\mathbf{A} = \left[\mathbf{I} - \mathbf{e}^b \otimes \mathbf{e}^b\right], \mathbf{C} = \left[\mathbf{I} - \frac{1}{2}\mathbf{e}^b \otimes \mathbf{e}^b\right]$, et la transformation orthogonale

$$\mathbf{\Omega}_Z\left(\mathbf{e}^b, \mathbf{e}^{b\perp}, \mathbf{Y}_3\right) = \begin{bmatrix} \cos\left(\frac{\pi}{2}\right) & -\sin\left(\frac{\pi}{2}\right) & 0 \\ \sin\left(\frac{\pi}{2}\right) & \cos\left(\frac{\pi}{2}\right) & 0 \\ 0 & 0 & 1 \end{bmatrix} \tag{8.25}$$

On en déduit la variation de la longueur de chaque poutre selon

$$\begin{aligned} \delta l^b &= \delta \mathbf{B}.\mathbf{e}^b + \mathbf{B}.\delta \mathbf{e}^b \\ &= \frac{\mathbf{B}}{l^b}.\left[\mathbf{I} + \mathbf{C}.\mathbf{A}\right].\delta \mathbf{B} \end{aligned} \tag{8.26}$$

Ces variations induisent les perturbations suivantes de l'effort normal

$$\delta N^{bo}\,\mathbf{e}^b = \frac{EA_b}{L}\begin{bmatrix} \left(\mathbf{e}^b \otimes \mathbf{e}^b\right) + \left(\frac{1}{l^b}\right)\left(\mathbf{e}^b \otimes \left(\mathbf{B} - \mathbf{B}_o\right)\right).\left(\mathbf{C}.\mathbf{P}\right) \\ -\frac{\left(B - B_o\right).\mathbf{e}^b}{\left(l^b\right)^2}\left(\left(\mathbf{e}^b \otimes \mathbf{B}\right).\left[\mathrm{I} + \mathbf{C}.\mathbf{P}\right]\right) \end{bmatrix}.\delta \mathbf{B} \tag{8.27}$$

$$N^{bo(k)}\,\delta \mathbf{e}^b = \left(\frac{N^{bo}}{l^b}\right)\mathbf{C}.\mathbf{P}.\delta \mathbf{B} \tag{8.28}$$

et de l'effort transverse

$$\delta T^{t^{bo(k)}}\mathbf{e}^{b\perp}=\left[\left(\frac{12EI_z}{(L)^3}\right)\left[\begin{array}{l}\left(\left(\mathbf{e}^{b\perp}\otimes\mathbf{e}^{b\perp}\right)+\left(\frac{1}{l^b}\right)\left(\mathbf{e}^{b\perp}\otimes\left(\mathbf{B}-\mathbf{B}_o\right)\right).\left(\boldsymbol{\Omega}_z.\mathbf{C}.\mathbf{P}\right)\right)\\ -\frac{\left(B-B_o\right).\mathbf{e}^{b\perp}}{\left(l^b\right)^2}\left(\left(\mathbf{e}^{b\perp}\otimes\mathbf{B}\right).\left[\mathrm{I}+\mathbf{C}.\mathbf{P}\right]\right)\end{array}\right]\right].\delta B$$
$$-\left[\left(\frac{2T^{t^{bo(k)}}}{\left(l^b\right)^2}\right)\left(\left(\mathbf{e}^{b\perp}\otimes\mathbf{B}\right).\left[\mathrm{I}+\mathbf{C}.\mathbf{P}\right]\right)\right]$$
$$+\left(\frac{-6EI_z}{(L)^2}\right)\left[\left(\mathbf{e}^{b\perp}\otimes\mathbf{Y}_3\right).\delta\Phi_o+\left(\mathbf{e}^{b\perp}\otimes\mathbf{Y}_3\right).\delta\Phi_e\right]$$

Avec

$$T_t^b\delta\mathbf{e}^{b\perp}=\left(\frac{T_t}{l^b}\right)\left(\boldsymbol{\Omega}_z.\mathbf{C}.\mathbf{P}\right).\delta\mathbf{B} \tag{8.29}$$

En insérant les equations (8.23-8.29) dans la relation d'équilibre (8.21), on obtient la relation suivante

$$\sum_{b\in B}\left[\begin{array}{l}\left[\begin{array}{l}\left(\frac{EA}{L}\left[\left(\mathbf{e}^b\otimes\mathbf{e}^b\right)+\left(\frac{1}{l^b}\right)\left(\mathbf{e}^b\otimes\left(\mathbf{B}-\mathbf{B}_o\right)\right).\left(\mathbf{C}.\mathbf{P}.\delta\mathbf{B}\right)-\frac{\left(\mathbf{B}-\mathbf{B}_o\right).\mathbf{e}^b}{\left(l^b\right)^2}\left(\left(\mathbf{e}^b\otimes\mathbf{B}\right).\left[\mathbf{I}+\mathbf{C}.\mathbf{P}\right]\right)\right]\right)+\\ \left(\frac{N^{bo}}{l^b}\right)\mathbf{C}.\mathbf{P}\end{array}\right]\\ \left[\left(\frac{12EI_z}{(L)^3}\right)\left[\left(\left(\mathbf{e}^{b\perp}\otimes\mathbf{e}^{b\perp}\right)+\left(\frac{1}{l^b}\right)\left(\mathbf{e}^{b\perp}\otimes\left(\mathbf{B}-\mathbf{B}_o\right)\right).\left(\boldsymbol{\Omega}_z.\mathbf{C}.\mathbf{P}\right)-\frac{\left(\mathbf{B}-\mathbf{B}_o\right).\mathbf{e}^{b\perp}}{\left(l^b\right)^2}\left(\left(\mathbf{e}^{b\perp}\otimes\mathbf{B}\right).\left[\mathbf{I}+\mathbf{C}.\mathbf{P}\right]\right)\right)\right]\right].\delta\mathbf{B}.\Delta v\\ -\left[\left(\frac{2T^{t^{bo(k)}}}{\left(l^b\right)^2}\right)\left(\left(\mathbf{e}^{b\perp}\otimes\mathbf{B}\right).\left[\mathrm{I}+\mathbf{C}.\mathbf{P}\right]\right)\right]\\ +\left(\frac{T_t}{l^b}\right)\left(\Omega_z.C.P\right)\end{array}\right] \tag{8.30}$$
$$+\sum_{b\in B}\left(\frac{-6EI_z}{(L)^2}\right)\left[\left(\mathbf{e}^{b\perp}\otimes\mathbf{Y}_3\right).\delta\Phi_o+\left(\mathbf{e}^{b\perp}\otimes\mathbf{Y}_3\right).\delta\Phi_e\right].\Delta v$$
$$+\sum_{b\in B}\left(N^{bo(k)}\mathbf{e}^b\right).\Delta v+\sum_{b\in B}\left(T_t^b\mathbf{e}^{b\perp}\right).\Delta v=0$$

De façon analogue, la perturbation de l'équilibre des moments s'écrit

$$\begin{aligned}
&\sum_{b\in B}\left(\frac{EI_z}{l^b}\right)\left[-\left(\mathbf{Y}_3\otimes\mathbf{Y}_3\right).\delta\Phi_o+\left(\mathbf{Y}_3\otimes\mathbf{Y}_3\right).\delta\Phi_e\right].\Delta w^{E(b)}+\\
&\sum_{b\in B}\left(\frac{EI_z}{l^b}\right)\left[\left(\mathbf{Y}_3\otimes\mathbf{Y}_3\right).\delta\Phi_o-\left(\mathbf{Y}_3\otimes\mathbf{Y}_3\right).\delta\Phi_e\right].\Delta w^{O(b)}+\\
&\sum_{b\in B}\left(M^{E(b)_0(k)}\mathbf{Y}_3.\Delta w^{E(b)}+M^{O(b)_0(k)}\mathbf{Y}_3.\Delta w^{O(b)}\right)+\sum_{b\in B}\left(T^{t^{bo(k)}}l^b\right)\mathbf{Y}_3.\Delta w^{C(b)}=0
\end{aligned}\tag{8.31}$$

On identifie à partir de la perturbation de l'effort normal des équations (8.27) et (8.28) les trois contributions à la matrice tangent : la rigidité linéaire, la rigidité de déplacement initiale et la contribution de la contrainte initiale, soit successivement :

$$\mathbf{K}_o=\frac{EA_b}{L}\left(\mathbf{e}^b\otimes\mathbf{e}^b\right),$$

$$\mathbf{K}_u=\frac{EA_b}{L}\left[\left(\frac{1}{l^b}\right)\left(\mathbf{e}^b\otimes\left(\mathbf{B}-\mathbf{B}_o\right)\right).\left(\mathbf{C.P}\right)-\frac{\left(\mathbf{B}-\mathbf{B}_o\right).\mathbf{e}^b}{\left(l^b\right)^2}\left(\left(\mathbf{e}^b\otimes\mathbf{B}\right).\left[\mathbf{I}+\mathbf{C.P}\right]\right)\right]$$

$$\mathbf{K}_\sigma=\left(\frac{N^{bo}}{l^b}\right)\mathbf{C.P}$$

On réécrit alors la loi de comportement sous forme matricielle selon

$$\left[\Delta v,\Delta w^{O(b)},\Delta w^{E(b)}\right]\begin{bmatrix}\left(\left[\left(\frac{EA}{L}\left[\left(\mathbf{e}^b\otimes\mathbf{e}^b\right)+\left(\frac{1}{l^b}\right)\left(\mathbf{e}^b\otimes\left(\mathbf{B}-\mathbf{B}_o\right)\right).\left(\mathbf{C}.\mathbf{P}.\delta\mathbf{B}\right)\right]\right)+\left[\left(\frac{N^{bo}}{l^b}\right)\mathbf{C}.\mathbf{P}\right]\right]+\left[\left(\frac{12EI_z}{(L)^3}\right)\left[\left(\left(\mathbf{e}^{b\perp}\otimes\mathbf{e}^{b\perp}\right)+\left(\frac{1}{l^b}\right)\left(\mathbf{e}^{b\perp}\otimes\left(\mathbf{B}-\mathbf{B}_o\right)\right).\left(\mathbf{\Omega}_z.\mathbf{C}.\mathbf{P}\right)\right)\right]\right]+\left[\left(\frac{T_t}{l^b}\right)\left(\mathbf{\Omega}_z.\mathbf{C}.\mathbf{P}\right)\right] & \left(\left(\frac{-6EI_z}{(L)^2}\right)\left(\mathbf{e}^{b\perp}\otimes\mathbf{Y}_3\right)\right) & \left(\left(\frac{-6EI_z}{(L)^2}\right)\left(\mathbf{e}^{b\perp}\otimes\mathbf{Y}_3\right)\right)\\ 0 & \left(\frac{EI_z}{l^b}\right)\left(\mathbf{Y}_3\otimes\mathbf{Y}_3\right) & -\left(\frac{EI_z}{l^b}\right)\left(\mathbf{Y}_3\otimes\mathbf{Y}_3\right)\\ 0 & -\left(\frac{EI_z}{l^b}\right)\left(\mathbf{Y}_3\otimes\mathbf{Y}_3\right) & \left(\frac{EI_z}{l^b}\right)\left(\mathbf{Y}_3\otimes\mathbf{Y}_3\right)\end{bmatrix}\begin{bmatrix}\delta\mathbf{B}\\ \delta\Phi_o\\ \delta\Phi_e\end{bmatrix}$$

$$+\left[\Delta v,\Delta w^{O(b)},\Delta w^{E(b)}\right]\begin{bmatrix}N^b\mathbf{e}^b+\left(T_t^b\mathbf{e}^{b\perp}\right)\\ \left(\frac{T^{t^{bo(k)}}l^b}{2}\right)\mathbf{Y}_3+M^O\mathbf{Y}_3\\ \left(\frac{T^{t^{bo(k)}}l^b}{2}\right)\mathbf{Y}_3+M^E\mathbf{Y}_3\end{bmatrix}=0$$

Les equations (8.30) et (8.31) fournissent le problème perturbé à résoudre avec une méthode itérative de Newton-Raphson, qui a une solution à une translation et une rotation rigides près ; il faut fixer un nœud au moins afin d'éviter que la matrice tangente devienne singulière.

La solution du problème de localisation à l'échelle de la cellule de référence porte sur les variables de position $\mathbf{B}^{b(k+1)}=\mathbf{B}^{b(k)}+\delta\mathbf{B}^{b(k)}$ du système d'équations (8.30) et (8.31); sa solution associée au problème d'homogénéisation fournit la loi de comportement nonlinéaire du milieu continu équivalent.

Nous avons négligé la partie nonlinéaire de la déformation dans l'expression des variables statiques ; on peut également négliger la rigidité de déplacement initiale compte tenu de la méthode de Lagrangian actualisé qui est employée.

L'algorithme qui actualise les variables lors du changement de configuration du réseau de poutres est décrit dans ce qui suit.

---

1. Initialisation : pour chaque poutre, longueur, et vecteur directeur. Vecteur position $\mathbf{x} = \mathbf{R}(\lambda^1, \lambda^2, \lambda^3)$

2. Transformation des expressions $\left(\frac{\partial \mathbf{U}}{\partial \lambda_i}\right)_{(\mathrm{Y}_1,\mathrm{Y}_2,\mathrm{Y}_3)} \mapsto \left(\frac{\partial \mathbf{U}}{\partial \lambda_i}\right)_{(\mathrm{e}_x,\mathrm{e}_y,\mathrm{e}_z)}$ and $\left(\frac{\partial \phi}{\partial \lambda_i}\right)_{(\mathrm{Y}_1,\mathrm{Y}_2,\mathrm{Y}_3)} \mapsto \left(\frac{\partial \phi}{\partial \lambda_i}\right)_{(\mathrm{e}_x,\mathrm{e}_y,\mathrm{e}_z)}$.

3. Pour chaque poutre $b \in \mathbf{B}_R$, definer la topologie initiale en terme de :

(a) Noeud origine et extrémité $O=O_R(b),\ E=E_R(b)$.

(b) Exprime déplacement relative entre les nœuds d'extrémité: $\Delta \mathbf{U}_1^b = \mathbf{u}_1^E - \mathbf{u}_1^O + \frac{\partial \mathbf{U}}{\partial \lambda^i}\delta^i$, rigidité de traction et de flexion $k_l = \frac{A^b E_s^b}{L^b}$ et $k_f = \frac{12 E_s^b I_z^b}{\left(L^b\right)^3}$

(c) Efforts au premier ordre : $N = k_l\left(\mathbf{e}^b.\left(\Delta \mathbf{U}_1^b\right)\right), T_t = k_f\left(\mathbf{e}^{b\perp}.\left(\Delta \mathbf{U}_1^b\right) - \frac{L^b}{2}\left(\mathbf{Y}_3\left(\phi_0^O + \phi_0^E\right)\right)\right)$.

(d) Moments au premier ordre :

$$M_1^O = k_f\frac{L^b}{12}\left(6\mathbf{Y}_3.\left(\Delta \mathbf{U}_1^b\right) + L^b\left(\mathbf{e}^{b\perp}.\left((4+\Phi_z)\phi_0^O + (2-\Phi_z)\phi_0^E\right)\right)\right), M_1^E = k_f\frac{L^b}{12}\left(6\mathbf{Y}_3.\left(\Delta \mathbf{U}_1^b\right) + L^b\left(\mathbf{e}^{b\perp}.\left((2-\Phi_z)\phi_0^O + (4+\Phi_z)\phi_0^E\right)\right)\right),$$

4. Calcul des inconnues cinématiques u_1^n et ϕ_0^n à partir des équations (8.4) et (8.7).

5. Identifie la microrotation homogénéisée.

6. Expression des forces et moments au second ordre selon :

(a) $\Delta \mathbf{U}_2^b = \mathbf{u}_2^E - \mathbf{u}_2^O$ (b) $N_2 = k_l\left(\mathbf{e}^b\left(\Delta \mathbf{U}_2^b\right)\right), T_{t2} = k_f\left(\mathbf{e}^{b\perp}.\left(\Delta \mathbf{U}_2^b\right) - \frac{L^b}{2}\left(\mathbf{Y}_3\left(\phi_1^O + \phi_1^E + \frac{\partial \phi}{\partial \lambda^i}\delta^i\right)\right)\right),$.

(c) $$M_{2y}^O = k_f\frac{L^b}{12}\left(6\mathbf{e}_z.\left(\Delta \mathbf{U}_2^b\right) + L^b\left(\mathbf{e}_y.\left((4+\Phi_z)\phi_1^O + (2-\Phi_z)\phi_1^E + (2-\Phi_z)\frac{\partial \phi}{\partial \lambda^i}\delta^i\right)\right)\right), M_2^E = k_f\frac{L^b}{12}\left(6\mathbf{e}_z.\left(\Delta \mathbf{U}_2^b\right) + L^b\left(\mathbf{e}_y.\left((2-\Phi_z)\phi_1^O + (4+\Phi_z)\phi_1^E + (4+\Phi_z)\frac{\partial \phi}{\partial \lambda^i}\delta^i\right)\right)\right),$$

Résoudre pour les variables u_2^n et ϕ_1^n à partir de (8.4) et (8.7).

7. ConstructIon des vecteurs contrainte et couple de contrainte $\mathbf{s}^{\mathrm{i}} = \sum_{b \in B_R}\left(F_{x1}^b\mathbf{e}^b + F_{y1}^b\mathbf{e}^{b\perp}\right)\delta^i$ et

$\mu^{\mathrm{i}} = \sum_{b \in B_R}\left(\frac{1}{2}\left(M_2^{E(b)} - M_2^{O(b)}\right)\mathbf{Y}_3\right)\delta^i$

8. Construction du tenseur des contraintes $\boldsymbol{\sigma} = \frac{1}{g}\mathbf{s}^{\mathrm{i}} \otimes \frac{\partial \mathbf{R}}{\partial \lambda^{\mathrm{i}}}$ et des couples de contraintes $\mathbf{m} = \frac{1}{g}\boldsymbol{\mu}^{\mathrm{i}} \otimes \frac{\partial \mathbf{R}}{\partial \lambda^{\mathrm{i}}}$,

tels que $\begin{Bmatrix} \boldsymbol{\sigma} \\ \mathbf{m} \end{Bmatrix} = \begin{bmatrix} \mathbf{K}^{s} & 0 \\ 0 & \mathbf{K}^{\mu} \end{bmatrix} \begin{Bmatrix} \grave{\mathrm{o}} \\ \chi \end{Bmatrix}$.

9. Calcul des proprieties mécaniques effectives $E_x^*, E_y^*, \nu_{xy}^*, G_{xy}^*, K_{55}^{\mu}, K_{66}^{\mu}$ pour cet incrément de chargement.

10. Calcul de l'incrément de contrainte en fonction de l'incrément de deformation.

11. Solution du problème inverse qui fournit le déplacement macroscopique consistent avec le chargement imposé.

11. Actualisation de la géométrie du treillis et nouveau calcul élastique sur cette nouvelle géométrie pour un nouvel incrément de chargement

---

8.5 Exemples de calcul de tissages en régime nonlinéaire

On analyse dans ce qui suit les réponses nonlinéaires de tissages monocouches d'armures toile et serge, pour des chargements uniaxial, biaxial et en cisaillement simple.

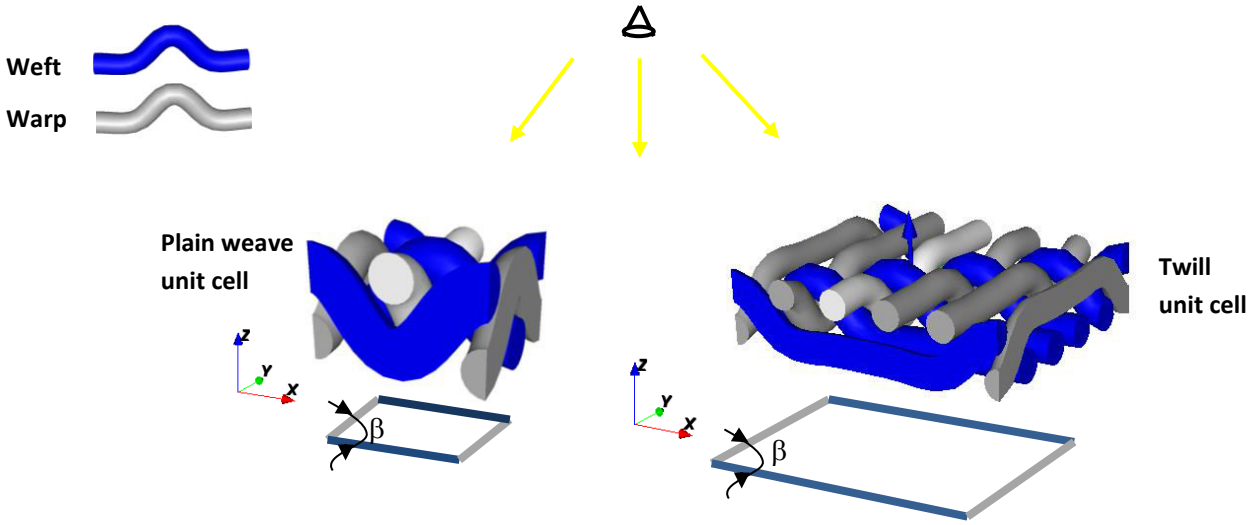

Figure 8.2 Cellule élémentaire représentative des armures toile et sergé.

Le tenseur gradient de la transformation s'exprime selon

$$F = \begin{bmatrix} 1+\varepsilon_{xx} & \gamma_{xy} \\ \gamma_{yx} & 1+\varepsilon_{yy} \end{bmatrix}$$

Il est appliqué sur la cellule élémentaire représentative du tissage avec des conditions limites de périodicité, avec ε et γ les déformations normale et de cisaillement respectivement. Les indices "x" et "y" désignent les directions des axes du système de coordonnées global. On rappelle qu'une partie seulement du gradient total de la transformation est contrôlé dans un chargement spécifique (il subsiste des composantes non spécifiées), de sorte qu'il faut déterminer un problème aux limites pour les composantes inconnues de la déformation non prescrite.

8.5.1 Comportement mécanique nonlinéaire de tissages d'armure toile

Les parameters géométriques et mécaniques de la cellule représentatives de l'armure toile du tissage sont donnés dans le tableau 3.6.

Tableau 8.1 : données d'entrée géométrique et mécanique pour un tissage d'armure toile équilibré

Armure toile					
Tissage équilibré	Chaine / Trame	*E*= 1889 MPa	*L* = 0.618 mm	ϑ =40°	*d* = 0.27 mm

Un état de traction uniaxiale tend à aligner les fils dans la direction de sollicitation en les désondulant, tandis que les ondulations du fil transverse augmentent. L'ondulation est définie par le paramètre C_r construit à partir des longueurs curvilignes du fil au sein de l'armure l_{yarn} au sein d'une période et de la longueur de périodicité l_{RUC}

$$C_{r_{11,22}}(\%) = \frac{l_{\text{yarn}_{1,2}} - l_{\text{RUC}_{1,2}}}{l_{\text{RUC}_{1,2}}}$$

Les indices "11" et "22" désignent les directions des axes du système de coordonnées globale (directions chaine et trame respectivement). Les tenseurs de déformation prescrits dans le cas de sollicitations uniaxiales dans les directions chaine et trame sont successivement

$$F_f = \begin{bmatrix} 1+\varepsilon_{xx} & \gamma = 0 \\ \gamma_{yx} = 0 & 1+\varepsilon_{yy} \end{bmatrix} = \begin{bmatrix} 1+\varepsilon_{xx} & 0 \\ 0 & \textit{indéter}\min\textit{ée} \end{bmatrix}$$

et

$$F_p = \begin{bmatrix} 1+\varepsilon_{xx} & \gamma_{xy} \\ \gamma_{yx} & 1+\varepsilon_{yy} \end{bmatrix} = \begin{bmatrix} \textit{indéter}\min\textit{ée} & 0 \\ 0 & 1+\varepsilon_{yy} \end{bmatrix}$$

On observe sur la réponse en chaine (fig. 8.3) une différence importante entre la réponse nonlinéaire et la réponse dans une situation linéaire (fictive), cette dernière étant obtenue en prolongeant la pente intiale à la réponse nonlinéaire. La rigidification progressive observée en fonction de la déformation est due à l'alignement des fils sollicités dans la direction de traction.

- **Traction uniaxiale sens chaine :**

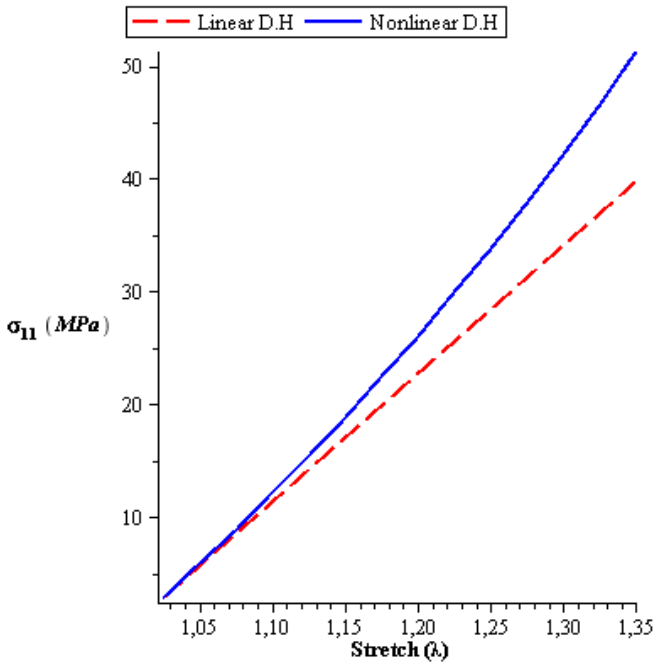

Figure 8.3. Mesure de contrainte de Cauchy en fonction de la déformation pour un essai virtuel de traction uniaxial sens chaine.

On représente ensuite les modules de traction $E_{h_{11}}, E_{h_{22}}$, les taux d'ondulation dans les deux directions $\%C_{r_1}, \%C_{r_2}$ et les coefficients de liage (contraction) $\nu_{h_{12}}, \nu_{h_{21}}$ dans la figure 8.4 (a, b, c) respectivement. Le module de traction effectif dans la direction de traction x augmente avec l'élongation, ce qui traduit un effet de durcissement du aux effets d'alignement des fils ; le module de traction dans la direction transverse y décroit en raison de l'augmentation d'ondulation concomitante. La contraction $\nu_{h_{21}}$ et le taux d'ondulation $\%C_{r_{11}}$ diminuent de façon monotone avec l'élongation ; le coefficient de Poisson $\nu_{h_{12}}$ croit jusqu'à un maximum (la contraction transverse est maximale pour $\lambda = 1.15$) puis décroit ensuite. Le taux d'ondulation $\%C_{r_{22}}$ augmente dans le sens trame en raison de la contraction dans cette direction.

(a)

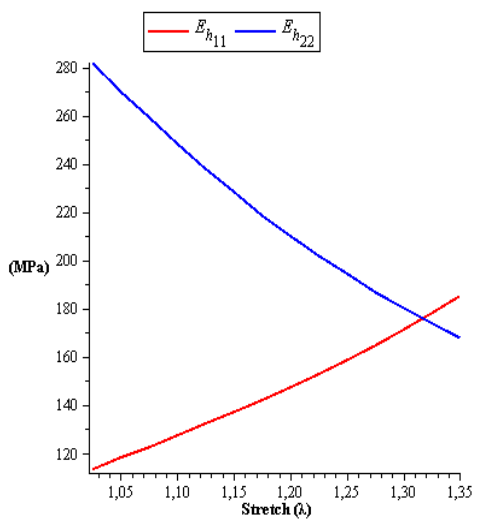

(b)

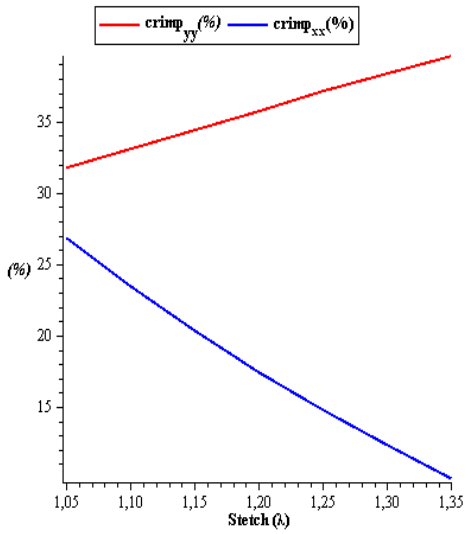

(c)

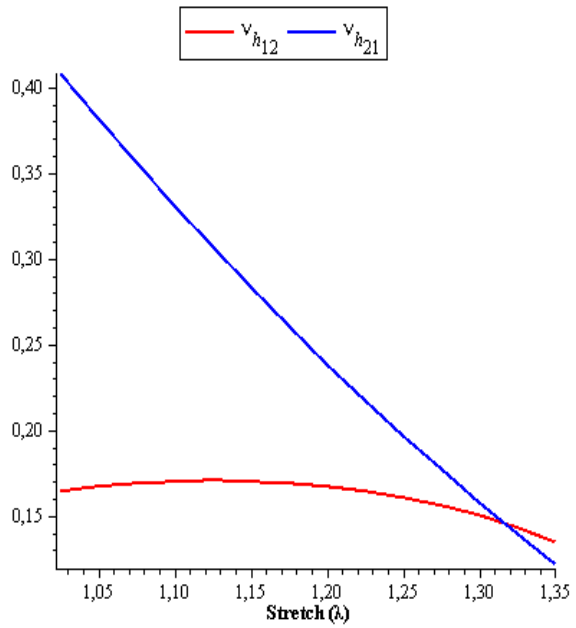

Figure 8.4: propriétés effectives simulées. (a) Modules de traction $E_{h_{11}}, E_{h_{22}}$ (b) Taux d'ondulation $\%C_{r_{11}}, \%C_{r_{22}}$. (c) Coefficients de contraction $\nu_{h_{12}}, \nu_{h_{21}}$ en fonction de la dilatation dans la direction x.

- **Traction uniaxiale sens trame**

On représente de la même façon l'évolution de la composante du tenseur de contrainte de Cauchy ainsi que celle des propriétés mécaniques effectives en fonction de la dilatation sens trame (direction y).

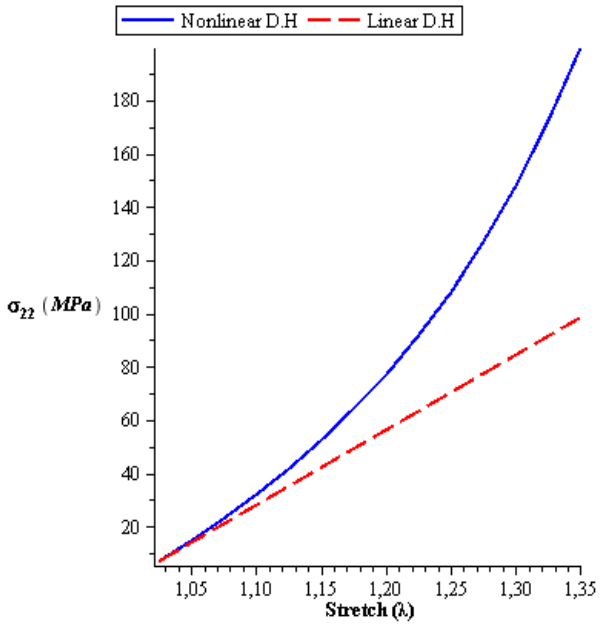

Figure 8.5. Composante selon y du tenseur de contrainte Cauchy en fonction de la dilatation dans la même direction

La différence entre les réponses linéaire et nonlinéaire (fig. 8.5) est de 102% pour un taux de déformation de 35% ; ceci est conforme à l'augmentation observée du module de traction $E_{h_{22}}$ dans la direction y et celle de la contraction $\nu_{h_{21}}$, figure 8.6 (a, c). A l'opposé, le module de traction dans la direction x, $E_{h_{11}}$ ainsi que la contraction $\nu_{h_{12}}$ diminuent. Le taux d'ondulation décroit dans la direction de sollicitation et augmente dans la direction transverse (figure 8.6 (b)).

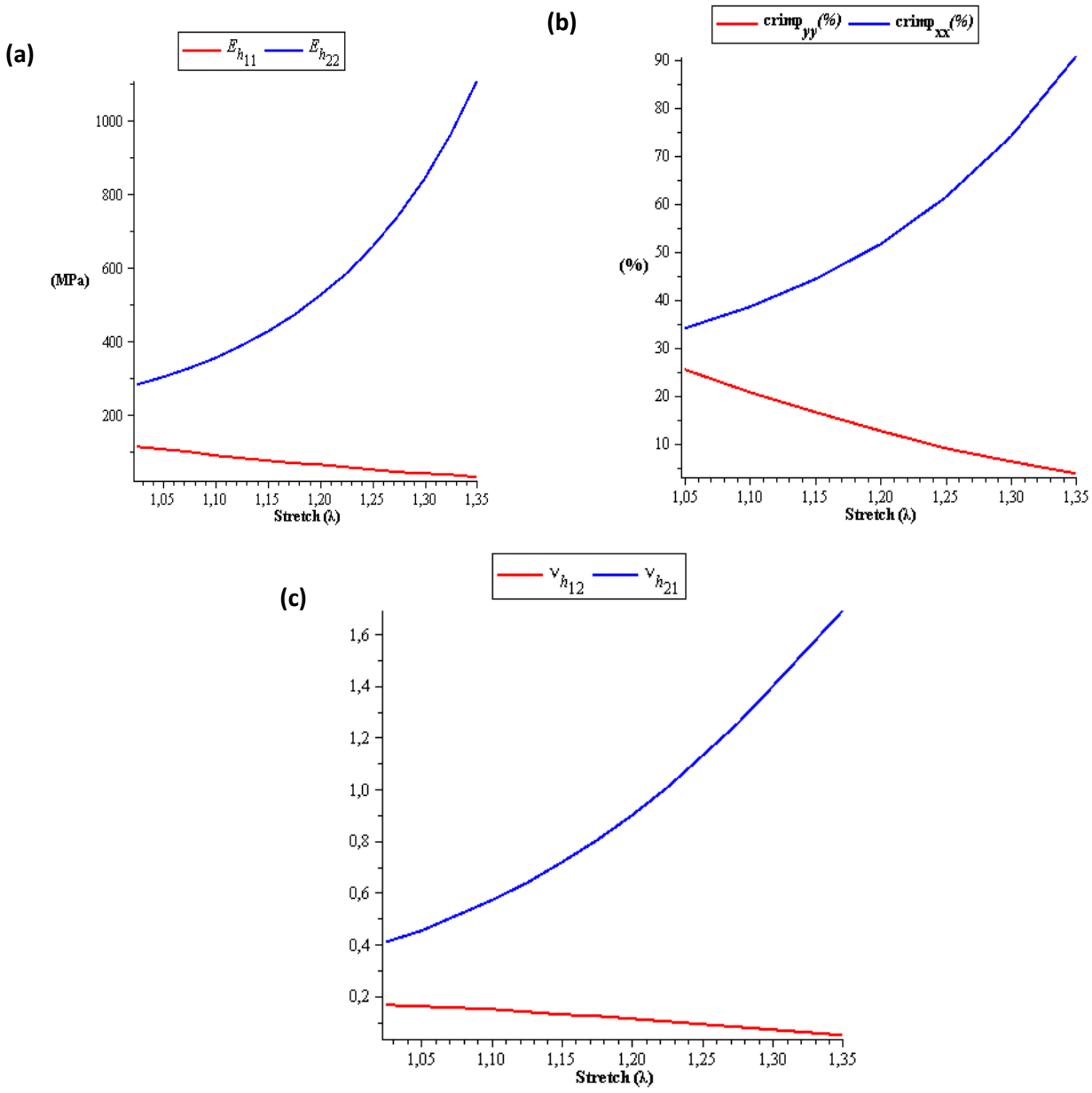

Figure 8.6. Propriétés effectives en function de la dilatation sens trame. (a) Modules de traction $E_{h_{11}}, E_{h_{22}}$ (b) Taux d'ondulation $\%C_{r_{11}}, \%C_{r_{22}}$. (c) Coefficients de Poisson $\nu_{h_{12}}, \nu_{h_{21}}$ en fonction de la dilatation dans la direction y.

- **Traction biaxiale**

Les simulations de traction biaxiale sont contrôlées par le rapport entre les deux déformations (sens chaine et trame), le paramètre scalaire

$$k = \frac{\varepsilon_2}{\varepsilon_1}$$

avec ε_1 la déformation imposée en chaine et ε_2 la déformation imposée sens trame. Le tenseur gradient de transformation prend la forme suivante

$$F = \begin{bmatrix} 1+\varepsilon_{xx} & \gamma_{xy}=0 \\ \gamma_{yx}=0 & 1+\varepsilon_{yy} \end{bmatrix}$$

La figure 8.7 (a,b) montre les évolutions du tenseur de Cauchy dans les directions x et y pour différentes valeurs du rapport de biaxialité, soit $k \in \{1,2,3\}$. Une réponse quasi linéaire est obtenue dans toutes les configurations de chargement ; le cas uniaxial (k=0) est construit de telle sorte qu'aucune contraction ne se produise dans la direction transverse.

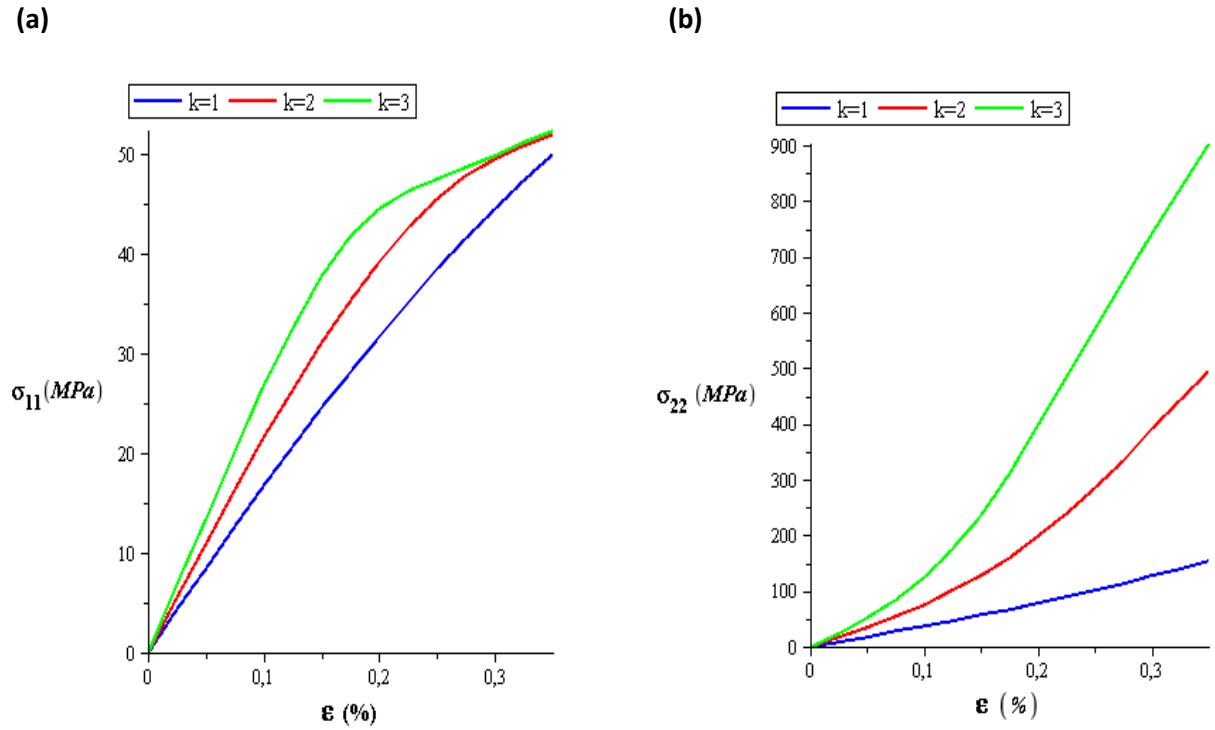

Fig. 8.7 Contrainte de Cauchy (a) direction x et (b) direction y en fonction de la déformation pour un tissage déséquilibré pour différentes valeurs du rapport de biaxialité.

On observe un durcissement de la réponse pour des rapports de biaxialité croissants.

▪ Réponse en flexion du tissage d'armure toile équilibré

La réponse en flexion de structures peut être calculée dans le régime nonlinéaire sur la base de la partie flexionnelle de la réponse micropolaire en grandes transformations, en mettant à profit le schéma incrémental décrit précédemment. Cette démarche est mise en œuvre pour le tissage monocouche d'armure toile aux fins d'illustration ; on rappelle auparavant les équations de la flexion pure des poutres.

On considère une poutre de longueur initiale L_o (non déformée) en figure3.20 (gauche); on suppose connu le lieu de la position de la section droite où $\rho\theta = L_o$, avec ρ le rayon de courbure et θ l'angle de flexion, comme étant l'axe neutre de la poutre: il s'agit du lieu où la longueur de la fibre déformée est identique à la longueur initiale de la configuration non déformée.

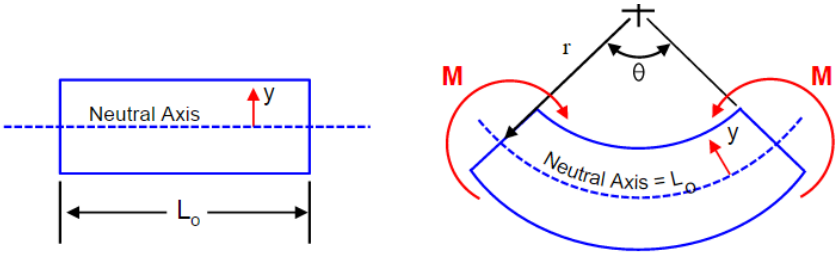

Figure 8.8 Flexion pure d'un élément de poutre et axe neutre

Soit y la distance d'un point matériel à l'axe neutre ; le rayon de courbure pour tout y est $(\rho - y)$ et la longueur finale de la fibre correspondante vaut

$$L = (\rho - y)\theta$$

La deformation de flexion est définie selon

$$\varepsilon = \frac{L - L_o}{L_o} = \frac{(\rho - y)\theta - \rho\theta}{\rho\theta}$$

$$\varepsilon = -\frac{y}{\rho} \qquad (8.32)$$

L'expression (8.32) montre que la deformation s'annule sur l'axe neutre (en $y = 0$), et varie linéairement en fonction de y. Pour des poutres épaisses, y prend des valeurs élevées, mais reste

petit pour des poutres élancées ; ceci explique que des poutres épaisses aient des rigidité en flexion plus importantes que des poutres élancées. Pour des angles θ , la courbure vaut $\kappa = \frac{1}{\rho}$.

La déformation de flexion s'exprime en fonction de la courbure selon

$$\varepsilon = \kappa y \tag{8.33}$$

L'angle d'ondulation du tissage est choisi en fonction de l'épaisseur h de l'armure dans le modèle ; on considère ici des angles faibles, soit $\theta_f \in \{5^\circ, 2^\circ\}$ (figure 8.9), comme le montre la figure 8.9 (a, b), et des déformations de flexion appliquées jusque 20%. Il en résulte alors selon (8.33) la courbure $\kappa = \varepsilon / h$; la hauteur de la cellule se calcule selon $h = L\sin(\theta_f)$. Le module de flexion effectif dépend a priori du rapport de l'épaisseur effective, h, à la longueur de la cellule élémentaire, paramètre $2L\cos\theta_f$, de telle sorte que $h/L = \tan\theta_f / 2 \cong \theta_f / 2$, compte tenu des faibles valeurs de l'angle. Cette analyse, bien que sommaire, explique les faibles effets de nonlinéarités attendus en flexion.

La figure 8.10 montre que la réponse nonlinéaire est plus souple que la réponse linéaire extrapolée, ce qui s'explique par le fait que la traction qui se développe lors de la flexion diminue l'ondulation initiale (une coque résistant par sa forme, elle devient a contrario plus souple lorsque l'épaisseur effective diminue). La flexion est donnée par la relation entre la composante du tenseur de couples de contraintes m_{xy} en fonction de la composante correspondante de la microcourbure κ_{xy} selon

$$m_{xy} = k_{33}\,\kappa_{xy}$$

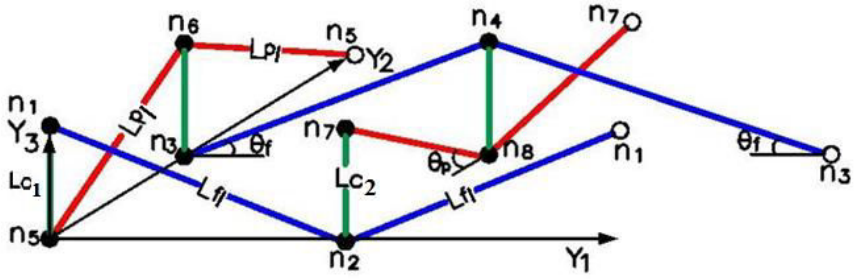

Fig. 8.9 A 3D lattice model of balanced plain weave.

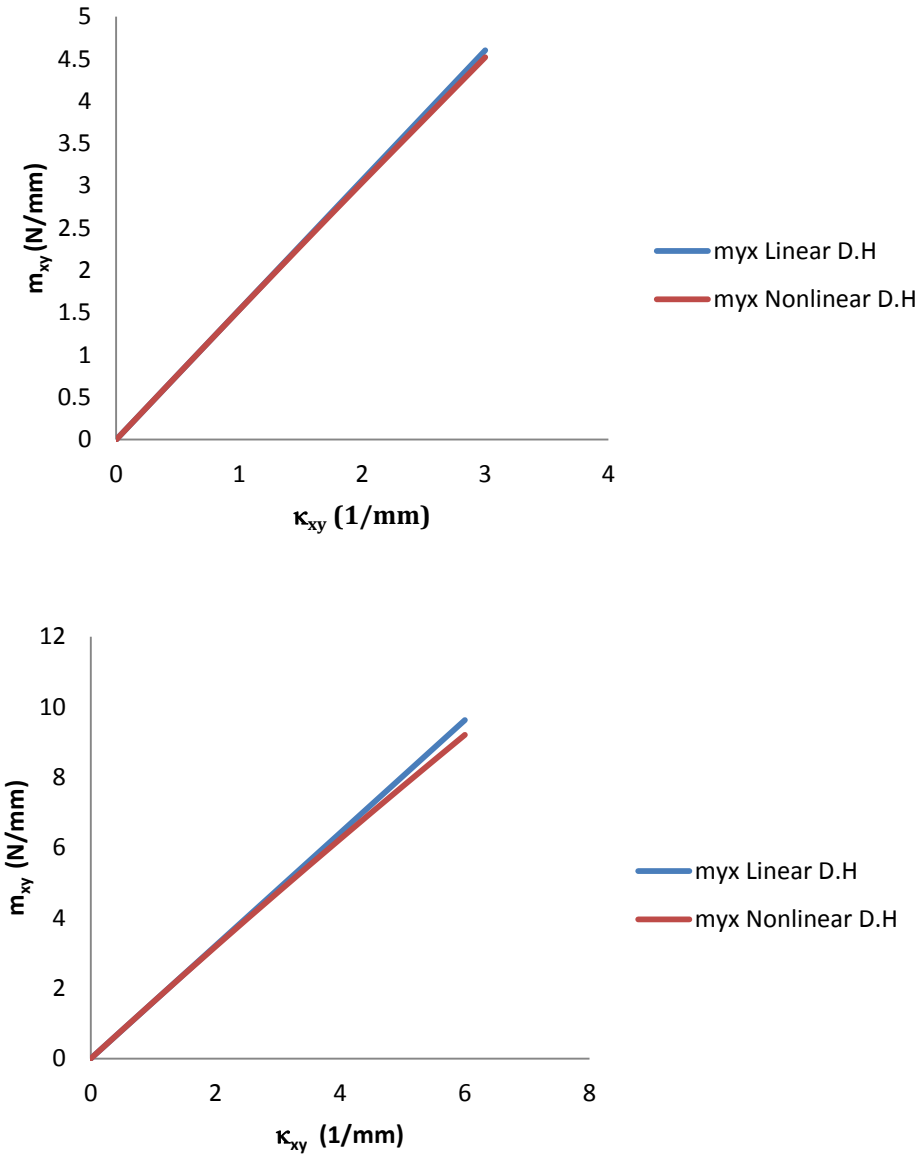

Figure 8.10. Evolution du couple de contraintes en function de la microcourbure pour les réponses nonlinéaire et linéaire extrapolée. (a) $\theta_f = 5^\circ$ (b) $\theta_f = 2^\circ$.

L'adoucissement observe correspond à une diminution du module de flexion homogénéisé k_{33} en fonction de la courbure matérielle. La longueur caractéristique en flexion est déterminée en fonction des rigidités effectives, selon :

$$l_c = \sqrt{K_{55}^{\mu} \Big/ 2\left(K_{33}^{s} + K_{34}^{s}\right)}$$

longueur qui décroit en function de la microcourbure, figure 8.11(a,b).

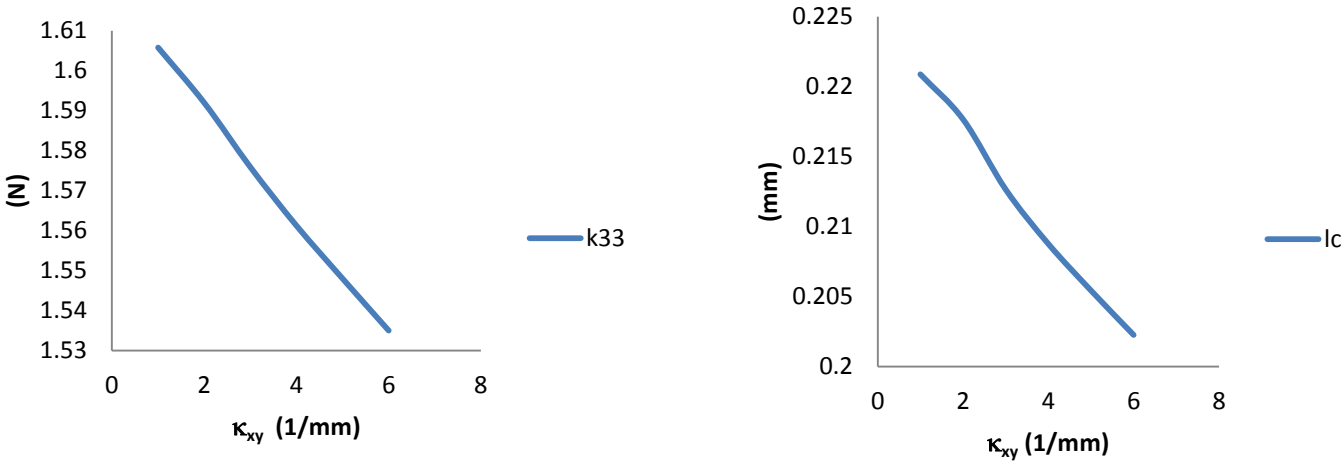

Figure 8.11 (a) Evolution du module micropolaire effectif K_{33}^{μ} en fonction de la courbure matérielle (b) Evolution de la longueur caractéristique en fonction de la microcourbure

8.6 Validation des réponses homogénéisées par des analyses éléments finis

On compare les réponses homogénéisées avec des résultats de simulation par éléments finis (ABAQUS), pour les trois chargements considérés précédemment ; on restreint ici la validation aux chargements uniaxial et équibiaxial. Les fils chaine et trame sont maillés par des éléments à 8 nœuds hexaèdre de type C3D8); le maillage de la cellule représentative du tissage toile équilibré comporte 14,804 éléments. Afin de prendre en compte le glissement relatif entre les fils, le contact avec frottement est pris en compte dans une approche de type maitre / esclave. Le comportement tangentiel des surfaces en contact dans le contexte du frottement de Coulomb est défini par une méthode de pénalité ; le coefficient de frottement est choisi 0.05, selon des données de (Peng and Cao, 2002). On applique sur le VER le tenseur gradient de transformation

$$\mathbf{F} = \begin{bmatrix} 1+\varepsilon_{xx} & \gamma_{xy} \\ \gamma_{yx} & 1+\varepsilon_{yy} \end{bmatrix}$$

en contrôlant les déplacements des quatre nœuds de la cellule élémentaire, dotée de conditions limites de périodicité. Les composantes $\varepsilon_{xx}, \varepsilon_{yy}, \gamma_{xy}$ sont les composantes normales et de cisaillement respectivement. Les réponses uniaxiale et équibiaxiale (fig. 8.12 et fig. 8.13) obtenues par homogénéisation sont en très bon accord avec les analyses EF, avec des écarts

respectifs de 1.41% et de 15 % (Fig. 8.13). Nous avons préféré l'élément de type C3D8 à l'élément C3D4, ce dernier faisant montre de performances plutôt faibles dans la littérature.

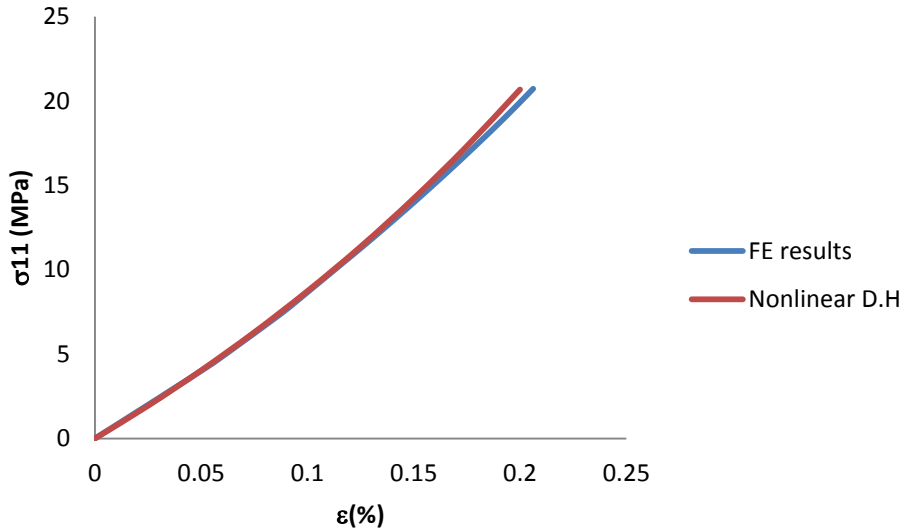

Fig. 8.12. Comparaison de la réponse uniaxiale en traction selon x pour le tissage d'armure toile équilibré obtenue par homogénéisation et par EF (ABAQUS).

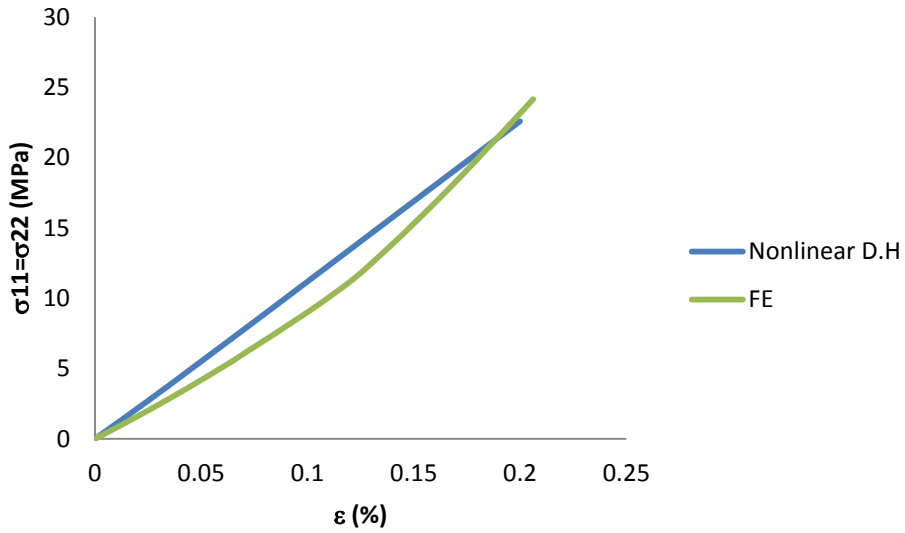

Fig. 8.13 Comparaison de la réponse équibiaxiale en traction selon x pour le tissage d'armure toile équilibré obtenue par homogénéisation et par EF (ABAQUS).

Les distributions des champs de déplacement et de contrainte pour les deux chargements sont représentées sur les Fig. 8.14 et Fig. 8.15. L'écart obtenu de 13% pour le test équibiaxial est lié selon nous à la présence de gradients internes des champs de déformation et de contrainte, ce qui

plaide pour une extension du modèle aux gradients d'ordre supérieur du déplacement (modèle du second gradient), qui sera développé dans l'avenir.

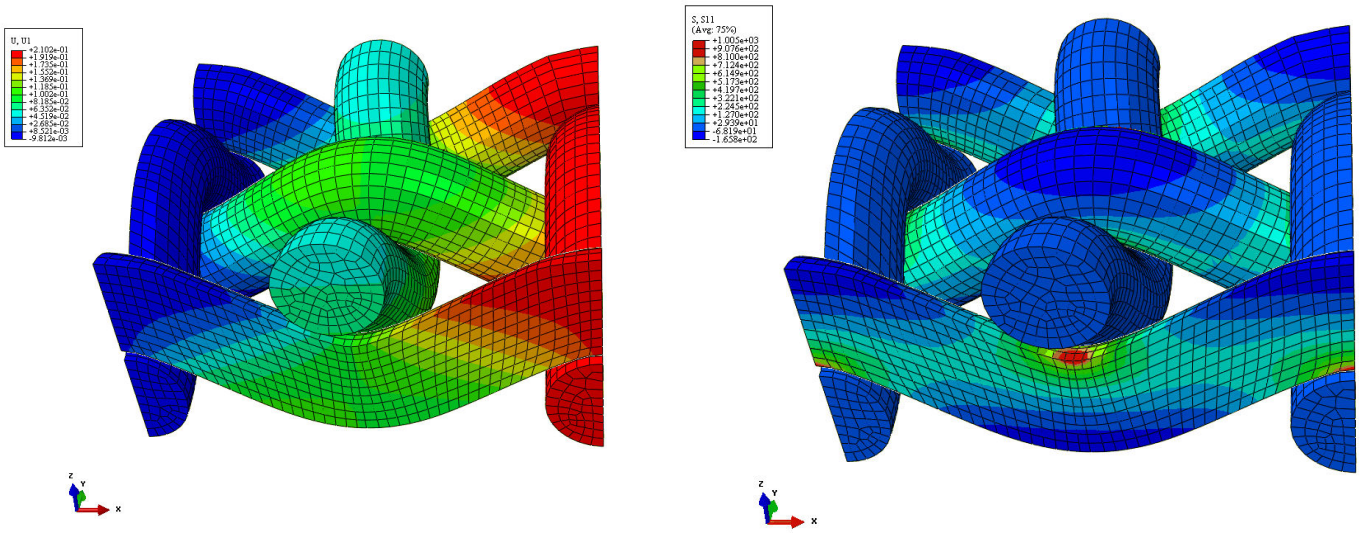

Fig. 8.14. Distribution des champs de déplacement (gauche) et contrainte (droite) pour le tissage monocouche d'armure toile soumis à une traction uniaxiale

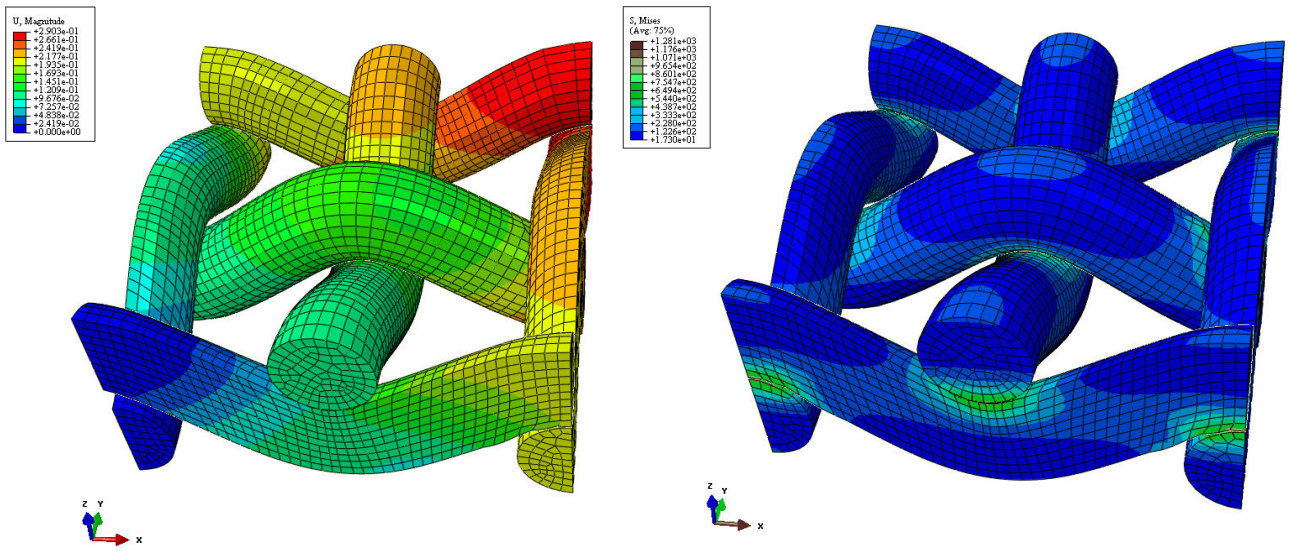

Fig. 8.15. Distribution des champs de déplacement (gauche) et contrainte (droite) pour le tissage monocouche d'armure toile soumis à une traction équibiaxiale

8.7 Identification d'une densité d'énergie hyperélastique

En vertu de son caractère prédictif, l'homogénéisation discrète asymptotique est mise à profit pour calibrer un modèle de comportement effectif hyperélastique ; cette démarche est mise en œuvre pour le tissage d'armure toile. On s'appuie sur une expression polynomiale de la densité d'énergie, qui s'exprime en fonction des dilatations principales λ_1, λ_2 et de l'angle de cisaillement θ, selon

$$\bar{W} = \sum_{\alpha=0}^{m} \frac{1}{\alpha+2} a_\alpha \left(\lambda_1^{\alpha+2} - 1\right) + \sum_{\beta=0}^{n} \frac{1}{\beta+2} b_\beta \left(\lambda_2^{\beta+2} - 1\right) + \sum_{\gamma=0}^{p} \frac{1}{\gamma+1} c_\gamma \cos^{\gamma+1}\theta + k_{r1}\lambda_1\lambda_2 + k_{r2}\left(\lambda_1\lambda_2\right)^2$$

- **Traction uniaxiale**

Un polynôme de degré trois est utilisé pour interpoler la courbe de réponse $S_{ii} - \lambda_i$ calculée par l'homogénéisation discrète. Les paramètres matériau de la loi de comportement, soit $a_\alpha, b_\beta, c_\gamma, k_{r1}, k_{r2}$, sont identifiés en minimisant l'écart quadratique entre la réponse prédite par l'homogénéisation discrète pour uen combinaison de tests virtuels en traction uniaxiale, cisaillement simple et traction biaxiale et celle obtenue par le modèle hyperélastique :

$$\underset{a_\alpha, b_\beta, c_\gamma, k_{r1}, k_{r2}}{\text{Min}} S^e\left(a_\alpha, b_\beta, c_\gamma, k_{r1}, k_{r2}\right) := \left\{ \left\| \mathbf{S}_{11}^{DH} - \mathbf{S}_{11} \right\|^2 + \left\| \mathbf{S}_{22}^{DH} - \mathbf{S}_{22} \right\|^2 + \left\| \mathbf{S}_{12}^{DH} - \mathbf{S}_{12} \right\|^2 \right\}^{1/2}$$

Les coefficients k_{r1}, k_{r2} sont nécessaires afin d'introduire une dépendance des deux composantes S_{11}, S_{22} en fonction des deux dilatations principales. Le second tenseur de Piola-Kirchoff est obtenu selon

$$\mathbf{S} = 2\frac{\partial \bar{W}}{\partial \mathbf{C}} = 2\left[\frac{\partial \bar{W}}{\partial \lambda_1}\frac{\partial \lambda_1}{\partial \mathbf{C}} + \frac{\partial \bar{W}}{\partial \lambda_2}\frac{\partial \lambda_2}{\partial \mathbf{C}} + \frac{\partial \bar{W}}{\partial \cos\theta}\frac{\partial \cos\theta}{\partial \mathbf{C}} \right]$$

Table 8.2: Jeu de paramètres de la densité d'énergie hyperélastique.

a_1 [MPa]	a_2 [MPa]	a_3 [MPa]	b_1 [MPa]	b_2 [MPa]	b_3 [MPa]	k_{r1} [MPa]	k_{r2} [MPa]	c_1 [MPa]	c_2 [MPa]	c_3 [MPa]
-7.73	-211.3	153.6	-106.5	-164.1	151.2	94.25	-14.39	4.83	10.514	3.521

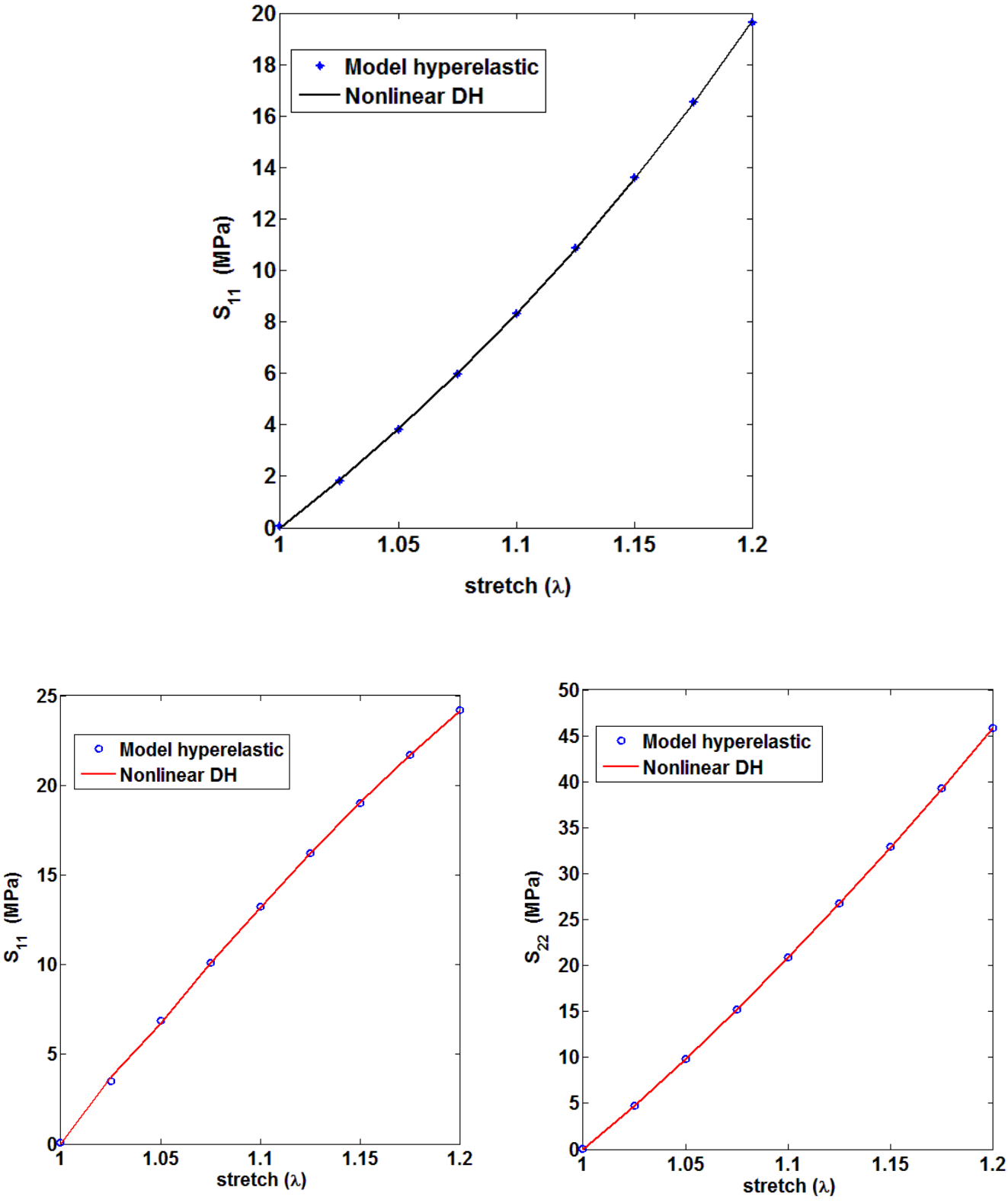

Fig. 8. 16. Evolution des composantes normales S_{11} et S_{22} du second tenseur de Piola-Kirchhoff en fonction des dilatations principales par l'homogénéisation et le modèle hyperélastique

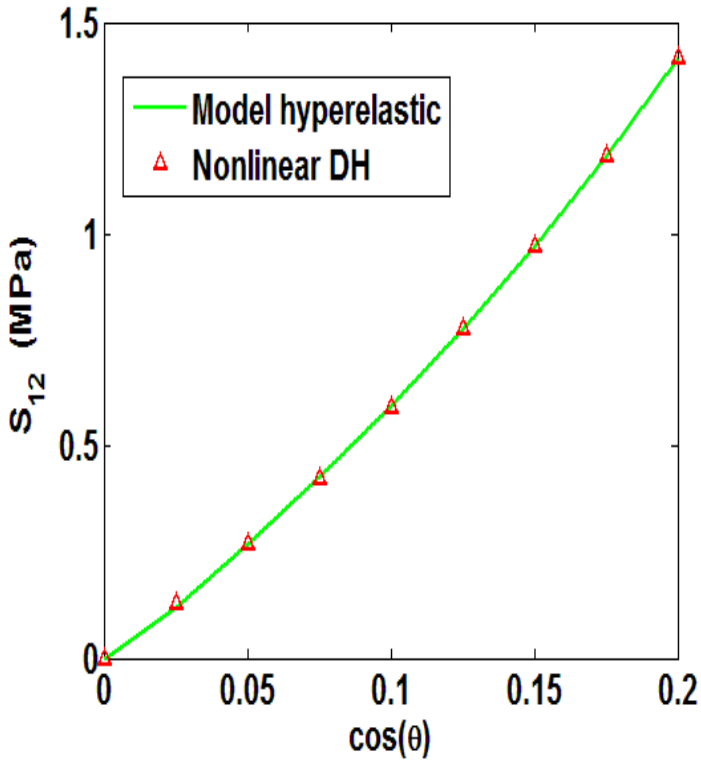

Fig. 8.17. Evolution de la composante de cisaillement du second tenseur de Piola-Kirchhoff S_{12} par l'homogénéisation et le modèle hyperélastique

Il est possible d'exprimer de façon alternative la densité d'énergie hyperélastiques en fonction des trois invariants de la déformation

$$I_1 + I_2 = \lambda_1 + \lambda_2, \quad I_1 I_2 = \lambda_1 \lambda_2, \quad I_{12} = \cos^2 \theta$$

ce qui permet de revenir à une formulation plus intrinsèque selon

$$\hat{W}(I_1, I_2, I_{12}) = W^{\text{stretch}}(I_1, I_2) + W^{\text{shear}}(I_{12})$$

En séparant les effets d'extension pure des effets de cisaillement.

Cette expression de la densité d'énergie ne prend pas en compte la présence éventuelle d'une matrice additionnelle, qui doit alors être ajoutée à $\hat{W}(I_1, I_2, I_{12})$.

8.8 Conclusion

L'homogénéisation discrète permet une étude systématique de la réponse nonlinéaire de réseaux de poutres quasi périodiques pour différents modes de déformation de la structure. Elle fournit le comportement anisotrope évolutif en fonction des déformations imposées. Une difficulté de la méthode est le contrôle des conditions limites en déformation, qui nécessite de calculer les déformations non prescrites à partie des modules effectifs actualisés (sur la nouvelle géométrie calculée). La méthode est très efficace et versatile, car elle permet de traiter tout type de structure 2D ou 3D. Le caractère prédictif permet d'identifier une densité d'énergie d'un milieu hyperélastique équivalent ; ceci permet ensuite de réaliser des calculs de structure de façon plus efficace. Les développements futurs porteront principalement sur la simulation de structures 3D (interlocks épais).

8.9 Références bibliographiques

Assidi, M., Ben Boubaker, B., Ganghoffer, J.F., 2011. Equivalent properties of monolayer fabric from mesoscopic modelling strategies. Int. J. Solids Struct. 48, 2920–2930.

Aimene Y., Hagege B., Sidoroff F., Salle E., Boisse P., 2008. "Hyperelastic approch for composite reinforcing forming simulations" ESAFORM 2008 International Journal of Material Forming, Springer Paris, Vol.1 pp. 811-814.

Aimene Y., Badel P., Vidal-Sallé E. Boisse P., 2008. "Analyse of textile composite reinforcement deformation using hyperelastic and hypoelastic constitutive laws", 11th Euromech-Mecamat conference: Mechanics of microstructured solids: cellular materials, fibre reinforced solids and soft tissues. Torino, Italie.

Belytschko T, Liu WK and Moran B 2000b Nonlinear Finite Elements for Continua and Structures.Wiley, Chichester, UK

Ben Boubaker, B., Haussy, B., Ganghoffer, J.F., 2007a. Consideration of the yarn-yarn interactions in meso/macro discrete model of the fabric. Part I: Single yarn behavior, Mechanics Research Comminucations 34, 359-370.

Bonet, J., & Wood, R. D., 1997. Nonlinear continuum mechanics for finite element analysis. Cambridge: Cambridge University Press.

Caillerie, D., Mourad, A., Raoult, A., 2006. Discrete homogenization in graphene sheet

modeling. J. Elast. 84, 33–68.

Charalambakis, N., 2010. Homogenization techniques and micromechanics Asurvey and perspectives. Appl.Mech.Rev.63(3),1–10.

Dos Reis, F., Ganghoffer, J.F., 2012. Construction of micropolar continua from the asymptotic homogenization of beam lattices . Computers and Structures 112–113 (2012) 354–363.

Goda, I., Assidi, M., Ganghoffer, J.F., 2013. Equivalent mechanical properties of textile monolayers from discrete asymptotic homogenization. International Journal of the Mechanics and Physics of Solids; 61(12):2537–2565.

Hohe, J., Becker, W., Effective mechanical behavior of hyperelastic honeycombs and two dimensional model foams at finite strain, International Journal of Mechanical Sciences, 45, 891‑913, 2003.

Janus-Michalska, M., Pęcherski, R. P., Macroscopic properties of open-cell foams based on micromechanical modeling, Technische Mechanik, Band 23, Heft 2-4, 221‑231, 2003.

Janus-Michalska, J., Effective models describing elastic behavior of cellular materials, Archives of Metallurgy and Materials, 50, 595‑608, 2005.

Janus-Michalska, J., Hyperelastic behavior of cellular structures based on micromechanical modeling at small strain, Arch. Mech., 63, 1, pp. 3‑23, Warszawa 2011.

Klaus-Jürgen Bathe, Saïd Bolourchi. Large Displacement Analysis of three-dimensional Beam Structures. International Journal for Numerical Methods in Engineering. VOL. 14, 961-986 (1979).

Mourad, A., 2003. Description topologique de l'architecture fibreuse et modélisation mécanique du myocarde. Ph.D. thesis, I.N.P.L. Grenoble.

Pradel F, Sab K. Homogenization of discrete media, 1998. J Phys IV France 1998;08:P317–24.

Pindera, M-J, Khatam, H., Drago, A.S., Bansal, Y.,2009. Micromechanics of spatially uniform heterogeneous media: A critical reviewand emerging approaches. Compos. Struct. 40, 349–378.

Realff, M.L., 1992. Mechanical properties of fabrics woven from yarns produced by different spinning technologies. Ph.D. Thesis, Massachusetts Institute of Technology.

Raoult, A., Caillerie, D., Mourad, A., 2008. Elastic lattices: equilibrium, invariant laws and homogenization. Ann. Univ. Ferrara 54, 297–318.

Realff, M.L., Boyce, M.C., Backer, S., 1997. A micromechanical model of the tensile behavior of woven fabric. Text. Res. J. 67, 445–459.

Shahkarami, A., Vaziri, R., 2007. A continuum shell finite element model for impact simulation of woven fabrics. Int. J. Imp. Eng. 34, 104–119.

Warren WE, Byskov E. Three-fold symmetry restrictions on two-dimensional micropolar material. Eur J Mech A/Solid 2002;21:779–92.

Wang, Y., Cuitino, A. M., Three-dimensional nonlinear open cell foams with large deformations, journals of the Mechanics and Physics of Solids, 48, 961–988, 2000.

Xue, P., Peng, X., Cao, J., 2003. A non-orthogonal constitutive model for characterizing woven composites. Compos. A 34, 183–193.

Xue, P., Cao, J. Chen, J., 2005. Integrated micro/macro-mechanical model of woven fabric composites under large deformation. Compos. Struct. 70, 69-80.

Modèles de comportement non linéaire des matériaux architecturés par des méthodes d'homogénéisation discrètes en grandes déformations. Application à des biomembranes et des textiles

Ce travail porte sur le développement de modèles micromécaniques pour le calcul de la réponse homogénéisée de matériaux architecturés, en particulier des matériaux se présentant sous forme de treillis répétitifs. Les matériaux architecturés et micro-architecturés couvrent un domaine très large de de propriétés mécaniques, selon la connectivité nodale, la disposition géométrique des éléments structuraux, leurs propriétés mécaniques, et l'existence d'une possible hiérarchie structurale. L'objectif principal de la thèse est la prise en compte des nonlinéarités géométriques résultant des évolutions importantes de la géométrie initiale du treillis, causée par une rigidité de flexion des éléments structuraux faible en regard de leur rigidité en extension. La méthode dite d'homogénéisation discrète est développée pour prendre en compte les non linéarités géométriques pour des treillis quais périodiques; des schémas incrémentaux sont construits qui reposent sur la résolution incrémentale et séquentielle des problèmes de localisation - homogénéisation posés sur une cellule de base identifiée, soumise à un chargement contrôlé en déformation. Le milieu continu effectif obtenu est en général un milieu micropolaire anisotrope, dont les propriétés effectives reflètent la disposition des éléments structuraux et leurs propriétés mécaniques. La réponse non affine des treillis conduit à des effets de taille qui sont pris en compte soit par un enrichissement de la cinématique par des variables de microrotation ou par la prise en compte des seconds gradients du déplacement. La construction de milieux effectifs du second gradient est faite dans un formalisme de petites perturbations. Il est montré que ces deux types de milieu effectif sont complémentaires en raison de l'analogie existant lors de la construction théorique des réponses homogénéisées, et par le fait qu'ils fournissent des longueurs internes en extension, flexion et torsion. Des applications à des structures tissées et des membranes biologiques décrites comme des réseaux de filaments quais-périodiques ont été faites. Les réponses homogénéisées obtenues sont validées par des comparaisons avec des simulations par éléments finis réalisées sur un volume élémentaire représentatif de la structure. Les schémas d'homogénéisation ont été implémentés dans un code de calcul dédié, alimenté par un fichier de données d'entrée de la géométrie du treillis et de ses propriétés mécaniques. Les modèles micromécaniques développés laissent envisager du fait de leur caractère prédictif la conception de nouveaux matériaux architecturés permettant d'élargir les frontières de l'espace 'matériaux-propriétés'.

Mots-clés : renforts tissés, analyse mésoscopique, Homogénéisation, second gradient, propriétés mécaniques, modelés micropolaires

Nonlinear constitutive models for lattice materials by discrete homogenization methods at large strains. Application to biomembranes and textiles

The present thesis deals with the development of micromechanical schemes for the computation of the homogenized response of architectured materials, focusing on periodical lattice materials. Architectured and micro-architectured materials cover a wide range of mechanical properties according to the nodal connectivity, geometrical arrangement of the structural elements, their moduli, and a possible structural hierarchy. The principal objective of the thesis is the consideration of geometrical nonlinearities accounting for the large changes of the initial lattice geometry, due to the small bending stiffness of the structural elements, in comparison to their tensile rigidity.

The so-called discrete homogenization method is extended to the geometrically nonlinear setting for periodical lattices; incremental schemes are constructed based on a staggered localization-homogenization computation of the lattice response over a repetitive unit cell submitted to a controlled deformation loading. The obtained effective medium is a micropolar anisotropic continuum, the effective properties of which accounting for the geometrical arrangement of the structural elements within the lattice and their mechanical properties.

The non affine response of the lattice leads to possible size effects which can be captured by an enrichment of the classical Cauchy continuum either by adding rotational degrees of freedom as for the micropolar effective continuum, or by considering second order gradients of the displacement field. Both strategies are followed in this work, the construction of second order grade continua by discrete homogenization being done in a small perturbations framework. We show that both strategies for the enrichment of the effective continuum are complementary due to the existing analogy in the construction of the micropolar and second order grade continua by homogenization. The combination of both schemes further delivers tension, bending and torsion internal lengths, which reflect the lattice topology and the mechanical properties of its structural elements. Applications to textiles and biological membranes described as quasi periodical networks of filaments are considered. The computed effective response is validated by comparison with FE simulations performed over a representative unit cell of the lattice. The homogenization schemes have been implemented in a dedicated code written in combined symbolic and numerical language, and using as an input the lattice geometry and microstructural mechanical properties. The developed predictive micromechanical schemes offer a design tool to conceive new architectured materials to expand the boundaries of the 'material-property' space.

Keywords: lattices, membranes, anisotropy, discrete homogenization, structural computations, hyperelasticity, micropolar continuum, second order continua, higher order tensile and flexural moduli, internal length